

Structural Integrity 8

Series Editors: José A. F. O. Correia · Abílio M. P. De Jesus

Emmanuel E. Gdoutos *Editor*

# Proceedings of the Second International Conference on Theoretical, Applied and Experimental Mechanics

 Springer

# Structural Integrity

Volume 8

## Series Editors

José A. F. O. Correia, Faculty of Engineering, University of Porto, Porto, Portugal  
Abílio M. P. De Jesus, Faculty of Engineering, University of Porto, Porto, Portugal

## Advisory Editors

Majid Reza Ayatollahi, School of Mechanical Engineering, Iran University of Science and Technology, Tehran, Iran

Filippo Berto, Department of Mechanical and Industrial Engineering, Faculty of Engineering, Norwegian University of Science and Technology, Trondheim, Norway

Alfonso Fernández-Canteli, Faculty of Engineering, University of Oviedo, Gijón, Spain

Matthew Hebdon, Virginia State University, Virginia Tech, Blacksburg, VA, USA

Andrei Kotousov, School of Mechanical Engineering, University of Adelaide, Adelaide, SA, Australia

Grzegorz Lesiuk, Faculty of Mechanical Engineering, Wrocław University of Science and Technology, Wrocław, Poland

Yukitaka Murakami, Faculty of Engineering, Kyushu University, Higashiku, Fukuoka, Japan

Hermes Carvalho, Department of Structural Engineering, Federal University of Minas Gerais, Belo Horizonte, Minas Gerais, Brazil

Shun-Peng Zhu, School of Mechatronics Engineering, University of Electronic Science and Technology of China, Chengdu, Sichuan, China

The *Structural Integrity* book series is a high level academic and professional series publishing research on all areas of Structural Integrity. It promotes and expedites the dissemination of new research results and tutorial views in the structural integrity field.

The Series publishes research monographs, professional books, handbooks, edited volumes and textbooks with worldwide distribution to engineers, researchers, educators, professionals and libraries.

Topics of interested include but are not limited to:

- Structural integrity
- Structural durability
- Degradation and conservation of materials and structures
- Dynamic and seismic structural analysis
- Fatigue and fracture of materials and structures
- Risk analysis and safety of materials and structural mechanics
- Fracture Mechanics
- Damage mechanics
- Analytical and numerical simulation of materials and structures
- Computational mechanics
- Structural design methodology
- Experimental methods applied to structural integrity
- Multiaxial fatigue and complex loading effects of materials and structures
- Fatigue corrosion analysis
- Scale effects in the fatigue analysis of materials and structures
- Fatigue structural integrity
- Structural integrity in railway and highway systems
- Sustainable structural design
- Structural loads characterization
- Structural health monitoring
- Adhesives connections integrity
- Rock and soil structural integrity

Springer and the Series Editors welcome book ideas from authors. Potential authors who wish to submit a book proposal should contact Dr. Mayra Castro, Senior Editor, Springer (Heidelberg), e-mail: [mayra.castro@springer.com](mailto:mayra.castro@springer.com)

More information about this series at <http://www.springer.com/series/15775>

Emmanuel E. Gdoutos  
Editor

# Proceedings of the Second International Conference on Theoretical, Applied and Experimental Mechanics

 Springer

*Editor*

Emmanuel E. Gdoutos  
Office of Theoretical  
and Applied Mechanics  
Academy of Athens  
Athens, Greece

ISSN 2522-560X

Structural Integrity

ISBN 978-3-030-21893-5

<https://doi.org/10.1007/978-3-030-21894-2>

ISSN 2522-5618 (electronic)

ISBN 978-3-030-21894-2 (eBook)

© Springer Nature Switzerland AG 2019

This work is subject to copyright. All rights are reserved by the Publisher, whether the whole or part of the material is concerned, specifically the rights of translation, reprinting, reuse of illustrations, recitation, broadcasting, reproduction on microfilms or in any other physical way, and transmission or information storage and retrieval, electronic adaptation, computer software, or by similar or dissimilar methodology now known or hereafter developed.

The use of general descriptive names, registered names, trademarks, service marks, etc. in this publication does not imply, even in the absence of a specific statement, that such names are exempt from the relevant protective laws and regulations and therefore free for general use.

The publisher, the authors and the editors are safe to assume that the advice and information in this book are believed to be true and accurate at the date of publication. Neither the publisher nor the authors or the editors give a warranty, expressed or implied, with respect to the material contained herein or for any errors or omissions that may have been made. The publisher remains neutral with regard to jurisdictional claims in published maps and institutional affiliations.

This Springer imprint is published by the registered company Springer Nature Switzerland AG  
The registered company address is: Gewerbestrasse 11, 6330 Cham, Switzerland

# Preface

This volume contains 50 six-page papers and 16 two-page abstracts presented at the “Second International Conference on Theoretical, Applied and Experimental Mechanics” (ICTAEM\_2) held in Corfu, Greece, June 23–26, 2019. The papers/abstracts are arranged in three topics and one special symposium with 35 and 31 papers/abstracts, respectively. The papers of the tracks have been contributed from open call, while the papers of the symposium have been solicited by Prof. Roman Kushnir to whom I am greatly indebted.

ICTAEM\_2 will focus in all aspects of theoretical, applied, and experimental mechanics including biomechanics, composite materials, computational mechanics, constitutive modeling of materials, dynamics, elasticity, experimental mechanics, fracture, mechanical properties of materials, micromechanics, nanomechanics, plasticity, stress analysis, structures, and wave propagation.

The attendees of ICTAEM\_2 will have the opportunity to interact with the most outstanding world leaders and get acquainted with the latest developments in the area of mechanics. ICTAEM\_2 will be a forum of university, industry, and government interaction and exchange of ideas in an area of utmost scientific and technological importance.

I am sure that besides the superb technical program, the attendees of ICTAEM\_2 will enjoy the majestic town of Corfu with its unique beaches and scenic beauty, many areas of historical interest and archeological importance, the delicious local cuisine, and the traditional Greek hospitality.

More than a hundred participants attended ICTAEM\_2. The participants of ICTAEM\_2 came from 18 countries. Roughly speaking 18% came from Europe, 17% from the Far East, 5% from the Americas, and 60% from other countries. I am happy and proud to have welcomed in Corfu well-known experts who came to discuss problems related to the analysis and prevention of failure in structures. The tranquility and peacefulness of this small town provided an ideal environment for a group of scientists and engineers to gather and interact on a personal basis. Presentation of technical papers alone is not enough for effective scientific communication. It is the healthy exchange of ideas and scientific knowledge, formal and informal discussions, together with the plenary and contributed papers that make a

fruitful and successful meeting. Informal discussions, personal acquaintance, and friendship play an important role.

I am proud to have hosted ICTAEM\_2 in the beautiful town of Corfu and I am pleased to have welcomed colleagues, friends, old and new acquaintances.

I very sincerely thank the authors who have contributed to this volume, the symposium/sessions organizers for their hard work and dedication, and the referees who reviewed the quality of the submitted contributions. The tireless effort of the members of the Organizing Committee as well as of other numerous individuals, and people behind the scenes is appreciated. I am deeply indebted to Dr. Stavros Shiaeles for his hard work and dedication in the organization of the conference. Finally, a special word of thanks goes to Dr. Maria Shiaeles for her continuous collaboration and support.

Athens, Greece  
March 2019

Emmanuel E. Gdoutos

# Contents

## Part I Materials: Properties, Manufacturing, Modelling

<b>Role of Compactness on Hardness and Reduced Modulus of Vaterite Determined with Nanoindentation</b> . . . . .	3
Radek Ševčík and Vladimír Hrbek	
<b>Approximate Mode Shape for Damped Structures</b> . . . . .	9
Wasiu A. Oke, Oluseyi A. Adeyemi, Kazeem A. Bello, and Adewale Adegbenjo	
<b>Deformation Behavior of Ferrite/Austenite Duplex Stainless Steel in Hot Compression Processing</b> . . . . .	15
Hezong Li, Suxia Huang, Qiusheng Li, Xiaopin An, Facai Ren, and Simon S. Wang	
<b>Material Strength Degradation Experiment and Statistical Expression Under Cyclic Loading</b> . . . . .	21
Liyang Xie, Hongyi Ma, and Guoliang Xu	
<b>Study of Effect of Phase Separation on Pores Orientation of Electrospun Nanofibre</b> . . . . .	27
S. O. Alayande, E. O. Dare, J. N. Edokpayi, O. A. Adeyemi, Adewale Adegbenjo, and T. A. M. Msagati	
<b>Deformation Model of <math>[\pm 45]_s</math> Cross-Ply Fiber Reinforced Plastics Under Tension</b> . . . . .	29
V. N. Paimushin, R. A. Kayumov, D. V. Tarlakovskii, and S. A. Kholmogorov	
<b>Segregation Resistance, Stiffness and Toughness of CNT Nanomodified Self Compacted Concrete</b> . . . . .	36
Myrsini Maglogianni, Panagiotis A. Danoglidis, Maria G. Falara, and Maria S. Konsta-Gdoutos	



<b>High Temperature Creep Properties of Cast Cobalt-Based Superalloys: A Comparison</b> .....	39
Marie Kvapilova, Vaclav Sklenicka, Petr Kral, and Jiri Dvorak	
<b>Sub-grain Plastic Strain Localization in CoCrNi Medium Entropy Alloy at Cryogenic Temperatures</b> .....	45
Wael Abuzaid and Luca Patriarca	
<b>Effects of Treatment on Microstructure and Deformation Behavior of Dissimilar Welded Joint Between Single Crystal and Polycrystalline Superalloy</b> .....	48
Yang Liu, Lei Wang, Xiu Song, Taosha Liang, and Guo Hua	
<b>Improved Post-crack Energy Absorption Capability of Cementitious Composites Reinforced with CNTs and PPs</b> .....	54
Panagiotis A. Danoglidis, Maria S. Konsta-Gdoutos, and Emmanuel E. Gdoutos	
<b>Molecular Dynamics Investigation of Dislocation Slip in Pure Metals and Alloys</b> .....	59
Alexander E. Mayer and Vasilij S. Krasnikov	
<b>Development and Validation of 3D DIC Based Residual Stress Testing Method</b> .....	65
Tomasz Brynk	
<b>Monogenic Filtering Based Automatic Defect Detection from a Single Fringe Pattern</b> .....	71
Rishikesh Kulkarni and Pramod Rastogi	
<b>Enhanced Post-crack Load Carrying Capacity of Nano and Micro Scale Carbon Fiber Reinforced Mortars</b> .....	75
Maria G. Falara, Maria S. Konsta-Gdoutos, and Emmanuel E. Gdoutos	
<b>Two-Point Bending Stress Determination of Ultra-Thin Glass Plates</b> ...	80
Po-Chi Sung, Wei-Chung Wang, and Yu-Wei Kuo	
<b>Investigation of Grating Collimation of Coherent Gradient Sensing Technique</b> .....	84
Po-Yu Chen and Wei-Chung Wang	
<b>The Mechanism of Grain Boundary in Hydrogen Embrittlement of Inconel 690 Alloy</b> .....	87
Lei Wang, Yang Liu, Cheng He, and Xiu Song	
<b>Determining Object Motion by Digital Image Correlation Method with Camera-Array Composed Cameras of Normal Frame Rate</b> .....	94
Chi-Hung Hwang, Tzu-Yu Kuo, and Wei-Chung Wang	

**Part II Fracture**

**Configurational Stability of a Crack Propagating in Mixed-Mode I + II + III** ..... 101  
 Jean-Baptiste Leblond, Alain Karma, Laurent Ponson, and Aditya Vasudevan

**Limiting Equilibrium of Interfacial Shear Cracks at the Corner Point of the Media-Separating Boundary of the Piece-Homogeneous Isotropic Plane** ..... 106  
 V. M. Nazarenko and A. L. Kipnis

**An Approach to Analysis of Fracture of Semi-bounded Body Under Compressing Along Interfacial Near-Surface Crack** ..... 110  
 V. L. Bogdanov and A. L. Kipnis

**Fracture of Composite Material at Compression Along Near-Surface Crack** ..... 114  
 Mykhailo Dovzhyk, Vyacheslav Bogdanov, and Vladimir Nazarenko

**Statistical Distribution of Pores in Solid and Molten Metals at Dynamic Tensile Fracture** ..... 119  
 Polina N. Mayer and Alexander E. Mayer

**Fatigue and Deformation of Light Magnesium Alloys** ..... 126  
 Daolun Chen

**Part III Miscellaneous (Biomechanics, Computational Mechanics, Dynamics, Nanomechanics, Plasticity, Structures, Wave Propagation)**

**Research on Contact Pressure of Friction Pair Based on Finite Element Method** ..... 135  
 Changlu Wang, Long Wu, Zichun Xu, Yaping Zhang, Hao Gao, and Yanzhong Wang

**Noise and Vibration Analysis of a Flux Switching Motor (FSM) with Segmental Rotor** ..... 142  
 Hedduri Sanket, M. N. Kishore, and Nagesh Suresh

**Quenching of Non-stationary Wave Due to Structural Transformation of Material** ..... 148  
 D. A. Indeitsev, B. N. Semenov, D. Yu. Skubov, and D. S. Vavilov

**Algorithms for System Identification** ..... 154  
 Todor Zhelyazov, Rajesh Ruphakety, and Simon Olaffson

**Mechanics of Earthquake Source Processes: Insights from Numerical Modeling** ..... 156  
 Nadia Lapusta

<b>Strategies to Improve Convergence After Degeneration of the Initial Finite Element Mesh</b> .....	159
Todor Zhelyazov	
<b>Parametric Study of Simulated Randomly Rough Surfaces Used in Contact Mechanics</b> .....	162
Rafael Schouwenaars, Miguel Ángel Ramírez, Carlos Gabriel Figueroa, Víctor Hugo Jacobo, and Armando Ortiz Prado	
<b>Simplified Analysis of the Early Stage Self-loosening of a Shear-Loaded Bolted Joint</b> .....	169
Vincent Rafik, Alain Daidié, Bertrand Combes, and Clément Chirol	
<b>Wave Scattering by Arrays of Shear Bands</b> .....	176
Davide Bigoni, Domenico Capuani, and Diana Giarola	
<b>Dynamic Failure of Granular Slopes: Due to Unidirectional Stress Transfer or Multi-dimensional Wave Propagation?</b> .....	182
Koji Uenishi and Tsukasa Goji	
<b>Part IV Symposium on: “Dynamic Response of Elastic and Viscoelastic Solids Elastostatic and Elastodynamic Problems for Thermosensitive and Nonhomogeneous Solids Dynamic Problems in Mechanics of Coupled Fields,” by Roman Kushnir</b>	
<b>Heat-Active Circular Interphase Inclusion in the Conditions of Smooth Contact with Half-Spaces</b> .....	187
Oleksandr Kryvyi and Yurii Morozov	
<b>Unsteady Elastic Diffusion Oscillations of a Timoshenko Beam with Considering the Diffusion Relaxation Effects</b> .....	193
O. A. Afanasieva, U. S. Gafurov, and A. V. Zemskov	
<b>Interphase Inclusion and Crack in an Inhomogeneous Anisotropic Plane</b> .....	199
Kostyantyn Arkhypenko and Oleksandr Kryvyi	
<b>Phenomenological Model of Pseudo-Elastic-Plastic Material Under Nonstationary Combining Loading</b> .....	205
Pavel Steblyanko, Yuri Chernyakov, Aleksandr Petrov, and Volodymyr Loboda	
<b>Plane Scattering Problem for an Inclusion of Non-classical Shape with a Thin Interphase Layer</b> .....	209
Roman Kushnir, Yaroslav Kunets, Valeriy Matus, and Oleksandr Trofymchuk	

**Stress State in a Finite Cylinder with Outer Ring-Shaped Crack at Non-stationary Torsion** ..... 215  
 Oleksandr Demydov and Vsevolod Popov

**Determination by Iterative Method of Diffraction Field at the Interaction Longitudinal Shear Wave with the System of Thin Rigid Inclusions** ..... 222  
 Vsevolod Popov

**Stress State Near Arbitrarily Oriented Cracks on the Continuation of a Rigid Inclusion Under Action of Longitudinal Shear Wave** ..... 229  
 A. S. Misharin and V. G. Popov

**Stress State of a Hollow Cylindrical Body with a System of Cracks Under Oscillations of Longitudinal Shear**..... 236  
 Olga Korylova and Vsevolod Popov

**The Wave Field of a Twice-Truncated Elastic Cone Under Torsion Moment Impact** ..... 242  
 K. Mysov and N. Vaysfel'd

**To the Solving of the Nonstationary Spatial Lamb—Cerutti Problem**..... 248  
 D. Prikazchikov, Yu. Protserov, and N. Vaysfeld

**The Model of Thin Electromagnetoelastic Shells Dynamics** ..... 254  
 V. A. Vestyak and D. V. Tarlakovskii

**Unsteady Electro-Magneto-Elastic Axisymmetric Oscillations of a Continuous Cylinder of Infinite Length**..... 259  
 Vladimir Vestyak and Vasily Scherbakov

**Transient Spatial Motion of Cylindrical Shell Under Influence of Non-stationary Pressure** ..... 264  
 Grigory V. Fedotenkov, Dmitry V. Tarlakovskii, and Andrey Yu Mitin

**Nonstationary Dynamic Problems for Elastic and Viscoelastic Piecewise Homogeneous Bodies** ..... 270  
 Pshenichnov Sergey

**The Wave Field of a Layer with a Cylindrical Cavity** ..... 277  
 Anna Fesenko and Nataly Vaysfel'd

**Features of Subsonic Stage of Contact Interaction of Viscoelastic Half-Plane and Absolutely Rigid Striker** ..... 283  
 Ekaterina Korovaytseva and Dmitry Tarlakovskii

**The Unsteady Contact Interaction Problem of an Absolutely Rigid Body and a Membrane**..... 289  
 Elena Yu Mikhailova, Grigory V. Fedotenkov, and Dmitry V. Tarlakovskii

<b>Static and Dynamic Models of Bending for Elastic Sandwich Plates . . .</b>	<b>294</b>
M. Yu. Ryazantseva and E. I. Starovoitov	
<b>Analysis of Vibration Insulation Properties of a Plate in an Elastic Medium Under the Influence of Different Types of Waves . . . . .</b>	<b>298</b>
N. A. Lokteva and D. V. Tarlakovskii	
<b>Studying of Influence of the Material Anisotropy on the Limit State of an Orthotropic Plate Weakened by a Periodic System of Collinear Cracks Under Biaxial Loading . . . . .</b>	<b>304</b>
Olga Bogdanova	
<b>The Boundary-Element Approach to Modeling the Dynamics of Poroelastic Bodies . . . . .</b>	<b>311</b>
Leonid Igumnov, Svetlana Litvinchuk, Aleksandr Ipatov, and Tatiana Iuzhina	
<b>Modeling Surface Waves on a Partially Saturated Poroelastic Half-Space . . . . .</b>	<b>316</b>
Leonid Igumnov, Svetlana Litvinchuk, Andrey Petrov, and Igor Vorobtsov	
<b>Part V Symposium on: “Elastostatic and Elastodynamic Problems for Thermosensitive and Nonhomogeneous Solids” by Roman Kushnir</b>	
<b>Residual Strength and Reliability of Corroded Pipelines—Monte-Carlo Approach for Consideration of Spatially Nonuniform Material Properties . . . . .</b>	<b>321</b>
Alexey Milenin, Elena Velikoivanenko, Galina Rozyinka, and Nina Pivtorak	
<b>Actual Problems of Structural Integrity Assessment of WWER-1000 Pressure Vessel Internals . . . . .</b>	<b>327</b>
O. V. Makhnenko and S. M. Kandala	
<b>Vibration of Titanium Blades of Turbomachines for Nuclear Power Plants with Erosive Damage . . . . .</b>	<b>334</b>
Yurii Vorobiov, Oleg Makhnenko, Nataliia Ovcharova, and Anton Olkhovskiy	
<b>Influence of Residual Stresses in the Cladding Zones of RPV WWER-1000 on Integrity Assessment . . . . .</b>	<b>341</b>
Oleh Makhnenko and Elena Kostenevich	

**Part VI Symposium on: “Dynamic Problems in Mechanics of Coupled Fields,” by Roman Kushnir**

**Damping of Hydroelastic Vibrations of the Plate Using Shunted Piezoelectric Element. Part I: Numerical Model** . . . . . 351  
 Sergey Lekomtsev, Dmitrii Oshmarin, and Natalya Sevodina

**Damping of Hydroelastic Vibrations of the Plate Using Shunted Piezoelectric Element. Part II: Experiment** . . . . . 357  
 Maksim Iurlov, Alexander Kamenskikh, Sergey Lekomtsev, and Dmitrii Oshmarin

**Stationary Dynamic Acoustoelasticity Problems of a Thin Plate in a Perfect Compressible Fluid, Taking into Account the Dissipation of Energy in the Plate and Liquid** . . . . . 364  
 V. N. Paimushin, R. K. Gazizullin, and D. V. Tarlakovskii

**Dynamics and Elastic Stability of an Electrostatically Actuated Microbeam Under Ultrafast Laser Pulse** . . . . . 370  
 A. V. Lukin, D. A. Indeitsev, I. A. Popov, O. V. Privalova, and L. V. Shtukin

**Author Index** . . . . . 377

**Part I**  
**Materials: Properties, Manufacturing,**  
**Modelling**



# Role of Compactness on Hardness and Reduced Modulus of Vaterite Determined with Nanoindentation

Radek Ševčík<sup>1</sup> and Vladimír Hrbek<sup>2</sup>

<sup>1</sup> Institute of Theoretical and Applied Mechanics of the Czech Academy of Sciences, Prosecká 76, 190 00 Praha 9, Czech Republic  
sevcik@itam.cas.cz

<sup>2</sup> Faculty of Civil Engineering, Czech Technical University in Prague, Thakurova 7/2077, 160 00 Praha 6, Czech Republic

**Abstract.** The influence of compaction degree of synthetic vaterite, the metastable polymorph of calcium carbonate, on determined mechanical properties was investigated using nanoindentation instrument. Specimens for measurements were prepared as pressed pellets with the application of three different forces—40, 60 and 80 kN. The highest values of reduced modulus and hardness were detected for vateritic pellet pressed at 60 kN. For this specimen, reduced modulus and hardness were found to be in ranges 74–10 and 5.2–0.3 GPa, respectively. Observation with scanning electron microscope showed increase compactness of pellet's microstructure and an increase in density and length of microcracks within vateritic pellets when higher pressing force was applied.

**Keywords:** Vaterite · CaCO<sub>3</sub> · Nanoindentation

## 1 Introduction

Calcium carbonate (CaCO<sub>3</sub>) is widely present on Earth and play crucial role in many industrial sectors and natural processes [1, 2]. Different modifications of CaCO<sub>3</sub> are known: it can exist as anhydrous polymorphs (vaterite, aragonite and calcite) or as hydrous phases (monohydrate, ikaite and amorphous calcium carbonate) [3] with different morphologies and variety of physico-chemical properties [1–3]. Due to their high importance, CaCO<sub>3</sub> formation and characterization are intensively studied, however, only limited information can be found about mechanical properties of synthetic products. Mainly only calcite, most abundant and thermodynamically stable CaCO<sub>3</sub> polymorph under Earth's surface conditions, was tested with nanoindentation [4–6]. In case of vaterite, data are available only for samples originated from biogenic [7–9] or biomimetic [10] processes. Some of our results of nanoindentation of synthetic vaterite were already published [5, 6].

In this article, we have investigated the influence of compactness's degree of powder synthetic vaterite on hardness and reduced modulus. Specimens were prepared as pressed pellets with applications of different forces. Mechanical properties were



determined using nanoindentation instrument and microstructure of prepared pellets were observed under scanning electron microscopy.

## 2 Experimental Part

### 2.1 Sample Preparation

Vaterite was synthesized as previously described without use of additives [11]. The composition of obtained powders was examined using quantitative phase analysis with the Rietveld method from collected X-ray diffraction patterns, confirming its purity 99 wt.% [11]. Testing specimens were prepared as pressed pellets made from 0.250 g of vaterite. Pellets were pressed for 30 s with force 40 kN, subsequently, for 30 s again with forces 40, 60 or 80 kN using hydraulic press (Trystom). No phase transformation was detected after pressing.

### 2.2 Nanoindentation Measurements

For mechanical testing of prepared specimens, nanoindenter TI 750 L Ubi (Hysitron) with three sided pyramidal diamond Berkovich indenter, was used. Indentation was done on area of  $190 \times 190 \mu\text{m}$  with the grid consists of  $20 \times 20$  indents with  $10 \mu\text{m}$  spacing between them. Quasi-static indentation was performed in load-controlled mode with maximum applied force was set to  $500 \mu\text{N}$ . The loading/unloading time was set to 2 s with a 5 s peak hold time.

### 2.3 Scanning Electron Microscopy

High-resolution field emission scanning electron microscope (SEM) Quanta 450 FEG (FEI) using a secondary electron detector was used to observe surfaces of testing specimens. Analyses were performed at 20 kV of accelerating voltage.

## 3 Results and Discussion

The mean load-displacement (P-h) curves for the vateritic pellets pressed with different forces are displayed on Fig. 1. Pellet pressed at lowest force (40 kN) showed maximum load ( $P$ ) at highest displacement ( $h$ ). Interestingly, the pellet pressed at 60 kN had maximum  $P$  at lowest  $h$  and the pellet pressed with 80 kN force exhibited maximum  $P$  between P-h curves for pellets pressed at 40 and 60 kN. Such behavior could be ascribed to the partial alteration of pellet's microstructure on testing specimen's surfaces of due to applied pressure and it will be further discussed in section dedicated to the SEM observations. On Fig. 1, results are compared with those obtained from specimen prepared also with grinding method, reported in [6]. It is clearly showed that mean P-h curve is significantly shifted to the higher values of  $h$ . Whereas, the maximum  $P$  of pressed pellets is located in the range of 80–130 nm, the maximum  $P$  of vaterite specimen prepared with grinding method is up to 240 nm. The mean values of determined elastic modulus ( $E_r$ ) and hardness ( $H$ ) are summarized in Table 1 and they

seem to be comparable without relevant difference for all specimens pressed as pressed pellets due to high confident intervals as a consequence of considerable decreased of  $E_r$  and  $H$  values with increased contact depths. If the values are reported in ranges, the influence of degree of compactness become more evident.  $E_r$  values of vateritic pellets pressed at 40, 60 and 80 kN were determined to be in the ranges of 60–15, 74–10 and 61–16 GPa, respectively.  $H$  values of vateritic pellets pressed at 40, 60 and 80 kN were determined to be in the ranges of 4.5–0.4, 5.2–0.3 and 4.2–0.3 GPa, respectively. So,  $E_r$  and  $H$  were found to increase with higher force of compactness, until 60 kN. At 80 kN force,  $E_r$  and  $H$  were detected to be more similar with pellets pressed at 40 kN instead of pellets pressed at 60 kN.

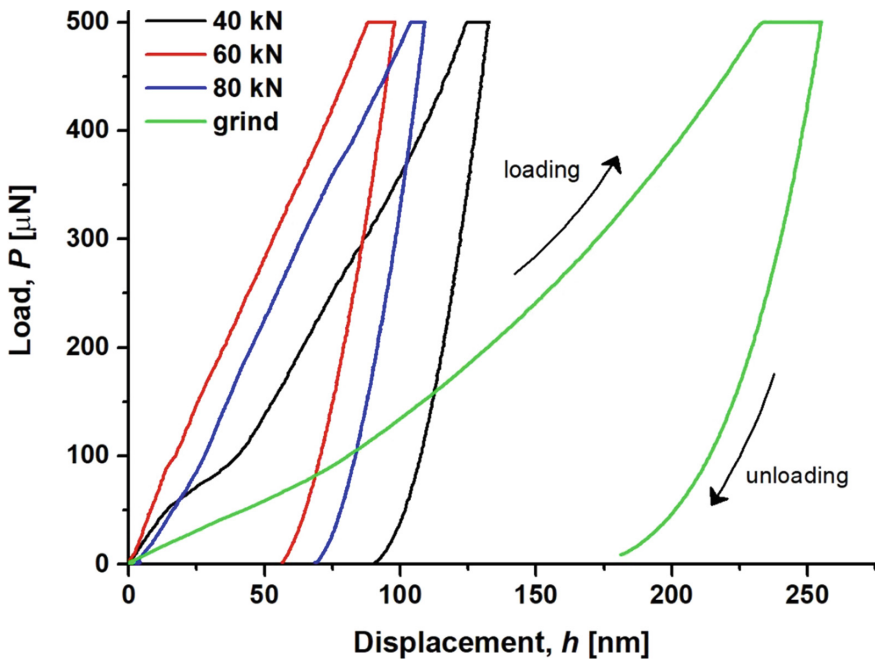


**Fig. 1.** Comparison of mean load-displacement ( $P$ - $h$ ) curves for pellets prepared from vaterite and pressed applying different forces (40–80 kN). The green curve represented  $P$ - $h$  curve for vaterite specimen prepared using grinding method (from [6]).

**Table 1.** Summary of mechanical testing results from nanoindentation. Mean values of reduced modulus ( $E_r$ ) and hardness ( $H$ ) for vaterite specimens prepared with pressing method (press) and grinding method (grind) are presented.

Sample	$E_r$ [GPa]	$H$ [GPa]
Vaterite 40 kN (press)	$27 \pm 9$	$1.2 \pm 0.8$
Vaterite 60 kN (press)	$34 \pm 12$	$1.6 \pm 0.9$
Vaterite 80 kN (press) [5]	$31 \pm 8$	$0.9 \pm 0.6$
Vaterite (grind) [6]	$10 \pm 5$	$0.3 \pm 0.2$

Such behavior may be explained observing of pellets microstructures under SEM. On Fig. 2a–c, the surfaces of samples are illustrated. It can be noticed that the degree of compactness is higher when the applied pressing force was higher.

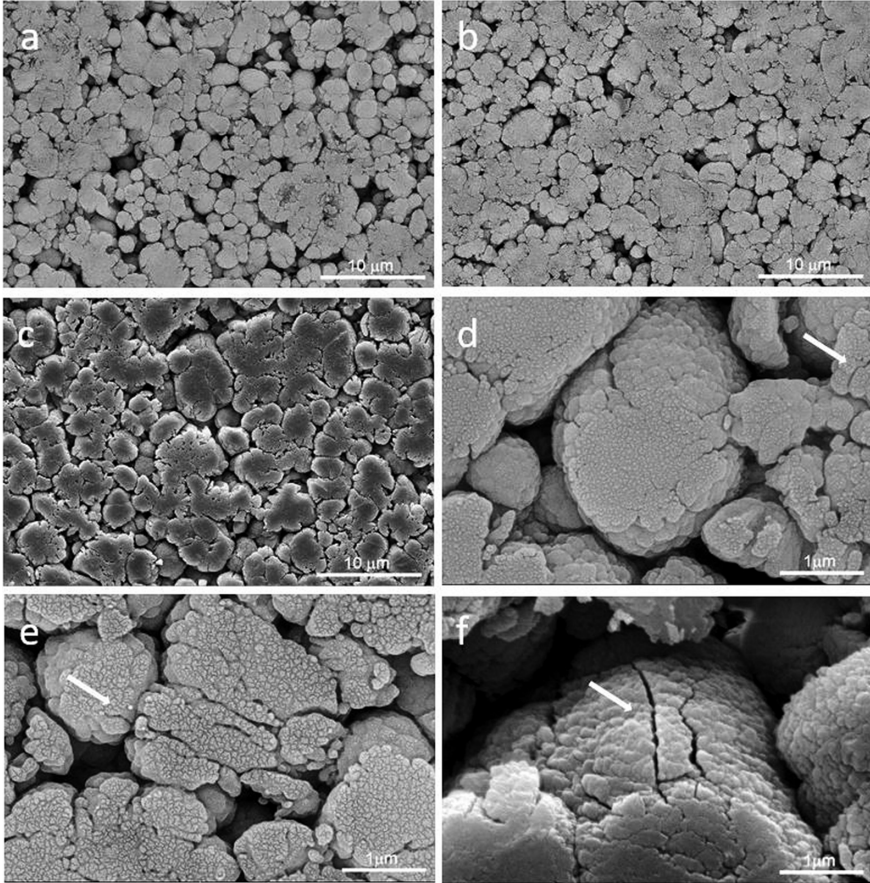


**Fig. 2.** Surfaces of prepared vateritic specimens at low magnifications (a, b, c—10,000 $\times$ ) and at high magnifications (d, e, f—80,000 $\times$ ). The formation of microcracks is highlighted with inserted arrows. Testing specimens were prepared with different applied forces: a, d—40 kN, b, e—60 kN, c, f—80 kN.

At the same time, larger bodies of vaterite particles were formed with increasing pressure. Together with higher degree of compactness, formation of microcracks was initiated (Fig. 2d–f, microcracks are indicated by arrows in Fig. 2d–f). Such microcracks were observed only in limited amount in case of pellet pressed at 40 kN. For pellet pressed at 60 kN, microcracks were present still only occasionally close to the surface. However, in pellet pressed at 80 kN, the density of microcracks resulted in much higher quantities. Interestingly, they were more pervasive not only on surfaces, but

penetrated in depth inside vaterite crystals (Fig. 2f). Thus, formation of these cracks may be the explanation of detected lower  $E_r$  and  $H$  values for pellet pressed at 80 kN compared to those pressed at 60 kN.

The comparison with literature data is limited to the few works dealing with the nanoindentation testing of vaterite. For samples of metastable polymorphs (vaterite and aragonite) embedded in epoxy resin and prepared using grinding method,  $E_r$  and  $H$  values were found to be almost three times lower [6]. Nonetheless, it is known that presence of epoxy resin may interfere with measurements [12]. For biogenic vaterite from fresh water carp astericus,  $E_r$  and  $H$  were found to be 57 and 3.2 GPa, respectively [8]. For biomimetic prismatic-type vateritic thin film,  $E_r$  and  $H$  were found to be  $32.5 \pm 2.4$  and  $2.2 \pm 0.2$  GPa, respectively [10]. Such values are higher as consequence of highly-organized structure present in biogenic and biomimetic materials [2, 3, 10]. Recently, vaterite coating on eggs were analyzed and  $E_r$  and  $H$  were found to be in ranges 1.8–5.8 GPa and 30–240 MPa depending on different female of the Greater Ani *Crotophaga major* [9]. Authors suggested that layers of vaterite may act as a shock absorber [9].

The preparation of samples for nanoindentation measurements as pressed pellets benefits from its timelessness, however, it was shown that degree of compaction played an important role in determined values of nanomechanical properties. In general, this method could be used for comparison of different powder samples using nanoindentation instrument.

## 4 Conclusion

In this paper, influence of degree of compactness on reduced modulus and hardness of synthetic vaterite was investigated using nanoindentation instrument. The testing vateritic specimens were produced as pressed pellets applying forces from 40 to 80 kN. The highest values of reduced modulus and hardness were detected for vateritic pellet pressed at 60 kN with reduced modulus and hardness found to be in ranges 74–10 and 5.2–0.3 GPa, respectively. With increasing pressure during production of pellets, the degree of compactness was higher, however, also the formation of microcracks was increased as confirmed by observations with scanning electron microscope. For pellet pressed at 80 kN, the microcracks were observe also within crystals of vaterite. This microscopic observation explained the decrease of mechanical properties of the sample pressed at 80 kN in comparison with the one pressed at 60 kN. Our study may help for designing of novel calcium carbonate based materials with enhanced properties.

**Acknowledgements.** The authors gratefully acknowledge support from the Czech Science Foundation GA ČR grant 17-05030S. We thank Mgr. Petra Mácová for help with preparation of testing specimens.

## References

1. Tegethoff, F.W.: Calcium carbonate—from the cretaceous period into the 21st century, 1st edn. Birkhauser Verlag, Basel (2001)
2. Sigel, A., Sigel, H., Sigel, R.K.O.: Biom mineralization: from nature to application, 1st edn. Wiley, Chichester (2008)
3. Van Driessche, A.E.S., Kellermeier, M., Benning, L.G., Gebauer, D.: New perspectives on mineral nucleation and growth: from solution precursors to solid materials. Springer, Cham (2017)
4. Calvaresi, M., Falini, G., Pasquini, L., Reggi, M., Fermani, S., Gazzadi, G.C., Frabboni, S., Zerbetto, F.: Morphological and mechanical characterization of composite calcite/SWCNT–COOH single crystals. *Nanoscale* **5**, 6944–6949 (2013)
5. Ševčík, R., Šašek, P., Viani, A.: Physical and nanomechanical properties of the synthetic anhydrous crystalline CaCO<sub>3</sub> polymorphs: vaterite, aragonite and calcite. *J. Mater. Sci.* **53**, 4022–4033 (2018)
6. Ševčík, R., Hrbek, V.: Influence of sample preparation on determined nanomechanical properties of metastable calcium carbonate polymorphs. In: Gdoutos, E.E. (ed.) *ICTAEM 2018*, pp. 3–7. Springer, Cham (2019)
7. Tai, C.Y., Chen, F.-B.: Polymorphism of CaCO<sub>3</sub> precipitated in a constant-composition environment. *AIChE J.* **44**, 1790–1798 (1998)
8. Ren, D., Meyers, M.A., Zhou, B., Feng, Q.: Comparative study of carp otolith hardness: lapillus and asteriscus. *Mater. Sci. Eng. C* **33**, 1876–1881 (2013)
9. Portugal, S.J., Bowen, J., Riehl, C.: A rare mineral, vaterite, acts as a shock absorber in the eggshell of a communally nesting bird. *Ibis* **160**, 173–178 (2018)
10. Xiao, C., Li, M., Wang, B., Liu, M-F., Shao, C., Pan, H., Lu, Y., Xu, B-B., Li, S., Zhan, D., Jiang, Y., Tang, R., Liu, X.Y., Cölfen, H.: Total morphosynthesis of biomimetic prismatic-type CaCO<sub>3</sub> thin films. *Nat. Commun.* **8**, 1398–1406 (2017)
11. Ševčík, R., Pérez-Estébanez, M., Viani, A., Šašek, P., Mácová, P.: Characterization of vaterite synthesized at various temperatures and stirring velocities without use of additives. *Powder Technol.* **284**, 265–271 (2015)
12. Dhama, N.K., Mukherjee, A., Reddy, M.S.: Micrographical, mineralogical and nano-mechanical characterisation of microbial carbonates from urease and carbonic anhydrase producing bacteria. *Ecol. Eng.* **94**, 443–454 (2016)



# Approximate Mode Shape for Damped Structures

Wasiu A. Oke<sup>1</sup>✉, Oluseyi A. Adeyemi<sup>2</sup>, Kazeem A. Bello<sup>1</sup>,  
and Adewale Adegbenjo<sup>3</sup>

<sup>1</sup> Department of Mechanical and Mechatronics Engineering, Afe Babalola University Ado-Ekiti (ABUAD), P.M.B 5454 Ado Ekiti, Nigeria  
wasiuad@abuad.edu.ng

<sup>2</sup> Department of Mechanical Engineering, First Technical University, Ibadan, Nigeria

<sup>3</sup> Center for Nanoengineering and Tribocorrosion, University of Johannesburg, Johannesburg, South Africa

**Abstract.** Mode shape is very important in dynamic analysis of the structures. It can be employed to assess dynamic interaction between a structure and its supports to avoid sudden failure. However, unlike undamped structures, exact mode shapes for damped structures are difficult to obtain due to the eigenvectors complexity. In practice, damped structures cannot be shunned and they are available in many engineering applications. Some undamped structures may become damped structures during the operations. Such structures include pipes conveying fluid and because of their roles globally, their dynamic analysis becomes vital to check their integrity to prevent abrupt failures. In this paper, different methods of obtaining approximate mode shapes of composite pipe conveying fluid were investigated. The pipe is modeled using the extended Hamilton's theory and discretized using wavelet-based finite element method. The pipe complex modal characteristics were obtained by solving the generalized eigenvalue problem and its mode shapes were computed.

**Keywords:** Mode shapes · Composite fluid pipe · Damped structures · Complex eigenvectors · Wavelets

## 1 Introduction

The pipes conveying fluid are commonly employed in pump discharge lines, marine risers, chemical plants, oil pipelines, and nuclear reactor components [1]. These pipes are subjected to flow-induced vibration as a result of turbulence in the flow. Hence, many researchers have been working on dynamic analysis of the fluid pipes in order to prevent the negative consequences of this vibration. However, the dynamic analysis of pipes conveying fluid is not as simple as that of empty pipes because the fluid flowing in the pipe will turn the system from undamped to damped system. This will lead to complex eigenvalues and eigenvectors and as a result, mode shapes constructions become complicated. While some researchers have discussed or mentioned the methods that can be used to obtain mode shapes of other structures, few researchers have

discussed how to obtain the mode shapes of pipes conveying fluid in one way or the other. Liu et al. [2] employed Frequency Response Function based method to calculate mode shapes of pipe conveying fluid while natural frequencies were obtained using a hybrid analytical numerical method based on the Transfer Matrix Method. Yun-dong and Yi-ren [3] studied the free vibration analysis of pipe conveying fluid with different boundary conditions using He's variational iteration method and mode shapes were obtained from real part of complex modes. Sarkar and Paidoussis [4] used semi-analytical approach to obtain the proper orthogonal modes of non-linear oscillation of a cantilevered fluid pipe with end-mass.

It can be observed from the review that more needs to be done on the construction of damped systems mode shapes. In this work, three methods that can be employed to obtain approximate mode shapes of damped structures or pipe conveying fluid at different velocities are presented. The extended Hamilton's theory was employed to model the composite pipe conveying fluid and discretized using the wavelet-based finite element method. The mode shapes were then constructed from the complex modal characteristics of the composite pipe-fluid vibrations obtained by solving the generalized eigenvalue problem.

## 2 Composite Pipe Conveying Fluid

As the fluid passes through the pipe of length  $L$  with inlet velocity  $v_1$  and discharge velocity  $v_2$ , the vibrational behavior of the system will be affected by the fluid-pipe interaction. The equilibrium of forces acting along the  $x$ -direction on the fluid element obtained in [5] can be expressed for the fluid in a pipe element of length  $dx$  as

$$F_\tau = A_i \frac{dP}{dx} dx \quad (1)$$

where  $F_\tau = \tau s dx$ . Besides, the strain energy  $U$  of the laminated composite pipe element conveying fluid and the total kinetic energy  $T$  can be defined as

$$U = \frac{1}{2} \int_0^{l_e} H(x) \left( \frac{\partial^2 y}{\partial x^2} \right)^2 dx, T = \frac{1}{2} \int_0^{l_e} M(x) V_p^2 dx + \frac{1}{2} \int_0^{l_e} m_f V_f^2 dx \quad (2)$$

where  $M(x) = \iint_{A_p} \rho_p dA_p = \sum_{\ell=1}^N \pi \rho_\ell (r_\ell^2 - r_{\ell-1}^2) \text{ kg/m}$

$$V_p = \frac{\partial y}{\partial t}, V_f = \frac{\partial y}{\partial t} + V \frac{\partial y}{\partial x}, A_p = \frac{\pi}{4} (D_o^2 - D_i^2), m_f = \rho_f A_f, A_f = \frac{\pi}{4} D_i^2$$

and  $H$  and  $M$  are stiffness and mass per unit length of the laminated composite pipe element;  $D_i$  and  $D_o$  are inner and outer pipe diameters;  $\rho_\ell$  and  $r_\ell$  are density and radius of  $\ell$ th layer. The Equation used in Ref. [6] can be modified for healthy composite pipe conveying fluid and it will become

$$H = (A_{11}R^3 + 2B_{11}R^2 + D_{11}R)\pi \quad (3)$$

where  $A_{11}$ ,  $B_{11}$ , and  $D_{11}$  are stiffness coefficients and  $R = 0.25(D_i + D_o)$ .

As a result of various sources of energy dissipation, fluid that is flowing through the pipes is always associated with losses. The major or minor loss can be used to describe the energy losses in the pipes. The energy loss in the components because of changes in velocity responsible for minor losses while the associated losses due to friction ( $h_f$ ) in the pipes and the viscosity are the cause of major losses [7, 8]. As a result of losses, Eq. (1) will become

$$F_\tau = A_f \frac{dP}{dx} dx = -h_f m_f g \quad (4)$$

### 3 Equation of Motion of Composite Pipe Conveying Fluid

By substituting Eqs. (1) and (2) in the extended Hamilton's principle, it becomes

$$\int_{t_1}^{t_2} \left\{ \left[ \int_0^{l_e} H(x) \frac{\partial^4 y}{\partial x^4} \delta y dx \right] - \left[ \delta \left( \frac{1}{2} \int_0^{l_e} m_e \left( \frac{\partial y}{\partial t} \right)^2 dx \right) + \delta \left( \frac{1}{2} \int_0^{l_e} 2m_f V \frac{\partial^2 y}{\partial t \partial x} dx \right) - \int_0^{l_e} m_f V^2 \frac{\partial^2 y}{\partial x^2} \delta y dx \right] - \left[ \int_0^{l_e} F_p \frac{\partial^2 y}{\partial x^2} \delta y dx \right] \right\} dt = 0 \quad (5)$$

Upon simplification of Eq. (5), the equation of motion for the laminated composite pipe conveying fluid can be obtained as

$$H(x) \frac{\partial^4 y}{\partial x^4} + m_e \frac{\partial^2 y}{\partial t^2} + 2m_f V \frac{\partial^2 y}{\partial t \partial x} + (F_p + m_f V^2) \frac{\partial^2 y}{\partial x^2} = 0 \quad (6)$$

where  $m_e = M(x) + m_f$  and  $F_p = -F_\tau$ .

### 4 Finite Element Formulation of Composite Pipe Conveying Fluid

The laminated composite pipe conveying fluid equation in Eq. (6) has been discretized using the Euler-Bernoulli pipe element in order to solve it, in which the B-spline wavelet on the interval was utilized. Consequently, Eq. (6) can then be expressed in a compressed form as



$$[M]_e \{\ddot{y}\}_e + [B]_e \{\dot{y}\}_e + [K]_e \{y\}_e = 0 \quad (7)$$

where

$$[M]_e = \int_0^{l_c} l_e m_e [T_B]^T \{\Psi\}^T \{\Psi\} [T_B] d\zeta, \quad [B]_e = \int_0^{l_c} C_b [T_B]^T \{\Psi\}^T \{\Psi'\} [T_B] d\zeta,$$

$$[K]_e = \int_0^{l_c} \frac{H}{l_c} [T_B]^T \{\Psi''\}^T \{\Psi''\} [T_B] d\zeta - \int_0^{l_c} \frac{1}{l_c} C_k [T_B]^T \{\Psi'\}^T \{\Psi'\} [T_B] d\zeta, \quad \text{and } C_b = 2m_f V,$$

$$C_k = F_p + m_f V^2$$

Hence, Eq. (7) is the equation of motion for the composite pipe conveying fluid. Furthermore, Eq. (7) can be expressed in state space using the state vectors  $\{\dot{z}\}$  and  $\{z\}$ , as

$$[\bar{M}]\{\dot{z}\} - [\bar{K}]\{z\} = 0 \quad (8)$$

where

$$[\bar{M}] = \begin{bmatrix} [I] & [0] \\ [0] & [M]_e \end{bmatrix}, \quad [\bar{K}] = \begin{bmatrix} [0] & [I] \\ -[K]_e & -[B]_e \end{bmatrix}, \quad \{z\} = \begin{bmatrix} \{y_1\} \\ \{y_2\} \end{bmatrix}, \quad \text{and}$$

$$\{\dot{z}\} = \begin{bmatrix} \{\dot{y}_1\} \\ \{\dot{y}_2\} \end{bmatrix}.$$

The state vectors can be stated for harmonic motion in the form

$$\{z\} = \{W\}e^{i\omega t}, \quad \{\dot{z}\} = i\omega\{W\}e^{i\omega t} \quad (9)$$

where  $\lambda = i\omega$  and  $\omega$  is frequency. Upon substituting Eq. (9) in Eq. (8), the generalized eigenvalue problem is obtained as

$$[[\bar{K}] - \lambda[\bar{M}]]\{W\} = 0 \quad (10)$$

## 5 Numerical Results and Discussions

In this section, the pinned-pinned composite pipe that has been considered in [9–11] and by other numerous researchers was considered with fluid flow in order to examine its vibration behavior and show the approximate mode shapes of a fluid-pipe or damped structure. First and foremost, the frequency of this pipe without fluid flow was obtained to validate the model and the results obtained for first frequency using current model is 98.76 while 98.65 Hz is obtained by [10, 11] using different solution methods. It can be observed that the result obtained in the present study agreed with other results.

Now, the pipe is then considered as the one conveying fluid. The  $2n$  complex conjugate  $\lambda$  and eigenvectors were obtained and as a result, the mode shapes are not easy to obtain as in undamped pipe. However, approximate mode shapes can be obtained from complex eigenvectors using three techniques: imaginary parts, real parts and absolute of complex eigenvectors. Mode shapes obtained from any of these techniques can be used for further analysis instead of using undamped modes that are not true mode shapes of the pipe when conveying fluid. Although, they are expected to be similar as long as the boundary conditions remain the same. The results obtained for the pipe conveying fluid at

different velocities are compared with mode shapes of the pipe without fluid (or undamped pipe) and some of them are as presented in Fig. 1. It is interesting to see that at lower velocities, the mode shapes obtained from the imaginary part of eigenvectors provide the mode shapes that are similar to mode shapes of pinned-pinned pipes. However, as velocity increases, the real part of eigenvectors gives the needed mode shapes but imaginary mode shapes are no longer portray correct mode shapes.

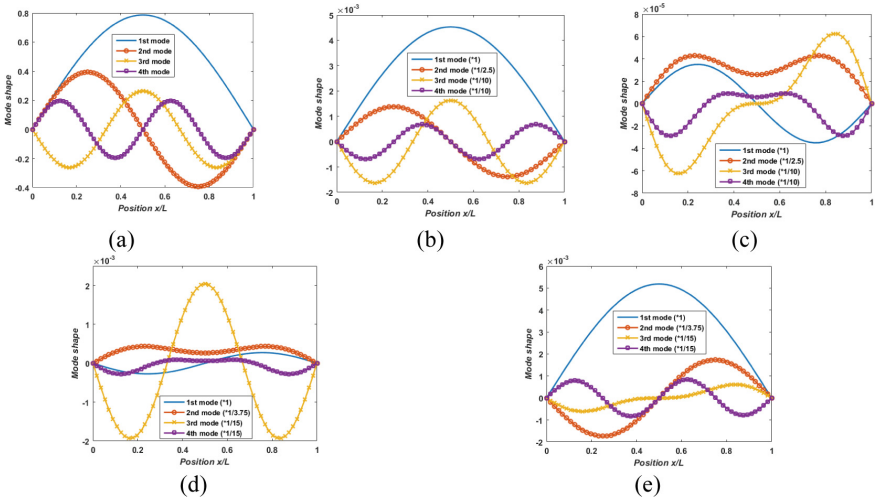


**Fig. 1.** **a** Mode shapes for empty pipe; **b** and **c** are imaginary and real mode shapes for pipe conveying fluid at  $V = 10$  m/s; **d** and **e** are imaginary and real mode shapes for pipe conveying fluid at  $V = 80$  m/s.

## 6 Conclusions

The structural mode shapes can be used: to appraise the dynamic interaction between the structures and their supports to avoid catastrophic failures, as a guide during the structural experimental analysis, and for further structural dynamic analysis. In this study, different methods for obtaining mode shapes of damped structures were examined in which composite fluid pipe was considered as a case study. It was discovered that at lower velocities, the mode shapes from absolute or imaginary part of eigenvectors can give approximate required mode shapes. On the other hand, the mode shapes from absolute or real part of eigenvectors can give approximate needed mode shapes at higher velocities. It can be seen that the three methods presented can be employed to obtain mode shapes of damped structure or fluid pipe for further analysis if necessary instead of using undamped mode shapes that are not true mode shapes and far more above the actual mode shapes. Besides, unlike it was reported in literature, it can be deduced that neither only real nor only imaginary part of complex eigenvectors is enough to obtain the correct approximate mode shapes of pipes conveying fluid at different velocities.

## References

1. Hu, Y.-J., Zhu, W.: Vibration analysis of a fluid-conveying curved pipe with an arbitrary undeformed configuration. *Appl. Math Model* **64**, 624–642 (2018)
2. Liu, M., Wang, Z., Zhou, Z., Qu, Y., Yu, Z., Wei, Q., Lu, L.: Vibration response of multi-span fluid-conveying pipe with multiple accessories under complex boundary conditions. *Eur J Mech A Solids* **72**, 41–56 (2018)
3. Yun-dong, L., Yi-ren, Y.: Vibration analysis of conveying fluid pipe via He's variational iteration method. *Appl Math Model* **43**, 409–420 (2017)
4. Sarkar, A., Paidoussis, M.P.: A cantilever conveying fluid: coherent modes versus beam modes. *Int J Non-Linear Mech* **39**(3), 467–481 (2004)
5. Wang, L.: Vibration and instability analysis of tubular nano- and micro-beams conveying fluid using nonlocal elastic theory. *Physica E* **41**(10), 1835–1840 (2009)
6. Oke, W.A., Khulief, Y.A.: Effect of internal surface damage on vibration behavior of a composite pipe conveying fluid. *Compos Struct* **194**, 104–118 (2018)
7. Young, D.F., Munson, B.R., Okiishi, T.H., Huebsch, W.W.: *A Brief Introduction to Fluid Mechanics*, 5th edn. Wiley, USA (2011)
8. Bansal, R.K.: *A textbook of fluid mechanics and hydraulic machines*, 9th edn. Laxmi Publications (P) Ltd, New Delhi, India (2010)
9. Oke, W.A., Khulief, Y.A.: Vibration analysis of composite pipes using the finite element method with B-spline wavelets. *J Mech Sci Technol* **30**(2), 623–635 (2016)
10. Hajianmaleki M, Qatu MS *Advances in composite materials—analysis of natural and man-made materials*. InTech (2011)
11. Qatu, M.S., Iqbal, J.: Transverse vibration of a two-segment cross-ply composite shafts with a lumped mass. *Compos Struct* **92**(5), 1126–1131 (2010)



# Deformation Behavior of Ferrite/Austenite Duplex Stainless Steel in Hot Compression Processing

Hezong Li<sup>1</sup>(✉), Suxia Huang<sup>1</sup>, Qiusheng Li<sup>1</sup>, Xiaopin An<sup>2</sup>,  
Facai Ren<sup>3</sup>, and Simon S. Wang<sup>1,4</sup>

<sup>1</sup> College of Mechanical and Equipment Engineering, Hebei University of Engineering, 056038 Handan, Hebei, China  
Lhzong@126.com

<sup>2</sup> Tianjin Bridge Welding Materials Group Company, 300380 Tianjin, China

<sup>3</sup> Shanghai Institute of Special Equipment Inspection and Technical Research, 200062 Shanghai, China

<sup>4</sup> Department of Aeronautical and Automotive Engineering, Loughborough University, LE11 3TU Loughborough, Leicestershire, UK

**Abstract.** The deformation behavior of Cr23 ferrite/austenite duplex stainless steel has been investigated at deformation temperatures from 1173 to 1473 K and strain rates from 0.01 to 10 s<sup>-1</sup> at a given total strain of 0.8. The results show that the flow stress is strongly influenced by the deformation temperature, the strain rate and the strain. There is a balance between the working hardening and the softening at strain rate of 1 s<sup>-1</sup> and elevated deformation temperature when the strain is in excess of 0.25. The softening mechanism of the dynamic recovery and dynamic recrystallization is prominent at lower strain rate less than 0.1 s<sup>-1</sup>. The Arrhenius-type constitutive model is used to predict the flow stress which is closed to the experimental data.

**Keywords:** Ferrite/austenite duplex stainless steel · Dynamic recrystallization · Deformation behavior

## 1 Introduction

Ferrite/austenite duplex stainless steels (FADSS) have been investigated since 1980s. These materials have excellent mechanical properties, such as, improved strength, corrosion resistance and good weldability and being used in chemical, petro-chemical, nuclear and energy plants [1–3]. In general, the variation of flow stress of materials during hot deformation processing, such as hot rolling, forging, and extruding, is very complex due to microstructure evolution with interaction metallurgical phenomena such as work hardening, dynamic recovery and dynamic recrystallization. Furthermore, the deformation distribution is not uniform because the hard austenite and soft ferrite phases would be deformed jointly at high temperature [4, 5]. Therefore, it is vital to understand the deformation behavior of FADSS to obtain the hot working parameters and thus improve its performance.

In this paper, hot deformation behavior of Cr23 material has been investigated in more details to evaluate the effect of high deformation temperatures on flow behavior with strain rate based on hot compression tests on Gleeble-1500D thermo-mechanical simulator.

## 2 Experimental Procedures

The chemical composition of Cr23 Ferrite/austenite duplex stainless steel used in this investigation was analyzed with an energy dispersive X-ray detector (EDS) and shown in Fig. 1 and Table 1.

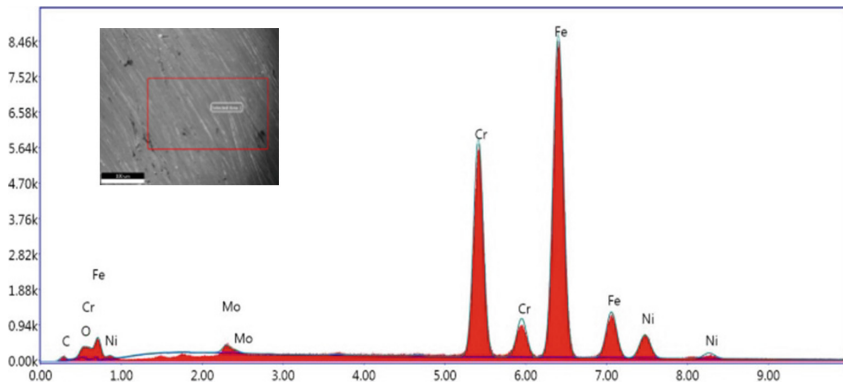


**Fig. 1.** EDS analysis of Cr23 FADSS

**Table 1.** Chemical composition of Cr23 FADSS (wt.%).

C	Mo	Cr	Ni	Mo	Mn	Cu	Fe
≤ 0.03	0.53	22.91	8.39	0.05–0.6	≤ 2.5	0.05–0.6	Bal.

Hot compression tests were conducted on a Gleeble-1500D thermos mechanical simulator at temperatures of 1173, 1273, 1373 and 1473 K, and strain rates of 0.01, 0.1, 1, and  $10\text{ s}^{-1}$ . Cylindrical specimens of 10 mm in diameter and 15 mm in height were used in this study. In order to reduce friction between the specimen and the punch and inhomogeneous deformation, the sticky graphite was painted on both ends of the specimens. At the same time, an inert gas (Argon) was injected around the specimens to prevent oxidation during the heating process. All of the specimens were preheated to 1473 K, held for 300 s to maintain composition homogenization and similar microstructure and then cooled to different deformation temperatures at a rate of  $10\text{ }^{\circ}\text{C/s}$ . Each specimen was held for 30 s to eliminate the internal thermal gradient at the compressing temperatures, and compressed to a total true strain of 0.8. Finally, the specimens were quenched in water as soon as possible.

### 3 Results and Discussions

#### 3.1 Flow Stress Analysis

The true stress-strain curves obtained from compression tests at different deformation temperatures and strain rates are shown in Fig. 2. Significant effects of deformation temperature and strain rate on the flow stress occurred. The flow softening phenomena are clearly observed on the flow curves due to dynamic recovery and dynamic recrystallization. The flow stress decreases with increasing deformation temperature and decreasing strain rate. This is because that the higher deformation temperature and lower strain rate promote higher mobility of grain boundary and there is enough time to maintain growth of new recrystallized grains. At higher deformation temperature of 1473 K, there is no obvious work hardening except at the strain rate of  $10\text{ s}^{-1}$ , but at lower deformation temperature of 1173 K, the work hardening is clearly seen (see Fig. 2a, d). Therefore, the dynamic recovery and dynamic recrystallization are the main softening mechanism during compression processing at lower strain rate. There is a parallel balance between the work hardening and softening at the strain rate of  $1\text{ s}^{-1}$  with different deformation temperature. Of course, the balance between working hardening and softening is more or less related to the deformation. When the strain is less than 0.25 at 1173 K, the work hardening is prominent over the softening mechanics, such as the dynamic recovery and dynamic recrystallization. When the strain increases over 0.25, the softening mechanics are exceeding the work hardening because of the deformation energy accumulation.

#### 3.2 Constitutive Model Developing

The flow stress, which is related to the deformation temperature ( $T$ ), the strain rate ( $\dot{\epsilon}$ ) and the strain ( $\epsilon$ ), can be expressed by the Arrhenius-type equation to analyze and predict the hot deformation behavior [6]. The constitutive model can be expressed as:

$$\sigma = \frac{1}{\alpha} \ln \left[ \left( \frac{Z}{A} \right)^{1/n} + \sqrt{\left( \frac{Z}{A} \right)^{2/n} + 1} \right] \quad (1)$$

where  $\alpha$ ,  $n$ ,  $A$  are the material constants.  $Z$  is the Zener-Hollomon parameter, which is related to the deformation and strain rate, and expressed as:

$$Z = \dot{\epsilon} \exp \left( \frac{Q}{RT} \right) \quad (2)$$

where  $Q$  is the activation energy for hot deformation,  $R$  is the gas constant, and  $T$  is the absolute temperature at which the hot deformation occurs.

In the constitutive equations, Eqs. (1) and (2), material parameters  $\alpha$ ,  $n$ ,  $A$ , and  $Q$  can be calculated at different deformation strain. Then, the relationship between each material parameter with the true strain can be expressed with a 6th order polynomial for the investigated material as follows:

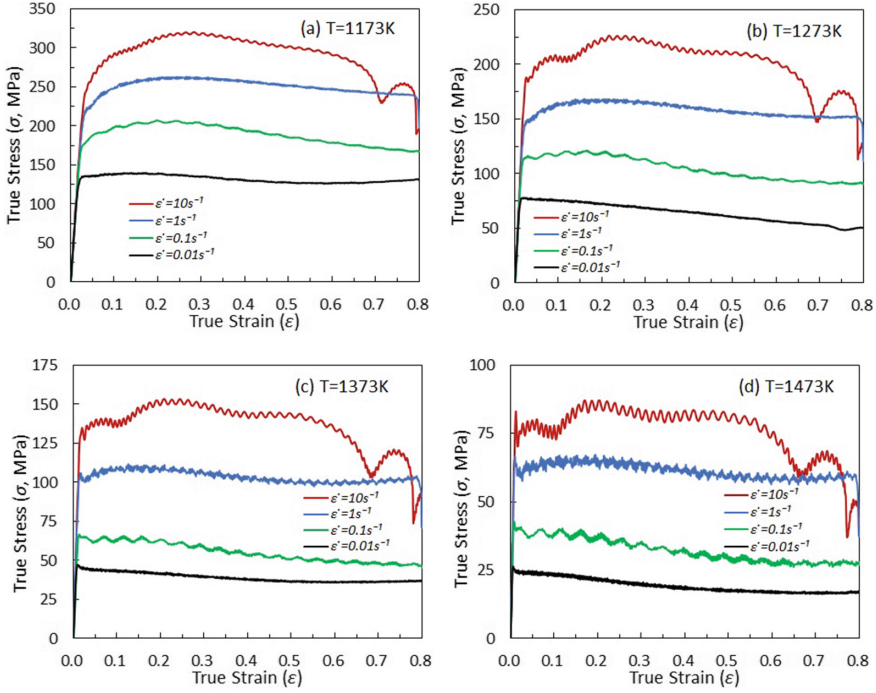


**Fig. 2.** True stress-True strain curves with different strain rates at different deformation temperatures of **a** 1173 K; **b** 1273 K; **c** 1373 K; **d** 1473 K.

$$\begin{aligned}
 \alpha &= 0.0115 - 0.0385\varepsilon + 0.4243\varepsilon^2 - 2.052\varepsilon^3 + 4.877\varepsilon^4 - 5.5286\varepsilon^5 + 2.3957\varepsilon^6 \\
 n &= 6.0846 - 34.604\varepsilon + 276.57\varepsilon^2 - 1185.3\varepsilon^3 + 2644.7\varepsilon^4 - 2902.3\varepsilon^5 + 1238.4\varepsilon^6 \\
 Q &= 584.33 - 3415.2\varepsilon + 37107\varepsilon^2 - 184186\varepsilon^3 + 442735\varepsilon^4 - 505894\varepsilon^5 + 220614\varepsilon^6 \\
 \ln A &= 50.419 - 301.5\varepsilon + 3284.1\varepsilon^2 - 16313\varepsilon^3 + 39234\varepsilon^4 - 44849\varepsilon^5 + 19561\varepsilon^6
 \end{aligned} \tag{3}$$

### 3.3 Verification of Developed Constitutive Model

The predicted values are compared with experimental data at different deformation temperatures, strain rates and the true strain, shown in Fig. 3, in which the scattered hollow points are experimental data and the predicted curves (solid lines) are obtained from the constitutive model based on Eqs. (1), (2) and (3). It is clearly shown that the predicted flow stress curves are in good agreement with experimental data over the entire strain range, especially at lower strain rate (0.01 and 0.1 s<sup>-1</sup>).

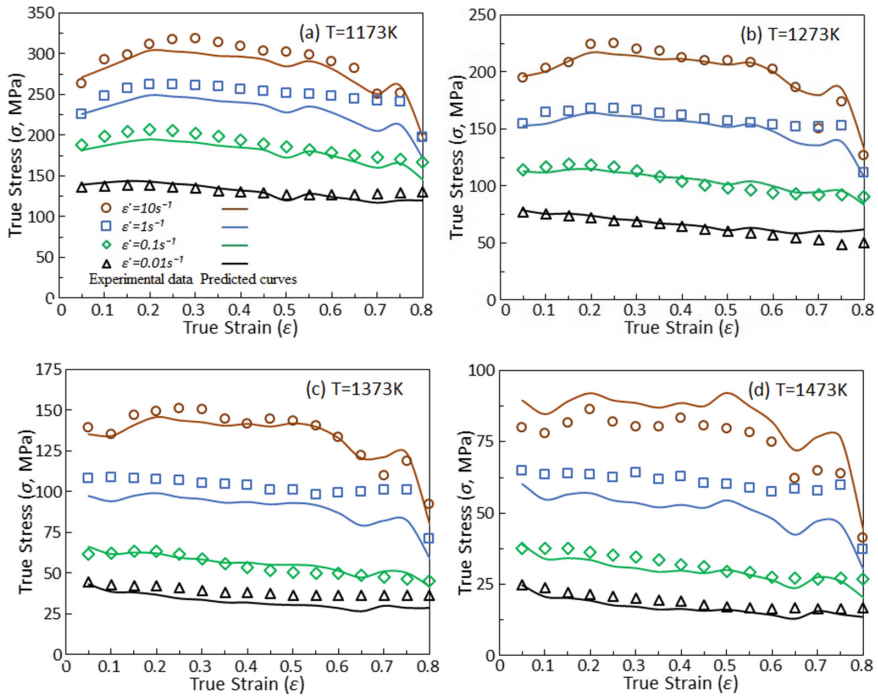


Fig. 3. Comparison of experimental data and predicted flow curves at different strain rate.

## 4 Conclusions

In this study, the deformation behavior and constitutive analysis of Cr23 FADSS were investigated with hot compression tests in high temperatures of 1173, 1273, 1373, and 1473 K, at different strain rates of 0.01, 0.1, 1 and  $10 \text{ s}^{-1}$  and at the strain of 0.8. Conclusions may be drawn as the followings:

- The deformation behavior of Cr23 FADSS is strongly influenced by the deformation temperature, strain rate and strain, and the flow stress decreases with increasing deformation temperature and decreasing strain rate.
- The dynamic recovery and the dynamic recrystallization are important softening mechanism in hot compression processing. There is a balance between the working hardening and softening at the strain rate  $1 \text{ s}^{-1}$  and when the true strain exceeded 0.25 at high deformation temperature.
- The Arrhenius-type constitutive model, developed with temperature, strain rate and strain, can be used to predict the flow stress, and the results showed good agreement between the modeled and the experimental data.

**Acknowledgements.** This work is funded by the Hebei Province Natural Science Foundation (No. E2013402064) and the Department of Education of Hebei Province (ZD20131049).



## References

1. Lo, K.H., Shek, C.H., Lai, J.K.L.: Recent developments in stainless steels. *Mater. Sci. Eng. R Rep.* **65**(4), 39–104 (2009)
2. Zou, D.N., Han, Y., Zhang, W., Fan, G.W.: Phase transformation and its effects on mechanical properties and pitting corrosion resistance of 2205 duplex stainless steel. *J. Iron. Steel Res. Int.* **17**(11), 67–72 (2010)
3. Garzón, C.M., Tschiptschin, A.P.: EBSD texture analysis of a high temperature gas nitrated duplex stainless steel. *Mater. Sci. Eng. A* **441**(1), 230–238 (2006)
4. Cizek, P.: The microstructure evolution and softening processes during high-temperature deformation of a 21Cr–10Ni–3Mo duplex stainless steel. *Acta Mater.* **106**, 129–143 (2016)
5. Yang, Y., Yan, B.: The microstructure and flow behavior of 2205 duplex stainless steels during high temperature compression deformation. *Mater. Sci. Eng. A* **579**, 194–201 (2013)
6. Zou, D.N., Wu, K., Han, Y., Zhang, W., Cheng, B., Qiao, G.J.: Deformation characteristic and prediction of flow stress for as-cast 21Cr economical duplex stainless steel under hot compression. *Mater. Des.* **51**, 975–982 (2013)



# Material Strength Degradation Experiment and Statistical Expression Under Cyclic Loading

Liyang Xie<sup>1</sup>(✉), Hongyi Ma<sup>1</sup>, and Guoliang Xu<sup>2</sup>

<sup>1</sup> Northeastern University, 110819 Shenyang, China  
lyxie@me.neu.edu.cn

<sup>2</sup> Beijing Strength Environment Institute, 100000 Beijing, China

**Abstract.** Cyclic loading leads to material strength degradation gradually until fatigue fracture occurs. Material strength degradation path is significant to fatigue life prediction and/or fatigue reliability estimation. Since the stochastic attributes of material strength, fatigue damage and fatigue life, material strength degradation test data are the type of partially left-censored. It makes material strength degradation behavior description difficult. The present paper presents a method to estimate residual strength distribution after  $n$  times of cyclic stress application, in which the strength degradation information contained by the early failed specimens is converted to equivalent residual strength at the expected cycle number. The strength degradation information conversion is based on an assumption that the residual strength is normal distributed, and the residual strength data are roughly symmetrical to the median. Such obtained residual strength probability density function and strength degradation path can be applied to predict fatigue life and evaluate reliability.

**Keywords:** Fatigue damage · Residual strength · Equivalent strength · Strength degradation path

## 1 Introduction

Strength is important material property. Under the action of cyclic stress higher than fatigue endurance strength, material strength will degrade continuously with fatigue damage accumulation. Since fatigue fracture occurs on residual strength being less than applied stress, strength degradation path directly affects the time of fatigue failure occurring. Since both material strength and the residual strength after a certain number of stress cycles are random variables, strength degradation path has to be tested with several groups of specimens subjected to different number of stress cycles (corresponding to different life ratios), respectively, by which the residual strength can be measured after different numbers of cyclic loading. Besides, since the randomness of fatigue life, some specimens may fail before the assigned stress cycle number, that produces left-censored strength data and make the corresponding residual strength measurement impossible.

Traditionally, residual strength estimation is made according to survived specimens only. That is, early failed specimens are not accounted for residual strength evaluation. That is obviously not reasonable, especially when the assigned cycle number at which the residual stress is tested is not much less than the mean life under the related stress level.

## 2 Material Residual Strength Experiment Under Cyclic Loading

Strength detection is a kind of destructive test. Residual strength test is usually conducted under several different life fractions such as  $n_i/N = 0.5, 0.6, 0.7, 0.8$  and  $0.9$ , respectively. Where  $n_i$  stands for the cycle numbers at which residual strength is detected,  $N$  stands for fatigue life under a suitably assigned cyclic stress level. Normally, it is assumed that residual strength is a function of life fraction (or the Miner cumulative damage  $n/N$ ) and cyclic stress level, and the cyclic stress level should be suitable to yield the interested fatigue life, e.g. high cycle fatigue or low cycle fatigue.

According to the regulation mentioned above, several metallic material residual strength experiments are performed. Test results from one of the experiments conducted under 240 MPa (amplitude of reversal cyclic stress), obtained from several groups of specimens designed to measure the residual strengths after different number of stress cycles are shown.

Shown in Fig. 1 is the fatigue life distribution of the material under reversal cyclic stress ( $\sigma_a = 240$  MPa). Because of the randomness of fatigue life under given cyclic stress level, there are normally two types of data, i.e. residual strength data of the specimens survived to the assigned cycle numbers and life data of the early failed specimens.

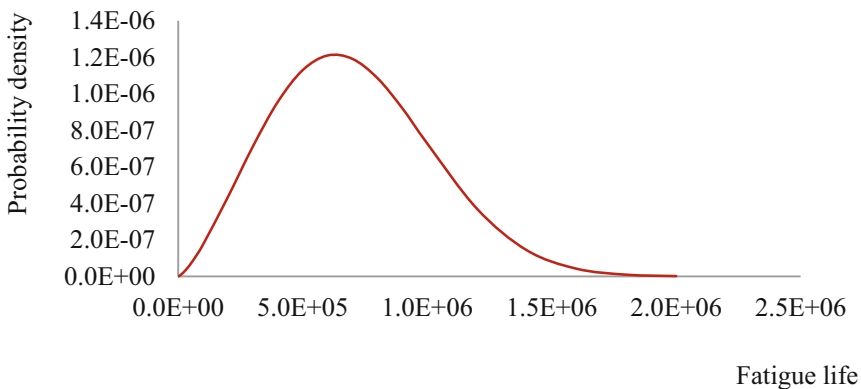
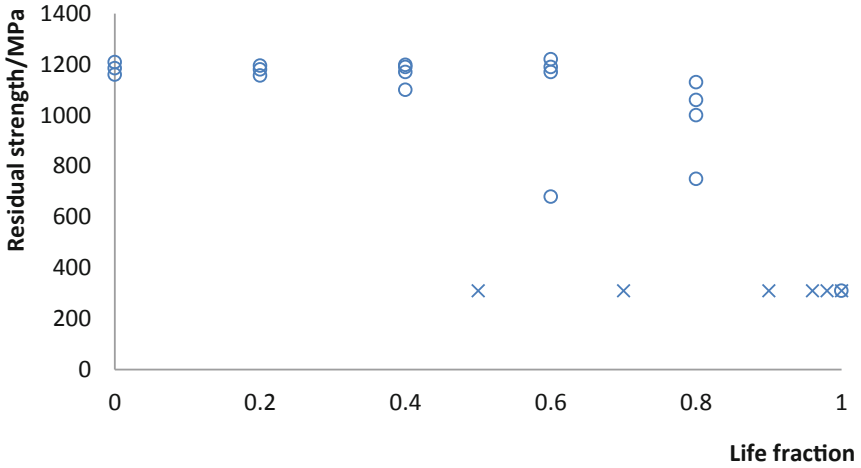
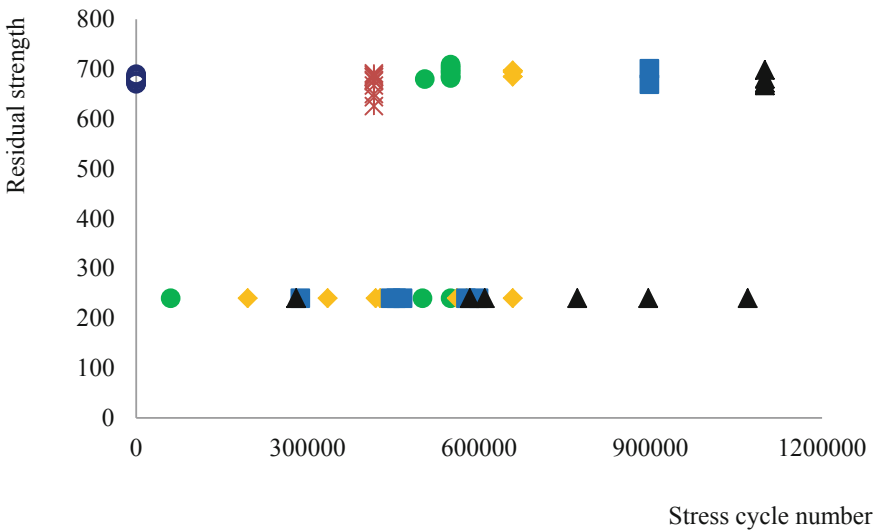


**Fig. 1.** Fatigue life distribution under cyclic stress ( $\sigma_a = 240$  MPa)



(a) o – residual strengths of survived specimens, x – lives early failed specimens



(b) Fatigue life (the lower line of points) and residual strength (the upper points)

**Fig. 2.** Test data—residual strength and fatigue life

Two typical groups of test results are shown in Fig. 2. Figure 2a shows that one specimen fails before the assigned life fraction 0.6, one specimen fails before the assigned life fraction 0.8, etc. Therefore, for the five specimens intended to measure the residual strength at the life fraction 0.8, only four residual strengths are obtained, the other one fails before this life fraction and the information provided is that its strength has degraded to the applied stress level before the life fraction.

### 3 Residual Strength Statistical Analysis and Strength Degradation Fitting

To fit the residual strength curve from the partial left-censored test data, appropriate statistical method is necessary. The situation of residual strength estimation is that, besides the specimens survived to the assigned stress cycles (the respective life fractions or cycle ratios) by which the residual strength can be detected, there are also some short life specimens failed before the assigned stress cycles. That is, no residual strength data corresponding to the assigned life fraction are available for these specimens. The short life specimens, i.e. the specimens with their fatigue lives shorter than the cycle numbers corresponding to assigned cycle ratio make the strength degradation curve fitting much more difficult or complicated, since such specimens cannot yield residual strength at the previously assigned stress cycles. On the other hand, no matter long or short the fatigue lives are, all the specimens contribute strength degradation information. How to get the implied strength degradation information from the short life specimens is the key to fit strength degradation curve.

To make use of the residual strength information contained by the early failed specimens, the present paper proposes a rule to treat the data as following. Taking the test results at a particular stress cycle number  $N$  as an example, the specimens with the fatigue lives longer than  $N$  provide residual strength directly, the early failed specimens provide fatigue lives. The information contained by the specimens with the fatigue lives shorter than  $N$  are converted into equivalent residual strengths at the cycle number  $N$  according to “median mirror image” assumption. For instance, five specimens are assigned to test residual strengths after cyclic stress acting  $N$  cycles. The test results are that there are four specimens have fatigue lives longer than  $N$  and thus four residual strengths are measured, the other specimen has a fatigue life shorter than  $N$ . The four residual strengths are 1198, 1190, 1170 and 1100, respectively. If there were five residual strengths normal distributed, the five values should be 1198, 1190, 1170, 1100 and  $S_5$ . Here, 1170 is the sample median. The “median mirror image” assumption means that all the data are roughly symmetrically located beside the median. That is, it is reasonable to let the difference  $S_4 - S_5 = S_1 - S_2$  now that no other information available. Therefore, let  $S_5 = S_4 - (S_1 - S_2) = 1092$ . Consequently, the residual stress at  $N$  can be estimated according to the five residual strength data including the equivalent one converted from the life data.

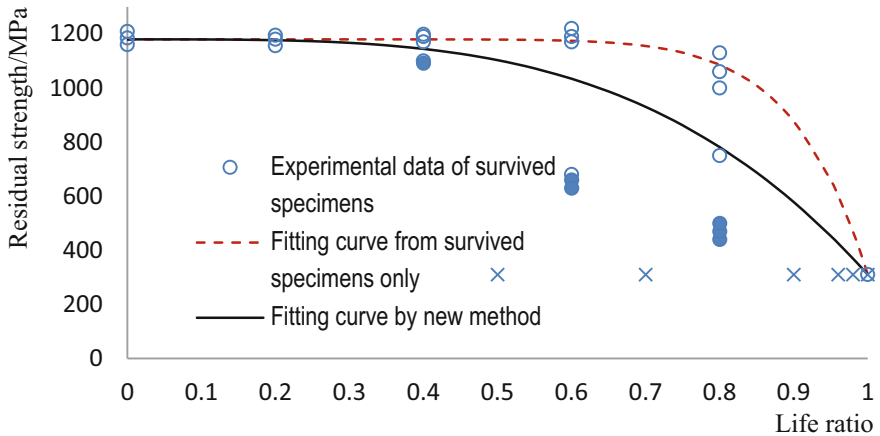


**Fig. 3.** Test data (o—residual strengths of survived specimens, X—lives measured with expected life ratio of short life specimens) and fitted residual strength curves by different methods

Another example is that, six specimens are assigned to test residual strengths after cyclic stress acting  $N$  cycles. The situation is that there are four specimens have the fatigue life longer than  $N$  and the respective residual strengths are measured, the other two specimens have fatigue lives shorter than  $N$ . The four residual strengths are 1060, 1030, 1000 and 750. If there were six residual strengths normal distributed, the five values should be 1060, 1030, 1000, 750,  $S_5$  and  $S_6$ . Here,  $(1000 + 750)/2 = 875$  is the sample median. By the “median mirror image” assumption,  $S_5 - S_6 = S_1 - S_2$ ;  $S_4 - S_5 = S_2 - S_3$ . Therefore,  $S_5 = 680$  and  $S_6 = 650$ .

Applying the real residual strength data directly detected and the equivalent residual strength converted from the early failed specimens, reasonable strength degradation curve can be fitted, shown in Fig. 3 in contrast to the strength degradation curve fitted according only to the real residual strength data.

## 4 Conclusions

For residual strength experiments under cyclic loading, the residual strength information contained by early failed specimens play an important role. This paper proposes a method to convert the life data of the early failed specimens into equivalent residual strengths. It is based on the so called “median mirror image” rule by which the residual strength data, including the equivalent strength data, are roughly symmetrically scattered around the median. It is shown that the material strength degradation curve fitted by the new method is considerably different from that fitted with the real residual strength data.

**Acknowledgements.** This research is subsidized by the Natural Science Foundation of China “Research on reliability theory and method of total fatigue life for large complex mechanical structures” (Grant No. U1708255) and The Collaborative Innovation Center of Major Machine Manufacturing in Liaoning.



# Study of Effect of Phase Separation on Pores Orientation of Electrospun Nanofibre

S. O. Alayande<sup>1</sup>✉, E. O. Dare<sup>2</sup>, J. N. Edokpayi<sup>3</sup>, O. A. Adeyemi<sup>1,4</sup>,  
Adeiwale Adegbenjo<sup>4</sup>, and T. A. M. Msagati<sup>5</sup>

<sup>1</sup> First Technical University, Ibadan, Nigeria  
{samson.alayande, oaadeyemi}@tech-u.edu.ng

<sup>2</sup> Federal University of Agriculture, Abeokuta, Nigeria  
dare3160@hotmail.com

<sup>3</sup> University of Venda, Thohoyandou 0950, South Africa  
joshuaedos@gmail.com

<sup>4</sup> University of Johannesburg, Johannesburg, South Africa  
waleeleect@gmail.com

<sup>5</sup> University of South Africa, Pretoria, South Africa  
msagatam@unisa.ac.za

**Abstract.** Nanoporous fibres are advanced materials with wide application in drug delivery, sensor, filtration, membrane, wound dressing, encapsulation and catalysis. Known mechanisms for pore formation in electrospun are temperature-induced phase separation (TIPS) and vapour induced phase separation (VIPS), these are crucial to application and classification. The underestimated factor electrospinning parameter (polymer concentration) resulted in polymer and solvent rich phases which are capable of manipulating orientation in the jet. In view of this, expanded polystyrene was electrospun at various concentration and voltage. The morphology of resultant fibres were examined with Secondary Electron (SE) and Back Scattering Electron (BSE) detectors, both revealed clear porous micrographs. The resultant phases formed during elongation override popular mechanism in the science of pore formation in electrospun fibre. Finally, pathway for polymer re-use in membrane science is presented.

**Keywords:** Nanofibre · Electrolysis · Pore orientation · Concentration · Mechanism

## 1 Introduction

A versatile, flexible and simple way of producing micro/nano fibres with hierarchical porosity in an organized or random manner is electrospinning technique [1–3]. The basic principle of electrospinning is well discussed in various text and reviews [4]. A notable feature of resultant fibres is the formation of pores. In view of this, electrospinning has found application in catalysis [4], filtration, drug delivery, encapsulation and membrane. Understanding of pore science in the fibre will promote application in tissue engineering, regenerative medicine and drug delivery.



Micrographs of porous fibres showed that pore formation does not solely depend on long acclaimed principles TIPS, VIPS, and breath figure, it is also dependent on polymer concentration [5]. Pore morphology examination using either SE or BSE was validated, either of the detectors can also be used for examination of porous materials. Finally, effect of polymer-rich phase as a principle in science of in electrospun fibre is established. Another pathway for re-use of EPS is presented in membrane technology (Fig. 1).

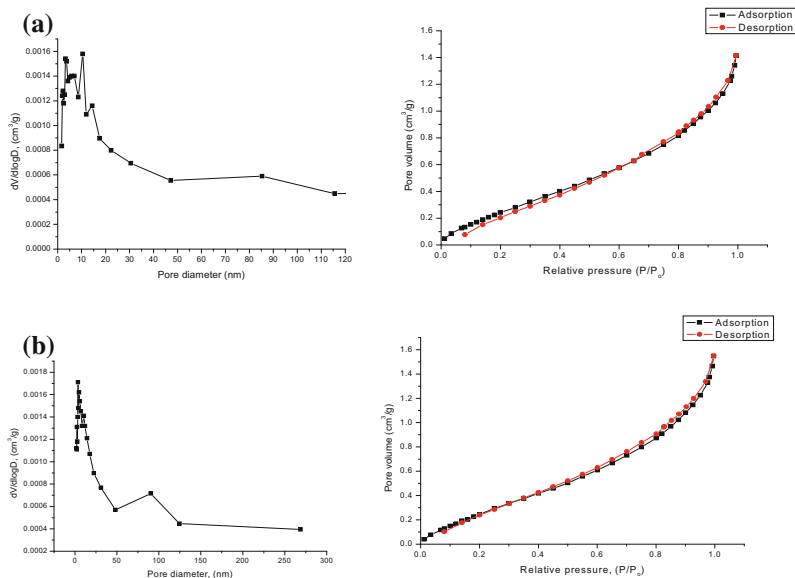


**Fig. 1.** **a** Pore distribution and Nitrogen adsorption-desorption isotherms of beaded fibre. **b** Pore distribution and Nitrogen adsorption-desorption isotherms of Porous fibre

## References

1. Lu, P., Xia, Y.: Maneuvering the internal porosity and surface morphology of electrospun polystyrene yarns by controlling the solvent and relative humidity. *Langmuir* **29**, 7070–7078 (2013)
2. Pierini, F., Lanzi, M., Nakielski, P., Kowalewski, T.A.: Electrospun polyaniline-based composite nanofibers: tuning the electrical conductivity by tailoring the structure of thiol-protected metal nanoparticles. *J. Nanomate* (Article ID 6142140), 1–8 (2017)
3. Pierini, F., Lanzi, M., Nakielski, P., Pawłowska, S., Zembrzycki, K.: Tomasz Aleksander Kowalewski Electrospun poly(3 hexylthiophene)/poly(ethylene oxide)/graphene oxide composite nanofibers: effects of graphene oxide reduction *Polym. Adv. Technol.* **27**, 1465–1475 (2016)
4. Ramakrishna, S., Fujihara, K., Teo, W.-E., Lim, T.-C., Ma, Z.: An Introduction to Electrospinning and Nanofibers, pp. 1–103. World Scientific Publishing Co. Pte. Ltd. (2005)
5. Alayande, S.O.: The development of nanoporous membranes for crude oil sorbent and spillage remediation (Ph.D. Thesis) Federal University of Agriculture, Abeokuta, Nigeria, pp. 1–305 (2015)



# Deformation Model of $[\pm 45]_S$ Cross-Ply Fiber Reinforced Plastics Under Tension

V. N. Paimushin<sup>1,2</sup>(✉), R. A. Kayumov<sup>1,3</sup>, D. V. Tarlakovskii<sup>4,5</sup>,  
and S. A. Kholmogorov<sup>1</sup>

<sup>1</sup> Kazan National Research Technical University Named After A.N. Tupolev,  
K.Marks str. 10, 420111 Kazan, Russia

vpajmushin@mail.ru

<sup>2</sup> Kazan Federal University, Kremlyovskay str. 18, 420008 Kazan, Russia

<sup>3</sup> Kazan State University of Architecture and Building Construction,  
Zelenaya Str. 1, 420043 Kazan, Russia

<sup>4</sup> Lomonosov Moscow State University, Leninskie Gory 1,  
119991 Moscow, Russia

<sup>5</sup> Moscow Aviation Institute (National Research University),  
Volokolamskoe Shosse 4, 125993 Moscow, Russia

**Abstract.** A series of experiments on tensile testing of specimens from cross-ply reinforced plastics made from unidirectional tape ELUR-P and cold-curing binder XT-118 and stacking sequence  $[\pm 45^\circ]$  were carried out. Tests were carried out on different specimens at three maximum stress values. It was established that the total axial strain can be represented as a sum of four components, including: reversible strain, residual (irreversible) strain, irreversible creep deformation and reversible creep strain due to the viscoelastic properties of the epoxy. The questions of the choice of relations for the description of the components of the strains and the identification of their mechanical characteristics are considered. The conclusion is formulated that for a hereditarily elastic model, one can use the Abel creep kernel and determine its parameters from an experiment for long holding times. To determine the parameters included in the irreversible creep relations, we use the results obtained immediately after the start of exposure at maximum stresses, and a method for their determination is proposed. After this is the initial modulus of elasticity. At the last stage, after determining the rheological characteristics and the initial modulus of elasticity, the nonlinear elastic reversible part of the strain can be singled out.

**Keywords:** Unidirectional CFRP · Specimen · Residual strain · Creep strain · Secant modulus of elasticity · Identification · Creep kernel

## 1 Introduction

Problems devoted to creep strain have received much attention from many researchers (see, in particular, [1–10]). An analysis of the work on the experimental study of the deformation of fiber reinforced composites shows that under shear stress, creep begins to manifest itself even at times calculated in minutes and even seconds.

To describe it, the model of a visco-elastic (hereditarily elastic) material is considered to be the most adequate for experiments. Its peculiarity is that after removal of the load, the creep deformations in the limit disappear. However, experiments conducted by the authors show that, nevertheless, some of the creep deformations are not restored. This suggests that this part of the creep deformations should be described by ratios of the incremental creep theory of the aging theory type. To determine the creep strain and the parameters of its models, the most convenient is an experiment conducted over a long period of time under constant load. However, it is impossible to separate the hereditarily elastic part of the strain and the irreversible strain of the creep. The following is one of the approaches for solving the problem of separation of these strains. It is also shown that traditional relations for determining the initial modulus of elasticity can lead to a significant underestimation of it, therefore, it is necessary to use modernized relations.

## 2 Experimental Results

To clarify the structure of creep strain, two series of experimental tensile studies of specimens from cross-ply fiber reinforced plastics, were carried out. In such specimens, under creep conditions, the creep properties are most pronounced. In this connection, the specimens were subjected to testing under two loading programs.

The first of them consists of three stages: tension up to stress  $\sigma_{\max}$  (35, 45 and 55 MPa), free unloading for  $\sigma = 0$  and further exposure (see Fig. 1). The second loading program consists of four stages: tension up to stress  $\sigma_{\max} = 45$  MPa, holding for  $t_e$  hours, free unloading to  $\sigma = 1.5$  MPa, and subsequent exposure for three days (see Fig. 2).

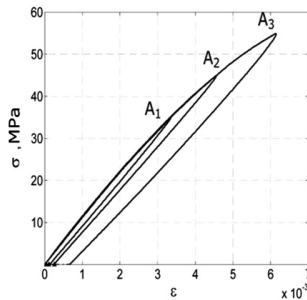


**Fig. 1.** First loading program.

From these results it follows that in addition to the elastic and hereditarily elastic components of strain, irreversible residual strain are formed.

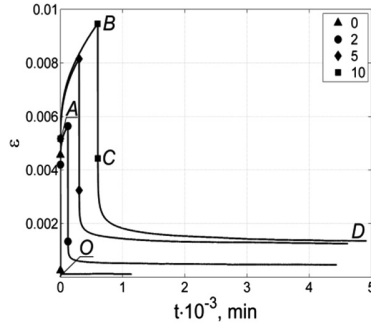


Fig. 2. Second loading program.

### 3 Methodology for Identification Deformation Model Parameters

Based on the analysis of the author's experiments and literature, it can be assumed that the full axial strain with sufficient accuracy can be represented as

$$\varepsilon = \frac{\sigma}{E_0} + \varepsilon_s^r + \varepsilon^v + \varepsilon^{nel} \quad (1)$$

Here  $\varepsilon^{nel}$ —the nonlinearly reversible part,  $\varepsilon_s^r$ —irreversible creep strain,  $\varepsilon^v$ —viscoelastic part of the strain.

In the following, we introduce a generalization of Kachanov's hypothesis [11], namely, we will assume that all components of the strain develop independently of each other, i.e.

$$\varepsilon^{nel} = \varepsilon^{nel}(\sigma), \quad \varepsilon^v = \int_0^t f(\sigma) H(\sigma, t - \tau) d\tau, \quad d\varepsilon_s^r/dt = F(\sigma, \varepsilon_s^r) \quad (2)$$

We first consider the problem of identifying the parameters of the hereditary model of deformation and the model of irreversible creep. Further reasoning will be based on the analysis of the results of experiments conducted according to the scenario corresponding to the second loading program (see Fig. 3).

First, by the time  $t_1$ , specimens are loaded to the maximum stress (in Fig. 3 this corresponds to point  $A_1$ ), then at this stress value the specimen is kept for some time  $\Delta t_m = t_m - t_1$ . Let us denote the experimental values of strain  $\varepsilon_1, \varepsilon_2, \varepsilon_3, \dots$  at points  $A_1, A_2, A_3, \dots$  at time points  $t_1, t_2, t_3, \dots$ . Then

$$\Delta_{ij}\varepsilon = [\varepsilon^v(\sigma_{\max}, t_i) + \varepsilon_s^r(\sigma_{\max}, t_i)] - [\varepsilon^v(\sigma_{\max}, t_j) + \varepsilon_s^r(\sigma_{\max}, t_j)] \quad (3)$$

To separate the creep strain and hereditary elasticity, we accept the experimentally confirmed hypothesis that the damping rate of irreversible creep strain occurs faster

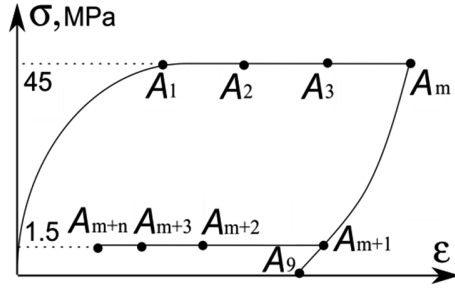


Fig. 3. Stress-strain diagram of second loading program.

than the damping rate of hereditary elasticity strain. Therefore, provided that  $t_m > t_i, t_j \gg t_1$ , we can write down with a small error:

$$\Delta_{ij}\varepsilon^{\text{exp}} = \varepsilon_i^{\text{exp}} - \varepsilon_j^{\text{exp}} \approx \varepsilon_i^v - \varepsilon_j^v, \quad t_i, t_j < t_m \tag{4}$$

Usually in experiment law  $\sigma = \zeta(t)$  is known. Then

$$\varepsilon_i^v = \int_0^{t_i} f(\zeta(\tau)) H(\zeta(\tau), t_i - \tau) d\tau \tag{5}$$

We approximate  $H$  by any system of functions  $H_k$

$$H(t - \tau) = \sum_{k=1}^K H_k(\alpha_k, t - \tau) \tag{6}$$

From (6), an overdetermined system of algebraic equations follows. By minimizing its quadratic residual constants  $\alpha_k$  are found. The authors of the experiments used the Abel's kernel:

$$H(t - \tau) = Bt - \tau^{-\alpha}, \quad 0 < \alpha < 1, \quad B > 0 \tag{7}$$

To describe the process of irreversible creep the theory of aging was adopted in one of the simplest variants regarding stress:

$$d\varepsilon_s^r/dt = \chi_0\sigma/(1 + \chi_1(\varepsilon_s^r)^m) \tag{8}$$

At small times, it is necessary to write down relations (4) already with allowance for irreversible creep strain. Minimizing the quadratic discrepancy between  $\Delta_{ij}\varepsilon^{\text{exp}}$  and  $\Delta_{ij}\varepsilon$ , we define the parameters included in relations (8).

The results of processing the experiments (see Fig. 4, in which the results of the experiment are indicated by markers, the solid line shows the results of the calculation) showed the acceptability of the assumptions used and the efficiency of the proposed approach. The solution to the problems described above gave the following results:

$$B = 6.0878 \cdot 10^{-7} \text{ sec}^{\alpha-1} / \text{MPa}, \alpha = 0.6151, \chi_0 = 1.2485 \cdot 10^{-7} (\text{sec} \cdot \text{MPa})^{-1},$$

$$\chi_1 = 1.8764 \cdot 10^4, m = 21.1 \quad (9)$$

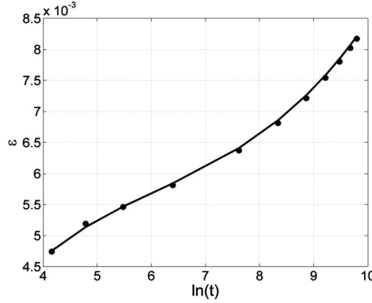


**Fig. 4.** Second loading program.

After that, the elastic modulus  $E_0$  can be determined from the increments of the stresses and the increments of the elastic part of the deformations over the initial small time interval. To determine the latter, viscoelastic deformations and irreversible creep deformations were subtracted from the total deformations. We note the following fact obtained from numerical experiments with creep kernel parameters with parameters (9). It turned out that for viscoelastic bodies described by models with weakly singular creep kernels, even at sufficiently high loading rates, the change in strain  $\Delta \varepsilon^v$  can be on the order of tens of percent of the total strain increment  $\Delta \varepsilon$ . Therefore, use to determine the elastic modulus  $E_0$  in accordance with known standards of the expression

$$E_0 = \Delta \sigma / \Delta \varepsilon \quad (10)$$

gives understated values. It necessary to determine from following relation

$$E_0 = \Delta \sigma / (\Delta \varepsilon - \Delta \varepsilon^v - \Delta \varepsilon_0^r) \quad (11)$$

Further, the problem of constructing the dependence of reversible strain  $\varepsilon^{nel}$  on stresses was considered. To find this dependence, we used the results of experiments obtained at stresses of 35, 45, 55 MPa. Values were from the following expression

$$\varepsilon^{nel}(\sigma) = \varepsilon - \left( \frac{\sigma}{E_0} + \varepsilon_0^r(\sigma, t) + \varepsilon^v(\sigma, t) \right) \quad (12)$$

The calculation results are shown in Table 1.

**Table 1.** Reversible strain

$\sigma_{\max}$ , MPa	$\varepsilon^{nel} \cdot 10^4$
35	2.356
45	6.883
55	10.105

Various types of approximations  $\varepsilon^{nel} = \varepsilon^{nel}(\sigma)$  were tested. Analysis of the results of numerical calculations leads to the conclusion that it is possible to use a variant of a piecewise continuous function, similar to the elastic-plastic case of deformation. Namely, there are no these strain up to a certain value  $\sigma = \sigma_{kr}$ , and then they develop depending on the stresses. This can be explained by the fact that at this stress the loss of stability of the phases of the composite begins. Of the functions considered, the most successful was hyperbolic (in Fig. 5 it is marked with a bold line). Expression for below:

$$\varepsilon^{nel} = a + c\sigma/(1 + b\sigma), \quad a = -0.00632, \quad c = 0.000643/\text{MPa}, \quad b = 0.0696/\text{MPa}$$

$$\sigma_{kr} \approx 31 \text{ MPa}$$

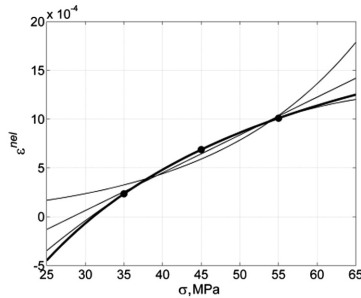


**Fig. 5.** Results of approximation.

**Acknowledgements.** The research results were obtained in the framework of the fulfilment of the state task of the Ministry Science and High Education of Russia No. 9.5762.2017/VU (project No. 9.1395.2017/PCh) and supported by Russian Science Foundation (project No. 19-19-00059).

## References

1. Rabotnov, U.N.: Creep of Structural Elements. Nauka, Moscow (1966)
2. Rzanicun, R.A.: Creep Theory. Gosstroyizdat, Moscow (1968)
3. Kachanov, L.M.: Creep Theory. Gos.izd.fiz.-mat.lit, Moscow (1960)

4. Udin, V.E., Volodin, V.P., Gubanova, G.N.: Features of the viscoelastic behavior of carbon plastics on the basis of the polymer matrix: a model study and calculation. *Mech. Compos. Mater.* **5**, 656–669 (1997)
5. Kayumov, R.A., Teregulov, I.G.: Structure of defining relations for hereditary-elastic materials reinforced with hard fibers. *J. Appl. Mech. Tech. Phys.* **3**, 120–128 (2005)
6. Giannadakis, K., Mannberg, P., Joffe, R., Varna, J.: The sources of inelastic behavior of Glass Fibre/Vinylester non-crimp fabric  $[\pm 45]_S$  laminates. *J. Reinf. Plast. Compos.* **30**(12), 1015–1028 (2011)
7. Paimushin, V.N., Kholmogorov, S.A., Kayumov, R.A.: Experimental investigation of residual strain formation mechanisms in composite laminates under cycling loading. *UCHENYE ZAPISKI KAZANSKOGO UNIVERSITETA-SERIYA FIZIKO-MATEMATICHESKIE NAUKI* **159**(4), 473–492 (2017)
8. Paimushin, V.N., Kholmogorov, S.A.: Physical-mechanical properties of a fiber-reinforced composite based on an ELUR-P carbon tape and XT-118 binder. *Mech. Compos. Mater.* **54**(1), 2–12 (2018)
9. Van Paeppegem, W., De Baere, I., Degrieck, J.: Modelling the nonlinear shear stress–strain response of glass fibre-reinforced composites. Part I: experimental results. *Compos. Sci. Technol.* **66**, 1455–1464 (2006)
10. Kayumov, R.A.: The extended task of identifying the mechanical characteristics of materials according to the results of structural tests. *Mech. Solids* **2**, 94–105 (2004)
11. Kachanov, L.M.: About failure time in creep conditions. *Izv. AN USSR. Otd.tehn.nauk* **8**, 26–31 (1958)





# Segregation Resistance, Stiffness and Toughness of CNT Nanomodified Self Compacted Concrete

Myrsini Maglogianni<sup>1</sup>(✉), Panagiotis A. Danoglidis<sup>1</sup>,  
Maria G. Falara<sup>1</sup>, and Maria S. Konsta-Gdoutos<sup>2</sup>

<sup>1</sup> School of Engineering, Democritus University of Thrace,  
671 00 Xanthi, Greece

myrsinimag@gmail.com

<sup>2</sup> Department of Civil Engineering, College of Engineering,  
University of Texas at Arlington, Arlington, TX, USA

**Abstract.** Self-Compacting Concrete (SCC) reinforced with well dispersed carbon nanotubes (CNTs) was successfully produced. The segregation resistance of fresh CNT-SCC mixture was assessed by conducting a non-destructive electrical resistivity technique. The addition of CNTs resulted in a more homogenous mixture as the CNT-SCC exhibited consistent resistivity values between different electrode pairs along the investigated column. The reinforcing efficiency of the CNTs was also demonstrated by improvements in flexural strength (53%), Young's modulus (68%), and flexural toughness (38%).

**Keywords:** Segregation resistance · Carbon nanotubes · Flexural strength · Young's modulus · Toughness

## 1 Introduction

While fibers are specified for an enhanced crack-bridging ability and to improve some mechanical properties of concrete matrix, inclusion of such fibers negatively affects the workability characteristics of SCC [1]. In this study, according to the author's knowledge, it is the first time that the evaluation of the homogeneity and flexural performance of a new type of SCC reinforcing with highly dispersed CNTs at amount of 0.1 wt%, took place.

## 2 Results

An electrical resistivity test was conducted to evaluate the segregation resistance of fresh SCC [2]. Three groups of mixtures were casted in  $4 \times 4 \times 16$  cm molds: SCC under intense segregation; homogenous SCC and 0.1 wt% CNT-SCC. The resistance was then measured in three electrode pairs, AB, BC and CD, along the column (Fig. 1a) with the nanomodified mixture exhibiting the lower spread in resistivity between the three parts.

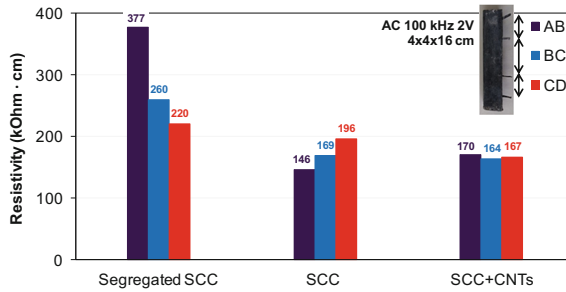


**Fig. 1.** Electrical resistivity of the three parts, AB, BC and CD of SCC mixture reinforced with 0.1 wt% CNTs

The mechanical properties of SCC nanocomposites were experimentally investigated by four-point bending tests on  $7 \times 8 \times 38$  cm prismatic specimens [3, 4]. The CNT network enables the stress transfer from the surrounding SCC matrix to the nanotube, thus enhancing the load bearing capacity of the nanomodified SCC matrix and resulting in increases in flexural strength (53%) Young's modulus (68%) and flexural toughness (38%) (Table 1).

**Table 1.** Mechanical properties of 28d SCC and 0.1 wt% CNT-SCC nanocomposites

Mix	Flexural strength (MPa)	Young's modulus (GPa)	Flexural toughness (MPa)
SCC	5.9	23.4	232
SCC + CNTs 0.1 wt%	9.0	39.4	372

### 3 Conclusions

In this study, the effect of highly dispersed 0.1 wt% CNTs on the segregation resistance, strength, stiffness and toughness of SCC was successfully evaluated. The experimental findings of electrical resistivity measurements indicated that the addition of CNTs was more efficient in improving the segregation resistance and the homogeneity of SCC mixture. The fiber-like structure of the CNTs and the raising dominance of a crack-bridging mechanism at the nanoscale results in exceptional increases in flexural strength (53%), Young's modulus (68%) and flexural toughness (38%).

### References

1. El-Dieb, A.S., Reda Taha, M.M.: Flow characteristics and acceptance criteria of fiber-reinforced self-compacted concrete (FR-SCC). *Con. Build. Mater.* **27**, 585–596 (2012)
2. Mesbah, H.A., Yahia, A., Khayat, K.H.: Electrical conductivity method to assess static stability of self-consolidating concrete. *Cem. Concr. Res.* **41**(5), 451–458 (2011)

3. ASTM C293/C293M—16 Standard Test Method for Flexural Strength of Concrete (Using Simple Beam With Center-Point Loading)
4. American Concrete Institute, Report on Fiber Reinforced Concrete, ACI 544.1R-96 (1996)



# High Temperature Creep Properties of Cast Cobalt-Based Superalloys: A Comparison

Marie Kvapilova<sup>1,2</sup>(✉), Vaclav Sklenicka<sup>1,2</sup>, Petr Kral<sup>1,2</sup>,  
and Jiri Dvorak<sup>1,2</sup>

<sup>1</sup> Institute of Physics of Materials, Academy of Sciences of the Czech Republic,  
Zizkova 22, 616 62 Brno, Czech Republic

kvapilova@ipm.cz

<sup>2</sup> CEITEC IPM, Institute of Physics of Materials,  
Academy of Sciences of Materials, Zizkova 22, 616 62 Brno, Czech Republic

**Abstract.** Cast cobalt-based superalloys have already found applications in the glass industry to construct glass shaping tools. The present study deals with the high temperature characterization of the two cast cobalt-based CoNb and CoTa superalloys which have been developed for precision casting of a rotary fibre-glass spinner disc for glass industry. The superalloys have been characterized through constant load creep tests at 1000, 1050 and 1100 °C in a tensile stress range from 20 to 100 MPa, with the aim to simulate the variation of mechanical properties occurring in a rotary fibreglass spinner disc at operational conditions. The results have been compared and discussed, with the aim to link the difference in creep properties to the evolution of creep damage and fracture in superalloys. It was found that the CoNb superalloy possesses longer creep life compared to the CoTa superalloy under the same loading conditions. Fractographic investigations of the creep fractured specimens of the examined superalloys revealed that the dominating creep fracture of the CoTa is of the ductile transgranular dimple fracture mode due to a loss of an external section of specimen (necking). By contrast, the final brittle fracture in the CoNb superalloys occurs via relatively fast propagation of the longest cracks after the ultimate state of creep damage is reached.

**Keywords:** Cobalt-based superalloys · Creep damage and fracture · Breakage of primary carbides

## 1 Introduction

Creep resistant nickel-based superalloys are currently used for the rotary fibreglass spinner discs with perforated walls which transform a stream of molten glass into thermally insulating glass wool by a centrifugal process. However, cobalt-based superalloys, materials even more resistant to high temperature creep could give a longer service life of the spinner discs [1]. Therefore, two high temperature cast high-chromium refractory cobalt-based superalloys have been developed for an investment casting of spinner discs [2]. During service, spinner discs are exposed to high temperature and severe environment of molten glass. For safe usage, the understanding of the creep behaviour and damage evolution leading to the final fracture of a material is

essential. In our previous work [3] the analyses of the creep data of CoTa and CoNb superalloys indicate that the creep behaviour of these superalloys obeys Monkman-Grant relationship which can be explained by a close relationship between creep deformation and fracture processes. This successive work on the same CoTa and CoNb superalloys aims to link the difference in creep properties to the differences in chemical compositions or to the presence of diverse precipitates in the microstructure. This is considered as an essential step to tailor the cobalt superalloys chemical composition and heat treatment for high temperature applications in glass industry.

## 2 Materials and Methods

The superalloys were elaborated in PBS Velká Bíteš, a.s. Czech Republic. The chemical compositions and abbreviated names of the tested investment cobalt-based superalloys are listed in Table 1. The superalloys were selected to investigate the individual strengthening effect of Nb and Ta additions. The superalloys were melted in an induction furnace and cast using an open furnace. Finally, the ingots were subjected to a homogenization annealing at 1150 °C for 90 min followed by air cooling.

**Table 1.** The chemical compositions (in wt%) and abbreviated names of tested Co-based superalloys.

Superalloy	Cr	Ni	W	C	Nb	Ta	Si	Mn	Fe	Co
CoNb	30.5	10.8	8.0	0.65	<b>2.48</b>	–	0.39	0.23	0.28	bal.
CoTa	29.3	23.0	7.0	0.60	–	<b>2.30</b>	1.0	0.22	4.9	bal.

Constant load creep tests in tension were carried out until the final fracture of the specimen [2]. Cylindrical creep specimens with a gauge of 50 mm in length and 3.5 mm in diameter were used in this study. The expected operational temperature of melted glass in the spinner discs is about 1050 °C. Therefore, the creep testing was conducted at 1000, 1050 and 1100 °C and at the different initial applied stresses  $\sigma$ . The details of creep testing and evaluation methods have been reported elsewhere [2, 3].

The microstructure of the studied superalloys in the as-received state and after creep exposures were observed by optical microscope, scanning electron microscope (SEM) and transmission electron microscope (TEM) [2]. Fractographic analyses of the creep damage and the fracture surfaces were performed by scanning electron microscope.

## 3 Results and Discussion

### 3.1 Creep Results

Representative standard creep curves of both superalloys at 1050 °C and the same value of the applied stress  $\sigma$  are shown in Fig. 1a. As demonstrated in Fig. 1a, the shape of standard creep curve for the CoTa superalloy differs considerably from that

conducted on the CoNb one. It is important to note that the standard creep curves in Fig. 1a do not clearly indicate the individual stages (like primary, stationary and tertiary) of creep [4]. However, these standard  $\varepsilon$  versus  $t$  curves can be easily replotted in the form of the instantaneous strain rate  $\dot{\varepsilon}$  versus time  $t$  as shown in Fig. 1b.

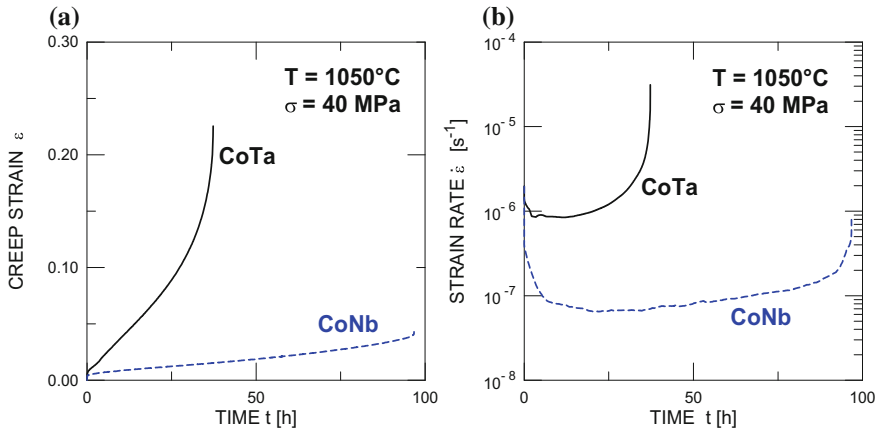


**Fig. 1.** Creep curves for both Co-based superalloys at  $1050^\circ\text{C}$  and  $40\text{ MPa}$ : **a** standard creep curves of strain  $\varepsilon$  versus time  $t$ , **b** modified creep curves of strain rate  $\dot{\varepsilon}$  versus  $t$ .

From Fig. 1b it is now clear that both curves exhibit a short primary stage in which strain rate  $\dot{\varepsilon}$  decreases with time, which has been attributed to strain hardening. The primary stage is followed by tertiary creep in which the strain rate  $\dot{\varepsilon}$  increases with time until the final fracture. In this stage the recovery rate and/or creep damage development may be high enough to balance strain hardening.

### 3.2 A Comparison of Creep Properties of the Superalloys

Significant differences were found in the “macroscopic” creep properties in the CoNb superalloy when compared to the CoTa superalloy under the same loading conditions. The results of creep tests carried out at three testing temperatures and selected applied stresses on both superalloys are summarized in Fig. 2. Inspection of Fig. 2 leads to three observations. First, the CoNb superalloy exhibits significantly better creep resistance than the CoTa one; the minimum creep rate  $\dot{\varepsilon}_m$  of the CoNb superalloy is less than that of the CoTa superalloy over all testing temperatures (Fig. 2a). Second, as depicted in Fig. 2b and in an agreement with previous results, the time to fracture (creep life)  $t_f$  of the CoNb superalloy is generally longer than that of the CoTa superalloy. Third, the strain to fracture  $\varepsilon_f$  of the CoTa superalloy is higher than that of the CoNb (Fig. 2c).

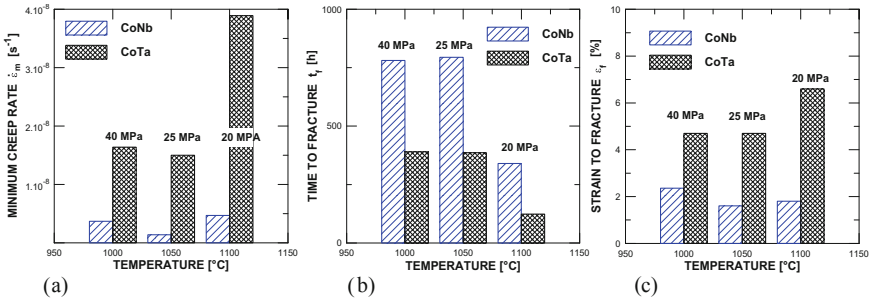


**Fig. 2.** Mutual comparison of selected creep data of the tested CoNb and CoTa superalloys: **a** the minimum creep rate  $\dot{\epsilon}_m$ , **b** the time to fracture  $t_f$ , and **c** the strain to fracture  $\epsilon_f$ .

### 3.3 Creep Fracture Strength

As it was mentioned earlier, the expected operational temperature of melted glass in the spinner discs should be about 1050 °C. Therefore, to evaluate the creep fracture strength of both tested superalloys, the experimentally determined values of the times to fracture  $t_f$  at 1050 °C were plotted against applied stress  $\sigma$  on a bilogarithmic scale in Fig. 3.

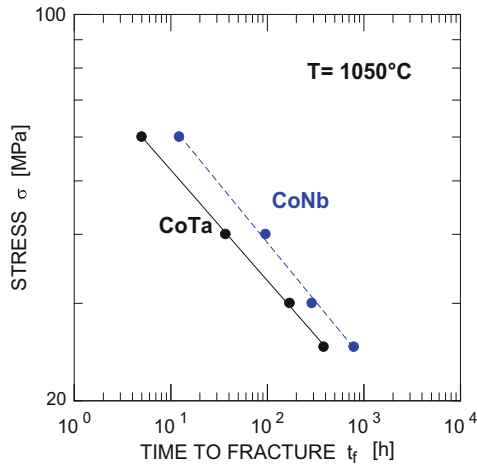


**Fig. 3.** Stress dependences of the time to fracture  $t_f$  at 1050 °C.

As depicted in Fig. 3, the dependences of  $t_f(\sigma)$  may have similar trend for both superalloys. In general, the slopes (i.e.  $t_f(\sigma)$ ) which are representing the apparent stress exponent of the time to fracture  $m = -(\partial \ln t_f / \partial \ln \sigma)_T$  [1, 2]. At temperature 1050 °C the values of  $m = 4.7$  (for CoNb) and  $m = 5.0$  (for CoTa) were found.

### 3.4 Creep Damage and Fracture

It was found that the creep damage initiation in the CoNb superalloy was exclusively related to the primary complex  $M_{23}C_6$  carbides and eutectics [1]. The decohesion at the interface between carbides and matrix transpired due to a loss of coherency and destruction of the primary carbides and eutectic phases occurring homogeneously in the whole specimen section and resulted in the main crack formation and propagation causing a premature brittle fracture. Conversely, the final ductile transgranular fracture of the CoTa superalloy at higher stresses is primarily a consequence of a strain-induced local instability of the dislocation microstructure and a very local breakage of isolated primary  $M_{23}C_6$  carbides [1]. However, at low stresses the mechanisms of creep damage and fracture in CoTa be getting similar like the mechanisms in CoNb (Fig. 4).

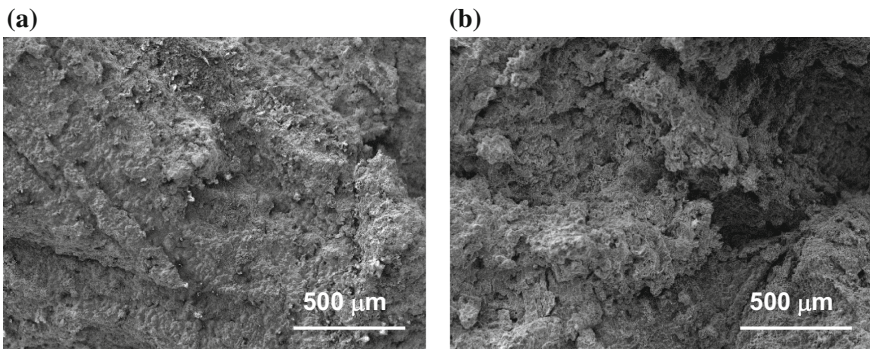


**Fig. 4.** SEM micrographs showing fracture surfaces in: **a** the CoNb and **b** the CoTa.

## 4 Concluding Remarks and Summary

Creep of the superalloy at high temperature (1050 °C) is one of the factors which require that each spinner is shut down in turn and a new spinner fitted. The main requirements for a satisfactory rotary process may be summarized as follows: (i) resistant to the high temperature environment, (ii) resistant to the high centrifugal stresses due to the high rotational speed (about 2300 rpm) and the stress concentrating effect of the many small holes in the rim, (iii) the need to insert hundreds of small holes through the wall, and (iv) resistance to the corrosion and extrusion of molten glass. Using finite element analysis [4] it can be shown that, essentially, there are three forces together acting, a centrifugal force acting radially outwards, a clockwise tangential moment and a force exerted by the molten glass. The highest stress was found at surfaces of holes which can cause the change in shape of initially circular holes to rhomboidal ones. The results are an increase of local excessive stress leading to formation of creep damage of the material and the final fracture when the creep fracture strength is reach (Fig. 5).



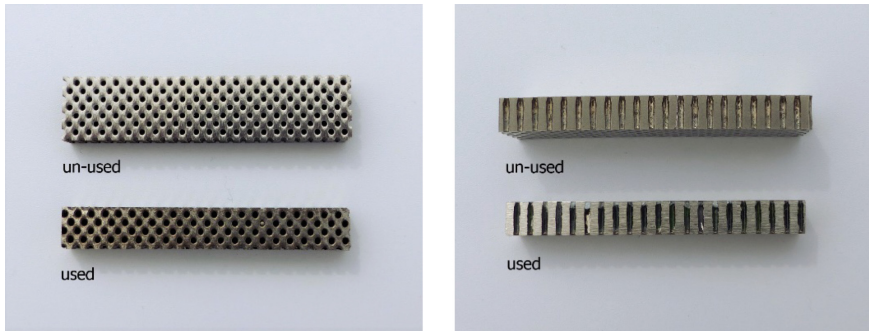


**Fig. 5.** Sections showing of the many small holes in the rim of spinner.

Finally, the results in Fig. 3 can be used to predict the adequate fracture strength for the predetermined creep life of the spinners made from both cobalt superalloys. Thus, for the predetermined creep life around 300 h we obtain 30.6 MPa for the CoNb and 26.5 MPa for the CoTa. Further, for creep life  $\sim 600$  h we will get 26.4 MPa (CoNb) and 23.1 MPa (CoTa), respectively. According to finite element analysis, in the region of the rim the principal stress indicates the value of about 22 MPa. Thus it would appear that both cast cobalt superalloys could sustain the stresses generated in use as a rotary fibreglass spinner. However, this is an answer to only one of the factors posed by the need to predict spinner life in glass fibre production.

**Acknowledgements.** The authors acknowledge financial support for this study provided by the Ministry of Industry and Trade of the Czech Republic within the framework program MPO ČR Trio under the Project No. FV10699. The research infrastructure IPMinfra supported by the Ministry of Education, Youth and Sports through the Project No. LM2015069 was used.

## References

1. Beltran, A.M.: Cobalt-Base Alloys, Superalloys II, Chap. 4, pp. 97–135. Wiley Inc., New York (1987)
2. Sklenička, V., Kvapilová, M., Král, P., Dvořák, J., Svoboda, M., Podhorná, B., Zýka, J., Hrbáček, K.: Joch, A: Degradation processes in high-temperature creep of cast cobalt-based superalloys. *Mater. Character.* **144**, 479–489 (2018)
3. Kvapilova, M., Kral, P., Dvorak, J., Sklenicka, V.: Creep fracture ductility of cobalt-based superalloys. In: Gdoutos, E.E. (ed.) *Proceedings of ICTAEM\_1 Conference*. pp. 184–189. Springer International Publishing AG, Cham, Switzerland (2018)
4. Zýka, J. et al.: Research Report No. UJP 1806. UJP PRAHA a.s., Czech Republic (2018)



# Sub-grain Plastic Strain Localization in CoCrNi Medium Entropy Alloy at Cryogenic Temperatures

Wael Abuzaid<sup>1</sup>(✉) and Luca Patriarca<sup>2</sup>

<sup>1</sup> American University of Sharjah, Sharjah, UAE  
wabuzaid@aus.edu

<sup>2</sup> Politecnico di Milano, Milan, Italy

**Abstract.** High and medium entropy alloys are currently attracting significant research interest due to their potential to achieve superior mechanical properties compared to traditional alloys systems. The CoCrNi alloy has been of particular interest owing to the simple single phase structure, superior fracture toughness, and exceptional strength and ductility at cryogenic temperatures. Previous works have been primarily focused on identifying the operative microstructural mechanisms responsible for improved ductility. The activation of deformation twinning at low deformation temperatures and high strains has been identified as a primary source for the improved ductility. However, detailed quantitative analysis focused on the deformation heterogeneities in the vicinity of grain boundaries, in particular at cryogenic temperatures, remains limited. Strain heterogeneities across grain boundaries reveal the micro-mechanisms responsible for the alloy strengthening and fracture properties, thus their measurements is of fundamental importance. The current work is dedicated to study the local strain accumulation in the vicinity of grains boundaries of plastically deforming CoCrNi. High resolution digital image correlation was used to measure and quantify the deformation heterogeneities at room temperature (298 K) and cryogenic temperature (77 K). The work aims to further elucidate the role of grain boundaries in improving the strength and ductility at cryogenic deformation temperatures.

**Keywords:** Medium entropy alloy · Strain localization · Cryogenic temperatures

## 1 Introduction

High entropy alloys is a promising class of materials with unique mechanical properties [1]. In particular, certain compositions have been shown to exhibit exceptional toughness combined with increased strength and ductility at cryogenic deformation temperatures [2, 3]. These desirable trends, which deviate from traditional alloys, have sparked intense research efforts to explain the observed properties. The FeMnNiCoCr system has been of particular interest owing to the simple single phase structure and exceptional strength and ductility at cryogenic temperatures [4]. More recent efforts have identified comparable superior properties in the equiatomic medium entropy alloy

CoCrNi, however with even better and unrivaled fracture toughness levels [5–8]. With such exceptional set of properties over a wide temperature range, the CoCrNi system is expected to have significant promise in temperature sensitive applications. This motivates further research to better understand the source of properties and the different microstructural aspects which influence the response of this alloy system.

Superior mechanical properties has been reported for polycrystalline [6] and single crystalline [5] CoCrNi alloy. The enhancement in mechanical properties has been typically attributed to the activation of mechanical twinning as an additional deformation mechanism [3, 9]. Although several studies have investigated the effect of annealing and grain size on the alloy properties, detailed quantitative analysis focused on the deformation heterogeneities in the vicinity of grain boundaries, in particular at cryogenic temperatures, remains limited. In this work, high resolution strain measurements were utilized to study the buildup of plastic strain heterogeneities in the vicinity of grain boundaries in CoCrNi at 77 K. In summary, the work aims to shed further insight on the effect of interfaces on the mechanical properties of CoCrNi medium entropy alloy.

## 2 Results

Figure 1 shows a representative stress-strain curve of a tensile sample deformed to  $\sim 4\%$  total strain at 77 K. The entire sample, tension grips, and extensometer, were entirely submerged in liquid nitrogen throughout the experiment. The stress drop observed during the loading cycle can be an indication of mechanical twinning. High resolution optical images were captured using an optical microscope prior and after deformation for full-field strain measurements using digital image correlation (DIC). The strain contour plot shown in Fig. 1c quantifies the residual plastic strains after

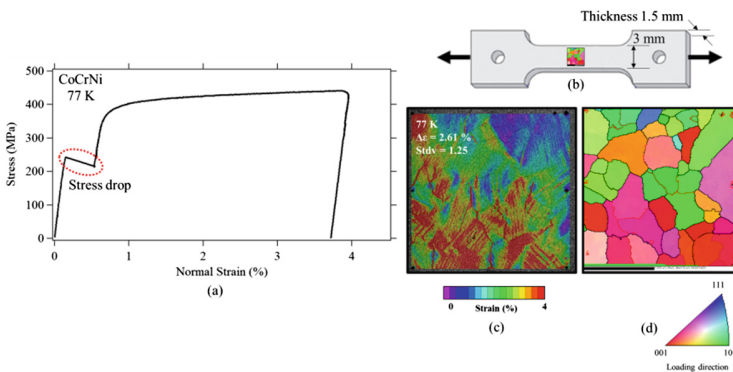


**Fig. 1.** **a** Stress-Strain curve of polycrystalline CoCrNi tension sample deformed at 77 K. **b** Schematic of the tensile specimen with an outline of the region of interest for EBSD and high resolution DIC measurements. **c** High resolution DIC measurements in the region of interest following unloading. EBSD grain orientation map showing the microstructure in the region of interest.

unloading the specimen. The microstructure in the region of interest covered with DIC measurements is shown in Fig. 1d. Deformation heterogeneities and strain localizations in the vicinity of grain boundaries can be clearly observed in the results presented in Fig. 1.

**Acknowledgements.** The corresponding author would like to acknowledge the financial support from the American University of Sharjah through the Office of Research (EFRG18-MSE-CEN-22).

## References

1. Miracle, D.B., Senkov, O.N.: A critical review of high entropy alloys and related concepts. *Acta Mater.* **122**, 448–511 (2017)
2. Zhang, Z., et al.: High-entropy alloy CrMnFeCoNi. *Nat. Commun.* **6**, 1–6 (2015)
3. Slone, C.E., Chakraborty, S., Miao, J., George, E.P., Mills, M.J., Niezgoda, S.R.: Influence of deformation induced nanoscale twinning and FCC-HCP transformation on hardening and texture development in medium-entropy CrCoNi alloy. *Acta Mater.* **158**, 38–52 (2018)
4. Gludovatz, B., George, E.P., Ritchie, R.O.: Processing, microstructure and mechanical properties of the CrMnFeCoNi high-entropy alloy. **67**(10), 2262–2270 (2015)
5. Uzer, B., et al.: On the mechanical response and microstructure evolution of NiCoCr single crystalline medium entropy alloys. *Mater. Res. Lett.* **6**(8), 442–449 (2018)
6. Dan Sathiaraj, G., et al.: Effect of annealing on the microstructure and texture of cold rolled CrCoNi medium-entropy alloy. *Intermetallics* **101**, 87–98 (2018)
7. Yoshida, S., Bhattacharjee, T., Bai, Y., Tsuji, N.: Friction stress and Hall-Petch relationship in CoCrNi equi-atomic medium entropy alloy processed by severe plastic deformation and subsequent annealing. *Scr. Mater.* **134**, 33–36 (2017)
8. Moravcik, I., et al.: Mechanical and microstructural characterization of powder metallurgy CoCrNi medium entropy alloy. *Mater. Sci. Eng., A* **701**, 370–380 (2017)
9. Laplanche, G., Kostka, A., Reinhart, C., Hunfeld, J., Eggeler, G., George, E.P.: Reasons for the superior mechanical properties of medium-entropy CrCoNi compared to high-entropy CrMnFeCoNi. *Acta Mater.* **128**, 292–303 (2017)



# Effects of Treatment on Microstructure and Deformation Behavior of Dissimilar Welded Joint Between Single Crystal and Polycrystalline Superalloy

Yang Liu<sup>1</sup>(✉), Lei Wang<sup>1</sup>, Xiu Song<sup>1</sup>, Taosha Liang<sup>1</sup>, and Guo Hua<sup>2</sup>

<sup>1</sup> Key Laboratory for Anisotropy and Texture of Materials (Ministry of Education), School of Materials Science and Engineering, Northeastern University, Shenyang 110819, China

liuyang@mail.neu.edu.cn

<sup>2</sup> High Temperature Material Research Institute, Central Iron and Steel Research Institute, Beijing 100081, China

**Abstract.** Dissimilar welding of Al + Ti rich and Nb rich nickel base superalloy has good welding performance. In this work, the tensile behavior of dissimilar Between Single Crystal and Polycrystalline Superalloy welded joint near its service temperatures (600–700 °C) was studied. The results show that the deformation behavior of the welded joint is closely related to the strength difference between difference regions. The yield strength (YS) and ultimate tensile strength (UTS) of the welded joint is dominated by the region with lower YS and UTS, which is Single Crystal Superalloy at 25–650 °C and Polycrystalline Superalloy at 660–700 °C. The plasticity of welded joint depends primarily on the magnitude of strength difference between different regions. Lower strength difference results in higher elongation. Both the UTS and elongation have peak values at 660 °C. The welded joints fail at Single Crystal Superalloy base metal at 25–650 °C while at Polycrystalline Superalloy base metal at 660–700 °C. The FZ has high strength and sufficient plasticity. Soft dendrites are surrounded and constrained by hard interdendrites. Fine discrete MC carbides and Laves phases in the interdendrites can effectively block the movement of dislocations from dendrites.

**Keywords:** Single crystal superalloy · Polycrystalline superalloy · Laser welding · Dissimilar welding · High temperature deformation

## 1 Introduction

Nickel base superalloys are important materials for high temperature applications in gas turbine engines owing to their excellent high temperature capability. Blade and disk are the crucial parts of the engine. In order to reduce engine weight and gain high thrust-to-weight ratio, dissimilar welding of blade to disk to replace traditional riveted joint attracts increasing attention [1–5]. Nickel base superalloys are heavily alloyed (by Co, Cr, Fe, Mo, Al, Ti, Nb, W, Ta and C, etc.) to ensure high temperature performance [6].

However, high alloying leads to poor fusion welding performance. Among those alloying elements, Al, Ti and Nb play important roles on the weldability. Nickel base superalloy with higher Al and Ti can precipitate more  $\gamma'$  and its strength is higher [7]. However,  $\gamma'$  precipitates faster at higher temperature even during welding [5]. The grain is strengthened while the grain boundary is weak. Hot cracking occurs easier under the welding thermal stress [8]. Adding high Nb into the nickel iron base superalloy is beneficial to the precipitation of  $\gamma''$ . Nevertheless, Nb has high segregation tendency and would promote the formation of  $\gamma$ -Laves eutectic which can lower the solidification temperature [9]. On the one hand, the hot cracking tendency increases [9, 10].

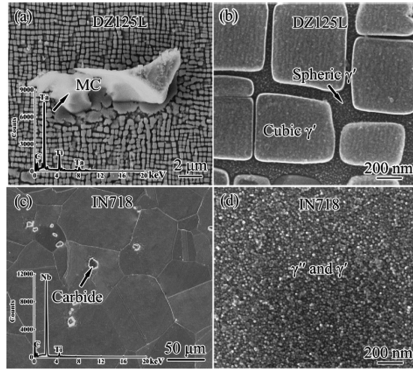
Based on the above reported work, we studied the dissimilar laser welding of DZ125L and IN718 [5]. In the present study, the deformation behavior of the laser welded DZ125L/IN718 joint near its working temperature (600–700 °C) was investigated. This research will provide guidance for improving the performance of such welded joint. It will also be instructive for reasonable material selection and design of new welded joint.

The DZ125L alloy was prepared by double vacuum melting, and then casted into slab with a withdrawal speed of 6 mm/min. Afterwards, it was solution treated at 1220 °C for 2 h followed by two-step aging at 1080 °C for 4 h and 900 °C for 16 h. The IN718 alloy was produced by vacuum induction melting and vacuum arc remelting, then hot forged and followed by solution treatment at 1020 °C for 1 h. Prior to laser welding, both the two base metals were mechanical and chemical cleaned to remove defects and contaminants near edges. After welding, postweld heat treatment (PWHT) of two-step aging at 720 °C for 8 h and 620 °C for 8 h was conducted. Tensile testing was conducted at 25, 600, 650, 660, 700 °C at  $10^{-3} \text{ s}^{-1}$  on a SANS CMT 5500 material testing machine equipped with a heating furnace. Three identical specimens were tested for data repeatability.

## 2 Results and Discussion

### 2.1 Microstructure and Microhardness Profile

Figure 1 shows the microstructure of the two base metals of DZ125L and IN718 alloys. The grain in the DZ125L is columnar. The primary dendrite arm distance is about 400  $\mu\text{m}$ . The cubic  $\gamma'$  with average size of  $550 \pm 43 \text{ nm}$  is dispersed in the matrix (Fig. 1a). In the  $\gamma$  channels, fine spheric  $\gamma'$  phase with average size of  $\sim 22 \text{ nm}$  can be observed (Fig. 1b). Moreover, the blocky MC carbides distribute in the interdendrites. Their sizes vary from 3 to 70  $\mu\text{m}$ . They are rich in Ti and Ta, as shown in the inset of Fig. 1a. The IN718 is polycrystal. The average grain size is  $81 \pm 29 \mu\text{m}$ . The blocky MC carbides with average size of  $8 \pm 3 \mu\text{m}$  can be seen at the grain boundaries (Fig. 1c). The EDS analysis in the inset of Fig. 1c shows that they are rich in Ti and Nb. In the higher magnified micrograph of Fig. 1d, fine  $\gamma''$  and  $\gamma'$  with average size of  $\sim 25 \text{ nm}$  can be observed.



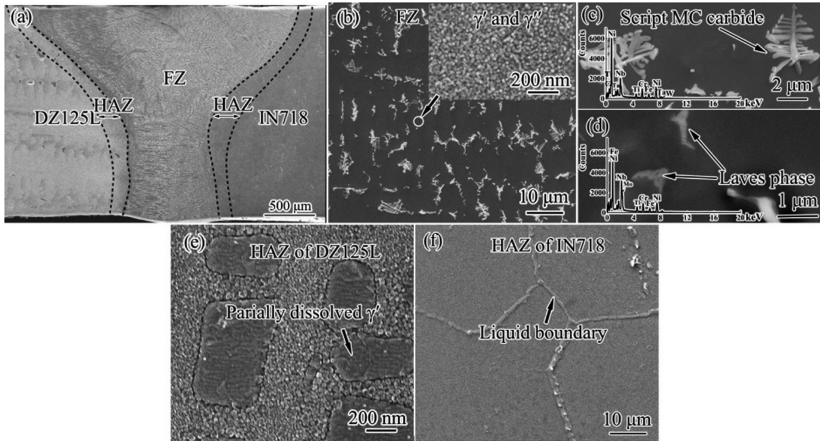
**Fig. 1.** SEM microstructure of the base metals. **a** MC carbide in DZ125L and its EDS analysis in the inset, **b** cubic  $\gamma'$  and spheric  $\gamma'$  in  $\gamma$  channel of DZ125L, **c** carbide in IN718 and its EDS analysis in the inset, and **d**  $\gamma''$  and  $\gamma'$  in IN718

Figure 2 shows the microstructures in the welded area including the FZ and the two HAZs. The shape of the FZ is funnel-like (Fig. 2a). The dendrite in FZ is fine. Its primary dendrite arm distance is  $7.1 \pm 1.9 \mu\text{m}$  in average. Discrete fine script MC carbides and irregular Laves phases distribute in the interdendrites and grain boundaries (Fig. 2b). The MC carbide is rich in Ti, Ta, Nb and W (inset of Fig. 2c). Its average size is  $5.1 \pm 1.6 \mu\text{m}$ . The Laves phase is smaller (Fig. 2d). Its size is  $1.3 \pm 0.3 \mu\text{m}$  in average and it mainly contains Cr, Fe, Ni, Nb and Mo (inset of Fig. 2d). The content of Laves and MC carbide cannot be accurately measured due to macro- and micro-segregation of elements [5]. There are only 0.62% of MC and 0.69% of Laves phases precipitated from the liquid metal. Their contents are much less than those of the base metals welded alone, respectively. Fine spheric  $\gamma'$  and  $\gamma''$  with average size of  $\sim 24 \text{ nm}$  disperse in the matrix (inset of Fig. 2b). Details on how to recognize these two phases in the FZ were reported in previous work [5].

The microhardness across the welded joint was measured at room temperature along the line  $\sim 1.3 \text{ mm}$  below the top surface and the hardness profile is given in Fig. 3. The average hardness values of different regions are  $399 \pm 8 \text{ HV}_{0.05}$  (DZ125L),  $423 \pm 7 \text{ HV}_{0.05}$  (the HAZ of DZ125L),  $494 \pm 6 \text{ HV}_{0.05}$  (FZ),  $457 \pm 10 \text{ HV}_{0.05}$  (the HAZ of IN718) and  $454 \pm 9 \text{ HV}_{0.05}$  (IN718), respectively. The FZ has the highest hardness, while the DZ125L has the lowest hardness.

## 2.2 Tensile Properties

Figure 4 shows the yield strength (YS), ultimate tensile strength (UTS) and elongation of the welded joint and the two base metals. The YS of the welded joint is not sensitive to deformation temperature at 25–660 °C. Their values are around 950 MPa. At 700 °C, the YS decrease slightly to  $914 \pm 28 \text{ MPa}$ . The YS is higher than that of the DZ125L base metal but lower than that of the IN718 base metal at 25–660 °C, whereas at 700 °C, the YS is higher than that of the IN718 base metal but lower than that of the DZ125L base metal.



**Fig. 2.** SEM microstructure of the welded areas of the DZ125L/IN718 welded joint. **a** Overview; **b** FZ and  $\gamma'$  and  $\gamma''$  in the inset, **c** MC carbides and its EDS, **d** Laves phase and its EDS, **e** HAZ of DZ125L showing the partially dissolved  $\gamma'$ , and **f** HAZ of IN718 showing the liquid grain boundary

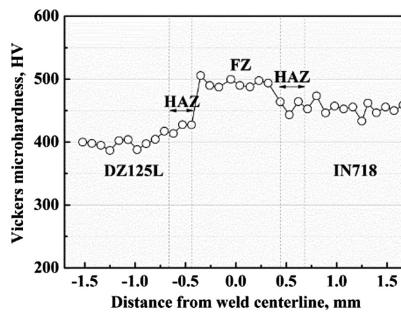


**Fig. 3.** Microhardness profile of the DZ125L/IN718 welded joint

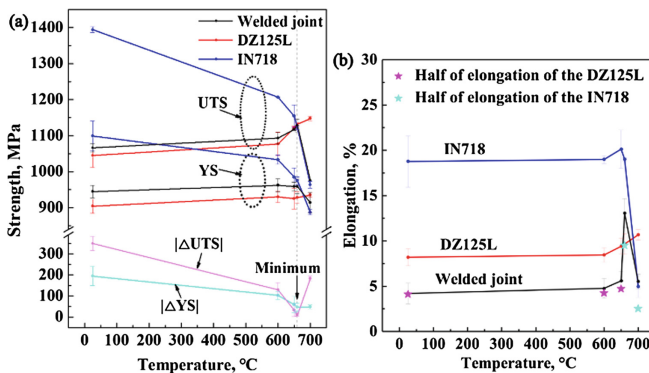


**Fig. 4.** Tensile properties of the DZ125L, IN718, and DZ125L/IN718 welded joints at different deformation temperatures. **a** YS, UTS and the mean absolute difference of YS and UTS between DZ125L and IN718, **b** total elongation



In contrast, the UTS of the welded joint increases from  $1066 \pm 11$  MPa to  $1128 \pm 18$  MPa with increasing temperature from 25 to 660 °C, while it decreases to  $976 \pm 7$  MPa at 700 °C. At 25–650 °C, the UTS is higher than that of the DZ125L base metal but lower than that of the IN718 base metal. At 660–700 °C, the UTS is higher than that of the IN718 base metal but lower than that of the DZ125L base metal.

Similar to the UTS, the elongation of the welded joint increases from  $4.2 \pm 1.1\%$  to  $13.1 \pm 1.6\%$  with increasing temperature from 25 to 660 °C, and it decreases to  $5.5 \pm 0.8\%$  at 700 °C, as shown in Fig. 4b. Basically, the elongations are low. They are slightly higher than half of that of the DZ125L base metal at 25–650 °C. They are obviously higher than half of that of the IN718 base metal at 660 and 700 °C.

### 2.3 Fracture Morphology

The welded joints failed at the DZ125L at 25–650 °C and failed at the IN718 at 660 and 700 °C. The fracture locations are far away from the welded areas (FZ and the two HAZs). Typical fracture morphologies are shown in Fig. 5. For the specimens failed at DZ125L, the fracture surfaces consist mainly of carbides and cleavage planes which exhibit quasi-brittle fracture features, as shown in Fig. 5c, f. It is reported that large MC carbides are easily broken even at early deformation stage and act as crack sources [11]. The great energy and stress concentration at the crack tip facilitate the formation of deformation twinning. Cracks propagate along the interface between deformation twins to form cleavage planes [12–14].

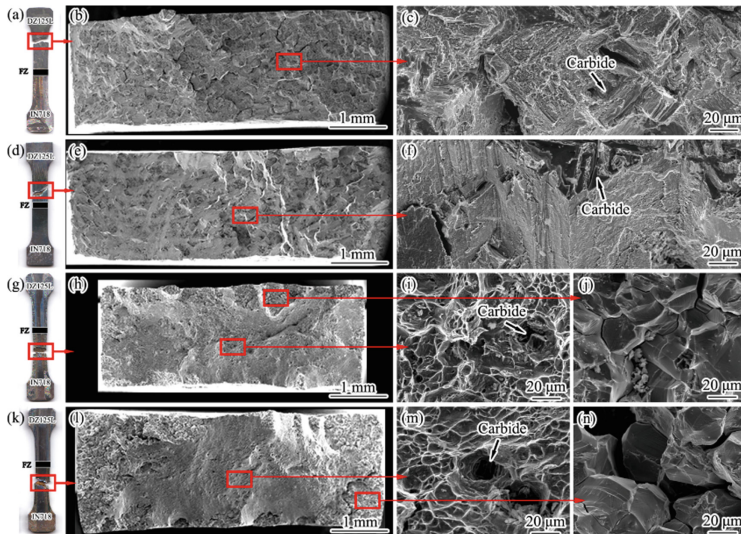


**Fig. 5.** Fracture morphology of the DZ125L/IN718 welded joints tensile deformed at different temperatures: **a–c** 25 °C, **d–f** 650 °C, **g–j** 660 °C, and **k–n** 700 °C

### 3 Conclusions

The strength of the welded joint depends on the strength of the subregions with lower YS and UTS. The YS of the welded joint is insensitive to deformation temperature from 25 to 660 °C. It decreases to a lower value at 700 °C. The UTS of the welded joint firstly increases then decreases with increasing temperature, peaked at 660 °C. The YS and UTS are slightly higher than those of the region with lower YS and UTS due to inhomogeneous plastic deformation. The FZ have both high strength and sufficient plasticity at high temperature. The dendrite core is strengthened by fine dispersed  $\gamma'$  and  $\gamma''$  and it is soft at high temperature. Interdendrite is strengthened by both fine dispersed  $\gamma'$  and  $\gamma''$  and fine discrete carbides and Laves phases, and it is hard comparatively. Soft dendrites are surrounded and constrained by hard interdendrites. Interdendrites can effectively hinder the movement of dislocation from dendrites. The soft dendrite carries higher plastic strain, while the interdendrite provides more strength.

**Acknowledgements.** This work was financially supported by the National Natural Science Foundation of China (51571052 and U1708253), and the Science and Technology Major Project (2017-VI-0002).

### References

1. Karadge, M., Preuss, M., Withers, P., Bray, S.: *Mater. Sci. Eng., A* **491**, 446–453 (2008)
2. Moosavy, H., Aboutalebi, M., Seyedein, S., Mapelli, C.: *Mater. Charact.* **82**, 41–49 (2013)
3. Moosavy, H., Aboutalebi, M., Seyedein, S., Goodarzi, M., Mapelli, C.: *Mater. Sci. Technol.* **30**, 339–347 (2014)
4. Roder, O., Albrecht, J., Lütjering, G.: *Mater. High Temp.* **23**, 171–177 (2014)
5. Liang, T., Wang, L., Liu, Y., Song, X.: *Met. Mater. Int.* **7**, 710–722 (2018)
6. Dupont, J.N., Lippold, J.C., Kiser, S.D.: *Welding Metallurgy and Weldability of Nickel-base Alloys*. Wiley, Canada (2009)
7. Xu, Y., Zhang, L., Li, J., Xiao, X., Cao, X., Jia, G., Shen, Z.: *Mater. Sci. Eng., A* **544**, 48–53 (2012)
8. Wang, Y.L., Ojo, O.A., Ding, R.G., Chaturvedi, M.C.: *Mater. Sci. Technol.* **25**, 68–75 (2009)
9. Xiao, H., Li, S., Han, X., Mazumder, J., Song, L.: *Mater. Des.* **122**, 330–339 (2017)
10. Antonsson, T., Fredriksson, H.: *Metall. Mater. Trans. B* **36**, 85–96 (2005)
11. Liang, T., Wang, L., Liu, Y., Song, X.: *J. Mater. Eng. Perform.* **27**, 721–727 (2018)
12. Xie, H., Yu, T., Yin, F., Tang, C.: *Mater. Sci. Eng., A* **580**, 99–104 (2013)
13. Xie, H.X., Wang, C.Y., Yu, T.: *J. Mater. Res.* **23**, 1597–1603 (2008)
14. Sun, F., Zhang, J., Harada, H.: *Acta Mater.* **67**, 45–57 (2014)



# Improved Post-crack Energy Absorption Capability of Cementitious Composites Reinforced with CNTs and PPs

Panagiotis A. Danoglidis<sup>1</sup>(✉), Maria S. Konsta-Gdoutos<sup>2</sup>,  
and Emmanuel E. Gdoutos<sup>3</sup>

<sup>1</sup> School of Engineering, Democritus University of Thrace,  
671 00 Xanthi, Greece  
pdanogli@civil.duth.gr

<sup>2</sup> Department of Civil Engineering, College of Engineering,  
University of Texas at Arlington, Arlington, TX, USA

<sup>3</sup> Academy of Athens, GR 106 79 Athens, Greece

**Abstract.** In this study a thorough investigation of the pre-peak and post-crack mechanical behavior of cement mortars reinforced with carbon nanotubes and polypropylene microfibers, took place. Flexural strength, Young's modulus, energy absorption capability and energy based dimensionless indices (toughness indices) were investigated. Prismatic specimens of neat mortar and mortars reinforced with 0.1 vol.% CNTs and 1.0 vol.% PPs were subjected to a three point close loop bending test. Combined networks of CNTs and PPs also incorporated in mortar matrix in order to investigate the synergistic effect of hybrid reinforcement on the mechanical properties of mortar composites in comparison to the singly-reinforced mortars. The experimental results showed an exceptional multi scale mechanical behavior of mortars as reflected from the load-deflection curves. Cement-based composites using carbon nanotubes or ladder scale reinforcement of CNTs and PPs are characterized by 1.9 times higher flexural strength and stiffness and 50% increased flexural toughness over the mortars reinforced with micro scale fibers alone. The post-crack energy absorption capability of multiscale reinforced mortars after the formation of the "first crack", is also outstandingly improved as indicated by the increases of the toughness indices  $I_5$ ,  $I_{10}$ ,  $I_{20}$ .

**Keywords:** Mortar · Carbon nanotubes · Polypropylene · Young's modulus · Toughness indices

## 1 Introduction

The use of micro scale fibers results to an improved post-crack behavior of cementitious materials by bridging the microcracks and delaying the formation of a through-specimen macrocrack [1]. However, they cannot prevent the initiation of cracks at the nanoscale, which affects the fundamental mechanical behavior of cement based materials [2]. The use of fibers at the nanoscale, such as carbon nanotubes (CNTs) and carbon nanofibers (CNFs), offers unprecedented improvements in the mechanical

properties of cement based materials [3, 4]. The purpose of the present study is to determine the synergistic effect of using CNTs and PPs on the flexural strength, Young's modulus and flexural toughness and to evaluate the post-cracking energy absorption capability of mortars reinforced with fibers at the nano and micro scale. Overall, the combination of CNTs and PPs provide better mechanical behavior at both the pre-peak and the post-crack area over the mortars reinforced with carbon nanotubes or polypropylene fibers alone. The synergistic interaction between the CNTs and PPs results in a multiscale reinforcing mechanism as: (i) inhibits the initiation and propagation of crack at the nanoscale, increasing the flexural strength (+108%) and stiffness (+87%); and (ii) provides a post-crack bridging mechanism after the formation of the "first crack" by improving the post-crack energy absorption capability of mortar composites as reflected by the higher values of the toughness indices  $I_5$ ,  $I_{10}$  and  $I_{20}$ .

## 2 Experimental Work

### 2.1 Materials and Specimens

Mortar composites were produced by using OPC Type I ( $w/c = 0.485$ ), standard sand ( $s/c = 2.75$ ), 0.1 vol.% multiwalled carbon nanotubes (CNTs) and 1.0 vol.% polypropylene fibers (PPs) at aspect ratios of 307 and 480, respectively. A total of four mortar samples were designed and examined: (i) plain mortar (M); (ii) M + CNTs; (iii) M + PPs, (iv) M + CNTs + PPs. CNTs were uniformly dispersed in aqueous suspension by the application of ultrasonication energy and the use of polycarboxylate based surfactant [5].  $40 \times 40 \times 160$  mm prisms were prepared for the determination of mechanical properties. Following demolding, the samples were cured in lime-saturated water for 28 days.

### 2.2 Experimental Determination of Flexural Strength, Young's Modulus, Energy Absorption Capability and Toughness Indices

Three-point bending tests were conducted on  $40 \times 40 \times 160$  mm prismatic specimens. The tests were performed using a 25 kN MTS servo-hydraulic, closed-loop testing machine under displacement control. The rate of displacement was kept at 0.1 mm/min. The flexural strength and Young's modulus were determined according to the ASTM C348-14. Flexural toughness and the dimensionless based toughness indices  $I_5$ ,  $I_{10}$  and  $I_{20}$  were evaluated by the analysis of the load-deflection curves of prismatic mortar beams as described by the ACI report on Fiber Reinforced Concrete [6].

## 3 Results and Discussion

Flexural strength and Young's modulus of 28d mortars reinforced with highly dispersed carbon nanotubes and/or polypropylene microfibers, are presented in Fig. 1. Comparing the results of plain mortar and mortar reinforced with 0.1 vol.% CNTs, 90% increase in both flexural strength and stiffness is observed. Mortars reinforced

with 1.0 vol.% PPs, exhibit almost the same flexural strength and stiffness with the plain mortar. The addition of micro scale fibers into the cementitious matrix mostly results in post-elastic property changes [7]. Interestingly, the simultaneous incorporation of CNTs along with PPs results in 1.9 times higher flexural strength and Young's modulus over the plain one. It is obvious that mortar either singly nanoreinforced or in combination with microscale fibers significantly enhance its fracture-dominant failure mode, therefore its flexural strength and modulus of elasticity.

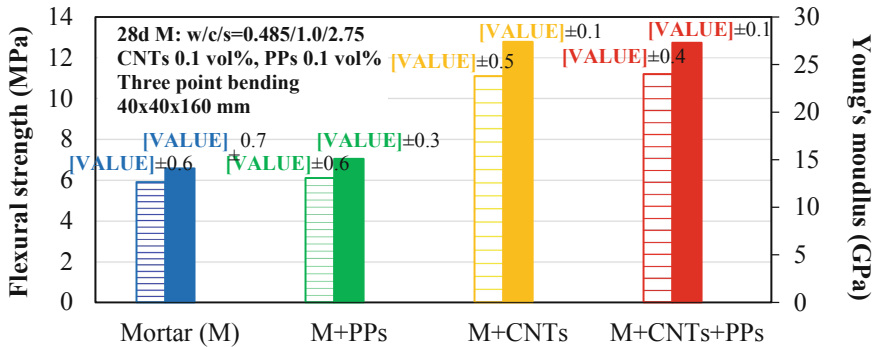
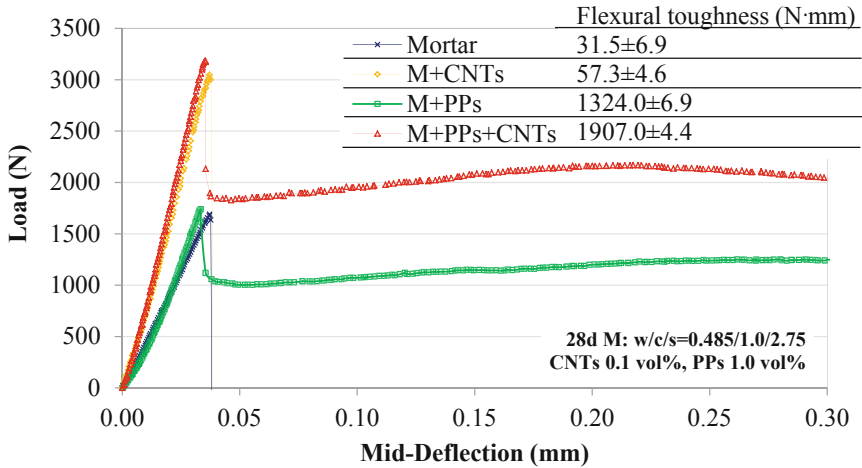


Fig. 1. Three point bending and uniaxial compression modulus of elasticity of 28d CNT.

Figure 2 presents load-deflection curves of 28d mortars with the ladder scale reinforcement of CNTs and PPs. As discussed above, the effect of the simultaneous addition of carbon nanotubes and polypropylene microfibers on the mortar matrix was outstanding. Similar to the mortar specimens reinforced with CNTs, the mortar composites with ladder scale reinforcement exhibit an exceptional pre-peak flexural behavior with almost the same peak load ( $\approx 3000$  N). The incorporation of CNTs provides a higher load transfer mechanism between the mortar matrix and the nanoscale fiber; therefore leading in such high increases in both flexural strength and Young's modulus (Fig. 1). Except of the increases in the strength and stiffness, it is also observed an increased energy absorption capability of hybrid mortars as reflected by the flexural toughness values calculated by the area under the load-deflection curves and also presented in Fig. 2. After the application of the peak load and the formation of first crack (Deflection > 0.04 mm) the hybrid mortars are further deformed to a large extend exhibiting an enhanced ability to sustain additional flexural loading and 50% higher energy absorption capability compared to the singly micro scale reinforced composites after the formation of the "first crack" and before their total failure.

To further examine the toughening effect of mortars modified with the nano and micro scale reinforcement Table 1 presents the toughness indices  $I_5$ ,  $I_{10}$  and  $I_{20}$  of 28d mortar reinforced with CNTs and/or PPs. As it is shown from Table 1 the addition of polypropylene fibers has a great effect of post-cracking toughness of mortars, as PP reinforced mortar composites exhibit a 3.4, 6.8 and 14.2 times higher energy absorption capability at the area up to a deflection of 3.0, 5.5. and 10.5 times the first-crack deflection. It should be mentioned here that toughness indices for the nanoreinforced



**Fig. 2.** Load-deflection curves and flexural toughness of 28d mortars reinforced with CNTs and/or PPs.

and plain mortar cannot be calculated as the materials does not exhibit any post-cracking mechanical behavior. Interestingly, the synergistic effect of carbon nanotubes and polypropylene fibers results in even higher improvement of the post-crack energy absorbing efficiency. Toughness indices of CNT and PP reinforced mortars are 26, 19 and 15% higher up to deflections of 3.0, 5.5 and 10.5 times the first-crack deflection, comparing to the singly micro scale fiber reinforced mortars.

**Table 1.** Toughness indices  $I_5$ ,  $I_{10}$  and  $I_{20}$  of 28d CNT and/or PP reinforced mortars.

	$I_5$	$I_{10}$	$I_{20}$
M + PPs	3.4	6.8	14.2
M + CNTs + PPs	4.3	8.1	16.3

## 4 Conclusions

The characterization of the pre-peak and post-crack mechanical behavior of cement mortars reinforced with nano and/or micro scale fibers, took place in this study. Carbon nanotubes and polypropylene fibers at volume fractions of 0.1 and 1.0%, respectively, were used for the matrix's reinforcement. The effect of the simultaneous use of CNTs and PPs on the mechanical properties of the mortar matrix, over the singly-reinforced mortars, was also investigated. The combination of CNTs and PPs provide better mechanical performance at both pre-peak and post-crack areas over the mortars reinforced with carbon nanotubes or polypropylene fibers alone. The addition of 0.1 vol.% CNTs leads to an enhanced pre-peak mechanical behavior, with 95% increased flexural strength and Young's modulus. On the other hand, the addition of micro scale

polypropylene fibers results only in post-crack changes as the mortar composites though exhibit no increase in flexural strength and stiffness, a 25 times higher energy absorption capability after the formation of the “first crack” is observed over the plain mortar and mortar reinforced with CNTs alone. Overall, the interaction between the CNTs and PPs results in an exceptional multiscale reinforcing mechanism, as composites exhibit 1.2 times higher flexural strength and Young’s modulus over the singly reinforced mortars. The enhanced bridging mechanism after the formation of the “first crack” by the simultaneous use of nano and micro scale fibers exceptionally improves the composites’ post-crack energy absorption capability as reflected by the higher toughness indices, compared to the microfiber reinforced mortar.

**Acknowledgements.** The authors would like to kindly acknowledge the financial support from the Academy of Athens under the Research Funding Program “Improving structural performance and monitoring of damage in nanomodified concrete composites using carbon nanotubes and carbon nanofibers” (200/877).

## References

1. Brandt, A.M.: Fibre reinforced cement-based (FRC) composites after over 40 years of development in building and civil engineering. *Compos. Struct.* **86**, 3–9 (2008)
2. Lawler, J.S., Zampini, D., Shah, S.P.: Permeability of cracked hybrid fiber reinforced mortar under load. *ACI Mater. J.* **99**(4), 379–385 (2002)
3. Gdoutos, E.E., Konsta-Gdoutos, M.S., Danoglidis, P.A.: Portland cement mortar nanocomposites at low carbon nanotube and carbon nanofiber content: a fracture mechanics experimental study. *Cement Concr. Compos.* **70**, 110–118 (2016)
4. Danoglidis, P.A., Konsta-Gdoutos, M.S., Gdoutos, E.E., Shah, S.P.: Strength, energy absorption capability and self-sensing properties of multifunctional carbon nanotube reinforced mortars. *Constr. Build. Mater.* **120**, 265–274 (2016)
5. Shah, S.P., Konsta-Gdoutos, M.S., Metaxa, Z.S.: Highly dispersed carbon nanotube reinforced cement based materials. United States Patent US9, 365, 456 (B2), 2016-06-14
6. American Concrete Institute: Report on Fiber Reinforced Concrete, ACI 544.1R-96 (1996)
7. Naaman, A.E., Shah, S.P., Throne, J.L.: Some developments in polypropylene fibers for concrete. *ACI Special Publication* **81**, 375–396 (1984)



# Molecular Dynamics Investigation of Dislocation Slip in Pure Metals and Alloys

Alexander E. Mayer<sup>(✉)</sup> and Vasilii S. Krasnikov

Chelyabinsk State University, Bratiev Kashirinykh Str. 129,  
454001 Chelyabinsk, Russia  
mayer@csu.ru

**Abstract.** Averaged accounting of motion and interaction of dislocations is a natural way to describe plasticity at macroscale in those metals, in which dislocation slip is the main mechanism. This approach describes the inertness of the plasticity development, which is crucial in dynamic problems. On the other hand, such models demand for additional equations and parameters. Molecular dynamics (MD) simulation of elementary processes in the dislocation ensemble at nanoscale is prospective tool for construction of these equations and fitting their parameters. We present MD simulation of the motion of single dislocation lines in pure metals and metals with precipitates. Influence of local stresses on the motion of dislocations in pure metals is discussed. The dislocation motion equation is derived and their parameters are fitted to MD simulations for Al, Cu and Mg. Also we discuss the model for dynamic interaction of dislocation and precipitate intended for description of plasticity in alloys.

**Keywords:** Dislocation plasticity · Motion of dislocations · Drag coefficient · Interaction with precipitate · Molecular dynamics

## 1 Introduction

Averaged accounting of motion and interaction of dislocations is a natural way to describe plasticity at macroscale in those metals, in which dislocation slip is the main mechanism [1–6]. Among other advantages, this approach allows one to describe the inertness of the plasticity development, which is crucial in dynamic problems, such as high-velocity impact [7] or powerful laser or electron irradiation of metals [8, 9]. Strain rates up to an inverse nanosecond are experimentally available [10–12], at these strain rates the material shear strength tends to its ultimate value [12]. The main disadvantages of the dislocation plasticity models are additional equations typically written for each slip system, and a number of parameters. Both, the form of equations and the values of parameters, have to be determined from elsewhere. Besides theoretical consideration and fitting with experimental data, the atomistic simulations of elementary processes in the dislocation ensemble at nanoscale can be used [13–16].

Here we present MD simulation of motion of single dislocation lines in pure metals and metals with precipitates. Influence of local stresses on the motion of dislocations in pure metals is discussed [15]. The dislocation motion equation is derived and their parameters are fitted to MD simulations for Al [15], Cu and Mg. Also we discuss the



model for dynamic interaction of dislocations and precipitates [16] intended for description of plasticity in alloys. Together with MD simulations of high-rate shear deformation used for verification of the dislocation kinetics equations [17] these results give exhausting information for formulation of continuum models of plasticity.

## 2 Motion of Dislocations in Pure Metals

MD simulations are performed using LAMMPS package [18]. OVITO [19] with the dislocation extraction algorithm (DXA) [20] are used for analysis of the atomic configurations and tracing position of dislocations. Atomsk [21] is implemented for obtaining of the initial configuration of single crystal with straight dislocation. The MD samples are oriented in such a way that the dislocation line lies along  $z$ -axis and moves along  $x$ -axis. The Burgers vector is directed either along  $x$ -axis (for edge dislocation) or along  $z$ -axis (for screw dislocation). Periodic boundary conditions are set along the dislocation line ( $z$ -axis) and direction of its motion ( $x$ -axis). One of the faces perpendicular to  $y$ -axis is fixed, while another one moves creating either  $\sigma_{xy}$  or  $\sigma_{yz}$  component of stress tensor, which provokes the motion of dislocation in the required direction. Two problem statements are considered: (i) initial instantaneous finite shear of the face and whole sample [15] (Figs. 1 and 2); (ii) shifting of face with constant speed [16], Fig. 3. Constant temperature is maintained in the MD system.

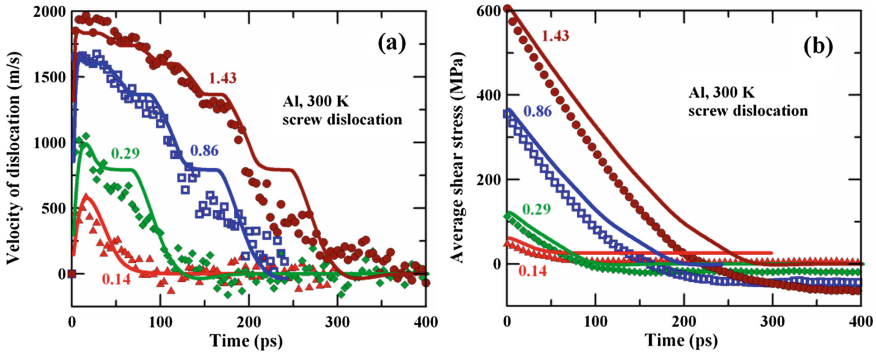


**Fig. 1.** Relaxation of initial shear in the case of screw dislocation in Al sample: **a** dislocation velocities and **b** shear stresses. Comparison of the dislocation motion equation [15] (solid lines) with MD data (symbols) for initial displacements of 0.14, 0.29, 0.86 and 1.43 nm is presented. The MD system size is  $74.4 \times 56.1 \times 10 \text{ nm}^3$ ; the temperature is equal to 300 K.

Variation of average shear stress, position and velocity of dislocation are compared with the theoretical model based on the dislocation motion equation [15], and the parameters of this equation are fitted, see Table 1. The model takes into account quasi-relativistic effect (infinite increase in the dislocation energy at the achievement of transverse sound speed) and the local character of the resolved shear stress, which moves the dislocation. Detailed analysis [15] of the relaxation of initial instant shear,

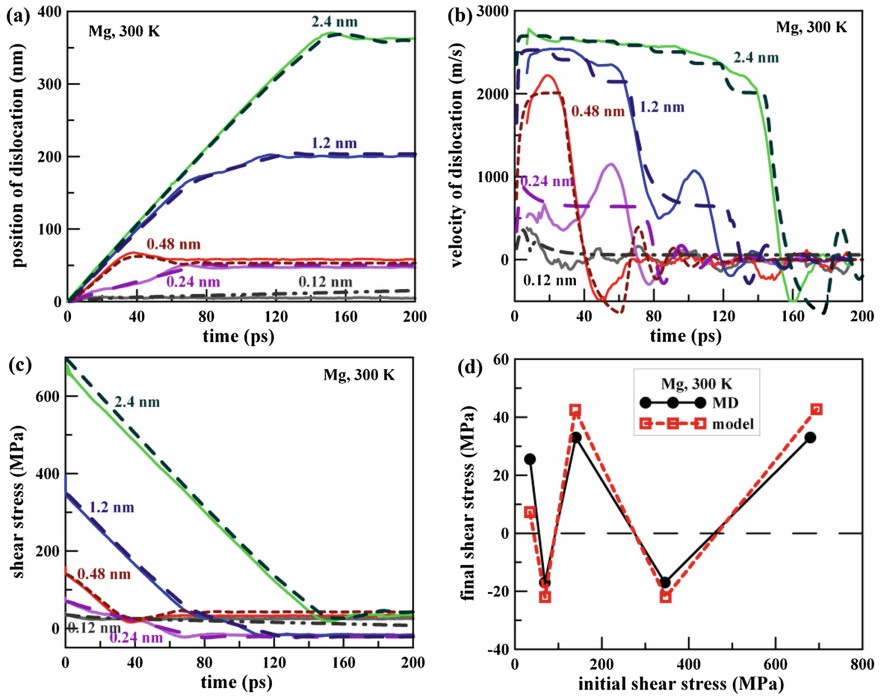


**Fig. 2.** Relaxation of initial shear in Mg sample containing straight edge dislocation in basal plane: time evolution of **a** positions of dislocations, **b** dislocation velocities and **c** shear stresses; **d** dependence of final shear stress upon initial one. Comparison of the dislocation motion equation [15] (solid lines) with MD data (symbols) for initial displacements of 0.12, 0.24, 0.48, 1.2 and 2.4 nm is presented. The MD system size is  $51 \times 52 \times 28 \text{ nm}^3$ ; the temperature is constant and equal to 300 K.

problem statement (i), showed that not the average over MD system, but local stresses, averaged through the region of the order of 10 nm in size, should be used in the dislocation motion equation. Besides it, the stress distribution is very heterogeneous near the dislocation line [15]: a moving dislocation leaves a relaxed area (trace) behind itself. This feature leads to step-wise change in velocity, Figs. 1a, 2b, at entering of trace of the previous dislocation, arising of negative velocities, Fig. 2b, and non-monotonic dependence of the final stress over initial one, Fig. 2d.

In the problem statement (ii) with continuous shift, the periodic entering into the traces of previous dislocations leads to oscillations of the dislocation velocity and average shear stress, Fig. 3. At fast shift, an unsaturated increase in shear stress takes place (Fig. 3 for 9 m/s) due to the restriction of the dislocation velocity [16].

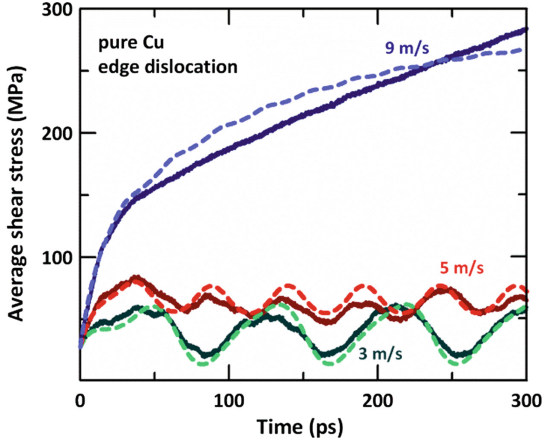


**Fig. 3.** Shear stresses in Cu sample with edge dislocation at boundary shift with constant velocities indicated near lines: MD data (solid lines) and calculations with using of the dislocation motion equation [15] (dashed lines). The MD system size is  $46 \times 43.8 \times 9.6 \text{ nm}^3$ ; the temperature is constant and equal to 300 K.

**Table 1.** Parameters of the dislocation motion equation [15] for 300 K: the drag coefficient  $B_0$  (at low velocity of dislocation) and the rest mass of dislocation  $m_0$ .

Parameter	Al (edge) [15]	Al (screw)	Mg (edge)	Cu (edge)
$B_0, 10^{-5} \text{ Pa s}$	1.45	1.69	1.54	1.20
$m_0, 10^{-16} \text{ kg/m}$	1.10	2.15	1.97	1.10

### 3 Interaction with Precipitates

MD simulation of the dislocation motion in metals with various obstacles, both the model ones (rigid obstacles and inclusions of various forms) and the obstacles repeating the structure of real precipitates of alloys [16] are performed. The simulations show that the main mechanism for overcoming of an obstacle is the formation of an Orowan loop around it. The shear deformation of the obstacle is a secondary process; it is observed either during the first or subsequent dislocation passing depending on the stiffness of the inclusion. Cutting of the obstacle occurs due to the shift by the Burgers vector of one part of the matrix surrounding the obstacle relative to the other part of it during each passage of the dislocation. When the displacement of the surrounding matrix becomes large enough, one part of the obstacle shifts relative to the other one. In some cases, when the obstacles are small in size or the dislocation passes near the edge of the obstacle, it can be avoided due to the ejection of a segment of the dislocation line into the adjacent plane (cross-slip) with emission of vacancies.

The mechanical model is formulated in [16] for description of the dynamics of dislocation with the formation of the Orowan loop. The model takes into account increase in the dislocation line energy due to increase of its size, which counteracts the

dislocation motion, and relaxation of stresses by dislocation, which promotes its motion. The model reflects the main tendencies observed in MD simulations [16], Fig. 4.

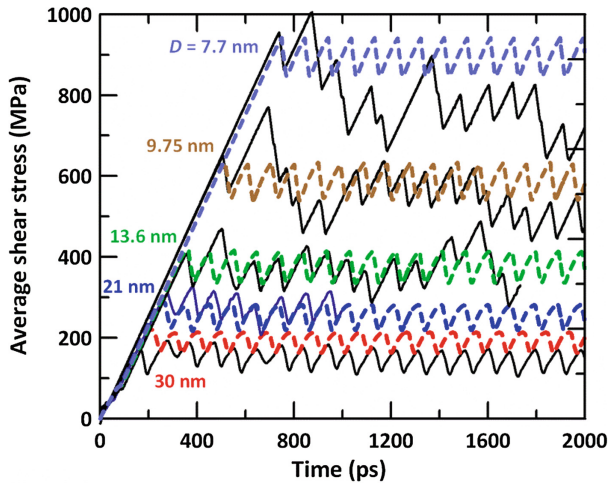


**Fig. 4.** Motion of edge dislocation in aluminum containing  $\theta'$  phase precipitates [16]: influence of the distance  $D$  between the centers of precipitates. MD simulations (black solid lines) and calculations on the basis of continuum model (color dashed lines) for evolution of shear stresses in sample at boundary shift with constant velocity of 3 m/s at constant temperature of 300 K are presented. The precipitate radius is 5 nm, the thickness is 2.2 nm. The system size is  $51.7 \times 60.3 \times D \text{ nm}^3$ , where  $D$  is indicated near lines.

## 4 Conclusions

Atomistic simulations of the dislocation motion in pure metals and alloys are used for formulation and verification of the mechanical models of continuum level, and fitting of the parameters of the models. Motion of dislocations creates heterogeneous distribution of stresses at nanoscale. Formation of Orowan loop is revealed to be the main mechanism of the overcoming of obstacles at dynamic loading.

**Acknowledgements.** Investigation of aluminum is supported by the Russian Science Foundation (Project 18-71-10038); investigation of copper and magnesium is supported by the Ministry of Science and Higher Education of the Russian Federation (State task 3.2510.2017/4.6).

## References

1. Austin, R.A., McDowell, D.L.: A dislocation-based constitutive model for viscoplastic deformation of FCC metals at very high strain rates. *Int. J. Plast.* **27**(1), 1–24 (2011)
2. Krasnikov, V.S., Mayer, A.E., Yalovets, A.P.: Dislocation based high-rate plasticity model and its application to plate-impact and ultra short electron irradiation simulations. *Int. J. Plast.* **27**(8), 1294–1308 (2011)

3. Barton, N.R., Bernier, J.V., Becker, R., Arsenlis, A., Cavallo, R., Marian, J., Rhee, M., Park, H.-S., Remington, B.A., Olson, R.T.: A multiscale strength model for extreme loading conditions. *J. Appl. Phys.* **109**(7), 073501 (2011)
4. Malygin, G.A., Ogarkov, S.L., Andriyash, A.V.: A dislocation kinetic model of the formation and propagation of intense shock waves in crystals. *Phys. Solid State* **55**(4), 787–795 (2013)
5. Merzhievskii, L.A.: Deformation models under intense dynamic loading (review). *Comb. Expl. Shock Waves* **51**(2), 269–283 (2015)
6. Luscher, D.J., Mayeur, J.R., Mourad, H.M., Hunter, A., Kenamond, M.A.: Coupling continuum dislocation transport with crystal plasticity for application to shock loading conditions. *Int. J. Plast.* **76**, 111–129 (2016)
7. Mayer, A.E., Khishchenko, K.V., Levashov, P.R., Mayer, P.N.: Modeling of plasticity and fracture of metals at shock loading. *J. Appl. Phys.* **113**, 193508 (2013)
8. Mayer, A.E., Borodin, E.N., Krasnikov, V.S., Mayer, P.N.: Numerical modelling of physical processes and structural changes in metals under intensive irradiation with use of CRS code: dislocations, twinning, evaporation and stress waves. *J. Phys.: Conf. Ser.* **552**, 012002 (2014)
9. Mayer, A.E., Mayer, P.N., Krasnikov, V.S., Pogorelko, V.V.: Multiscale models of metal behaviour and structural change under the action of high-current electron irradiation. *J. Phys.: Conf. Ser.* **830**, 012072 (2017)
10. Agranat, M.B., Ashitkov, S.I., Komarov, P.S.: Metal behavior near theoretical ultimate strength in experiments with femtosecond laser pulses. *Mech. Solids* **49**(6), 643–648 (2014)
11. Smith, R.F., Eggert, J.H., Rudd, R.E., Swift, D.C., Bolme, C.A., Collins, G.W.: High strain-rate plastic flow in Al and Fe. *J. Appl. Phys.* **110**(12), 123515 (2011)
12. Kanel, G.I., Zaretsky, E.B., Razorenov, S.V., Ashitkov, S.I., Fortov, V.E.: Unusual plasticity and strength of metals at ultra-short load durations. *Phys.-Usp.* **60**(5), 490–508 (2017)
13. Krasnikov, V.S., Kuksin, A.Yu., Mayer, A.E., Yanilkin, A.V.: Plastic deformation under high-rate loading: the multiscale approach. *Phys. Solid State* **52**(7), 1386–1396 (2010)
14. Norman, G.E., Yanilkin, A.V.: Homogeneous nucleation of dislocations. *Phys. Solid State* **53**(8), 1614–1619 (2012)
15. Krasnikov, V.S., Mayer, A.E.: Influence of local stresses on motion of edge dislocation in aluminum. *Int. J. Plast.* **101**, 170–187 (2018)
16. Krasnikov, V.S., Mayer, A.E.: Dislocation dynamics in aluminum containing  $\theta'$  phase: atomistic simulation and continuum modeling. *Int. J. Plast.* (2019)
17. Mayer, A., Krasnikov, V., Pogorelko V.: Limit of ultra-high strain rates in plastic response of metals. In: Gdoutos, E. (eds) *Proceedings of the First International Conference on Theoretical, Applied and Experimental Mechanics. ICTAEM 2018. Structural Integrity*, vol. 5, pp. 273–278. Springer, Cham (2019)
18. Plimpton, S.: Fast parallel algorithms for short-range molecular dynamics. *J. Comput. Phys.* **117**, 1–19 (1995)
19. Stukowski, A.: Visualization and analysis of atomistic simulation data with OVITO—the Open Visualization Tool. *Modell. Simul. Mater. Sci. Eng.* **18**, 015012 (2010)
20. Stukowski, A., Bulatov, V.V., Arsenlis, A.: Automated identification and indexing of dislocations in crystal interfaces. *Modell. Simul. Mater. Sci. Eng.* **20**, 085007 (2012)
21. Hirel, P.: Atomsk: a tool for manipulating and converting atomic data files. *Comput. Phys. Commun.* **197**, 212–219 (2015)



# Development and Validation of 3D DIC Based Residual Stress Testing Method

Tomasz Brynk<sup>(✉)</sup>

Faculty of Materials Science and Technology, Warsaw University  
of Technology, Woloska 141 Str., 02-507 Warsaw, Poland  
tomasz.brynk@pw.edu.pl

**Abstract.** The paper describes the methodology of residuals stress determination on the basis of displacement fields measurement near drilled holes by means of 3D Digital Image Correlation. Detailed information concerning testing procedure are presented and supplemented by exemplary tests results for steel sample uniaxially loaded to 300 MPa. Determined values of residual stress calculated with inverse method algorithm are compared to the ones obtained with traditional method with near the hole strain measurements by means of tensometric rosette. In both cases 2 mm mill was used to drill the flat bottom hole with 0.25 mm increase steps. The influence of FEM model geometry used to deliver correction terms to the analytical model, necessary in the case of blind holes, is discussed. Determined residual stress from DIC based method agreed reasonably with traditional method.

**Keywords:** Residual stress · 3D digital image correlation · Inverse method

## 1 Introduction

The most popular method of residual stress determination is based on strain measurements near the drilled hole by means of specially designed rosettes usually consisting of three tensometers. Stress relaxation caused by material removal causes small deformation on the surface dependent on stress distribution. The method is standardized, however has some drawback related to time consuming tensometers fixing procedure, hole eccentricity sensitivity and limited drill diameters range (dependent on the available tensometric rosettes geometry). Overmentioned disadvantages might be overcome by replacing tensometers with non-contact optical measurements by means of Digital Image Correlation (DIC) method. Moreover, DIC measurements deliver much more data (hundreds or thousands data points) in comparison to tensometric rosettes (usually three readings, only) allowing to use over-deterministic procedures for stress calculations and improvement of the method accuracy.

## 2 Methodology

### 2.1 Development of Testing Stand

Testing stand aimed for displacement fields measurements near drilled holes by means of 3D DIC has been developed. 3D DIC system utilizes digital images of the object surface (with contrast in the form of speckle pattern) registered before and after deformation with at least two cameras. In two cameras system they are placed in 30–60° angle to each other which gives an opportunity to place driller between them and eliminate the need of removing camera while drilling. During presented tests upgraded stand was used (see Fig. 1). Preliminary tests which results are presented elsewhere [1] revealed the need for construction stiffness improvement and better cameras fixing. Hole depth was controlled by a stepper motor steered with Arduino microcontroller.

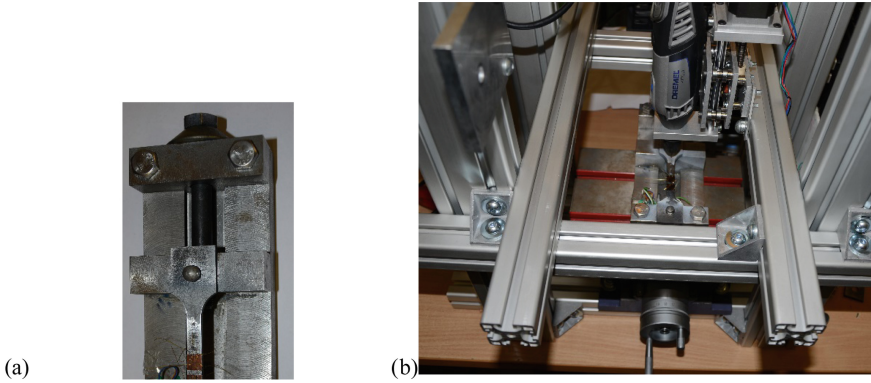


**Fig. 1.** Experimental set-up: **a** loading table with mounted sample, **b** frame with driller. Development of calculation algorithms.

### 2.2 Development of Calculation Algorithms

Equations describing displacement field near drilled hole are available in the form [2]:

$$u_r = A(\sigma_x + \sigma_y) + B[(\sigma_x - \sigma_y) \cos 2\theta + 2\sigma_{xy} \sin 2\theta] \quad (1)$$

$$u_\theta = C[(\sigma_x - \sigma_y) \sin 2\theta - 2\sigma_{xy} \cos 2\theta] \quad (2)$$

where:

$u_r$  radial displacement,  
 $u_\theta$  angular displacement,  
 $\sigma_x, \sigma_y, \sigma_{xy}$  residual stress components

In the through hole case there are available analytical equations for A, B and C coefficients:

$$A = \frac{r_0}{2E}(1 + \nu)\rho \quad (3)$$

$$B = \frac{r_0}{2E} [4\rho - (1 + \nu)\rho^3] \quad (4)$$

$$C = \frac{r_0}{2E} [2(1 - \nu)\rho + (1 + \nu)\rho^3] \quad (5)$$

where:

- $r_0$  hole radius,
- $E$  Young's modulus,
- $\nu$  Poisson's ratio,
- $\rho$  distance from the hole center to hole radius ratio ( $r/r_0$ ).

Blind hole case is not straightforward due to the lack of direct analytical solutions. However, correction terms replacing A, B and C might be introduced from Finite Element Modelling (FEM) results for uniaxial loading case as proposed in [2] and presented in author previous work [1]. These correction terms are depended on elastic constants, hole geometry and distance from the hole center and valid for arbitrary residual stress components values.

Correction terms for analytical equations were determined from FEM models of two geometries. First one geometry agreed with sample gauge section dimensions while the second one was designed for more general cases and was in the form of  $20 \times 20 \times 4$  mm plate. Images of meshes for both models are presented in Fig. 2. Element death technique was used to simulate material removal caused by drilling.

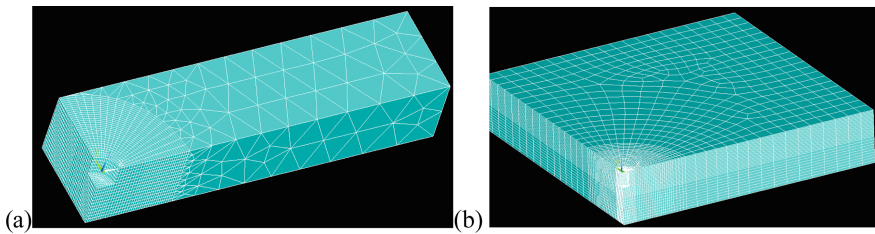


**Fig. 2.** FEM model meshes for: **a** sample and **b** plate case.

Correction terms were determined for different discrete  $r/r_0$  values. 4th order polynomial was fitted to obtained data allowing to use them for arbitrary coordinates combinations for fixed hole depth.



Inverse method iterative algorithm has been developed for residual stress calculations from DIC data. The aim of calculations was to determine the optimized set of  $\sigma_x$ ,  $\sigma_y$ ,  $\sigma_{xy}$  as well as coordinates of the hole center and rigid body motion and rotation by minimizing global difference between model and DIC measured displacements. Algorithm reliability has been preliminary validated using artificial FEM generated displacement fields for different biaxial residual stress conditions as the input data. The results agreed with less than 1% error.

### 2.3 Experimental Work

Experimental work covered an attempt to determine residual stress in steel sample of  $10 \times 4$  mm cross section uniaxially loaded to 300 MPa. Prior testing sample was annealed to relieve any possible residual stress coming from material processing. Sample was loaded and locked in special table (Fig. 1a) and final stress was determined from Hook's law basing on attached extensometer readings. After achieving desire uniaxial stress level extensometer was removed, sample surface prepared for DIC measurements by black and white paint spraying and the loading table with sample mounted to testing stand. 1.5 mm diameter hole was drilled with diameter in 0.25 mm consecutive steps to final depth of 2 mm. For each step three digital images were registered for 3D DIC measurements. Reported  $\sigma_x$  values are averages from the results of model parameters optimization for three DIC measurements for the same hole depth.

Additionally drilling procedure was done on the same sample in the center of tensometric rosette fixed after sample loading. In this case residual stress were determined in accordance to ASTM standard [3].

## 3 Results and Discussion

Exemplary displacement fields maps from DIC measurements sample geometry based model after parameters optimization are shown in Fig. 3. The results of dominating component average values are presented in Fig. 4.

In general, the results obtained with DIC based method agreed well with those from standardized procedure, especially when FEM model geometry used for blind hole correction was depicting sample gauge section and calculation were made for hole depth exceeding 0.75 mm. It suggest necessity for dedicated FEM model geometry development to deliver blind hole correction terms in the cases when residual stress has to be determined near an object edge.

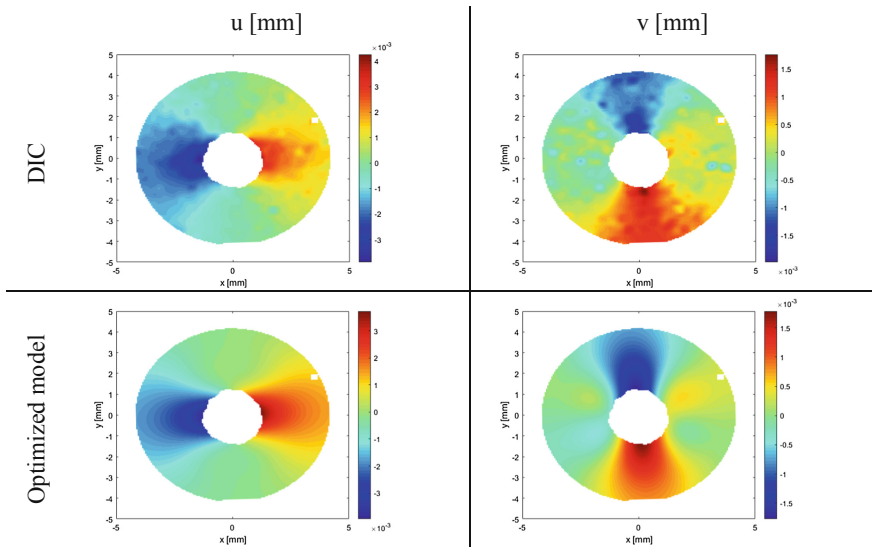


**Fig. 3.** Exemplary displacement field maps from DIC measurements and corrected analytical model (Sample geometry model correction, 2 mm hole depth).

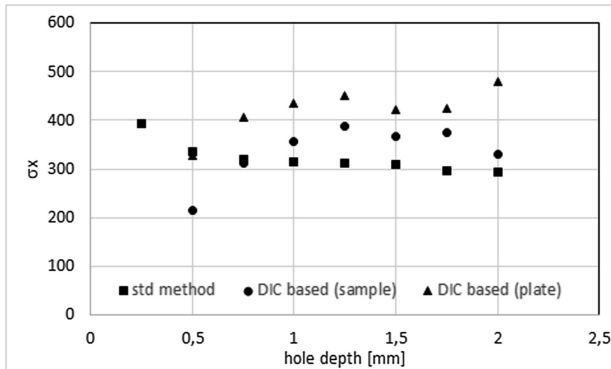


**Fig. 4.** Results of  $\sigma_x$  determined from DIC based and standardized method.

## 4 Conclusions

Residual stress in steel sample loaded to known stress level has been determined with the improved stand and calculations algorithm based on displacement fields measurements near drilled blind holes by means of 3D DIC. Obtained results agreed reasonably with standardized method, validating proposed testing procedure. This methodology might be used for holes geometry not limited by available tensometric rosettes sizes and related mills diameters.

**Acknowledgements.** This work was supported by The National Science Center under contract 2016/21/D/ST8/02019.

## References

1. Makino, A., Nelson, D.: Residual-stress determination by single-axis holographic interferometry and hole drilling-part I: theory. *Exp. Mech.* **34**(1), 66–78 (1994)
2. Brynk, T., Romelczyk-Baishya, B.: Residual stress estimation based on 3D DIC displacement field measurement around drilled holes. *Procedia Struct. Integr.* **13**, 1267–1272 (2018)
3. ASTM E837



# Monogenic Filtering Based Automatic Defect Detection from a Single Fringe Pattern

Rishikesh Kulkarni<sup>1</sup>(✉) and Pramod Rastogi<sup>2</sup>

<sup>1</sup> Department of Electronics and Electrical Engineering,  
Indian Institute of Technology Guwahati, Guwahati, India  
rishik.k@iitg.ernet.in

<sup>2</sup> Applied Computing and Mechanics Laboratory, Ecole Polytechnique  
Federale de Lausanne, Lausanne, Switzerland

**Abstract.** We propose a fringe analysis algorithm for the automatic detection of defects from a single fringe pattern (FP). Typically, the surface defects exhibit high fringe density areas in the FP. Consequently, high fringe density regions can be utilized as a signature for detecting and locating the surface defects. An algorithm based on monogenic filtering of the FP is proposed for an efficient computation of the fringe density. The defect related high density fringe areas are segmented from the defect-free region based on a threshold derived from the fringe density histogram. The algorithm is found to be noise robust and it does not require any pre-processing of the FP. A single FP based analysis approach is suitable in identifying defects using interferometric systems in an industrial environment. Simulation and experimental results are provided to demonstrate the feasibility of the proposed algorithm.

**Keywords:** Fringe analysis · Interferometry · Monogenic filtering

## 1 Introduction

Optical interferometric measurement techniques such as digital holographic interferometry, electronic speckle pattern interferometry, and shearography have been employed in the applications of defect detection, deformation analysis and non-destructive testing [1–3]. In these techniques, the information on the measurand is recorded in the form of a sinusoidal variation in intensity, usually termed as a *fringe pattern*. In general, phase shifting interferometry has to be employed for performing quantitative measurement [4]. Since phase shifting is sensitive to vibrations, it is desirable to perform deformation analysis using a single recording of a fringe pattern. In this work, we propose a frequency selective filtering based on monogenic representation of the fringe pattern for surface defect detection.

## 2 Monogenic Filtering Based Fringe Analysis

The FP can be represented as,

$$I(\mathbf{r}) = a(\mathbf{r}) + b(\mathbf{r}) \cos \phi(\mathbf{r})$$

where,  $\mathbf{r} = [x, y]^T$  indicates the pixel spatial coordinates of the FP;  $a(\mathbf{r})$  and  $b(\mathbf{r})$  represent the background intensity and the fringe amplitude, respectively;  $\phi(\mathbf{r})$  represents the phase embedded in the fringe pattern. In deformation analysis using electronic speckle pattern interferometry and holographic interferometry, this phase is proportional to surface displacement. On the other hand, in shearography, the phase is proportional to surface displacement derivative.

Adaptive monogenic filtering has been considered in [5] for the purpose of fringe normalization and denoising. In this work, we propose to use the adaptive monogenic filtering operation for the estimation of fringe density at each pixel. At a given pixel  $\mathbf{r}'$ , the FP within a small window can be expressed as a single frequency sinusoid as,

$$I(\mathbf{r}) = A \cos[\boldsymbol{\omega}_0^T(\mathbf{r} - \mathbf{r}') + \phi],$$

where,  $\boldsymbol{\omega}_0 = [\omega_x, \omega_y]^T$  represent the local frequency vector. If an appropriate filter is designed, the local amplitude  $A$  and phase  $\phi$  can be estimated accurately. To do so, we need to obtain a two-dimensional analytic signal, i.e. monogenic signal, corresponding to the FP. For the computation of monogenic signal, we consider an isotropic log-Gabor filter, which is given as

$$H(\boldsymbol{\omega}) = \exp\left(-\frac{\left(\log\left(\frac{|\boldsymbol{\omega}|}{\omega_0}\right)\right)^2}{2(\log \sigma)^2}\right).$$

The bandwidth of the filter passband depends on the shape parameter  $\sigma$ . The FP filtered by  $H(\boldsymbol{\omega})$  constitutes the real part of the monogenic signal. The two imaginary parts of the monogenic signal are computed using a complex valued filter

$$H_O(\boldsymbol{\omega}) = \frac{j\omega_x - \omega_y}{|\boldsymbol{\omega}|} H(\boldsymbol{\omega}), \quad j = \sqrt{-1}.$$

The real and imaginary components of the output of this filter corresponds to the two odd parts of the monogenic signal. Let  $I_e(\mathbf{r})$ ,  $I_{01}(\mathbf{r})$  and  $I_{02}(\mathbf{r})$  represent the real and imaginary components of the monogenic signal. The local amplitude estimate is obtained as,

$$I_o(r) = \sqrt{I_{01}(r)^2 + I_{02}(r)^2}$$

$$A(r) = \sqrt{I_e(r)^2 + I_o(r)^2}$$

The local amplitude is computed using a number of filter frequencies ( $\omega_0$ ), say  $K$ . The frequencies are selected such that low and high fringe frequencies corresponding to slow phase variations and noise, respectively, are filtered out. Subsequently, at each pixel, the maximum filter output amplitude among all the filter outputs is computed. This maximum amplitude map clearly indicate the defective region with high amplitude against the low amplitude defect-free region. The amplitude map is normalized and a threshold is applied to obtain a binary map segmenting the defective and defect-free region. The threshold is computed based on the histogram of the maximum amplitude map.

### 3 Simulation and Experimental Results

A simulation example is provided in Fig. 1a with a typical shearogram recorded in shearography setup. Four defect locations with different fringe densities are present. The FP is corrupted by additive noise. Spatially varying background intensity and fringe amplitudes are considered in the simulation. Figure 1b shows the maximum amplitude map. The binary image in Fig. 1c clearly indicates the identified defective regions. Figure 1d is provided for the purpose of illustration.

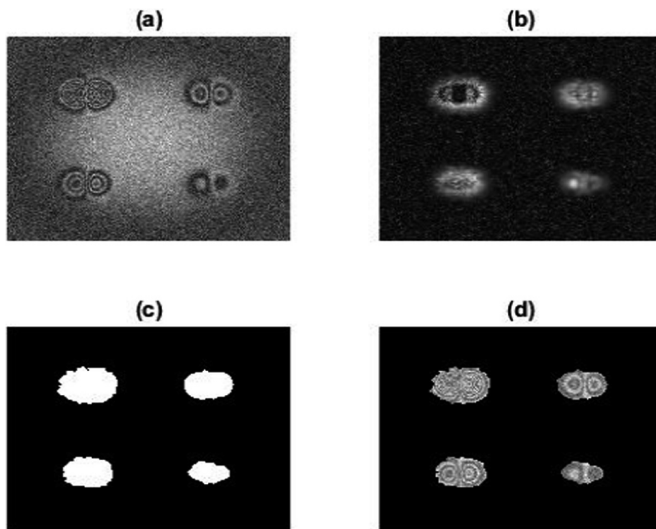


**Fig. 1.** Simulation results: **a** simulated shearogram with four defects, **b** monogenic filter amplitude, **c** binary image indicating defect locations and **d** high density fringes present at the defect locations.

Figure 2a shows the FP recorded in a holographic interferometry setup corresponding to out-of-plane deformation of an aluminum plate. A circle indicating the point of loading is shown in the figure. The proposed algorithm is implemented to

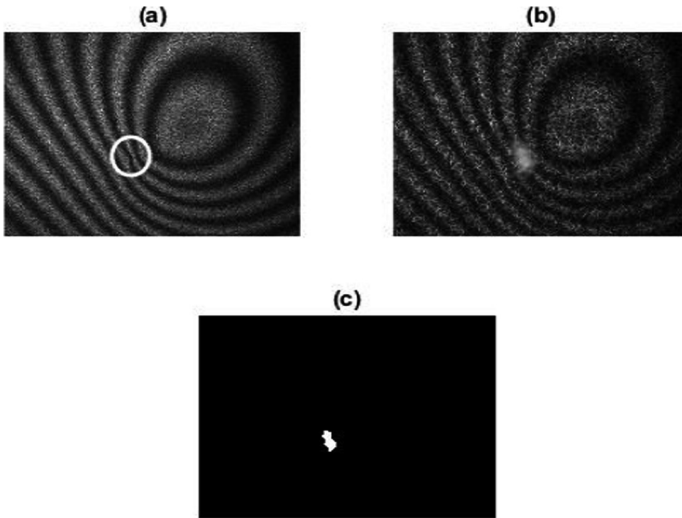


**Fig. 2.** Experimental results: **a** fringe pattern recorded in a holographic interferometry setup corresponding to out-of-plane deformation of an aluminum plate, **b** monogenic filter amplitude and **c** binary image indicating the point of loading.

locate the point of load. Figure 2b, c show the maximum amplitude map and identified defect map, respectively.

## 4 Conclusion

A noise robust fringe analysis algorithm is proposed for the automatic identification of surface defects. A monogenic filtering based algorithm effectively computes the local fringe amplitude map at different filter frequencies based on which high fringe density areas are identified. The simplicity of implementation and simulation and experimental results substantiates the practical applicability of the proposed method.

## References

1. Jacquot, P.: Speckle interferometry: a review of the principal methods in use for experimental mechanics applications. *Strain* **44**, 57–69 (2008)
2. Servin, M., Quiroga, J.A., Padilla, M.: *Fringe Pattern Analysis for Optical Metrology: Theory, Algorithms, and Applications*. Wiley-VCH (2014)
3. Kulkarni, R.D., Rastogi, P.: *Single and Multicomponent Digital Optical Signal Analysis: Estimation of Phase and Its Derivatives*. Institute of Physics publishing (2017)
4. Vandenrijt, J., Georges, M.: Automated defect detection algorithm applied to shearography in composites. In: *Fringe 2013*, pp. 237–240. Springer, Berlin (2014)
5. Guerrero, J.A., Marroquin, J.L., Rivera, M., Quiroga, J.A.: Adaptive monogenic filtering and normalization of ESPI fringe patterns. *Opt. Lett.* **30**, 3018–3020 (2005)



# Enhanced Post-crack Load Carrying Capacity of Nano and Micro Scale Carbon Fiber Reinforced Mortars

Maria G. Falara<sup>1</sup>(✉), Maria S. Konsta-Gdoutos<sup>2</sup>,  
and Emmanuel E. Gdoutos<sup>3</sup>

<sup>1</sup> School of Engineering, Democritus University of Thrace,  
671 00 Xanthi, Greece  
mfalara@civil.duth.gr

<sup>2</sup> Department of Civil Engineering, College of Engineering,  
University of Texas at Arlington, Arlington, TX, USA

<sup>3</sup> Academy of Athens, 106 79 Athens, Greece

**Abstract.** A thorough investigation of the pre-peak, first crack and post-crack flexural response, energy absorption performance and ductility of cement mortar composites with hybrid reinforcement using nano and micro scale carbon fibers took place in this study. Young's modulus, energy absorption capability and energy based dimensionless indices (toughness indices) were investigated through the Linear Elastic Fracture Mechanics theory. Prismatic notched specimens of neat mortar and mortars reinforced with 0.1 vol.% CNFs and/or 0.5 vol.% CFs were subjected to a three-point close loop bending test, using the crack mouth opening displacement, CMOD. Combined networks of CNFs and CFs were incorporated in mortar matrix in order to investigate the synergistic effect of hybrid reinforcement on the mechanical properties of the single-reinforced mortars. The experimental results showed an exceptional multi scale mechanical performance of nano and micro scale fiber reinforced mortars as reflected from the load-CMOD response of specimens. The energy absorption capability and load carrying capacity of multiscale reinforced mortars after the formation of the initial crack (first crack), are outstandingly improved as indicated by the 138 and 100% increases of the proposed size independent toughness indices, up to the peak load and the ultimate failure, respectively.

**Keywords:** Carbon nanofibers · Carbon fibers · Energy absorption capability · Toughness indices

## 1 Introduction

The most important properties that structural materials such as mortars and concrete can provide are strength, stiffness, flexural toughness and post-cracking energy absorption capability. Failure in cement based materials is a gradual multi-scale process. In order to improve the load-bearing capacity of cementitious materials, crack growth must be delayed at the nano, micro and eventually at the macro scale. Microfibers, such as carbon fibers (CFs) can improve the post-peak behavior by



bridging the microcracks and delaying the formation of a through-specimen macrocrack [1, 2]. However, cracks in cementitious materials initiate from the nanoscale where microfibers are not effective. Carbon nanofibers (CNFs) exhibit several distinct advantages as reinforcing materials for cementitious composites. Effectively dispersed nanoscale fibers are able to control the matrix cracks at the nanoscale, resulting in essentially improved flexural strength, stiffness and energy absorption ability as well as enhanced flexural toughness [3]. The ladder scale reinforcement, with the simultaneous use of carbon nanofibers and microscale PVA fibers in cement paste yielded remarkable improvement in flexural strength and stiffness up to 50 and 84%, respectively, and the composites also exhibited 33 times higher flexural toughness [4]. This study aims to evaluate the synergistic effect of carbon fibers at the nano and micro scale on the flexural strength, Young's modulus, flexural toughness and the post-cracking energy absorption capability of hybrid nano- and micro-modified mortars. The synergistic interaction between the carbon fibers at the nano and micro scale results in a multiscale reinforcing mechanism as: (i) inhibits the initiation and propagation of cracks at the nanoscale, increasing the flexural strength (+108%) and stiffness (+96%) and the proportionality of load-CMOD response until the "first crack"; and (ii) provides an enhanced post-crack bridging mechanism after the formation of the "first crack". The combined nano and micro scale fiber networks exceptionally improve the post-crack energy absorption capability of micro scale fiber mortar composites as reflected by the  $\approx 2.0$  times higher toughness indices, up to peak load and ultimate failure, respectively.

## 2 Experimental Work

### 2.1 Materials and Specimens

In this study, mortar samples were produced by adding 0.1 vol.% CNFs and/or 0.5 vol.% CFs to Type I ordinary Portland cement (OPC) 42.5R and standard sand according to EN 196-1, at a water to cement ratio (w/c) 0.485 and sand to cement ratio (s/c) 2.75. Effective dispersion was achieved by adding the fibers to an aqueous polycarboxylate based surfactant solution, at a surfactant to fibers weight ratio of 4.0 and applying ultrasonic energy [5]. After mixing, notched  $20 \times 20 \times 80$  mm prisms were prepared to conduct 3 point bending mechanical testing. Following demolding, the samples were cured in lime-saturated water for 28 days.

### 2.2 Experimental Determination of Flexural Strength, Young's Modulus and Toughness Indices

Three point bending tests were conducted on  $20 \times 20 \times 80$  mm specimens according to the procedure based on ASTM C348-14. The test was performed using a 25 kN MTS servo-hydraulic, closed-loop testing machine. Flexural strength and Young's modulus were determined according to the Linear Elastic Fracture Mechanics theory and the ASTM C348-14 [6]. The toughness indices are determined by dividing the area under the load-CMOD curve up to a specified point by the CMOD at which "first crack" is deemed to have occurred [7].

### 3 Results and Discussion

Flexural strength and Young's modulus of 28d mortars reinforced with highly dispersed carbon nanofibers and/or microfibers, are presented in Fig. 1. Comparing the results of plain mortar and mortar reinforced with 0.1 vol.% CNFs,  $\approx 94\%$  increase in both flexural strength and stiffness is observed. Mortars reinforced with 0.5 vol.% CFs, exhibit almost the same flexural strength and stiffness with the plain mortar. The addition of micro scale fibers into the cementitious matrix mostly results in post-elastic property changes [8]. However, the simultaneous incorporation of nano and micro scale fibers results in 2.1 times higher flexural strength and 1.9 times higher Young's modulus over the plain one.

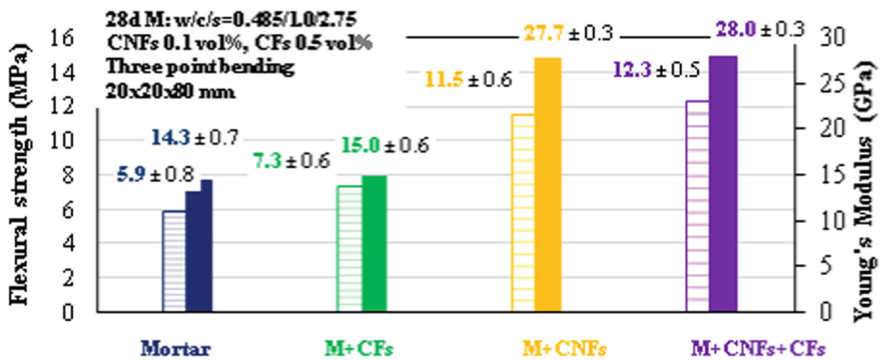
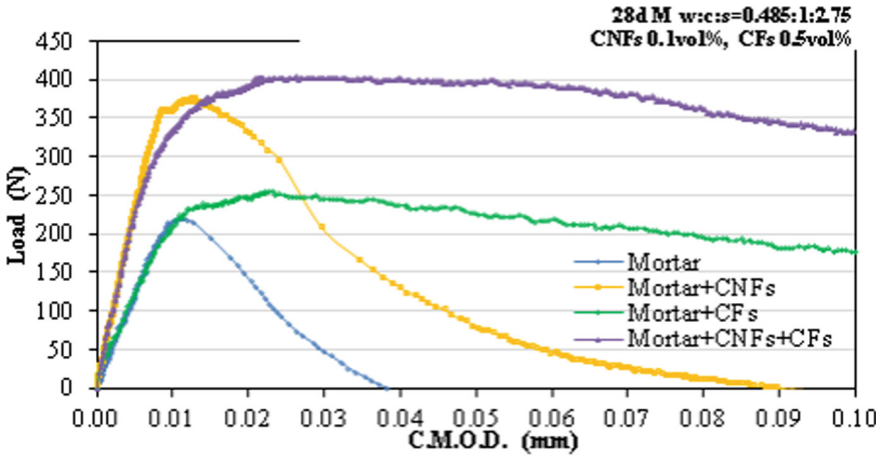


Fig. 1. Flexural strength and Young's modulus of 28d plain mortar and mortars reinforced with CNFs and/or CFs.

Figure 2 presents load-CMOD curves of 28d mortars with the ladder scale reinforcement of CNFs and CFs. The addition of CNFs doubles the flexural toughness of neat mortar matrix as reflected by the bigger area under the load-CMOD curve. The energy absorption capability of the mortars reinforced with microscale CFs is approximately 12 times higher than the toughness exhibited by the neat or nanomodified mortar. It is obvious that the addition of microscale fibers has a considerable positive influence on the post elastic energy absorption capability of mortar composites. Interestingly, the energy absorption capability of mortars reinforced with hybrid networks of CNF-CF is almost 105% higher than that exhibited from the mortars singly reinforced with CFs.

The flexural toughness, however, cannot be used as a true material property since it is size and geometry dependent. For this reason, energy-based dimensionless indices (toughness indices) were developed and used to interpret the material's post-cracking behavior. Toughness indices identify the pattern of the material behavior up to a selected bending strain criteria, according to ACI 544R-1 report on fiber reinforced concrete [9]. The addition of CFs however has a great effect on post-cracking toughness of mortars, as both the  $T_{PL}/T_{FC}$  and  $T_U/T_{FC}$  ratios are greatly enhanced from 1.3 up to 4.4 and 4.9 up to 59.5, respectively. Toughness index of CNF-CF reinforced



**Fig. 2.** Load-CMOD curves of 28d mortars reinforced with CNFs and/or CFs.

mortars is 1.6 higher up to the application of the peak load, comparing to the micro scale fiber reinforced mortars. The hybridization of the mortar matrix has also a higher impact at the post peak area up to failure, as the mortar reinforced with both CNFs and CFs exhibit 74% higher toughness index comparing to the mortar reinforced only with the carbon micro scale fibers (Table 1).

**Table 1.** Toughness indices up to peak load and ultimate failure of 28d plain mortar and hybrid mortar nanocomposites reinforced with CNFs and CFs

Sample	$T_{PL}/T_{FC}$	$T_U/T_{FC}$
M	1.3	4.9
M + CNFs	1.6	5.5
M + CFs	4.4	59.5
M + CNFs + CFs	7.4	103.6

## 4 Conclusions

The principal objective of this study is a thorough mechanical characterization at the pre-peak and post-crack area of cement mortars reinforced with single or multiple nano and micro scale fiber reinforcement. The combination of CNFs and CFs provide better mechanical performance at both pre-peak and post-crack over the mortars reinforced with microscale fibers alone. The addition of 0.1 vol.% CNFs leads to an enhanced pre-peak mechanical behavior, with 95 and 94% increased flexural strength and Young’s modulus, respectively. On the other hand, the addition of micro scale carbon fibers results only in post-crack changes as the mortar composites though exhibit no increase in flexural strength and stiffness, a 14 times higher energy absorption capability after the formation of the “first crack” is observed over the plain mortar and

mortar reinforced only with CNFs, respectively. The enhanced bridging mechanism after the formation of the “first crack” by the simultaneous use of nano and micro scale fibers exceptionally improves the composites’ post-crack energy absorption capability as reflected by the  $\approx 2.0$  times higher toughness indices, up to peak load and ultimate failure, respectively.

**Acknowledgements.** The authors would like to kindly acknowledge the financial support from the Academy of Athens under the Research Funding Program “Improving structural performance and monitoring of damage in nanomodified concrete composites using carbon nanotubes and carbon nanofibers” (200/903).

## References

1. Shah, S.P., Ouyang, C.: Mechanical behavior of fiber reinforced cement-based composites. *J. Am. Ceram. Soc.* **74**(11), 2727–2953 (1991)
2. Brandt, A.M.: Fibre reinforced cement-based (FRC) composites after over 40 years of development in building and civil engineering. *Compos. Struct.* **86**, 3–9 (2008)
3. Gdoutos, E.E., Konsta-Gdoutos, M.S., Danoglidis, P.A.: Portland cement mortar nanocomposites at low carbon nanotube and carbon nanofiber content: a fracture mechanics experimental study. *Cement Concr. Compos.* **70**, 110–118 (2016)
4. Metaxa, Z.S., Konsta-Gdoutos, M.S., Shah, S.P.: Mechanical properties and nanostructure of cement-based materials reinforced with carbon nano-fibers and polyvinyl alcohol (PVA) microfibers. *ACI Spec. Publ. Adv. Mater. Sci. Concr.* **270**, 115–126 (2010)
5. Shah, S.P., Konsta-Gdoutos, M.S., Metaxa, Z.S.: Highly dispersed carbon nanotube reinforced cement based materials. United States Patent US9,365,456 (B2), 14 June 2016
6. Danoglidis, P.A., Konsta-Gdoutos, M.S., Gdoutos, E.E., Shah, S.P.: Strength, energy absorption capability and self-sensing properties of multifunctional carbon nanotube reinforced mortars. *Constr. Build. Mater.* **120**, 265–274 (2016)
7. Barr, B.I.G., Gettu, R., Al-Oraimi, S.K.A., Bryars, L.S.: Toughness measurement—the need to thing again. *Cement Concr. Compos.* **18**, 281–297 (1996)
8. Toutanji, H.A., El-Korchi, T., Katz, R.N.: Strength and reliability of carbon-fiber reinforced cement composites. *Cement Concr. Compos.* **16**, 15–21 (1994)
9. American Concrete Institute: Report on Fiber Reinforced Concrete. ACI 544.1R-96 (1996)



# Two-Point Bending Stress Determination of Ultra-Thin Glass Plates

Po-Chi Sung, Wei-Chung Wang<sup>(✉)</sup>, and Yu-Wei Kuo

Department of Power Mechanical Engineering, National Tsing Hua University,  
30013 Hsinchu, Taiwan, Republic of China  
wawang@pme.nthu.edu.tw

**Abstract.** Based on the large deflection beam theory and the deflection beam profile equation, a two-point bending stress determination method for ultra-thin glass plates was proposed in this paper. The full-profile bending stress distribution as the ultra-thin glass plate is bent with any contact angle and any compression displacement in the two-point bending test can be determined by the proposed method. In experiment, the widths and heights of the profile as well as the compression forces of a 100  $\mu\text{m}$  thickness ultra-thin glass plate bent with different contact angles and compression displacements were measured. Measurement results of the widths and heights of the profiles as well as the compression forces are in good agreement with the theoretical values.

**Keywords:** Ultra-thin glass plate · Bending stress · Large deflection beam theory · Two-point bending test · Enhanced exposure theory of photoelasticity

## 1 Introduction

The residual stress and micro defect produced by the cutting processing may reduce the flexibility of the ultra-thin glass plate. Two-point bending test has been one of industrial standards to be used to inspect the ultra-thin glass plate after cutting. In the common inspection standard, the bending stress on the profile center when the ultra-thin glass plate is coming to be fractured is regarded as the strength of the ultra-thin glass plate in two-point bending test. Therefore, the previous investigations of two-point bending test [1, 2] only developed the theories to determine the bending stress on the profile center of the specimen. It means that those theories reported in [1, 2] can be applied only in the situation that the fracture is generated right on the profile center. However, in general, the fracture is not on the profile center.

Exactly determining the bending stress at the fracture point will help manufacturers and users accurately define the quality of ultra-thin glass plates. Sung et al. [3] proposed a method to determine the full-profile bending stress of ultra-thin glass plate by using the enhanced exposure theory of photoelasticity (EEToP) [4]. Nevertheless, a correlation between the full-profile bending stress distribution and the compression displacement needs to be explored.

In this paper, a method capable of determining the full-profile bending stress with any contact angle and compression displacement in two-point bending test was proposed. In this method, the large deflection beam theory was utilized and the deflection

beam profile equation was proposed to derive the general equation for two-point bending stress determination. An ultra-thin glass plate was bent with different contact angles and compression displacements. Measurement results of the widths and heights of the profile as well as the compression forces of the ultra-thin glass plate were compared with the theoretical values to verify the feasibility of this method.

## 2 Experimental Setup

The test specimen was a 100  $\mu\text{m}$  thickness ultra-thin glass plate (OA-10G, Nippon Electric Glass Co., Ltd.) with 140 mm in length and 70 mm in width. The experimental setup involved a self-made two-point bending frame and a digital still camera. The compression load and displacement by the built-in load cell and graduated scale can be measured by the two-point bending frame, respectively. The digital still camera was placed in the lateral side of the two-point bending frame to capture the profile image of the ultra-thin glass plate under bending. By analyzing the profile image, the width and height of the profile as well as the contact angle can be obtained. Then, through these three values, the deflection beam profile equation proposed in this study can be expressed.

## 3 Experimental Results

With the different compression displacements, measurement results of the widths and heights of the profiles as well as the compression forces of the ultra-thin glass plate are all well-matched with the theoretical values in the large deflection beam theory. The maximum absolute difference rates between the measurement results and the theoretical values in the width and height of profile as well as the compression force are 1.76, 2.26, and 4.78%, respectively. Figure 1 shows the comparison between the real profile (green line) and the profile reconstructed by the deflection beam profile equation (blue line) of the ultra-thin glass plate with the compression displacement of 22.06 mm. The good match between the real and reconstructed profiles demonstrates the correctness of the proposed deflection beam profile equation. By integrating the deflection beam

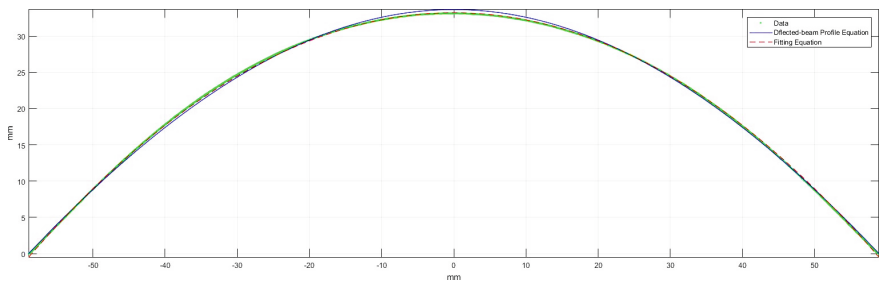


**Fig. 1.** The comparison between the real profile (green line) and the profile reconstructed by the deflection beam profile equation (blue line) when the compression displacement is 22.06 mm.

profile equation into the large deflection beam theory, the general equation of the full-profile bending stress determination can be derived. Figure 2 shows results of the bending stress distribution of the ultra-thin glass plate with the compression displacement of 22.06 mm. Apparently, in the bending stress distribution the stress value is maximum on the profile center and gradually decreases to zero from the center to the side of the profile. Thus, as long as the location of the fracture point on the profile is known, the bending stress at the fracture point can be exactly determined.

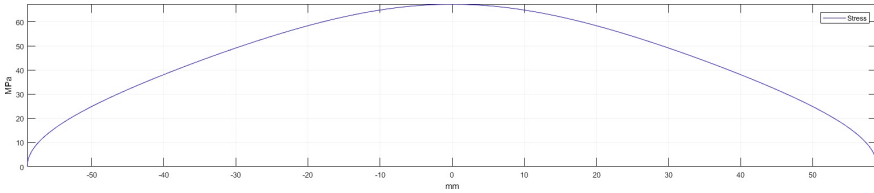


**Fig. 2.** Results of the bending stress distribution when the compression displacement is 22.06 mm.

## 4 Conclusions

In this paper, the general equation of the full-profile two-point bending stress determination was derived by using the large deflection beam theory and the proposed deflection beam profile equation. The required parameters in the general equation, i.e. the width and height of the profile as well as the contact angle, can be obtained from the profile image. Besides, to make the stress distribution on the edge of the ultra-thin glass plate under bending could be more precisely determined, the full-profile bending stress determination results could be combined with the residual stress measurement results on the edge of the ultra-thin glass plate by EEToP [5]. Therefore, the method and system proposed in this paper may assist the manufacturers and users of ultra-thin glass plate in improving the inspection standard and increasing the product quality.

**Acknowledgements.** This paper was supported in part by the Ministry of Science and Technology (Grant no. MOST 106-2221-E-007-048 and 105-2221-E-007-047-MY3), Taiwan, Republic of China.

## References

1. Matthewson, M.J., Kurkjian, C.R., Gulati, S.T.: Strength measurement of optical fibers by bending. *J. Am. Ceram. Soc.* **69**, 815–821 (1986)
2. Gulati, S.T., Westbrook, J., Carley, S., Vepakomma, H., Ono, T.: Two point bending of thin glass substrate. *SID Symp. Dig. Tech. Pap.* **42**(1), 652–654 (2011)
3. Sung, P.C., Wang, W.C., Yeh, Y.L.: An optical stress quantifying method for curved glass plates. In: 18th International Conference on Experimental Mechanics (ICEM18), Paper No. 142, pp. 1–2. The Egg, Brussels, Belgium (2018)

4. Wang, W.C., Sung, P.C., Lu, Z.Y., Yeh, Y.L., Chen, P.Y.: Stress measurement method and system for optical materials. United States Patent, Patent Application Number: 15/618,145, Patent Number: 10067012, Application Date: 2017/06/09, Issued Date: 2018/09/04
5. Sung, P.C., Wang, W.C., Lin, M.C., Kuo, Y.W., Hsu, T.H.: Micro-scale non-destructive stress measurement for ultra-thin glass plates. In: Gdoutos, E. (ed.) Proceedings of the First International Conference on Theoretical, Applied and Experimental Mechanics (ICTAEM 2018), Structural Integrity, vol. 5, pp. 136–138. Springer, Cham (2019)





# Investigation of Grating Collimation of Coherent Gradient Sensing Technique

Po-Yu Chen and Wei-Chung Wang<sup>(✉)</sup>

Department of Power Mechanical Engineering, National Tsing Hua University,  
30013 Hsinchu, Taiwan, Republic of China  
wawang@pme.nthu.edu.tw

**Abstract.** In this paper, the grating collimation of coherent gradient sensing (CGS) technique was investigated. Due to the basic principle of the CGS technique, two gratings are used to obtain the interference fringe pattern, therefore, the accuracy of the CGS technique is directly influenced by the collimation of the two gratings. In order to investigate the grating collimation of the CGS technique, a standard specimen was implemented. The measurement results show that the error becomes larger when the rotational misalignment between the gratings was increased.

**Keywords:** Collimation · Grating · Coherent gradient sensing technique · Rotational misalignment

## 1 Introduction

The coherent gradient sensing (CGS) technique [1] has been widely adopted for measuring the curvature and topography of the specimen. The schematic of CGS technique is shown in Fig. 1. Interference fringe pattern is produced by the collimated light passing through two gratings with the same pitch. The fringe pattern is filtered by the aperture and is recorded by the CCD camera. In the CGS system, the two grating lines must be arranged in parallel. If one of the two gratings has rotational misalignment, the recorded pattern fringe becomes inclined. Consequently, unwanted error will be produced. This rotational misalignment was observed by Tippur [1] and Dhanotia [2]. However, the error caused by grating rotational misalignment has not been investigated. Therefore, the variation of fringe patterns and the error produced by different inclinations between the two gratings were investigated in this paper.

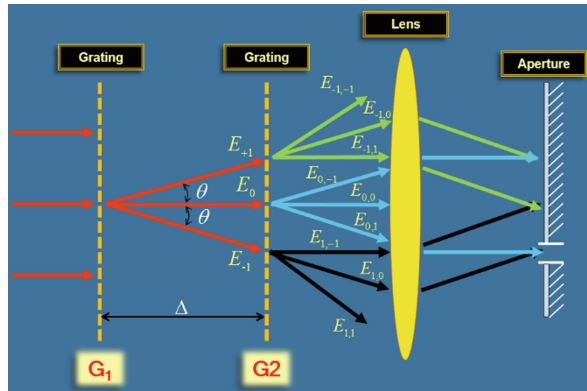


**Fig. 1.** Schematic of the CGS technique.

## 2 Results and Discussions

In order to investigate the grating rotational misalignment of the CGS system, a standard specimen (spherical mirror with  $5 \pm 0.005$  m radius of curvature) was employed. Figure 2a shows the CGS fringe patterns generated by the two gratings when they are in parallel. Hereinafter, this parallel condition is called parallel. Figure 2b and c show the CGS fringe patterns when the angles between the two gratings are one and two degrees, respectively. Hereinafter, these two conditions are called 1 degree and 2 degrees, respectively. It can be observed that the fringe patterns are inclined when the two gratings are not parallel to each other. Besides, as the angle between the two gratings becomes larger, the fringe pattern is more inclined.

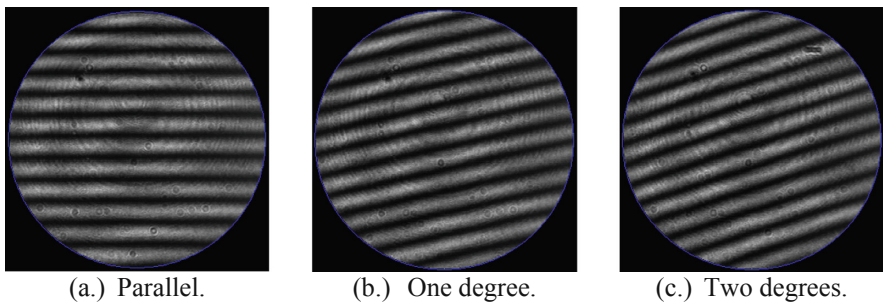


**Fig. 2.** The CGS fringe patterns produced without and with rotational misalignment between gratings.

It is interested to point out that the profile of the standard specimen can be obtained by using the calculated phases through numerical integration. In this paper, the calculated profile results obtained from the conditions parallel and 1 degree (case 1) as

well as conditions parallel and 2 degrees (case 2) were compared to each other. The experimental results showed that the difference of the maximum height of the standard specimen between the results obtained by cases 1 and 2 are 11% and 18%, respectively. Moreover, the shape of the specimen is not a concentric circle when the grating rotational misalignment presents.

**Acknowledgements.** This paper was supported in part by the Ministry of Science and Technology (Grant no. MOST 105-2221-E-007-047-MY3), Taiwan, Republic of China.

## References

1. Tippur, H.V., Krishnaswamy, S., Rosakis, A.J.: A coherent gradient sensor for crack tip deformation measurements: analysis and experimental results. *Int. J. Fract.* **48**, 193–204 (1991)
2. Dhanotia, J., Prakash, S.: Collimation testing using coherent gradient sensing. *Opt. Lasers Eng.* **49**, 1185–1189 (2011)



# The Mechanism of Grain Boundary in Hydrogen Embrittlement of Inconel 690 Alloy

Lei Wang<sup>1(✉)</sup>, Yang Liu<sup>1</sup>, Cheng He<sup>2</sup>, and Xiu Song<sup>1</sup>

<sup>1</sup> Key Laboratory for Anisotropy and Texture of Materials, Northeastern University, 110819 Shenyang, China  
wanglei@mail.neu.edu.cn

<sup>2</sup> Hangzhou Steam Turbine & Power Group Co., Ltd., 310020 Hangzhou, China

**Abstract.** The effects of grain boundary on tensile deformation behaviors of Inconel 690 alloy precharged with hydrogen were investigated by changing the grain size, in order to clarify the mechanism of hydrogen embrittlement of the alloy. The results show that tensile strength and elongation of precharged alloy decreases, and the decreasing degree is gradually reduced with the increase of grain size, indicating that the interaction between grain boundary and hydrogen dominate hydrogen embrittlement of Inconel 690 alloy. Hydrogen could easily migrate towards the grain boundaries following the moving dislocations during tensile, and then enrich at grain boundaries, when the strain rate is relatively low. Thus, the accumulation of hydrogen results in dislocations pile-up, and if such dislocations pile-up reaches a critical degree, the hydrogen-induced cracking will initiate at grain boundaries, which leads to the brittle intragranular fracture characteristics. That means hydrogen-enhance dislocation pile-up is the main reason for hydrogen embrittlement of Inconel 690 alloy. Therefore, how to control the ratio of grain boundary could be considered as the key to avoid the hydrogen embrittlement.

**Keywords:** Inconel 690 alloy · Grain boundary · Hydrogen embrittlement

## 1 Introduction

The vapor generator made of Inconel 690 alloy is one of the current choices for pressurized water reactor (PWR) of nuclear power plant, because this alloy exhibits good mechanical properties and superior stress corrosion resistance when exposed to PWR [1]. However, after long-term servicing, the plasticity and toughness of the Inconel 690 alloy is usually reduced by the high-temperature and high-pressure hydrogen, even hydrogen-induced fracture will occur. Therefore, considering the safety assessment of nuclear power plants, it is necessary to study the relationship between the diffusion and enrichment of hydrogen and fracture behaviors of Inconel 690 alloy, in order to explore the hydrogen embrittlement mechanism of the alloy.

It has been found that hydrogen could be absorbed in Ni-based alloys under PWR, resulting in hydrogen brittlement [2, 3]. Especially hydrogen could enrich at the grain boundaries, which is the main hydrogen trapping site. However, it is clear that the grain

boundary and the carbides are both typical irreversible hydrogen trapping sites in the alloy [4, 5]. The presence of hydrogen trapping sites could play the key role on the effective hydrogen diffusivity and potential alloy susceptibility to hydrogen embrittlement. Also it has been reported that hydrogen atoms can also accumulate at the interface between carbides and matrix, leading to weaken the interface bonding force [6, 7]. Up to now, the essence of hydrogen embrittlement of Inconel 690 alloy has not been clear yet. In order to clarify the essence of hydrogen embrittlement and eliminate the influence of grain boundary carbides on hydrogen embrittlement, the tensile behaviors of the hydrogen precharged alloys with different grain sizes were investigated. And the hydrogen embrittlement mechanisms were also discussed.

## 2 Experimental

The Inconel 690 alloy was fabricated by double vacuum melting, forging, and then rolled to form the bar. The chemical compositions of Inconel 690 alloy (wt%) were C 0.018, Fe 8.19, Cr 29.3, Cu 0.02, Co 0.018, Si 0.05, Al 0.23, Ti 0.2, Nb 0.06, Mn 0.34, P 0.005, S 0.002, B 0.002, Ni balance. Three heat treatment processes were used to change the grain size for controlling the grain boundary ratio (as shown in Table 1).

**Table 1.** Heat-treatment parameters of Inconel 690 alloy

Group	Solution treatment	Aging treatment
A	1070 °C × 300 s, AC	720 °C × 3.6 ks, AC
B	1070 °C × 900 s, AC	720 °C × 3.6 ks, AC
C	1070 °C × 1.8 ks, AC	720 °C × 3.6 ks, AC

Before hydrogen charging, the specimens were carefully cleaned by ultrasonic vibrations with acetone and alcohol. High pressure thermal charging method was used. In this study, the reactor pressure is 10 MPa, and the hydrogen purity was 99.99% (vol.%). The reactor temperature is about 300 °C, and the hydrogen charging time is about 240 h. A LECO hydrogen analyzer (TCH600) was used to measure the hydrogen contents. The hydrogen contents of the sample A, B and C were all about 25 µg/g. The specimens were kept in the freezer to reduce the hydrogen loss, and the mechanical tests were completed as early as possible after hydrogen charging.

Dog-bone-type tensile specimens were prepared in accordance with ASTM E08-2008. The loading direction of the specimens was parallel with the forging direction. The gage dimensions were  $\phi 5 \text{ mm} \times 25 \text{ mm}$ . ASANS-CMT5105 testing machine was used with an initial strain rate of  $3 \times 10^{-4} \text{ s}^{-1}$ .

Internal friction test is carried out on dynamic mechanical analyzer (DMA). The measurement mode is forced vibration with the frequency is 1 Hz, and the applied strain is 0.001%. The temperature range is form room temperature to 350 °C. The data measured in the experiment are processed by Origin software. The microstructures of Inconel 690 alloy of each group with different grain boundary ratios were observed by

an OLYMPUS GX71 Optical Microscope (OM), and TECNAIG<sup>2</sup> Transmission Electron Microscope (TEM). Fracture surfaces were observed using a JEOL 6510A scanning electron microscope (SEM).

### 3 Results and Discussions

#### 3.1 Fracture Surfaces Observations

Figure 1 shows the microstructure of Inconel 690 alloy with different grain boundary ratios. It can be seen that the matrix is austenite grain, and the  $M_{23}C_6$  carbides are distributed at the grain boundaries (Fig. 1d). By quantitative analysis, the grain size of group A, B and C is about 60, 100, and 130  $\mu\text{m}$ , respectively. The grain boundary ratio of group A, B and C sample is 0.031, 0.019, and 0.013%.

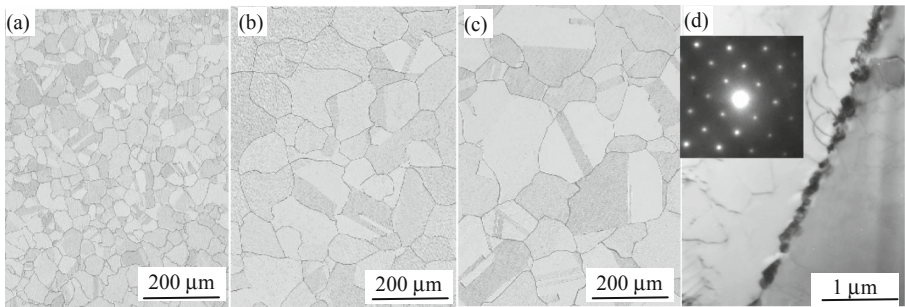


**Fig. 1.** Microstructure of Inconel 690 alloy with different grain sizes: **a** group A; **b** group B; **c** group C; **d** TEM morphology of grain boundary carbides and corresponding SAED.

#### 3.2 Effect of Grain Boundary on Tensile Properties

Figure 2a shows that the tensile strength of group A sample after charging hydrogen decreases by 45 MPa, which is about 6.8%, and the elongation decreased by 24.6%,

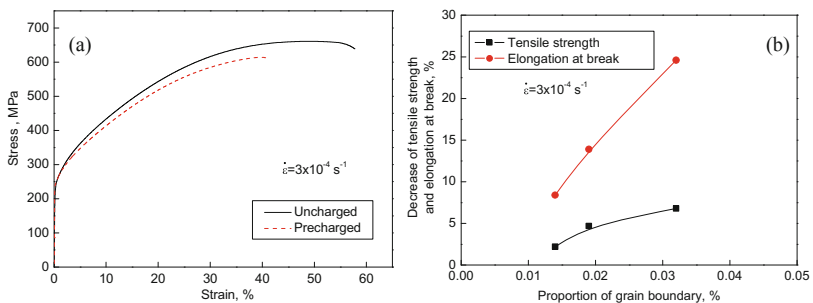


**Fig. 2.** **a** Stress-strain curves of Inconel 690 alloy at group A; **b** decrease of tensile strength and fracture elongation versus proportion of grain boundary

indicating the obvious hydrogen embrittlement. In this study, in order to clarify the hydrogen embrittlement mechanism, the effect of grain boundary ratio on tensile properties of hydrogen charged samples of the testing alloy was analyzed. Figure 2b shows the tensile properties of the three groups of samples, and the decreasing degree of tensile strength and fracture elongation with proportion of grain boundary was compared. The results show that tensile strength and elongation of hydrogen precharged alloy with different grain boundary ratio all decrease. In addition, compared with that of group A sample, the tensile strength of group B sample decrease by 29 MPa, which is about 4.7%, and the elongation decreases by 13.9%. While, the tensile strength of group C sample decreases by 13 MPa, which is about 2.2%, and the elongation decreases by 8.4%. That means, with the increase of grain size, the decreasing degree of tensile strength and the elongation increases after charging hydrogen.

Figure 3 shows the fracture morphology of Inconel 690 alloy with a grain size of 100  $\mu\text{m}$  before and after charging hydrogen. It is still a typical dimple fracture surface of the alloy before charging hydrogen, while after charging hydrogen, the fracture morphology changed into mixed fracture morphology with intergranular fracture as the main feature, which shows that hydrogen influence on the alloy grain boundary.

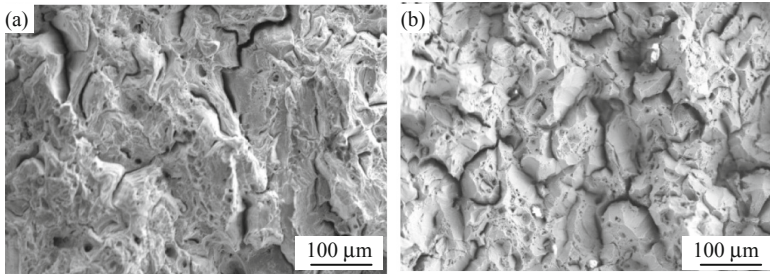


**Fig. 3.** Microfractography of Inconel 690 alloy before (a) and after (b) charging

### 3.3 Hydrogen Embrittlement Mechanism

According to the previous studies results about the hydrogen embrittlement of Inconel 690 alloy, hydrogen atoms in the alloy easily migrate towards grain boundaries and carbides at the grain boundaries in the form of Cottrell hydrogen atmosphere following the moving dislocations during the tensile deformation [8, 9]. With further deformation, hydrogen atoms would enrich at the grain boundaries and then be captured by grain boundaries or grain boundary carbides, resulting in hydrogen embrittlement, because the grain boundary and carbides are both strong traps for hydrogen in Ni-based alloy. While the results in the present study show that the decrease of tensile strength and elongation of the samples after charging hydrogen gradually decreases, with the decrease of grain boundary ratio. That means the decrease of tensile properties of the testing alloy is mainly due to the enrichment of hydrogen at grain boundaries, and it is the interaction between grain boundary and hydrogen dominate hydrogen embrittlement. In order to clarify the interaction between grain boundary and hydrogen during

the tensile deformation, the internal friction curves of hydrogen uncharged and charged samples are tested, as shown in Fig. 4. The S-K-K internal friction peak of Inconel 690 alloy after subtracting background is shown in Fig. 4, which is  $0.86 \times 10^{-4}$  in undeformed sample, while it is  $2.08 \times 10^{-4}$  and  $2.77 \times 10^{-4}$  in the samples at the tensile deformation of 2% of hydrogen uncharged and charged samples, respectively. It can be seen that the S-K-K internal friction peak of the sample after charging hydrogen is significantly higher than that of the sample without charging hydrogen under the same deformation of 2%. That means that the dislocation density inside the hydrogen charged sample is higher than that of uncharged sample.

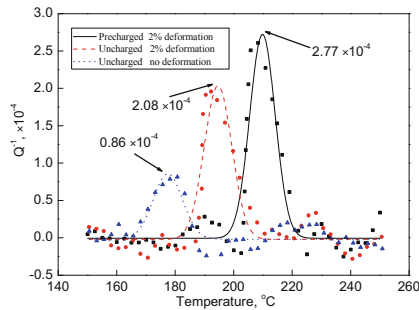


**Fig. 4.** The height of S-K-K peak after subtracting background of the tensile specimen

Figure 5 illustrates typical dislocation configurations at grain boundary and within the grains in the alloys under 2% deformation with hydrogen charged and uncharged specimens. It is obvious that the dislocation density near the grain boundary is significantly higher than that of the uncharged sample, while the dislocation density within the grain is nearly not changes. That result is well coordinated with that by internal friction tests, showing that the accumulation of hydrogen at grain boundary causes a significant increase in dislocation density near the grain boundaries of the alloy.

Therefore, during the deformation, the hydrogen atoms charged into the alloy mostly migrate towards the grain boundaries with dislocations in the form of Cottrell hydrogen atmosphere and enrich at the grain boundaries. That could greatly promote the dislocations pile-up near the grain boundaries. However, if the dislocation accumulation at the grain boundary reaches a critical degree, hydrogen-induced cracking will initiate, which tends to propagate along the grain boundaries at a very high speed, causing the fracture. That is why the obvious brittle intragranular fracture appears on the fracture surface in hydrogen charging alloy. In summary, hydrogen induced dislocation pile-up is the main reason for hydrogen embrittlement of Inconel 690 alloy.



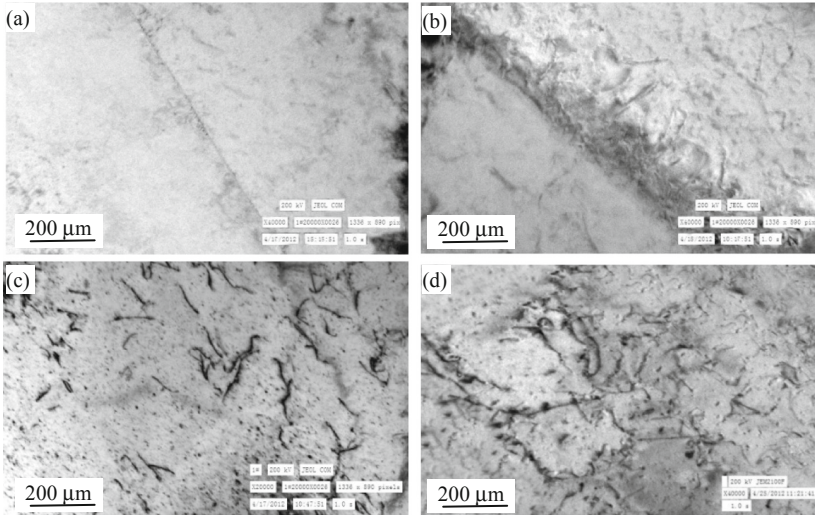


**Fig. 5.** Dislocation configuration of GH690 alloy after 2% deformation near the grain boundary, **a** uncharged and **b** precharged; and within the grain, **c** uncharged and **d** precharged

## 4 Conclusions

- (1) With the increase of grain boundary ratio, the decreasing degree of tensile strength and elongation gradually increases, which indicates that the main reason for hydrogen-induced brittleness of Inconel 690 alloy is related to the interaction between grain boundary and hydrogen.
- (2) Hydrogen atoms can migrate together with the moving dislocations during the tensile deformation in the form of Cottrell hydrogen atmosphere and enrich at the grain boundaries, which can change the fracture features of Inconel 690 alloy and reducing the strength and plasticity of the alloy.
- (3) The accumulation of hydrogen at the grain boundary results in dislocations pile-up, thus the hydrogen-induced cracking will initiate, which leads to the brittle intragranular fracture characteristics.


## References

1. Zhu, J.Z.: Operation of PWR Nuclear Power Plant, pp. 33–38. Atomic Energy Press, Beijing (2000)
2. Young, B.A., Gao, X., Srivatsan, T.S., et al.: The response of alloy 690 tubing in a pressurized water reactor environment. *Mater. Des.* **28**(2), 373–379 (2007)
3. Angeliu, T.M., Was, G.S.: Behavior of grain boundary chemistry and precipitates upon thermal treatment of controlled purity alloy 690. *Metall. Trans. A* **21**(8), 2097–2107 (1990)
4. Chu, W.Y.: Hydrogen Damage and Delayed Fracture, P50-52. Metall. Industry Press, Beijing (1988)

5. Robertson, I.M.: The effect of hydrogen on dislocation dynamics. *Eng. Frac. Mech.* **68**(6), 671–692 (2001)
6. Wang, F.Q., Wang, L., Liu, Y., et al.: Effect of hydrogen on fracture toughness and fracture behavior of GH690 alloy. *Corr. Sci. Prot. Tech.* **20**(05), 380–384 (2010)
7. Wang, F.Q., Wang, L., Liu, Y., et al.: Hydrogen embrittlement behavior of GH690 alloy. *J. Zhengzhou Univ. (Eng. Sci.)* **30**(01), 34–38 (2009)
8. Ferreira, P.J., Robertson, I.M., Birnbaum, H.K.: Hydrogen effects on the interaction between dislocations. *Acta Mater.* **46**(5), 1749–1757 (1998)
9. Stenerud, G., Johnsen, R., Olsen, J.S., et al.: Effect of hydrogen on dislocation nucleation in alloy 718. *Int. J. Hydrogen Energy* **42**(24), 15933–15942 (2017)



# Determining Object Motion by Digital Image Correlation Method with Camera-Array Composed Cameras of Normal Frame Rate

Chi-Hung Hwang<sup>1</sup> , Tzu-Yu Kuo<sup>2</sup>, and Wei-Chung Wang<sup>2</sup>

<sup>1</sup> Instrument Technology Research Center, NARLabs, Hsinchu, Taiwan  
chihunghwang@gmail.com

<sup>2</sup> Department of Power Mechanical Engineering, National Tsing Hua University,  
Hsinchu, Taiwan

**Abstract.** In this study, a camera-array constructed by four regular CCD cameras which can provide 20 frames per second output is used for taking images and then analyzed by digital image correlation method to determine the motion route of an object. The object for tracking is prepared by spraying to form artificial random dots on the surface. The camera-array is first calibrated by using black-white chess board to align all image centers of cameras within 2 pixels. No special time-synchronization among cameras is implemented for camera-array, images are taken by a triggering signal and then analyzed by digital image correlation method to obtain whole filed displacement field with respect to reference frame which is taken before object moved. The test object first is first moved horizontally and then vertical away from and back to the original with maximum 20 mm, the motion at different time interval is then calculated by averaging the displacement field evaluated by DIC. The motion-path determined by DIC matches well to the predefined route but with small zig zag noise can be found from the plot. The result reveals the proposed camera-array can improve temporal resolution and provide motion route, however, the reason for zig zag motion departure is given in the end of this paper which is helpful to improve the proposed method.

**Keywords:** Digital image correlation · Motion route · Camera-array · Frame rate

## 1 Introduction

Digital image correlation method (DIC) is an image based strain measurement method which has been well and widely used for measuring object displacement and strain field. For traditional image processing method, motion of an object can be determined by finding maximum cross-correlation of images taken at different status. DIC method calculates the integer-pixel displacement also based on finding extreme value of cross-correlation of two images; however, as shown in Fig. 1, different from the typical image processing method, DIC is always applied to deformable object for displacement determination; therefore, the object image is always divided into image set instead of using whole image for calculating the cross-correlation value and high spatial

resolution is then can be achieved. In addition, considering DIC method is always applied to deformable object; obviously, deformation must be considered while calculating the cross-correlation value. Therefore, interpolation and shape functions are always used for subset whenever DIC is applied. The differences for determining motion of an object by using typical image processing method (IMP) and DIC method can be briefly itemized as

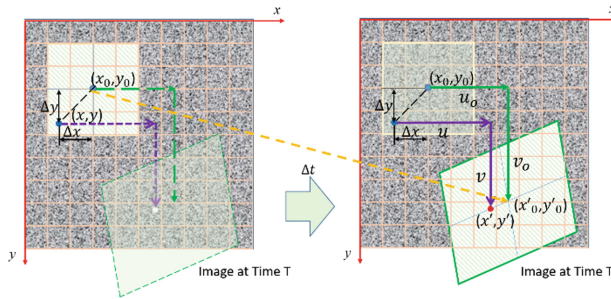


**Fig. 1.** Digital image correlation method determines the displacement field by tracing characteristic pattern between two video-frames.

- (1) DIC can provide reliable motion route and deformation field at the same time all over the object, IMP can provide motion path of discrete points of an object;
- (2) DIC need artificial random marks on the surface for tracking motion of an object; in general, IMP tracks object motion need stickers or tags which different from the background are attached to the object; it is worth to mention that the motion/displacement of an object can also be tracked cross video-streamlines based on automatically determined characteristic points of reference image but the relation between points are not confirmed;
- (3) DIC method consider an object to be deformable makes motion tracking becomes an ill-posed inverse problem; but IMP method treat an object as rigid body (at least there is no constrain among tracking marks) and some iteration method such as iterative closest point algorithm can be applied for solving the unknowns directly.

Obviously, tracking motion of an object can obtain much more message than traditional image tracking method; therefore, in this paper tracking an object subject to in-plane motion by using DIC method would be performed and discussed. Meanwhile, the accurate of motion route also relies on the temporal resolution, high temporal resolution would end up more detail motion information; therefore, the temporal resolution issue would also be considered by using camera-array system in this paper.

## 2 Experiments and Discussions

As shown in Fig. 2, a camera-array consists of four 2 Mpixels monochromatic digital CCD cameras and arranged into  $2 \times 2$  array format, the camera frame rate is 20 fps with global shutter. The camera-array is integrated by a HMI by using NI-MAX virtual instrument which provides necessary functions for triggering cameras, taking images and storing captured images. The virtual instrument also provide image shifting functions; therefore, the camera-array is calibrated by placing a b/w chess board to the same location of the test object, then taking series images to determine the averaged departure in pixels among cameras. The determined departures are then compensated by shifting the images. Limited by the hardware, the departures of image centers among four cameras are reduced to be less than 2 pixels.



**Fig. 2.** Camera-array used for taking images for motion-tracking by DIC method

The motion of the test object is moved to  $(0, 0)$ ,  $(+10, 0)$ ,  $(0, 0)$ ,  $(0, +10)$  and  $(0, 0)$  in sequence by two motor-stages with encoder; the motion route indicates the object is moved first +10 mm in horizontal and then moved  $-10$  mm horizontally back to the origin, afterward moved +10 mm vertically and returned back to the origin again by moving  $-10$  mm vertically. The motion is completed in 3.5 s which yields 11.5 m/s averaged motion speed and 280 images recorded. By using commercial available VIC-2D from Correlated Solutions Ltd., the typical U, V displacement fields are then determined as shown in Figs. 3 and 4. The images shown in Figs. 3 and 4 are only 8 images out of the captured 280 images, from which 4 images are for object moved horizontally and the other 4 images are for vertical movement. Obviously, while object moved vertically, the 4 images of first line of Fig. 4 are all rendered with zero displacement and no displacement gradient can be found, same results can also be seen for the images shown along the second line of Fig. 3. Moreover, from images shown in first line of Fig. 3 and second line of Fig. 4 which reveal the horizontal and vertical motion respectively; however, the determined displacements cannot provide enough information of real motion route which reflect the fact that if the temporal resolution is too low then the determined motion route would totally depart from the fact. In this study, for presenting the calculated the motion route efficiency, the motion route would

be represented by average displacement  $(\bar{u}, \bar{v})$  of each image frame which can be calculated by equation

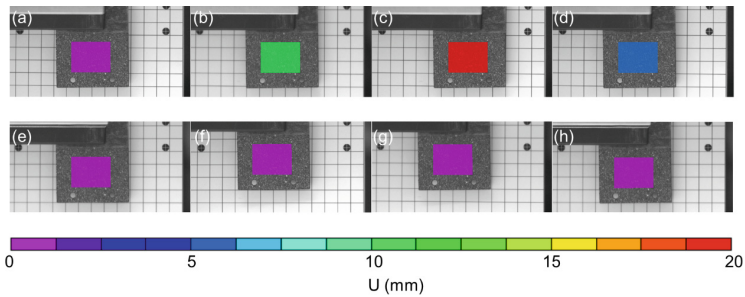


**Fig. 3.** Determined displacement along horizontal direction

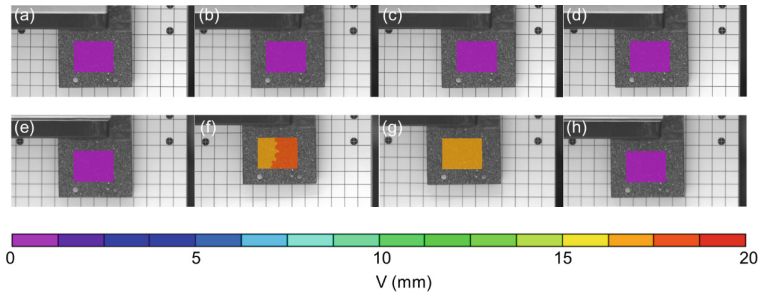


**Fig. 4.** Determined displacement along vertical direction

$$(\bar{u}, \bar{v}) = \left( \frac{\sum_{i,j}^{m,n} U(i,j)}{m \times n}, \frac{\sum_{i,j}^{m,n} V(i,j)}{m \times n} \right)$$

Figure 5 shows the motion route of the object by calculating the averaged displacement  $(\bar{u}, \bar{v})$  frame by frame of all 280 images and the motion route fits well with the given code for motor-stages but there is zig zag noise can be seen all over the plot. To explore the causing reason, the calibration result are reinvestigated again. Taking upper left camera as first and reference camera and then numbering the cameras clockwise in sequence, then the departures of the image centers among all four cameras are recalculated with respect to reference image; as shown in Fig. 6. In fact, the image center departures can be considered as virtual U and V displacement corresponding to the departure distance along x- and y-axis. Based on the support evidence, the zig zag noise reported from Fig. 5 might be caused because of image center errors are still

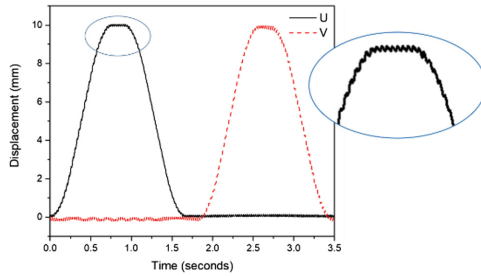


**Fig. 5.** Plot of DIC determined motion in horizontal and vertical direction

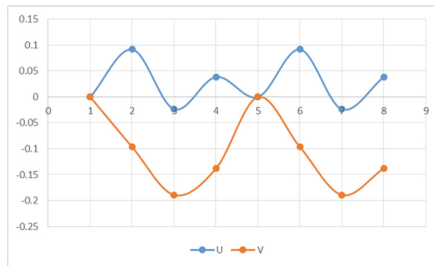


**Fig. 6.** Residual pseudo-displacement after camera-calibration causes zig zag phenomenon for DIC determined motion-track

available. However, this result reveals the measuring system might can be improved by adopting mechanical adjusting mechanism for physically shifting the locations/orientations of cameras.

### 3 Conclusions

In this study, according to the experimental results and discussions, the achievements can be concluded as

- (1) The proposed system together with calibration procedure can completely and accurately reconstructs route of the round-trip movements along horizontal and vertical direction with motion speed is 11.5 m/s in details.
- (2) The phenomenon of zig zag has been identified and the reason for this irregular movement have been discussed; the residual image center departures among cameras is considered to be the major reasons for introduce zig zag with strong evidences presented to support the conclusion.
- (3) Camera-array is a potential optical system for measurement displacement/deformation/strain field of a movement object.

**Acknowledgements.** This paper was supported in part by the Ministry of Science and Technology, Taiwan (Grant no. MOST-106-2221-E-492-013 and MOST-107-2221-E-492-012).

# **Part II**

## **Fracture**





# Configurational Stability of a Crack Propagating in Mixed-Mode I + II + III

Jean-Baptiste Leblond<sup>1</sup> (✉), Alain Karma<sup>2</sup>, Laurent Ponson<sup>1</sup>,  
and Aditya Vasudevan<sup>1,2</sup>

<sup>1</sup> Faculté des Sciences et Ingénierie, Sorbonne Université,  
Campus Pierre et Marie Curie, CNRS, UMR 7190,  
Institut Jean Le Rond d'Alembert, Cedex 05, 75252 Paris, France  
jbl@lmm.jussieu.fr

<sup>2</sup> Physics Department and Center for Interdisciplinary Research on Complex  
Systems, Northeastern University, Boston, MA 02115, USA

**Abstract.** In some previous papers, we presented some linear stability analyses of the coplanar propagation of a crack loaded in mixed-mode I + III, using a propagation criterion combining a Griffith-type energetic condition and Goldstein and Salganik's "principle of local symmetry". In the last one, the local value of the fracture energy was no longer considered as a constant but heuristically permitted to depend upon the ratio of the local mode III to mode I stress intensity factors. As a result, a much improved agreement of theory and experimental observations was obtained for the "threshold" value of the ratio of the unperturbed mode III to mode I stress intensity factors, above which coplanar propagation becomes unstable. This analysis is extended here to the situation, of considerable practical significance, where a small additional mode II loading component is present in the initially planar configuration of the crack. This component induces a small, general kink of this crack from the moment it is applied. The main novelty resulting from its application is that the instability modes, present above the threshold, must drift along the crack front during its propagation. It is hoped that this prediction will be useful to theoretically interpret a number of experiments where such a drifting motion was indeed observed but left unexplained.

**Keywords:** Configurational stability · Mode I + II + III · Griffith condition · Principle of local symmetry · Drifting motion

## 1 Introduction

In a previous paper [1], we proposed an interpretation of the experimentally well-known instability of coplanar crack propagation in mode I + III, based on a linear stability analysis. This analysis was itself based on two elements: (i) analytical expressions of the stress intensity factors (SIFs) for a 3D crack slightly perturbed both within and out of its original plane [2, 3]; (ii) a "double" propagation criterion combining Griffith's energetic condition involving the fracture energy [4], and Goldstein and Salganik's "principle of local symmetry" (PLS) according to which the SIF of mode II must remain zero on the entire crack front and throughout the entire

propagation [5]. With these hypotheses instability modes were indeed evidenced for values of the mode mixity ratio—ratio of the mode III to mode I SIFs applied remotely—larger than some “threshold” value depending only on Poisson’s ratio. Unfortunately, for typical values of this material parameter, the predicted threshold values were much larger than those actually observed in most experiments.

To try and resolve this paradox, in a more recent paper [6], we re-examined the linear stability analysis of a propagating 3D crack in mode I + III conditions, with the extra hypothesis that the fracture energy may depend upon the local mixity ratio, with a constitutive relationship between these two quantities motivated by experimental observations. We showed that such a dependence suffices, provided that it is strong enough, to significantly lower the threshold value of the mode mixity ratio for instability, bringing it in a range of values more consistent with experiments.

However, in actual experiments a small mode II component is also frequently present, generating a small general kink of the crack. The aim of this paper is to investigate the modifications brought into the linear stability analysis of the propagating crack by introduction of such an additional loading component.

## 2 General Geometrical and Mechanical Hypotheses

We consider an initially flat semi-infinite crack, occupying the domain  $x < 0$  within the plane  $y = 0$ , obtained through machining of the specimen, or propagation in mode I fatigue, or any other possible means. A static load including mode II and III components, of sufficient magnitude to induce crack propagation, is applied on this pre-crack. A general kink of the crack ensues, with possibly superimposed perturbations of the crack front and surface growing in an unstable manner.

Figure 1 provides 2D schematic illustrations, in the plane  $Oxy$ , of the configurations of the crack in its initial state and after some propagation under such conditions. On the right the full line represents the fundamental, kinked but unperturbed configuration, and the dotted line a kinked *and perturbed* configuration. (Note that since the perturbation is assumed to already be nonzero at  $x = 0$ , it must necessarily extend over some small distance in the region  $x < 0$ .)

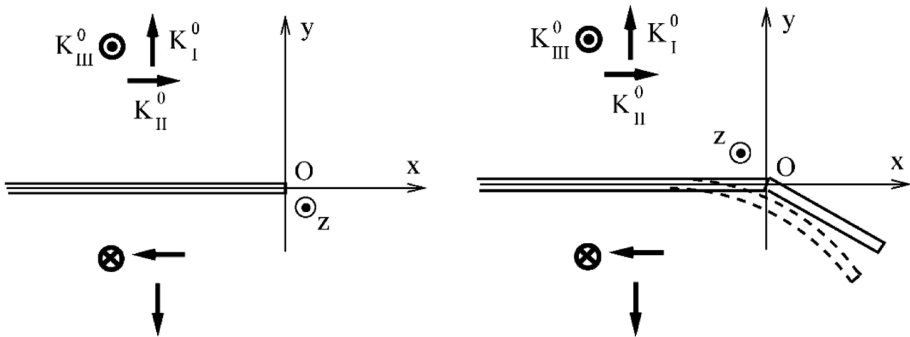


**Fig. 1.** Configurations of the crack before (left) and during (right) propagation in mixed mode I + II + III.

The SIFs in the initial configuration being denoted  $K_I^0, K_{II}^0, K_{III}^0$ , we define the dimensionless ratios

$$\varphi^0 = \frac{K_{II}^0}{K_I^0}; \rho^0 = \frac{K_{III}^0}{K_I^0}. \quad (1)$$

The ratio  $\varphi^0$  is assumed to be much smaller than unity, because the mode II component of the loading generates a general kink angle proportional to it to first order; thus if it were allowed to be large, the kink angle could also be large, and this would prohibit use of first-order formulae for the perturbed SIFs [2, 3], which demand small slopes of the crack surface with respect to the initial crack plane.

### 3 First Stability Analysis

In a first linear stability analysis, the fracture energy is assumed to possibly depend upon the ratio of the local mode III to mode I SIFs:

$$G_c(x, z) = G_c[\rho(x, z)], \rho(x, z) = \frac{K_{III}(x, z)}{K_I(x, z)} \quad (2)$$

according to the phenomenological formula

$$G_c(\rho) = G_c^{\text{Mode I}}(1 + \gamma|\rho|^\kappa) \quad (3)$$

where  $G_c^{\text{Mode I}}$  denotes the value of  $G_c$  in pure mode I, and  $\gamma$  and  $\kappa$  positive, dimensionless material parameters. (The inequality  $\gamma > 0$  means that presence of mode III *increases* the value of  $G_c$ .)

With this assumption, the calculations resulting from combination of the first-order formulae for the perturbed SIFs [2, 3] and the conditions resulting from the double criterion reveal extremely heavy. In order to keep them reasonable, it is assumed that the ratio  $\rho^0$  is small like  $\varphi^0$ , and all expressions are expanded only to first order in the pair  $(\varphi^0, \rho^0)$ .

The result of the stability analysis is as follows. Just like in the case of a mixed mode I + III loading envisaged earlier [1, 6], coplanar propagation becomes unstable when the ratio  $\rho^0$  exceeds some threshold value; and above the threshold, the instability modes correspond to a perturbed crack front having the shape of an elliptic helix, of central axis coinciding with the unperturbed front, and semi-axes growing in proportion and exponentially with the distance  $x$  of propagation of the crack. There is however a major novelty: *the helix no longer moves in the general direction  $x$  of propagation of the crack, but drifts along the front as it propagates.* This effect results, in the approach adopted, from combination of existence of a general mode II loading component and dependence of the fracture energy upon mode mixity. (The drift velocity is proportional to both  $K_{II}^0$  and  $\gamma$  and thus vanishes when either of these parameters is zero.)

Figure 2 illustrates both the absence and presence of a drifting motion of the instability modes, in the absence and presence of a mode II loading component.

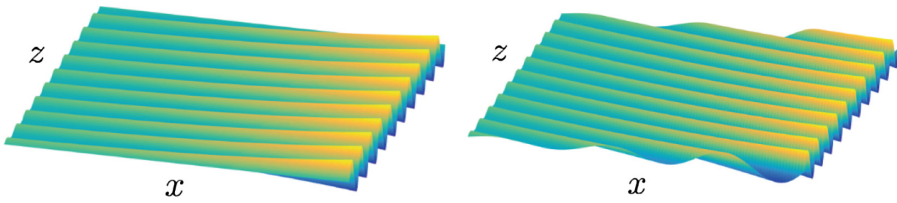


**Fig. 2.** Schematic representation of the geometry of instability modes. Left, no general mode II, no drift; right, presence of general mode II, existence of a drift.

## 4 Second Stability Analysis

The conclusions of the preceding analysis raise an issue pertaining to the conditions found necessary for existence of a drifting motion of instability modes along the crack front. Indeed, in the absence of general mode II, the absence of a drifting motion of instability modes finds its root in the invariance of both the geometry and the loading in a rotation of  $180^\circ$  about the direction  $x$  of general propagation of the crack. Introduction of a general mode II component destroys this invariance, so that a drifting motion of instability modes along the crack front is no longer a priori impossible, and may reasonably be expected to occur no matter whether or not the fracture energy depends upon mode mixity. But the preceding stability analysis says otherwise since it predicts that a  $\rho$ -dependent  $G_c$ , in addition to a nonzero  $K_{II}^0$ , is necessary for the instability modes to drift.

To investigate this question, the stability analysis is repeated with a constant  $G_c$ , in order to see whether a drifting motion can be predicted under the sole condition that  $K_{II}^0$  be nonzero. However the hypothesis of a small  $\rho^0$  is now discarded, since the preceding analysis has unambiguously shown that with a small  $\rho^0$ , there is no drifting motion in the absence of a dependence of  $G_c$  upon  $\rho$ .

The output of the new calculation is that a drifting motion of instability modes indeed exists under such conditions; this motion results from higher order terms in the pair  $(\varphi^0, \rho^0)$  disregarded in the preceding analysis. The drift velocity is however much smaller than with a  $\rho$ -dependent  $G_c$ .

## 5 Perspectives

Many experiments have evidenced crack propagation in mode I + III in the form of tilted facets. In many cases these facets have been observed not to propagate in the direction of general propagation of the crack, but to drift along the front as it propagates. No clear and irrefutable explanation of this phenomenon has been provided.

The preceding results concerning the prediction of a drifting motion of instability modes offer an interesting perspective for the interpretation of such experiments. The first point of comparison of theory and experiments will simply be the *sign* of the drift. If the theory is found to successfully predict the sign actually observed, it will remain to see whether experimental drift angles can be satisfactorily predicted by the theory, and whether this will require assuming a  $\rho$ -dependent  $G_c$  or not.

Whatever the conclusions of future studies, an important feature of the present work has been to emphasize the importance of existence of a small mode II loading component upon existence of a drift.

## References

1. Leblond, J.B., Karma, A., Lazarus, V.: Theoretical analysis of crack front instability in mode I +III. *J. Mech. Phys. Solids* **59**, 1872–1887 (2011)
2. Gao, H., Rice, J.R.: Shear stress intensity factors for planar crack with slightly curved front. *ASME J. Appl. Mech.* **53**, 774–778 (1986)
3. Movchan, A.B., Gao, H., Willis, J.R.: On perturbation of plane cracks. *Int. J. Solids Struct.* **35**, 3419–3453 (1998)
4. Griffith, A.: The phenomena of rupture and flow in solids. *Phil. Trans. R. Soc. Lond. Ser. A* **221**, 163–198 (1920)
5. Goldstein, R.V., Salganik, R.L.: Brittle fracture of solids with arbitrary cracks. *Int. J. Fract.* **10**, 507–523 (1974)
6. Leblond, J.B., Karma, A., Ponson, L., Vasudevan, A.: Configurational stability of a crack propagating in a material with mode-dependent fracture energy—part I: mixed-mode I+III. Submitted to *J. Mech. Phys. Solids* (2018)



# Limiting Equilibrium of Interfacial Shear Cracks at the Corner Point of the Media-Separating Boundary of the Piece-Homogeneous Isotropic Plane

V. M. Nazarenko and A. L. Kipnis<sup>(✉)</sup>

S.P. Timoshenko Institute of Mechanics of the National Academy of Science of Ukraine, Kiev, Ukraine  
a.l.kipnis@gmail.com

**Abstract.** An exact solution of symmetric problem on the elastic equilibrium of piece-homogeneous isotropic plane with the interface of media in the form the sides of angle, which contains the interfacial shear cracks is constructed by the Wiener—Hopf method. The case of smooth contact between sides of cracks is investigated. The stress intensity factor at the end of the shear crack is determined.

**Keywords:** Interface of media · Corner point · Interfacial shear crack · Wiener—hopf method

Under the conditions of plane deformation, the elastic equilibrium the piece-homogeneous isotropic plane with the interface of media in the form of the sides of angle which contains the interfacial shear cracks propagated from its the corner point is investigated in the static symmetric problem framework (see Fig. 1). We propose that friction is absent between the sides of cracks. The asymptotic of the stress field on infinity is the same with the asymptotic of the stress field near the corner point in the corresponding problem for the piece-homogeneous plane without interfacial cracks (see Fig. 2).

The boundary conditions of corresponding symmetric problem of elasticity theory are as follows:

$$\theta = \pi - \alpha, \tau_{r\theta} = 0, u_\theta = 0; \theta = -\alpha, \tau_{r\theta} = 0, u_\theta = 0;$$

$$\theta = 0, \langle \sigma_\theta \rangle = \langle \tau_{r\theta} \rangle = 0, \langle u_\theta \rangle = 0;$$

$$\theta = 0, r < l, \tau_{r\theta} = 0; \theta = 0, r > l, \langle u_r \rangle = 0; \theta = 0, r \rightarrow \infty, \tau_{r\theta} = Cg r^{\lambda_0} + o(1/r).$$

Here  $0 \leq \theta \leq \pi$ ;  $\langle a \rangle$ —jump of  $a$ ;  $g(\alpha, e_0, \nu_1, \nu_2)$  ( $e_0 = E_1/E_2$ )—is known function;  $\lambda_0$ —is unique on interval  $] -1; 0[$  root of next equation

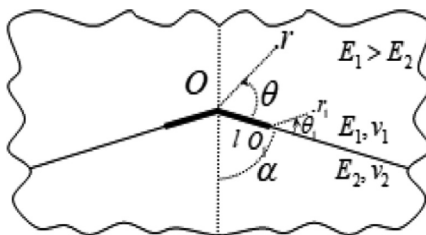


Fig. 1. Piece-homogeneous isotropic plane with interior interfacial shear cracks

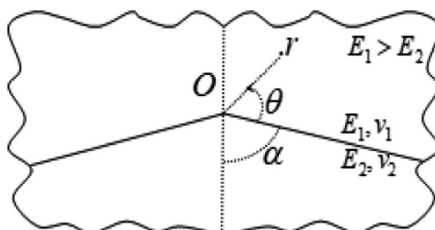


Fig. 2. Piece-homogeneous isotropic plane with the interface of media in the form the sides of angle

$$\Delta(-x - 1) = 0, \Delta(z) = \delta_0(z) + \delta_1(z)e + \delta_2(z)e^2,$$

$$\delta_0(z) = (\sin 2z\alpha + z \sin 2\alpha)[\varkappa_1 \sin 2z(\pi - \alpha) + z \sin 2\alpha],$$

$$\delta_1(z) = (1 + \varkappa_1)(1 + \varkappa_2) \sin^2 z\pi - (\sin 2z\alpha + z \sin 2\alpha)[\varkappa_1 \sin 2z(\pi - \alpha) + z \sin 2\alpha] - [\sin 2z(\pi - \alpha) - z \sin 2\alpha](\varkappa_2 \sin 2z\alpha - z \sin 2\alpha),$$

$$\delta_2(z) = [\sin 2z(\pi - \alpha) - z \sin 2\alpha](\varkappa_2 \sin 2z\alpha - z \sin 2\alpha),$$

$$e = \frac{1 + \nu_2}{1 + \nu_1} e_0, \quad \varkappa_{1,2} = 3 - 4\nu_{1,2}$$

Using the Mellin's integral transform [1], the theory of elasticity problem is reduced to the Wiener-Hopf functional equation [2] of the following form

$$\Phi^+(p) + \frac{\tau}{p + \lambda + 1} = \text{Actg } p\pi G(p)\Phi^-(p),$$

$$A = \frac{(1 + \varkappa_1)[1 + \varkappa_1 + (1 + \varkappa_2)e]}{2[\varkappa_1 + (1 + \varkappa_1 \varkappa_2)e + \varkappa_2 e^2]}, \quad G(p) = \frac{G_1(p)}{G_2(p)},$$

$$G_1(p) = [\varkappa_1 + (1 + \varkappa_1 \varkappa_2)e + \varkappa_2 e^2][a_0(p) + a_1(p)e] \sin p\pi,$$

$$G_2(p) = [1 + \varkappa_1 + (1 + \varkappa_2)e][b_0(p) + b_1(p)e + b_2(p)e^2]\cos p\pi,$$

$$a_0(p) = (1 + \varkappa_1)[\cos 2p(\pi - \alpha) - \cos 2\alpha](\sin 2p\alpha + p \sin 2\alpha),$$

$$b_0(p) = (\sin 2p\alpha + p \sin 2\alpha)[\varkappa_1 \sin 2p(\pi - \alpha) + p \sin 2\alpha],$$

$$b_1(p) = (1 + \varkappa_1)(1 + \varkappa_2)\sin^2 p\pi - (\sin 2p\alpha + p \sin 2\alpha)[\varkappa_1 \sin 2p(\pi - \alpha) + p \sin 2\alpha] - [\sin 2p(\pi - \alpha) - p \sin 2\alpha](\varkappa_2 \sin 2p\alpha - p \sin 2\alpha),$$

$$b_2(p) = [\sin 2p(\pi - \alpha) - p \sin 2\alpha](\varkappa_2 \sin 2p\alpha - p \sin 2\alpha), \quad \tau = -Cgl^{\lambda_0},$$

$$\Phi^+(p) = \int_1^\infty \tau_{r\theta}(\rho l, 0)\rho^p d\rho, \quad \Phi^-(p) = \frac{E_1}{4(1 - \nu_1^2)} \int_0^1 \left\langle \frac{\partial u_r}{\partial r} \right\rangle \Big|_{\theta=0} r = \rho l \rho^p d\rho,$$

which took place in the strip of complex plane contains the imagine axis. The factorization of the equation coefficient on the imagine axis carried out by its splitting into two functions: the function which factorizes using gamma-functions [3] and the function which factorizes according Gakhov's formula [4]. Using these factorizations, the exact analytical solution of the Wiener–Hopf equation, which expresses by Cauchy type integrals and gamma-functions, is built.

Based on the solution of Wiener–Hopf equation, the formula for the stress intensity factor at the end of the shear crack is obtained:

$$K_{II} = \frac{2\sqrt{2}(1 + \varkappa_2 e)g\Gamma(\lambda_0 + 3/2)}{[1 + \varkappa_1 + (1 + \varkappa_2)e]\Gamma(\lambda_0 + 2)G^+(-\lambda_0 - 1)} Cl^{\lambda_0 + 1/2}.$$

The dependence of the dimensionless stress intensity factor  $K_{II}^0 = -K_{II}/(Cl^{\lambda_0 + 1/2})$  on the angle  $\alpha$  for various values of the parameter  $e_0 = E_1/E_2 > 1$  ( $\nu_1 = \nu_2 = 0, 3$ ) is shown in the Fig. 3.

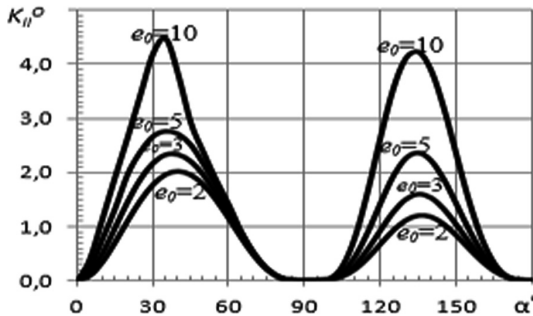


Fig. 3. The dimensionless stress intensity factor for various values of the parameter  $e_0$



**Table 1.** Maximums of function  $K_{II}^0(\alpha)$  ( $v_1 = v_2 = 0, 3$ )

$e_0$	2	3	5	10
$\alpha_{\max 1}^\circ$	42.4	37.1	35.3	33.5
$K_{II}^0(\alpha_{\max 1})$	2.0224	2.3371	2.7663	4.5121
$\alpha_{\max 2}^\circ$	139.2	135.4	134.1	132.4
$K_{II}^0(\alpha_{\max 2})$	1.2025	1.6012	2.3644	4.2363

The values  $\alpha_{\max 1}^\circ, \alpha_{\max 2}^\circ$  of the angle  $\alpha$  at which the function  $K_{II}^0(\alpha)$  will take the greatest values at each of the intervals  $]0; \pi/2[, ]\pi/2; \pi[$  and the corresponding values of the function are listed in the Table 1.

Proceeding on the force fracture criterion, the equation for determent the breaking load is obtained:

$$C = \frac{[1 + \varkappa_1 + (1 + \varkappa_2)e]\Gamma(\lambda_0 + 2)G^+(-\lambda_0 - 1)K_{IIc}}{2\sqrt{2}(1 + \varkappa_2e)g \Gamma(\lambda_0 + 3/2)l^{\lambda_0 + 1/2}}$$

Crack starts when the loading parameter  $C$ , which increases with the external loading increasing, will reach its critical value.

Analyzing the formula for stress intensity factor and guiding by the criterion the crack stabilizing equilibrium, next result was obtained. If interfacial small-scale shear cracks were born at the corner point of the media-separating boundary of isotropic elastic body than their equilibrium is unstable in case of smooth contact between sides of these cracks. After reaching the limit equilibrium state, the dynamic mode crack propagation will take place.

## References

1. Uflyand, Y.S.: Integral Transformations in Elasticity Theory Problems. Nauka, Leningrad (1967) (in Russian)
2. Nobl, B.: Applying the Wiener—Hopf Method for Solving Partial Derivatives Differential Equations. Inostr. lit, Moscow (1962). (in Russian)
3. Lavrentiev, M.A., Shabat, B.V.: The Theory of Complex Variable Methods. Nauka, Moscow (1973). (in Russian)
4. Gakhov, F.D.: Boundary-Value Problems. Nauka, Moscow (1977). (in Russian)



# An Approach to Analysis of Fracture of Semi-bounded Body Under Compressing Along Interfacial Near-Surface Crack

V. L. Bogdanov and A. L. Kipnis<sup>(✉)</sup>

S.P. Timoshenko Institute of Mechanics of the National Academy of Science of Ukraine, Kiev, Ukraine  
a.l.kipnis@gmail.com

**Abstract.** The problem of compressing a piece-homogeneous half-plane with forces directed along the near-surface crack located in the interface of two materials is considered. The problem relates to non-classical problems of fracture mechanics, since under such a loading scheme the stress-strain state realized in the body is homogeneous and in the corresponding expressions for stresses and displacements near the crack there are no singular components. Due to the fact that the stress intensity factors are equal to zero, the classical Griffiths-Irwin fracture criteria are inapplicable for the problem under consideration. In this situation, the start of crack propagation is associated with the local stability loss of the equilibrium state of a part of the material in the region adjacent to the crack. Using the approaches of the linearized theory of deformed bodies stability, the mathematical formulation of the problem was carried out.

**Keywords:** Piece-homogeneous half-plane · Compressing along crack · Interfacial crack · Linearized theory of deformed bodies stability

Under the conditions of plane deformation the piece-homogeneous half-plane  $x_2 \leq h$  with a free of loading boundary surface  $x_2 = h$  and rectilinear media-separating boundary  $x_2 = 0$  is considered (Fig. 1). Let media 1 (the strip  $0 \leq x_2 \leq h$ ) and media 2 (the half-plane  $x_2 \leq 0$ ) are rigidly linked. Media-separating boundary between materials 1 and 2 contains free of loading opened crack, which has the length equals  $2a$ . The materials are compressed on infinity along the  $Ox_1$  axis by the uniformly distributed loading such that equals shortenings along this axis are provided for both materials 1 and 2.

Research is carried out within the linearized theory of deformed bodies stability [1–4]. Boundary conditions of the problem under the consideration are the follows

$$\begin{aligned}
 t_{22}^{(\pm)} = 0, \quad t_{21}^{(\pm)} = 0, \quad x_2 = 0, \quad |x_1| < a; \\
 t_{22}^{(+)} = t_{22}^{(-)}, \quad t_{21}^{(+)} = t_{21}^{(-)}, \quad u_1^{(+)} = u_1^{(-)}, \quad u_2^{(+)} = u_2^{(-)}, \quad x_2 = 0, \quad |x_1| \geq a; \quad (1) \\
 t_{22}^{(+)} = 0, \quad t_{21}^{(+)} = 0, \quad x_2 = h.
 \end{aligned}$$

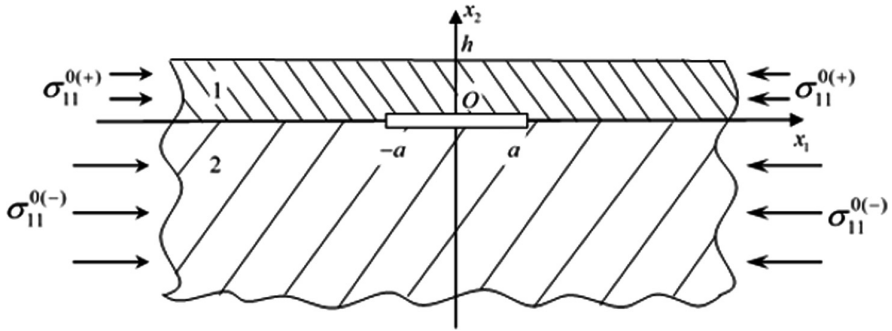


Fig. 1. The piece-homogeneous half-plane with a crack

Hereinafter, the superscript “+” in brackets denotes the values related to the material of the strip *I*, and the superscript “-” in brackets denotes the half-plane 2.

Considering only those forms of loss of stability that “at infinity” attenuate in the same way as the corresponding solutions of plane static problems of the linear theory of elasticity [4], we write the last two conditions in (1) in the equivalent form:

$$\frac{\partial u_1^{(+)}}{\partial x_1} = \frac{\partial u_1^{(-)}}{\partial x_1}, \quad \frac{\partial u_2^{(+)}}{\partial x_1} = \frac{\partial u_2^{(-)}}{\partial x_1} \quad \text{when } x_2 = 0, \quad |x_1| > a$$

We introduce complex variables

$$z_k^{(+)} = x_1 + \mu_k^{(+)} x_2, \quad k = 1, 2$$

for material *I* and

$$z_k^{(-)} = x_1 + \mu_k^{(-)} x_2, \quad k = 1, 2$$

For material 2, where values  $\mu_{1,2}^{(\pm)}$  for each of the materials are the roots of the corresponding characteristic equation [2, 3]

$$\begin{aligned} \mu^{(\pm)4} + 2A^{(\pm)}\mu^{(\pm)2} + A_1^{(\pm)} &= 0, \\ 2A^{(\pm)} &= \frac{\omega_{1111}^{(\pm)}\omega_{2222}^{(\pm)} + \omega_{2112}^{(\pm)}\omega_{1221}^{(\pm)} - (\omega_{1122}^{(\pm)} + \omega_{1212}^{(\pm)})^2}{\omega_{2222}^{(\pm)}\omega_{2112}^{(\pm)}}, \\ A_1^{(\pm)} &= \frac{\omega_{1111}^{(\pm)}\omega_{1221}^{(\pm)}}{\omega_{2222}^{(\pm)}\omega_{2112}^{(\pm)}}. \end{aligned}$$

The values  $\omega_{ijkl}^{(\pm)} = \omega_{ijkl}^{(\pm)}(\lambda_1, \lambda_2)$  are components of the fourth-rank tensors  $\tilde{\omega}^{(\pm)}$  and characterize the chosen material model. Similar representations were obtained [2, 3] for

the case of incompressible bodies. We note the advantage of the approach used here, proposed in [2, 3], within which the specification of the material model occurs only at the final stage of solving the problem, which allows us to conduct research in general form for elastic and elastic-plastic, isotropic and orthotropic bodies, for small and finite subcritical deformations.

Consider the case when for each of materials of strip and half-plane, the corresponding characteristic equation has equal roots ( $\mu_1^+ = \mu_2^+$ ,  $\mu_1^- = \mu_2^-$ ).

Then following representations take place

$$\begin{aligned}
 t_{22} &= \operatorname{Re}\{\Psi(z_1) + \bar{z}_1\Phi'(z_1) + \gamma_{22}^{(2)}\Phi(z_1)\}, \\
 t_{21} &= \operatorname{Re}\{\mu_1\gamma_{21}^{(1)}[\Psi(z_1) + \bar{z}_1\Phi'(z_1)] + \gamma_{21}^{(2)}\Phi(z_1)\}, \\
 t_{21} &= \operatorname{Re}\{-\mu_1[\Psi(z_1) + \bar{z}_1\Phi'(z_1)] + \gamma_{12}^{(2)}\Phi(z_1)\}, \\
 t_{21} &= \operatorname{Re}\{\mu_1^2\gamma_{11}^{(1)}[\Psi(z_1) + \bar{z}_1\Phi'(z_1)] + \gamma_{11}^{(2)}\Phi(z_1)\}, \\
 \frac{\partial u_k}{\partial x_1} &= \operatorname{Re}\{\gamma_k^{(1)}[\Psi(z_1) + \bar{z}_1\Phi'(z_1)] + (\gamma_k^{(1)} + \gamma_k^{(2)})\Phi(z_1)\}, \quad k = 1, 2, \\
 z_1 &= x_1 + \mu_1 x_2.
 \end{aligned} \tag{2}$$

Expressions (2) determinates stresses and derivatives from displaces in materials 1 and 2 (you only need to put in all quantities the index “+” or “-”) using two analytical functions of complex variables in case of equal roots. Coefficients  $\gamma_{ij}^{k(\pm)}$ ,  $\gamma_j^{k(\pm)}$ ,  $i, j, k = 1, 2$  are known functions of tensor's  $\tilde{\omega}^{(\pm)}$  [2, 3] components. Functions  $\Phi^{(+)}$ ,  $\Psi^{(+)}$  are analytical in the strip  $0 < \operatorname{Im}z_1^{(+)} < \left|\mu_1^{(+)}\right|h$  and functions  $\Phi^{(-)}$ ,  $\Psi^{(-)}$  are analytical in the half-plane  $\operatorname{Im}z_1^{(-)} < 0$ .

Substituting expressions (2) in boundary conditions (1) we obtain boundary conditions of the problem in terms of analytical functions of complex variables

$$\begin{aligned}
 \operatorname{Re}\{\Psi^{(\pm)}(x_1) + x_1\Phi^{(\pm)'}(x_1) + \gamma_{22}^{(2)(\pm)}\Phi^{(\pm)}(x_1)\} &= 0, \\
 \operatorname{Re}\{\mu_1^{(\pm)}\gamma_{21}^{(1)(\pm)}[\Psi^{(\pm)}(x_1) + x_1\Phi^{(\pm)'}(x_1)] + \gamma_{21}^{(2)(\pm)}\Phi^{(\pm)}(x_1)\} &= 0, \quad |x_1| < a; \\
 \operatorname{Re}\{[\Psi^{(+)}(x_1) + x_1\Phi^{(+)'}(x_1)] - [\Psi^{(-)}(x_1) + x_1\Phi^{(-)'}(x_1)] \\
 + \gamma_{22}^{(2)(+)}\Phi^{(+)}(x_1) - \gamma_{22}^{(2)(-)}\Phi^{(-)}(x_1)\} &= 0, \\
 \operatorname{Re}\{\mu_1^{(+)}\gamma_{21}^{(1)(+)}[\Psi^{(+)}(x_1) + x_1\Phi^{(+)'}(x_1)] - \mu_1^{(-)}\gamma_{21}^{(1)(-)}[\Psi^{(-)}(x_1) + x_1\Phi^{(-)'}(x_1)] \\
 + \gamma_{21}^{(2)(+)}\Phi^{(+)}(x_1) - \gamma_{21}^{(2)(-)}\Phi^{(-)}(x_1)\} &= 0, \\
 \operatorname{Re}\{\gamma_1^{(1)(+)}[\Psi^{(+)}(x_1) + x_1\Phi^{(+)'}(x_1)] - \gamma_1^{(1)(-)}[\Psi^{(-)}(x_1) + x_1\Phi^{(-)'}(x_1)] \\
 + (\gamma_1^{(1)(+)} + \gamma_1^{(2)(+)})\Phi^{(+)}(x_1) - (\gamma_1^{(1)(-)} + \gamma_1^{(2)(-)})\Phi^{(-)}(x_1)\} &= 0,
 \end{aligned} \tag{3}$$

$$\operatorname{Re}\{\gamma_2^{(1)(+)}[\Psi^{(+)}(x_1) + x_1\Phi^{(+)'}(x_1)] - \gamma_2^{(1)(-)}[\Psi^{(-)}(x_1) + x_1\Phi^{(-)}(x_1)] + (\gamma_2^{(1)(+)} + \gamma_2^{(2)(+)})\Phi^{(+)}(x_1) - (\gamma_2^{(1)(-)} + \gamma_2^{(2)(-)})\Phi^{(-)}(x_1)\} = 0, \quad |x_1| \geq a;$$

$$\operatorname{Re}\{[\Psi^{(+)}(x_1 + \mu_1^{(+)}h) + (x_1 + \mu_1^{(+)}h)\Phi^{(+)'}(x_1 + \mu_1^{(+)}h)] + \gamma_{22}^{(2)(+)}\Phi^{(+)}(x_1 + \mu_1^{(+)}h)\} = 0,$$

$$\operatorname{Re}\{\mu_1^{(+)}\gamma_{21}^{(1)(+)}[\Psi^{(+)}(x_1 + \mu_1^{(+)}h) + (x_1 + \mu_1^{(+)}h)\Phi^{(+)'}(x_1 + \mu_1^{(+)}h)] + \gamma_{21}^{(2)(+)}\Phi^{(+)}(x_1 + \mu_1^{(+)}h)\} = 0.$$

It should be noted that all the expressions presented above for each of the areas “1” and “2” are written using two functions of the complex variable, which are analytical in the area occupied by the corresponded material. One of the possible approaches to solving the formulated problem is transition to the one (for each of the materials) function in these expressions, which is analytic in the whole complex plane, which will allow reducing the boundary problem to the conjugation problem of two analytical functions defined in the whole complex plane. An essential complication in the implementation of this approach is the fact that the conjugation of analytic functions is performed not on the border of the half-plane, but on the inner interface line of the media  $x_2 = 0$ , which leads to the appearance of an additional condition follows from the last of conditions (3) already on the border of the half-plane itself.

## References

1. Bogdanov, V.L., Guz, A.N., Nazarenko, V.M: Spatial problems of the fracture of materials loaded along cracks (Review). *Int. Appl. Mech.* **51**(5), 489–560 (2015)
2. Guz, A.N.: *Fracture mechanics of composite materials under compression*. Nauk. dumka, Kiev (1990). (in Russian)
3. Guz, A.N: *Fundamentals of the three-dimensional theory of stability of deformable bodies*. Springer, Berlin, Hiedelberg, New York (1999)
4. Muskhelishvili, N.I.: *Some basic problems of the mathematical theory of elasticity*. Nauka, Moscow (1966). (in Russian)



# Fracture of Composite Material at Compression Along Near-Surface Crack

Mykhailo Dovzhyk<sup>1</sup>(✉), Vyacheslav Bogdanov<sup>2</sup>,  
and Vladimir Nazarenko<sup>1</sup>

<sup>1</sup> S.P. Timoshenko Institute of Mechanics, National Academy  
of Sciences of Ukraine, Nesterov Str. 3, 01057 Kiev, Ukraine  
Dovzhyk. M. V@ukr. net

<sup>2</sup> National Academy of Sciences of Ukraine,  
Volodymyrska 54, 01030 Kiev, Ukraine

**Abstract.** Nonclassical problem of fracture mechanics for near-surface crack under the action of compressive loads, directed along crack was investigated. The axisymmetrical problem for penny-shaped crack was considered. There are two approaches that are used to investigate such problems “beam approximation” and three-dimensional linearized theory of stability of deformable bodies for finite and small subcritical strains. Within the limits of the offered in second approach the problem was reduced to the solution of system of integral equations Fredholm with a side condition. Using the Bubnov-Galerkin method and numerically analytic technique, the problem was reduced to system of linear equations. As an example numerical research for a composite material was conducted. Critical loads were obtained for small and large distance between crack and free surface. Results for the composite materials behavior were also present and discussed.

**Keywords:** Composite materials · Compression along near-surface crack · Stress intensity factors

## 1 Compression Along Cracks

Fracture of material at compression along cracks is one of the nonclassical problems of fracture mechanics. In this case, the classical approaches of fracture mechanics such as Griffiths-Irwin don't work. Currently, there are two approaches that are used to investigate such problems [1]. The first of them is the use of approximate calculation schemes and approximate theories [2]. Within the framework of this approach, has the greatest application the “beam approximation”, when the part between the crack and the free surface (between the cracks) is replaced by a thin-walled element: beam, plate or shell, which are investigated in the framework of the applied theory of stability of thin systems. However, this method has significant drawbacks: it is necessary to carry out separate investigations to determine the possibilities of its application depending on the distance between the cracks, but even having determined this distance, there remains the question of choosing the conditions for fixing of thin-walled element. The second approach is based on the basic relationships and methods of the three-

dimensional linearized theory of stability of deformable bodies for finite and small subcritical strains [3]. At the same time, the destruction process is identified as the moment of local stability loss within the framework of a rigorous linearized theory of elasticity. In [4] using the second approach was found the conditions of applicability of the “beam approximation” for elastic materials with near surface crack. And it’s interesting find such conditions for composite materials.

**1.1 Problem Formulation**

We considered a half-space from composite material with penny-shaped crack of radius  $a$  which is situated in the plane  $x_3 = 0$  with center on  $Ox_3$  see Fig. 1. The initial stresses that operated along a crack correspond to biaxial uniform compression and defined from.

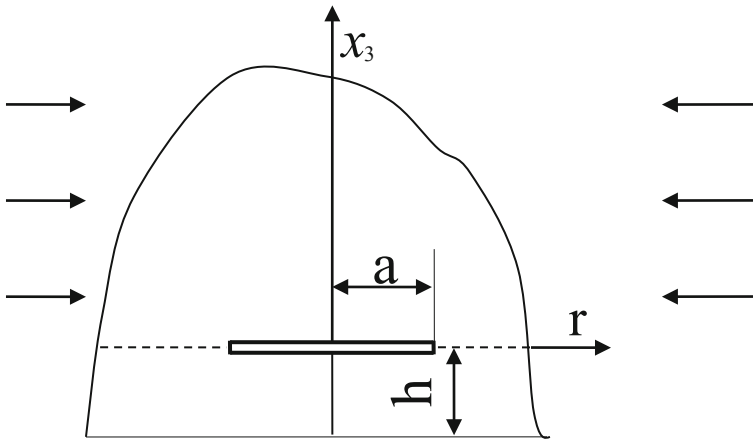


**Fig. 1.** Compression of half-space along penny-shaped crack.

Within the limits of the second approach the problem was reduced to the solution of system of integral equations Fredholm with a side condition [5]

$$\begin{aligned}
 f(\xi) + \frac{1}{\pi k} \int_0^1 M_1(\xi, \eta) f(\eta) d\eta + \frac{1}{\pi k} \int_0^1 N_1(\xi, \eta) g(\eta) d\eta &= 0, \\
 g(\xi) + \frac{1}{\pi k} \int_0^1 M_2(\xi, \eta) g(\eta) d\eta + \frac{1}{\pi k} \int_0^1 N_2(\xi, \eta) f(\eta) d\eta + \tilde{C}_1 &= 0, \\
 \int_0^1 g(\xi) d\xi &= 0 \quad (0 \leq \xi \leq 1, 0 \leq \eta \leq 1), \\
 f(\xi) &\equiv \varphi(a\xi), \quad g(\xi) \equiv \psi(a\xi).
 \end{aligned}
 \tag{1}$$

## 1.2 Exploratory Procedure

We used the procedure on the basis of a method Bubnov-Galerkin for solve integral equations (1) and search of critical shortening and stress. As system of coordinate functions power functions were used.

$$f(x) = \sum_{i=0}^N F_i x^i, \quad g(x) = \sum_{i=0}^N G_i x^i. \quad (2)$$

For further calculations, the numerical analytical procedure proposed in [4], which allowed us to obtain results for elastic materials, was used. Unlike the previous works [6, 7] where after substitution of coordinate functions (2) to system the numerical integration was executed. Here the procedure which allows analytically to calculate integrals for the chosen system of coordinate functions using a package of symbolic computations was used. It has allowed to achieve at the further numerical calculations higher exactitude of evaluations at the expense of a numerical integration lapse exclusion. For acceleration of integrals solutions the recurrence relations were used.

Using a method offered in [4] Fredholm integral equations (1) have been transformed to system of the equations with corresponding factors  $F_{1ji}$ ,  $G_{1ji}$  and variables  $F_i$ ,  $G_i$ ,  $\tilde{C}_1$ ,  $i, j \in [0, N]$ .

$$\begin{aligned} \sum_{i=0}^N F_i F_{1ji} + \sum_{i=0}^N G_i G_{1ji} &= 0; \\ \sum_{i=0}^N F_i F_{2ji} + \sum_{i=0}^N G_i G_{2ji} + \tilde{C}_1 &= 0; \\ \sum_{i=0}^N \frac{1}{i+1} G_i &= 0, \quad 0 \leq j \leq N. \end{aligned} \quad (3)$$

## 1.3 Results

As an example the task for near surface penny-shaped crack in half space from laminate composite with isotropic layers was conducted.

In macrovolumes such composite may be considered transversely-isotropic medium. In the case considered, crack are located in plane  $x_3 = const$ , parallel to interface boundary of layers. Dependence of critical dimensionless compressive stress  $\sigma_{11}^0/E$  on ratio of the dimensionless distance between a crack and free surface  $\beta = h/a$  are given in Figs. 2 and 3 and Table 1 (for  $\nu = \nu_1 = \nu_2$ , fiber concentration  $c_1$  is 0.7 and fiber aspect ratio is 10).

Critical values of  $\sigma_{11}^0/E$  at  $\beta \rightarrow \infty$  go asymptotically to values 0.0965, which are equal to respective critical values at surface instability of half-space. For a thin plate



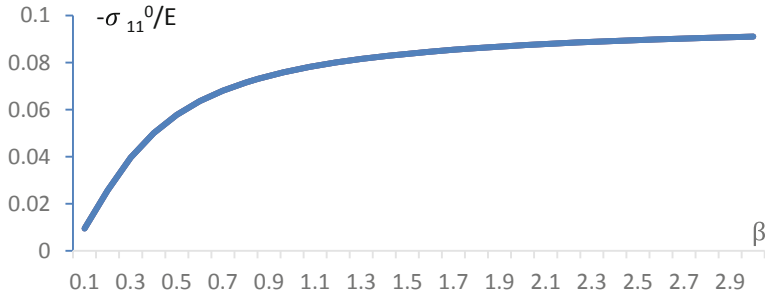


**Fig. 2.** Dependence of critical dimensionless compressive stress on ratio of the dimensionless distance between a crack and free surface.

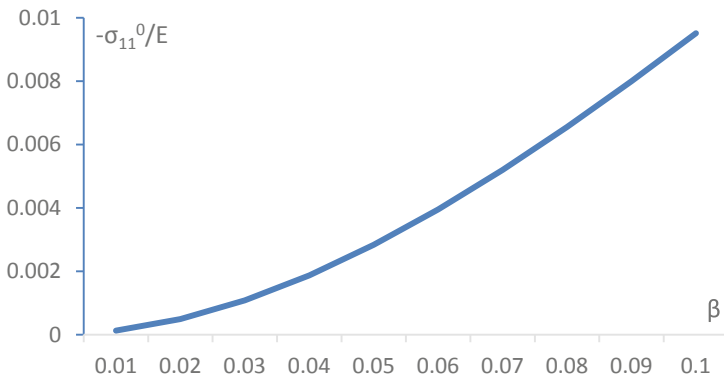


**Fig. 3.** Dependence of critical dimensionless compressive stress on ratio of the dimensionless distance between a crack and free surface for small distance.

critical stress can be found as  $\sigma_{cr} = A_{cr}\beta^2$  and for small dimensionless distance between a crack and free surface coefficient A found in Table 1.

Critical compressive stress was obtained for composite materials for large and small distances between the crack and fry surface. Analysis of the results was allowed to

**Table 1.** Critical compressive stress for small dimensionless distance between a crack and free surface.

$\beta$	Critical compressive stress ( $\sigma_{11}^0/E$ )	A
$1 \times 10^{-2}$	$-1.268 \times 10^{-4}$	-1.268
$1 \times 10^{-3}$	$-1.290 \times 10^{-6}$	-1.290
$1 \times 10^{-4}$	$-1.287 \times 10^{-8}$	-1.287
$1 \times 10^{-5}$	$-1.285 \times 10^{-10}$	-1.285
$1 \times 10^{-6}$	$-1.1284 \times 10^{-12}$	-1.284
$1 \times 10^{-9}$	$-1.284 \times 10^{-18}$	-1.284

determine the conditions of applicability of the “beam approximation”. Beam approximation good work for small distance between the crack and the free surface (when  $\beta < 0.01$  computing error less than 1%) and bad work in else case (when  $\beta > 0.1$  computing error more than 5%).

## References

1. Guz, A.N.: Establishing the foundations of the mechanics of fracture of materials compressed along cracks (review). *Int. Appl. Mech.* **50**, 1–57 (2014)
2. Obreimoff, I.W.: The splitting strength of mica. *Proc. Roy. Soc. London* **127**, 290–297 (1930)
3. Guz, A.N.: On one criterion of fracture of solids in compression along the cracks. Plane problem. *Docl. Akad. Nauk SSSR.* **259**, 1315–1318 (1980). (in Russian)
4. Guz, A.N., Dovzhik, M.V., Nazarenko, V.M.: Fracture of a material compressed along a crack located at a short distance from the free surface. *Int. Appl. Mech.* **47**(6), 627–635 (2011)
5. Guz, A.N., Nazarenko, V.M.: Mechanics of fracture of materials in compression along the cracks (review). *Highly elastic materials. Sov. Appl. Mech.* **25**(9), 3–32 (1989)
6. Guz, A.N., Knukh, V.I., Nazarenko, V.M.: Compressive failure of materials with two parallel cracks: small and large deformation. *Theoret. Appl. Fract. Mech.* **11**, 213–223 (1989)
7. Bohdanov, V.L.: Mutual influence of two parallel coaxial cracks in a composite material with initial stresses. *Mater. Sci.* **44**, 530–540 (2008)



# Statistical Distribution of Pores in Solid and Molten Metals at Dynamic Tensile Fracture

Polina N. Mayer<sup>(✉)</sup> and Alexander E. Mayer

Chelyabinsk State University, Bratiev Kashirinykh Str. 129,  
454001 Chelyabinsk, Russia  
polina.nik@mail.ru

**Abstract.** Knowledge about the evolution of the size distribution of pores during fracture of material is essential for formulation and verification of the fracture models. Here we continue our previous study on the size distribution of pores in molten and solid metals in conditions of high-rate tension. We expand the previous molecular dynamics simulations on larger systems and lower strain rates. This simulations show that behaviour of solid metals can be more complex than in the case of melts. Solid metals can exhibit secondary nucleation of voids in intersection of lattice defects created by plastic growth of primary pores. Also we compare the obtained molecular dynamics results with theoretical model that takes into account nucleation of pores due to thermal fluctuations and variation of their sizes, which is governed by viscous flow in the case of melt or plasticity in the case of solid metals.

**Keywords:** Tensile fracture · Evolution of pore ensemble · Size distribution · Nucleation and size variation · Molecular dynamics

## 1 Introduction

Dynamic tensile fracture at unloading of a rapidly heated layer or reflection of a shock pulse from a free surface is peculiar to both solids [1–3] and molten substances [4–7]. Dynamic tension follows the compression and transfers matter into a metastable state with the subsequent relaxation by means of nucleation and growth of pores. The dynamic tensile (spall) fracture is characterized by formation and interaction of multiple pores of different sizes, which eventually leads to fragmentation [8] or formation of main crack. The study of the size distribution of pores [9, 10] and the reasons of its evolution can significantly contributes formulation of the fracture model and allow one to take into account important statistical aspects of fracture.

We showed previously by means of molecular dynamics (MD) simulations that the exponential size distribution of pores is typical at the stage of their initial nucleation for both molten and solid metals [10]. The following relaxation of tensile stresses leads to collapse of small pores, and the size distribution of pores is transformed into normal one in the most cases [10]. In present paper we expand the MD simulations on larger systems and lower strain rates. Also we compare the MD results with theoretical model

that takes into account nucleation of pores due to thermal fluctuations and variation of their sizes, which is governed by viscous flow in the case of melt or plasticity in the case of solid metals.

## 2 Size Distribution of Pores in Melt

The problem statement and results of MD study for the case of melt are described in details in [10]. Increase in the system size and decrease in the strain rate do not alter the main conclusions about evolution of the pore size distribution in metal melt at tension. Exponential size distribution is revealed in all the investigated cases at the stage of the initial nucleation of pores after reaching the dynamic tensile strength. The following decrease in tensile stress due to growth of the void volume stops the nucleation and leads to collapse of smallest voids driven by surface tension. The collapse transforms the size distribution of pores into normal one. At very late stages, the size distribution is corrupted due to pore merging. Formation of normal size distribution can absent at very high strain rates (more than 10–100/ns depending on specific metal), at which merging starts before the collapse significantly contributes.

Let us consider how a theoretical model taking into account nucleation and size variation of pores can describe these statistical regularities observed in MD simulations. Critical radius at negative pressure  $P$  is  $R_{cr} = 2\gamma/(-P)$ , where  $\gamma$  is the coefficient of surface tension. Large pores with radii  $R > R_{cr}$  grow due to tension of matter, while smaller pores collapse due to surface tension. It is generally accepted that initial supercritical pores arise due to thermal fluctuations. The probability  $p$  of nucleation of a new critical pore during the time interval  $(t - t_j)$  from the previous nucleation instant  $t_j$  can be obtained by time integration of the nucleation rate [7].

$$p = N \int_{t_j}^t \left(\frac{c}{a}\right) \exp\left(-\frac{16\pi\gamma^3}{3kTP^2}\right) dt', \quad (1)$$

where  $N$  is the number of atoms in the system;  $c$  is the sound velocity;  $a$  is the average interatomic distance. In numerical realization of the theoretical model, a pseudorandom number  $\xi$  uniformly distributed within the range  $[0, 1]$  is generated each time step, and new supercritical pore is introduced if  $\xi \leq p$ . Its initial radius is defined as

$$R_{j+1}(t_{j+1}) = \sqrt{R_{cr}^2 + \frac{3kT}{4\pi\gamma} \ln\left(\frac{p}{\xi}\right)}, \quad (2)$$

which takes into account stochastic variation of the nucleated pore size. Subsequent evolution of each pore in the system is described by Rayleigh-Plesset equation [7].

$$\ddot{R}_i = -\frac{3\dot{R}_i}{2R_i} + \frac{1}{\rho R_i} \left(-P - \frac{2\gamma}{R_i} - 4\eta \frac{\dot{R}_i}{R_i}\right), \quad i = 1, \dots, j, \quad (3)$$

where  $\rho$  is the melt density;  $\eta$  is the viscosity of the melt. Tracing of nucleation and size variation of pores allows one to calculate the total volume of voids

$$V_p = \sum_{i=1}^j \frac{4\pi}{3} R_i^3, \quad (4)$$

the volume occupied by melt  $V_m = V - V_p$  and, consequently, the pressure in the system  $P(V_m, T)$ . Thus, we obtain the closed model predicting the melt reaction on tension, which determines the current volume  $V$  of the system.

Figure 1 shows the results of comparison between the theoretical model and the MD simulations for pressure and number of pores in the system. Variation of two model parameters, the surface tension coefficient and the melt viscosity coefficient, allows us to obtain a good correspondence. The initial monotonic decrease in pressure with melt tension is interrupted by abrupt nucleation of pores. Increase in total volume of voids leads to increase in pressure and collapse of all small voids as mentioned in [10, 11]. Subsequent oscillations of pressure are observed in both the model and the MD data, while the amplitude of oscillations is larger in the case of model. For higher strain rates, the pressure oscillations are less pronounced [8, 11].

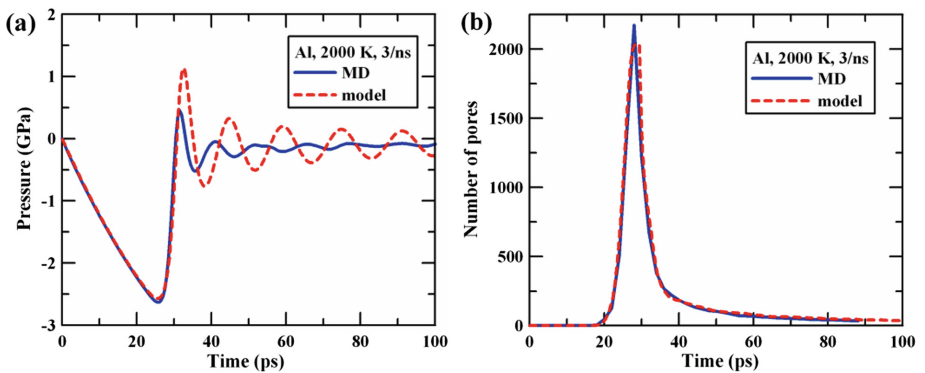


**Fig. 1.** Comparison of MD data (solid lines) and theoretical model (dashed lines) for the case of aluminum melt: time evolution of **a** pressure and **b** number of pores. The melt temperature is 2000 K; uniform tension with the true strain rate of 3/ns. The initial system size is  $86 \times 86 \times 86 \text{ nm}^3$ ; it contains 32 million atoms in MD.

The theoretical model gives not only the average parameters like pressure and number of voids, but also individual trajectories of pores and their size distributions. Individual trajectories show that initial growth changes to subsequent collapse and elimination from the ensemble for the most of the pores. Only largest pores emerged at the very beginning of the nucleation stage survive after the pressure increase. The number of pores continuously decreases with time. Here we restrict calculation by achieving the void volume fraction about  $0.2 \div 0.25$ . Very late stages of tension with

larger fraction of pores require another description proposed in [11] with taking into account strong the interaction between pores.

The size distributions of pores are analyzed as proposed in [10]. The sample distribution is compared with the exponential and normal trial distributions, both are defined on the finite interval restricted by minimal and maximal pore radius. Parameters of trial distributions are estimated to fit the sample mean and the sample variance.

Figure 2 shows that the developed theoretical model describes the evolution of the size distribution of pores observed in MD. Figure 2a and b correspond to beginning and end of the nucleation stage, respectively. One can see that the size distribution is close to exponential one at this stage. The following collapse of small pores leads to establishment of normal size distribution, see Fig. 2c and d. The calculated  $K$  ranges of pore radii coincide with the results of MD simulations [10].

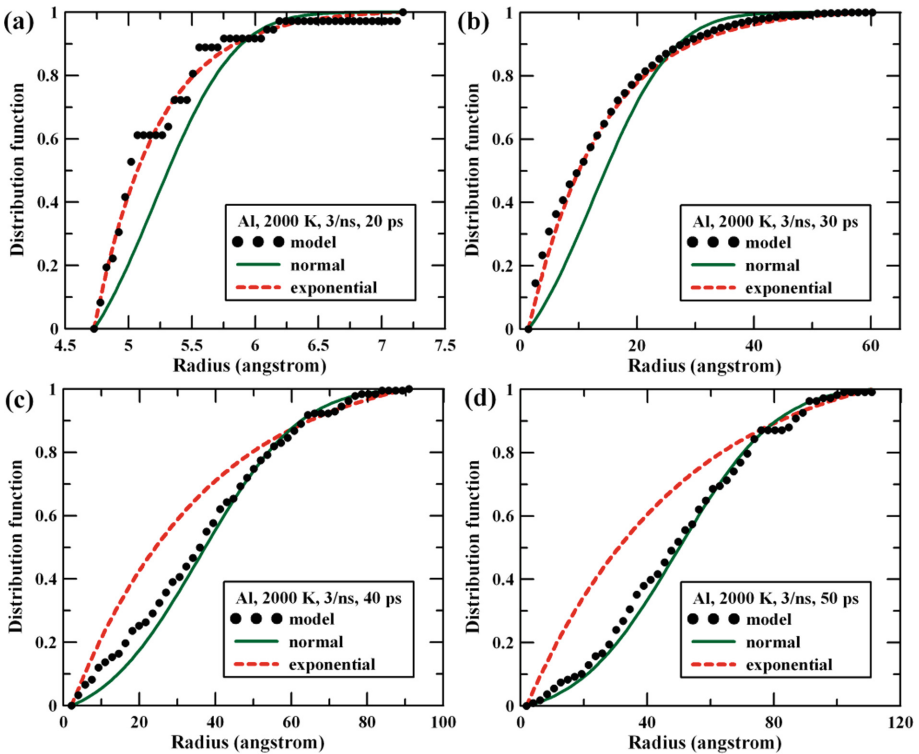


**Fig. 2.** Size distributions of pores calculated with theoretical model (circles) and its approximation by exponential (dashed red line) and normal (solid green line) distributions: evolution in time. The aluminum melt temperature is 2000 K; uniform tension with the true strain rate of 3/ns. The initial system size is  $86 \times 86 \times 86 \text{ nm}^3$ .

### 3 Size Distribution of Pores in Solid Metal

MD simulations are performed for aluminum single crystals using LAMMPS [12] and interatomic potential [13]; OVITO [14] is used for data visualization. The pore search algorithm is described in [10]. It consists in dividing the volume of the system into domains with sizes smaller than interatomic distances, defining empty domains as being farther from the center of atoms than the average interatomic distance, and combining all empty domains with adjoining faces into a separate pore. The type of size distribution is defined from comparison of cumulative distribution functions. Determination of parameters is based on the coincidence of variance and/or mean for model and sample distributions [10]. We consider both uniaxial and triaxial (uniform) tension with strain rates of 1/ns and 3/ns at a constant temperature of 300 K.

Increase in tensile stress up to 8–9 GPa leads to nucleation of pores (primary nucleation), see Fig. 3a. The formation and growth of pores leads to stress relaxation, as a result, the smallest pores become unstable (subcritical) and collapse; the number of pores decreases slightly. During further tension, the stresses in the system are maintained in the range from 0 to 1 GPa, and the number of pores can both smoothly decrease (at the strain rate of 3/ns) and increase (at 1/ns). Thus, the secondary nucleation of pores is possible at considerably lower level of stress (about 1 GPa) than the primary one. The cause of secondary nucleation at lower tensile stresses is the formation of lattice defects around the primary pores during their plastic growth.

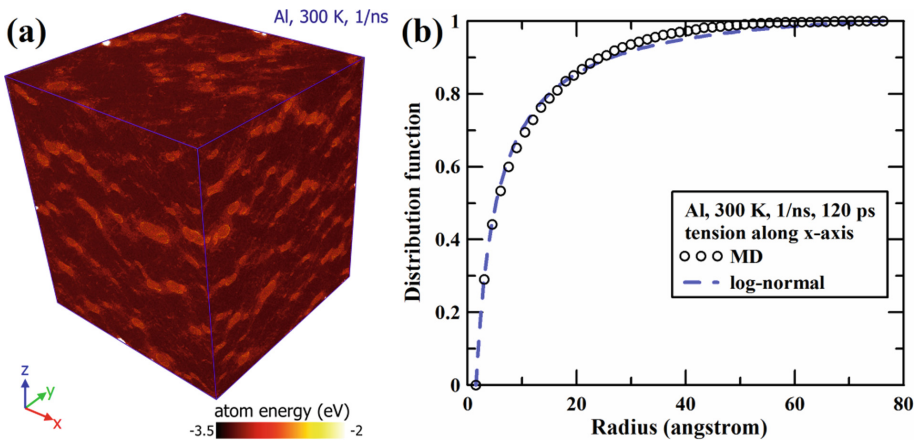


**Fig. 3.** Pores in solid aluminum: **a** MD system with atoms colored in correspondence with their total energy (light areas correspond to pores); **b** size distributions of pores from MD (circles) and its approximation by lognormal distribution (dashed line). The temperature of aluminum single crystal is 300 K; uniaxial tension with the true strain rate of 1/ns; the time moment is 120 ps from the beginning of tension. The MD system contains 108 million atoms.

Similar to the case of metal melts [10], the pore size distribution is close to exponential one at the stage of primary nucleation. Further, a normal distribution can be

established due to the collapse of the smallest pores. Besides it, a lognormal distribution is a good approximation in many cases, see Fig. 3b.

In the case of solid metals, the theoretical model includes the equations of plasticity driven growth of each pore [15] instead of the Rayleigh-Plesset equation (3). The nucleation part is the same as for melt.

## 4 Conclusions

MD simulations of formation and evolution of multiple pores in the course of tension of matter can be used for verification and calibration of physically-based models of fracture. Comparison of the MD results with the model predictions allows one to test both the nucleation and the size variation equations and their interplay for prediction of the statistical features of the pore ensemble.

**Acknowledgements.** Investigation of metal melts is supported by the Russian Science Foundation (Project 17-71-10205); investigation of solid metals is supported by the Ministry of Science and Higher Education of the Russian Federation (State task 3.2510.2017/4.6).

## References

1. Kanel, G.I., Zaretsky, E.B., Razorenov, S.V., Ashitkov, S.I., Fortov, V.E.: Unusual plasticity and strength of metals at ultra-short load durations. *Phys. Usp.* **60**(5), 490–508 (2017)
2. De Ressaiguier, T., Hemery, S., Lescoute, E., Villechaise, P., Kanel, G.I., Razorenov, S.V.: Spall fracture and twinning in laser shock-loaded single-crystal magnesium. *J. Appl. Phys.* **121**(16), 165104 (2017)
3. Krasnyuk, I.K., Pashinin, P.P., Semenov, A.Y., Khishchenko, K.V., Fortov, V.E.: Study of extreme states of matter at high energy densities and high strain rates with powerful lasers. *Laser Phys.* **26**(9), 094001 (2016)
4. Ashitkov, S.I., Komarov, P.S., Ovchinnikov, A.V., Struleva, E.V., Agranat, M.B.: Strength of liquid tin at extremely high strain rates under a femtosecond laser action. *JETP Lett.* **103**, 544–548 (2016)
5. Kanel, G.I., Savinykh, A.S., Garkushin, G.V., Razorenov, S.V.: Dynamic strength of tin and lead melts. *JETP Lett.* **102**, 548–551 (2015)
6. Struleva, E.V., Ashitkov, S.I., Komarov, P.S., Khishchenko, K.V., Agranat, M.B.: Strength of iron melt at high extension rate during femtosecond laser ablation. *J. Phys. Conf. Ser.* **774**, 012098 (2016)
7. Mayer, A.E., Mayer, P.N.: Continuum model of tensile fracture of metal melts and its application to a problem of high-current electron irradiation of metals. *J. Appl. Phys.* **118**(3), 035903 (2015)
8. Mayer, P.N., Mayer, A.E.: Late stages of high rate tension of aluminum melt: molecular dynamic simulation. *J. Appl. Phys.* **120**(7), 075901 (2016)
9. Rawat, S., Raole, P.M.: Molecular dynamics investigation of void evolution dynamics in single crystal iron at extreme strain rates. *Comput. Mater. Sci.* **154**, 393–404 (2018)
10. Mayer, P.N., Mayer, A.E.: Size distribution of pores in metal melts at non-equilibrium cavitation and further stretching, and similarity with the spall fracture of solids. *Int. J. Heat Mass Transf.* **127C**, 643–657 (2018)



11. Mayer, P.N., Mayer, A.E.: Evolution of foamed aluminum melt at high rate tension: a mechanical model based on atomistic simulations. *J. Appl. Phys.* **124**(3), 035901 (2018)
12. Plimpton, S.: Fast parallel algorithms for short-range molecular dynamics. *J. Comput. Phys.* **117**, 1–19 (1995)
13. Zope, R.R., Mishin, Y.: Interatomic potentials for atomistic simulations of the Ti-Al system. *Phys. Rev. B* **68**, 024102 (2003)
14. Stukowski, A.: Visualization and analysis of atomistic simulation data with OVITO—the open visualization tool. *Modell. Simul. Mater. Sci. Eng.* **18**, 015012 (2010)
15. Krasnikov, V.S., Mayer, A.E.: Plasticity driven growth of nanovoids and strength of aluminum at high rate tension: molecular dynamics simulations and continuum modeling. *Int. J. Plast.* **74**, 75–91 (2015)



# Fatigue and Deformation of Light Magnesium Alloys

Daolun Chen <sup>(✉)</sup>

Department of Mechanical and Industrial Engineering,  
Ryerson University, Toronto, Canada  
dchen@ryerson.ca

**Abstract.** Lightweighting has been deemed as one of the most effective strategies to improve fuel efficiency and reduce human-induced emissions in the automotive and aerospace industry. Magnesium alloy, as an ultra-lightweight metallic material, has recently received significant attention in the transportation industry to reduce the vehicle weight due to its high strength-to-weight ratio, dimensional stability, good machinability and recyclability. However, the hexagonal close-packed (hcp) crystal structure of magnesium alloys gives only limited slip systems and develops sharp deformation textures, leading to strong mechanical anisotropy and tension-compression yield asymmetry caused by the presence of twinning in compression and detwinning in tension when loading along the extrusion or rolling direction. For the vehicle components subjected to dynamic loading, such asymmetry could exert an unfavorable effect on the performance. This issue could be overcome through texture weakening via addition of rare-earth (RE) elements and other alloying elements to refine grains and generate nano-sized precipitates. To ensure the structural integrity, durability, and safety of load-bearing structural components, understanding the characteristics and mechanisms of deformation and fatigue of magnesium alloys is vitally important. In this talk, a few examples on the cyclic deformation behavior of extruded magnesium alloys containing both high and low RE contents will be presented in comparison with RE-free extruded magnesium alloys. Moreover, twinning, twin growth, and twin-twin interactions during uniaxial compression in the extrusion direction and de-twinning in the transverse direction will also be discussed.

**Keywords:** Magnesium alloy · Fatigue · Deformation · Texture · Twinning · Detwinning

## 1 Introduction

The titles such as “Why lightweighting is a game changer in automotive design”, and “Lightweighting is top priority for automotive industry” have recently grabbed the headlines. Vehicle lightweighting is nowadays recognized as one of the decisive strategies to improve fuel efficiency and reduce anthropogenic climate-changing, environment-damaging, costly, and human death-causing emissions [1–4], since every 10% reduction in weight can lead to 6–8% increase in fuel efficiency. Lightweight magnesium alloy has the potential to reduce component weight up to 70%. However,

the hexagonal close-packed (hcp) crystal structure of magnesium alloys limits the availability of slip systems and results in strong mechanical anisotropy and tension-compression yield asymmetry due to the presence of twinning and the associated deformation texture. For the components subjected to dynamic cyclic loading, such asymmetry could play an unfavorable part in the material performance and compromise the structural integrity, safety, and durability of highly-loaded structural components. This issue could be surmounted through weakening the basal texture via the addition of rare-earth (RE) elements, e.g., Y, Gd and Ce, and other alloying elements to refine grain sizes and generate strengthening precipitates. Then the formation and growth of deformation twins could be blocked. The underlying deformation characteristics and mechanisms of these magnesium alloys have thus been studied.

## 2 Results and Discussion

In the past ten years, Dr. Chen's team at Ryerson University, Toronto, Canada, has studied extensively fatigue and deformation behavior of various magnesium alloys including both cast (e.g., AZ91 [5], AM60 [6], ZK60 [7]) and wrought (e.g., AZ31 [8, 9], AM30 [10], ZEK100 [11], ME20 [12], GW103K [13, 14], NZ30K [15], ZM31 [16, 17]) magnesium alloys, focusing mainly on the twinning, twin growth, and twin-twin interactions during uniaxial compression in the extrusion direction and de-twinning in the transverse direction. For instance, as shown in Fig. 1, during cyclic deformation the stress-strain hysteresis loops of the mid-life cycles of the extruded GW103K (Mg-10Gd-3Y-0.5Zr) alloy in different material states were nearly symmetrical, which were somewhat similar to those of fcc metals (e.g., Al, Cu and Ni) as a result of the dislocation slip-dominated deformation [14, 18].

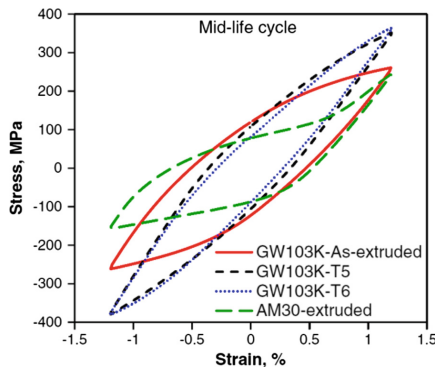


**Fig. 1.** Typical stress-strain hysteresis loops of the mid-life cycles at a given total strain amplitude of 1.2% in push-pull fatigue tests ( $R = -1$ ) for the extruded RE-free AM30 and high RE-containing GW103K alloy in different alloy states, respectively [14, 18].

This is in contrast to that of RE-free AM30 and AZ31 magnesium alloys, where a skewed asymmetrical shape appeared due to the occurrence of twinning in compression and detwinning in tension [8–10, 18]. In addition to the finer grain sizes in the GW103K alloy, a large number of nano-sized plate-shaped precipitates in T5 and T6 conditions can effectively impede the formation and propagation of twins (Fig. 2).

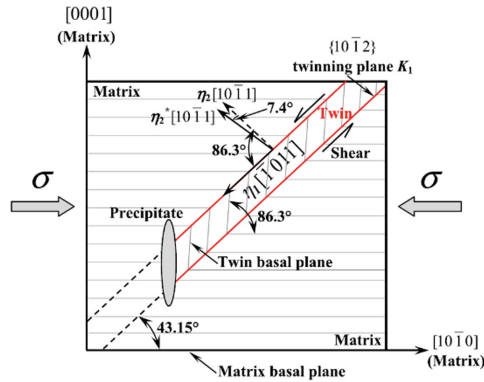


**Fig. 2.** A schematic illustration of the interaction between a plate-shaped precipitate and  $\{10\bar{2}\}$  extension twin in the GW103K alloy [13, 18].

When the compressive loading direction is parallel to the extrusion direction (ED),  $\{10\bar{2}\}$  extension twinning occurs as a consequence of the presence of basal texture with the  $c$ -axes of hcp unit cells in the majority of grains being perpendicular to the ED. With increasing compressive strain, the extension twins grow wider via the movement of twinning dislocations along the twin boundaries and also more extension twins are formed, as seen from Fig. 3. Various interesting twinning characteristics, such as (1) the operation of one twin variant exhibiting a morphology of parallel twins, (2) the operation of two twin variants present at an angle (either blocked or penetrated each other), and (3) more complicated twin-twin interactions (e.g., ladder-like structures, and branching-like structures with three twin variants operated) were observed. Also,  $\{11\bar{2}1\}$  embryonic twin structures were spotted [19].

After the compressive deformation in the ED to a certain amount (say, 4.3%) with the generation of a sufficient number of  $\{10\bar{2}\}$  extension twins which are also wide enough, changing the compressive loading direction to the normal direction (ND) will result in the occurrence of detwinning, i.e., the disappearance or narrowing or shortening of the pre-existing extension twins, as illustrated in Fig. 4. This leads to the recovery of the pre-deformed material to its initial state to some extent. Furthermore, such a change of compressive loading direction also causes the presence of  $\{10\bar{1}1\}$  and  $\{10\bar{1}3\}$  contraction twins as well as the impingement of  $\{10\bar{1}1\}$  contraction twins nucleated in the grain matrix on a pre-existing  $\{10\bar{2}\}$  extension twin [20].

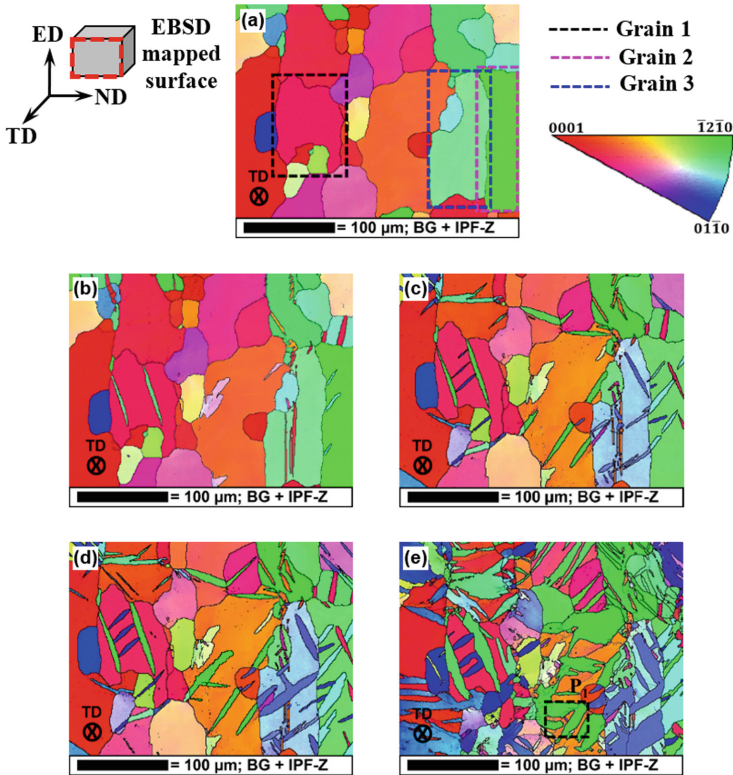


**Fig. 3.** EBSD orientation maps of an extruded AZ31 magnesium alloy compressed along the extrusion direction at a strain amount of **a** 0%, **b** 1.2%, **c** 2.5%, **d** 5.5%, and **e** 8% [19].

### 3 Concluding Remarks

Fatigue and deformation behavior of magnesium alloys are of vital importance for the lightweight structural applications. The commercially available RE-free wrought magnesium alloys (e.g., AZ31 and AM30) exhibit strong hysteresis loop asymmetry during cyclic deformation due to the occurrence of  $\{10\bar{1}2\}$  extension twinning in compression and partial detwinning in tension when the cyclic loading direction is parallel to the ED. The presence of a large number of extension twins causes significant cyclic hardening, arising from the twin-twin, twin-dislocation, and twin-grain boundary interactions. The addition of RE elements can effectively hinder the twinning as a result of the formation of nano-sized precipitates, grain refinement, solid solution effect, interfacial segregation and pinning effect. The suppression of twinning paves the way for the dislocation slip-dominated deformation, leading to nearly symmetrical hysteresis loops and cyclic stabilization. To better understand the twinning-detwinning mechanisms, uniaxial compression tests were conducted. When the compressive loading direction is along the ED,  $\{10\bar{1}2\}$  extension twinning occurs. With increasing compressive strain, the extension twins become increasingly wider via the motion of

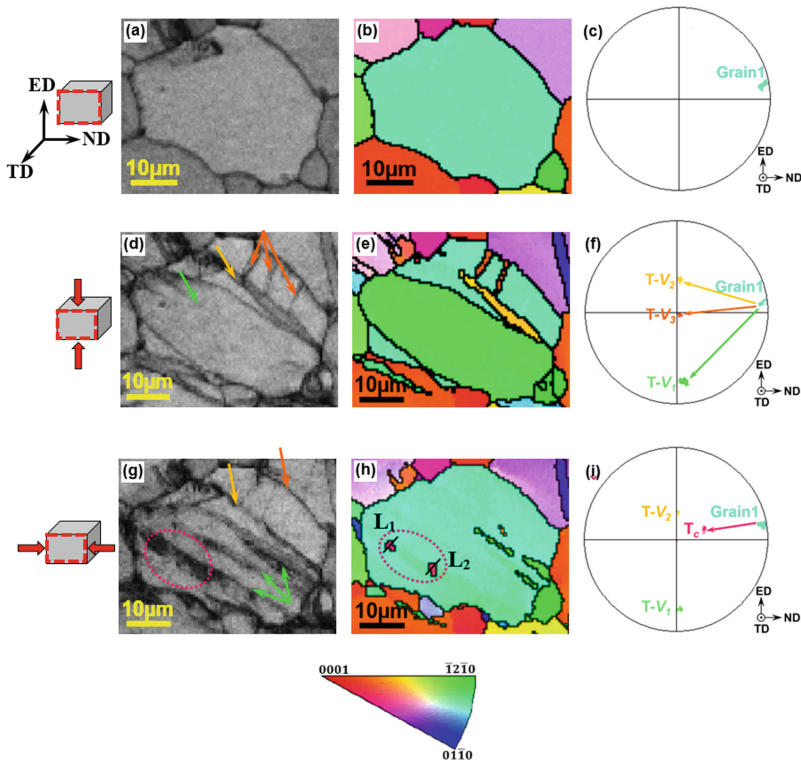


**Fig. 4.** EBSD band contrast maps, orientation maps, and the corresponding  $\{0001\}$  pole figures of the matrix and the twins of the central grain compressed at **a, b, c** 0%, **d, e, f** 4.3% ED, and **g, h, i** 4.3% ED–4.3% ND, respectively [20].

twinning dislocations along the twin boundaries in conjunction with the formation of more extension twins. Some interesting twinning characters, such as the operation of a single twin variant and two twin variants, more complicated twin-twin interactions (e.g., ladder-like structures, and branching-like structures), and  $\{11\bar{2}1\}$  embryonic twin structures are observed. When the compressive loading direction is changed to the ND, detwinning (i.e., the vanishing or narrowing or shortening of the pre-existing extension twins) occurs, along with the formation of  $\{10\bar{1}1\}$  and  $\{10\bar{1}3\}$  contraction twins and the impingement of  $\{10\bar{1}1\}$  contraction twins nucleated in the matrix on a pre-existent  $\{10\bar{1}2\}$  extension twin. More studies via in situ EBSD and high-resolution transmission electron microscopy as well as atomic simulations are needed to further deepen the understanding of the intriguing twinning and detwinning mechanisms in magnesium alloys.

**Acknowledgements.** The author would like to acknowledge the financial support of Natural Sciences and Engineering Research Council of Canada (NSERC), Premier's Research Excellence Award, NSERC-DAS, Canada Foundation for Innovation, and Ryerson Research Chair program, and thank his current and former graduate students and PDFs including Dr. F. Mokdad, Dr. F. A.

Mirza, Dr. N. Tahreen, Dr. D. Sarker, Dr. D. R. Ni, Dr. C. L. Fan, Dr. W. P. Jia, Mr. S. M. A. K. Mohammed, Ms. S. Begum, Mr. H. A. Patel, Mr. X. Z. Lin, Ms. M. Luk, Mr. A. R. Emami, and Mr. K. Wang, and his research collaborators in this aspect including Prof. S. D. Bhole, Prof. J. Friedman, Prof. D. Y. Li, Prof. M. A. Wells, Prof. A. Luo, Dr. S. Xu, Dr. K. Sadayappan, Prof. X. Q. Zeng, Dr. D. J. Li, Prof. B. L. Xiao, Prof. Z. Y. Ma, Prof. X. Q. Jiang, Prof. D. F. Zhang, and Prof. F. S. Pan.

## References

1. Barrett, S.: Choices in the climate common. *Science* **362**, 1217 (2018)
2. Diffenbaugh, N.S., Singh, D., Mankin, J.S.: Unprecedented climate events: historical changes, aspirational targets, and national commitments. *Sci. Adv.* **4**(2), eaao3354 (2018)
3. Anenberg, S.C., Miller, J., Minjares, R., Du, L., Henze, D.K., Lacey, F., Malley, C.S., Emberson, L., Franco, V., Klimont, Z., Heyes, C.: Impacts and mitigation of excess diesel-related NO<sub>x</sub> emissions in 11 major vehicle markets. *Nature* **545**, 467–471 (2017)
4. Rockström, J., Gaffney, O., Rogelj, J., Meinshausen, M., Nakicenovic, N., Schellnhuber, H. J.: A roadmap for rapid decarbonization. *Science* **355**, 1269–1271 (2017)
5. Patel, H.A., Chen, D.L., Bhole, S.D., Sadayappan, K.: Cyclic deformation and twinning in a semi-solid processed AZ91D magnesium alloy. *Mater. Sci. Eng. A* **528**(1), 208–219 (2010)
6. Patel, H.A., Chen, D.L., Bhole, S.D., Sadayappan, K.: Low cycle fatigue behavior of a semi-solid processed AM60B magnesium alloy. *Mater. Des.* **49**, 456–464 (2013)
7. Hadadzadeh, A., Mokdad, F., Amirkhiz, B.S., Wells, M.A., Williams, B., Chen, D.L.: Bimodal grain microstructure development during hot compression of a cast-homogenized Mg-Zn-Zr alloy. *Mater. Sci. Eng. A* **724**, 421–430 (2018)
8. Lin, X.Z., Chen, D.L.: Strain controlled cyclic deformation behavior of an extruded magnesium alloy. *Mater. Sci. Eng. A* **496**(1–2), 106–113 (2008)
9. Begum, S., Chen, D.L., Xu, S., Luo, A.A.: Low cycle fatigue properties of an extruded AZ31 magnesium alloy. *Int. J. Fatigue* **31**(4), 726–735 (2009)
10. Begum, S., Chen, D.L., Xu, S., Luo, A.A.: Strain-controlled low cycle fatigue properties of a newly developed extruded magnesium alloy. *Metall. Mater. Trans. A* **39**, 3014–3026 (2008)
11. Mokdad, F., Chen, D.L.: Strain-controlled low cycle fatigue properties of a rare-earth containing ZEK100 magnesium alloy. *Mater. Des.* **67**, 436–447 (2015)
12. Mirza, F.A., Wang, K., Bhole, S.D., Friedman, J., Chen, D.L., Ni, D.R., Xiao, B.L., Ma, Z. Y.: Strain-controlled low cycle fatigue properties of a rare-earth containing ME20 magnesium alloy. *Mater. Sci. Eng. A* **661**, 115–125 (2016)
13. Mirza, F.A., Chen, D.L., Li, D.J., Zeng, X.Q.: Low cycle fatigue of a rare-earth containing extruded magnesium alloy. *Mater. Sci. Eng. A* **575**, 65–73 (2013)
14. Mirza, F.A., Chen, D.L., Li, D.J., Zeng, X.Q.: Cyclic deformation behavior of a rare-earth containing extruded magnesium alloy: effect of heat treatment. *Metall. Mater. Trans. A* **46** (3), 1168–1187 (2015)
15. Mirza, F.A., Chen, D.L., Li, D.J., Zeng, X.Q.: Low cycle fatigue of an extruded Mg-3Nd-0.2Zn-0.5Zr magnesium alloy. *Mater. Des.* **64**, 63–73 (2014)
16. Tahreen, N., Zhang, D.F., Pan, F.S., Jiang, X.Q., Li, C., Li, D.Y., Chen, D.L.: Characterization of hot deformation behavior of an extruded Mg-Zn-Mn-Y alloy containing LPSO phase. *J. Alloy. Compd.* **644**, 814–823 (2015)
17. Tahreen, N., Zhang, D.F., Pan, F.S., Jiang, X.Q., Li, D.Y., Chen, D.L.: Strengthening mechanisms in magnesium alloys containing ternary I, W and LPSO phases. *J. Mater. Sci. Technol.* **34**(7), 1110–1118 (2018)

18. Mirza, F.A., Chen, D.L.: Fatigue of rare-earth containing magnesium alloys: a review. *Fatigue Fract. Eng. Mater. Struct.* **37**, 831–853 (2014)
19. Mokdad, F., Chen, D.L., Li, D.Y.: Single and double twin nucleation, growth, and interaction in an extruded magnesium alloy. *Mater. Des.* **119**, 376–396 (2017)
20. Mokdad, F., Chen, D.L., Li, D.Y.: Twin-twin interactions and contraction twin formation in an extruded magnesium alloy subjected to an alteration of compressive direction. *J. Alloy. Compd.* **737**, 549–560 (2018)



**Part III**  
**Miscellaneous (Biomechanics,  
Computational Mechanics, Dynamics,  
Nanomechanics, Plasticity, Structures,  
Wave Propagation)**



# Research on Contact Pressure of Friction Pair Based on Finite Element Method

Changlu Wang<sup>1</sup>, Long Wu<sup>2</sup>, Zichun Xu<sup>3</sup>(✉), Yaping Zhang<sup>3</sup>,  
Hao Gao<sup>4</sup>, and Yanzhong Wang<sup>3</sup>

<sup>1</sup> Beautiful China Development Institute, 365004 Sanming, China

<sup>2</sup> Fujian Provincial Collaborative Innovation Center for Green Casting,  
Forging and Advanced Manufacturing, 365004 Sanming, China

<sup>3</sup> School of Mechanical Engineering and Automation, Beihang University,  
100191 Beijing, China  
1019856685@qq.com

<sup>4</sup> Engineering Research Center, Fujian Province University for Modern  
Mechanical Design and Manufacturing Technology, 365004 Sanming, China

**Abstract.** The brake is a device that realizes mechanical speed reduction and braking, and its key component is the friction pair. In this paper, the problem of the brake pressure distribution characteristic of the friction pair is studied. The dynamic and static contact pressure of the friction pair is simulated by ABAQUS. Based on MATLAB and statistical moment analysis methods, the simulation results of contact pressure under different working conditions are analyzed.

**Keywords:** Friction pair · Static contact pressure · Dynamic contact pressure

## 1 Static Contact Pressure Simulation Model of Friction Pair

The object of this paper is the friction pair, which is used in the all-disc brake. The friction pair is mainly composed of a static friction disc and a dynamic friction disc. The static and dynamic friction disc are both composed of a friction plate and a friction plate base, and the friction plates have a circumferentially uniform arrangement on the friction disk. Therefore, the simplified structural model of the friction pair of the single dynamic friction plate and the plurality of static friction plates is established by the symmetry distribution of the friction plates (see Fig. 1).

The static contact pressure simulation of friction pairs is the contact pressure simulation of friction pairs under pure extrusion without relative sliding between the dynamic friction plate and the static friction plate. In order to eliminate the influence of the loading input on the friction pair, the loading method is to apply uniform pressure on the upper surface of the dynamic friction plate. The general static solver of ABAQUS is used in this paper. The “CPRESS” information of the 927 unit nodes involved in the dynamic friction plate is mainly analyzed, and the static contact pressure response of the friction pair is finally obtained.

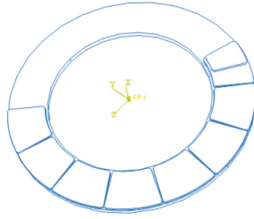


**Fig. 1.** Friction pair structure model.

## 2 Static Contact Pressure Analysis of Friction Pair

Qualitative observation of the simulation results, Fig. 2 is the static contact pressure of the dynamic friction plate of the friction pair with a loading pressure of 0.8 MPa. It can be seen that the static contact pressure of the friction pair is not uniform, which has obvious geometric symmetry. From the numerical point of view, the edge contact pressure of the friction plate is smaller, the maximum contact pressure appears in the interior near the outer edge and the center pressure of the friction plate is relatively uniform.

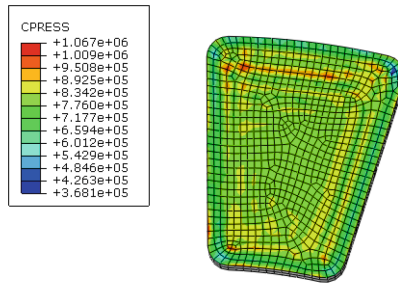


**Fig. 2.** Simulation results of friction pair contact pressure under 0.8 MPa loading pressure (left).

In view of the non-uniformity of the static contact pressure, it is assumed that the contact pressure on the dynamic friction plate node has the statistical characteristic. As shown in Fig. 3, it is the distribution of the static contact pressure of the friction pair under 0.8 MPa. The horizontal coordinate scale is the scale after the node pressure value is taken as  $\log_{10}$ , and the longitudinal coordinate is the frequency of the node pressure value. The horizontal coordinate position corresponding to the vertical dotted line is the average pressure corresponding position of the theoretical node pressure when the loading force is 0.8 MPa, and the horizontal coordinate position corresponding to the vertical solid line is the corresponding pressure position after taking the arithmetic mean of the contact pressure of 927 nodes. Its value is 826,989.51 Pa. The

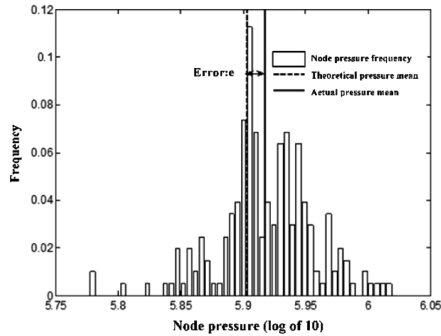


**Fig. 3.** Contact pressure distribution of friction pair nodes under 0.8 MPa (right).

error from the theoretical loading value is approximately 3.37%. Therefore, it can be considered that the simulation value is basically consistent with the theoretical value, and the simulation is effective.

As mentioned in the previous paragraph, the static node pressure distribution has a probability distribution characteristic. In this paper, the first-order center moment, second-order center moment, third-order center moment and kurtosis of the node contact pressure samples are mainly studied. The first-order center moment represents the mean value of the sample and the second-order center moment represents the variance of the sample. The third-order center moment characterizes the symmetry of the sample with respect to the mean, and the kurtosis characterizes the similarity between the sample distribution and the normal distribution [1].

The contact pressure response under loading conditions of 0.8, 0.6, 0.4, and 0.2 MPa was simulated. Figure 4a–d show the relationship between the first-order, second-order, third-order center moment and kurtosis and loading conditions, respectively. As can be seen from Fig. 4a, the first-order center moment is linear with the loading conditions. The error between the simulation result and the theoretical result is less than 5% within the operating conditions. It can be seen from Fig. 4b that the second-order center moment is constantly increasing with the loading condition, which means that the dispersion of the contact pressure on the friction pair becomes larger, and the surface pressure unevenness of the friction plate increases with the pressure. It can be seen from Fig. 4c that the third-order center moment has a tendency to become smaller with the loading condition, which is close to zero. Therefore, the contact pressure of the friction pair node has a good symmetry centered on the mean. It can be seen from Fig. 4d that the kurtosis of the contact pressure of the friction plate node tends to decrease with the pressure and is close to zero. Therefore, the larger the loading pressure in the static case, the closer the contact pressure distribution is to the normal distribution.

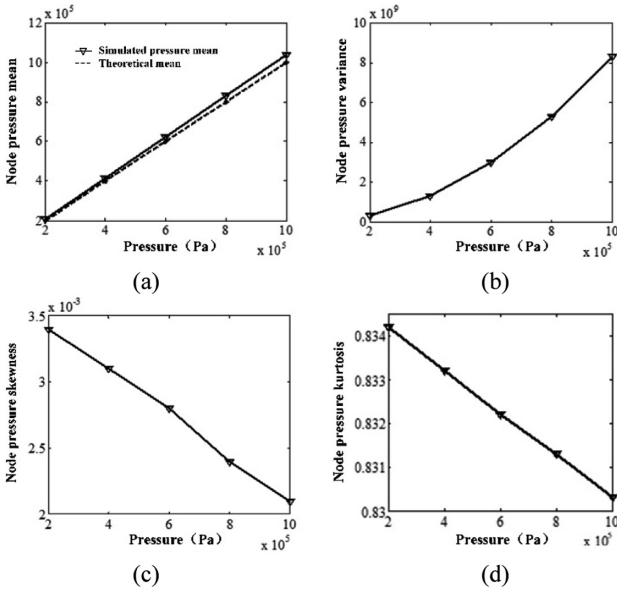


**Fig. 4.** The first four-order central moment of the contact pressure value of nodes under different working conditions.

### 3 Dynamic Contact Pressure Simulation Model of Friction Pair

The dynamic contact pressure simulation model of friction pair is the simulation of the contact pressure between the dynamic friction plate and the static friction plate under extrusion and relative sliding. The model is modified based on the friction pair static contact pressure simulation model, and its structural model is identical to the former structural model. The difference between the two is in the boundary constraint in the simulation setup. The dynamic contact pressure simulation of the friction pair adds a rotation boundary to the dynamic friction plate. The solver for this model is the dynamic solver for ABAQUS, and this model inherits the meshing of static models and processes the contact pressure response results in the same way.

There are two input parameters for the friction pair dynamic contact pressure simulation model: the relative sliding speed of the friction pair and the loading pressure. One variable is set to increase and another variable is set as an input parameter in order to study the effect of two factors on the contact pressure response. The relative sliding speed is between 0 and 60 m/s, and the theoretical loading pressure is between 0 and 0.8 MPa. Therefore, the simulation conditions of Table 1 are set.

**Table 1.** Dynamic contact pressure simulation of friction pair.

Test number	1	2	3	4	5	6	7	8	9
Relative sliding speed (m/s)	10	20	30	40	50	60	30	30	30
Pressure (MPa)	0.8	0.8	0.8	0.8	0.8	0.8	0.6	0.4	0.2

### 4 Dynamic Contact Pressure Analysis of Friction Pair

Qualitative observation of the simulation results, Fig. 5b-d are the dynamic contact pressure of the friction pair under different speed conditions, which is significantly different from the static contact pressure of Fig. 5a. The former loses the distribution symmetry of the latter. The maximum pressure is multiplied and the pressure distribution is more concentrated. However, the dynamic contact pressure distribution under different operating conditions has similar characteristics.

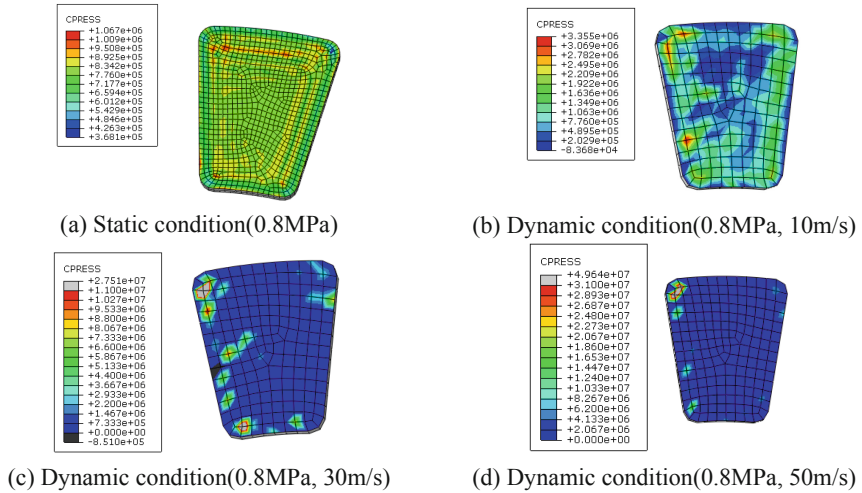


**Fig. 5.** Dynamic contact pressure simulation results of friction pair.

Figure 6 shows the distribution of the contact pressure of the contact nodes under the condition of 0.8 MPa and 40 m/s. It can be seen that there is a big difference between the static situation and the dynamic situation. The static node pressure distribution is concentrated near the theoretical pressure value. The dynamic node pressure distribution is dispersed, but the overall node pressure distribution state still presents a bell shape. The average value of the samples is  $8.2435 \times 10^5$  Pa, which is 3.04% different from the theoretical value ( $8.00 \times 10^5$  Pa). It can be considered that the simulation can reflect a certain degree of authenticity.

As shown in Fig. 7, only the first moment of the contact pressure of the node has a significant tendency, because the average value of contact pressure increases with the linear velocity of friction plate. It can be seen from Fig. 7a that the contact unevenness of friction plate is intensified as the linear velocity changes of friction plate. It can be seen from Fig. 7b that in the dynamic case, the friction plate contact pressure has a significant dispersion compared with the static contact pressure, that is, the contact pressure is not uniform. The symmetry of the pressure distribution of the friction plate can be seen from Fig. 7c. Whether static or dynamic condition, the skewness of node pressure samples is negative, which means that the distribution is negatively skewed. In

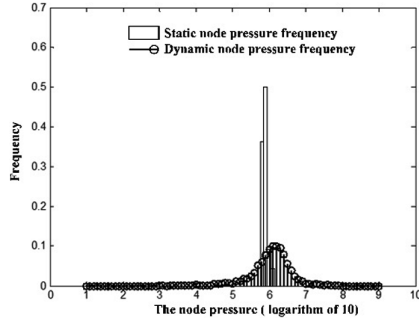


Fig. 6. Dynamic node contact pressure distribution of friction pair.

the dynamic case, the value is more concentrated on the left side than that in the static case, which means that the pressure node has a large probability of large pressure value, but its skewness value is relatively small, which can be approximated as symmetric distribution. The difference between normal distribution and pressure distribution of friction plate can be seen from Fig. 7d. The pressure distribution is steeper than the normal distribution generally.

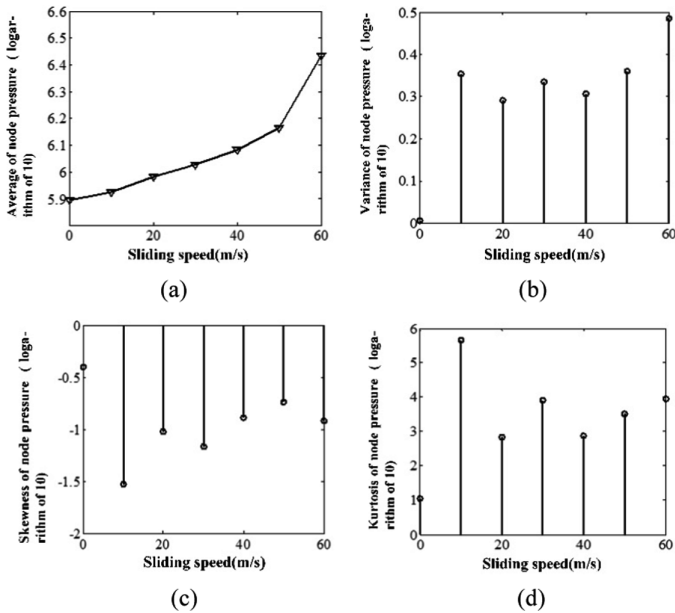


Fig. 7. First four-order center moment of dynamic contact pressure.

## 5 Conclusion

The static pressure at the frictional plate edge is small, and the maximum static pressure appears at a certain distance from the frictional plate edge. The distribution of the dynamic pressure destroys the symmetry of the static pressure distribution. Its distribution is roughly that the dynamic contact pressure at the edge of the friction plate is large and the contact pressure inside the friction plate is small. Along the velocity direction, the dynamic contact pressure at the front of the friction plate is greater than that at the back. This conclusion is similar to Gao's conclusion [2] to some extent that the maximum dynamic contact pressure appears at the entrance and the minimum at the exit. It is found that the distribution of static contact pressure values approximates a normal distribution with a theoretical value, and the distribution of dynamic contact pressure values has a higher kurtosis than the normal distribution.

## References

1. Wang, Q., Chang, Z., Cao, X: Random Data Processing Method. China University of Petroleum Publishers (2011)
2. Huang, J., Gao, C., Lin, X.: Study on the contact pressure distribution of a disc brake. *Acta Mech. Solida Sin.* **03**, 297–302 (2007)





# Noise and Vibration Analysis of a Flux Switching Motor (FSM) with Segmental Rotor

Hedduri Sanket<sup>1</sup>(✉), M. N. Kishore<sup>2</sup>, and Nagesh Suresh<sup>3</sup>

<sup>1</sup> Mechanical Engineering, PES University, Bengaluru, India  
sankethedduri@gmail.com

<sup>2</sup> Crucible of Research and Innovation, PES University, Bengaluru, India

<sup>3</sup> Computational Mechanics, PES University, Bengaluru, India

**Abstract.** Flux Switching Motor (FSM) with segmental rotor is a new class of electric motor, with both AC and DC windings on the stator. The rotor is devoid of any windings. FSM with its high torque density, compactness, less heat production and high ruggedness can prove to be an ideal motor topology to be used for the propulsion systems of electric vehicles. The objective of this study is to investigate the noise and vibration characteristics of an FSM with segmental rotor due to the electromagnetic forces acting on the motor and optimize the design to reduce noise and vibration levels.

**Keywords:** Flux switching motor · Vibration · Noise · Electromagnetic analysis · Electro-mechanical interaction

## 1 Introduction

When a rotor spins, unbalance lateral forces and moments are generated due to limitations in machining and assembly accuracy. These forces and moments give rise to vibration at the same frequency as rotational speed. If the excitation frequency matches that of any of the natural frequencies of the rotor, resonance takes place, leading to higher vibration and noise and sometimes costly failures. There are many reasons for induction of rotor dynamic instability, viz., electro-mechanical interactions, misalignments, air gap eccentricity, etc.

## 2 Methodology

A flux-switching motor of 1 kW power rating, having 8 rotor segments was designed from scratch and 3D CAD model developed. Modal analysis was done to obtain natural frequencies and mode shapes of the rotor. Transient magnetic analysis was then performed to get the electromagnetic forces acting on the rotor and stator. Based on the results of transient magnetic analysis, the rotor and stator design were optimized to, avoid magnetic saturation of the material, provide a low reluctance path for the magnetic flux lines and avoid magnetic flux leakage. Impulse excitation exerted on the rotor by electromagnetic forces was used as the load for vibration transient analysis and the rotor response found out.

### 3 Configuration and Design of FSM

Figure 1 shows the construction of an FSM. It consists of stator, windings (coils), rotor segments and rotor core. Based on available research literature, 7-segment and 8-segment rotors are considered to be the optimum options for a 12-pole stator. The rationale behind opting 8 rotor segments was that, more number of rotor segments result in less torque ripples and even number of segments have lesser noise and vibration problems [1]. The configuration of the 8-segment FSM is as listed in Table 1. Table 2 shows the materials assigned for different parts of the motor.

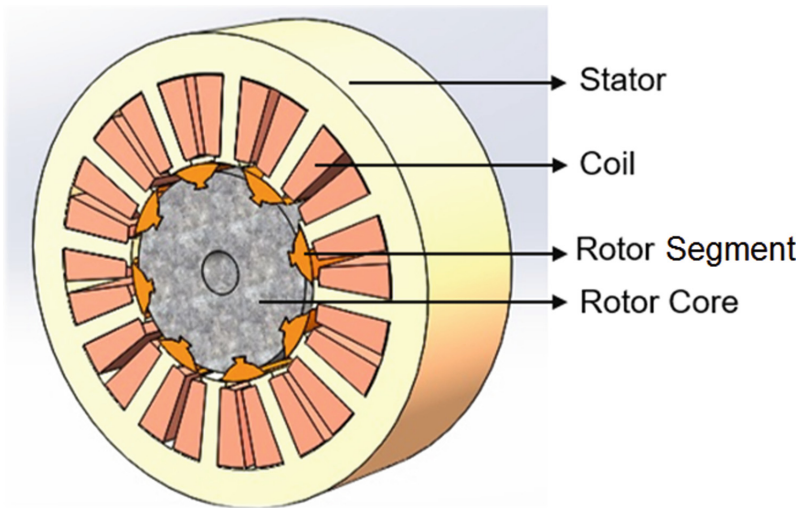


Fig. 1. Flux-switching motor with segmental rotor

## 4 Electromagnetic Simulation

### 4.1 FSM Design Optimization

Providing a low reluctance path for magnetic flux, by optimizing the rotor and stator design would not only result in an increased torque output but also reduce vibration and noise levels. Avoiding magnetic saturation of the rotor and stator material would lead to higher efficiency. The magnetic flux density was studied and the dimensions of the stator tooth was iterated to limit the magnetic flux density to around 1.5 T. The same process was employed to finalize rotor segment design. Magnetic flux density of the motor is shown in Fig. 2. It was observed that most of the magnetic flux on the stator and the rotor segments was below 1.44 T, and hence magnetic saturation was avoided. Presence of magnetic flux above 1.6 T (saturation limit) was observed in a very small localized area.

**Table 1.** Motor configuration

Parameter	Value
Rating of the motor	1 kW
Rated speed	3000 RPM
Number of AC phase	3
Number of AC excited coils	6 (96 turns each)
Number of DC excited coils	6 (96 turns each)
Number of stator poles	12
Number of rotor segments	7 and 8
AC supply current	5 A, 400 Hz
DC supply current	5 A
Air gap	0.5 mm

**Table 2.** Material configuration

Part	Material
Rotor segments	M36 electrical steel
Rotor core	AISI 304 stainless steel (non-electrical steel)
Stator	M36 electrical steel
Windings	AWG 12 copper

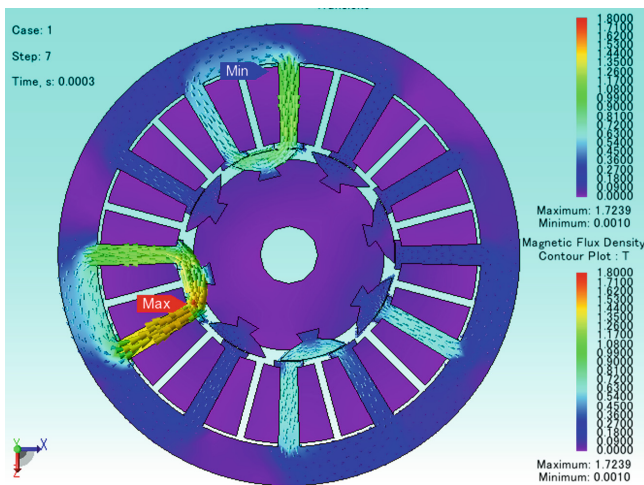


**Fig. 2.** Magnetic flux density distribution contour plot

### 4.2 Electromagnetic Force Calculation

The most important vibration excitation is the reluctance force produced in the air gap between the stator and rotor. The reluctance force of electric motor is electromagnetic force which has two components, radial ( $F_{rad}$ ) and tangential ( $F_{tan}$ ) components. In electromagnetic FEA calculations, the material boundaries are chosen on edge of the stator tip [2]. Equations (1) and (2) give the formulae for radial and tangential electromagnetic forces respectively. The integral is performed over the length of the stator tip edge length,  $l$ .

$$F_{rad} = \frac{L_{stk}}{2\mu_0} \oint (B_n^2 - B_t^2) dl \tag{1}$$

$$F_{tan} = \frac{L_{stk}}{\mu_0} \oint (B_n \cdot B_t) dl \tag{2}$$

where  $B_n$  and  $B_t$  are the normal and tangential components of magnetic flux density respectively,  $\mu_0 = 4\pi \times 10^{-7}$  H/m, is permeability of vacuum and  $L_{stk}$  is stack length of the machine.

Figure 3 shows the maximum nodal force (EMF) acting on the rotor at any point in time. Average absolute total EMF for the 8-segment rotor was found to be 75.86 N.

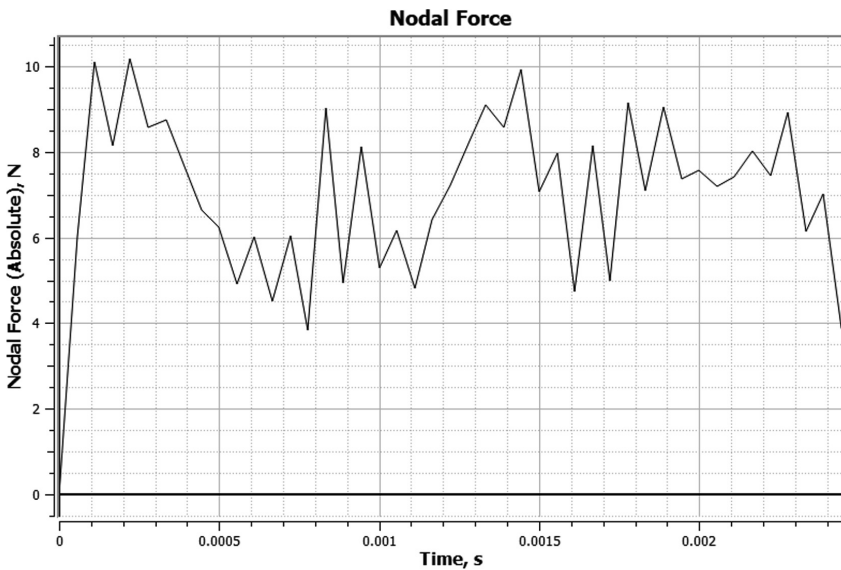


Fig. 3. Maximum nodal force (EMF) versus time

**Table 3.** Modal analysis results

Mode	Frequency (Hz)
7	13,342
8	13,349
9	14,801
10	14,808

## 5 Rotor Noise and Vibration Characteristics

### 5.1 Modal Analysis

A free-free eigen value analysis was then carried out to find out the natural frequencies of the rotor (Table 3). The values of the first six modes were zero or near zero, which verified structural integrity of the FE model.

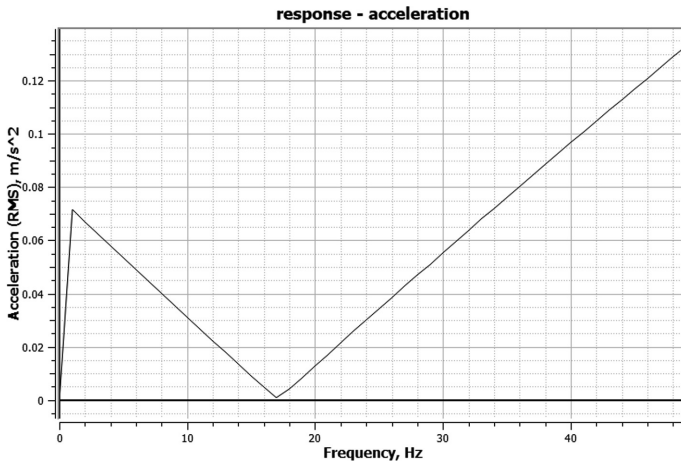


**Fig. 4.** Rotor response in the operational frequency range

### 5.2 Rotor Response to EMF

The response of the rotor was found for operational frequency range of 0–50 Hz (0–3000 RPM). From Fig. 4 and the modal analysis results, it can be concluded that the rotor is very much safe in the operation range. Equation (3) gives the equation for Sound Pressure Level (SPL) in decibels.

$$SPL = 20 \log_{10} \frac{P_1}{P_0} \tag{3}$$

where  $P_I$  is actually measured sound pressure level of a given sound, and  $P_0$  is a reference value of 20  $\mu\text{Pa}$ , which corresponds to the lowest hearing threshold of the young, healthy ear.

It was observed that in the operational frequency range of 0–50 Hz, the maximum sound pressure level (SPL) was 101.49 dBA at a rotational velocity of 3000 RPM or 50 Hz.

## 6 Conclusion

In this paper, an effort was made to find out the noise and vibration characteristics of a 1 kW 8-segment FSM rotor due to the EMF acting on the rotor. The rotor and stator design were optimized to reduce noise and vibration by avoiding magnetic saturation of the material, providing a low reluctance path for the magnetic flux lines and preventing magnetic flux leakage.

Modal analysis of the rotor revealed that its natural frequencies lie very far away and hence the rotor is safe in the operation range. The results were analytically verified. Response of the rotor due to the EMF was found out. A maximum Sound Pressure Level of 101.49 dBA was found out at the maximum operation speed (50 Hz) of the rotor. It is to be considered that this analysis was done for the bare rotor, which was not physically connected to the whole motor, through bearings, in which case, the effective mass of the system increases and the SPL comes down. SPL can also be further reduced by using acoustic padding inside the motor.

## References

1. Zulu, A.: Flux Switching Machines Using Segmental Rotors, pp. 87–88. Newcastle University, UK (2010)
2. Xin, G.E.: Simulation of Vibrations in Electrical Machines for Hybrid-Electric Vehicles, p. 7. Chalmers University of Technology, Sweden (2014)



# Quenching of Non-stationary Wave Due to Structural Transformation of Material

D. A. Indeitsev<sup>1,2,3(✉)</sup>, B. N. Semenov<sup>1,2</sup>, D. Yu. Skubov<sup>3</sup>,  
and D. S. Vavilov<sup>1,4</sup>

- <sup>1</sup> Institute for Problems in Mechanical Engineering, V.O. Bolshoj Pr. 61, 199178 St. Petersburg, Russia  
londr@yandex.ru
- <sup>2</sup> St. Petersburg State University, Universitetskaya Emb. 13B, 199034 St. Petersburg, Russia
- <sup>3</sup> St. Petersburg Polytechnic University, Polytechnicheskaya 29, 195251 St. Petersburg, Russia
- <sup>4</sup> Mozhaisky Military Space Academy, Jdanovskaya 13, 197198 St. Petersburg, Russia

**Abstract.** In the present paper a new model for describing structural transformation of solids under external impact is discussed. We suppose that the material consists of two crystalline lattices with close physical properties, connected by nonlinear interaction force. The relative displacement of the components is considered to be an additional degree of freedom responsible for transition of material to a new equilibrium position. Using experimental data on shock-wave loading and analogy between continuous model and its discrete representation allows to evaluate the unknown parameters and to reveal the mechanism of energy transfer from macro to micro level. Also it becomes possible to predict the parameters of external impact, necessary to start the process of transition to another state. The results of analytical investigation are confirmed by numerical solution of the original problem.

**Keywords:** Structural transformations · Non-stationary wave · Discrete model

## 1 Introduction

Mathematical modeling such phenomena as rearrangement of crystalline lattice under external impact always requires the introduction of additional equations, providing the connection between micro and macro level. These equations usually contain unknown parameters, which are difficult to estimate. In the present paper we consider the problem of structural transformations caused by shock-wave loading. Recent experiments on high-speed deformation of metals demonstrate in a certain range of impactor velocities propagation of the shock wave leads to nucleation of reticulate structures of  $0.1 - 0.3 \mu\text{m}$  in diameter that do not disappear after removal of the stress [1]. At the macro level, the process of structure formation is revealed through energy losses, which can be observed experimentally [2]. At the same time, the transition dynamics is

accompanied by the oscillations with a certain frequency on the time profile of the particle velocity on the free surface of the sample (see Fig. 1).

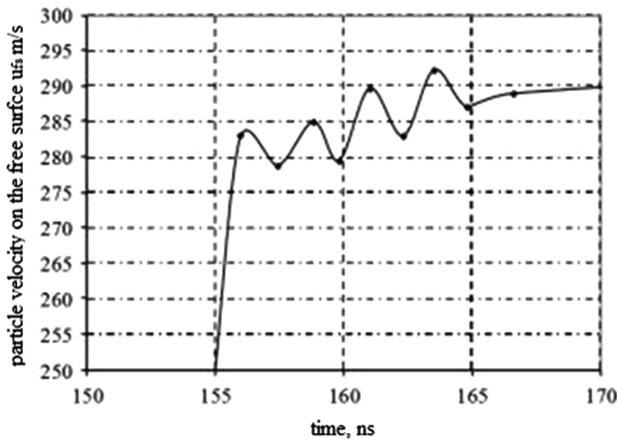


Fig. 1. Oscillations on the time profile.

To describe this process we introduce a one dimensional model of two-component material, consisting of two similar lattices [3, 4]. Supposing that each of them obeys the Hooke’s law, one can write the governing equations for the center of mass displacement  $U = \frac{\rho_1 u_1 + \rho_2 u_2}{\rho_1 + \rho_2}$  and for the relative displacement  $z = u_1 - u_2$  in the following form

$$\begin{aligned} \frac{\partial^2 U}{\partial x^2} - \frac{1}{c_u^2} \frac{\partial^2 U}{\partial t^2} &= \alpha \frac{\partial^2 z}{\partial x^2} \\ \frac{\partial^2 z}{\partial x^2} - \frac{1}{c_z^2} \frac{\partial^2 z}{\partial t^2} &= \beta R(z, \dot{z}) + \gamma \frac{\partial^2 U}{\partial t^2} \end{aligned} \tag{1}$$

Here the following notation is used:  $c_u^2 = \frac{E_1 + E_2}{\rho_1 + \rho_2}$ ,  $c_z^2 = \frac{E_1 E_2 (\rho_1 + \rho_2)}{(E_1 + E_2) \rho_1 \rho_2}$ , where  $E_k$  ( $k = 1, 2$ ) signifies Young modulus. Parameters  $\alpha$ ,  $\beta$  and  $\gamma$  are defined by the physical properties of material:  $\alpha = \frac{E_2 \rho_1 - E_1 \rho_2}{(E_1 + E_2)(\rho_1 + \rho_2)}$ ,  $\beta = \frac{E_1 + E_2}{E_1 E_2}$ ,  $\gamma = \frac{E_2 \rho_1 - E_1 \rho_2}{E_1 E_2}$ . The interaction force between the components is denoted as  $R$ . Taking into account the periodic structure of the lattice [5], its analytical expression is given by

$$R = K \sin \lambda z + \nu \dot{z}. \tag{2}$$

where  $K$  defines its maximum value and  $\nu$  characterizes dissipation. The parameter  $\lambda = \frac{2\pi}{d}$  is inversely proportional to the period of the lattice  $d$ . Supplementing Eq. (1) with appropriate boundary and initial conditions, we are able to formulate a nonlinear Cauchy problem, but any attempt of solving is useless without evaluating the parameters of the interaction force.



## 2 Continuous Model

After introducing dimensionless variables  $\tilde{x} = \frac{x\omega^*}{c_1}$ ,  $\tilde{t} = \omega^*t$ ,  $\tilde{U} = U\lambda$ ,  $\tilde{z} = z\lambda$ ,  $\tilde{\sigma} = \frac{c_1\lambda\sigma}{\omega^*(E_1 + E_2)}$ ,  $\tilde{v} = \frac{v\omega^*}{K\lambda}$ , where  $\omega^* = \sqrt{\left(1 + \frac{E_1}{E_2}\right)\frac{K\lambda}{\rho_1}}$  and  $\sigma = \sigma_1 + \sigma_2$ , Eq. (1) can be presented as

$$\begin{aligned} \frac{\partial^2 \tilde{U}}{\partial \tilde{x}^2} - \frac{1}{\tilde{c}_u^2} \frac{\partial^2 \tilde{U}}{\partial \tilde{t}^2} &= \alpha \frac{\partial^2 \tilde{z}}{\partial \tilde{x}^2} \\ \frac{\partial^2 \tilde{z}}{\partial \tilde{x}^2} - \frac{1}{\tilde{c}_z^2} \frac{\partial^2 \tilde{z}}{\partial \tilde{t}^2} &= \sin \tilde{z} + \tilde{v} \dot{\tilde{z}} + \delta \frac{\partial^2 \tilde{U}}{\partial \tilde{t}^2}, \end{aligned} \tag{3}$$

where  $\tilde{c}_u^2 = \frac{(1-\gamma\delta)}{1-\delta}$ ,  $\tilde{c}_u^2 = \frac{1}{1-\gamma\delta}$ ,  $\delta = 1 - \frac{c_1^2}{c_2^2}$ . Here  $c_k^2 = \frac{E_k}{\rho_k}$  ( $k = 1, 2$ ) signifies the velocities of sound and, the coefficient  $\chi = \frac{\rho_1}{\rho_1 + \rho_2}$  denotes the mass fraction of the first component. Furthermore, we assume that parameters  $c_1$  and  $c_2$  do not differ much. In this case two branches on the dispersion graph (see Fig. 2) corresponding to the center of mass displacement and relative motion are located sufficiently close to each other. It means that we can expect energy transfer from one branch to another due to existence of nonlinear forces. Also taking an approximate value for cutoff frequency  $\omega^*$  from experimental data (see Fig. 1), we are able to estimate the interaction force between the components.

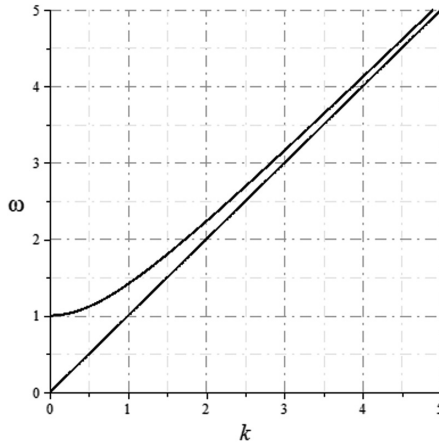


**Fig. 2.** Dispersion curves

### 3 Discrete Model

In spite of a rapid development of numeric methods one-dimensional discrete models still retain their significance. Structural element from the rheological model of two-component medium is represented by the nonlinear system of coupled oscillators with close natural frequencies  $\delta = \frac{\omega_2^2 - \omega_1^2}{\omega_1^2}$ . Denoting their displacements as  $x_1$  and  $x_2$  it is possible describe its dynamics analogously to continuous problem, taking for unknown functions the center of mass displacement  $x = \frac{1}{2}(x_1 + x_2)$  and the relative displacement  $z = x_1 - x_2$ . In dimensionless variables the governing equations are given by

$$\begin{aligned} \ddot{x} + x &= \frac{\delta z}{4} \\ \ddot{z} + n\dot{z} + z + \kappa \sin z &= \delta x \end{aligned} \tag{4}$$

At the same time the correspondence between continuous and discrete systems is established by the following relations

$$\kappa = \frac{4\pi Kd}{E}, \quad n = \frac{\omega^{*2}d^2\nu}{\pi c_1 K} \tag{5}$$

In linear system ( $\kappa = 0$ ) we obtain beat oscillations with the period  $T = \frac{4\pi}{\delta}$  depending on the difference between physical properties of the lattices. The appearance of nonlinear term changes its dynamics dramatically. The specific feature of the process for sufficiently large value of initial velocity for  $x$  is the time point separating two different regimes (see Fig. 3). Note that the amplitude of oscillations at the second one is reduced in comparison with initial value due to dynamics of the relative displacement.

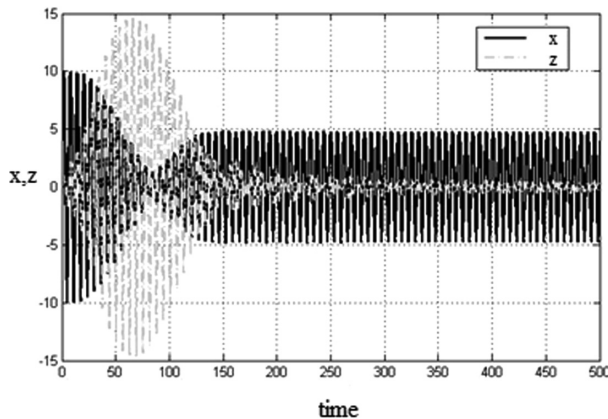


Fig. 3. Dynamics of discrete model

To realize the energy transfer it is important that its duration  $\tau_e = \frac{2\pi}{\delta}$  won't exceed the relaxation time  $\tau_r = \frac{1}{n}$  of the partial system. Otherwise, the oscillations of the relative displacement will be damped before the center of mass displacement has enough time to be excited. This implies that  $n \leq \frac{\delta}{2\pi}$ .

### 4 Conclusion

After the necessary estimates of parameters are provided, we return to the original continuous problem given by Eq. (3) considered in the half space  $0 < x < \infty$ . Initial conditions are assumed to be zero, as for the boundary conditions a rectangular pulse of  $\tau$  duration is applied at  $x = 0$

$$\sigma|_{x=0} = \sigma_0(H(t) - H(t - \tau)), \tag{6}$$

where  $H(t)$  is the Heaviside step function. Numeric solution of the problem is obtained basing on finite difference method. The strain distribution in the two-component rod is presented in Fig. 4.

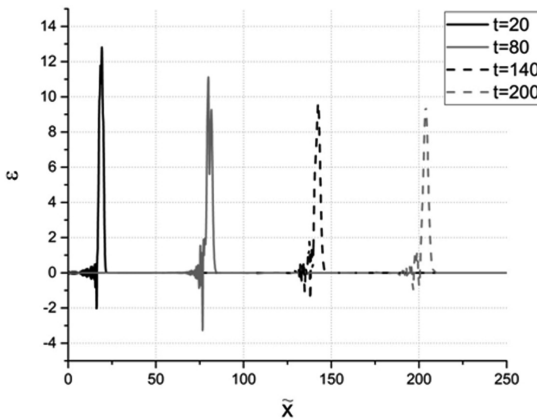


**Fig. 4.** Strain distribution in the two-component rod

The same effect of reduction of initial pulse caused by energy transfer as in the discrete model is observed. In conclusion it should be noted that the nonlinear problem turns to be rather sensitive to small changes in parameters and any attempt of discovering the required effect is useless without preliminary analysis.

The work was performed within the RSF Project No. 15-19-00182.

## References

1. Meshcheryakov, Y.I., Zhigacheva, N.I., Divakov, A.K., Makarevich, I.P., Barakhtin, B.K.: Turbulence and dissipative structures in shock-loaded copper. *Russ. J. Phys. Chem.* **1**(6), 623–629 (2007)
2. Meshcheryakov, Y.I., Savenkov, G.G.: Oscillations of the plastic wave front under high-rate loading. *J. Appl. Mech. Tech. Phys.* **42**(6), 1023–1028 (2001)
3. Indeitsev, D.A., Naumov, V.N., Semenov, B.N.S.: Dynamic effects in materials of complex structure. *Mech. Solids* **42**(5), 672–691 (2007)
4. Aero, E.L., Bulygin, A.N.: Strongly nonlinear theory of nanostructure formation owing to elastic and nonelastic strains in crystalline solids. *Mech. Solids* **42**(5), 807–822 (2010)
5. Braun, O.M., Kivshar, Y.: *The Frenkel-Kontorova Model: Concepts, Methods, and Applications*. Springer Science and Business Media (2013)



# Algorithms for System Identification

Todor Zhelyazov<sup>1(✉)</sup>, Rajesh Ruphakety<sup>2</sup>, and Simon Olafsson<sup>2</sup>

<sup>1</sup> Technical University of Sofia, 8, Kliment Ohridski Blvd, 1000 Sofia, Bulgaria  
elovar@yahoo.com

<sup>2</sup> Earthquake Engineering Research Center (EERC), University of Iceland,  
Austurvegur 2a, 800 Selfoss, Iceland  
{rajesh, simon}@hi.is

**Abstract.** Implementations of different algorithms designed for material constant identification are discussed in this contribution. Identification is performed by varying the input variables (i.e., the material constants) and juxtaposing the results obtained by analysis of the model and some benchmark example. In order to reduce the iterations needed to achieve a good agreement with desired results, different numerical strategies can be employed. One of the possibilities is to use a genetic algorithm. The combination of finite element analysis and identification algorithm is a strong tool but it is time consuming and very demanding in computational resources. A surrogate modeling can be employed to reduce computational time. Generally, it consists in replacing the original model with a simplified one. Two approaches are taken into consideration herein: the polynomial chaos expansion and the artificial neural network. The efficiency of the above-mentioned algorithms is to be assessed in terms of computational resource.

**Keywords:** FEM · Material constants identification · Artificial neural network

Implementations of different algorithms designed for material constants identification are discussed in this contribution.

Commonly, identification is performed by varying the input variables (i.e., the material constants) and juxtaposing the results obtained by analysis of the model and some benchmark example.

In order to reduce the iterations needed to achieve a good agreement with desired results, different numerical strategies can be employed. One of the possibilities is to use a genetic algorithm [1]. A typical iteration comprises three modules: analysis module, comparison module and modification module. The results (obtained for example by finite element analysis) in the analysis module are compared to the target set of data points in the comparison module. On the basis of the assessment of the ‘distances’ (in the considered space) between points obtained by numerical analysis and benchmark points, modifications of the input variables (referred to as ‘crossover’ and ‘mutations’) can be performed in order to obtain a better fit with target data in the subsequent iteration(s).

In this context, combination of finite element analysis and identification algorithm is a strong tool for accurate calibration of model constants. However, it is well known that this strategy is time consuming and very demanding in computational resources.

A surrogate modeling can be employed to reduce computational time. Generally, surrogate modeling consists in replacing the original model with a simplified one. Different approaches have been proposed in literature: polynomial chaos expansion (PCE), support vector machine, Kriging metamodel, artificial neural network (ANN) etc. [2–6].

The polynomial chaos expansion of a response variable for a random input vector  $\mathbf{X}$  and finite variance can be defined as follows [2]:

$$Y = \sum_{\alpha} \beta_{\alpha} \psi_{\alpha}(X) \quad (1)$$

In Eq. (1) indices  $\alpha_i$  are ordered lists of integers,  $\beta$  are deterministic coefficients,  $\psi$  represent multivariate orthonormal basis functions with respect to joint probability density function of the input variables.

Generally, the artificial neural network is a parallel signal processing system designed to solve a specified task. The ANN can be formalized by a sorted triple  $(N, V, \omega)$  [7].  $N$  is a given set of neurons,  $V$  is a set containing all defined connections between neurons  $i$  and  $j$  from  $N$ :

$$V \equiv \{(i, j) | i, j \in N\} \quad (2)$$

and  $\omega(i, j)$  is a function which defines the weight of a specified connection.

The weights of the connections as well as the structure of the neural network can be changed during solution.

The efficiency of the above-mentioned algorithms is to be assessed in terms of computational resources and time (i.e., number of iterations needed to obtain a satisfactory fit with the target set of data points).

## References

1. Goldberg, D.E.: Genetic Algorithms in Search, Optimization and Machine Learning. Addison-Wesley, Reading (1989)
2. Ghamen, R.G., Spanos, P.D.: Stochastic Finite Elements: Spectral Approach. Springer, Berlin (1991)
3. Hurtado, J.E.: An examination of methods for approximating implicit limit state functions from viewpoint of statistical learning theory. Struct. Saf. **26**(3), 271–293 (2004)
4. Kaymaz, I.: Application of Kriging method to structural reliability problems. Struct. Saf. **27**(2), 133–151 (2005)
5. Echard, B., Gayton, N., Lemaire, M.: AK-MCS: an active learning reliability method combining Kriging and Monte Carlo simulation. Struct. Saf. **33**(2), 145–154 (2011)
6. Lehký, D., Šomodíková, M.: Reliability calculation of time-consuming problems using a small-sample artificial neural network-based response surface method. Neural Comput. Appl. **28**, 1249–1263 (2017)
7. Kriesel, D.: A Brief Introduction to Neural Networks. [http://www.dkriesel.com/en/science/neural\\_networks](http://www.dkriesel.com/en/science/neural_networks)



# Mechanics of Earthquake Source Processes: Insights from Numerical Modeling

Nadia Lapusta<sup>(✉)</sup>

California Institute of Technology, Pasadena, CA 91125, USA  
lapusta@caltech.edu

**Abstract.** Many major faults separate two tectonic plates that slowly move past each other in opposite directions. The relative motion is accommodated by faults by both sudden dramatic rupture events perceived as earthquakes and much slower, quasi-static fault slips. We study the mechanics of these rupture processes using dynamic-fracture ideas and continuum-mechanics modeling that incorporates laboratory-derived fault friction laws [1–3], shear heating, and effects of pore fluids [4–6]. The modeling can reproduce all stages of the past behavior of some fault segments—including locked, slowly moving, and earthquake-producing—with remarkable qualitative, and often quantitative, agreement. In part, it reveals the potential physics behind the unexpected extreme events, such the 2011 Mw 9.0 Tohoku earthquake in Japan [6, 7] that caused up to 40-m tsunami and numerous casualties. The modeling has been used to study situations in which energy-related quantities estimated from seismic shaking based on traditional fracture mechanics theory are valid and when they are not [8]. Such continuum-mechanics-based models, when further developed, will enable us to incorporate our increasing understanding of earthquake source physics into the assessment of seismic hazards and seismicity response to perturbations of natural or anthropogenic origins.

**Keywords:** Numerical modeling · Dynamic fracture · Earthquake mechanics

## 1 Introduction: Fault Slip Modes and Interface Friction

Faults in the earth's crust accommodate slow relative motion between tectonic plates through a combination of slow slip and dynamic rupture events perceived as earthquakes. The slow and fast slip is often assumed to occur on fault segments with different friction properties. Rate-and-state friction paradigm has been developed ([1] and references therein), based on laboratory experiments at slow slip velocities, in which interface friction depends on the slip velocity (defined as the rate of the relative shear across the interface) and an evolving state variable. The rate-and-state fault models associate creeping regions with velocity-strengthening (VS) steady-state friction, suggesting that they act as barriers to earthquake ruptures since their strength increases with their slip velocity (also called slip rate). Indeed, earthquakes often arrest at the boundaries of creeping regions. The regions that host earthquakes are associated with velocity-weakening (VW) steady-state friction [1–3].

## 2 Possibility of Dynamic Rupture on Fault Segments Currently Considered Stable

However, experimental and theoretical studies reveal that several dynamic weakening mechanisms, such as flash heating thermal pressurization of pore fluids, can be activated at high seismic slip rates [4, 5]. As earthquake rupture penetrates into the VS fault areas, it significantly increases slip rates there, potentially activating the additional coseismic weakening and turning the stable fault areas into seismogenic ones.

We have explored such behavior in a numerical continuum-mechanics modeling with frictional and hydro-mechanical fault properties measured using rock samples obtained from the Chelungpu fault, the site of the 1999 Chi-Chi earthquake [6]. The modeling reproduces a number of both long-term and coseismic observations about faults that hosted the 2011 Tohoku and 1999 Chi-Chi earthquakes. Moreover, only models in which a shallow creeping region dynamically ruptures can reproduce the proposed 1000-year recurrence interval proposed for the Tohoku-like events [7]. In short, it is physically plausible for a creeping fault region to sustain dramatic seismic slip, and this may have occurred in the 2011 Tohoku-Oki and 1999 Chi-Chi earthquakes.

The possibility that seismic rupture can be sustained in a creep-prone, VS region due to coseismic weakening implies that earthquake ruptures can potentially penetrate below the locked seismogenic zone, into the deeper creeping fault extensions [8]. Our strike-slip fault models mimicking segments of the San Andreas Fault (SAF) show that the depth extent of the largest events is determined by the boundary where enhanced coseismic weakening stops being efficient. The depth extent of coseismic rupture influences the seismicity pattern throughout the post-seismic and inter-seismic period, due to changes in the stress distribution on the fault interfaces. When large events are confined in the traditionally defined seismogenic region, with velocity-weakening (VW) rate-and-state friction properties, streaks of microseismicity are seen at and above the VS/VW transition due to stress concentration between the locked and creeping regions being in the VW area. In the cases with deeper penetration due to the enhanced dynamic weakening, the microseismicity streaks disappear, as the stress concentrations are buried deeper, in the interseismically stable VS regions, and cannot nucleate dynamic events. These characteristic behaviors resemble the observed seismicity activity on the Parkfield and Carrizo segments on SAF, respectively.

The much larger occasional extent of earthquake ruptures in our numerical models than what would be inferred based on currently locked fault areas highlights the potential for extreme, unexpected earthquake events. To improve our understanding of earthquake hazard, we need to study the structure, properties, and past behavior of creeping regions to evaluate their propensity for coseismic weakening, and hence their ability to sustain large seismic slip.



### 3 Estimation of Energy-Related Quantities for Earthquake Rupture

Observational seismological studies of earthquakes seek to understand their source physics by determining averaged quantities from remote observations, such as static stress drop and radiation efficiency. These inferences rely on the use of idealized fracture mechanics models, whereas the actual spatial distribution of slip and local stress change may be different from such models throughout the ruptured area. The relationship between average rupture characteristics inferred observationally and their actual values is therefore not obvious. We have been exploring this relation using our modeling. Our preliminary results [9] indicate that the validity of the seismological estimates significantly depend on the rupture mode and may not be valid for the typical style of large earthquake ruptures observed. If these conclusions withstand the further numerical interrogation for a broader parameter range, then inferences about energy budget of large earthquake rupture would need to be reconsidered.

### References

1. Dieterich, J.H.: Applications of rate- and state-dependent friction to models of fault slip and earthquake occurrence. *Treatise Geophys.* **4**, 107–129 (2007)
2. Lapusta, N., Rice, J.R., Ben-Zion, Y., Zheng, G.: Elastodynamic analysis for slow tectonic loading with spontaneous rupture episodes on faults with rate- and state-dependent friction. *J. Geophys. Res.* **105**, 23765–23789 (2000)
3. Lapusta, N., Liu, Y.: Three-dimensional boundary integral modeling of spontaneous earthquake sequences and aseismic slip. *J. Geophys. Res.* **114**, B09303 (2009)
4. Rice, J.R.: Heating and weakening of faults during earthquake slip. *J. Geophys. Res. Solid Earth* **111**, B05311 (2006)
5. Rubino, V., Rosakis, A.J., Lapusta, N.: Understanding dynamic friction through spontaneously evolving laboratory earthquakes. *Nat. Commun.* (2017) <https://doi.org/10.1038/ncomms13020>
6. Noda, H., Lapusta, N.: Stable creeping fault segments can become destructive as a result of dynamic weakening. *Nature* (2013) <https://doi.org/10.1038/nature11703>
7. Cubas, N., Lapusta, N., Avouac, J.-P., Perfettini, H.: Numerical modeling of long-term earthquake sequences on the NE Japan megathrust: comparison with observations and implications for fault friction. *Earth Planet. Sci. Lett.* **419** (2015)
8. Jiang, J., Lapusta, N.: Deeper penetration of large earthquakes on seismically quiescent faults. *Science* **352** (2016)
9. Lambert, V., Perry, S., Lapusta, N.: Energy budget of earthquakes: connecting remote observations with local physical behavior. AGU Fall Meeting Abstract (2018)



# Strategies to Improve Convergence After Degeneration of the Initial Finite Element Mesh

Todor Zhelyazov<sup>(✉)</sup>

Technical University of Sofia, 8, Kliment Ohridski Blvd, 1000 Sofia, Bulgaria  
elovar@yahoo.com

**Abstract.** In some cases, the finite element solution does not converge because of severe distortions in the finite elements of the initially generated mesh. Numerical strategies aimed to overcome such issues are discussed in this contribution. The context is the numerical simulation of concrete/RC beams strengthened with composite material. The structural element is considered as a multiple-component system: constitutive relations and local failure criteria are defined for all components, i.e., for all materials: concrete, steel and composite material. A damage-based constitutive law is retained for concrete. As a result of this procedure application, zones of reduced or of zero or rigidity are formed in the medium which is initially defined as homogeneous and isotropic. A new initial state for the subsequent post-failure solution is defined on the basis of the state at the time preceding the loss of convergence. After homogenization, zones containing distorted finite elements are ‘healed’.

**Keywords:** FEM · Large displacement response · Post failure behavior

In some cases, the finite element solution does not converge because of severe distortions in the finite elements of the initially generated finite element mesh. This ‘premature’ (compared to the experimentally obtained results) numerical failure can result in underestimation of the mechanical performances of the modeled structure.

Numerical strategies aimed to overcome such issues are discussed in this contribution. They can potentially appear in the context of the numerical simulation of concrete/reinforced concrete beams strengthened with composite material.

Generally, the overall behavior of such structural elements is governed mainly by the behavior of concrete. The behavior of concrete is the most complex one compared to the responses of the other materials used in the structural element.

In this contribution, the structural element is considered as a multiple-component system: constitutive relations and local failure criteria are defined for all components, i.e., for all materials: concrete, steel and composite material(s).

A damage-based constitutive law is retained for concrete: a damage variable is integrated in the stress-strain relationship [1, 2].

According to the damage mechanics fundamentals, the damage variable quantifies the mechanical damage accumulated in the material. The evolution of the damage variable depends on a quantity ‘constructed’ from the positive values of the principal strains [3].

Two thresholds are associated with the damage variable: the lower threshold (i) and upper threshold (ii). When the lower threshold is reached by the above-defined quantity, damage starts to grow. If the upper threshold is reached by the damage variable a local failure occurs: it can be stated that a meso-crack is initiated/propagates where the upper damage threshold is reached.

As a result of the application of such procedure zones of zero rigidity are formed in the medium which is initially defined as homogeneous and isotropic. Moreover, zones of reduced rigidity (or zones of modified mechanical characteristics) are formed along with the damage accumulation throughout the loading history (see Fig. 1).

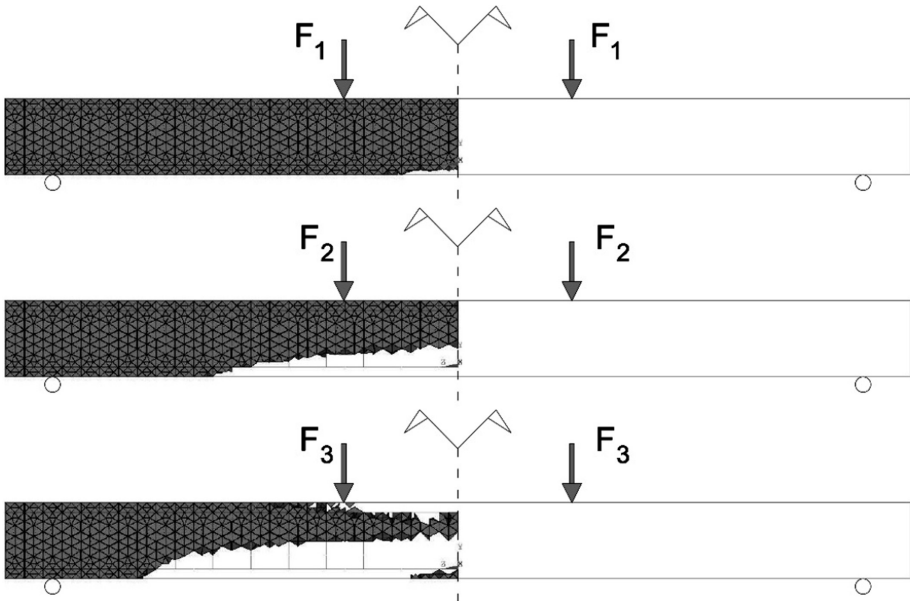


**Fig. 1.** Damage zone propagation for three consecutive values of the applied load  $F$ : finite elements in which damage variable exceeds a specified value are not displayed; taking into account the symmetries only a quarter-model space is considered in the finite element simulation of the four-point bending test.

All these factors eventually contribute to the accumulation of severe distortions in the remaining finite elements (the finite elements which are not deactivated via the numerical engine designed to model damage and crack propagation).


As it has been already stated, the distortion of some finite elements could result in the loss of convergence. Therefore, if a ‘premature’ numerical failure occurs, these finite elements should be ‘healed’ before continuing solution. This could involve the definition of a new initial state (for the subsequent post-failure solution) on the basis of the state preceding the loss of convergence. This approach also involves homogenization since damage accumulation and propagation leads to forming adjacent finite elements of different material properties. Results of homogenization should be carefully assessed in order to minimize possible loss of accuracy in the subsequent analysis.

## References

1. Marigo, J.J.: Formulation d'une loi d'endommagement d'un matériau élastique. CR Acad. Sci. Paris **292**(2), 1309–1312 (1981)
2. Lemaitre, J.: A Course on Damage Mechanics. Springer, Berlin (1996)
3. Mazars, J.: Application de la Mécanique de l'Endommagement au Comportement Non-linéaire et à la Rupture du Béton de Structure. PhD thesis, Paris 6 University, Paris, France (1984)



# Parametric Study of Simulated Randomly Rough Surfaces Used in Contact Mechanics

Rafael Schouwenaars<sup>1</sup> , Miguel Ángel Ramírez<sup>1</sup>,  
Carlos Gabriel Figueroa<sup>2</sup>, Víctor Hugo Jacobo<sup>1</sup>,  
and Armando Ortiz Prado<sup>1</sup>

<sup>1</sup> Departamento de Materiales y Manufactura, Facultad de Ingeniería,  
Edificio O, Universidad Nacional Autónoma de México,  
Avenida Universidad 3000, 04510 Coyoacán, Mexico City, Mexico  
raf\_schouwenaars@yahoo.com

<sup>2</sup> Departamento de Materiales y Manufactura, Facultad de Ingeniería,  
Universidad Nacional Autónoma de México, PIIT, Vía de la Innovación 410,  
Apodaca, Nuevo León, Mexico

**Abstract.** The study and numerical simulation of randomly rough surfaces is a fundamental topic in contact mechanics. Existing theory permits calculating the distributions of values such as height, slopes and gradients based on the power spectrum of the surface. Determination of derived quantities like summit height or radius distribution tends to become mathematically intractable. An alternative approximation is then to simulate the random surfaces to obtain these distributions empirically. Here, a direct Monte-Carlo approach is presented in which distributions of summit heights and curvatures are obtained directly from the theoretical formulae. Results are compared to distributions calculated from simulated surfaces, over a wide range simulation parameters. The latter approach induces significant statistical dispersion as compared to the former. The summit radius distribution is narrower for the simulated surfaces than predicted by theory.

**Keywords:** Random surface · Roughness · Fractal dimension · Monte Carlo simulation · Contact mechanics

## 1 Introduction

From the early development of surface profilers, it was recognised that roughness is a random process [1]. More recently, it has been found that roughness can often be described as a fractal stochastic process [2, 3]. In general, the difference between fractal and non-fractal descriptions resides in the power spectrum. The use of fractal descriptions has been criticised by several authors [4, 5], as surface roughness often has a non-random component (a pattern). Patterns would appear as discrete peaks in the power spectrum, contrary to the random part which produces a continuous spectrum. Only the latter part is studied if randomly rough surfaces are considered.

The first model for the contact of randomly rough surfaces was proposed by Greenwood and Williamson (GW) [6]. They considered a set of spherical asperities, with

a fixed radius and randomly distributed heights, each one in Hertzian contact with the mating surface. This model has been modified in later studies, to consider the distribution of asperity radius [7], elliptical asperities [8], plastic deformation [9–11], elastic interaction between neighbouring asperities [7, 12] and coalescence of asperities into larger contact patches [12]. Analyses which use the full surface topography but do not involve the definition of spherical asperities are the boundary element method [13–15] and finite element method [16–18]. A broader review was given recently in ref. [19].

Several methods for the generation of randomly rough surfaces exist [20]. In the spectral method, the surface is constructed by the sum of cosine waves with random phase angle and wave vectors, with amplitudes determined from the power spectrum. The theoretical background for this method was established long before computer simulation of random surfaces became a topic of interest [21, 22]. Statistical distribution of height, slopes, gradients and the number of local maxima can be found as simple mathematical expressions. Calculation of further properties, such as the height or radius distribution of asperities, become very cumbersome [23]. This work presents a new approach to obtain the joint statistical distribution of surface curvature and height from theory. The results, in terms of asperity radius, height and density, will be compared to simulations using the spectral method. In the latter, the cut-of radius and number of wave components will be treated as simulation parameters.

## 2 Theory and Simulation Methods

### 2.1 Fundamentals

The statistical analysis of randomly rough surfaces, defined by their power spectral density (PSD), is based on the calculation of the moments of the PSD [21]. The PSD for isotropic fractal surfaces is written as:

$$p_R(r) = \begin{cases} \frac{H(ab)^{2H}}{\pi(b^{2H}-a^{2H})} r^{-2(H+1)} & r \in [a, b] \\ 0 & r \notin [a, b] \end{cases} \quad (1)$$

where  $r$  is the length of the wave vector,  $a$  and  $b$  are the lower and upper cut-of radius and  $H$  the Hurst exponent, which relates to the fractal dimension  $D$  as  $H = 3 - D$ . The PSD has been normalised such that its integral over frequency space is equal to 1. The lower cut-of radius was set equal to 1. The  $n$ th (polar) moment of the PSD is:

$$M_n = \frac{2H}{n-2H} \frac{b^n a^{2H} - a^n b^{2H}}{(b^{2H} - a^{2H})} \quad (2)$$

With  $0 < H \leq 1$ , the limit for  $b \rightarrow \infty$  is finite only for  $n = 0$ , i.e. without an upper cut-off limit, the moments do not exist. The number of local maxima per unit area is given by:

$$n_{Asp} = \frac{1}{8\sqrt{3}} \frac{M_4}{M_2} = \frac{1}{8\sqrt{3}} \left( \frac{1-H}{2-H} \right) \frac{a^4 b^{2H} - a^{2H} b^4}{a^2 b^{2H} - a^{2H} b^2} \quad (3)$$

From the generalised central limit theorem, it follows that the joint probability distribution for surface heights and slopes follows a Gaussian distribution, written as:

$$p_V(\mathbf{v}) = (2\pi|\Sigma|)^{-3} \exp\left(-\frac{1}{2} \mathbf{v} \cdot \Sigma^{-1} \cdot \mathbf{v}\right) \quad (4)$$

where  $\mathbf{v}$  is the vector of random variables and  $\Sigma$  the correlation matrix. As heights and curvatures are of interest in this work,  $\mathbf{v}$  has the components  $z^{(0,0)}(x, y)$ ,  $z^{(2,0)}(x, y)$ ,  $z^{(1,1)}(x, y)$  and  $z^{(0,2)}(x, y)$ , with  $z$  the surface height as a function of  $x$  and  $y$  and the numbers between parentheses indicate the  $(n, m)$ th derivative with respect to  $x$  and  $y$  respectively. The correlation matrix is found as [24]:

$$\Sigma = \begin{pmatrix} M_0 & -\frac{M_2}{2} & 0 & -\frac{M_2}{2} \\ -\frac{M_2}{2} & \frac{3M_4}{8} & 0 & \frac{M_4}{8} \\ 0 & 0 & \frac{M_4}{8} & 0 \\ -\frac{M_2}{2} & \frac{M_4}{8} & 0 & \frac{3M_4}{8} \end{pmatrix} \quad (5)$$

$z^{(0,0)}(x, y)$ ,  $z^{(2,0)}(x, y)$  and  $z^{(0,2)}(x, y)$  are correlated variables while  $z^{(1,1)}(x, y)$  is independent.

## 2.2 Direct Monte-Carlo Simulation

A random vector of 3 uncorrelated Gaussian variables with given mean and variance is easily composed by calculating  $n$  random numbers independently. For the correlated variables ( $z^{(0,0)}$ ,  $z^{(2,0)}$ ,  $z^{(0,2)}$ ) one must diagonalize  $\Sigma$ , which corresponds to a rotation in random variable space. Three independent random numbers are then generated with mean 0 and variance  $\Sigma_i$ , with  $\Sigma_i$  the  $i$ th eigenvalue of  $\Sigma$ . The resulting vector is rotated back to the original reference system and an independently chosen value for  $z^{(1,1)}$  is added to complete the random vector. For each random vector thus created, the Gaussian curvature is found as follows:

$$K = \frac{z^{(2,0)}z^{(0,2)} - z^{(1,1)2}}{(1 + z^{(1,0)2} + z^{(0,1)2})^2} \quad (6)$$

The term in the denominator is equal to 1 at a stationary point, hence  $K = \det(H)$ , with  $H$  the Hessian matrix of the surface at a given point. For the point to be a maximum, the additional conditions that  $K > 0$  and  $z^{(2,0)} + z^{(0,2)} < 0$ . The determinant of  $H$  is equal to the product of the mean curvatures; the geometric mean radius of curvature  $\rho = \det(H)^{-1/2}$ .

The simulation is performed by creating  $10^5$  random vectors for the height and the second derivatives. As the first derivatives are independent from the former values, the

numerator in Eq. (6) will be independent of the first derivatives ( $K$  is not). Hence, to determine the distribution of  $\rho$ , the first derivatives need not be simulated.

### 2.3 Surface Monte-Carlo Simulation

Random surfaces were simulated by means of the spectral method [13, 15], with a cut-off radius  $b$  and  $c$  components in the sum. Surfaces were produced on a unit square with step size  $2^{-m}$ , resulting in  $(2^{-m} + 1) \times (2^{-m} + 1)$  grid points. In the examples,  $m = 9$ . The value of  $b$  was varied from  $2^6$  to  $2^{10}$ , with steps of 1/2 in the exponent.  $c$  was varied in the same way. The entire simulation was performed twice, producing 162 random surfaces. Direct Monte Carlo simulation was performed for the same values of  $b$ , using  $10^5$  random vectors for each simulation.  $H$  was set equal to 0.5 in all simulations.

An asperity is defined as a point which is higher than its 8 neighbours. A second-order polynomial (Taylor expansion) is fitted through the asperity and its 8 neighbours:

$$z(x, y) = z(0, 0) + \frac{\partial z}{\partial x} \Delta x + \frac{\partial z}{\partial y} \Delta y + \frac{1}{2} \frac{\partial^2 z}{\partial x^2} \Delta x^2 + \frac{\partial^2 z}{\partial x \partial y} \Delta x \Delta y + \frac{1}{2} \frac{\partial^2 z}{\partial y^2} \Delta y^2 \quad (7)$$

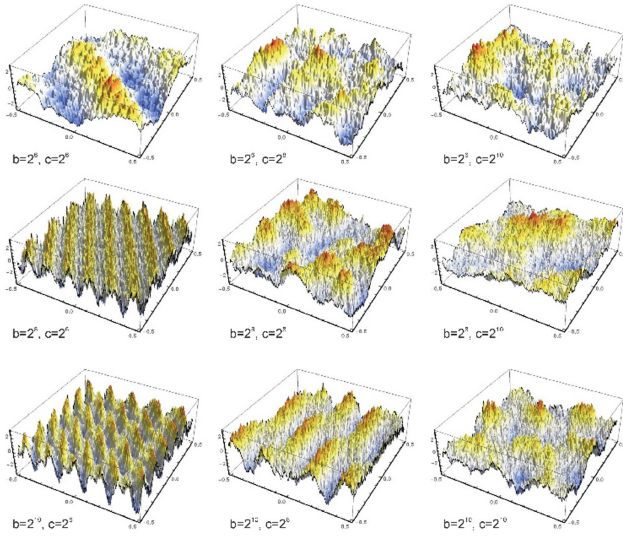
The partial derivatives are determined by the fitting procedure. The geometric mean radius is  $\rho = \det(H)^{-1/2}$ . To verify the quality of the produced surfaces, the fractal dimension was calculated by the triangular prism method, according to Ref. [24].

## 3 Results

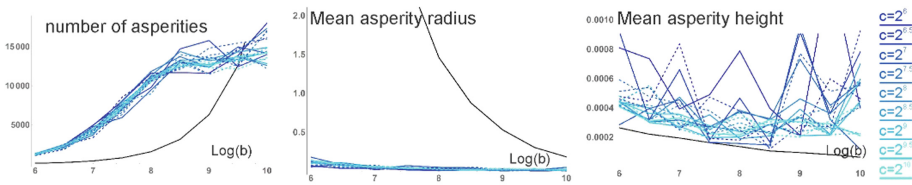
Figure 1 presents the plots of the surfaces for different combinations of  $b$  and  $c$ . A response surface analysis was executed for the full set of 162 surfaces, analysing the behaviour of the Hurst exponent and the coefficient of determination ( $R^2$ ) of the regression used in determining  $H$ . An optimal combination of both can be found at  $b = 2^8$  and  $c = 2^{10}$ . A low value of  $c$  creates the risk that the roughness is dominated by a few long wavelengths. Low values of  $b$  produce surfaces which are not fractal at the lowest wavelengths, while a value of  $b$  which is too high only induces random noise.

Figure 2 compares the results of direct Monte Carlo simulation to surface simulation. The number of asperities in the surface simulations is not related to what is predicted by the theoretical formulas. The average curvature is underestimated, and the average height of asperities is too low. The effect of  $c$  in the simulations is smaller than the statistical spread on the individual data. A final set of simulations was performed to verify whether coincidence can be obtained between the surface simulations and the direct Monte Carlo approach. The spectral method with  $m = 11$ ,  $b = 2^9$  and  $c = 2^{10}$ ,  $m = 9$ ,  $b = 2^8$  and  $c = 2^{10}$  was compared to results of the midpoint algorithm [21] for  $m = 11$  and  $m = 9$  and direct Monte Carlo for  $b$  in the range of  $2^{11}$ – $2^{14}$ . The asperity height distribution for direct Monte Carlo is independent from  $b$ , but the asperity radius distribution shifts to the right upon decreasing  $b$  (Fig. 3). Surface simulations miss the smallest radii and drops to zero much more rapidly at higher radii, explaining the much lower average radius observed in Fig. 2b.





**Fig. 1.** Examples of simulated surfaces for different values of  $b$  and  $c$ .



**Fig. 2.** Comparison of surface simulation to direct Monte Carlo simulation (black curve).

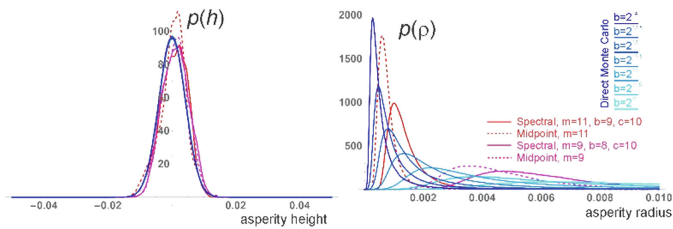


**Fig. 3.** Probability distributions for asperity height and radius, for different simulations.

## 4 Conclusions

A new method to simulate the statistics of asperity heights and radii, based on the mathematical theory of randomly rough surfaces was presented and compared to surface simulations by means of the spectral method. No clear relationship was found between the asperity density in direct and surface simulations. The mean asperity radius

is seriously underestimated in the latter technique and the radius distribution misses both the small radii and the heavy tail. As surface measurements involve some of the same problems as surface simulations (finite measurement area, finite resolution, finite precision), they cannot be used to decide which approach is better. Hence, precise measurement and simulation of physical properties such as contact stiffness and thermal or electrical conductivity will be needed to decide on the optimal method for surface simulation.

**Acknowledgements.** This work was sponsored by DGAPA grant IN114718. Technical support by G. Álvarez, I. Cueva and E. Ramos is acknowledged.

## References

1. Whitehouse, D.J., Archard, J.F.: The properties of random surfaces of significance in their contact. *Proc. Roy. Soc. A.* **316**, 97–121 (1970)
2. Majumdar, A., Bhushan, B.: Role of fractal geometry in roughness characterization and contact mechanics of surfaces. *J. Tribol.* **112**, 205–216 (1990)
3. Majumdar, A., Bhushan, B.: Fractal model of elastic-plastic contact between rough surfaces. *J. Tribol.* **113**, 1–11 (1991)
4. Whitehouse, D.J.: Fractal or fiction. *Wear* **249**, 345–353 (2001)
5. Borodich, F.M., Pepelyshev, A., Savencu, O.: Statistical approaches to description of rough engineering surfaces at nano and microscales. *Tribol. Intern.* **103**, 197–207 (2016)
6. Greenwood, J.A., Williamson, J.B.P.: Contact of nominally flat surfaces. *Proc. Roy. Soc. A.* **295**, 300–319 (1966)
7. Ciavarella, M., Delfino, V., Demelio, G.A.: “Re-vitalized” Greenwood and Williamson model of elastic contact between fractal surfaces. *J. Mech. Phys. Sol.* **54**, 2569–2591 (2006)
8. Greenwood, J.A.: A simplified elliptic model of rough surface contact. *Wear* **261**, 191–200 (2006)
9. Yang, J., Komvopoulos, K.: A mechanics approach to static friction of elastic–plastic fractal surfaces. *J. Tribol.* **127**, 315–324 (2005)
10. Yan, W., Komvopoulos, K.: Contact analysis of elastic-plastic fractal surfaces. *J. Appl. Phys.* **84**, 3617–3624 (1998)
11. Kogut, L., Etsion, I.: Elastic-plastic contact analysis of a sphere and a rigid flat. *J. Appl. Mech.* **69**, 657–662 (2002)
12. Afferrante, L., Carbone, G., Demelio, G.: Interacting and coalescing Hertzian asperities: a new multiasperity contact model. *Wear* **278**, 28–33 (2012)
13. Pohrt, R., Popov, V.L.: Normal contact stiffness of elastic solids with fractal rough surfaces. *Phys. Rev. Lett.* **108**(10), 104301 (2012)
14. Pohrt, R., Qiang, L.: Complete boundary element formulation for normal and tangential contact problems. *Физическая мезомеханика* **17**(3) (2014)
15. Putignano, C., Afferrante, L., Carbone, G., Demelio, G.: A new efficient numerical method for contact mechanics of rough surfaces. *Int. J. Solids Struct.* **49**(2), 338–343 (2012)
16. Hyun, S., Pei, L., Molinari, J.F., Robbins, M.O.: Finite-element analysis of contact between elastic self-affine surfaces. *Phys. Rev. E* **70**(2), 026117 (2004)
17. Pei, L., Hyun, S., Molinari, J.F., Robbins, M.O.: Finite element modeling of elasto-plastic contact between rough surfaces. *J. Mech. Phys. Solids* **53**(11), 2385–2409 (2005)
18. Yastrebov, V.A., Ancaix, G., Molinari, J.F.: From infinitesimal to full contact between rough surfaces: evolution of the contact area. *Int. J. Solids Struct.* **52**, 83–102 (2015)

19. Müser, M.H., Dapp, W.B., Bugnicourt, R., Sainsot, P., Lesaffre, N., et al.: Meeting the contact-mechanics challenge. *Tribol. Lett.* **65**(4), 118 (2017)
20. Saupe, D.: Algorithms for random fractals. In: Peitgen, H.O., Saupe, D. (eds.) *The Science of Fractal Images*, pp. 71–136 [Barnsley, M.F., Devaney, L., Mandelbrot, B.B., Peitgen, H. O., Saupe, D., Voss, R.F. (eds.)]. Springer, New York (1988)
21. Longuet-Higgins, M.S.: The statistical analysis of a random, moving surface. *Philos. Trans. Roy. Soc. A* **249**, 321–387 (1957)
22. Longuet-Higgins, M.S.: Statistical properties of an isotropic random surface. *Philos. Trans. Roy. Soc. A* **250**, 157–174 (1957)
23. Nayak, P.R.: Random process model of rough surfaces. *J. Lubr. Technol.* **93**, 398–407 (1971)
24. Schouwenaars, R., Jacobo, V.H., Ortiz, A.: The effect of vertical scaling on the estimation of the fractal dimension of randomly rough surfaces. *Appl. Surf. Sci.* **425**, 838–846 (2017)



# Simplified Analysis of the Early Stage Self-loosening of a Shear-Loaded Bolted Joint

Vincent Rafik<sup>1,2(✉)</sup>, Alain Daidié<sup>1</sup>, Bertrand Combes<sup>1</sup>,  
and Clément Chirol<sup>2</sup>

<sup>1</sup> Université de Toulouse, Institut Clément Ader, UMR CNRS 5312,  
INSA/UPS/ISAE/Mines Albi, 3 rue Caroline Aigle, 31400 Toulouse, France  
vincent.rafik@airbus.com

<sup>2</sup> AIRBUS France, Materials & Processes, Assembly Technology, Rue Marius  
Tercé, 31200 Toulouse, France

**Abstract.** The self-loosening of a joint through unscrewing of the bolt is a phenomenon mainly occurring when the assembly is solicited by transverse repeated loads. Previous works highlighted that the transversal sliding of the bearing surfaces, either in the threads or underneath the bearing surfaces of bolts and/or nuts, is its root cause and that this phenomena begins during the first loading cycles. In order to study the early stage of this self-loosening, a simplified numerical model has been developed. The latter factors the bearing surfaces of the bolt, the preload, the friction coefficient, the amplitude of the shear-load and the fastener's material. Through measurements and interpretation of the results, the shearing of the fastener has been identified as the main deformation leading to the self-loosening of the assembly, while the bending of the fastener shank limits the self-loosening. Moreover, according to the values of preload and shear-load, the behaviors were identified and an interpretation has been proposed.

**Keywords:** Self-loosening · Bolted joints · Shear-load · Finite elements analysis

## 1 Introduction

### 1.1 The Self-loosening in the Literature

A few scientists such as Reid [1], Hattori [2] or Dinger [3] highlighted that in some specific conditions, the self-loosening of the fasteners clamping the pieces of a structure together can be noticed. This phenomena might be due to an excessive cycled shear-loading of the parts. In order to focus on this phenomena, several papers are studying the self-loosening of a single bolted joint to get rid of the additional phenomena implied by the bolting sequence in a multi bolted assembly [4–7].

Junker [4] is the first to have studied this phenomena. Thanks to a specific test bench, he considered the sliding of the bearing surfaces of the fasteners and the bolt's bending as its root cause. Dinger [3] and Zhou [5] studied the influence of the bolt coating on the self-loosening of the joint. They noticed that the lower was the friction coefficient, the most severe was its self-loosening as it can be seen on Fig. 1.

Whichever the coating Zhou considered, the loss of normal strength could be observed. Indeed, the higher was the friction coefficient, the latter and the slower was the phenomena.

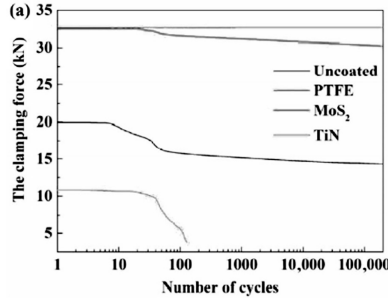


Fig. 1. Loosening curve for different fastener coatings [5]

Zadoks interested himself in the behavior of the sliding surfaces [6]. He factored the transverse sliding and the plate and bolt deformation in order to propose an explanation to the self-loosening. He described the phenomena thanks to ratios between the relative circumferential and transverse velocities, either in the threads or under the head. According to Jiang [7], the loosening curves can be split into two parts, Fig. 2. Moreover, he stated that the early loosening “Stage I”, is driving the phenomena as the first movement or deformation, breaking the bolt’s steadiness, were the most important one.

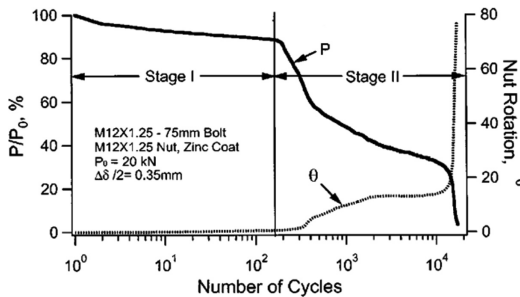


Fig. 2. The self-loosening sequence, [7]

### 1.2 Purpose of the Study

Understanding which process implies the early self-loosening might help us to avoid the loss of preload due to the rotation of the fastener. To do so, a simplified numerical models of the contact between the fastener’s bearing surfaces and the clamped part will

be developed. Once this model has been validated thanks to specific tests, an analysis will be done in order to identify the process and more specifically the deformation, either shearing or bending, leading to the self-loosening of the assembly. Finally, an analytical approach will aim at proposing a definition of the loosening load, the effort implying the loss of preload.

## 2 The Numerical Analysis

### 2.1 Presentation of the Model

We will study an assembly of three plates (Fig. 3a) tightened together by a bolt, solicited transversally by a sinusoidal shaped load. Our model, developed on Abaqus (Fig. 3b), only represents the head of the fastener, a part of its shank and its bearing plates. The bolt (diameter 9.52 mm, in red), is in titanium whereas the plate (with bore clearance of 30  $\mu\text{m}$ , in light grey) is in aluminum. The simulation is composed of 3 steps. The first one is an axial loading  $F_0$  to apply a preload on section  $S_b$ . A maximum preload of 28,000 N, chosen according to Airbus standards, corresponds to 60% of the yield strength for the Ti4Al6V. The second one is an axial torque  $C_0$  applied to the section  $S_b$ , to consider the reaction of the nut's threads on the bolt's threads due to the preload. The last one is the shear-loading of the assembly by a sinusoidal shear-load  $F_t(t)$  at a frequency of 5 Hz, applied to the cylinder  $C_t$ .

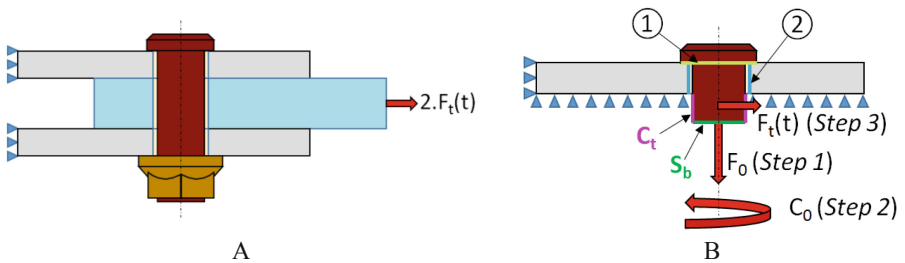


**Fig. 3.** Definition of the complete assembly (a) and the model (b)

Two contacts with Coulomb friction are modeled (Fig. 3b):

- **Contact ①:** Between the aluminum coated bolt's head and the primer coated bearing surface of the plate,  $f = 0.06$ .
- **Contact ②:** Between the aluminum coated bolt's rod and the uncoated hole of the plate,  $f = 0.08$ .

The variation of three parameters will be tested. Their values are presented Table 1. The influence of the preload and shear-load will aim at identifying the process leading to the self-loosening whereas the Young modulus of the bolt will highlight which deformation implies the phenomena.

**Table 1.** Definition of the parameters

Parameters	Shear-load (N)	Preload (N)	Young modulus (GPa)
Number of values	50	5	10
Range of values	30–25,000	500–25,000	60–250

## 2.2 The Results

### Influence of the Shear-Load

In a first step, the influence of the amplitude of the shear-load has been investigated. For each preload value, the loosening speed (i.e. the mean rotation of the bolt for one loading cycle, measured in steady state after a stabilization time) has been plotted

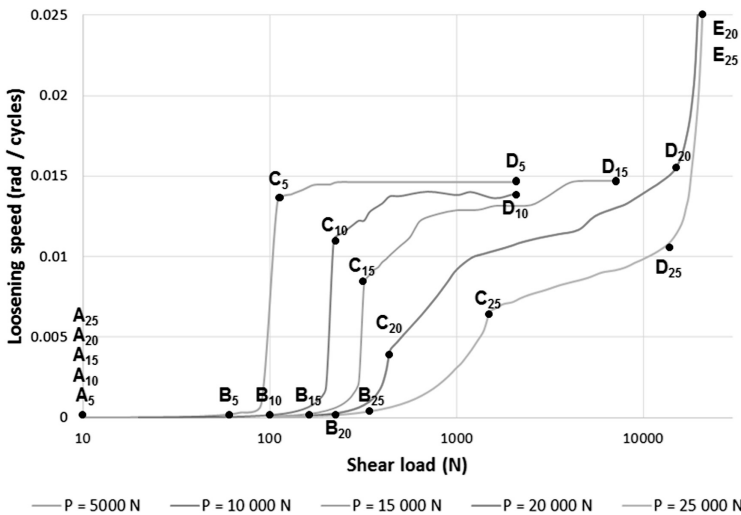


**Fig. 4.** Comparison of loosening speed versus shear-load, for different preloads.

versus the amplitude of the shear-load, Fig. 4.

The curves can be split into several parts from A to E:

- **Part AB:** The head of the fastener sticks to its bearing surface. Therefore, the bolt cannot rotate.
- **Part BC:** Beyond a certain shear-load, the head starts to slip on the plate. The loosening of the fastener can be noticed. Up to a preload of 15,000 N, this part is vertical, which correspond to the Coulomb theory. The corresponding loading will be qualified as “loosening load”. As soon as the solicitation reaches it, the distance of the head’s slipping will be the clearance as the bending is negligible. For higher preload, the shear-load necessary for the head to slip will imply the fastener bending. Then, the slipping distance will be lower as well as the loosening speed.

- **Part CD:** For low preload, once the fastener slides, its shank will contact the plate hole. The sliding will be stopped and the loosening speed will be the same whatever the shear-load in the part CD. For higher preload, the fastener will bend more, the slipping distance and the loosening speed will be lower. But when the shear-load increases, the contact between the shank and its hole gets closer to the head. So the slipping distance and the loosening speed increases with the shear-load.
- **Part DE:** The shear-load is sufficiently high to cause the plastic deformation of the hole, causing its ovalization, then the possible sliding distance becomes larger and the loosening angle caused by the head slipping is higher.

### Influence of the Preload

Then, the influence of the normal stress has been investigated. In order to do so, the preload and the torque applied during the first and second simulation steps has been changed a simulation from another. For each of them, the evolution of the loosening load, defined by points B on Fig. 4, has been plotted on Fig. 5.

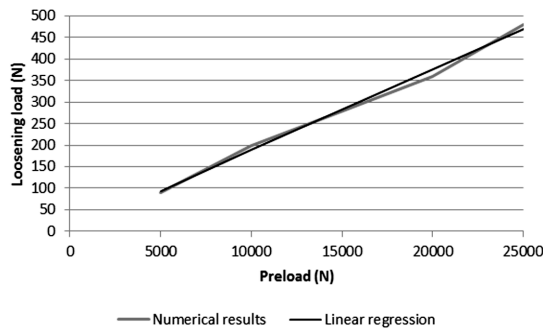


**Fig. 5.** Loosening load versus the preload.

The loosening load is proportional to the preload, which matches the Coulomb theory. This result shows that for this level of shear-load and for any preload considered, the plate's deformation is negligible as the fastener will slide on the plate for a specific load which could be calculated thanks to an analytical model with simple hypothesis.

### Influence of the Young Modulus

Bending and shearing of the shank are caused by the shear-loading of the fastener. In order to define which one implies the loss of preload, the influence of the fastener material has been investigated. The loosening speed for preload of 28,000 N and shear-load of 10,000 N for different Young modulus of the bolt has been plotted Fig. 6.



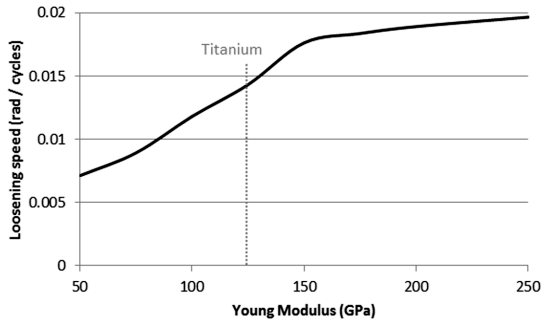


**Fig. 6.** Influence of the Young modulus on the loosening speed.

We observe that the higher the fastener's Young modulus is, the lower its bending deformation is, and the more severe its self-loosening. So we can conclude that the bending of the bolt prevents the self-loosening. This can be attributed to the contact of the bolt shank and its hole, that happens earlier when the shank bends, and which decreases the amplitude of the sliding of the head on the plate as seen before.

### 3 Conclusion

The self-loosening is a phenomenon characterized by a loss of preload within the joint coming from unscrewing. Its root cause is the sliding of the bolt's bearing surface caused by an excessive shear-load. It has been proven that the early stage of the phenomena is driving the subsequent rotation. In order to study the behavior of the bolt during the first cycles, a simplified numerical model including only a part of the bolt and a plate has been developed. Thanks to it, the influences of the preload, the amplitude of shear-load and the fastener material have been investigated.

The results highlighted that whichever the preload and beyond a certain shear-load, the bolt will self-loosen, matching the Coulomb theory. However, for high value of preload, this simple theory is not sufficient as the bending of the bolt shank induces a contact of the shank on its hole, which reduces the sliding of the bolt head and the unscrewing. Finally, the shearing of the bolt has been identified as the main solicitation implying the self-loosening. Indeed, the higher is the bolt's bending rigidity, the more severe is its self-loosening.


### References

1. Reid, J.D.: Detailed modeling of bolted joints with slippage. *Finite Elem. Anal. Des.* **41**, 547–562 (2005)
2. Hattori, T.: Loosening and sliding behaviour of bolt-nut fastener under transverse loading. In: 14th International Conference on Experimental Mechanics. EPJ Web of Conferences, 08002, p. 1–8 (2010)

3. Dinger, G.: Design of multi-bolted joints to prevent self-loosening failure. *J. Mech. Eng. Sci.* **230**(15), 2564–2578 (2016)
4. Junker, G.H.: New criteria for self-loosening of fasteners under vibration. *Soc. Automot. Eng.* **78**, 314–335 (1969)
5. Zhou, J.: Anti-loosening performance of coatings on fasteners subjected to dynamic shear load. *Friction* **6**, 32–46 (2018)
6. Zadoks, R.I.: An investigation of the self-loosening behavior of bolts under transverse vibration. *J. Sound Vib.* **208**(2), 189–209 (1997)
7. Jiang, Y.: A study of early stage self-loosening of bolted joints. *J. Mech. Des.* **125**, 518–526 (2003)



# Wave Scattering by Arrays of Shear Bands

Davide Bigoni<sup>1</sup>, Domenico Capuani<sup>2</sup>(✉) , and Diana Giarola<sup>1</sup>

<sup>1</sup> DICAM, University of Trento, Via Mesiano 77, 38123 Trento, Italy

<sup>2</sup> DA, University of Ferrara, Via Quartieri 8, 44121 Ferrara, Italy  
domenico.capuani@unife.it

**Abstract.** A plane-strain model of multiple shear bands, arranged in different configurations, is presented in order to investigate the effects of their dynamic interaction. Reference is made to a material stressed to the verge of instability and subject to incoming harmonic waves of small amplitude. It is shown that shear band arrays may be subject to resonance and corresponding shear band growth or, conversely, to shear band annihilation. At the same time, multiple scattering may bring about focusing or, conversely, shielding from waves.

**Keywords:** Shear band · Wave propagation · Pre-stress

## 1 Introduction

Interaction of shear bands has been documented so far for quasi-static deformation processes [1], where it has been shown that different shear band patterns emerge as related to load conditions and material properties of the samples, and where parallel, aligned, and converging shear bands [2] are frequently observed. In dynamics, results are restricted to high strain-rate loading, where numerical simulations [3] have been presented. In this context, experiments on metallic glass [4] show the development of a complex texture of multiple shear bands, with complex interactions.

Direct experimental investigation on the fine development of shear bands in a material and their effect on the stress field during time-harmonic vibrations remains difficult to be carried out, so that mechanical modelling represents the worthwhile way to shed light on a complex phenomenon, whose comprehension is a key point for engineering materials with enhanced mechanical properties.

In this paper, shear bands of finite length are idealized as discontinuity surfaces, formed inside the infinite medium at a certain stage of a continuous deformation. Each shear band is seen as a weak surface whose faces can freely slide, but are constrained to remain in contact.

## 2 Constitutive Equations

The incremental behaviour of an infinite, incompressible, nonlinear elastic material, homogeneously deformed under plane strain condition, is considered. According to Biot [5], the constitutive relations between the nominal stress increment  $i_{ij}$  and the

gradient of incremental displacement  $v_{i,j}$  (a comma denotes partial differentiation) can be expressed in the principal reference system of Cauchy stress (here denoted by axes  $x_1$  and  $x_2$ ) as follows

$$\dot{i}_{ij} = \mathbf{K}_{ijkl}v_{l,k} + \dot{p}\delta_{ij} \quad (1)$$

where repeated indices are summed and range between 1 and 2,  $\delta_{ij}$  is the Kronecker delta,  $\dot{p}$  is the incremental hydrostatic stress and  $\mathbf{K}_{ijkl}$  are the instantaneous moduli. These moduli possess the major symmetry  $\mathbf{K}_{ijkl} = \mathbf{K}_{klij}$  and are functions of principal components of Cauchy stress,  $\sigma_1$  and  $\sigma_2$ , describing the pre-stress, and of two incremental moduli  $\mu$  and  $\mu_*$  (which can depend arbitrarily on the current stress and strain) corresponding to shearing parallel to, and at  $45^\circ$  to, the principal stress axes. The non-null components are:

$$\begin{aligned} \mathbf{K}_{1111} &= \mu_* - \frac{\sigma}{2} - p, & \mathbf{K}_{1122} &= \mathbf{K}_{2211} - \mu_*, & \mathbf{K}_{2222} &= \mu_* + \frac{\sigma}{2} - p \\ \mathbf{K}_{1212} &= \mu + \frac{\sigma}{2}, & \mathbf{K}_{1221} &= \mathbf{K}_{2112} = \mu - p, & \mathbf{K}_{2121} &= \mu - \frac{\sigma}{2} \end{aligned} \quad (2)$$

with

$$\sigma = \sigma_1 - \sigma_2, \quad p = (\sigma_1 + \sigma_2)/2. \quad (3)$$

Equation (1) is complemented by the incompressibility constraint for incremental displacement  $v_i$

$$v_{i,i} = 0. \quad (4)$$

Constitutive Eqs. (1)–(4) describe a broad class of material behaviors, including all possible elastic incompressible materials which are isotropic in an initial state, but also materials which are orthotropic with respect to the principal stress directions.

### 3 The Boundary Value Problem

In Fig. 1 possible different arrays of shear bands, each one of total length  $2l$ , are represented together with local reference systems  $(\hat{x}_1, \hat{x}_2)$  centered on each shear band, with  $\hat{x}_1$ -axis aligned parallel to the shear band, and rotated at an angle  $\theta$  with respect to the principal reference system  $(x_1, x_2)$  introduced for constitutive Eq. (1).

According to the model described in [6], by introducing the jump operator for a generic function  $f$ , smooth on two regions labeled “+” and “–”, and discontinuous across the surface  $S_n$  of the  $n$ th shear band, as

$$\llbracket f \rrbracket = f^+ - f^- \quad (5)$$

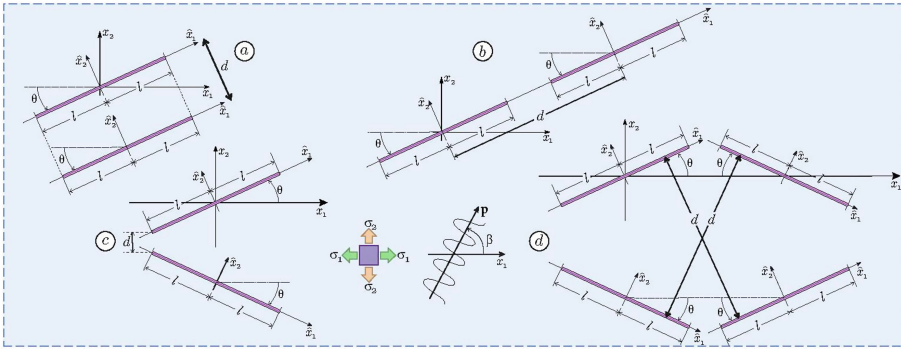


**Fig. 1.** Arrays of shear bands: **a** parallel; **b** aligned; **c** converging; **d** with 4 shear bands.

where  $f^\pm$  denote the limits approached by function  $f$  at the faces of the discontinuity surface, the boundary conditions at shear band surface  $S_n$  can be written as

$$[[\hat{v}_2]] = 0, \quad [[\hat{t}_{22}]] = 0, \quad \hat{t}_{21} = 0 \tag{6}$$

with  $\hat{v}_i$ ,  $\hat{t}_{ij}$  being incremental displacement and incremental stress components in the local reference system.

Time-harmonic incident shear waves of circular frequency  $\Omega$  characterized by incremental displacement field  $\mathbf{v}^{inc}(\mathbf{x})$ , with amplitude  $A$  and phase velocity  $c$ , propagation direction  $\mathbf{p}$  and direction of motion  $\mathbf{d}$ , are considered

$$\mathbf{v}^{inc} = A d e^{i\frac{\Omega}{c}(\mathbf{x}\cdot\mathbf{p}-ct)} \tag{7}$$

so that the total incremental displacement field  $\mathbf{v}(\mathbf{x})$  is given by the sum of the incident and of the scattered field  $\mathbf{v}^{sc}(\mathbf{x})$ .

The dynamic response of the medium in terms of total incremental displacement field can be found by adopting integral representations for the wave-fields as is shown in [7], using the infinite body Green function [8]. The system of boundary integral equations in the unknown scalar functions  $[[\hat{v}_1]]$  at each  $S_n$ , i.e. the jumps of tangential incremental displacement across the faces of each shear band, has been given in [7].

## 4 Numerical Examples

Using a collocation method, the boundary integral equation system in [7] can be transformed into a linear algebraic system where the unknown nodal values of displacement jumps across shear band faces can be determined in terms of known nodal values of incident tangential tractions on shear bands. To this purpose, each shear band is subdivided into  $Q$  line elements ( $Q = 100$ ), and a quadratic variation of the incremental displacement jump is assumed within each line element, with the exception of two line elements situated at the shear band tips, where a square root variation is adopted to take into account the singularity at the shear band tip.

A ductile low-hardening metal, modelled through the  $J_2$ -deformation theory of plasticity [9–11], with the hardening exponent  $N = 0.4$  (representative of a medium carbon steel) is considered. A level of prestress close to the elliptic boundary, with  $k = \sigma/2\mu = 0.87$  and  $\zeta = \mu/\mu_* = 0.26$ , corresponding to shear band inclination  $\theta \cong \pm 26^\circ$ , is assumed so that some shear bands are expected to be already formed.

The material response to shear waves with angle of incidence  $\beta$  (see Fig. 1) and wavenumber  $\Omega l/c_1 = 1$  ( $c_1$  is the propagation velocity in the direction of  $x_1$ -axis), is shown in terms of modulus of the incremental deviatoric strain field for arrays of shear bands which are parallel (Fig. 2), aligned (Fig. 3), converging (Fig. 4) or formed by

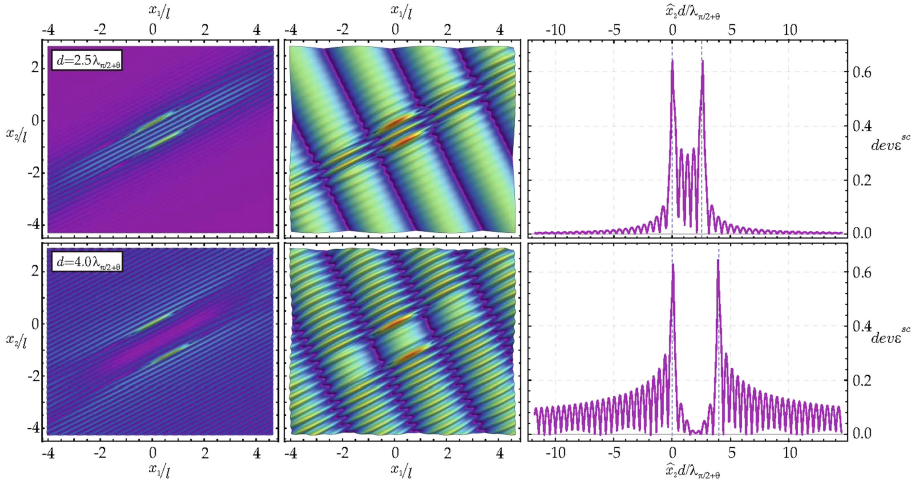


Fig. 2. Parallel shear bands with parallel incident wave ( $\beta = \theta$ ).

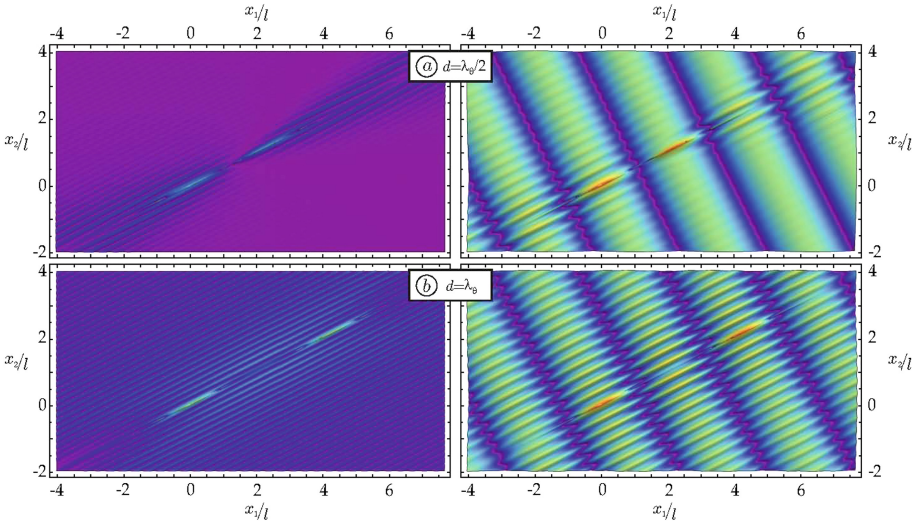
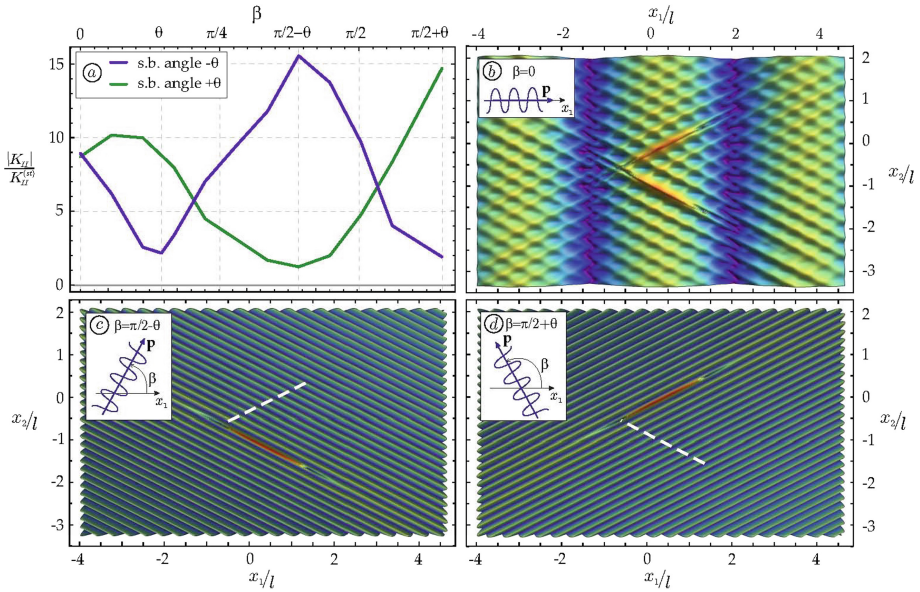
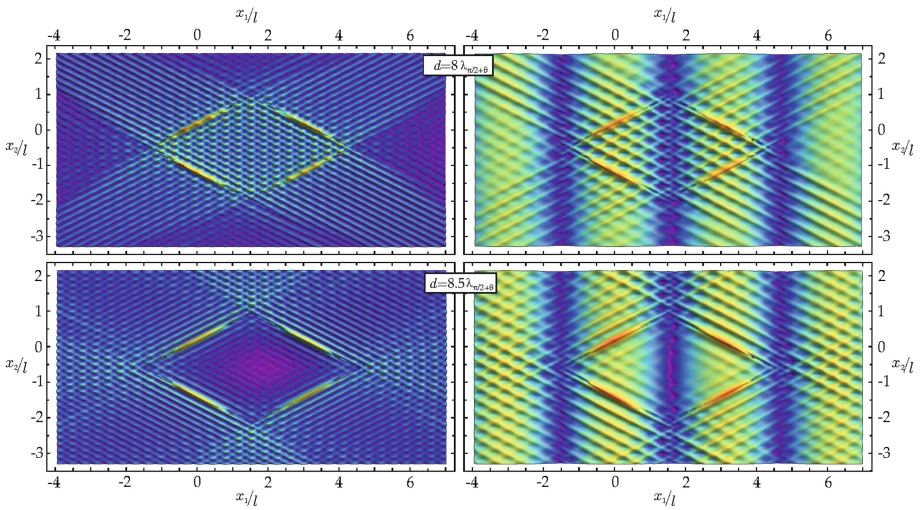


Fig. 3. Aligned shear bands with parallel incident wave ( $\beta = \theta$ ).



**Fig. 4.** Converging shear bands with different angles of wave incidence (distance  $d = l/10$ ).



**Fig. 5.** Four shear bands with horizontal incident wave ( $\beta = 0$ ).

four shear bands (Fig. 5). In all figures, maps show the scattered wave-field on the left hand side and the total wave-field on the right hand side, with the exception of Fig. 4 where only the total wave-field is reported.

In Fig. 2, graphs on the right side are cross-sections of the scattered deviatoric strain along  $\hat{x}_2$ -axis, at the shear band centre. The two cases differ only in the distance  $d$  between the shear bands, with  $d = 2.5\lambda_{\pi/2+\theta}$  or  $d = 4\lambda_{\pi/2+\theta}$ , where  $\lambda_\alpha$  is the wavelength in the propagation direction singled out by angle  $\alpha$ . Analogously, in Fig. 3 where  $\alpha = \theta$ .

In Fig. 4a, the dimensionless stress intensity factor is reported as a function of the angle  $\beta$  of wave incidence. It can be seen that when the wave travels orthogonal to one shear band, the relevant shear band tip is unloaded. This effect, which corresponds to annihilation of a shear band, is visible in parts (c) and (d) of the same figure, where one shear band (dashed white line) “disappears”, while the other one is “highlighted”.

In Fig. 5, focusing of signal is noted in the area circumscribed by shear bands at a distance  $d = 8\lambda_{\pi/2+\theta}$ , whereas shielding is evidenced at a distance  $d = 8.5\lambda_{\pi/2+\theta}$  producing an “island of stress relief”.

**Acknowledgements.** Financial support from the ERC advanced grant ERC-2013-ADG-340561-INSTABILITIES and from the University of Ferrara (FAR) is gratefully acknowledged.

## References

1. He, J., et al.: Local microstructure evolution at shear bands in metallic glasses with nanoscale phase separation. *Sci. Rep.* **6**, 25832 (2016)
2. Qu, R.T., Liu, Z.Q., Wang, G., Zhang, Z.F.: Progressive shear band propagation in metallic glasses under compression. *Acta Mater.* **91**, 19–33 (2015)
3. Bonnet-Lebouvier, A.S., Molinari, A., Lipinski, P.: Analysis of the dynamic propagation of adiabatic shear bands. *Int. J. Solids Struct.* **39**, 4249–4269 (2002)
4. Ruan, H.H., Zhang, L.C., Lu, J.: A new constitutive model for shear banding instability in metallic glass. *Int. J. Solids Struct.* **48**, 3112–3127 (2011)
5. Biot, M.A.: *Mechanics of Incremental Deformations*. Wiley, New York (1965)
6. Giarola, D., Capuani, D., Bigoni, D.: The dynamics of a shear band. *J. Mech. Phys. Solids* **112**, 472–490 (2018). <https://doi.org/10.1016/j.jmps.2017.12.004>
7. Giarola, D., Capuani, D., Bigoni, D.: Dynamic interaction of multiple shear bands. *Sci. Rep.* **8**(16033), 1–7 (2018). <https://doi.org/10.1038/s41598-018-34322-w>
8. Bigoni, D., Capuani, D.: Time-harmonic Green’s function and boundary integral formulation for incremental nonlinear elasticity: dynamics of wave patterns and shear bands. *J. Mech. Phys. Solids* **53**, 1163–1187 (2005). <https://doi.org/10.1016/j.jmps.2004.11.007>
9. Argani, L.P., Bigoni, D., Capuani, D., Movchan, N.V.: Cones of localized shear strain in incompressible elasticity with prestress: Green’s function and integral representations. *Proc. R. Soc. A* **470**, 20140423 (2014). <https://doi.org/10.1098/rspa.2014.0423>
10. Argani, L.P., Misseroni, D., Piccolroaz, A., Vinco, Z., Capuani, D., Bigoni, D.: Plastically-driven variation of elastic stiffness in green bodies during powder compaction: part I. Experiments and elastoplastic coupling. *J. Eur. Ceram. Soc.* **36**, 2159–2167 (2016). <https://doi.org/10.1016/j.jeurceramsoc.2016.02.012>
11. Argani, L.P., Misseroni, D., Piccolroaz, A., Capuani, D., Bigoni, D.: Plastically-driven variation of elastic stiffness in green bodies during powder compaction. Part II: micromechanical modelling. *J. Eur. Ceram. Soc.* **36**, 2169–2174 (2016). <https://doi.org/10.1016/j.jeurceramsoc.2016.02.013>





# Dynamic Failure of Granular Slopes: Due to Unidirectional Stress Transfer or Multi-dimensional Wave Propagation?

Koji Uenishi<sup>1,2</sup>(✉) and Tsukasa Goji<sup>2</sup>

<sup>1</sup> Department of Advanced Energy, University of Tokyo,  
Kashiwa 277-8561, Japan

uenishi@k.u-tokyo.ac.jp

<sup>2</sup> Department of Aeronautics and Astronautics, University of Tokyo,  
Tokyo 113-8656, Japan

**Abstract.** In order to numerically study fracture development in solids, models composed of discrete elements are often assumed instead of those based on continuum mechanics. Although realistic results have been obtained through the investigation of discontinua, the real fracture process in discrete media, in particular that under dynamic loading conditions, has not been experimentally scrutinized thoroughly. Here, we employ experimental technique of dynamic photoelasticity in conjunction with high speed cinematography and trace evolution of fracture inside discontinuous media. Especially, we consider dynamics of two-dimensional dry granular slopes consisting of penny-shaped birefringent elastic particles and having some inclination angle. The observations of transient stress and fracture development owing to dynamic impact on the top slope surface indicate that at least two specific failure patterns exist and whichever occurs seems to be governed by force-chain-like unidirectional stress transfer and continua-like multi-dimensional wave propagation.

**Keywords:** Dynamic slope failure · Fracture dynamics · Waves and fracture · Force chain · Granular media

## 1 Unexpected Earthquake-Induced Slope Failure

Although the strong influence of tsunamis was highlighted, the seismic waves generated by the 2011 off the Pacific coast of Tohoku, aka Great East Japan, earthquake did directly affect the natural and man-made structures severely, particularly in the northeastern part of Japan. One unexpected and puzzling phenomenon found on that occasion is the dynamically induced tensile cracks in fill slopes in Sendai that extended rather straight and parallel to the upper edge in the top slope surface [1]. To be peculiar, the cracks were located some meters away from the edge, and basically no other damage to the slopes appeared. Very similar open cracks were produced exactly in the same slopes by the 1978 Miyagi-ken-oki earthquake [2]. It is noteworthy that the slopes were reinforced with steel pipe piles after the 1978 quake using the conventional countermeasures that normally take into account the body wave effect. Not well-known, but this kind of seismic failure was reported at other sites including California,

the United States, in 1906, 1957 and 1989, as well as the South Island, New Zealand, in 2011. Efforts have been made to reproduce the observed failure pattern through the mechanical analyses of body wave interaction with continuum model slopes, but the exact mechanisms behind have not been fully identified. Even in time-dependent simulations of discontinuous granular slopes, the effect of wave propagation on dynamic fracture is usually neglected and only granular mass flow, i.e. almost simultaneous and total collapse of a slope is illustrated. Hence the single damage, or tensile cracks in the top surface, cannot be numerically produced.

## 2 Experimental Observations of Impact-Generated Wave Propagation and Particle Motion in Granular Slopes

Lately, from a time-harmonic analysis of continua [2] and a dynamic particle simulations [1], we have theoretically suggested more significant roles played by Rayleigh surface waves than body waves in producing tensile cracks in slopes. Also experimentally, utilizing the technique of dynamic photoelasticity, we have examined the propagation of Rayleigh waves in vertical and inclined model slopes made of continuous polycarbonate [3]. In this contribution, experimentally but in place of continua, we study wave propagation and fracture evolution in a two-dimensional dry granular slope composed of penny-shaped photoelastic particles [4]. We trace the particle motion and stress development inside every particle due to dynamic impact on the top free surface of the slope that is imparted, e.g. by an airsoft gun-launched projectile. The photographs taken by a high speed digital video camera show the presence of at least two failure patterns in the granular slope that are controlled by the mode of energy transmission. One is mass flow or total collapse of the slope related to unidirectional stress transfer that is similar to force chains found in quasi-static models. The other is toppling failure-like separation of the slope face only, which is induced by propagation of multi-dimensional waves caused and widely radiated owing to impact.

**Acknowledgements.** This study has been financially supported by the Japan Society for the Promotion of Science (JSPS) through the “KAKENHI: Grant-in-Aid for Scientific Research (C)” Program (No. 16K06487).

## References

1. Uenishi, K., Sakurai, S.: Dynamic tensile cracking in slopes possibly induced by Rayleigh surface waves. *Geomech. Geoeng.* **10**, 212–222 (2015)
2. Uenishi, K.: On a possible role of Rayleigh surface waves in dynamic slope failures. *Int. J. Geomech.* **10**, 153–160 (2010)
3. Uenishi, K., Takahashi, T.: Rayleigh waves and dynamic tensile cracking in slopes. In: *Proceedings of the 17th U.S. National Congress of Theoretical and Applied Mechanics*, S-04-341, Michigan State University, East Lansing (2014)
4. Uenishi, K., Goji, T.: Dynamic fracture and wave propagation in a granular medium: a photoelastic study. *Procedia Struct. Integrity* **13**, 769–774 (2018)

## **Part IV**

**Symposium on: “Dynamic Response  
of Elastic and Viscoelastic Solids  
Elastostatic and Elastodynamic  
Problems for Thermosensitive and  
Nonhomogeneous Solids Dynamic  
Problems in Mechanics of Coupled  
Fields,” by Roman Kushnir**



# Heat-Active Circular Interphase Inclusion in the Conditions of Smooth Contact with Half-Spaces

Oleksandr Kryvyi<sup>1</sup>  and Yurii Morozov<sup>2</sup> 

<sup>1</sup> National University “Odessa Maritime Academy”, Odessa, Ukraine  
kryvyi-od@math.onma.edu.ua

<sup>2</sup> Institute of Mechanical Engineering, Odessa National Polytechnic University,  
Odessa, Ukraine

**Abstract.** The method of Singular Integral Relations (SIR) for solving problems of stationary thermoelasticity for a piecewise homogeneous transversely isotropic space is generalized. Using the SIR method, the stationary thermoelasticity problem for interphase circular inclusion that is in smooth contact with piecewise homogeneous transversely isotropic space is reduced directly to a system of two-dimensional singular integral equations (SIE) with nuclei, which are expressed through elementary functions. An exact solution has been built for the said SIS; as a result, dependences of the translational displacement of the inclusion on temperature, the resulting load, the main momentum and the thermomechanical characteristics of transversely isotropic materials have been obtained. The order of the features of stresses and displacements jump is determined. Expressions for the stress intensity factor at the boundary of the inclusion are obtained, as well as numerical dependences of these coefficients on the polar angle, temperature and loads.

**Keywords:** Thermoelasticity problem · Interphase circular inclusion · Singular integral equations · Piecewise-homogeneous transversely isotropic space

## 1 Formulation of the Problem

Let the heat active absolutely rigid interphase inclusion occupying a circular area  $\Omega = \left\{ \sqrt{x_1^2 + x_2^2} \leq a \right\}$ , in the plane  $x_3 = 0$  of the connection of two different transversely isotropic half-spaces, is in smooth contact with the specified half-spaces. The inclusion of an arbitrary applied load, which leads to the resultant force  $\mathbf{P} = (P_1, P_2, P_3)$  and the main moment  $\mathbf{M} = (M_1, M_2, M_3)$ . The location of the face of inclusion after deformation describe the function

$$\begin{aligned} \zeta_6^\pm &= \zeta_6^0 + \vartheta_0^\pm(x_1, x_2), & \zeta_k^\pm &= \zeta_k^0, & k &= 4, 5, (x_1, x_2) \in \Omega \\ \zeta_4^0 &= \delta_1 - \varphi_3 x_3, & \zeta_5^0 &= \delta_2 + \varphi_3 x_1, & \zeta_6^0 &= \delta_3 + \varphi_2 x_2 + \varphi_1 x_2, \end{aligned} \quad (1)$$

$$\{\zeta_k^\pm\}_{k=1}^8 = \{\sigma_3(x_1, x_2, \pm 0), \sigma_4(x_1, x_2, \pm 0), \sigma_5(x_1, x_2, \pm 0), u_1(x_1, x_2, \pm 0), \\ u_2(x_1, x_2, \pm 0), u_3(x_1, x_2, \pm 0), T(x_1, x_2, \pm 0), Q(x_1, x_2, \pm 0)\},$$

$$\sigma = \{\sigma_k\}_{k=1}^6 = \{\sigma_x, \sigma_y, \sigma_z, \tau_{yz}, \tau_{xz}, \tau_{xy}\}, \quad \mathbf{u} = \{u_k\}_{k=1}^3 = \{u, v, w\},$$

$\vartheta_0^\pm(x_1, x_2)$  setting the form of inclusion, respectively, when  $x_3 = \pm 0$ ;  $\delta_k, \varphi_k, k = 1, 2, 3$ —translational movements and turning angles around the corresponding axes;  $T(x_1, x_2, x_3)$ —temperature;  $Q(x_1, x_2, x_3)$ —heat flow.

On the inclusion of specified heat flux, and the inclusion faces are in smooth contact with the half-spaces. In this case the boundary conditions in a plane  $x_3 = 0$  we shall write so

$$\chi_4^\pm(x_1, x_2) = (1 \pm 1)\zeta_4^0, \quad \chi_5^\pm(x_1, x_2) = (1 \pm 1)\zeta_5^0$$

$$\chi_6^\pm(x_1, x_2) = \vartheta^\pm(x_1, x_2) + (1 \pm 1)\zeta_6^0, \quad \vartheta^\pm = \vartheta_0^+ \pm \vartheta_0^-, \quad (x_1, x_2) \in \Omega$$

$$\zeta_8^\pm(x_1, x_2, \pm 0) = q(x_1, x_2), \quad (x_1, x_2) \in \Omega;$$

$$\chi_k^-(x_1, x_2) = 0, \quad k = \overline{1, 7}, \quad (x_1, x_2) \notin \Omega, \quad \lambda_3^+ \partial_2 \zeta_7(x_1, x_2, +0) = \lambda_3^- \partial_2 \zeta_7(x_1, x_2, -0), \tag{2}$$

$$\chi_k^\pm = \langle \zeta_k(x_1, x_2) \rangle^\pm = \zeta_k^+(x_1, x_2) \pm \zeta_k^-(x_1, x_2), \quad k = \overline{1, 8}, \quad (x_1, x_2) \in \Omega$$

For definiteness, we assume that the heat flux given in the region  $\Omega$  varies linearly

$$q(x_1, x_2) = q_0 \sum_{i,j=0}^1 b_{ij} x_1^i x_2^j$$

Given the conditions (2) and using the method of the SIR [2–6], relatively unknown jumps of the normal stresses, the tangential displacements and temperature  $\chi_k^-(x, y)$  ( $k = 1, 4, 5, 7$ ), we obtain the following system of two-dimensional SIE.

$$\frac{1}{2\pi} \iint_{\Omega} \left\{ q_{21} \chi_1^- \partial_2 \frac{1}{r_0} + q_{23} \chi_4^- \partial_{12}^2 \frac{1}{r_0} + \chi_5^- \left[ q_{23} \partial_2^2 \frac{1}{r_0} - \tilde{q}_{12} \partial_1^2 \frac{1}{r_0} \right] \right\} d\xi_1 d\xi_2 = g_1(x_1, x_2)$$

$$\frac{1}{2\pi} \iint_{\Omega} \left\{ q_{21} \chi_1^- \partial_1 \frac{1}{r_0} + \chi_4^- \left[ q_{23} \partial_1^2 \frac{1}{r_0} - \tilde{q}_{12} \partial_2^2 \frac{1}{r_0} \right] + q_{23} \chi_5^- \partial_{12}^2 \frac{1}{r_0} \right\} d\xi_1 d\xi_2 = g_2(x_1, x_2) \tag{3}$$

$$\frac{1}{2\pi} \iint_{\Omega} \left\{ q_{41} \chi_1^- \frac{1}{r_0} + q_{43} \left[ \chi_4^- \partial_1 \frac{1}{r_0} + \chi_5^- \partial_2 \frac{1}{r_0} \right] \right\} d\xi_1 d\xi_2 = g_3(x_1, x_2),$$

$$\begin{aligned}
& -\frac{q_{65}}{2\pi} \iint_{\Omega} \chi_7^- \frac{1}{r_0^3} dt d\tau = \chi_8^+ \\
g_j &= -q_{24} \partial_{3-j} \chi_6^- - q_{25} \iint_{\Omega} \chi_7^- \partial_{3-j} \frac{1}{r_0} d\xi_1 d\xi_2, \quad j = 1, 2, \\
g_3 &= \chi_6^+ - q_{44} \chi_6^- - q_{45} \iint_{\Omega} \chi_7^- \frac{1}{r_0} d\xi_1 d\xi_2
\end{aligned}$$

To determine the unknowns  $\delta_3$ ,  $\varphi_1$ ,  $\varphi_2$  need to use the following conditions of force and moment equilibrium.

$$\iint_{\Omega} \chi_1(x_1, x_2) dx_1 dx_2 = P_3, \quad \iint_{\Omega} \begin{pmatrix} x_1 \\ x_2 \end{pmatrix} \chi_1(x_1, x_2) dx_1 dx_2 = \begin{pmatrix} M_1 \\ M_2 \end{pmatrix} \quad (4)$$

## 2 The Solution of the SIE

Following the work [1–8] after the introduction of combinations of jumps and sums  $\tau^\pm = \chi_3^\pm + i\chi_2^\pm$ ,  $u^\pm = \chi_4^\pm + i\chi_5^\pm$ , and the transition to the polar coordinates, we look for the solution of the problem in the form

$$v_j^\pm(\rho, \varphi) = \sum_{n=-\infty}^{\infty} V_n^{j,\pm}(\rho) e^{in\varphi}, \quad V_n^{j,-}(\rho) = \frac{1}{2\pi} \int_{-\pi}^{\pi} v_j^-(\rho, \varphi) e^{-in\varphi} d\varphi, \quad j = 1, 3, 5, \quad (5)$$

where

$$\begin{aligned}
v_1^\pm(r, \varphi) &= v_1^\pm(\rho \cos \varphi, \rho \sin \varphi), \quad v_3^\pm(r, \varphi) = e^{-i\varphi} u^\pm(\rho \cos \varphi, \rho \sin \varphi), \\
\{v_k^\pm\}^8 &= \{\langle \sigma_z \rangle^\pm, \langle \tau_{z\varphi} \rangle^\pm, \langle \tau_{z\rho} \rangle^\pm, \langle u_\rho \rangle^\pm, \langle v_\varphi \rangle^\pm, \langle w \rangle^\pm, \langle T \rangle^\pm, \langle q \rangle^\pm\} \\
u^\pm(\rho \cos \varphi, \rho \sin \varphi) &= e^{i\varphi} u^\pm(\rho, \varphi), \quad u^\pm = v_4^\pm + iv_5^\pm
\end{aligned}$$

Relatively  $V_n^{j,\pm}(\rho)$ , a system of integral equations with Weber-Sonin cores was obtained, the decision of the latter [1, 4–6] allowed us to obtain explicit expressions for the jumps of the normal stresses and tangential displacements:

$$\begin{aligned}
v_1^-(\rho, \varphi) &= \frac{2}{\pi} \frac{\rho}{\sqrt{a^2 - \rho^2}} \left\{ \frac{2}{b_{21}^* |\mathbf{B}|} \delta_3 + h_0 + \frac{\tilde{s}_{21} b_{11}^* a^{-3}}{2\beta_1} \operatorname{Re}(f_n^T e^{-i\varphi}) + \beta_2 \operatorname{Re}(\phi_{12} e^{i\varphi}) \right\} \\
&\quad - s_{11} \mathbf{W}_{0,0}^* [F_0^-(\rho)] - \tilde{s}_{11} V_0^{5,-} - \tilde{s}_{11} \operatorname{Re}(V_1^{5,-} e^{i\varphi}),
\end{aligned} \quad (6)$$

$$v_3^-(\rho, \varphi) = -\frac{2s_{21}}{\pi\rho} \{a^{-1}f_*\sqrt{a^2 - \rho^2} - L[F_0^-(\rho)]\} - \tilde{s}_{21}\{(\sqrt{a^2 - \rho^2} - a)a^{-1}f_0^T + \tilde{s}_{21}\frac{2b_{00}}{3\rho}(a^3 - (a^2 - \rho^2)^{3/2})\} + V_{-1}^{3,-}(\rho)e^{-i\varphi} + V_1^{3,-}(\rho)e^{i\varphi} \quad (7)$$

$$V_{-1}^{3,-} = \frac{1}{\pi} \left\{ \frac{\tilde{\beta}_1}{2\beta_1} \frac{\tilde{s}_{21}}{a^3} \tilde{f}_1^T + \frac{b_{22}^*(2\beta_1 - \tilde{\beta}_1)}{\beta_1} \phi_{12} \right\} \sqrt{a^2 - \rho^2} + \frac{4}{3} \tilde{s}_{21} (b_{10} + b_{01}i) \int_0^\rho r^2 \sqrt{a^2 - r^2} dr$$

$$V_1^{3,-}(\rho) = \rho^{-2} \tilde{s}_{21} \left\{ \frac{2f_1^T}{\pi a^3} \int_0^\rho \frac{r^3 dr}{\sqrt{a^2 - r^2}} - \frac{4}{3} (b_{10} - b_{01}i) \int_0^\rho r^3 \sqrt{a^2 - r^2} dr \right\}$$

$$\beta_1 = \left[ \frac{b_{21}^* \tilde{q}_{23}^- + 2}{2\tilde{q}_{23}^-} \right], \quad \beta_2 = \frac{b_{12}^* \beta_1 - b_{22}^* b_{11}^*}{2\beta_1}, \quad h_0 = \frac{b_{11}^*}{b_{21}^*} a^{-1} (s_{21} f_* + \tilde{s}_{21} f_0^T),$$

$$f_* = \int_0^a \frac{t F_0^-(t) dt}{\sqrt{a^2 - t^2}}, \quad f_n^T = \pi \int_0^a V_n^{5,-}(\rho) \rho^{n+1} d\rho, \quad V_0^{5,-}(\rho) = 2b_{00} \sqrt{a^2 - \rho^2},$$

$$V_{\pm 1}^{5,-} = \frac{4}{3} (b_{10} \mp b_{01}i) \rho \sqrt{a^2 - \rho^2}, \quad s_{j1} = b_{j1}^* q_{24} + b_{j2}^* q_{44}, \quad \tilde{s}_{j1} = b_{j1}^* q_{25} + b_{j2}^* q_{45}$$

$$\mathbf{B} = \{b_{jm}\}^2 = \begin{pmatrix} q_{21} & \tilde{q}_{23}^+ \\ q_{41} & q_{43} \end{pmatrix}, \quad |\mathbf{B}| = q_{21}q_{43} - q_{41}\tilde{q}_{23}^+, \quad \tilde{q}_{23}^\pm = 0.5(q_{23}^- \pm q_{23}^+)$$

Expressions for translational displacements will be determined from the conditions (8)

$$\delta_3 = \frac{b_{21}^* |\mathbf{B}|}{4a} P_3 - \beta_* f_* - \beta_T f_0^T$$

$$\varphi_1 = \frac{3\beta_2}{2a^3} M_1 - \frac{3}{2a^3} \beta_2 \beta_1^T \text{Im}(f_1^T), \quad \varphi_2 = \frac{3}{8a^3} \beta_2 M_2 - \frac{3}{8a^3} \beta_2 \beta_1^T \text{Re}(f_1^T) \quad (8)$$

$$\beta_* = \frac{b_{21}^* |\mathbf{B}| (b_{11}^* s_{21} - s_{11} b_{21}^*)}{2a}, \quad \beta_T = \frac{b_{21}^* |\mathbf{B}| (b_{11}^* \tilde{s}_{21} - \tilde{s}_{11} b_{21}^*)}{2a},$$

$$\beta_1^T = \frac{4}{3} a^3 \frac{b_{11}^* \tilde{s}_{21}}{\beta_1} - \tilde{s}_{11} 2\pi$$

In Figs. 1 and 2 present the dependence of the generalized intensity coefficient (GIC) from the polar angle  $\varphi$  of the heat flux  $q_0$  and the resulting moments  $M_1, M_2$ . The magnitudes of the moments in Figs. 1 and 2 differ by an order of magnitude, i.e.  $M_1 = M_2 = 20$  for the first picture and  $M_1 = M_2 = 200$  for the second. It can be seen from the figures that the value of the heat flux and the moments on the inclusion significantly affect the values of GIC. The GIC values also depend on the polar angle, which shows the anisotropy effect of the thermoelastic properties of materials on the GIC.

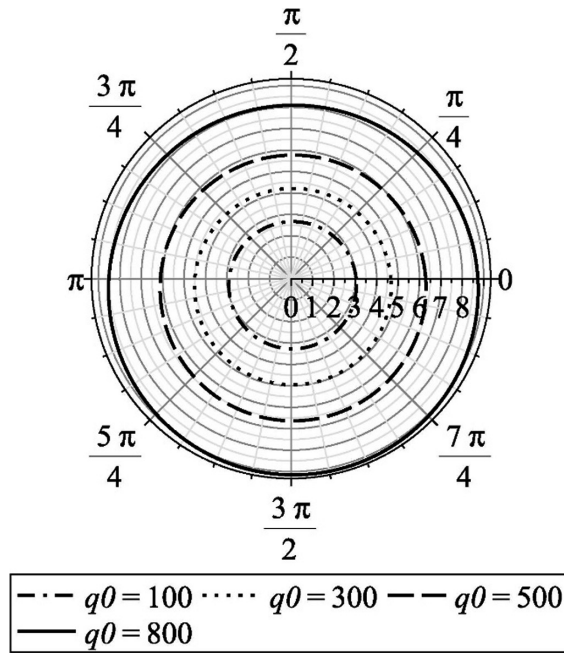


**Fig. 1.** The generalized intensity coefficient (GIC) from the polar angle  $\varphi$  of the heat flux  $q_0$  and the resulting moments  $M_1 = M_2 = 20$

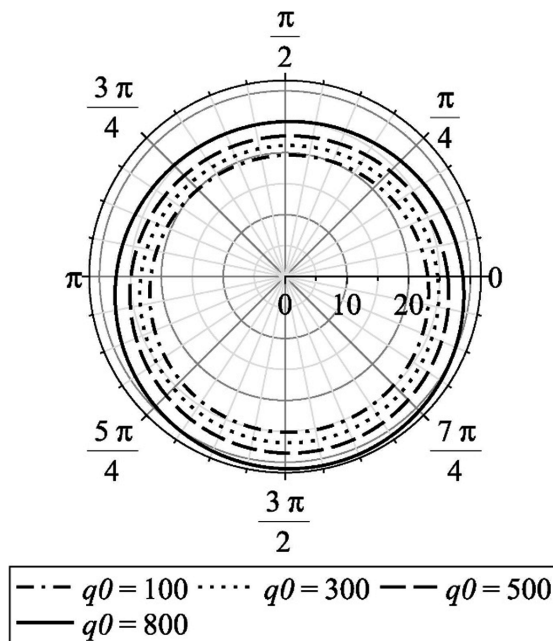


**Fig. 2.** The generalized intensity coefficient (GIC) from the polar angle  $\varphi$  of the heat flux  $q_0$  and the resulting moments  $M_1 = M_2 = 200$



Similarly can be obtained the exact solution of the problem of stationary thermoelasticity with different conditions of contact interaction of interfacial inclusions with a piecewise homogeneous transversely isotropic space.

## References

1. Efimov, V.V., Krivoi, A.F., Popov, G.Y.: Problems on the stress concentration near a circular imperfection in a composite elastic medium. *Mech. Solids* **33**(2), 35–49 (1998). Springer ISSN: 0025-6544
2. Kryvyi, O.: The discontinuous solution for the piece-homogeneous transversal isotropic medium. *Oper. Theory Adv. Appl.* **191**, 387–398 (2009). [https://doi.org/10.1007/978-3-7643-9921-4\\_25](https://doi.org/10.1007/978-3-7643-9921-4_25)
3. Kryvyi, O.F.: Singular integral relations and equations for a piecewise homogeneous transversally isotropic space with interphase defects. *J. Math. Sci.* **176**(4), 515–531 (2011). <https://doi.org/10.1007/s10958-011-0419-2>
4. Kryvyi, O.F.: Interface crack in the inhomogeneous transversely isotropic space. *Mater. Sci.* **47**(6), 726–736 (2012). <https://doi.org/10.1007/s11003-012-9450-9>
5. Kryvyi, O.F.: Interface circular inclusion under mixed conditions of interaction with a piecewise homogeneous transversally isotropic space. *J. Math. Sci.* **184**(1), 101–119 (2012). <https://doi.org/10.1007/s10958-012-0856-6>
6. Kryvyi, O.F.: Delaminated interface inclusion in a piecewise homogeneous transversely isotropic space. *Mater. Sci.* **50**(2), 245–253 (2014). <https://doi.org/10.1007/s11003-014-9714-7>
7. Kryvyi, O., Morozov, Y.: Interphase circular inclusion in a piecewise-homogeneous transversely isotropic space under the action of a heat flux. In: Gdoutos, E. (eds.) *Proceedings of the First International Conference on Theoretical, Applied and Experimental Mechanics. ICTAEM 2018. Structural Integrity*, vol. 5. Springer, Cham (2019). [https://doi.org/10.1007/978-3-319-91989-8\\_94](https://doi.org/10.1007/978-3-319-91989-8_94)
8. Kriviy, O.F., Morozov, Y.A.: Rozv'yazok zadachI teploprovIdnostI dlya transversalno-Izotropnogo kuskovo-odnorIdnogo prostoru z dvoma krugovimi vklyuchennyami. *Matematichni metodi ta fiziko-mehanichni polya*. T. 60, № 2, S. 130–141. *Rezhim dostupu* (2017) [http://nbuv.gov.ua/UJRN/MMPPhMP\\_2017\\_60\\_2\\_15](http://nbuv.gov.ua/UJRN/MMPPhMP_2017_60_2_15)



# Unsteady Elastic Diffusion Oscillations of a Timoshenko Beam with Considering the Diffusion Relaxation Effects

O. A. Afanasieva<sup>1</sup>, U. S. Gafurov<sup>1,2</sup>, and A. V. Zemskov<sup>1,2</sup>(✉)

<sup>1</sup> Moscow Aviation Institute (National Research University), Moscow, Russia  
azemskov1975@mail.ru

<sup>2</sup> Institute of Mechanics, Lomonosov Moscow State University, Moscow, Russia

**Abstract.** The unsteady Timoshenko beam oscillations with mass transfer considering are investigated. In general formulation, the beam is under the action of tensile forces, bending moments and shearing forces given at its ends. The densities of diffusion fluxes are also given at ends. All the above factors are in the plane of the beam bend. To solve the obtained problem, the Laplace integral transform on time and Fourier series expansion on spatial coordinate are used.

**Keywords:** Mechanodiffusion · Elastic diffusion · Timoshenko beam · Unsteady oscillations

## 1 Problem Formulation

The plane unsteady oscillations problem of Timoshenko beam is considered. The scheme of the applied forces and bending moments, as well as the orientation of the axes of the rectangular Cartesian coordinate system is shown in Fig. 1.

The equations of beam transverse oscillations are obtained on the basis of the Hamilton variational principle as a condition for the functional stationarity. Variation of the functional  $H(u_i, \eta^{(q)})$  has the form [1]

$$\delta H = \int_{t_1}^{t_2} d\tau \int_G \left( \ddot{u}_i - \frac{\partial \sigma_{ij}}{\partial x_j} - F_i \right) \delta u_i dG + \sum_{q=1}^N \int_{t_1}^{t_2} d\tau \int_G \left( \dot{\eta}^{(q)} + \frac{\partial J_i^{(q)}}{\partial x_i} - Y^{(q)} \right) \delta \eta^{(q)} dG$$

$$+ \int_{t_1}^{t_2} \iint_{\Pi_\sigma} (\sigma_{ij} n_j - P_i) \delta u_i dS d\tau + \sum_{q=1}^N \int_{t_1}^{t_2} \iint_{\Pi_J} (J_i^{(q)} - I_i^{(q)}) n_i \delta \eta^{(q)} dS d\tau,$$

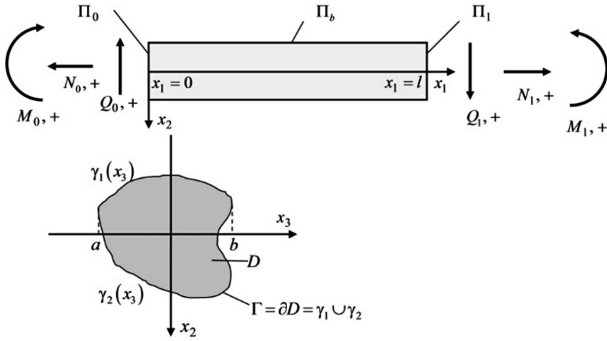


Fig. 1. Illustration to problem formulation.

where  $\sigma_{ij}$  and  $J_i^{(q)}$  are the stress tensor components and the diffusion flux vector respectively, which are defined as follows ( $q = \overline{1, N}$ ) [1–3]:

$$\sigma_{ij} = C_{ijkl} \frac{\partial u_k}{\partial x_l} - \sum_{q=1}^N \alpha_{ij}^{(q)} \eta^{(q)}, \quad J_i^{(q)} + \tau_q \dot{J}_i^{(q)} = -D_{ij}^{(q)} \frac{\partial \eta^{(q)}}{\partial x_j} + \Lambda_{ijkl}^{(q)} \frac{\partial^2 u_k}{\partial x_j \partial x_l}.$$

Here the dots denote the time derivative. All quantities are dimensionless. For them the following notation is used

$$x_i = \frac{x_i^*}{l}, \quad u_i = \frac{u_i^*}{l}, \quad \tau = \frac{Ct}{l}, \quad C_{ijkl} = \frac{C_{ijkl}^*}{C_{1111}}, \quad C^2 = \frac{C_{1111}^*}{\rho}, \quad \alpha_{ij}^{(q)} = \frac{\alpha_{ij}^{*(q)}}{C_{1111}},$$

$$D_{ij}^{(q)} = \frac{D_{ij}^{*(q)}}{Cl}, \quad \Lambda_{ijkl}^{(q)} = \frac{m^{(q)} D_{ij}^{*(q)} \alpha_{kl}^{*(q)} n_0^{(q)}}{\rho RT_0 Cl}, \quad F_i = \frac{\rho l F_i^*}{C_{1111}}, \quad Y^{(q)} = \frac{l Y^{*(q)}}{C},$$

where  $t$  is time;  $x_i^*$  are rectangular Cartesian coordinates;  $\rho$  is the medium density;  $u_i^*$  are displacement vector components;  $C_{ijkl}^*$  are elastic constant tensor components;  $T_0$  is initial temperature;  $D_{ij}^{*(q)}$  are the self-diffusion coefficients;  $R$  is the universal gas constant;  $m^{(q)}$  is the molar mass;  $\eta^{(q)} = n^{(q)} - n_0^{(q)}$  is the concentration increment of  $q$ -th component in the  $N$ -component medium;  $n_0^{(q)}$  and  $n^{(q)}$  are the initial and actual concentrations (mass fractions);  $\alpha_{ij}^{*(q)}$  are coefficients characterizing the medium volumetric changes due to diffusion;  $l$  is beam length;  $P_i, I_i^{(q)}$  are mechanical and diffusive surface perturbations  $F_i$  and  $Y^{(q)}$  are mechanical and diffusive bulk perturbations;  $\tau^{(q)}$  is relaxation time of diffusion perturbations.

Further, for the bending equations formulation, we assume that:

- the beam material is a homogeneous orthotropic continuum ( $\lambda$  and  $\mu$  are Lamé coefficients)

$$C_{ijkl} = \lambda \delta_{ij} \delta_{kl} + \mu (\delta_{ik} \delta_{jl} + \delta_{il} \delta_{jk}), \quad \Lambda_{\alpha\alpha\beta\beta}^{(q)} = \Lambda_q, \quad \alpha_{\alpha\alpha}^{(q)} = \alpha_q, \quad D_{\alpha\alpha}^{(q)} = D_q,$$

- the transverse deflections are considered small,
- the cross-sections that are normal to the beam axis before deformation, remain flat even after deformation (the hypothesis of flat sections).

Then the desired values linearization by the spatial variable  $x_2$  takes the form [4, 5]:

$$u_1(x_1, x_2, \tau) = u(x_1, \tau) + x_2 \chi(x_1, \tau), \quad u_2(x_1, x_2, \tau) = v(x_1, \tau) + x_2 \psi(x_1, \tau), \\ \eta^{(q)} = N_q(x_1, \tau) + x_2 H_q(x_1, \tau).$$

Using the necessary condition for the functionals stationarity, we obtain the unsteady plane bending model of Timoshenko elastic diffusion beam

$$\ddot{v} - \mu k^2 (v'' - \chi') + F_1 = 0, \\ \ddot{\chi} - \chi'' - \frac{F}{J_3} \mu k^2 (v' - \chi) + \sum_{q=1}^N \alpha_q H_q' + F_2 = 0, \quad (1.1) \\ \dot{H}_q + \tau_q \ddot{H}_q - D_q H_q'' - \Lambda_q \chi''' + F_{q+2} = 0;$$

$$\left( \chi' + \sum_{q=1}^N \alpha_q H_q \right) \Big|_{x_1=0} = f_{21}(\tau), \quad \left( \chi' + \sum_{q=1}^N \alpha_q H_q \right) \Big|_{x_1=1} = f_{22}(\tau), \quad (1.2)$$

$$v|_{x_1=0} = f_{11}(\tau), \quad v|_{x_1=1} = f_{12}(\tau), \quad H_q|_{x_1=0} = f_{q+2,1}(\tau), \quad H_q|_{x_1=1} = f_{q+2,2}(\tau),$$

$$F_1(x, \tau) = -\frac{q(x, \tau)}{F}, \quad F_2(x, \tau) = -\frac{m(x, \tau)}{J_3}, \quad F_{q+2}(x, \tau) = -\frac{z^{(q)}(x, \tau)}{J_3}, \\ f_{11}(\tau) = V_0(\tau), \quad f_{12}(\tau) = V_1(\tau), \quad f_{q+2,1}(\tau) = H_{q0}(\tau), \quad f_{q+2,2}(\tau) = H_{q1}(\tau), \\ f_{21}(\tau) = -\frac{M_0(\tau)}{J_3}, \quad f_{22}(\tau) = -\frac{M_1(\tau)}{J_3}.$$

where  $F$  is the cross-sectional area,  $J_3$  is moment of inertia of the beam section relative to the axis  $Ox_3$ ,  $m$  is the linearly distributed moment,  $q$  is the linearly distributed transverse load;  $z^{(q)}$  is the linearly distributed sources of mass transfer. The remaining external force factors are presented in Fig. 1.

The coefficient  $k$  considering the uneven distribution of tangential stresses over the beam cross-section [5]. If the tangential stresses are distributed according to the Zhuravsky formula, then for a rectangular beam section of unit thickness and height  $h$  there is an equality  $k^2 = 5/6$ .

## 2 Solution Method

The solution of the problem (1.1), (1.2) is represented as  $(k = \overline{1, N+1})$  [6, 7]:

$$\begin{aligned} \left\{ \begin{array}{l} v(x, \tau) \\ \chi(x, \tau) \\ \eta_q(x, \tau) \end{array} \right\} &= \sum_{k=1}^{N+2} \int_0^\tau \left[ \left\{ \begin{array}{l} G_{1k}(x, \tau - t) \\ G_{2k}(x, \tau - t) \\ G_{q+2,k}(x, \tau - t) \end{array} \right\} f_{k1}(t) + \left\{ \begin{array}{l} G_{1k}(1-x, \tau - t) \\ G_{2k}(1-x, \tau - t) \\ G_{q+2,k}(1-x, \tau - t) \end{array} \right\} f_{k2}(t) \right] dt \\ &+ \sum_{k=1}^{N+2} \int_0^\tau \int_0^1 \left\{ \begin{array}{l} \tilde{G}_{1k}(x, \xi, \tau - t) \\ \tilde{G}_{2k}(x, \xi, \tau - t) \\ \tilde{G}_{q+2,k}(x, \xi, \tau - t) \end{array} \right\} F_k(\xi, t) d\xi dt. \end{aligned} \tag{2.1}$$

Here  $x = x_1$ ;  $G_{mk}$  are surface Green's functions satisfying the equations

$$\begin{aligned} \ddot{G}_{1k} - \mu k^2 (G''_{1k} - G'_{2k}) &= 0, \\ \ddot{G}_{2k} - G''_{2k} - \frac{F}{J_3} \mu k^2 (G'_{1k} - G_{2k}) + \sum_{q=1}^N \alpha_q G'_{q+2,k} &= 0, \\ \dot{G}_{q+2,k} + \tau_q \ddot{G}_{q+2,k} - D_q G''_{q+2,k} + \Lambda_q G'''_{2k} &= 0; \end{aligned} \tag{2.2}$$

and boundary conditions:

$$\begin{aligned} G_{1k}|_{x_1=0} = \delta_{1k} \delta(\tau), \quad G_{1k}|_{x_1=1} = 0, \quad G_{q+2,k}|_{x_1=0} = \delta_{q+2,k} \delta(\tau), \quad G_{q+2,k}|_{x_1=1} = 0, \\ \left( G'_{2k} - \sum_{j=1}^N \alpha_j G_{j+2,k} \right) \Big|_{x_1=0} = \delta_{2k} \delta(\tau), \quad \left( G'_{2k} - \sum_{j=1}^N \alpha_j G_{j+2,k} \right) \Big|_{x_1=1} = 0. \end{aligned} \tag{2.3}$$

$\tilde{G}_{mk}$  are bulk Green's functions satisfying the equations

$$\begin{aligned} \ddot{\tilde{G}}_{1k} - \mu k^2 (\tilde{G}''_{1k} - \tilde{G}'_{2k}) + \delta_{1k} \delta(x - \xi) \delta(\tau) &= 0, \\ \ddot{\tilde{G}}_{2k} - \tilde{G}''_{2k} - \frac{F}{J_3} \mu k^2 (\tilde{G}'_{1k} - \tilde{G}_{2k}) + \sum_{q=1}^N \alpha_q \tilde{G}'_{q+2,k} + \delta_{2k} \delta(x - \xi) \delta(\tau) &= 0, \\ \dot{\tilde{G}}_{q+2,k} + \tau_q \ddot{\tilde{G}}_{q+2,k} - D_q \tilde{G}''_{q+2,k} + \Lambda_q \tilde{G}'''_{2k} + \delta_{q+2,k} \delta(x - \xi) \delta(\tau) &= 0. \end{aligned}$$

and homogeneous boundary conditions corresponding to (2.3).

To find the surface Green's functions, the Laplace transform and Fourier series expansion are used. As a result, we obtain the following representations for the surface Green functions  $G_{mk}$ .

$$\left\{ \begin{array}{l} G_{1k}(x, \tau) \\ G_{q+2,k}(x, \tau) \end{array} \right\} = \sum_{n=1}^{\infty} \left\{ \begin{array}{l} G_{1k}^s(\lambda_n, \tau) \\ G_{q+2,k}^s(\lambda_n, \tau) \end{array} \right\} \sin \lambda_n x,$$

$$G_{2k}(x, \tau) = \frac{G_{2k}^c(0, \tau)}{2} + \sum_{n=1}^{\infty} G_{2k}^c(\lambda_n, \tau) \cos \lambda_n x,$$

$$G_{ik}^s(\lambda_n, \tau) = \sum_{j=1}^{2N+2} A_{ik}^{(j)}(\lambda_n) e^{s_j(\lambda_n)\tau}, \quad A_{ik}^{(j)}(\lambda_n) = \frac{P_{ik}(\lambda_n, s_j(\lambda_n))}{P'(\lambda_n, s_j(\lambda_n))},$$

$$G_{q+2,1}^s(\lambda_n, \tau) = \sum_{j=1}^{2N+2} A_{q+2,1}^{(j)}(\lambda_n) e^{s_j(\lambda_n)\tau}, \quad A_{q+2,1}^{(j)}(\lambda_n) = \frac{P_{q+2,1}(\lambda_n, s_j(\lambda_n))}{P'(\lambda_n, s_j(\lambda_n))},$$

$$G_{q+2,p+2}^s(\lambda_n, \tau) = \sum_{l=1}^2 \left[ A_{q+2,p+2}^{(2N+2+l)}(\lambda_n) + \frac{2\lambda_n(D_q \delta_{pq} - \Lambda_q \alpha_p)}{1 + 2\tau_q \xi_l(\lambda_n)} \right] e^{\xi_l(\lambda_n)\tau} + \sum_{j=1}^{2N+2} A_{q+2,p+2}^{(j)}(\lambda_n) e^{s_j(\lambda_n)\tau},$$

$$G_{q+2,2}^s(\lambda_n, \tau) = \sum_{l=1}^2 \left[ A_{q+2,2}^{(2N+2+l)}(\lambda_n) - \frac{2\Lambda_q \lambda_n}{1 + 2\tau_q \xi_l(\lambda_n)} \right] e^{\xi_l(\lambda_n)\tau} + \sum_{j=1}^{2N+2} A_{q+2,2}^{(j)}(\lambda_n) e^{s_j(\lambda_n)\tau},$$

$$A_{q+2,p+2}^{(j)}(\lambda_n) = \frac{P_{q+2,p+2}(\lambda_n, s_j(\lambda_n))}{Q'_q(\lambda_n, s_j(\lambda_n))}, \quad A_{q+2,2}^{(j)}(\lambda_n) = \frac{P_{q+2,2}(\lambda_n, s_j(\lambda_n))}{Q'_q(\lambda_n, s_j(\lambda_n))},$$

$$\xi_{1,2}(\lambda_n) = \frac{-1 \pm \sqrt{1 - 4\tau_q D_q \lambda_n^2}}{2\tau_q},$$

where  $P(\lambda_n, s)$ ,  $P_{km}(\lambda_n, s)$  are polynomials depend on  $s$ . Their explicit form is not given here.  $s_j(\lambda_n)$  are simple zeros of polynomial  $P(\lambda_n, s)$ ;  $Q_q(\lambda_n, s) = (s + \tau_q s^2 + D_q \lambda_n^2)P(\lambda_n, s)$ .

Algorithm for the bulk Green's functions  $\tilde{G}_{mk}$  is similar. Substituting the obtained expressions for the Green's functions into convolutions (2.1), we obtain the problem solution of the Timoshenko beam bending in formulation (1.1) and (1.2).

Thus, the coupled unsteady model of elastodiffusive Timoshenko beam oscillations is presented. An algorithm for the surface Green functions constructing of the problem is proposed. Based on the developed model, the interaction of mechanical and diffusion fields is investigated.

## References

1. Zemskov, A.V., Tarlakovskii, D.V.: Postanovka zadachi o nestatsionarnykh uprugodiffuzionnykh kolebaniyakh balki Eilera-Bernulli. In: XXIV International Symposium “Dynamic and Technological Problems of a Mechanics of Constructions and Continuous Mediums” dedicated to A.G. Gorshkov, vol. 2, pp. 152–157 (2018) (in Russian)
2. Davydov, S.A., Zemskov, A.V.: Unsteady one-dimensional perturbations in multicomponent thermoelastic layer with cross-diffusion effect. *J. Phys. Conf. Ser.* **1129**, 012009 (2018)
3. Knyazeva, A.G.: Model of medium with diffusion and internal surfaces and some applied problems. *J. Mater. Phys. Mech.* **7**(1), 29–36 (2004)
4. Mikhailova, E.Y., Tarlakovskii, D.V., Fedotenkov, G.V.: *Obshchaya teoriya uprugikh obolochek*. MAI, Moscow, Russia (2018) (in Russian)
5. Gorshkov, A.G., Medvedsky, A.L., Rabinsky, L.N., Tarlakovsky D.V.: *Volny v sploshnykh sredakh*. Fizmatlit, Moscow, Russia (2004) (in Russian)
6. Davydov, S.A., Zemskov, A.V., Tarlakovskii, D.V.: An elastic half-space under the action of one-dimensional time-dependent diffusion perturbations. *Lobachevskii J. Math.* **36**(4), 503–509 (2015)
7. Igumnov, L.A., Tarlakovskii, D.V., Zemskov, A.V.: A two-dimensional nonstationary problem of elastic diffusion for an orthotropic one-component layer. *Lobachevskii J. Math.* **38**(5), 808–817 (2017)



# Interphase Inclusion and Crack in an Inhomogeneous Anisotropic Plane

Kostyantyn Arkhypenko  and Oleksandr Kryvviy 

National University “Odessa Maritime Academy”, Odessa, Ukraine  
krivoy-odessa@ukr.net

**Abstract.** In the inhomogeneous anisotropic plane the problem about interaction between interphase crack and inclusion, which is in the conditions of full cohesion, was considered. Using the method of singular integral relations for interphase defects, the problem was reduced to the system of singular integral equations, and the method for its solution is proposed. As a result, the effect of the distance between defects, the loading applied to them and the properties of anisotropic materials on the features of the stress fields in the neighborhood of defects was investigated. In particular, the critical distance between the crack and the inclusion, according to which the mutual influence of the defects is significant, was established. It was also established under what loads it is advisable to remain within the singular statement of the problem without taking into account the contact zones of the crack edges.

**Keywords:** Inhomogeneous anisotropic plane · Interphase crack and inclusion · Systems of singular integral equations · Stresses · Stress intensity factor

## 1 Statement of the Problem

The inhomogeneous anisotropic plane consisting of two different anisotropic half-planes was considered. The conjunction line of these half-planes is the  $Oy$  axis on which the crack  $L_1 : \{x = 0, y \in [a; b]\}$  and the absolutely rigid, thin inclusion  $L_2 : \{x = 0, y \in [c; d]\}$ , ( $a < b < c < d$ ), which is in the conditions of full cohesion with anisotropic materials, are located. At the infinity the forces are applied that generate the stresses  $\sigma_x(\pm 0, y) = \sigma(y)$ ,  $\tau_{xy}(\pm 0, y) = \tau(y)$ ,  $y \in [a; b]$  on the crack edges. The shapes of the inclusion edges  $u_*^\pm(y) = u(\pm 0, y)$ ,  $y \in L_2$  are given, and the arbitrary load is applied to the inclusion, which reduces to the resultant force  $\mathbf{P} = (P_1, P_2)$  and creates the moment  $P_0$  relatively to the inclusion center.

To reduce the problem to the system of singular integral equations (SIE) the method of singular integral relations was applied [1–10]. As a result, the following matrix SIE was obtained relatively to the unknown stresses jumps  $H_j^-(y)$ ,  $j = 1, 2$  and the derivatives of displacements  $H_j^-(y)$ ,  $j = 3, 4$ .

$$\mathbf{B}^{(j)} \cdot \mathbf{t}^{(j)}(y) + \mathbf{C}^{(j)} \cdot \Gamma_1[\mathbf{t}^{(j)}] + \mathbf{C}_*^{(j)} \cdot \Gamma_2[\mathbf{t}^{(j)}] = \mathbf{p}^{(j)}(y), \quad y \in L_j, j = 1, 2. \quad (1)$$



$$\Gamma_j[f] = \frac{1}{\pi} \int_{L_j} \frac{f(t)dt}{t-y}, \mathbf{t}^{(1)}(y) = \begin{pmatrix} H_3^-(y) \\ H_4^-(y) \end{pmatrix}, \mathbf{t}^{(2)}(y) = \begin{pmatrix} H_1^-(y) \\ H_2^-(y) \end{pmatrix},$$

$$\mathbf{p}^{(1)}(y) = 2l \begin{pmatrix} \sigma(y) \\ \tau(y) \end{pmatrix}, \mathbf{p}^{(2)}(y) = 2l \begin{pmatrix} 0 \\ \delta + g^+(y) \end{pmatrix}, \mathbf{B}^{(1)} = \begin{pmatrix} r_4^- & 0 \\ 0 & -r_4^- \end{pmatrix},$$

$$\mathbf{B}^{(2)} = \begin{pmatrix} r_{54}^- & 0 \\ 0 & -r_{54}^- \end{pmatrix}, \mathbf{C}^{(1)} = \begin{pmatrix} -r_1^+ & r_2^+ \\ r_3^+ & -r_1^+ \end{pmatrix}, \mathbf{C}_*^{(1)} = \begin{pmatrix} r_{14}^+ & r_{24}^+ \\ -r_{34}^+ & -r_{14}^+ \end{pmatrix},$$

$$\mathbf{C}^{(2)} = \begin{pmatrix} -r_{15}^+ & -r_{25}^+ \\ -r_{35}^+ & -r_{15}^+ \end{pmatrix}, \mathbf{C}_*^{(2)} = \begin{pmatrix} -r_{14}^+ & r_{24}^+ \\ -r_{34}^+ & r_{14}^+ \end{pmatrix},$$

where  $2l = r_2^+ r_3^+ - (r_1^+)^2 - (r_4^-)^2$ , and  $r_j^\pm, r_{ij}^\pm$  depend from the elastic properties of anisotropic half-planes [1],  $2g^+(y) = (u_*^+(y) + u_*^-(y))'_y$ ,  $\delta$ —the unknown angle of inclusion rotation. The statement of the problem completes the additional conditions

$$\int_a^b \mathbf{t}^{(1)}(y)dy = 0, \int_c^d \mathbf{t}^{(2)}(y)dy = \mathbf{P}, \int_c^d H_1^-(y)ydy = P_0. \tag{2}$$

## 2 Solution the System of SIE

Using the approach of works [1–6], the matrix SIE (1) was applied as follows

$$\mathbf{J}^{(j)} \cdot \boldsymbol{\tau}^{(j)}(y) + \Gamma_j[\boldsymbol{\tau}^{(j)}] + \mathbf{V}^{(j)} \cdot \Gamma_{3-j}[\boldsymbol{\tau}^{(3-j)}] = \mathbf{U}^{(j)} \cdot \mathbf{p}^{(j)}(y), \quad y \in L_j, j = 1, 2 \tag{3}$$

$$\boldsymbol{\tau}^{(j)}(y) = (\mathbf{S}^{(j)})^{-1} \cdot \mathbf{t}^{(j)}(y), \mathbf{U}^{(j)} = (\mathbf{C}^{(j)} \cdot \mathbf{S}^{(j)})^{-1}, \mathbf{V}^{(j)} = \mathbf{U}^{(j)} \cdot \mathbf{C}_*^{(j)} \cdot \mathbf{S}^{(3-j)}$$

$$\mathbf{S}^{(1)} = \begin{pmatrix} r_2^+ & r_2^+ \\ r_1^+ - i\lambda_{01} & r_1^+ + i\lambda_{01} \end{pmatrix}, \mathbf{S}^{(2)} = \begin{pmatrix} -r_{25}^+ & -r_{25}^+ \\ r_{15}^+ - i\lambda_{02} & r_{15}^+ + i\lambda_{02} \end{pmatrix}, \mathbf{J}^{(j)} = \begin{pmatrix} \lambda_{2j-1} & 0 \\ 0 & \lambda_{2j} \end{pmatrix},$$

$$\lambda_j = (-1)^{j+1} i r_4^- d_1^{-1} \lambda_{01}, \quad j = 1, 2, \lambda_{01} = \text{sgn}(r_4^-) \cdot \sqrt{d_1}, \quad d_1 = r_2^+ \cdot r_3^+ - (r_1^+)^2,$$

$$\lambda_j = (-1)^{j+1} i r_{54}^- d_2^{-1} \lambda_{02}, \quad j = 3, 4, \lambda_{02} = \text{sgn}(r_{54}^-) \sqrt{d_2}, \quad d_2 = r_{25}^+ \cdot r_{35}^+ - (r_{15}^+)^2.$$

The analysis of the solutions of the matrix SIE (3) led to the conclusion that the stresses at the ends of the crack and inclusion have a root singularity reinforced oscillation. The latter makes it possible to construct the solutions in the form of series by Jacobi polynomials  $P_n^{\gamma_j, \lambda_j}(\xi)$ :

$$T_j(\xi) = \tau_j \left( \frac{b-a}{2} \xi + \frac{b+a}{2} \right) = \sum_{n=1}^{\infty} q_{jn} \cdot Q_n^{\gamma_j}(\xi) + q_{j0} \cdot \omega_j^{-1}(\xi), \quad |\xi| \leq 1, j = \overline{1, 4}, \tag{4}$$

$$Q_n^{j\bar{j}}(\xi) = (1 - \xi)^{\bar{j}j}(1 + \xi)^{j\bar{j}}P_n^{\bar{j}j\bar{j}j}(\xi), \omega_j^{-1}(\xi) = (1 - \xi)^{\bar{j}j}(1 + \xi)^{j\bar{j}}, \quad j = 1, 2,$$

$$\gamma \begin{bmatrix} j \\ 2+j \end{bmatrix} = -\frac{1}{2} + i(-1)^{j+1}\alpha \begin{bmatrix} 1 \\ 2 \end{bmatrix}, \alpha_j = \frac{1}{2\pi} \ln \frac{1 - \alpha_{0j}}{1 + \alpha_{0j}}, \alpha_{01} = |r_4^-| \sqrt{d_1^{-1}}, \alpha_{02} = |r_{54}^-| \sqrt{d_2^{-2}}.$$

To determine the unknown coefficients  $q_{km}$ , using the method of orthogonal polynomials, an infinite system of linear algebraic equations was obtained. For the latter, the reduction method [11] was applied, and the exponential rate of its convergence to the exact solution was proved.

As a result, the coefficients  $q_{km}$  of the expression (4) is defined and the rotation angle of the inclusion  $\delta$  is obtained by the formula:

$$\delta = \frac{\sqrt{1 - \alpha_{02}^2}}{8l \cdot u_{12}^{(2)}} q_{31} - \frac{(1 + 4\alpha_2^2)^{-1}}{2l\pi \cdot u_{12}^{(2)}} \left( A \sum_{j=1}^2 v_{1j}^{(2)} \sum_{n=1}^{\infty} q_{jn} J_{0n}^{3j} + F_{30}^0 \right) \quad (5)$$

The expression (4) makes it possible to obtain formulas for the generalized stress intensity factors (GSIF) at the vertices of the crack and inclusion:

$$K_T^{1\pm} = \frac{\sqrt{b-a}\sqrt{1 - \alpha_{01}^2}}{2l} \left| \left( -r_1^+ S_{11}^{(1)} + r_2^+ S_{21}^{(1)} \right) \Sigma_1^{\pm} \right|, \quad (6)$$

$$K_T^{2\pm} = \frac{\sqrt{b-a}\sqrt{1 - \alpha_{01}^2}}{2l} \left| \left( r_3^+ S_{11}^{(1)} - r_1^+ S_{21}^{(1)} \right) \Sigma_1^{\pm} \right|,$$

$$K_I^{1\pm} = \frac{\sqrt{d-c}}{2l} \left| \left( r_{14}^+ \cdot S_{11}^{(2)} + r_{24}^+ \cdot S_{21}^{(2)} \right) \Sigma_3^{\pm} \right|$$

$$K_I^{2\pm} = \frac{\sqrt{d-c}}{2l} \left| \left( r_{34}^+ \cdot S_{11}^{(2)} + r_{14}^+ \cdot S_{21}^{(2)} \right) \Sigma_3^{\pm} \right|, \quad \Sigma_3^{\pm} = \sqrt{1 - \alpha_{02}^2} \Sigma_2^{\pm} \pm \frac{2P_1^{(1)}}{\pi(d-c)},$$

$$\Sigma_j^{\pm} = \sum_{n=1}^{\infty} \frac{q_{2j-1n} (0.5 \mp i\alpha_{2j-1})_n}{(\pm 1)^n n!}, \quad j = 1, 2.$$

where  $K_T^{j\pm}$ —GSIF for normal ( $j = 1$ ) and shear stresses ( $j = 2$ ) at the vertices of the crack  $a$  and  $b$  respectively, and  $K_I^{j\pm}$ —GSIF for normal ( $j = 1$ ) and shear stresses ( $j = 2$ ) at the vertices of the inclusion  $c$  and  $d$  respectively.

### 3 Numerical Results and Conclusions

In the numerical implementation, was considered the composite anisotropic plane consisting of the combination of such anisotropic materials [10]: fiberglass single reinforced (material  $m1$ ), fiberglass orthogonally reinforced (material  $m2$ ), fiberglass STET (material  $m3$ ), fiberglass ACTT(b) (material  $m4$ ). In each figure the curve 1 corresponds to the plane, composing of material  $m1$  ( $x < 0$ ) and material  $m2$  ( $x > 0$ ),

curve 2—the plane, composing of material  $m4$  ( $x < 0$ ) and material  $m3$  ( $x > 0$ ), curve 3—the plane, composing of material  $m2$  ( $x < 0$ ) and material  $m4$  ( $x > 0$ ). The stresses' fields near the crack and the inclusion essentially depend on the distance between these defects. Figure 1 displays the dependence of GSIF for the normal stress from the distance between the defects when  $\sigma(y) = -1$ ,  $\tau(y) = 0$ ,  $\mathbf{P} = 0$  and  $P_0 = 0$  for the lower (1a) and upper (1b) crack's vertices.

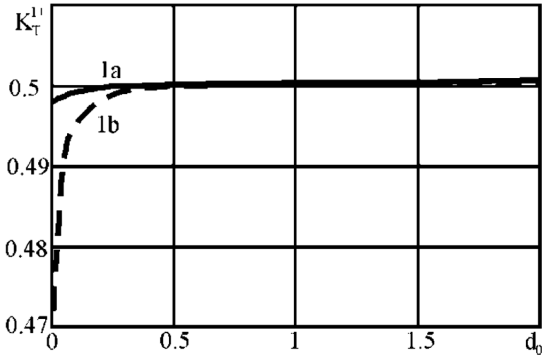


Fig. 1. The dependence of GSIF for the normal stress from the distance between the defects

From the figure above, we can conclude that when defects approach each other, GSIF decreases for the crack, and the decrease is greater for the vertex closer to the inclusion. For the inclusion GSIF, on the contrary, increases with approaching, and increases more for the vertex closer to the crack. If only the inclusion is under the load, then the GSIF behavior is just the opposite, i.e., GSIF for the crack increases, but for the inclusion, on the contrary, decreases. Thus, the effect of defects on stresses' fields becomes significant when  $d_0 \leq 0.25$ .

The contact zones between the crack edges were also investigated for the different loadings of both defects. As it turned out, any tangential load both on the crack and on the inclusion causes the contact of the edges at both vertices of the crack, and one of these zones is much smaller, than the other. According to this, we can assume that only one contact zone arises on the crack. When the crack is under the constant normal load, and the tangential load is less than the normal one, and the resultant force on the inclusion is smaller than the normal load, or these forces are completely absent, then both contact zones are so small that their sizes can be neglected comparing to the crack size. The contact zones' sizes, can be compared with the crack size when the crack is only under the tangential load or when the tangential load is bigger than normal. So, for example, setting only the tangential load on the crack and assuming that the inclusion is free of load, the contact zone on the crack is equal to half of its length.

Figure 2 shows the dependences of the contact zone's length  $l_z$  on the ratio of loads  $P_1/\sigma$ , when the crack is under the load  $\sigma(y) = -1$ ,  $\tau(y) = 0$ , and the inclusion is under the load, which reduces to the resultant force  $\mathbf{P} = (P_1, 0)$  ( $0 \leq P_1 \leq 50$ ) and creates a zero moment relatively to the center of inclusion ( $P_0 = 0$ ). As can be seen

from Fig. 2 for the appearance of the contact zone  $l_z$ , the length of which is equal 1% of the crack length, it is necessary that the normal component  $P_1$  of the resultant force applied to the inclusion is 20 times greater than the normal load on the crack for less rigid materials that consist the anisotropic plane, or even more for more rigid materials.

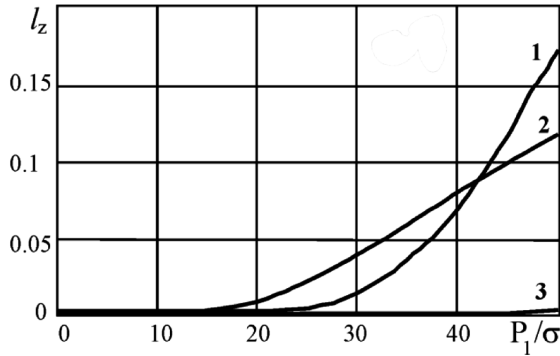


**Fig. 2.** The dependences of the contact zone's length  $l_z$  on the ratio of loads  $P_1/\sigma$

If the crack is under the normal load, then for the appearance of 1% contact zone, it is necessary that the tangential load applied to the crack is 3 times more by absolute value than the normal load on the crack for more rigid materials or even more for less rigid materials.

Thus, the mutual influence of the interphase crack and inclusion becomes significant if the distance between them is less than a quarter from one of their lengths. If the crack is under the normal load, then to increase the contact area of the crack edges to sizes that can't be neglected, it is necessary that the crack or inclusion is under tangential load. So the tangential load on the crack should be at least three times greater than the normal one for more rigid materials which are consisted the plane, or even more—for less rigid materials. The load on the inclusion must be 20 times bigger that the normal load on the crack for less rigid materials or even bigger for more rigid materials. So, the application of oscillatory model of the crack was established for this problem.

Similarly, the problems concerning interphase crack and inclusion under other contact interaction conditions with half-planes can be considered.

## References

1. Krivoi, A.F., Radiollo, M.V.: Specific features of the stress field near inclusions in a composite anisotropic plane. *Izv. Akad. Nauk SSSR Mekh. Tverd. Tela*. № 3, 84–92 (1984)
2. Krivoi, A.F., Radiollo, M.V.: Fundamental solution of a plane problem of elasticity theory for a composite anisotropic medium. *J. Sov. Math.* **60**(2), 1365–1368 (1992). <https://doi.org/10.1007/BF01679639>

3. Krivoi, A.F.: A fundamental solution for a four-component anisotropic plane. *Vest. Odessk. Nats. Univ. Fiz. Mat. Nauki* **8**, 140–149 (2003)
4. Krivoy, O.F., Arkhipenko, K.M.: A crack extending onto conjunction line between two different anisotropic half-planes. *Math. Methods Phys. Mech. Fields* **48**(3), 110–116 (2005)
5. Krivoi, A.F., Popov, G.Y.: Interface tunnel cracks in a composite anisotropic space. *J. Appl. Math. Mech.* **72**(4), 689–700 (2008). <https://doi.org/10.1016/j.jappmathmech.2008.08.001>
6. Kryvyi, O.F.: Tunnel inclusions in a piecewise homogeneous anisotropic space. *Math. Methods Phys. Mech. Fields* **50**(2), 55–65 (2007)
7. Krivoi, A.F., Popov, G.Y.: Features of the stress field near tunnel inclusions in an inhomogeneous anisotropic space. *Appl. Mech.* **44**(6), 626–634 (2008). <https://doi.org/10.1007/s10778-008-0084-4>
8. Kryvyi, O.F.: Tunnel internal crack in a piecewise homogeneous anisotropic space. *J. Math. Sci.* **198**(1), 62–74 (2014). <https://doi.org/10.1007/s10958-014-1773-7>
9. Kryvyi, O.F.: Mutual influence of an interface tunnel crack and an interface tunnel inclusion in a piecewise homogeneous anisotropic space. *J. Math. Sci.* **208**(4), 409–416 (2015). <https://doi.org/10.1007/s10958-015-2455-9>
10. Arkhpenko, K.M., Kryvyi, O.F.: Some boundary-value problems for anisotropic quarter plane. *IOP Conf. Ser. J. Phys. Conf. Series* **991**, 1–7 (2018). <https://doi.org/10.1088/1742-6596/991/1/012004>
11. Popov, G.Y.: Concentration of elastic stresses near dies, cuts, thin inclusions and reinforcements. *Science, Moscow* (1982)



# Phenomenological Model of Pseudo-Elastic-Plastic Material Under Nonstationary Combining Loading

Pavel Steblyanko<sup>1</sup>(✉), Yuri Chernyakov<sup>2</sup>, Aleksandr Petrov<sup>2</sup>,  
and Volodymyr Loboda<sup>2</sup>

<sup>1</sup> Dnipro State Technical University, Kamianske 51918, Ukraine  
caf-vmi@ukr.net

<sup>2</sup> Dnipro National University named after Oles Honchar, Dnipro 49010, Ukraine

**Abstract.** The study of the behavior of bodies from pseudo-elastic-plastic materials requires the development of special algorithms for calculating the stress-strain state. When constructing the physical relations, it was assumed that the deformation at a point is represented as a sum of the elastic component, the deformation jump at the phase transition, the plastic deformation and the deformation caused by temperature changes. A numerical method of enhanced accuracy based on the use of two-dimensional spline functions is proposed for solving multidimensional nonstationary problems of thermo-elastic-plastic theory for bodies produced of pseudo-elastic-plastic materials. The basic equations comprising heat conduction, equilibrium or motion equations and geometric relations are written. The boundary and initial conditions are formulated in a general form and numerical examples are considered.

**Keywords:** Pseudo-elastic-plastic material · Phase transitions

## 1 Introduction

Pseudo-elastic-plasticity is the ability of a loaded material to accumulate deformations of a certain value at a higher temperature mode, and then return to its original state after unloading (through a hysteresis loop). The main mechanism is the inverse martensitic transformation between the phases of a solid, which can occur at room temperature. Such a transformation may be caused by a change in temperature or stress. The material is also characterized by non-linear mechanical behaviour, high internal damping and high yield stress.

Alloys that demonstrate shape memory and pseudo-elastic-plasticity are the following: NiTi AuCd, CuAlNi, CuSn, CuZn, NiFeGa, NiTiNb, NiNiGa, NiFeGa, NiPi, NiPeGa, NiPiGi [1, 3].

Such characteristics make SMA suitable for use in various devices or as component parts in some advanced composite materials. NiTi alloy leads in most of these applications due to its structural properties.

The first SMAs were developed in the middle of the last century; however, there are no strict and reliable determining models of the continual level necessary for engineering applications of these materials. The relationship between microscopic and macroscopic behavior is very complex and has not yet been developed to the extent required by such models. This is partly due to the rather strong dependence of the mechanical reactions on temperature, loading rate, range of deformation, geometry of the body under study, thermo mechanical history and nature of the environment as well as the interaction between these parameters themselves.

## 2 Phenomenological Model

One aspect of general non-stationary problems solution for inelastic bodies is the choice of the constitutive relations between the stresses and strains. This choice is justified by consistency with the experiment and is closely related to the processes of deformation under investigation. In a general case the strain values are functions of the process of stresses and temperatures variations, which are determined by the characteristics of the entire preceding process of physical factors variations, and not just the current values. Detailed information on this issue can be found in [2].

When constructing the physical relations, it was assumed that the deformation at a point is represented as the sum of the elastic component, the deformation jump at the phase transition, the plastic deformation and the deformation caused by the temperature variations.

The instant thermo mechanical surface is under construction of experiment on a simple stretching of samples at the various fixed temperatures. This function for some classes of originally isotropic materials with the big degree of accuracy does not depend on the type of stress state. As a result, it can be determined using tensile experiments on cylindrical specimens.

Figure 1 shows a typical plot of dependencies  $\sigma$  from  $\epsilon$  that are determined as a result of experiments for a pseudo-elastic-plastic material.

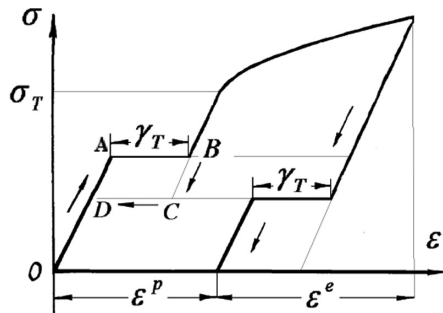


Fig. 1. Diagram of pseudo-elastic-plastic alloy.

The diagrams have an initial linear section OA. The processes of deformation on it are reversible. The increase and decrease of the stress follow a straight line, and the deformations are small. At point C, the elastic component of the total deformation of the sample disappears. Jump deformation caused by phase transition disappears also, and remains only plastic deformation. The total strain tensor can be represented as

$$\hat{\varepsilon} = \hat{\varepsilon}_e + \hat{\varepsilon}_T + \hat{\varepsilon}_p + \hat{\varepsilon}_\Theta.$$

where  $\hat{\varepsilon}_T = \gamma_T \frac{\partial f_e}{\partial \hat{\sigma}}$ ,  $\hat{\varepsilon}_p = \lambda \frac{\partial f_p}{\partial \hat{\sigma}}$ ,  $\hat{\varepsilon}_\Theta = \alpha(T - T_0)$ ,  $f_e(\hat{\sigma}) = 0$ ,  $f_p(\hat{\sigma}) = 0$ , which respectively define the boundaries of the surfaces in the space of stresses. During the transition across the surface  $f_e(\hat{\sigma}) = 0$ , the elastic deformation increases abruptly, and during the transition through the surface  $f_p(\hat{\sigma}) = 0$  plastic deformations occur in the body. Figure 1 also shows the elastic unloading of the sample along the straight line BC, which is assumed to be parallel to the line OA. Such representation of the unloading mechanism displays in general terms only the actual process of the material deformation under small deformations. For large strains (10% or more), the sample unloading process will be non-linear.

### 3 Numerical Results

In [4] a variant of the method of enhanced accuracy, developed for solving non-stationary problems of the theory of thermo-elasticity and thermo-plasticity is presented. The main unknowns are displacement rates, stresses, strains and temperature.

Let's consider the problem of non-stationary deformation of a cylindrical NiTi alloy tube with a notch. A cylindrical coordinate system is used here  $x \in [0; L]$ ,  $r \in [R_0; R_1]$ ,  $\varphi \in [0; 2\pi]$ ,  $t \in [0, \infty)$ .

At the edge  $x = 0$  the stretching rate is zero. At the other end  $x = L$  the rate of stretching  $v = V_0$  is set. The side edges of the tube are stress-free. The load-free notch through the thickness of the tube is defect which tip is modeled at a point with coordinates  $x = l$ ,  $r = R_1 - h$ ,  $\varphi = 0$ .

The sought values are the velocities; stress; deformation and temperature.

To account for the heat released as result of a phase transition the temperature is determined from the solution of the thermal conductivity equation with a mobile source of heat. This source takes into account the heat release at a moving point of a cylindrical body when moving from point A to point B (Fig. 1). It is established that the heat source moves in a spiral which develops over time.

Consider a series of numerical results obtained for a cylindrical tube. Here the outer radius is 5 cm, the inner radius is 4 cm, the tube length is 30 cm. The circumference is divided into 58 sectorial elements. The thickness of the tube is taken as 2 elements, the length as 60 elements, the notch is 3 cm below the upper rigidly fixed end, the lower end is stretched during 100 s at a speed of 0.0001 m/s.

Figure 2 shows the distribution of strains with active loading for the indicated time points.



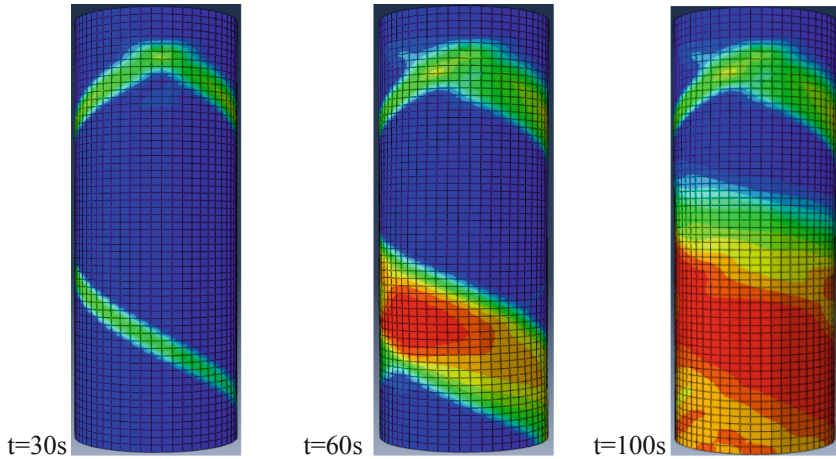


**Fig. 2.** Distribution of plastic deformations for different points in time.

The obtained results show that the boundary of the spiral-shaped deformation change propagates with a constant speed which depends only on the mechanical properties of the material. In the process of heat generation due to phase transitions the temperature distribution along the plate axis becomes uniform over time.

## 4 Conclusions

An experimental substantiation of the phenomenological model of the behaviour of a pseudo-elastic-plastic material with shape memory has been carried out. The model gives the opportunity to quantitatively evaluate the complex interactions between stresses.

A new class of non-stationary problems of the theory of thermo-elastic-plasticity for pseudo-elastic-plastic materials with shape memory has been solved.

## References

1. Abeyaratne, R., Knowles, J.K.: *Evolution of Phase Transitions*. Cambridge University Press (2006)
2. Petrov, A., Chernyakov, Y., Steblyanko, P., Demichev, K., Haydurov, V.: Development of the method with enhanced accuracy for solving problems from the theory of thermo-pseudoelastic-plasticity. *East. Eur. J. Enterp. Technol.* **4/7**(94), 25–33 (2018)
3. Shaw, J.A., Kyriakides, S.: On the nucleation and propagation of phase transformation fronts in a NiTi alloy. *J. Acta Mater.* **45**, 683–700 (1997)
4. Steblyanko, P., Shevchenko, Y.: Computational methods in stationary and non-stationary thermal-plasticity problems. In: *ETS-Encyclopedia of Thermal Stresses*, vol. 7, pp. 630–636. Springer, New York (2014)



# Plane Scattering Problem for an Inclusion of Non-classical Shape with a Thin Interphase Layer

Roman Kushnir<sup>1</sup>(✉), Yaroslav Kunets<sup>1</sup>, Valeriy Matus<sup>1</sup>,  
and Oleksandr Trofymchuk<sup>2</sup>

<sup>1</sup> Pidstryhach Institute for Applied Problems of Mechanics and Mathematics,  
Ukrainian National Academy of Sciences, Lviv, Ukraine  
dyrector@iapmm.lviv.ua

<sup>2</sup> Institute of Telecommunications and Global Information Space,  
Ukrainian National Academy of Sciences, Kiev, Ukraine

**Abstract.** The null-field method is applied to two-dimensional problems on P- and SV-waves scattering on an elastic inclusion of non-classical shape with a thin interphase layer of low rigidity. The interaction between the inclusion and its surrounding is modeled by means of the effective conditions imposed on the contour of the inclusion. The amplitudes of the scattering waves are analyzed in a far-wave field.

**Keywords:** Scattering of P- or SV-waves · Elastic inclusion of Non-classical cross-section · Thin interphase layer · Effective boundary condition · Null-field approach

## 1 Introduction

Solutions of problems on scattering of elastic waves on local nonhomogeneities are important for proper mathematical modeling of wave generation processes in matrix- and fiber-composites. One of the features of such materials is the occurrence of zones with slackening of connection between the structural elements. In [1–4], the contact imperfections between the elements of a fiber composite were modeled by a thin interphase layer of constant thickness. The vast majority of relevant research papers are focused on structures with elastic filling compounds of classical shapes, e.g., the circular [2, 3] or spherical [4, 5] ones. The interphase layer was either treated as an elastic solid perfectly connected with both a matrix and a fiber or simulated in its interaction with the surrounding by means of effective imperfect conditions on the interface between the matrix and inclusion.

The null-field method can be regarded as an efficient tool for the analysis of scattering problems for the waves of different physical nature on object of complex shape. By this means, the interaction of elastic waves with volumetric inclusions have been usually considered under the conditions of perfect contact between the nonhomogeneity and the surrounding. In [6], this method has been employed for the scattering of SH-waves in the presence of a thin piezoelectric interlayer. Herein, the same

method is extended to the case of P- an SV-waves scattering on an inclusion of non-classical shape under the presence of a thin elastic interphase layer of variable thickness and small rigidity.

## 2 Problem Formulation and Scattered Far Field

Consider a homogeneous unbounded elastic solid (a matrix) in two dimensions with density  $\rho_1$  and Lamé moduli  $\lambda_1$  and  $\mu_1$ . Assume the solid to contain an inclusion  $W_2$  of a non-classical shape with the corresponding material parameters  $\rho_2, \lambda_2, \mu_2$ . The inclusion is coated by a thin elastic layer  $W_0$  with parameters  $\rho_0, \lambda_0, \mu_0$  (Fig. 1). The elastic system undergoes the steady-state oscillations in time. In what follows, the time multiplier  $\exp(-i\omega t)$  is omitted, where  $\omega$  is the angular frequency and  $t$  is time. The displacement vectors  $\mathbf{u}_j(\mathbf{x}), j = 0, 1, 2, \mathbf{u}_1(\mathbf{x}) = \mathbf{u}^{in}(\mathbf{x}) + \mathbf{u}^{sc}(\mathbf{x})$ , in the composite meet the two-dimensional motion equations:

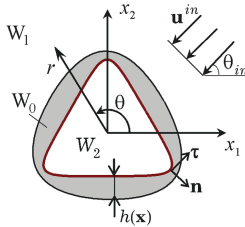


Fig. 1. Problem configuration

$$k_{pj}^{-2} \nabla \nabla \cdot \mathbf{u}_j(\mathbf{x}) + k_{sj}^{-2} \nabla \times \nabla \times \mathbf{u}_j(\mathbf{x}) + \mathbf{u}_j(\mathbf{x}) = 0, \quad \mathbf{x} \in W_j, \quad j = 1, 2, \quad (1)$$

$$(\lambda_0 + \mu_0) \nabla \nabla \cdot \mathbf{u}_0(\mathbf{x}) + \mu_0 \nabla^2 \mathbf{u}_0(\mathbf{x}) + \omega \rho_0 \mathbf{u}_0(\mathbf{x}) = 0, \quad \mathbf{x} \in W_0,$$

where  $\mathbf{x} = (x_1, x_2)$  are Cartesian coordinates,  $\mathbf{u}^{in}(\mathbf{x})$  is a wave that incident upon the inclusion,  $k_{pj} = \omega [\rho_j / (\lambda_j + 2\mu_j)]^{1/2}$  and  $k_{sj} = \omega (\rho_j / \mu_j)^{1/2}$ ,  $j = 1, 2$ , are the wave numbers of the P- and SV-waves in the composite. The scattered field  $\mathbf{u}^{sc}(\mathbf{x})$  meets the radiation conditions at infinity [1]

$$\mathbf{u}^{sc}(\mathbf{x}) = \sum_{\alpha=p,s} \frac{\exp(ik_{\alpha 1} r + i\pi/4)}{(8\pi k_{\alpha 1} r)^{1/2}} \mathbf{f}^\alpha(\omega, \theta) + O(r^{-1}), \quad r \rightarrow \infty, \quad (2)$$

$$x_1 = r \cos \theta, \quad x_2 = r \sin \theta, \quad 0 \leq \theta \leq 2\pi,$$

where  $\mathbf{f}^\alpha(\omega, \theta)$  are vectors of complex scattering amplitude for the longitudinal ( $\alpha = p$ ) an transversal ( $\alpha = s$ ) waves,  $(r, \theta)$  are polar coordinates.

The wave numbers of the matrix and inclusion, the thickness of the layer  $h(\mathbf{x})$  and its elastic parameters meet the conditions:

$$k_{\alpha j} \max_{\mathbf{x} \in \partial W_2} |h(\mathbf{x})| \leq 1, \quad \alpha = p, s, \quad j = 1, 2,$$

$$\varepsilon = a^{-1} \max_{\mathbf{x} \in \partial W_2} h(\mathbf{x}) \leq 1, \quad \max(\lambda_0, \mu_0) / \max(\lambda_j, \mu_j) \ll 1, \quad j = 1, 2,$$

where  $\varepsilon$  is a small dimensionless parameter,  $a$  is a characteristic size of the domain  $W_2$ . Under such conditions, the dynamic interaction between the thin layer and its surrounding can be asymptotically modeled by means of effective contact conditions on the contour of the inclusion  $S = \partial W_2$  [7]:

$$\begin{aligned} \mathbf{u}_1(\mathbf{X}) - \mathbf{u}_2(\mathbf{X}) &= h(\mathbf{X})(\eta_0^{-1} \mathbf{n}\mathbf{n} + \mu_0^{-1} \boldsymbol{\tau}\boldsymbol{\tau}) \cdot \mathbf{t}_1(\mathbf{u}_1), \quad \mathbf{x} \in S, \\ \mathbf{t}_1(\mathbf{u}_1) &= \mathbf{t}_2(\mathbf{u}_2), \quad \mathbf{x} \in S, \end{aligned} \quad (3)$$

where  $\mathbf{t}_j(\mathbf{u}_j) = \mathbf{n}\lambda_j \nabla \cdot \mathbf{u}_j + 2\mu_j \frac{\partial \mathbf{u}_j}{\partial n} + \mu_j \mathbf{n} \times (\nabla \times \mathbf{u}_j)$  is a stress vector,  $\mathbf{n}$  and  $\boldsymbol{\tau}$  are the external unit normal and a unit tangential vector on  $S$ ,  $\eta_0 = (\lambda_0 + 2\mu_0)$ .

Analytical-numerical solution to problem (1)–(3) in the far zone of wave scattering can be evaluated by means of the null-field method [6, 8]. The incident and scattered waves are to be represented as decompositions by cylindrical vector functions:

$$\mathbf{u}^{in}(\mathbf{x}) = u_0 \sum_{\alpha=p,s} \sum_{\sigma=1}^2 \sum_{m=0}^{\infty} a_{\alpha\sigma m}^{in} \text{Re} \boldsymbol{\Phi}_{\alpha\sigma m}^1(\mathbf{x}), \quad (4)$$

$$\mathbf{u}^{sc}(\mathbf{x}) = u_0 \sum_{\alpha=p,s} \sum_{\sigma=1}^2 \sum_{m=0}^{\infty} f_{\alpha\sigma m} \boldsymbol{\Phi}_{\alpha\sigma m}^1(\mathbf{x}) \quad |\mathbf{x}| > r_1, \quad (5)$$

$$\boldsymbol{\Phi}_{p\sigma m}^j(\mathbf{x}) = \varepsilon_m^{1/2} \nabla \psi_{p\sigma m}^j(\mathbf{x}), \quad \boldsymbol{\Phi}_{s\sigma m}^j(\mathbf{x}) = \varepsilon_m^{1/2} \nabla \times \mathbf{e}_z \psi_{s\sigma m}^j(\mathbf{x}), \quad j = 1, 2,$$

$$\psi_{\alpha\sigma m}^j(\mathbf{x}) = H_m^{(1)}(k_{\alpha j} r) C_{\sigma m}(\theta), \quad \text{Re} \psi_{\alpha\sigma m}^j(\mathbf{x}) = J_m(k_{\alpha j} r) C_{\sigma m}(\theta), \quad j = 1, 2,$$

$$C_{1m}(\theta) = \cos(m\theta), \quad C_{2m}(\theta) = \sin(m\theta),$$

where  $u_0$  is the amplitude of the incident wave,  $r_1$  is the radius of a circle circumscribing the scatterer,  $(\mathbf{e}_r, \mathbf{e}_\theta, \mathbf{e}_z)$  are the unit vectors of the cylindrical coordinate system,  $J_m(x)$  and  $H_m^{(1)}(x)$  are Bessel and Hankel functions of the first kind and order  $m$ , respectively,  $\varepsilon_m = 2 - \delta_{m0}$ ,  $\delta_{mn}$  is the Kronecker delta. The relation between the known coefficients  $a_{\alpha\sigma m}^{in}$  in the series for an incident wave and the quested-for coefficients  $f_{\alpha\sigma m}$  in the series for a scattered wave, in view of fixed incidence and observation angles,  $\theta_{in}$  and  $\theta$ , can be expressed through the transition matrix with elements  $T_{\alpha\sigma m, \alpha' \sigma' m'}$  of the form

$$f_{\alpha\sigma m} = \sum_{\alpha', \sigma', m'} T_{\alpha\sigma m, \alpha' \sigma' m'} a_{\alpha' \sigma' m'}^{in} \quad (6)$$

For an incident plane P-wave, Eq. (4) implies

$$\mathbf{u}^{in}(\mathbf{x}) = u_0 \mathbf{g} \exp(ik_{p1} \mathbf{g} \cdot \mathbf{x}), \quad a_{p\sigma m}^{in} = \frac{\varepsilon_m^{1/2} C_{\sigma m}(\theta_{in})}{i^{m+1} k_{p1}}, \quad a_{s\sigma m}^{in} = 0.$$

In the case of an SV-wave, we have

$$\mathbf{u}^{in}(\mathbf{x}) = -u_0 \mathbf{g} \times \mathbf{e}_z \exp(ik_{s1} \mathbf{g} \cdot \mathbf{x}), \quad a_{p\sigma m}^{in} = 0, \quad a_{s\sigma m}^{in} = \frac{\varepsilon_m^{1/2}}{i^{m-1} k_{s1}} C_{\sigma m}(\theta_{in}),$$

where the unit vector  $\mathbf{g} = -(\cos \theta_{in}, \sin \theta_{in})$  determines the direction of the wave incidence.

By making use of the known internal and external boundary-integral representations of the wave fields [8], we obtain a system of equations for the null-field method:

$$\int_S [\mathbf{u}_1 \cdot \mathbf{t}_1(\Phi_{\alpha\sigma m}^1) - \Phi_{\alpha\sigma m}^1 \cdot \mathbf{t}_1(\mathbf{u}_1)] dS = 4iu_0 \mu_1 k_{s1}^2 a_{\alpha\sigma m}^{in}, \quad (7)$$

$$\int_S [\mathbf{u}_2 \cdot \mathbf{t}_2(\text{Re}\Phi_{\alpha\sigma m}^2) - \mathbf{t}_2(\mathbf{u}_2) \cdot \text{Re}\Phi_{\alpha\sigma m}^2] dS = 0,$$

$$\int_S [\mathbf{u}_1 \cdot \mathbf{t}_1(\text{Re}\Phi_{\alpha\sigma m}^1) - \mathbf{t}_1(\mathbf{u}_1) \cdot \text{Re}\Phi_{\alpha\sigma m}^1] dS = -4iu_0 \mu_1 k_{s1}^2 f_{\alpha\sigma m}, \quad (8)$$

$$\alpha = p, s, \quad \sigma = 1, 2, \quad m = \overline{0, \infty}.$$

The unknown displacements and stresses on the contour of an inclusion can be found from the relations (7) in the form of series by the system of trigonometric functions:

$$\mathbf{u}_1(\mathbf{x}) - \mathbf{u}_2(\mathbf{x}) = u_0 \sum_{\sigma'=1}^2 \sum_{m'=0}^{\infty} \mathbf{x}_{1\sigma'm'} C_{\sigma'm'}(\theta),$$

$$\mathbf{u}_2(\mathbf{X}) = u_0 \sum_{\sigma'=1}^2 \sum_{m'=0}^{\infty} \mathbf{x}_{2\sigma'm'} C_{\sigma'm'}(\theta), \quad \mathbf{X} \in S, \quad (9)$$

$$\mathbf{x}_{j\sigma'm'} = \sum_{\alpha'=p,s} x_{j\alpha'\sigma'm'} \mathbf{e}_{\alpha'}, \quad \mathbf{e}_p \equiv \mathbf{n} \quad \mathbf{e}_s \equiv \boldsymbol{\tau}, \quad j = 1, 2.$$

Substituting (9) into the null-field Eq. (7) with account for the contact conditions (3), we derive a system of linear algebraic equations of infinite order for determination of the coefficients  $x_{jp\sigma'm'}$  and  $x_{js\sigma'm'}$ :

$$\begin{aligned} \sum_{\alpha', \sigma', m'} \left( a_{\alpha \sigma m, \alpha' \sigma' m'}^1 x_{1\alpha' \sigma' m'} + a_{\alpha \sigma m, \alpha' \sigma' m'}^2 x_{2\alpha' \sigma' m'} \right) &= 4ik_{s1}^2 \mu_1 a_{\alpha \sigma m}^{in} \\ \sum_{\alpha', \sigma', m'} \left( a_{\alpha \sigma m, \alpha' \sigma' m'}^3 x_{1\alpha' \sigma' m'} + a_{\alpha \sigma m, \alpha' \sigma' m'}^4 x_{2\alpha' \sigma' m'} \right) &= 0, \end{aligned} \quad (10)$$

$$\alpha = p, s, \quad \sigma = 1, 2, \quad m = \overline{0, \infty};$$

$$\begin{aligned} a_{\alpha \sigma m, \alpha' \sigma' m'}^1 &= \mathbf{e}_{\alpha'} \cdot \int_S \mathbf{t}_1(\Phi_{\alpha \sigma m}^1) \cdot (\mathbf{nn} + \tau\tau) C_{\sigma' m'}(\theta) dS \\ &\quad - \mathbf{e}_{\alpha'} \cdot \int_S h^{-1}(\theta) (\eta_0 \mathbf{nn} + \mu_0 \tau\tau) \cdot \Phi_{\alpha \sigma m}^1 C_{\sigma' m'}(\theta) dS \\ a_{\alpha \sigma m, \alpha' \sigma' m'}^2 &= \mathbf{e}_{\alpha'} \cdot \int_S \mathbf{t}_1(\Phi_{\alpha \sigma m}^1) C_{\sigma' m'}(\theta) dS, \\ a_{\alpha \sigma m, \alpha' \sigma' m'}^3 &= -\mathbf{e}_{\alpha'} \cdot \int_S (\eta_0 \mathbf{nn} + \mu_0 \tau\tau) \cdot \operatorname{Re} \Phi_{\alpha \sigma m}^2 \frac{C_{\sigma' m'}(\theta)}{h(\theta)} dS, \\ a_{\alpha \sigma m, \alpha' \sigma' m'}^4 &= \mathbf{e}_{\alpha'} \cdot \int_S \mathbf{t}_2(\operatorname{Re} \Phi_{\alpha \sigma m}^2) C_{\sigma' m'}(\theta) dS. \end{aligned}$$

For the amplitudes of the wave fields, Eqs. (2) and (8) yield:

$$\begin{aligned} \mathbf{f}^p(\omega, \theta) &= u_0 f^p(\omega, \theta) \mathbf{e}_r, \quad \mathbf{f}^s(\omega, \theta) = u_0 f^s(\omega, \theta) \mathbf{e}_\theta, \\ f^\alpha(\omega, \theta) &= \frac{(-1)^{\delta_{zs}} i k_{\alpha 1}}{u_0 \mu_1 k_{s1}^2} \sum_{\sigma, m} \varepsilon_m^{1/2} i^{-m} C_{\sigma m}(\theta) \int_S [\mathbf{u}_1 \cdot \mathbf{t}_1(\operatorname{Re} \Phi_{\alpha \sigma m}^1) - \\ &\quad - \mathbf{t}_1(\mathbf{u}_1) \cdot \operatorname{Re} \Phi_{\alpha \sigma m}^1] dS. \end{aligned} \quad (11)$$

Representation (11) with account for (9) can be given in the form

$$f^\alpha(\omega, \theta) = 4(-1)^{\delta_{zs}} k_{\alpha 1} \sum_{\sigma, m} \sum_{\alpha', \sigma', m'} \varepsilon_m^{1/2} i^{-m} C_{\sigma m}(\theta) T_{\alpha \sigma m, \alpha' \sigma' m'} a_{\alpha' \sigma' m'}^{in},$$

where elements  $T_{\alpha \sigma m, \alpha' \sigma' m'}$  of T-matrix are related to the inverse matrix of system (10).

### 3 Numerical Simulation and Conclusions

A solution of system (10) is constructed by means of the reduction method. We analyzed the amplitudes of P- and SV-waves scattering on an inclusion of circular, elliptic, square and triangular shapes with smoothed angles. For the considered scatters, the order of reduction  $M$  of system (10) was selected as  $M = 6 + m_d$  at  $k_{p1} a \leq 3$  and

$M = E(2ka) + m_d$  at  $3 < k_p a \leq 5$ , where  $E(x)$  is an integer part of  $x$ . Parameter  $m_d$  was selected from a numerical experiment.

It is shown that for small rigidity of the interphase layer and different mechanical properties of the matrix and the inclusion, the spectra of scattering amplitude exhibit clearly defined low-frequency resonance induced by the rotational oscillations of the fiber as a rigid solid. Beyond this resonance, the scattering amplitude is nearly identical to the scattering amplitude on a void of corresponding shape. If the material mismatch parameter of the thin interphase layer is comparative to its thickness, the spectra of scattering amplitudes do not exhibit the resonance behavior in the ranges of low and medium frequencies. When increasing the wave dimension of the scatterer, the effect of the interphase layer is neglected.

The corrugating of an interphase layer coating a circular inclusion does not have a critical effect in the amplitudes of scattered waves, with an exception for the ranges of resonant frequencies, where this effect is significant. Under the bistatic probing at the resonant frequencies of inclusions with soft coating, when the corrugating order is greater than four periods of the sinusoid, the amplitudes of scattered waves are rather the same as for a coating of constant thickness  $0.75\varepsilon$ .

## References

1. Martin, P.A.: Boundary integral equations for the scattering of elastic waves by elastic inclusions with thin interface layers. *J. Nondestruct. Eval.* **11**, 167–174 (1992)
2. Wong, D.C., Sung, J.C.: Dynamic response of an inclusion with compliant interface in an elastic medium due to a plane shear wave. *Appl. Math. Model.* **18**, 3–13 (1994)
3. Wang, X., Sudak, L.J.: Scattering of elastic waves by multiple elastic circular cylinders with imperfect interface. *Waves Random Complex Media* **17**(2), 159–187 (2007)
4. Butrak, I.O., Kil'nitskaya, T.I., Mykhas'kiv, V.V.: The scattering of an harmonic elastic wave by a volume inclusion with a thin interlayer. *J. Appl. Math. Mech.* **76**(3), 342–347 (2012)
5. Liu, Z., Zhang, X., Mao, Y., Zhu, Y.Y., Yang, Z., Chan, C.T., Sheng, P.: Locally resonant sonic materials. *Science* **289**, 1734–1736 (2000)
6. Kunets, Y., Kushnir, R., Matus, V., Trofymchuk, O.: Interaction of antiplane shear waves with elastic fiber in the presence of a thin interphase piezoceramic layer. In: Gdoutos, E. (ed.) *Proceedings of the First International Conference on Theoretical, Applied and Experimental Mechanics, Structural Integrity*, vol. 5, pp. 401–403. Springer, Berlin (2019)
7. Kit, H.S., Kunets, Y.I., Yemets, V.F.: Elastodynamic scattering from a thin-walled inclusion of low rigidity. *Int. J. Eng. Sci.* **37**, 331–345 (1999)
8. Matus, V., Kunets, Y., Mykhas'kiv, V., Boström, A., Zhang, Ch.: Wave propagation in 2-D elastic composites with partially debonded fibers by the null field approach. *Waves Random Complex Media* **19**, 654–669 (2009)



# Stress State in a Finite Cylinder with Outer Ring-Shaped Crack at Non-stationary Torsion

Oleksandr Demydov<sup>(✉)</sup>  and Vsevolod Popov

National University “Odesa Maritime Academy”, Odesa, Ukraine  
{alexandr.v.demidov, dr.vg.popov}@gmail.com

**Abstract.** The axisymmetric dynamic problem of determining the stress state in the vicinity of a ring-shaped crack in a finite cylinder is solved. The source of the loading is the rigid circular plate, which is joined with one of the cylinder ends and loaded by the time-dependent torque. The proposed method consists in the difference approximation of only the time derivative. To do this, specially selected non-equidistant nodes and special representation of the solution in these nodes are used. Such an approach allows the original problem to be reduced to a sequence of boundary value problems for the homogeneous Helmholtz equation. Each such problem is solved by using integral Fourier and Hankel transforms, with their subsequent reversal. As a result, integral representations were obtained for the angular displacement through unknown tangential stresses in the plane of the crack. From boundary condition on a crack, an integral equation is obtained, which, as a result of using the Weber-Sonin integral operator and a series of transformations, is reduced to the Fredholm integral equation of the second kind. The numerical solution found made it possible to obtain an approximate formula for calculating the stress intensity factor (SIF).

**Keywords:** Stress intensity factor · Ring-shaped crack · Finite cylinder · Finite differences · Non-stationary torsion

## 1 Introduction

The analysis of modern scientific literature shows that the stress state of cylindrical bodies with cracks under static loading has been studied sufficiently enough, but works with the analysis of the stress state under dynamic loading conditions is much smaller. As a rule, the researchers study cylinders of infinite length [1–3].

The complexity of theoretical studies of dynamic problems is due to the necessity of using the Laplace integral transform in time with subsequent numerical inversion. However, this task is not only mathematically complicated, but incorrect.

These difficulties can be avoided by use mixed numerical-experimental methods. In [4], the dynamic tension and in [5] the dynamic torsion of finite cylinders with ring cracks was investigated. But these methods, like all the experimental ones, are characterized by the disadvantages associated with the need to carry out experiments for each particular sample. This complicates the study of the impact of cylinder geometric dimensions on SIF values.



Recently, there have appeared works in which the modified method of finite difference in time is applied [6]. Using this method, in this paper, the problem of determining the SIN in the vicinity of a ring-shaped crack in a finite cylinder under the action of torque is solved. So far, such a problem has been considered only in a stationary formulation [7] and for a harmonic moment [8, 9].

## 2 Problem Formulation

Consider an isotropic finite elastic cylinder with height  $a$  and radius  $r_0$  (Fig. 1). The cylinder is related to the cylindrical coordinate system, whose centre coincides with the centre of the bottom end, and the axis  $Oz$  with the axis of the cylinder.

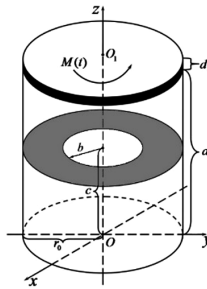


Fig. 1. Cylinder with outer ring-shaped crack.

The bottom end of the cylinder is rigidly fixed and its top end is joined with a rigid plate with thickness  $d$  and the same radius. The plate suffers the action of a time-dependent torsional moment  $M(t)$ . The cylinder contains a ring-shaped crack parallel to its ends and occupies the region  $z = c, b \leq r \leq r_0, 0 \leq \varphi \leq 2\pi$ . The lateral surface of the cylinder and the surface of the crack are free of stresses.

The cylinder is in state of the axisymmetric torsional deformation and only the angular displacement  $\bar{w}(r, z, t)$  will be nonzero. Next, to formulate the initial boundary value problem, we proceed to dimensionless quantities using the formulas:

$$\bar{w}(r, z, t) = r_0 \cdot w(\eta, \zeta, \tau), \quad \gamma = a/r_0, \quad l = c/a, \quad \beta = b/r_0$$

$$r = r_0 \eta, \quad 0 \leq \eta \leq 1, \quad z = a \zeta, \quad 0 \leq \zeta \leq 1, \quad t = r_0 \tau / c_2, \quad \tau \in (0, +\infty), \quad c_2^2 = G \cdot \rho^{-1},$$

where  $\rho, G$ —density and shear modulus for the cylinder material.

Then, dimensionless displacement will satisfy the equation with zero initial conditions:

$$D_{\eta\zeta} w = \frac{\partial^2 w}{\partial \tau^2}, \quad D_{\eta\zeta} = \frac{\partial^2}{\partial \eta^2} + \frac{1}{\eta} \frac{\partial}{\partial \eta} - \frac{1}{\eta^2} + \frac{1}{\gamma^2} \frac{\partial^2}{\partial \zeta^2}. \tag{1}$$

We formulate boundary conditions in relative dimensionless quantities.

On the cylinder ends, they have the form:

$$w|_{\zeta=0} = 0, \quad w|_{\zeta=1} = \alpha(\tau)\eta, \quad 0 \leq \eta \leq 1, \quad \tau \in [0, +\infty), \quad (2)$$

where  $\alpha(\tau)$ —unknown angle of rotation of the plate. It is determined from the equation of the motion of the plate:

$$\pi\gamma m_0 \ddot{\alpha}(\tau) = 2(M_0(\tau) - M_R(\tau)), \quad \alpha(0) = 0, \quad \dot{\alpha}(0) = 0, \quad (3)$$

where  $m_0$ —a mass ratio of the plate and cylinder,  $M_0, M_R$ —dimensionless moments.

On the lateral surface of the cylinder, there must be fulfilled the equality:

$$\tau_{\varphi r}(1, \zeta, \tau) = 0, \quad 0 \leq \zeta \leq 1, \quad \tau \in [0, +\infty). \quad (4)$$

For the condition on the crack, we have:

$$\tau_{\varphi z}(\eta, l, \tau) = \chi(\eta, \tau), \quad \tau \in (0, +\infty), \quad \chi(\eta, \tau) = \bar{\chi}(r_0\eta, r_0\tau/c_2), \quad (5)$$

where  $\chi(\eta) \equiv 0, \beta \leq \eta \leq 1$ , and  $\bar{\chi}(r, t)$ —unknown tangential stresses acting in the crack plane.

To solve the formulated initial boundary value problem (1)–(5), we apply a method based on the difference approximation of time derivatives, detailed in [6]. For this purpose, we create a time grid:

$$\tau_k = \sum_{v=1}^k h_v, \quad h_v = \tau_k - \tau_{k-1}, \quad (\tau_0 = 0), \quad k = 1, 2, 3, \dots, h_i \neq h_j$$

We introduce the designation  $w(\eta, \zeta, \tau_k) = w_k(\eta, \zeta)$  and use the left-sided finite difference for time derivatives. Then, from zero initial conditions and Eq. (1), we find

$$w_0 = 0, \quad D_{\eta\zeta} w_1 = \frac{w_1}{h_1^2}, \quad D_{\eta\zeta} w_k - \frac{w_k}{h_k^2} = \frac{w_{k-2}}{h_k h_{k-1}} - \frac{w_{k-1}}{h_k} \left( \frac{1}{h_k} + \frac{1}{h_{k-1}} \right), \quad k = 2, 3, \dots \quad (6)$$

Next, according to [6], we write the angular displacement, the angle of rotation of the plate, the stresses in the cylinder and the moment in the form of a linear combination of new functions:

$$w_k = \sum_{v=1}^k C_{kv} U_v, \quad \alpha_k = \sum_{v=1}^k C_{kv} A_v, \quad \tau_{\varphi rk} = \sum_{v=1}^k C_{kv} \tau_{\varphi rv}, \quad \tau_{\varphi zk} = \sum_{v=1}^k C_{kv} \tau_{\varphi zv}, \quad (7)$$

$$M_{0k} = \sum_{v=1}^k C_{kv} \mu_{0v},$$

where  $C_{kv}$  determined by the formulas:

$$C_{kk} = 1, \quad k = 1, 2, 3, \dots, \quad C_{k,k-1} = \frac{h_{k-1}}{h_{k-1} - h_k}, \quad k = 2, 3, \dots$$

$$C_{k,v} = \frac{h_v^2}{h_k^2 - h_v^2} \cdot \left( \frac{h_k}{h_{k-1}} C_{k-2,v} - \left( 1 + \frac{h_k}{h_{k-1}} \right) C_{k-1,v} \right), \quad k = 3, 4, \dots; \quad v = 1, 2, \dots, k - 2.$$

Then the functions  $U_v$  satisfy the homogeneous Helmholtz equation

$$D_{\eta\zeta} U_v - \kappa_v^2 U_v = 0, \quad v = 1, 2, 3, \dots, \quad \kappa_v = h_v^{-1}. \tag{8}$$

The boundary conditions on the cylinder surface for these functions can be written as follows:

$$U_v|_{\zeta=0} = 0, \quad U_v|_{\zeta=1} = A_v \eta, \quad \tau_{\varphi_{rv}}|_{\eta=1} = 0. \tag{9}$$

The conditions for the crack will take the form:

$$\tau_{\varphi_{zv}}|_{\zeta=l} = \chi_v(\eta), \quad 0 \leq \eta \leq 1, \quad \chi_v(\eta) \equiv 0, \quad \beta \leq \eta \leq 1, \quad \chi_k = \sum_{v=1}^k C_{kv} \chi_v. \tag{10}$$

And Eq. (3) takes the form:

$$\pi \gamma m_0 \chi_v^2 A_v = 2(\mu_{0v} - \mu_{Rv}), \quad \mu_{Rv}(\tau) = 2\pi \int_0^1 \eta^2 \tau_{\varphi_{zv}}|_{\zeta=1} d\eta, \tag{11}$$

where  $\mu_{0v}$  can be found from the recurrence relation.

### 3 Solution of the Problem

The solution of the boundary value problem (7)—(11) is represented in the form:

$$U_v(\eta, \zeta) = U_v^0(\eta, \zeta) + U_v^1(\eta, \zeta), \quad U_v^0(\eta, \zeta) = A_v \eta \frac{\text{sh}(\gamma \zeta \chi_v)}{\text{sh}(\gamma \chi_v)}. \tag{12}$$

The first term is the solution to the problem in the absence of crack. The second term is the solution to Eq. (8). It satisfies the zero conditions on the cylinder ends and lateral surface and on the surface of the crack it satisfies the condition:

$$\tau_{\varphi_{zv}}^1(\eta, l) = \chi_v(\eta) - \tau_{\varphi_{zv}}^0(\eta, l), \quad 0 \leq \eta \leq 1. \tag{13}$$

The functions  $U_v^1(\eta, \zeta)$  are found separately for the parts of the cylinder separated by the crack plane:

$$U_v^1(\eta, \zeta) = U_v^-(\eta, \zeta), \quad \zeta \in [0, l), \quad U_v^1(\eta, \zeta) = U_v^+(\eta, \zeta), \quad \zeta \in (l, 1]. \quad (14)$$

In order to find  $U_v^\pm(\eta, \zeta)$ , it is necessary to solve Eq. (8) with boundary conditions:

$$\begin{aligned} U_v^-|_{\zeta=0} = 0, \quad U_v^+|_{\zeta=1} = 0, \quad \tau_{\phi_{zv}}^\pm(\eta, l) = \chi_v(\eta) - \tau_{\phi_{zv}}^0(\eta, l), \quad 0 \leq \eta \leq \beta, \\ \tau_{\phi_{rv}}^-(1, \zeta) = 0, \quad 0 \leq \zeta \leq l, \quad \tau_{\phi_{rv}}^+(1, \zeta) = 0, \quad l \leq \zeta \leq 1. \end{aligned} \quad (15)$$

The solution to these boundary value problems is constructed by the integral transform method, similarly to [8]. It contains unknown tangential stresses acting in the crack plane. To find them, we obtain an integral equation for them by using the condition of continuity of angular displacements in the crack plane for  $\eta \in [0, \beta]$ .

By using the procedure proposed in [8], we reduce this equation to a Fredholm equation of the second kind for an unknown function associated with tangential stresses acting in the crack plane:

$$g_v(s) + \frac{1}{2\pi} \int_{-1}^1 g_v(y)[F(y-s) + Q(y-s)]dy = \frac{A_v s}{\text{ch}(\gamma \kappa_v(1-l))}, \quad (16)$$

where  $F(Y)$  and  $Q(Y)$  are expressed via uniformly convergence integrals and series, and  $A_v$  determined from Eq. (11).

An approximate solution to Eq. (16), as in [8, 10], is sought in the form of an interpolation polynomial. To solve Eq. (16), we approximate its integrals according to the quadrature Gauss-Legendre formula and obtain a system of linear algebraic equations for the values of the unknown function in the interpolation nodes. As a result of the solution of the system, the unknown function is approximated by the interpolation polynomial.

The solution of Eq. (16) allowed us to obtain a formula for calculating the dimensionless SIF:

$$K(\tau_k) = \frac{\overline{K}(t_k)}{G\sqrt{b}}, \quad K(\tau_k) = \sum_{v=1}^k C_{kv} K_v, \quad K_v = \frac{\sqrt{2}}{\pi} g_v(1). \quad (17)$$

### 4 Numerical Results

Using Formula (17), there was performed a numerical study of the dependence of the SIF on the dimensionless time  $\tau$  for different load cases. The time grid nodes were condensed near the point  $\tau = 0$ . The results of calculations are shown in Fig. 2 in the form of graphs of time dependencies of dimensionless SIFs. During these calculations

it was considered that the relative thickness of the plate is  $\delta = d/a = 0.1$ , the relative height of the cylinder is  $\gamma = a/r_0 = 2$ , the crack is located in the middle plane of the cylinder  $l = c/r_0 = 0.5$ , and the relative inner crack radius is  $b = b/r_0 = 0.5$ .

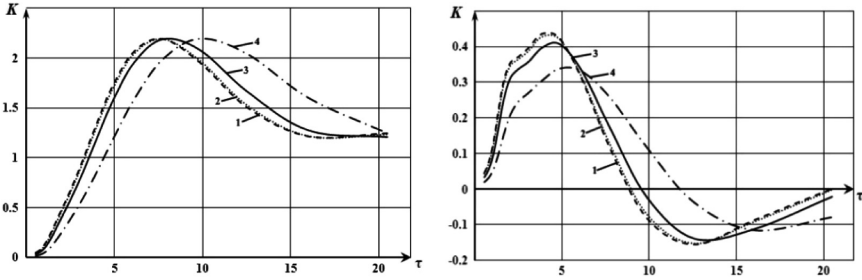


**Fig. 2.** Time dependence of dimensionless SIFs for different types of load:  $M_0(\tau) = H(\tau)$  (left);  $M_0(\tau) = H(\tau) - H(\tau - 1)$  (right).

The charts have been constructed for the case of the action of a suddenly applied torsional load (Fig. 2 (left)), and the case of specifying the torsional load by a suddenly applied moment of the unit length (Fig. 2 (right)). Curve 1–4 correspond to different values of the relative plate density:  $\bar{\rho} = \rho_{\text{plate}}/\rho_{\text{cyl}} : 0.1; 0.25; 1; 4$ .

From the graphs in Fig. 2 it can be seen that in all considered types of loading, during the transient process, the maximum SIF values are observed. When a sudden constant load is applied, this maximum is 1.5–2 times higher than the static value of SIF. Hence, it is most likely that the destruction of the cylinder will occur during the transient period. In addition, as can be seen from Fig. 2, an increase in the mass of the plate leads to an increase in the time until the SIF reaches its maximum value. However, it almost does not affect the maximum value itself, in the case of the action of a suddenly applied torsional load. In the case of the action of a load by a suddenly applied moment of the unit length, a decrease in the magnitude of the SIF maximum is observed. It can be explained by the fact that SIF does not have time to reach its maximum during the action of the load.

## 5 Conclusion

The paper proposes a method for solving the problem of determining the stress-strain state of an elastic finite cylindrical body with an outer ring-shaped crack that is under torsional loading. This technique is based on the differential approximation of the time derivative and use of a time grid with specially selected nodes. Numerical results demonstrate the effectiveness of such an approach when investigating the transient processes that occur immediately after load application. But arise some problems in applying this technique for large time intervals, due to the step-by-step accumulation of errors.

## References

1. Shindo, Y., Li, W.: Torsional impact response of a thick-walled cylinder with a circumferential edge crack. *J. Press. Vessel Technol.* **112**, 367–373 (1990)
2. Bai, H., Shah, A.H., Popplewell, N., Datta, S.K.: Scattering of guided waves by circumferential cracks in composite cylinders. *Int. J. Solids Struct.* **39**, 4583–4603 (2002)
3. Dimarogonas, A., Massouros, G.: Torsional vibration of a shaft with a circumferential crack. *Eng. Fract. Mech.* **15**, 439–444 (1981). [https://doi.org/10.1016/0013-7944\(81\)90069-2](https://doi.org/10.1016/0013-7944(81)90069-2)
4. Andreikiv, O.E., Boiko, V.M., Kovchyk, S.E., Khodan, I.V.: Dynamic tension of a cylindrical specimen with circumferential crack. *Mater. Sci.* **36**, 382–391 (2000). <https://doi.org/10.1007/BF02769599>
5. Ivanyts'kyi, Y.L., Boiko, V.M., Khodan', I.V., Shtayura, S.T.: Stressed state of a cylinder with external circular crack under dynamic torsion. *Mater. Sci.* **43**, 203–214 (2007). <https://doi.org/10.1007/s11003-007-0023-2>
6. Savruk, M.P.: New method for the solution of dynamic problems of the theory of elasticity and fracture mechanics. *Mater. Sci.* **39**, 465–471 (2003). <https://doi.org/10.1023/B:MASC.0000010922.84603.8d>
7. Popov, P.V.: The problem of the torsion of a finite cylinder with a ring-shaped crack. *Mashynoznavstvo.* **9**, 15–18 (2005). [in Ukrainian]
8. Popov, V.H.: Torsional oscillations of a finite elastic cylinder containing an outer circular crack. *Mater. Sci.* **47**, 746–756 (2012). <https://doi.org/10.1007/s11003-012-9452-7>
9. Vaisfeld, N.D.: A nonstationary dynamic problem of torsion of a hollow elastic cylinder. *Phys. Math. Sci.* **6**, 95–99 (2001) (in Russian)
10. Demydov, O.V., Popov, V.H.: Nonstationary torsion of the finite cylinder with circular crack. *Phys. Math. Sci.* **1**, 131–142 (2017) (in Ukrainian)



# Determination by Iterative Method of Diffraction Field at the Interaction Longitudinal Shear Wave with the System of Thin Rigid Inclusions

Vsevolod Popov<sup>(✉)</sup>

National University “Odesa Maritime Academy”, Odesa 65029, Ukraine  
dr.vg.popov@gmail.com

**Abstract.** The problem of the diffraction field determination is arising as a result of the longitudinal shear wave interaction with the thin rigid inclusions system arbitrarily situated in an infinity body was solved. Inclusions are considered to be fully coupled to the elastic medium and are moving. Unknown amplitudes of inclusions are determined from the equations of motion. The solution method is based on the submission diffraction field displacement as sum of discontinuous solutions to the Helmholtz equation, the constructed for each inclusion. As result the original problem is reduced to the system of the singular integral equations for unknown jumps of stresses on the inclusions surface, The iterative method of this system solving, where the zero approximation are the solutions of the integral equations for the single inclusions, is proposed. This integral equation for single inclusions are numerical solved the mechanical quadrature method. The final result is the approximate formulas for calculating stress intensity factors and the amplitudes of the oscillations.

**Keywords:** Thin ridged inclusion · Wave interaction · Integral equations · Iterative method

## 1 Introduction

Nowadays methods of mechanics of deformable bodies (potentials method, discontinuous solutions method, etc.) make it easy to reduce the problem of determination of wave fields in a body with system of thin inclusions or cracks to the solution systems of integral equations. But, the main attention is paid to bodies with systems of cracks. Research of dynamic stress state bodies with systems of thin rigid inclusions is much less. One of the first works in this direction, probably should be considered [1], where is solved the problem of diffraction of waves on two parallel thin rigid inclusions. Interaction of waves with periodic systems of curvilinear inclusions is considered in [2]. The method of explosive articles decisions wave fields and stress intensity factors (SIF) for elastic waves diffraction on systems of radially placed inclusions are defined of discontinuous solutions method in [3, 4]. Achievements in solving dynamic problems for bodies with arbitrary systems of inclusions are associated with the development of for boundary integral equations and boundary elements methods can be seen in

[5, 6]. But when applying methods, based on the reducing the original boundary value problems for bodies with inclusions to systems of integral equations, there is a significant problem. It consists in the need to solve systems of integral equations of large dimension. That's why during calculation of SIF and wave fields, authors of the limited case of a few, often just two, inclusions. Thus the determination of dynamic stress state and wave fields in bodies with systems of thin rigid inclusions is not completely solved. In the submitted article, iterative method for determination of SIF and wave fields in the interaction of the longitudinal shear waves of  $N$  inclusions.

## 2 Statement of the Problem

Let an elastic body that is in a longitudinal shear strain condition,  $N$  through thin rigid inclusions are situated. These inclusions are occupied on the plane  $Oxy$  by the segments length  $2d_k$  and with centers at points with coordinates  $(a_k, b_k), k = 1, 2, \dots, N$  (Fig. 1).

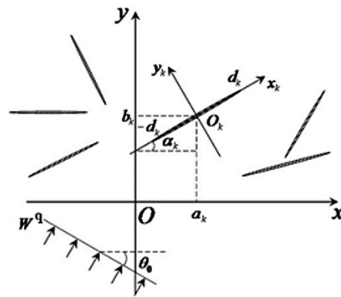


Fig. 1. The system of the thin ridged inclusions in the body

The wave of longitudinal shear interacts with them which is propagated in the body and causing the following displacement along axis  $Oz$ :

$$W^q(x, y) = A e^{i\kappa_2(x \cos \theta_0 + y \sin \theta_0)}, \quad \kappa_2^2 = \frac{\rho \omega^2}{G}, \tag{1}$$

where  $\omega$ —the frequency of the oscillations,  $\rho, G$ —density and modulus of shear of the body,  $\theta_0$ —the angle between the direction of propagation of the wave and the positive direction of the axis  $Ox$ . Multiplier  $e^{-i\omega t}$  which determines dependency from time here and then rejected. Let  $W(x, y)$  is the only different from 0 in the conditions of longitudinal shear strain component of the vector of displacements caused by waves reflected from the defects. Then it must to satisfy the Helmholtz equation.

$$\Delta W + \kappa_2^2 W = 0, \tag{2}$$

where  $\Delta$ —the Laplace operator in a system of coordinates  $Oxy$ .



This equation must be seen with conditions on the inclusions for the formulation that the local coordinate systems  $O_k x_k y_k$  connected with each of them. It is assumed that inclusion is completely coupled with an elastic medium that leads to equation

$$W_k(x_k, 0) = c_k - W_k^q(x_k, 0), W_k^q(x_k, 0) = -Ae^{ik_2 z_{0k}}, \tag{3}$$

$$z_{0k} = a_k \cos \theta_0 + b_k \sin \theta_0 + x_k \cos(\alpha_k - \theta_0) - y_k \sin(\alpha_k - \theta_0), \quad k = 1, 2, 3, \dots, N.$$

Also the surface impurities cause a discontinuity stress unknown jumping which denomination

$$\tau_{zy_k}(x_k, +0) - \tau_{zy_k}(x_k, -0) = \chi_{1k}(x_k), -d_k < x_k < d_k, k = 1, 2, \dots, N. \tag{4}$$

In equality (3) consists of -unknown displacement inclusions under the influence of propagating wave. They are determined from the equations of motion of inclusions, which in the case of harmonic oscillation are of the form

$$m_k \omega^2 c_k = \int_{-d_k}^{d_k} \chi_{1k}(x_k) dx_k, \quad k = 1, 2, \dots, N \tag{5}$$

where  $m_k$ -mass of  $k$ -th inclusion.

When formulated conditions the problem of determination the displacement and stress of the diffraction field in the body and SIF for inclusions is posed.

### 3 Solution of the Problem

For the solution of the problem for each inclusion with a number  $l$  in a coordinate system  $O_l x_l y_l$ , connected with it, of discontinuous solutions of Eq. (2) [7, 8] from jumping (4) are built

$$W_l^d(x_l, y_l) = \int_{-d_l}^{d_l} \frac{\chi_{1l}(\eta)}{G} r_2(\eta - x_l, y_l) d\eta, \quad l = 1, 2, \dots, N. \tag{6}$$

Displacement of the scattered wave field in the coordinate system  $Oxy$  is represented in the form of

$$W(x, y) = \sum_{l=1}^N W_l^g(x, y), \tag{7}$$

where  $W_l^g(x, y)$  are obtained from (6) as a result of the  $l$  coordinate transformation. But in order to use the formulas (7) it is necessary to determine the unknown jumps of

stress (4) on the inclusions. For determination of the unknown jumps  $\chi_{1l}(x_l)$  from the conditions (3) the system of integral equations must be obtained. That the received system has received singularity Cauchy type, (3) is replaced by the following equivalent equalities

$$\frac{\partial W_k}{\partial x_k}(x_k, 0) = -\frac{\partial W_k^q}{\partial x_k}(x_k, 0), W_k(-d_k, 0) = c_k - W_k^q(-d_k, 0), k = 1, 2, \dots, N. \quad (8)$$

After transformations of coordinates in the (7) and substitution to (8) the following system of singular integral equations with additional conditions is obtained:

$$\begin{aligned} & \frac{1}{2\pi} \int_{-1}^1 \varphi_k(\tau) \left( -\frac{1}{\tau-\zeta} + F_k(\tau-\zeta) \right) d\tau \\ & + \sum_{\substack{l=1 \\ l \neq k}}^N \frac{1}{2\pi} \varphi_l(\tau) R_{kl}(\tau, \zeta) d\tau = -i\kappa_0 A_0 \cos(\alpha_k - \theta_0) e^{i\kappa_0 r_0 k(\zeta)}, \\ & \frac{\gamma_k}{2\pi} \int_{-1}^1 \varphi_k(\tau) [\ln(1+\tau) + D_k(\tau+1)] d\tau + \sum_{\substack{l=1, \\ l \neq k \\ k=1,2,\dots,N}}^N \frac{\gamma_l}{2\pi} \int_{-1}^1 \varphi_l(\tau) D_{lk}(\tau) d\tau = c_{0k} - A_0 e^{i\kappa_0 r_0 k(-1)}, \end{aligned} \quad (9)$$

In this system, introduced the notation

$$\begin{aligned} \varphi_l(\tau) &= \chi_l(d_l \tau) / G, k = 1, 2, \dots, N; \eta = d_l \tau, x_k = d_k \zeta, \gamma_k = d_k / d \\ \kappa_0 &= \kappa_2 d, d = \max(d_1, d_2, \dots, d_N). \\ c_{0k} &= -\frac{1}{2\gamma_k h_{0k} \kappa_0^2 \rho_k} \int_{-1}^1 \varphi_k(\tau) d\tau, c_{0k} = \frac{c_k}{d}, \bar{\rho}_k = \frac{\rho_k}{\rho}, h_{0k} = \frac{h_k}{d_k}. \end{aligned}$$

where  $h_k, \rho_k$  are the thickness and density of the material of  $k$ -th inclusion.

### 4 Iterative Method Solution

The system of integral Eqs. (9) can be solved approximately using the by the mechanical quadrature method, as in [3–6]. But the immediate use of this method requires solving a system of linear algebraic equations, which is proportional to the number of inclusions  $N$ . Therefore, the iterative method for solving the system (9) is proposed for elimination of this problem. For this, the zero approximation is solution of  $N$  separate equations for single inclusion. Then an iterative process continues by solving the next equations at every step

$$\begin{aligned}
 \frac{1}{2\pi} \int_{-1}^1 \varphi_k^{(i)}(\tau) \left( -\frac{1}{\tau-\zeta} + F_k(\tau-\zeta) \right) d\tau &= -i\kappa_0 A_0 \cos(\alpha_k - \theta_0) e^{i\kappa_0 r_{0k}(\zeta)} \\
 &\quad - \sum_{\substack{l=1 \\ l \neq k}}^N \frac{\gamma_l}{2\pi} \int_{-1}^1 \varphi_l^{(i-1)}(\tau) R_{kl}(\tau, \zeta) d\tau; \\
 \frac{\gamma_k}{2\pi} \int_{-1}^1 \varphi_k^{(i)}(\tau) (\ln(1+\tau) + D_k(\tau+1)) d\tau &= c_{0k}^{(i)} - A_0 e^{-i\kappa_0 r_{0k}(-1)} \\
 &\quad - \sum_{\substack{l=1 \\ l \neq k}}^N \frac{\gamma_l}{2\pi} \int_{-1}^1 \varphi_l^{(i-1)}(\tau) D_{kl}(\tau, \zeta) d\tau;
 \end{aligned} \tag{10}$$

Solution of integral Eqs. (10) is based on the representation of unknown functions in the form

$$\varphi_k^{(i)}(\tau) = \frac{\psi_k^{(i)}(\tau)}{\sqrt{1-\tau^2}}, \quad k = 1, 2, \dots, N, \quad i = 1, 2, \dots \tag{11}$$

The formula (11) provide an opportunity to numerically solve Eqs. (10) method of mechanical quadratures [9]. As a result, Eqs. (10) are reduced to the solution of systems of linear algebraic equations sequence that differ only in the right sides of. As it is known [10] stresses in the body around the thin rigid inclusions are described stress intensity factors  $K_l^\pm$  near its ends  $x_l = \pm d_l$ . After solving the system (10) their approximate value by results of the  $i$ -th iteration are calculated on formulas.

$$k_l^\pm = \frac{K_l^\pm}{G_l \sqrt{2d_l}} = \psi_l^{(i)}(\pm 1), \quad l = 1, 2, \dots, N \tag{12}$$

### 5 Results of Numerical Analyses

One of the main purposes of the numerical analysis was to study practical convergence of iterative method is proposed. This was a system with three inclusions of the same length  $2d$  is considered. Inclusions are placed at the sides of the proper triangle with sides long  $4d$ , as shown in Fig. 2 (left). The thickness and density of the inclusions here are of the implementation of the specified number of iterations. We can considered to be the same:  $h_{0k} = 0.05$ ,  $\bar{\rho}_{0k} = 1$ . It was assumed that plane wave of longitudinal shear, propagating along the positive direction of the axis. interacts with inclusions  $0y(\theta_0 = 90^\circ)$ .

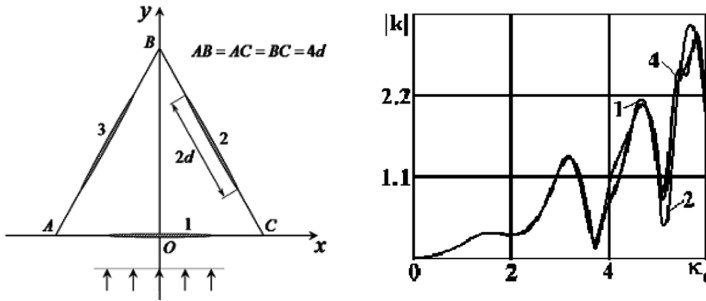


**Fig. 2.** The system of three inclusions (left); the dependence of SIF by dimensionless wave number for other numbers of iteration (right)

Figure 2 (right) shows the dependency graphs of absolute value of the dimensionless SIF  $|k_1| = |k_1^-| = |k_1^+|$  for first inclusion of the dimensionless wave number  $\kappa_0 = \kappa_2 d$ . Curve 1 corresponds to the values SIF obtained as a result of the immediate solution of the system of integral Eqs. (9) mechanical quadrature methods. Curves 2, 4 show the value of the SIF is obtained by the formula (12) as a result see that after 4 iterations the results are obtained by different methods almost do not differ. The continuation of the iterative process leads to the complete coincidence of the results. And at the frequencies of oscillations such that convergence results is observed already after two iterations.

## 6 Conclusions

The above results allow making the following general conclusions. Effective iterative method of solving the problem by definition stress condition and diffraction fields in body with arbitrary system of thin rigid inclusions at the interaction with the longitudinal shear waves. This method can be used for systems of inclusions with implicate geometry and sufficiently tightly placed inclusions. Numerical investigation has determined that the configuration of a system of inclusions, their size and relative locating substantially influence the value of the SIF. Interaction repeatedly reflected from inclusions of the waves provides dependence to SIF on the frequency of implicate shape with lots of maximums and minimums.

## References

1. Jain, D.L., Kanval, R.P.: Diffraction of elastic waves by two coplanar parallel rigid strips. *Int. J. Solids Struct.* **10**(11), 925–937 (1972). [https://doi.org/10.1016/0020-7225\(72\)90002-X](https://doi.org/10.1016/0020-7225(72)90002-X)
2. Nazarenko, O.M., Lozhkin, O.M.: Plane problem of diffraction of elastic harmonic waves on periodic curvilinear inserts. *Mater. Sci.* **43**(2), 249–255 (2007). <https://doi.org/10.1007/s11003-007-0028-x>

3. Popov, V.G.: Diffraction of elastic shear waves on radially distributed rigid inclusions. *Int. Appl. Mech.* **32**(8), 624–630 (1996). <https://doi.org/10.1007/BF02740760>
4. Popov, V.G.: Interaction of plane elastic waves with systems of radial defects [in Russian]. *Izv. Ross. Akad. Nauk. Mekh. Tverdogo Tela.* **4**, 118–129 (1999)
5. Liu, E., Zhang, Z.: Numerical study of elastic wave scattering by cracks or inclusions using the boundary integral equation method. *J. Comput. Acoust.* **9**(3), 1039–1054 (2001). <https://doi.org/10.1142/S0218396X01001315>
6. Lei, J., Yang, Q., Wang, Y.-S., Zhang, C.: An investigation of dynamic interaction between multiple cracks and inclusions by TDBEM. *Compos. Sci. Technol.* **69**(7–8), 1279–1285 (2009). <https://doi.org/10.1016/J.COMPSCITECH.2009.03.005>
7. Popov, V.G.: Comparison of displacement fields and stresses in the diffraction of elastic shear waves at various defects: crack and thin rigid inclusion [in Russian]. *Dyn. syst.* **12**, 35–41 (1993)
8. Popov, V.G.: Investigation of the fields of displacements and stresses in the case of diffraction of shear elastic waves on thin rigid exfoliated inclusions [in Russian]. *Izv. Ross. Akad. Nauk. Mekh. Tverdogo Tela.* **3**, 139–146 (1992)
9. Belotserkovskii, S.M., Lifanov, I.K.: Numerical methods in singular integral equations and their use in ferrodynamics, the theory of elasticity and electrodynamics [in Russian]. Nauka, Moscow (1985)
10. Sulym, H.T.: Foundations of the Mathematical theory of thermoelastic equilibrium of deformed bodies with thin inclusions [in Ukrainian]. *Doslidno-Vydavnychi Tsent NTSh, Lviv* (2007)



# Stress State Near Arbitrarily Oriented Cracks on the Continuation of a Rigid Inclusion Under Action of Longitudinal Shear Wave

A. S. Misharin<sup>(✉)</sup> and V. G. Popov

National University “Odessa Maritime Academy”, 8, Didrikhson Str., 65029  
Odessa, Ukraine

{as.mishandr, dr.vg.popov}@gmail.com

**Abstract.** The problem about determining of the dynamic stress intensity factors (SIF) for the cracks that are located at an angle from the ends of the inclusion is solved. The inclusion is located in an unbounded elastic body, in which the longitudinal shear harmonic waves are propagated. Unknown amplitude of inclusions are determined from the equations of motion. Boundary conditions are formed in the assumption that the inclusion is fully coupled with the medium (matrix), and the surface of cracks are not loaded. The method of the solution is based on the presentation of displacements in the body as a superposition of three discontinuous solutions which are built respectively to the cracks and the inclusion. As result the original problem is reduced to the system of the singular integral equations for unknown jumps of stresses and displacements to the defect. For the numerical solution of the system the method is developed. It takes into consider the real asymptotic of the unknown functions and uses the special quadrature formulas for singular integrals.

**Keywords:** Stress intensity factors · Singular integro-differential equations · Cracks · Inclusion · Elastic wave

## 1 Introduction

In the field of construction technology and mechanical engineering, the structures and parts of machines quite often contain elements or technological defects that can be considered as thin inclusions of high stiffness. But studies [1] show that thin stiff inclusions cause a significant concentration of stresses in the environment, which can lead to the formation of cracks propagating at certain angles relative to the plane of inclusion. The stress intensity factors (SIF) for cracks on the continuation of inclusion, which are located on the same line, in a static setting, were studied in research papers [2–4]. A similar problem for a half-plane with a crack on the continuation of the inclusion was solved in [5]. The problems of determining the dynamic stress state near the defects, which are thin inclusions, from the ends of which cracks propagate at certain angles, were hardly solved. This is associated with the difficulties that arise when solving integro-differential equations with fixed singularities. The problems of determining the dynamic stress state in the vicinity of V-shaped cracks and inclusions, as well as cracks in the form of polyline, were solved in research papers [6–8].

The same research papers also propose a numerical method for solving integral and integro-differential equations with fixed singularities. This method considers the real asymptotics of the solution in the vicinity of singular points and is based on the use of special quadrature formulas for singular integrals. In this paper, a similar method is used in solving the following problem.

## 2 Statement of the Problem

An elastic isotropic medium in a state of out-of-plane deformation is considered. It has a through defect in the form of absolutely stiff inclusion from the ends of which cracks propagate at arbitrary angles. In the plane  $Oxy$  the inclusion and cracks are located as shown in Fig. 1.

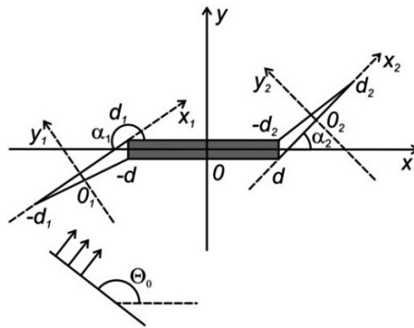


**Fig. 1.** The inclusion from the ends of which cracks propagate at arbitrary angles.

The defect interacts with a flat harmonic wave of longitudinal offset causing displacement:

$$w_0(x, y) = Ae^{i\kappa_2(x \cos \theta_0 + y \sin \theta_0)}, \quad \kappa_2^2 = \rho\omega^2/G \tag{1}$$

where  $\omega$ —the frequency of the oscillations,  $\rho, G$ —density and modulus of shear of the body. Multiplier  $e^{-i\omega t}$  which determines dependency from time here and then rejected. Under such conditions, the single non-zero  $z$ —component of the displacement vector, satisfies the Helmholtz equation:

$$\Delta w + \kappa_2^2 w = 0 \tag{2}$$

where  $\Delta$ —Laplace operator in the coordinate system  $Oxy$ .

To formulate the boundary conditions for a defect, let us associate the local coordinate system  $O_l x_l y_l, l = 1, 2$  with each crack, where the center of such coordinate system coincides with the middle of the corresponding crack (Fig. 1).

Let  $w_l(x_l, y_l)$ ,  $l = 1, 2$  be the displacement in the coordinate system associated with  $l$ —crack. Then, if there are no load on the crack edges, the following equations should be satisfied:

$$\tau_{yz}(x_l, 0) = 0, \quad x_l \in [-d_l, d_l], \quad l = 1, 2. \tag{3}$$

In addition, on the surface of cracks, the displacements  $w_l(x_l, y_l)$ ,  $l = 1, 2$  endure breaks with unknown jumps, for which the following designations are introduced:

$$w_l(x_l, +0) - w_l(x_l, -0) = \chi_l(x_l), \quad x_l \in [-d_l, d_l], \quad l = 1, 2. \tag{4}$$

Let us formulate the boundary conditions on inclusion from the conditions of ideal bonding:

$$w(x, 0) = a, \quad x \in [-d, d] \tag{5}$$

where  $a$ —unknown amplitude of longitudinal (along  $Oz$  axis) oscillations of inclusion. On the surface of inclusion, the stress  $\tau_{yz}(x, y)$  has a break with an unknown jump, for which the designation is introduced:

$$\tau_{yz}(x, +0) - \tau_{yz}(x, -0) = \chi(x), \quad x \in [-d, d]. \tag{6}$$

The unknown amplitude is determined from the following equation:

$$-m\omega^2 a = \int_{-d}^d \chi(\eta) d\eta + P, \quad m = 2d\rho_v h \tag{7}$$

### 3 Solution of the Problem

To solve the formulated problem in the coordinate system associated with defects, the discontinuous solutions of Eq. (2) with jumps (4) and (6) are constructed. These discontinuous solutions are found using the formulas [9]:

$$w^d(x, y) = \int_{-d}^d \frac{\chi(\eta)}{G} r_2(\eta - x, y) d\eta, \quad w_l^d(x_l, y_l) = \int_{-d_l}^{d_l} \chi_l(\eta) \frac{\partial}{\partial y_l} r_2(\eta - x_l, y_l) d\eta, \tag{8}$$

where  $r_2(\eta - x, y) = -i4^{-1}H_0^{(1)}(\kappa_2 \sqrt{(\eta - x)^2 + y^2})$ ,  $H_0^{(1)}(z)$ —Hankel function.

Displacement are searched as superposition:

$$w(x, y) = w^d(x, y) + w_1^g(x, y) + w_2^g(x, y), \tag{9}$$



where  $w_l^g(x, y)$ ,  $l = 1, 2$  are found by formulas (8) after transition to coordinates  $Oxy$ . In order to decisively determine the displacement of the diffraction field, it is necessary to find unknown jumps (4), (6). To do this, we need to use the conditions (3), (5). In this case, the equality (5) is replaced by two equivalent equalities:

$$\frac{\partial w^d(x, 0)}{\partial x} = 0, \quad w^d(d, 0) = a. \tag{10}$$

After substituting (9) into the boundary conditions (3) and (10), we obtain a system of integro-differential equations for the unknown jumps. This system, after extraction of singular components of kernels and transition to the interval  $[-1, 1]$  takes the following form:

$$\begin{cases} \frac{1}{2\pi} \int_{-1}^1 \left( \frac{Q(\tau, \zeta)}{\tau - \zeta} + G(\tau, \zeta) + R(\tau, \zeta) \right) F(\tau) d\tau + \frac{1}{2\pi} \int_{-1}^1 (\kappa_0^2 D \ln|\tau - \zeta| + R_0(\tau, \zeta)) \Phi(\tau) d\tau = Z(\zeta), \\ \frac{1}{2\pi} \int_{-1}^1 \varphi_0(\tau) [\gamma \ln|1 + \tau| + R_1(\tau)] d\tau - \frac{1}{\pi} \int_{-1}^1 \varphi_2(\tau) R_2(\tau) d\tau = -A_0 e^{-i\kappa_0 \gamma \cos \theta_0}, \end{cases} \tag{11}$$

$G(\tau, \zeta) = \{g_{lj}(\tau, \zeta)\}$ ,  $l, j = 0, 1, 2$ —the matrix, whose nonzero elements are equal:

$$\begin{aligned} g_{10}(\tau, \zeta) &= \gamma \sin \beta_1 \tau^+ / p_1(\tau^+, \zeta^-), \quad g_{20}(\tau, \zeta) = \gamma \sin \beta_2 \tau^- / p_2(\tau^-, \zeta^+), \\ g_{01}(\tau, \zeta) &= -\tau^- / p_1(\zeta^+, \tau^-), \quad g_{02}(\tau, \zeta) = \tau^+ / p_2(\zeta^-, \tau^+); \\ F(\tau) &= (\varphi_0(\tau), \varphi_1(\tau), \varphi_2(\tau))^T = (f_0(\tau), f_1(\tau), f_2(\tau))^T, \\ p_j(x, y) &= \gamma^2 x^2 + 2\gamma \gamma_j xy \cos \beta_j + \gamma_j^2 y^2, \quad j = 1, 2, \quad \tau^\pm = 1 \pm \tau, \quad \zeta^\pm = 1 \pm \zeta, \\ f_l(\tau) &= \chi_l(\eta) d_l^{-1}, \quad x_l = d_l \zeta, \quad \eta = d_l \tau, \quad \gamma_l = d_l b^{-1}, \quad f_0(\tau) = \chi(\eta) G, \quad \eta = d\tau, \quad \gamma = db^{-1}, \quad b = \max(d, d_l). \end{aligned}$$

### 4 Approximate Solution of a System of Integro-Differential Equations

The presence of singular component of the system (11) of fixed singularities affects the behavior of its solution in the vicinity of points  $\zeta = \pm 1$  [10]. The asymptotics of the solution in the neighborhood of these points is determined by the method described in [11]. As a result, it was found that unknown functions should be sought in the following form:

$$\begin{aligned} f_l(\tau) &= (1 + (-1)^l \tau)^{\delta_l} (1 - (-1)^l \tau)^{-1/2} \psi_l(\tau), \quad l = 1, 2, \quad f_0(\tau) \\ &= (1 + \tau)^{\delta_1} (1 - \tau)^{\delta_2} \psi_0(\tau), \end{aligned} \tag{12}$$

where power indicators are found by the following formulas:

$$\delta_l = -(\pi + 2\beta_l)/(2\pi + 2\beta_l), \quad 0 < \beta_l < \pi, \quad l = 1, 2, \quad \beta_1 = \alpha_1 - \pi, \quad \beta_2 = \alpha_2.$$

Moreover, for functions with such singularities to be solutions of the system (11), the following equalities must be fulfilled [11]:

$$\psi_1(1) = (\gamma_1/\gamma)^{\delta_1} \psi_0(-1), \quad \psi_2(-1) = (\gamma_2/\gamma)^{\delta_2} \psi_0(1). \tag{13}$$

and the functions  $\psi_l(\tau)$ ,  $l = 0, 1, 2$ , are considered to be such that they satisfy the Holder condition on the interval  $[-1, 1]$ . Further solution is based on the approximation of these functions by interpolation polynomials:

$$\psi_l(\tau) = \sum_{m=1}^n \psi_{lm} \frac{P_{ln}(\tau)}{(\tau - \tau_{lm})[P_{ln}(\tau_{lm})]^l}, \quad l = 0, 1, 2, \tag{14}$$

$\psi_{lm} = \psi_l(\tau_{lm})$ ,  $P_{0n}(\tau) = P_n^{\delta_2, \delta_1}(\tau)$ ,  $P_{1n}(\tau) = P_n^{-\delta_1, -1/2}(\tau)$ ,  $P_{2n}(\tau) = P_n^{-1/2, -\delta_2}(\tau)$ —Jacobi polynomials,  $\tau_{lm}$ —the roots of these polynomials.

For integrals with a Cauchy kernel, we apply the following quadrature formulas from [12]. Similar formulas for integrals with fixed singularities were obtained in [13]. To calculate integrals that contain directly unknown functions  $f_l(\tau)$ ,  $l = 0, 1, 2$ , and for integrals with a logarithmic function, the formulas from [6] are applied.

The application of quadrature formulas leads to the replacement of the system of integro-differential Eqs. (11) by a system of linear algebraic equations with respect to the values of functions  $\psi_l$ ,  $l = 0, 1, 2$  in the interpolation nodes.

For the destruction mechanics, the stress intensity factors (SIF) are of particular interest, whose approximate values are expressed by the following formulas through the solution of system (11):

$$k_l = K_l 2^{\delta_l - 1} G^{-1} / \sqrt{d_l} = \psi_l((-1)^l), \quad l = 1, 2. \tag{17}$$

## 5 Results of Numerical Analyses

When conducting a numerical implementation, the primary goal was to study the practical convergence of the proposed method of numerical solution. For this purpose, the defect shown in Fig. 1 was considered at  $\alpha_1 = \pi + \beta$ ,  $\alpha_2 = \beta$ ,  $\beta_1 = \beta_2 = \beta$ . Cracks and inclusion have the same length  $d = d_l$ ,  $l = 1, 2$ . Dimensionless SIF vales were calculated by formulas (17). And as a result of symmetry, we have that  $|k_1| = |k_2| = |k|$ . The calculation is performed at an angle  $\beta = 45^\circ$ . When receiving SIF values with an error not exceeding 0, 1% it suffices up to 20 interpolation nodes in (14). And for waves with a low frequency, such that, for a dimensionless wave number  $\kappa_0 \leq 2$  it suffices 5 nodes ( $\kappa_0 = \kappa_2 b$ ,  $b = \max(d, d_l)$ ).

A study of the influence of cracks location on the SIF value when changing the angle values  $\beta$  depending on the dimensionless value of the wave number was

conducted. Positions of the cracks is determined by the angle  $\beta$ , which they form with the plane of inclusion. Calculation results are shown in Fig. 2 for angles  $\beta = 5, 30, 60, 90, 120, 150, 175^\circ$ . At sharp angles, we observe a decrease in SIF values as the angle  $\beta$  increases. At obtuse angles, on the contrary, there is an increase in SIF values as the angle  $\beta$  increases. SIF values are minimal when the cracks are perpendicular to the inclusion. In general, as a result of the complexity of the wave field created by the reflection of waves from a defect, the dependence of SIF on frequency has significant maxima, the magnitude and position of which are affected by the configuration of the defect.

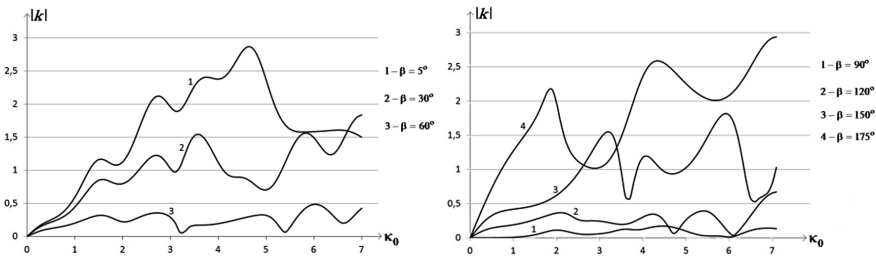


Fig. 2. Dependence of SIF on the position of cracks with respect to inclusion.

## 6 Conclusions

Taking into account the true asymptotics of solutions and the application of special quadrature formulas for singular integrals improves the convergence of numerical methods for solving singular equations. The conducted numerical analysis has established the significant influence of the position of cracks relative to the inclusion on the change of SIF.

## References

1. Sulim, G.T.: Fundamentals of the Mathematical Theory of Thermoelastic Equilibrium of Deformable Solids With Thin Inclusions. Research-published. NTSH Center, Lviv (2007)
2. Berezhnitsky, L.T., Panasyuk, V.V., Stashchuk, N.G.: Interaction of Rigid Linear Inclusions and Cracks in a Deformed Body. Science Dumka, Kiev (1983)
3. Berezhnitskii, L.T., Staschuk N.G.: Coefficients of Stress Intensity Near a Crack on the Extension of a Linear Rigid Inclusion. Dokl. Academy of Sciences of Ukraine. Ser. A. № 11, 30–46 (1981)
4. Berezhnitsky, L.T., Stashchuk, N.G., Gromyak, R.S.: On the determination of the critical size of a macrocrack arising on the extension of a linear rigid inclusion. Probl. Strength 2, 68–71 (1989)
5. Akopyan, V.N., Amirjanyan A.A.: Stress state of a half-plane with an absolutely rigid inclusions and cracks on the boundary. In: Proceedings of the National Academy of Sciences of Armenia. Mechanics, vol. 68(1), 25–36 (2015)

6. Popov, V.G.: The stressed state of two cracks emerging from one point with harmonic fluctuations of longitudinal displacement. *Izv. Ros. Akad. Nauk, Mekh. Tverd. Tela* № 2, 91–100 (2018)
7. Litvin, O.V., Popov, V.G.: The interaction of harmonic wave of longitudinal shear with v-shaped inclusion. *Math. Methods Phys. Mech. Fields. T.* **60**(1), 96–106 (2017)
8. Popov, V.G.: A crack in the shape of a three-link broken line under the action of a longitudinal shear wave. *J. Math. Sci.* **222**(2), 112–120 (2017)
9. Popov, V.G.: Comparison of displacement fields and stresses in the diffraction of elastic shear waves at various defects: crack and thin rigid inclusion. *Dyn. syst.* **12**, 35–41 (1993)
10. Duduchava, R. V.: *Integral Equations of Convolution with Discontinuous Presymbols, Singular Integral Equations with Fixed Singularities, and their Applications to Problems of Mechanics.* Razmadze Inst. of Math., Academy of Sciences of Gruz. SSR, Tbilisi (1979)
11. Popov, V.G.: Diffraction of elastic shear waves by the inclusion of a complex shape located in an unbounded elastic medium. In: *Hydroaeromechanics and the Theory of Elasticity: Numerical and Analytical Methods for Solving Problems of Hydroaerodynamics and Elasticity Theory*, pp. 121–127. Dnepropetr. state. Univ., Dnepropetrovsk (1986)
12. Andreev, A.V.: Direct numerical method for solving singular integral equations of the first kind with generalized kernels. *Izv. RAN. MTT* **1**, 126–146 (2005)
13. Misharin, A.S., Popov, V.G.: Stress state near arbitrarily oriented cracks on the continuation of a rigid inclusion under the action of the shear harmonic forces. In: *The Problems of Dynamics of Interaction of Deformable Media.* Institute of Mechanics, NAS RA, Yerevan (2018)



# Stress State of a Hollow Cylindrical Body with a System of Cracks Under Oscillations of Longitudinal Shear

Olga Kyrylova<sup>(✉)</sup> and Vsevolod Popov

National University “Odesa Maritime Academy”, Odesa, Ukraine  
{olga.i.kyrylova, dr.vg.popov}@gmail.com

**Abstract.** The problem of determining the stress state near the through-cracks in an infinite hollow cylinder of arbitrary cross-section under oscillations of longitudinal shear is solved. The method allows satisfying the conditions separately on the surface of cracks and on the borders of the cylinder. The solution scheme is based on the use of discontinuous solutions of equations of motion of elastic medium with jumps of displacements on the surface of defects. For this displacement are represented by the sums of discontinuous solutions, built for each defect, and an unknown characteristic function. Designed presentation enables fulfilling separately the boundary conditions on the surface of defects that leads to the set of systems of integral equations, which don't depend from the shape of the boundaries of the body. Then the unknown coefficients of represented characteristic function are determined from the conditions on the boundaries of the body by the collocation method.

**Keywords:** Hollow cylinder of arbitrary cross section · Harmonic oscillations · Crack · Stress intensity factors · The system of cracks

## 1 Introduction

Research of the stress state of bodies with cracks is actual for formulation the conditions for the fracture of bodies and diagnoses such defects, based on information about their influence on resonant frequency. The results obtained in this direction it is mainly up to infinity and semi-infinite bodies with defects [1–4]. Situations where the body occupy finite area, considered much less. This is due to the fact that when applying the method of boundary integral equations of the initial boundary value problems are reduced to the related systems of integral equations defined and surface defects and on the boundary of the body [5–7]. As a result, numerical solution essentially more complicated, especially in the case of systems defects and multiplies connected areas. Method that allowing independently consistently satisfying the boundary conditions on defects and on the surface of the body is proposed there.

## 2 Statement of the Problem

Hollow elastic cylindrical body with axis parallel to the axis  $Oz$  of the cross section plane  $xOy$  which is a two connected area that is bounded by arbitrary smooth curves is considered. These curves in a polar coordinate system, the pole of which coincides with the center of coordinates system  $xOy$  are defined by the equations:

$$r = r_0\psi_0(\varphi), \quad r = r_1\psi_1(\varphi); \quad 0 \leq \varphi < 2\pi.$$

The first equation defines the outside boundary of the cross-section, and the second equation defines inside. The cylinder contains  $N$  through cracks. These cracks in cross section plane occupied segments of  $2a_k, k = \overline{1, N}$  length with centers at points  $(c_k, d_k)$  that do not intersect with the boundaries of cross section and among themselves (Fig. 1).

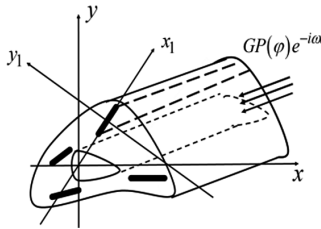


Fig. 1. Infinite cylindrical body with cracks.

The longitudinal shear oscillation proceeds in the cylinder as a result of the harmonic load  $GP(\varphi)e^{-i\omega t}$  on the outside boundary, where  $G$  is shear module,  $\omega$  is the frequency of oscillation. The multiplier  $e^{-i\omega t}$  is everywhere on omitted. Only the  $z$ -component of the vector of displacement is different from 0, which satisfies the Helmholtz equation

$$\Delta w + \kappa_2^2 w = 0; \quad \kappa_2^2 = \omega^2 \rho / G, \tag{1}$$

$\Delta$ -is the Laplace operator in a polar coordinate system. Due to the load on the outside surface of the body and on the supposition about the fixity inside surface next conditions are fulfilled on them

$$\tau_{nz}(r_0\psi_0(\varphi), \varphi) = GP(\varphi), \quad w(r_1\psi_1(\varphi), \varphi) = 0, \quad 0 \leq \varphi < 2\pi. \tag{2}$$

For the formulation of boundary conditions on the cracks with the center of each the local coordinate system  $x_kO_ky_k, k = \overline{1, N}$  is associated (Fig. 1).

Let  $w_k(x_k, y_k)$  is the  $z$ -component of the vector of displacement after the transformation from polar coordinates to Cartesian  $x_kO_ky_k$ . Cracks are considered to be free from stresses:

$$\tau_{zy_k}(x_k, 0) = 0, \quad |x_k| < a_k, \quad k = \overline{1, N} \tag{3}$$

Also displacement is discontinuous on the surfaces of the cracks with jumps

$$\tau_{zy_k}(x_k, 0) = 0, \quad |x_k| \leq a_k, \quad \chi_k(\pm a_k) = 0 \quad k = \overline{1, N} \tag{4}$$

Under such conditions, the problem of determining the wave field in the body and stress state in the vicinity of the cracks is posed.

### 3 Solution of the Problem

For each of the cracks in the local coordinate system  $x_l O_l y_l$  discontinues solution of Eq. (1) [8] with jumping (4) is built

$$w_l^{(d)}(x_l, y_l) = \frac{\partial}{\partial y_l} \int_{-a_l}^{a_l} \chi_l(\eta) r_2(\eta - x_l, y_l) d\eta, \tag{5}$$

where  $r_2(\eta - x_l, y_l) = -\frac{i}{4} H_0^{(1)}\left(\kappa_2 \sqrt{(\eta - x_l)^2 + y_l^2}\right)$ ,  $H_0^{(1)}$ —Hankel function.

Then in a polar system displacement is represented in the form of:

$$w^{(g)}(r, \varphi) = w_0^{(g)}(r, \varphi) + \sum_{l=1}^N w_l^{(g)}(r, \varphi) \tag{6}$$

where  $w_l^{(g)}(r, \varphi)$  are discontinuous solutions (5) after the transition to polar coordinates,  $w_0^{(g)}(r, \varphi)$  is some unknown function which conditions (2) on the surface of the body would be satisfied. Further, this function is represented as a linear combination of the partial solutions of Helmholtz Equation [9]:

$$w_0^{(g)}(r, \varphi) = r_0 \sum_{s=1}^M (A_s g_s(r, \varphi) + B_s h_s(r, \varphi)) \tag{7}$$

$$h_{2m-1}(r, \varphi) = H_{m-1}(\kappa_2 r) \cos(m-1)\varphi, \quad h_{2m}(r, \varphi) = H_m(\kappa_2 r) \sin m\varphi$$

$$g_{2m-1}(r, \varphi) = J_{m-1}(\kappa_2 r) \cos(m-1)\varphi, \quad g_{2m}(r, \varphi) = J_m(\kappa_2 r) \sin m\varphi$$

After transition in (7) to the Cartesian coordinates  $x_k O_k y_k$  and substitution to (4) system of integro-differential equations for functions  $\varphi_l(\tau) = \chi_l(a_l \tau)/a_l$  is obtained.

Formulas (7) and the linearity of this system allow to represent the unknown function in form:

$$\varphi_l(\tau) = a_l \sum_{s=1}^M \left( A_s \varphi_{sl}^{(1)}(\tau) + B_s \varphi_{sl}^{(2)}(\tau) \right); \quad \varphi_l'(\eta) = \sum_{s=1}^M \left( A_s \left( \varphi_{sl}^{(1)}(\tau) \right)' + B_s \left( \varphi_{sl}^{(2)}(\tau) \right)' \right).$$

As a result of these actions the set of systems of integral equations for  $\varphi_{sk}^{(i)}(\tau)$  are obtained finally

$$\begin{aligned} & \frac{1}{2\pi} \int_{-1}^1 (\varphi_{sk}^{(i)}(\tau))' \left[ \frac{1}{\tau-\zeta} + R_k^{(1)}(\tau-\zeta) \right] d\tau + \frac{1}{2\pi} \int_{-1}^1 \varphi_{sk}^{(i)}(\tau) \left[ -\gamma_k^2 \kappa_0^2 \ln|\tau-\zeta| + R_k^{(0)}(\tau-\zeta) \right] d\tau \\ & + \sum_{\substack{l=1 \\ l \neq k}}^N \left[ \frac{1}{2\pi} \int_{-1}^1 (\varphi_{sl}^{(i)}(\tau))' F_{kl}^{(1)}(\tau, \zeta) d\tau + \frac{1}{2\pi} \int_{-1}^1 \varphi_{sl}^{(i)}(\tau) F_{kl}^{(0)}(\tau, \zeta) d\tau \right] = f_{sk}^{(i)}(\zeta), \end{aligned} \tag{8}$$

$$f_{sk}^{(1)}(\zeta) = -r_0 \frac{\partial g_s(a_k \zeta; 0)}{\partial y_k}, \quad f_{sk}^{(2)}(\zeta) = -r_0 \frac{\partial h_s(a_k \zeta; 0)}{\partial y_k}, \quad k=1, \dots, N; s=1, \dots, M; \quad i=1, 2.$$

Solution of systems (8) is based on the representation of derivatives of unknown functions in the form [10]:

$$\left( \varphi_{sk}^{(i)}(\tau) \right)' = \frac{\psi_{sk}^{(i)}(\tau)}{\sqrt{1-\tau^2}}, \quad k = 1, 2, \dots, N \tag{9}$$

Then the mechanical quadrature method with (8) the set of systems of linear algebraic equations for the knots values of unknown function  $\left( \psi_{sk}^{(i)} \right)_m = \psi_{sk}^{(i)}(\tau_m)$  are obtained with (8). Where  $T_n(\tau)$  is Chebyshev's polynomial,  $\tau_m$  is its roots. Unknown coefficients  $A_k, B_k$  in (7) are determined by condition (2) in the boundaries of the body. After the its realization and applying of the collocation method systems of linear algebraic equations for these coefficients are obtained

$$\begin{aligned} & \sum_{s=1}^M A_s \left( \sum_{m=1}^n a_m \psi_{sm}^{(1)} \sum_{l=1}^n D_{lm} G(Z_l, \sigma_r) + F_s^1(\sigma_r) \right) \\ & + \sum_{s=1}^M B_s \left( \sum_{m=1}^n a_m \psi_{sm}^{(2)} \sum_{l=1}^n D_{lm} G(Z_l, \sigma_r) + F_s^2(\sigma_r) \right) = P(\sigma_r), \\ & \sum_{s=1}^M A_s \left( \sum_{m=1}^n a_m \psi_{sm}^{(1)} \sum_{l=1}^n D_{lm} E(Z_l, \sigma_r) + g_s(\sigma_r) \right) + \sum_{s=1}^M B_s \left( \sum_{m=1}^n a_m \psi_{sm}^{(2)} \sum_{l=1}^n D_{lm} E(Z_l, \sigma_r) + h_s(\sigma_r) \right) = 0, \\ & \sigma_r = \frac{2\pi r}{M}, \quad r = 1, \dots, M. \end{aligned} \tag{10}$$

Values that define the possibility of developing cracks, there are stress intensity factors (SIF)  $K_l^\pm$  near its edges  $x_l = \pm a_l$ , After the solution (8) and (10) its dimensionless value are founded

$$k_l^\pm = \frac{K_l^\pm}{G\sqrt{a_l}} = \frac{(-1)^{n+1}}{2n} \left( \sum_{s=1}^M A_s \sum_{m=1}^n (-1)^m \psi_{sm}^{(1)} (\text{ctg } \frac{\gamma_m}{2})^{\pm 1} + \sum_{s=1}^M B_s \sum_{m=1}^n (-1)^m \psi_{sm}^{(2)} (\text{ctg } \frac{\gamma_m}{2})^{\pm 1} \right),$$

$$\gamma_m = \frac{\pi(2m-1)}{2n}.$$



### 4 The Results of Numerical Analyses

As an example, the cylindrical body with cross-section bounded of two ellipses (Fig. 2) was considered when the next load surface  $P(\varphi) = \sin 2\varphi$ .

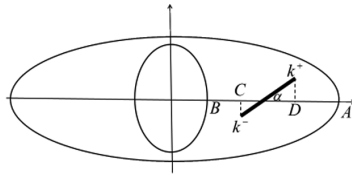


Fig. 2. The cross section of cylindrical body with crack.

Eccentricities of internal and external ellipses are same and equal  $\varepsilon = 0,5$ , the ratio of axes of the ellipses is  $r_1/r_0 = 0,5$ . The dependence of the absolute values of the SIF on dimensionless wave numbers  $\kappa_0 = \kappa_2 r_0$  was studied for different angles of inclination of the cracks to the axis of the ellipse. Figure 3 corresponds to the case of a crack with a length equal to one third of the distance  $AB$  between the vertexes of ellipses, and centered on the axis of the cross section. Curves 1–5 are illustrating the change of SIF  $|k^+|$  with increase of the wave number for the following angles,  $0^\circ, 30^\circ, 45^\circ, 60^\circ, 90^\circ$  respectively. We can see that until reach the first resonance frequency absolute value of SIF decreases with increase factor of crack inclination angle. Crack inclination angle also substantially affects the number and value of resonant frequencies. So, for the angles of inclination  $\alpha = 0^\circ$  and  $\alpha = 90^\circ$  there is no resonance for  $\kappa_0 \approx 2, 6$ , which is observed for the other angles. However, all the cases revired are characterized by resonant behavior of SIF for  $\kappa_0 \approx 3, 8$ .

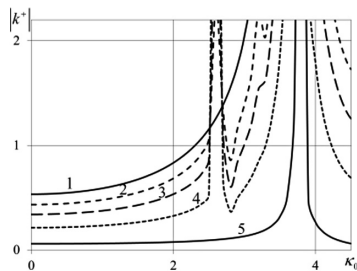


Fig. 3. Dependence of SIF on wave number when changing cracks inclination angle.

### 5 Conclusions

Effective analytical-numerical method for determining the dynamic stresses in hollow cylindrical body with arbitrary cross-section with through cracks for longitudinal shear strain conditions was proposed. This method allows solving separate integral equations

on defects and satisfying the conditions on the boundary of body, which facilitates numerical realization. The method can be generalized to the case of the plane deformation state and more difficult problems. Some difficulties in applying this method arise when approaching the defect to the crack and unsmooth the boundaries of the body. But in general, the proposed method allows the approximate calculation of SIF and study the impact on their value of geometrical parameters of the cracks and the body in a wide frequency area. It is shown that the presence of cracks in an elastic hollow cylinder for harmonic load is accompanied by both the intensity of the dynamic stresses in the vicinity of defects, and the resonant nature of their changes. In the considered frequency area opportunities of achievement one or two resonances depending on the position of the cracks in the body are revealed.

## References

1. Popov, V.G.: Comparative Analysis of Diffraction Fields During the Passage of Elastic Waves Through Defects of Different Nature [in Russian]. *Izv. RAN, Mekh. Tverdogo Tela*. **4**, 99–109 (1995)
2. Ang, D.D., Knopoff, L.: Diffraction of scalar elastic waves by a finite strip. *Proc. Math. Sci. USA* **51**(4), 593–598 (1964)
3. Mykhas'kiv, V., Zhabdynskiy, I., Zhang, Ch.: Elastodynamic analysis of multiple crack problem in 3-D bi-materials by a BEM. *Int. J. Num. Meth. Biomed. Eng.* **26**(12) 1934–1946, (2010)
4. Popov, V.G.: Interaction of plane elastic waves with systems of radial defects [in Russian]. *Izv. RAN Mehanika tverdogo tela*. **4**, 118–129 (1999)
5. Chirino, F., Domingues, J.: Dynamic analysis of cracks using boundary element method. *Eng. Fract. Mech.* **34**(5–6), 1051–1061 (1989)
6. Bobylev, A.A., Dobrova, Y.A.: Application of the Boundary Element Method to the Calculation of Forced Vibrations of Finite-Sized Elastic Bodies with Cracks[in Russian]. *Visnyk of Kharkov National University* **590**(1), 49–54 (2003)
7. Zhang, Ch.: A 2D hypersingular time-domain traction BEM for transient elastodynamic crack analysis. *Wave Motion* **35**(1), 17–40 (2002)
8. Popov, V.G.: Comparison of displacement fields and stresses in the diffraction of elastic shear waves at various defects: crack and thin rigid inclusion [in Russian]. *Dyn. Syst.* **12**, 35–41 (1993)
9. Vekua, N.P.: *Systems of Singular Integral Equations and Some Boundary-Value Problems* [in Russian]. Nauka, Moscow (1970)
10. Belotserkovskiy, S.M., Lifanov, I. K.: *Numerical Methods in Singular Integral Equations* [in Russian]. Moskow, Nauka (1985)



# The Wave Field of a Twice-Truncated Elastic Cone Under Torsion Moment Impact

K. Mysov<sup>(✉)</sup> and N. Vaysfel'd

Department of Mathematics, Physics and IT, Odesa Mechnikov University,  
Dvoryanska Str.2, 65082 Odesa, Ukraine  
kmysov2309@gmail.com, vaysfeld@onu.edu.ua

**Abstract.** The problem of an elastic twice-truncated cone wave field estimation is considered for a steady state torsional oscillations. The G. Ya. Popov integral transformation with regard to an angular coordinate is applied. It allows the reduction of the original problem to a one-dimensional boundary value problem in the transformation's domain. The solution of this boundary value problem is derived in an explicit form. The dependence of the eigenfrequencies on the cone's geometric parameters is investigated.

**Keywords:** Twice truncated cone · Steady state torsional oscillations · G. ya. popov integral transformation

## 1 Introduction

An important task widely common in engineering practice is to determine the dynamic stress state of a cone under the impact of a non-stationary load. A particularly important point is the ability to calculate the eigenfrequencies required to evaluate the dynamic stability of the constructions.

The solving of the initial boundary value problems for cone-shaped elastic bodies is not a new problem, however, there are many unresolved issues, especially when the cone is twice-truncated. A thick-walled twice-truncated cone from two-dimensional, functionally graded materials exposed to the combined load is considered at [1]. In [2] the stress state of a twice-truncated cone resting on a rigid base of the lateral surface under a uniform load applied at a larger base is investigated. An axisymmetric problem for a twice-truncated anisotropic cone is solved in [3] with the help of the straight lines method for three-dimensional elasticity equations. The general solution for axisymmetric boundary value problems for a twice-truncated cone is derived in [4]. More complicated, an axially mixed problem for a twice-truncated hollow cone under its own weight was considered in [5]. Significantly less problems are confirmed with an investigation of the dynamic field of conical bodies. An axisymmetric dynamic problem for a twice truncated dynamic cone first was considered at [6], but a lot of unresolved questions connected with eigenvalues investigation still remain.

## 2 Statement of the Problem

The twice truncated elastic cone is considered in the spherical coordinate system  $a < r < b, -\psi \leq \theta \leq \psi, -\pi \leq \varphi < \pi$  (Fig. 1).

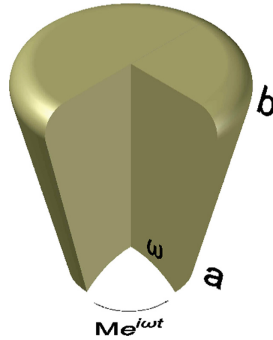


Fig. 1. Geometry of the problem

The problem is stated for the case of steady-state oscillations and for all mechanical characteristics representation  $\tilde{f}(r, \theta, \varphi, t) = e^{i\omega t}f(r, \theta, \varphi)$  takes place, where  $\omega$  is the steady state frequency, factor  $e^{i\omega t}$  will be omitted in all next formulas.

An absolutely rigid overlay is in adhesion with the bottom spherical face  $r = a, -\psi \leq \theta \leq \psi, -\pi \leq \varphi < \pi$ . The torsion dynamic moment impacts the cone through this rigid overlay:

$$w|_{r=a} = \alpha l \sin \theta \cos \theta, \tag{1}$$

here  $w(r, \theta) = u_\varphi(r, \theta)$  the only non-zero displacement in this problem statement,  $l = b - a$  and  $\alpha$  is the unknown rotation angle. This rotation angle should be found further from the movement equation of the overlay

$$2\pi a^3 \int_0^\psi \sin^2 \theta \tau_{r\varphi}(a, \theta) d\theta + M + \omega^2 \alpha J = 0, \tag{2}$$

where  $M$  is torque, applied to overlay,  $J$  is overlay's known inertia moment.

The cone's surface  $a < r < b, \theta = \psi, -\pi \leq \varphi < \pi$  is free from stress

$$\tau_{\theta\varphi}|_{\theta=\psi} = 0. \tag{3}$$

The upper spherical face of the cone  $r = b, -\psi \leq \theta \leq \psi, -\pi \leq \varphi < \pi$  is fixed

$$w|_{r=b} = 0. \tag{4}$$

It is required to determine the displacement satisfying the boundary conditions (1), (3), (4) and the torsion equation

$$(r^2 w')' + \frac{(\sin \theta w^\bullet)^\bullet}{\sin \theta} - \frac{w}{\sin^2 \theta} = -r^2 q^2 \frac{\partial^2 w}{\partial r^2}, \tag{5}$$

where  $w^\bullet = \frac{\partial w(r, \theta)}{\partial \theta}$ ,  $q = \frac{\omega}{c}$  is the wave number and  $c = \sqrt{\frac{G}{\rho}}$ , is the shear wave speed,  $\rho$  is density and  $G$  is the shear modulus.

### 3 The Problems Solving

The integral G. Ya. Popov transformation [7] is applied to derived problem (1), (3)–(5)

$$w_k(r) = \int_0^\psi \sin \theta P_{\nu_k}^1(\cos \theta) w(r, \theta) d\theta \tag{6}$$

with the inverse transformation formula

$$w(r, \theta) = \sum_{k=0}^\infty \frac{P_{\nu_k}^1(\cos \theta) w_k(r)}{\|P_{\nu_k}^1(\cos \theta)\|^2}, \tag{7}$$

where  $P_{\nu_k}^1(\cos \theta)$  is associated Legendre's function of the first kind,  $\nu_k$  are the roots of the transcendental equation

$$\left. \frac{\partial P_{\nu_k}^1(\cos \theta)}{\partial \theta} \right|_{\theta=\psi} - \text{ctg } \omega P_{\nu_k}^1(\cos \psi) = 0 \tag{8}$$

Thus, in the transformation's domain, a one-dimensional boundary value problem is written:

$$\begin{aligned} (r^2 w_k')' - \nu_k(\nu_k + 1)w_k - r^2 q^2 w_k &= 0 \\ w_k|_{r=b} &= 0 \\ w_k|_{r=a} &= \alpha l \gamma_k, \quad \gamma_k = \frac{\sin^3 \psi P_{\nu_k}^1(\cos \psi)}{(\nu_k - 2)(\nu_k + 3)} \end{aligned} \tag{9}$$

the solution of boundary value problem (9) is constructed in the form [8]

$$w_k(r) = \Psi_{0k}(r) \alpha l \gamma_k \tag{10}$$

where  $\{\Psi_{0k}(r), \Psi_{1k}(r)\}$  is the system of the basis solutions

$$\begin{aligned}
 \Psi_{0k}(r) &= a^{\frac{1}{2}} r^{-\frac{1}{2}} (J_{\bar{\nu}_k}(qr) Y_{\bar{\nu}_k}(qb) - J_{\bar{\nu}_k}(qb) Y_{\bar{\nu}_k}(qr)) \Delta^{-1} \\
 \Psi_{1k}(r) &= -b^{\frac{1}{2}} r^{-\frac{1}{2}} (J_{\bar{\nu}_k}(qr) Y_{\bar{\nu}_k}(qa) - J_{\bar{\nu}_k}(qa) Y_{\bar{\nu}_k}(qr)) \Delta^{-1} \\
 \Delta &= J_{\bar{\nu}_k}(qa) Y_{\bar{\nu}_k}(qb) - J_{\bar{\nu}_k}(qb) Y_{\bar{\nu}_k}(qa)
 \end{aligned}
 \tag{11}$$

here  $J_{\bar{\nu}_k}(qr)$  and  $Y_{\bar{\nu}_k}(qr)$  are Bessel's functions of the first and second kind respectively. G. Ya. Popov inverse integral transformation (7) is applied to the expression (10). It leads to the final formula for the displacement

$$w(r, \theta) = \left(\frac{a}{r}\right)^{\frac{1}{2}} \alpha l \sin^2 \psi \sum_{k=0}^{\infty} \frac{P_{\nu_k}^1(\cos \theta) P_{\nu_k}^1(\cos \psi)}{(\nu_k - 1)(\nu_k + 2) \|P_{\nu_k}^1(\cos \theta)\|^2} \frac{J_{\bar{\nu}_k}(qr) Y_{\bar{\nu}_k}(qb) - J_{\bar{\nu}_k}(qb) Y_{\bar{\nu}_k}(qr)}{J_{\bar{\nu}_k}(qa) Y_{\bar{\nu}_k}(qb) - J_{\bar{\nu}_k}(qb) Y_{\bar{\nu}_k}(qa)}
 \tag{12}$$

Formula (12) determines the cone's displacement, if the rotation angle  $\alpha$  is known. To find it one must use the formula (5)

$$\alpha = -\frac{M}{\omega^2 J}
 \tag{13}$$

Taking into account the correspondent (13) an explicit solution of the problem (1-5) is derived.

### 4 Discussion of the Numerical Results

From the point of view of mechanical applications, the most important is to find the eigenfrequencies. It requires the solving of the transcendental equation

$$D(\omega) = \prod_{k=0}^N \left( J_{\bar{\nu}_k} \left( \omega \frac{a}{c} \right) Y_{\bar{\nu}_k} \left( \omega \frac{b}{c} \right) - J_{\bar{\nu}_k} \left( \omega \frac{b}{c} \right) Y_{\bar{\nu}_k} \left( \omega \frac{a}{c} \right) \right) = 0
 \tag{14}$$

The following input parameters were selected for the calculation.  $N = 5$ ,  $G = 45.5 \times 10^{10} \text{ g/cm}^2$ ,  $\rho = 8.92 \text{ g/cm}^3$ ,  $a = 10 \text{ cm}$ ,  $b = 3a$ ,  $c = 2.26 \times 10^5 \text{ cm/c}$ ,  $V = 0.1 \text{ cm}^3$ ,  $m = \rho V = 0.892 \text{ g}$ ,  $J = 2.43 \text{ g} \cdot \text{cm}^2$ ,  $M = 120 \cdot 10^{10} \text{ g} \cdot \text{cm}^2/\text{c}^2$ , where  $V$  and  $m$  are an overlay's volume and mass respectively.

For three different cone angles  $\psi = 15^\circ, 45^\circ, 75^\circ$  the first eigenfrequencies are evaluated and shown in Table 1.

**Table 1.** Eigenfrequencies dependence from cone's opening angle

$\Psi(^{\circ})$	$\Omega_i = \frac{2\omega_i l}{\pi c}, i = 1, \dots, 5$				
15	2.08253	4.04742	6.03272	8.02487	10.0200
45	2.08253	4.04742	4.63559	6.03272	6.23599
75	2.08253	3.25786	4.04742	4.58078	4.90631

In Table 2 one can see how changing the cone size influences the values of first eigen frequencies ( $\psi = 45^{\circ}$ ).

**Table 2.** Eigenfrequencies dependence from cone's linear size

$b$	$1.5a$	$2a$	$3a$	$10a$
$\Omega_1$	2.01231	2.03500	2.08253	2.25799

In Fig. 2 one can see values  $k_1 = \frac{\tau_{r\varphi}(b,\theta)}{|\alpha|G}$  where  $0 \leq \theta \leq \psi$  and displacement  $k_2 = \frac{w(r,\psi)}{|\alpha|}$  where  $a < r < b$  for different cone opening angles  $\psi = 45^{\circ}$  and  $\psi = 75^{\circ}$ .

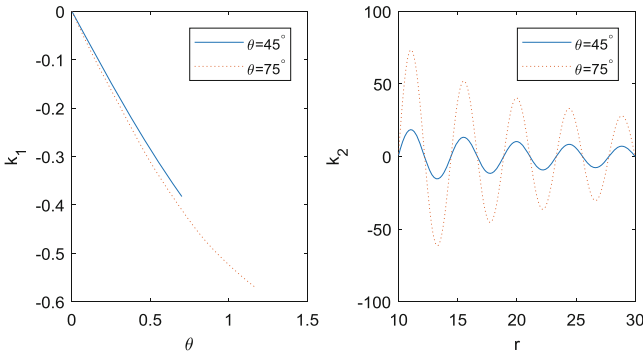


**Fig. 2.** The values of  $k_1$  and  $k_2$  dependencies

### 5 Concluding Remarks

The explicit formulas for the wave field of a twice-truncated cone under dynamic torsion impact are derived in this paper. The dependence of the eigenfrequencies on the opening angle and the linear size of the cone was stated. The explicit formulae of stress and displacement were derived.

It is established that increasing the opening angle, the first eigenfrequencies are decreased, however, when increasing the cone's linear size, they are increased.

The proposed approach can be used to determine the dynamic stress and displacement of a twice-truncated cone in the case when the load is applied to the body weakened by a spherical defect (a crack or a thin absolutely hard inclusion).

## References

1. Kamran, A., Manouchehr, S., Mehdi, A.: Elastic solution of a two dimensional functionally graded thick truncated cone with finite length under hydrostatic combined loads. *Acta Mech.* **217**(1–2), 119–134 (2011)
2. Savchenko, V.I., Shokot'ko, S.G., Uspenskii, A.A.: Study of the stress-strain state of truncated elastic cones. *Strength Mater.* **9**(7), 817–821 (1977)
3. Uspenskii, A.A.: State of stress of an anisotropic cone under an axisymmetric load. *Soviet Appl. Mech.* **13**(5), 436–440 (1977)
4. Popov, G.Y.: On the axisymmetrical problems of elasticity for the truncated hollow cone. *J. Appl. Math. Mech.* **69**(3), 417–426 (2005)
5. Vaisfel'd, N.D., Popov, G.Y., Reut, A.V.: Axisymmetric problem of stressed state for a twice truncated cone. *J. Math. Sci.* **201**(2), 229–244 (2014)
6. Mysov, K., Vaysfeld, N.: Steady state torsion of twice truncated elastic cone. *Young Scientist* **10**(62), 118–121 (2018)
7. Popov, G.Y.: New transforms for the resolving equations in elastic theory and new integral transforms, with applications to boundary-value problems of mechanics. *Int. Appl. Mech.* **39**(12), 1400–1424 (2003)
8. Popov, G.Y., Abdimanapov, S.A., Efimov, V.V.: *Green's Functions and Matrix of One-dimensional Boundary Value Problems*. Rauan, Almati (1999)





# To the Solving of the Nonstationary Spatial Lamb—Cerutti Problem

D. Prikazchikov<sup>1</sup>, Yu. Protserov<sup>2</sup>, and N. Vaysfeld<sup>2</sup>(✉)

<sup>1</sup> Department of Mathematics, Keele University, Staffordshire ST55BG, UK

<sup>2</sup> Department of Mathematics, Physics and IT, Odesa Mechnikov University,  
Dvoryanska str. 2, 65082 Odesa, Ukraine  
vaysfeld@onu.edu.ua

**Abstract.** The nonstationary Lamb-Cerutti problem was solved in the spatial statement for the elastic half-plane. Explicit formulae in the Laplace transform domain were derived. The solution was provided in detail for the case of steady state tangential and normal loads. Explicit formulae for the stresses and displacements of the half-space for both normal and tangent load were obtained.

**Keywords:** Lamb-Cerutti problem · Nonstationary · Spatial · Explicit form · Integral transforms

## 1 Introduction

In many three-dimensional contact problems, such as the indentation of a cylinder into an elastic half space, it is necessary to have formulae defining the stress and displacements of a half-space, not only under normal, but also under tangential load on its surface. In the static statement these solutions are studied sufficiently fully (Cerutti's problem) in two-dimensional formulation. However, in the dynamic spatial statement the Cerutti's problem, as distinct from Lamb's problem [1, 2], is not fully investigated [3]. In the proposed paper the explicit solution of a nonstationary spatial Cerutti problem is constructed in the Laplace transform domain. Also the formulae for the displacements and stress of a half-space under steady state tangential load are derived for the spatial statement.

## 2 The Statement of the Problem

The elastic half-space  $-\infty < x, y < \infty$ ,  $z \geq 0$  meets the nonstationary normal and tangent loadings at the surface  $Z = 0$  at moment  $t = 0$

$$\begin{aligned}\sigma_z(x, y, z, t)|_{z=0} &= -f(x, y)D(t) \\ \tau_{zx}(x, y, z, t)|_{z=0} &= -g(x, y)D(t) \\ \tau_{zy}(x, y, z, t)|_{z=0} &= -h(x, y)D(t)\end{aligned}$$

One must estimate the wave field of the half-space satisfying the equations of motion and zero initial conditions

$$\begin{cases} \Delta u + \mu_0 \frac{\partial \theta}{\partial x} = c_2^{-2} \frac{\partial^2 u}{\partial t^2} \\ \Delta v + \mu_0 \frac{\partial \theta}{\partial y} = c_2^{-2} \frac{\partial^2 v}{\partial t^2}, \quad \theta = \frac{\partial u}{\partial x} + \frac{\partial v}{\partial y} + \frac{\partial w}{\partial z}, \\ \Delta w + \mu_0 \frac{\partial \theta}{\partial z} = c_2^{-2} \frac{\partial^2 w}{\partial t^2} \end{cases}$$

where  $\mu_0 = (1 - 2\mu)^{-1}$ ,  $c_1^2 = (\lambda + 2G)\rho^{-1}$ ,  $c_2^2 = G\rho^{-1}$ ,  $\mu$  is Poisson’s coefficient,  $\lambda$ ,  $G$ —Lame’s coefficients,  $\rho$ —density of elastic medium. Following Popov [1, 2] the functions  $Z = \frac{\partial u}{\partial x} + \frac{\partial v}{\partial y}$ ,  $Z^* = \frac{\partial v}{\partial x} - \frac{\partial u}{\partial y}$  were considered and Lamé’s system was transformed to the two coupled equations and a separate one

$$\begin{cases} \Delta w + \mu_0 \frac{\partial}{\partial z} \left( Z + \frac{\partial w}{\partial z} \right) = c_2^{-2} \frac{\partial^2 w}{\partial t^2} \\ \Delta Z + \mu_0 \nabla_{xy} \left( Z + \frac{\partial w}{\partial z} \right) = c_2^{-2} \frac{\partial^2 Z}{\partial t^2}, \quad \Delta Z^* = c_2^{-2} \frac{\partial^2 Z^*}{\partial t^2}, \quad \nabla_{xy} = \frac{\partial^2}{\partial x^2} + \frac{\partial^2}{\partial y^2} \end{cases} \quad (1)$$

The new functions are input instead of the stress:  $\sigma_z = 2G\mu_0 \left( \mu Z + (1 - \mu) \frac{\partial w}{\partial z} \right)$ ,  $\tau = \frac{\partial \tau_{xx}}{\partial x} + \frac{\partial \tau_{xy}}{\partial y} = G \left( \nabla_{xy} w + \frac{\partial Z}{\partial z} \right)$ ,  $\tau^* = \frac{\partial \tau_{xy}}{\partial x} - \frac{\partial \tau_{xx}}{\partial y} = G \frac{\partial Z^*}{\partial z}$ .

The boundary conditions are rewritten in the form

$$\begin{aligned} 2G\mu_0 \left( \mu Z + (1 - \mu) \frac{\partial w}{\partial z} \right) \Big|_{z=0} &= -f(x, y)D(t) \\ \tau \Big|_{z=0} &= G \left( \nabla_{xy} w + \frac{\partial Z}{\partial z} \right) \Big|_{z=0} = - \left( \frac{\partial g}{\partial x} + \frac{\partial h}{\partial y} \right) D(t) \\ \tau^* \Big|_{z=0} &= G \frac{\partial Z^*}{\partial z} \Big|_{z=0} = - \left( \frac{\partial h}{\partial x} - \frac{\partial g}{\partial y} \right) D(t) \end{aligned} \quad (2)$$

The initial conditions are reformulated in terms of the new functions as well

$$w \Big|_{t=0} = Z \Big|_{t=0} = Z^* \Big|_{t=0} = 0, \quad \frac{\partial w}{\partial t} \Big|_{t=0} = \frac{\partial Z}{\partial t} \Big|_{t=0} = \frac{\partial Z^*}{\partial t} \Big|_{t=0} = 0.$$

### 3 Solving the Problem

The Laplace transform with regard to variable  $t$  and Fourier transform with the regard to variables  $x$  and  $y$  were applied sequentially to Lamé’s Eq. (1) and boundary conditions (2)

$$\langle w_{\alpha\beta p}(z), Z_{\alpha\beta p}(z), Z_{\alpha\beta p}^*(z) \rangle = \int_{-\infty}^{\infty} e^{i\beta y} dy \int_{-\infty}^{\infty} e^{i\alpha x} dx \int_0^{\infty} \langle w(x, y, z, t), Z(x, y, z, t), Z^*(x, y, z, t) \rangle e^{-pt} dt.$$

It is derived in the transform domain that

$$\begin{cases} w''_{\alpha\beta p}(z) - \gamma^2 q_2^2 w_{\alpha\beta p}(z) + (1 - \gamma^2) Z'_{\alpha\beta p} = 0 \\ Z''_{\alpha\beta p}(z) - \gamma^{-2} q_1^2 Z_{\alpha\beta p}(z) + (1 - \gamma^{-2}) N^2 w'_{\alpha\beta p} = 0, \quad Z_{\alpha\beta p}^{*''}(z) - q_2^2 Z_{\alpha\beta p}^* = 0 \end{cases} \quad (3)$$

The boundary conditions are reformulated

$$\begin{aligned} (1 - 2\gamma^2) Z_{\alpha\beta p}(0) + w'_{\alpha\beta p}(0) &= -\gamma^2 G^{-1} f_{\alpha\beta} D_p \\ N^2 w_{\alpha\beta p}(0) - Z'_{\alpha\beta p}(0) &= -iG^{-1} (\alpha g_{\alpha\beta} + \beta h_{\alpha\beta}) D_p \end{aligned} \quad (4)$$

$$Z_{\alpha\beta p}^{*'}(0) = -iG^{-1} (\beta g_{\alpha\beta} - \alpha h_{\alpha\beta}) D_p. \quad (5)$$

Here  $k_i = pc_i^{-1}, \gamma = k_1 k_2^{-1}, N^2 = \alpha^2 + \beta^2, q_i = \sqrt{N^2 + k_i^2} (i = 1, 2)$ .

The solution of the Eq. (3), satisfying the boundary condition (5) and decreasing on infinity has the form  $Z_{\alpha\beta p}^*(z) = iG^{-1} q_2^{-1} (\beta g_{\alpha\beta} - \alpha h_{\alpha\beta}) D_p e^{-q_2 z}$ .

The governing Eqs. (3) are then written in vector form as  $L_2[\vec{y}(z)] = I \vec{y}''(z) + A \vec{y}'(z) + B \vec{y}(z) = 0$ , where

$$\vec{y}(z) = \begin{pmatrix} w_{\alpha\beta p}(z) \\ Z_{\alpha\beta p}(z) \end{pmatrix}, A = \begin{pmatrix} 0 & 1 - \gamma^2 \\ (1 - \gamma^{-2}) N^2 & 0 \end{pmatrix}, B = \begin{pmatrix} -\gamma^2 q_2^2 & 0 \\ 0 & -\gamma^{-2} q_1^2 \end{pmatrix}, I$$

—unit matrix.

The solution of this vector equation is constructed on the base of matrix solution  $L_2[Y(z)] = 0$ , through the substitution  $Y(z) = e^{sz} I$ , leading to

$$Y(z) = \frac{1}{2\pi i} \int_C e^{sz} M^{-1}(s) ds,$$

where  $M^{-1}(s) = \frac{1}{(s^2 - q_1^2)(s^2 - q_2^2)} \begin{pmatrix} s^2 - \gamma^{-2} q_1^2 & -(1 - \gamma^2)s \\ -(1 - \gamma^{-2}) N^2 s & s^2 - \gamma^2 q_2^2 \end{pmatrix}$ , and C is a closed

contour covering the poles  $s_{1,2} = \pm q_1$  and  $s_{3,4} = \pm q_2$ . The decreasing on infinity matrix solution  $Y(z)$  is derived after evaluation of a contour integral (taking into consideration the poles  $s_2$  and  $s_4$ ). The vector solution takes the form

$$\vec{y}(z) = Y(z) \begin{pmatrix} A_1 \\ A_2 \end{pmatrix},$$

where constants  $A_1$  and  $A_2$  are found from the boundary conditions (4). To find the unknown displacements one must use the expressions found for transformations of new inputted functions

$$\begin{aligned}
 u_{\alpha\beta p}(z) &= iN^{-2}[\alpha Z_{\alpha\beta p}(z) - \beta Z_{\alpha\beta p}^*(z)], & v_{\alpha\beta p}(z) &= iN^{-2}[\beta Z_{\alpha\beta p}(z) + \alpha Z_{\alpha\beta p}^*(z)] \\
 w_{\alpha\beta p}(z) &= G^{-1}R^{-1}(N)\{[(2N^2 + k_2^2)e^{-q_1z} - 2N^2e^{-q_2z}]q_1f_{\alpha\beta} \\
 &\quad + [2q_1q_2e^{-q_1z} - (2N^2 + k_2^2)e^{-q_2z}]i(\alpha g_{\alpha\beta} + \beta h_{\alpha\beta})\}D_p
 \end{aligned} \tag{6}$$

where  $R(N) = (2N^2 + k_2^2)^2 - 4N^2\sqrt{N^2 + k_1^2}\sqrt{N^2 + k_2^2}$ .

Let us apply the inverse Laplace's and Fourier's transforms to the derived formulae. The displacement  $w(x, y, z, t)$  is written in the form

$$\begin{aligned}
 w(x, y, z, t) &= \frac{1}{8\pi^3 iG} \int_{-\infty}^{\infty} \int_{-\infty}^{\infty} f(\xi, \eta) d\xi d\eta \int_{\varepsilon-i\infty}^{\varepsilon+i\infty} D_p e^{p t} dp \int_{-\infty}^{\infty} \int_{-\infty}^{\infty} \frac{R_1(N)}{R(N)} q_1 e^{-i\alpha(x-\xi) - i\beta(y-\eta)} d\alpha d\beta \\
 &\quad - \frac{1}{8\pi^3 iG} \frac{\partial}{\partial x} \int_{-\infty}^{\infty} \int_{-\infty}^{\infty} g(\xi, \eta) d\xi d\eta \int_{\varepsilon-i\infty}^{\varepsilon+i\infty} D_p e^{p t} dp \int_{-\infty}^{\infty} \int_{-\infty}^{\infty} \frac{R_2(N)}{R(N)} e^{-i\alpha(x-\xi) - i\beta(y-\eta)} d\alpha d\beta \\
 &\quad - \frac{1}{8\pi^3 iG} \frac{\partial}{\partial y} \int_{-\infty}^{\infty} \int_{-\infty}^{\infty} h(\xi, \eta) d\xi d\eta \int_{\varepsilon-i\infty}^{\varepsilon+i\infty} D_p e^{p t} dp \int_{-\infty}^{\infty} \int_{-\infty}^{\infty} \frac{R_2(N)}{R(N)} e^{-i\alpha(x-\xi) - i\beta(y-\eta)} d\alpha d\beta \\
 R_1(N) &= (2N^2 + k_2^2)e^{-q_1z} - 2N^2e^{-q_2z}, & R_2(N) &= 2q_1q_2e^{-q_1z} - (2N^2 + k_2^2)e^{-q_2z}.
 \end{aligned}$$

As may be seen, the double integrals are dependent on the expressions  $N = \sqrt{\alpha^2 + \beta^2}$  and  $q_i = \sqrt{\alpha^2 + \beta^2 + k_i^2}$  ( $i = 1, 2$ ). It is possible to transform them into a single integral with the help of a well-known correspondence

$$\int_{-\infty}^{\infty} \int_{-\infty}^{\infty} F\left(\sqrt{\alpha^2 + \beta^2 + c}\right) e^{-i\alpha x - i\beta y} d\alpha d\beta = \int_0^{\infty} F\left(\sqrt{\rho^2 + c}\right) J_0\left(\rho\sqrt{x^2 + y^2}\right) \rho d\rho,$$

where  $J_0(x)$  is the Bessel's function. The transformed displacement is written as

$$\begin{aligned}
 4\pi^2 iGw(x, y, z, t) &= \int_{\varepsilon-i\infty}^{\varepsilon+i\infty} D_p e^{p t} dp \int_0^{\infty} F(\rho, x, y) \frac{R_1(\rho)}{R(\rho)} q_1 \rho d\rho \\
 &\quad - \frac{\partial}{\partial x} \int_{\varepsilon-i\infty}^{\varepsilon+i\infty} D_p e^{p t} dp \int_0^{\infty} G(\rho, x, y) \frac{R_2(\rho)}{R(\rho)} \rho d\rho - \frac{\partial}{\partial y} \int_{\varepsilon-i\infty}^{\varepsilon+i\infty} D_p e^{p t} dp \int_0^{\infty} H(\rho, x, y) \frac{R_2(\rho)}{R(\rho)} \rho d\rho,
 \end{aligned}$$

where

$$\begin{aligned}
 &\langle F(\rho, x, y), G(\rho, x, y), H(\rho, x, y) \rangle \\
 &= \int_{-\infty}^{\infty} \int_{-\infty}^{\infty} \langle f(\xi, \eta), g(\xi, \eta), h(\xi, \eta) \rangle J_0\left(\rho\sqrt{(x-\xi)^2 + (y-\eta)^2}\right) d\xi d\eta
 \end{aligned}$$

The other displacements are found in a similar manner.

The derived solutions contain the functions  $F(\rho, x, y), G(\rho, x, y), H(\rho, x, y)$ , represented by double integrals and their derivatives. Let's consider the subcase when an external load is applied by the rectangular area  $|x| \leq a, |y| \leq b$  and uniformly distributed there with intensity  $A_x, A_y, A_z$  along the corresponding directions. It leads

to  $F(\rho, x, y) = A_z \int_{-a}^a \int_{-b}^b J_0 \left( \rho \sqrt{(x - \xi)^2 + (y - \eta)^2} \right) d\xi d\eta$ , where after Sonin's formula [4] and some additional transformations, one derives

$$F(\rho, x, y) = \frac{8}{\pi \rho^2} A_z \int_0^{\pi/2} \sin(a\rho \cos \psi) \sin(b\rho \sin \psi) \cos(x\rho \cos \psi) \cos(y\rho \sin \psi) \frac{d\psi}{\cos \psi \sin \psi}.$$

Similar correspondences are constructed for  $G(\rho, x, y)$  and  $H(\rho, x, y)$ .

Let us focus on the case when the external load is harmonic in time, i.e.  $D(t) = e^{i\omega t}$ . The explicit solutions are written for  $p = i\omega$ :

$$\begin{aligned} \frac{w(x, y, z, t)}{(2\pi G)^{-1} e^{i\omega t}} &= \int_0^\infty F(\rho, x, y) \frac{S_1(\rho)}{S(\rho)} \gamma_1 \rho d\rho - \frac{\partial}{\partial x} \int_0^\infty G(\rho, x, y) \frac{S_2(\rho)}{S(\rho)} \rho d\rho \\ &\quad - \frac{\partial}{\partial y} \int_0^\infty H(\rho, x, y) \frac{S_2(\rho)}{S(\rho)} \rho d\rho \end{aligned} \tag{7}$$

Here  $S(\rho) = (2\rho^2 - \chi_2^2)^2 - 4\rho^2 \gamma_1 \gamma_2$ ,  $S_1(\rho) = (2\rho^2 - \chi_2^2) e^{-\gamma_1 z} - 2\rho^2 e^{-\gamma_2 z}$

$$S_2(\rho) = 2\gamma_1 \gamma_2 e^{-\gamma_1 z} - (2\rho^2 - \chi_2^2) e^{-\gamma_2 z} \quad \chi_i = \omega c_i^{-1}, \quad \gamma_i = \sqrt{\rho^2 - \chi_i^2}, \quad i = 1, 2$$

As it is seen, if the denominator of (7) is zero  $S(\rho) = (2\rho^2 - \chi_2^2)^2 - 4\rho^2 \gamma_1 \gamma_2 = 0$ , one arrives at the Rayleigh equation. Its unique root is  $\rho = \chi_R = \omega c_R^{-1}$ , connected with the velocity  $c_R$  of Rayleigh's wave propagation ( $\chi_1 < \chi_2 < \chi_R$ ). The damping is introduced in a medium to direct the energy flow in Rayleigh's wave from the load's location. After a contour integration procedure the formulae for the displacements are written.

For the tangential load  $g \neq 0, f = h = 0$  the displacement has the form

$$\begin{aligned} \frac{w(x, y, z, t)}{(2\pi i G)^{-1} e^{-i\omega t}} &= \frac{\partial}{\partial x} \left\{ \pi \frac{G(\chi_R, x, y)}{S'(\chi_R)} S_2(\chi_R) \chi_R \right. \\ &\quad - \int_0^{\chi_1} G(\xi, x, y) \frac{2\sqrt{\chi_1^2 - \xi^2} \sqrt{\chi_2^2 - \xi^2} \sin\left(z\sqrt{\chi_1^2 - \xi^2}\right) + (2\xi^2 - \chi_2^2) \sin\left(z\sqrt{\chi_2^2 - \xi^2}\right)}{(2\xi^2 - \chi_2^2)^2 + 4\xi^2 \sqrt{\chi_1^2 - \xi^2} \sqrt{\chi_2^2 - \xi^2}} \xi d\xi \\ &\quad - \int_{\chi_1}^{\chi_2} \frac{G(\xi, x, y) (2\xi^2 - \chi_2^2)}{(2\xi^2 - \chi_2^2)^4 + 16\xi^4 (\xi^2 - \chi_1^2) (\chi_2^2 - \xi^2)} \left[ 2(2\xi^2 - \chi_2^2) \sqrt{\xi^2 - \chi_1^2} \sqrt{\chi_2^2 - \xi^2} e^{-z\sqrt{\xi^2 - \chi_1^2}} \right. \\ &\quad \left. \left. + (2\xi^2 - \chi_2^2)^2 \sin\left(z\sqrt{\chi_2^2 - \xi^2}\right) - 4\xi^2 \sqrt{\xi^2 - \chi_1^2} \sqrt{\chi_2^2 - \xi^2} \cos\left(z\sqrt{\chi_2^2 - \xi^2}\right) \right] \xi d\xi \right\} \end{aligned}$$

Other formulae are not given here due to the limited size of the article.

## 4 Conclusions

1. The explicit solutions of nonstationary spatial Lamb's and Cerutti's problems are constructed in the Laplace's transform domain.
2. The problem was studied in detail for the case of steady-state normal and tangential loads. The wave field in the half-space was derived in explicit form for the spatial statement of the problem.

**Acknowledgements.** Support through the Erasmus + KA107 framework is gratefully acknowledge. The authors are also indebted to Prof J. Kaplunov for fruitful discussions.

## References

1. Popov, G.Y., Vaisfeld, N.: On a new approach to the Lamb problem solution. *Doklady Phys.* **55**(5), 246–251 (2010)
2. Sretenskii, L.N.: In *Problems of Continuum Mechanics*, pp. 411–427. Akad. Nauk SSSR, Moscow (1961)
3. Kaplunov, J., Prikazchikov, D.: Asymptotic theory for Rayleigh and Rayleigh-type waves. *Adv. Appl. Mech.* **50**, 1–106 (2017)
4. Sonin, N.Y.: *The Investigation of Cylindrical Functions and Special Polynomials* (in Russian). Gostexizdat, Moscow (1954)



# The Model of Thin Electromagnetoelastic Shells Dynamics

V. A. Vestyak<sup>1(✉)</sup> and D. V. Tarlakovskii<sup>1,2</sup>

<sup>1</sup> Moscow Aviation Institute (National Research University), Moscow, Russia  
v. a. vestyak@mail.ru

<sup>2</sup> Institute of Mechanics, Lomonosov Moscow State University, Moscow, Russia

**Abstract.** Interacting with electromagnetic field, thin linear elastic homogeneous anisotropic shell with a smooth median surface is exploring. The equations of its movement are used, taking into account the rotation of the normal fiber and compression. The components of the electromagnetic field together with the Maxwell equations and the generalized Ohm's law are linearized along the transverse coordinate. In the surface pressure on the shell and the momentum per unit area, electromagnetic components are distinguished, they are found using the expression for the Lorentz force. Physical law for the shell, taking into account piezoelectric effects, closes the system of equations. A special case of equations for an isotropic shell is given.

**Keywords:** Electromagnetoelasticity · Coupled problems · Time-dependent axisymmetric problems · Green's functions

## 1 Problem Formulation

Interacting with electromagnetic field, thin linear elastic homogeneous anisotropic shell with a smooth median surface is exploring

$$\Pi : \mathbf{r} = \mathbf{r}_0(\xi^1, \xi^2), (\xi^1, \xi^2) \in D \subset R^2, \quad (1)$$

where  $\mathbf{r}$ —radius vector,  $\xi^1, \xi^2$ —curvilinear coordinates.

Its equation of motion is [1] (time derivatives are indicated with dots):

$$\begin{aligned} \rho h \ddot{u}^i &= \nabla_j T^{ji} - b_j^i Q^j + q^i, \rho h \ddot{w} = \nabla_i Q^i + b_{ij} T^{ij} + q, \\ \rho I \ddot{\psi}^i &= \nabla_j M^{ij} - Q^i + m^i, \rho I \ddot{\psi}_3 = \nabla_i \mu^i - N + m, I = h^3 / 12; \end{aligned} \quad (2)$$

$$Q^i = \hat{Q}^i + b_j^i \mu^j, T^{ij} = \hat{T}^{ij} + b_k^i M^{kj}, N = \hat{N} - b_{ij} M^{ij}; \quad (3)$$

$$\begin{aligned} \hat{T}^{ij} &= \int_{-h/2}^{h/2} \sigma^{ij} dz, M^{ij} = \int_{-h/2}^{h/2} z \sigma^{ij} dz, \hat{Q}^i = \int_{-h/2}^{h/2} \sigma^{i3} dz, \\ \mu^i &= \int_{-h/2}^{h/2} z \sigma^{i3} dz, \hat{N} = \int_{-h/2}^{h/2} \sigma^{33} dz; \end{aligned} \quad (4)$$

$$\begin{aligned}
 2\varepsilon_{ij} &= \alpha_{ij} + \alpha_{ji}, 2\kappa_{ij} = \beta_{ij} + \beta_{ji}, \alpha_{ij} = \nabla_i u_j - b_{ij} w, \\
 \beta_{ij} &= \nabla_i \psi_j - b_{ij} \psi_3 + b_i^k \alpha_{kj}, -\vartheta_i = \nabla_i w + b_i^k u_k, \theta_k = \psi_k - \vartheta_k.
 \end{aligned} \tag{5}$$

Here latin indexes take on values of 1,2; index «3» corresponds to the normal coordinate  $z$ ;  $\rho$ —material density;  $h$ —thickness;  $u_i$  и  $w$ —tangential and normal movement;  $\psi_i$ —angles of normal rotation to the surface of the fiber;  $\psi_3$ —its deformation;  $b_{ij}$ —components of surface curvature tensor  $\Pi$ ;  $\sigma^{ij}, \sigma^{i3}, \sigma^{33}$ —voltage tensor components;  $q^i, q$  and  $m^i, m$ —coordinates of surface pressure vectors and moment, referred to the unit area.

The electromagnetic field is described by Maxwell's equations, linearized relatively to the initial state by the generalized Ohm's law and physical relations (subscript "0" indicates the initial field; components of vectors and tensors here and further correspond to the coordinate system  $\xi^1, \xi^2, z$ ) [2]:

$$\text{rot } \mathbf{E} = -c^{-1} \dot{\mathbf{B}}, \text{rot } \mathbf{H} = c^{-1} (4\pi \mathbf{j} + \dot{\mathbf{D}}), \text{div } \mathbf{D} = 4\pi \rho_e; \tag{6}$$

$$\mathbf{j} = \sigma(\mathbf{E} + c^{-1}[\mathbf{v}, \mathbf{B}_0]) + \rho_{e0} \mathbf{v}; \tag{7}$$

$$\begin{aligned}
 D^i &= e^{ij} E_j + e^{i3} E_3 + \kappa^{ijk} \varepsilon_{jk} + 2\kappa^{ij3} \varepsilon_{j3} + \kappa^{i33} \varepsilon_{33}, \\
 D_3 &= e^{3j} E_j + e^{33} E_3 + \kappa^{3jk} \varepsilon_{jk} + 2\kappa^{3j3} \varepsilon_{j3} + \kappa^{333} \varepsilon_{33}, \\
 B^i &= \mu^{ij} H_j + \mu^{i3} H_3 + \gamma^{ijk} \varepsilon_{jk} + 2\gamma^{ij3} \varepsilon_{j3} + \gamma^{i33} \varepsilon_{33}, \\
 B_3 &= \mu^{3j} H_j + \mu^{33} H_3 + \gamma^{3jk} \varepsilon_{jk} + 2\gamma^{3j3} \varepsilon_{j3} + \gamma^{333} \varepsilon_{33}.
 \end{aligned} \tag{8}$$

Here  $\mathbf{E}$  and  $\mathbf{H}$ —electric and magnetic field strength vectors;  $\mathbf{D}$  and  $\mathbf{B}$ —electric and magnetic induction vectors;  $\mathbf{j}$  and  $\mathbf{v}$ —current density and medium velocity vectors;  $\rho_e$ —charge density;  $c$ —speed of light;  $\sigma$ —conductivity coefficient;  $e^{ij}, e^{i3}$  и  $\mu^{ij}, \mu^{i3}$ —components of dielectric and magnetic permeability tensors;  $\kappa^{ijk}, \kappa^{ij3}, \kappa^{i33}, \kappa^{333}$  and  $\gamma^{ijk}, \gamma^{ij3}, \gamma^{i33}, \gamma^{333}$ —components of the piezoelectric and piezomagnetic constant tensors.

The relations (1–8) are supplemented by a generalization of Hooke's law and a linearized expression for the Lorentz force  $\mathbf{F}_e$  [2]:

$$\begin{aligned}
 \sigma^{ij} &= C^{ijkl} \varepsilon_{kl} + C^{ij33} \varepsilon_{33} - (\kappa^{ijk} E_k + \kappa^{ij3} E_3 + \gamma^{ijk} H_k + \gamma^{ij3} H_3) / 4\pi, \\
 \sigma^{i3} &= 2C^{i3k3} \hat{\varepsilon}_{k3} - (\kappa^{i3k} E_k + \kappa^{i33} E_3 + \gamma^{i3k} H_k + \gamma^{i33} H_3) / 4\pi, \\
 \sigma^{33} &= C^{33kl} \varepsilon_{kl} + C^{3333} \varepsilon_{33} - (\kappa^{33k} E_k + \kappa^{333} E_3 + \gamma^{33k} H_k + \gamma^{333} H_3) / 4\pi;
 \end{aligned} \tag{9}$$

$$\mathbf{F}_e = \rho_{e0} \mathbf{E} + \rho_e \mathbf{E}_0 + c^{-1}([\mathbf{j}_0, \mathbf{B}] + [\mathbf{j}, \mathbf{B}_0]). \tag{10}$$

where  $C^{ijkl}, C^{ij33}, C^{i3k3}, C^{3333}$ —components of the elastic constant tensor.

We assume that the initial electromagnetic characteristics do not depend on the coordinate and restrict ourselves to a linear approximation for the components of the electromagnetic field like the theory of elastic shells. (here  $i = 1, 2, 3$ ):



$$\begin{aligned}
 E_i &= e_i(\xi^1, \xi^2, t) + z\chi_i(\xi^1, \xi^2, t), H_i = h_i(\xi^1, \xi^2, t) + z\varphi_i(\xi^1, \xi^2, t), \\
 D_i &= d_i(\xi^1, \xi^2, t) + z, \delta_i(\xi^1, \xi^2, t)B_i = b_i(\xi^1, \xi^2, t) + z\beta_i(\xi^1, \xi^2, t), \\
 j_i &= y_i(\xi^1, \xi^2, t) + zv_i(\xi^1, \xi^2, t), \rho_e = r_e(\xi^1, \xi^2, t) + z\lambda_e(\xi^1, \xi^2, t).
 \end{aligned}
 \tag{11}$$

Then the linearized version of equalities (7) is written as ( $g$ —second invariant of the metric tensor  $g_{ij}$  of coordinates (1); here and further in analogous equations, the indexes  $i$  and  $j$  form a circular permutation of the numbers 1 and 2):

$$\begin{aligned}
 y^i &= \sigma[e^i + (-1)^j c^{-1} g_2(\dot{u}_j B_{03} - \dot{w} B_{0j}) + \rho_{e0} \dot{u}^i], \\
 v^i &= \sigma[\chi^i + (-1)^j c^{-1} g_2(\dot{\psi}_j B_{03} - \dot{\psi}_3 \hat{B}_{0j}) + \rho_{e0} \dot{\psi}^i], \\
 y_3 &= \sigma[e_3 + c^{-1} g_2(\dot{u}_1 B_{02} - \dot{u}_2 B_{01})] + \rho_{e0} \dot{w}, \\
 v_3 &= \sigma[\chi_3 + c^{-1} g_2(\dot{\psi}_1 B_{02} - \dot{\psi}_2 B_{01})] + \rho_{e0} \dot{\psi}_3, g_2 = \sqrt{g}.
 \end{aligned}
 \tag{12}$$

The right parts of Eqs. (2) are presented in the form of two items ( $F_e^i, F_{e3}$ —coordinates of vector  $\mathbf{F}_e$ ; indexes «\*» and «e» correspond to mechanical and electromagnetic components):

$$q^i = q_*^i + q_e^i, m^i = m_*^i + m_e^i, q = q_* + q_e, m = m_* + m_e,
 \tag{13}$$

where

$$q_e^i = \rho \int_{-h/2}^{h/2} F_e^i dz, q_e = \rho \int_{-h/2}^{h/2} F_{e3} dz, m_e^i = \rho \int_{-h/2}^{h/2} z F_e^i dz, m_e = \rho \int_{-h/2}^{h/2} z F_{e3} dz.$$

Using (10–12), we obtain the following formulas for electromagnetic components:

$$\begin{aligned}
 q_e^i &= h[\rho_{e0} e^i + r_e E_0^i + (-1)^j c^{-1} g_2(j_{0j} b_3 - j_{03} b_j + y_j B_{03} - y_3 B_{0j})], \\
 q_e &= h[\rho_{e0} e_3 + r_e E_{03} + c^{-1} g_2(j_{01} b_2 - j_{02} b_1 + y_1 B_{02} - y_2 B_{01})], \\
 m_e^i &= I[\rho_{e0} \chi^i + \lambda_e E_0^i + (-1)^j c^{-1} g_2(j_{02} \beta_3 - j_{03} \beta_2 + v_2 B_{03} - v_3 B_{02})], \\
 m_e &= I[\rho_{e0} \chi_3 + \lambda_e E_{03} + c^{-1} g_2(\hat{j}_{01} \beta_2 - \hat{j}_{02} \beta_1 + v_1 \hat{B}_{02} - v_2 \hat{B}_{01})].
 \end{aligned}
 \tag{14}$$

Linearization along the coordinate of relations (9) brings equalities (4) to the following form of physical law for the shell:

$$\begin{aligned}
 \hat{T}^{ij} &= h \left[ C^{ijkl} \varepsilon_{kl} + C^{ij33} \Psi_3 \right] - \frac{1}{4\pi} (\kappa^{ijk} e_k + \kappa^{ij3} e_3 + \gamma^{ijk} h_k + \gamma^{ij3} h_3) \\
 M^{ij} &= I \left[ C^{ijkl} \kappa_{kl} - \frac{1}{4\pi} (\kappa^{ijk} \chi_k + \kappa^{ij3} \chi_3 + \gamma^{ijk} \varphi_k + \gamma^{ij3} \varphi_3) \right], \\
 \hat{Q}^i &= h \left[ C^{i3k3} \theta_k - \frac{1}{4\pi} (\kappa^{i3k} e_k + \kappa^{i33} e_3 + \gamma^{i3k} h_k + \gamma^{i33} h_3) \right], \\
 \mu^i &= I \left[ C^{i3k3} (b'_k \theta_l + \nabla_k \Psi_3) - \frac{1}{4\pi} (\kappa^{i3k} \chi_k + \kappa^{i33} \chi_3 + \gamma^{i3k} \varphi_k + \gamma^{i33} \varphi_3) \right], \\
 \hat{N} &= h \left[ C^{33kl} \varepsilon_{kl} + C^{3333} \Psi_3 - \frac{1}{4\pi} (\kappa^{33k} e_k + \kappa^{333} e_3 + \gamma^{33k} h_k + \gamma^{333} h_3) \right].
 \end{aligned} \tag{15}$$

Application of a similar procedure to Eqs. (6) gives the following result ( $H$  и  $K$ —mean and gaussian curvatures of the surface  $\Pi$ ):

$$g_2 \dot{b}^i = (-1)^i c \left( \frac{\partial e_3}{\partial \xi^2} + b_2^k e_k - \chi_2 \right), \quad g_2 \dot{b}_3 g_2 = c(\nabla_2 e_1 - \nabla_1 e_2); \tag{16}$$

$$g_2 (\dot{d}^i + 4\pi y^i) = (-1)^j c \left( \frac{\partial h_3}{\partial \xi^j} + b_j^k h_k - \varphi_j \right), \tag{17}$$

$$g_2 (\dot{d}_3 + 4\pi y_3) = c(\nabla_1 h_2 - \nabla_2 h_1);$$

$$\nabla_k d^k - 2Hd_3 + \delta_3 = 4\pi r_e; \tag{18}$$

$$g_2 \dot{\beta}^i = (-1)^i c \left( \frac{\partial \chi_3}{\partial \xi^j} + b_j^k \chi_k + b_j^k \frac{\partial e_3}{\partial \xi^k} + c_j^k e_k \right), \tag{19}$$

$$g_2 \dot{\beta}_3 = c(\nabla_2 \chi_1 - \nabla_1 \chi_2 + b_2^k \nabla_k e_1 - b_1^k \nabla_k e_2);$$

$$g_2 (\dot{\delta}^i + 4\pi v^i) = (-1)^j c \left[ \frac{\partial \varphi_3}{\partial \xi^2} + b_j^k \left( \varphi_k + \frac{\partial h_3}{\partial \xi^k} + b_k^n h_n \right) \right], \tag{20}$$

$$g_2 (\dot{\delta}_3 + 4\pi v_3) = c(\nabla_1 \varphi_2 - \nabla_2 \varphi_1 + b_1^k \nabla_k h_2 - b_2^k \nabla_k h_1);$$

$$\nabla_k \delta^k - 2H\delta_3 + b^{nk} \nabla_n d_k - 2(2H^2 - K)d_3 = 4\pi \lambda_e. \tag{21}$$

Thus, the closed system of equations for an anisotropic electromagnetically elastic shell includes the equations of motion (2), equalities (3), (5), (12), (13), (14), (15) and Eqs. (16–21). This system is greatly simplified for isotropic conductors, which are materials with the following physical characteristics. (here and further indexes  $i, j, k, l$  take values 1, 2, 3):

$$\begin{aligned}
 C^{ijkl} &= \lambda g^{ij} g^{kl} + \mu (g^{ik} g^{jl} + g^{il} g^{jk}), \\
 \kappa^{ijk} &= 0, \quad \gamma^{ijk} = 0, \quad e^{ij} = \varepsilon_e g^{ij}, \quad \mu^{ij} = \mu_e g^{ij},
 \end{aligned}$$

where  $\lambda$  and  $\mu$ —elastic constants of Lamé;  $\varepsilon_e$  and  $\mu_e$ —dielectric and magnetic permeability coefficients.

In this case, equalities (15) are transferred to the physical law for the elastic shell [1], and ratios (8) take the form:

$$D^i = \varepsilon_e E^i, B^i = \mu_e H,$$

Which is, according to (11), equivalent to equalizes

$$d^i = \varepsilon_e e^i, \delta^i = \varepsilon_e \chi^i, b^i = \mu_e h^i, \beta^i = \mu_e \varphi^i$$

and leads to a decrease in the number of unknowns on (12).

## References

1. Mikhailova E.Y., Tarlakovskii D.V., Fedotenkov G.V.: General theory of elastic shells: Tutorial. MAI, 112p. (2018) (in Russian)
2. Tarlakovskii, D.V., Vestyak, V.A., Zemskov, A.V.: Dynamic Processes in Thermo-Electro-Magneto-Elastic and Thermo-Elasto-Diffusive Media. Encyclopedia of Thermal Stresses, vol. 2, pp. 1064–1071. Springer, Dordrecht, Heidelberg, New York, London (2014)



# Unsteady Electro-Magneto-Elastic Axisymmetric Oscillations of a Continuous Cylinder of Infinite Length

Vladimir Vestyak<sup>(✉)</sup> and Vasily Scherbakov

Moscow Aviation Institute (National Research University),  
125993 Moscow Volokolamskoe Shosse, 4, Russian Federation  
v.a.vestyak@mail.ru, vasily.a.scherbakov@gmail.com

**Abstract.** In the present work is considered an axisymmetric time-dependent waves of an infinite cylindrical body. The body material is taken to be isotropic and electro magneto elastic. Piezoelectric effects are not taken into account. The deformation process is described by a system of equation with respect to radial and angular components of deformation of the body points in cylindrical coordinate system. In additional, it takes into account the effect of current density, surface charges, electric and magnetic fields. All parameters and ratios are reduced to dimensionless form. To solve the problem, are used the Fourier transformation of angles and the Laplace transformation of time. Then, the resulting expressions expansion in series in terms of a small parameter. The small parameter characterizes the relationship between mechanic and electro-magnetic fields. To move into the space of the originals using the inverse Laplace transformation via residue theorem.

**Keywords:** Electromagnetoelasticity · Axisymmetric waves · Residue theorem · Coupled problems · Time-dependent axisymmetric problems · Green's functions

## 1 Problem Statement

### 1.1 Basic Equations

Consider the unsteady oscillations of a continuous cylinder of infinite length with a radius  $R$ . The material of a cylindrical body is considered electro magneto elastic and isotropic. Piezoelectric effects will not be taken into account. The flat deformed state of the continuous medium will be investigated, therefore all the required functions of the problem will depend on three parameters:  $\tau$ —time,  $r$ —radial coordinate and  $\theta$ —angular coordinate. The interaction of mechanical and electromagnetic fields is described by the following system of equations [1–4]:

– equations of motion respect to displacement

$$\ddot{u}_r = (1 - \eta^2) \frac{\partial I_1}{\partial r} + \eta^2 \Delta u_r - \frac{\eta^2}{r^2} \left( 2 \frac{\partial u_\theta}{\partial \theta} + u_r \right) + \alpha F_{er}, \quad (1)$$

$$\ddot{u}_\theta = \frac{(1 - \eta^2)}{r} \frac{\partial I_1}{\partial \theta} + \eta^2 \Delta u_\theta + \frac{\eta^2}{r^2} \left( 2 \frac{\partial u_r}{\partial \theta} - u_\theta \right) + \alpha F_{e\theta}, \quad (2)$$

where  $I_1 = \frac{1}{r} \left[ \frac{\partial(ru_r)}{\partial r} + \frac{\partial u_\theta}{\partial \theta} \right]$ ,  $\Delta = \frac{1}{r} \frac{\partial}{\partial r} \left( r \frac{\partial}{\partial r} \right) + \frac{1}{r^2} \frac{\partial^2}{\partial \theta^2}$ ;

– Maxwell's equations

$$\begin{aligned} \frac{1}{r} \left[ \frac{\partial(rE_\theta)}{\partial r} - \frac{\partial E_r}{\partial \theta} \right] &= -\dot{H}, \quad -\frac{\partial H}{\partial r} = \eta_e^2 (\gamma j_\theta + \dot{E}_\theta), \\ \frac{1}{r} \frac{\partial H}{\partial \theta} &= \eta_e^2 (\gamma j_r + \dot{E}_r), \quad \frac{1}{r} \left[ \frac{\partial(rE_r)}{\partial r} + \frac{\partial E_\theta}{\partial \theta} \right] = \rho_e; \end{aligned} \quad (3)$$

– Ohm's law

$$j_r = E_r + H_0 \dot{u}_\theta + \rho_{e0} \dot{u}_r / \gamma, \quad j_\theta = E_\theta - H_0 \dot{u}_r + \rho_{e0} \dot{u}_\theta / \gamma; \quad (4)$$

– Lorentz force

$$F_{er} = \rho_{e0} E_r + \rho_e E_{0r} + \gamma (j_{0\theta} H + j_\theta H_0), \quad F_{e\theta} = \rho_{e0} E_\theta + \rho_e E_{0\theta} - \gamma (j_{0r} H + j_r H_0); \quad (5)$$

– Physical relationships of electromagnetism

$$D_r = E_r, D_\theta = E_\theta, B = H. \quad (6)$$

Here  $u_r, u_\theta$ —components of the displacement vector;  $F_{er}, F_{e\theta}$ —components of the Lorentz force;  $E_r, E_\theta$ —components of electric field;  $H, B$ —components of magnetic field;  $j_r, j_\theta$ —components of current density;  $\rho_e$ —volume charge density;  $D_r, D_\theta$ —components of electric displacement field. All of these parameters are unknown and depend on three variables:  $\tau, r$  and  $\theta$ .  $H_0, \rho_{e0}, E_{0r}, E_{0\theta}, j_{0r}$  and  $j_{0\theta}$  are the parameters of the initial electromagnetic field and do not depend on time.

The above equations are dimensionless. In order to make these equations dimensionless, the following substitutions were applied (the “-” sign indicates a dimensional parameter):

$$\begin{aligned}
 r &= \frac{\bar{r}}{R}, \tau = \frac{c_1 t}{R}, u_k = \frac{\bar{u}_k}{R}, H = \frac{\bar{H} \mu_e c_1}{c E_*}, B = \frac{\bar{B} c_1}{c E_*}, \rho_e = \frac{4\pi \bar{\rho}_e R}{\varepsilon E_*}, \\
 E_k &= \frac{\bar{E}_k}{E_*}, D_k = \frac{\bar{D}_k}{\varepsilon E_*}, j_k = \frac{\bar{j}_k}{\sigma E_*}, F_{ek} = \frac{\bar{F}_{ek} R}{\lambda + 2\mu}, \eta_e = \frac{c_1}{c_e}, \\
 \alpha &= \frac{\varepsilon E_*^2}{4\pi(\lambda + 2\mu)}, \gamma = \frac{\gamma_e R}{c_1} = \frac{4\pi\sigma R}{\varepsilon c_1}, c_1^2 = \frac{\lambda + 2\mu}{\rho}, c_2^2 = \frac{\mu}{\rho}, \\
 \eta &= \frac{c_2}{c_1}, \gamma_e = \frac{4\pi\sigma}{\varepsilon}, c_e^2 = \frac{c^2}{\mu_e \varepsilon},
 \end{aligned}$$

where  $c_1$  and  $c_2$ —propagation velocities of tension-compression waves and shear waves;  $E_*$ —characteristic level of electric field;  $\lambda$  and  $\mu$ —Lame’s parameters;  $\varepsilon$  and  $\mu_e$ —dielectric and magnetic permeability coefficients;  $k = r, \theta$ ;  $c$ —light speed in vacuum;  $\sigma$ —conductivity coefficients.

### 1.2 Initial and Boundary Conditions

It is assumed that at the initial moment of time, there are no perturbation in the solid body.

As conditions on the boundary of a cylindrical body, the following are assumed:

$$u_r(\tau, r, \theta)|_{r=1} = U_r(\tau, \theta), u_\theta(\tau, r, \theta)|_{r=1} = 0.$$

At the point at  $r = 0$ , disturbances in a cylindrical body are considered limited:

$$u_r(\tau, r, \theta)|_{r=0} = O(1), u_\theta(\tau, r, \theta)|_{r=0} = O(1).$$

The system of Eqs. (3–6) can be reduced to a system of equations of two equations:

$$\begin{aligned}
 \eta_e^2 (\ddot{E}_r + \gamma \dot{E}_r) &= N_{11}(E_r) + N_{12}(E_\vartheta) - \eta_e^2 (\rho_{e0} \ddot{u}_r + \gamma H_0 \ddot{u}_\theta), \\
 \eta_e^2 (\ddot{E}_\vartheta + \gamma \dot{E}_\vartheta) &= N_{21}(E_r) + N_{22}(E_\vartheta) + \eta_e^2 (\gamma H_0 \ddot{u}_r - \rho_{e0} \ddot{u}_\theta), \\
 N_{11} &= \frac{1}{r^2} \frac{\partial^2}{\partial \vartheta^2}, N_{12} = -\frac{1}{r} \frac{\partial}{\partial \vartheta} \left( \frac{\partial}{\partial r} + \frac{1}{r} \right), \\
 N_{21} &= -\frac{1}{r} \frac{\partial}{\partial \vartheta} \left( \frac{\partial}{\partial r} - \frac{1}{r} \right), N_{22} = \frac{\partial}{\partial r} \left[ \frac{1}{r} \frac{\partial(r)}{\partial r} \right].
 \end{aligned} \tag{7}$$

## 2 Solution Methods

To solve the problem of the field of displacement and the electric field are expressed through the vector and scalar potentials:

$$\begin{aligned} \mathbf{u} &= \text{grad}\varphi + \text{rot}\boldsymbol{\psi}, \\ E &= \text{grad}\varphi_e + \text{rot}\boldsymbol{\psi}_e, \\ \text{div}\boldsymbol{\psi} &= 0, \text{div}\boldsymbol{\psi}_e = 0, \end{aligned} \tag{8}$$

where  $\varphi$  and  $\varphi_e$ —scalar potentials,  $\boldsymbol{\psi}$  and  $\boldsymbol{\psi}_e$ —vector potentials.

The Lorentz force vector can also be represented via scalar and vector potentials:

$$\mathbf{F}_e = \text{grad}\Phi + \text{rot}\boldsymbol{\Psi}, \tag{9}$$

where

$$\Delta\Phi = \text{div}F_e = \frac{1}{r} \frac{\partial(rF_{er})}{\partial r} + \frac{1}{r} \frac{\partial F_{e\theta}}{\partial \theta}, \Delta\Psi = -\text{rot}F_e = -\frac{1}{r} \frac{\partial(rF_{e\theta})}{\partial r} + \frac{1}{r} \frac{\partial F_{er}}{\partial \theta}.$$

In order to fulfill the axisymmetric conditions, it is necessary that the defining parameters of the problem, as well as the vector and scalar potentials correspond to the following equations:

$$\begin{aligned} u_r &= u_r(\tau, r, \theta), u_\theta = u_\theta(\tau, r, \theta), u_z \equiv 0, F_{ez} \equiv 0, E_r = E_r(r, \theta, t), \\ E_\theta &= E_\theta(r, \theta, t), E_z = E_{0z} \equiv 0, E_{0r} = E_{0r}(r, \theta), E_{0\theta} = E_{0\theta}(r, \vartheta), \\ \varphi &= \varphi(r, \theta, t), \varphi_e = \varphi_e(r, \theta, t), F_{er} = F_{er}(r, \theta, t), E_\theta = E_\theta(r, \theta, t), \\ \psi_r &= \psi_\theta \equiv 0, \psi_{er} = \psi_{e\theta} \equiv 0, \psi_z = \psi = \psi(r, \theta, t), \psi_{ez} = \psi_e = \psi_e(r, \theta, t), \\ H_r &= H_{0r} = H_\theta = H_{0\theta} \equiv 0, H_z = H(r, \theta, t), H_{0z} = H_0(r, \vartheta). \end{aligned}$$

By substituting (8) and (9) into systems (1), (2) and (7), we obtain a system of equations for  $\varphi$ ,  $\boldsymbol{\psi}$  and  $\varphi_e, \boldsymbol{\psi}_e$ .

First, the unknown functions are decomposed into a complex Fourier series:

$$\begin{aligned} \varphi(\tau, r, \theta) &= \sum_{n=-\infty}^{+\infty} \varphi_n^F(\tau, r) e^{i\theta}, \psi(\tau, r, \theta) = \sum_{n=-\infty}^{+\infty} \psi_n^F(\tau, r) e^{i\theta}, \\ \varphi_e(\tau, r, \theta) &= \sum_{n=-\infty}^{+\infty} \varphi_{en}^F(\tau, r) e^{i\theta}, \psi_e(\tau, r, \theta) = \sum_{n=-\infty}^{+\infty} \psi_{en}^F(\tau, r) e^{i\theta}, \end{aligned}$$

then, the Laplace transforms in time are applied to the obtained coefficients  $\varphi_n^F(\tau, r) \dots \psi_{en}^F(\tau, r)$  ( $s$ —conversion parameter):

$$\begin{aligned} \varphi_n^F(\tau, r) &\xrightarrow{L} \varphi_n^{FL}(s, r), \\ &\dots \\ \psi_{en}^F(\tau, r) &\xrightarrow{L} \psi_{en}^{FL}(s, r). \end{aligned}$$

The resulting coefficients  $\varphi_n^{FL}(s, r) \dots \psi_{en}^{FL}(s, r)$  are expanded in a power series for a small parameter  $\alpha$ :

$$\varphi_n^{FL} = \sum_{m=0}^{\infty} \varphi_{nm}^{FL} \alpha^m, \dots, \psi_{en}^{FL} = \sum_{m=0}^{\infty} \psi_{enm}^{FL} \alpha^m.$$

After that we get a new recurrent system of differential equations for the coefficient of expansion  $\varphi_{nm}^{FL} \dots \psi_{nm}^{FL}$ .

And finally in order to move obtained  $\varphi_{nm}^{FL} \dots \psi_{nm}^{FL}$  parameters into the space of the originals it is using the inverse Laplace transformation via residue theorem.

## References

1. Wang, X., Dong, K.: Magneto-thermodynamic stress and perturbation of magnetic field vector in a non-homogeneous thermoelastic cylinder. *Eur. J. Mech. A.* **25**(1), 98–109 (2006)
2. Vest'yak V.A., Lemeshev V.A. Rasprostraneniye nestatsionarnykh radialnykh vozmushcheniy ot tsilindricheskoy polosti v elektromagnitnouprugoy srede. // *Mater. XIV Intern. Symp. "Dynamic and technolo-ronmental problems of mechanics of structures and continua"*, vol. 1. pp. 59–60. named A.G. Gorshkov. Moscow. (2008)
3. Gorshkov, A.G., Medvedsky, A.L., Rabinsky, L.N., Tarlakovsky, D.V.: *Waves in continuous mediums. Textbook for Higher Education Institutions*, p. 472. Fizmatlit, Moscow (2004)
4. Vest'yak, V.A., Lemeshev, V.A., Tarlakovsky, D.V.: One-dimensional time-dependent waves in an electromagnetoelastic half-space or in a layer. *Doklady Phys.* **54**(6), 262–264 (2009)





# Transient Spatial Motion of Cylindrical Shell Under Influence of Non-stationary Pressure

Grigory V. Fedotenkov<sup>1,2</sup>(✉), Dmitry V. Tarlakovskii<sup>1,2</sup>,  
and Andrey Yu Mitin<sup>2</sup>

<sup>1</sup> Institute of Mechanics Lomonosov Moscow State University, Moscow 119192  
Michurinsky Prospekt 1, Russia

greghome@mail.ru

<sup>2</sup> Moscow Aviation Institute, National Research University, Moscow 125993  
Volokolamskoyeshosse 4, Russia

**Abstract.** This paper investigates a transient spatial problem for cylindrical shell of a Timoshenko-type subjected to external pressure distributed over some area belonging to a lateral surface. The approach to the solution is based on the Influence Function Method. There has been constructed an integral representation of the solution with a kernel in form of a spatial influence function for a cylindrical shell which is found analytically by expansion in Fourier series and Laplace and Fourier integral transformations. This paper proposes and implements an original algorithm of analytical reversion of Fourier and Laplace integral transforms based on connection of Fourier integral with an expansion in Fourier series based on connection of Fourier integral with expansion in Fourier series at variable interval with examples of calculations.

**Keywords:** Timoshenko-type circular cylindrical shell ·  
Superposition method · Spatial influence function · Fourier series ·  
Integral transformations · Non-stationary spatial motion

## 1 Statement of Problem

### 1.1 Shell Motion Equations

Let us consider a problem of motion of an infinitely long Timoshenko-type circular cylindrical shell under non-stationary pressure  $P(\alpha, z, \tau)$  distributed over some arbitrary area belonging to a lateral surface of the shell (Fig. 1).  $P(\alpha, z, \tau) = p(\alpha, z, \tau)H(\tau)\theta(D)$  where  $H(\tau)$  is Heaviside function and a  $\theta(D)$  is a characteristic function of the set  $D$ :

$$\theta(D) = \begin{cases} 1, & M \in D; \\ 0, & M \notin D, \end{cases}, \text{ where } M(\alpha, z) \text{ is a point of the shell's lateral surface.}$$

To describe movements of the shell motion we will use spatial motion equations in displacements of a Timoshenko model [1]. In the normal orthogonal coordinate system  $\alpha z$ ,  $\alpha \in [0, 2\pi]$ ,  $z \in (-\infty, \infty)$  they are written as follows:

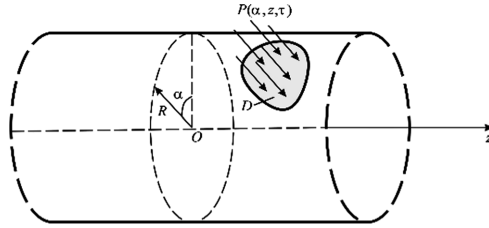


Fig. 1. Statement of problem

$$\frac{\partial^2 \mathbf{W}}{\partial \tau^2} = L \cdot \mathbf{W} + \mathbf{P}, L = (L_{ij})_{5 \times 5}, \mathbf{W} = (u, v, w, \chi_1, \chi_2)^T, \mathbf{P} = (0, 0, P, 0, 0)^T, \quad (1)$$

where  $u, v, w$  are angular, axial and normal displacements,  $\chi_1, \chi_2$  are angles of rotation of sections due to shear deformations,  $L$  is matrix operator whose elements are defined by the following differential operators [1]:

$$\begin{aligned} L_{11} &= \partial^2 / \partial \alpha^2 + \eta^2 (\partial^2 / \partial z^2 - k^2), L_{12} = (1 - \eta^2) \partial^2 / \partial \alpha \partial z, L_{13} = (1 + k \eta^2) \partial / \partial \alpha, \\ L_{14} &= -\gamma^2 \partial^2 / \partial \alpha^2 + \eta^2 k^2, L_{15} = -\gamma^2 (1 - 2 \eta^2) \partial^2 / \partial \alpha \partial z, L_{21} = L_{12}, \\ L_{22} &= \partial^2 / \partial z^2 + \eta^2 \partial^2 / \partial \alpha^2, L_{23} = (1 - 2 \eta^2) \partial / \partial z, L_{24} = -\gamma^2 \eta^2 \partial^2 / \partial \alpha \partial z, \\ L_{25} &= -\gamma^2 \eta^2 \partial^2 / \partial \alpha^2, L_{31} = -L_{13}, L_{32} = -L_{23}, L_{33} = \eta^2 k^2 (\partial^2 / \partial \alpha^2 + \partial^2 / \partial z^2) - 1, \\ L_{34} &= \eta^2 k^2 \partial / \partial \alpha, L_{35} = \eta^2 k^2 \partial / \partial z, L_{41} = \gamma^{-2} L_{14}, \\ L_{42} &= \gamma^{-2} L_{24}, L_{43} = -\gamma^{-2} L_{34}, L_{44} = \partial^2 / \partial \alpha^2 + \eta^2 (\partial^2 / \partial z^2 - k^2 \gamma^{-2}), \\ L_{45} &= L_{12}, L_{51} = \gamma^{-2} L_{15}, L_{52} = \gamma^{-2} L_{25}, L_{53} = -\gamma^{-2} L_{35}, L_{54} = L_{12}, \\ L_{55} &= \partial^2 / \partial z^2 + \eta^2 (\partial^2 / \partial \alpha^2 - k^2 \gamma^{-2}), \end{aligned}$$

Here and after all variables and parameters are reduced to a dimensionless form. The corresponding system of dimensionless values is written as follows (dimensional values are primed):

$$\begin{aligned} u &= u' / R, v = v' / R, w = w' / R, z = z' / R, \tau = c_1 t / R, \eta^2 = c_2^2 / c_1^2, \\ c_1^2 &= (\lambda + 2\mu) / \rho, c_2^2 = \mu / \rho, \gamma^2 = h^2 / 12R^2, P = P' R / h(\lambda + 2\mu), k^2 = 5/6, \end{aligned}$$

where  $R$  and  $h$  are radius and thickness of the shell,  $t$  is dimensional time,  $\tau$  is dimensionless time,  $c_1, c_2$  are speeds of strain stress wave and shear in the shells's material,  $\lambda, \mu, \rho$  are elastic Lamé parameters and density of the shell,  $k$ -is shear coefficient.

We believe that at the initial moment of time the sell is motionless which corresponds to zero initial conditions

$$u|_{\tau=0} = v|_{\tau=0} = w|_{\tau=0} = \chi_1|_{\tau=0} = \chi_2|_{\tau=0} = \dot{u}|_{\tau=0} = \dot{v}|_{\tau=0} = \dot{w}|_{\tau=0} = \dot{\chi}_1|_{\tau=0} = \dot{\chi}_2|_{\tau=0} = 0. \tag{2}$$

Let us state the problem as to find normal displacements of the shell  $w(\alpha, z, \tau)$  under non-stationary normal pressure arbitrarily distributed over some arbitral area belonging to a lateral surface of the shell.

### 1.2 Resolving Integral Relation

The solution method is based on the superposition principle [1–5] which stipulates that normal displacement  $w(\alpha, z, \tau)$  are linked with the pressure  $p(\alpha, z, \tau)$  by means of integral convolution operator by dimensional variables and time:

$$w(\alpha, z, \tau) = \int_0^\tau dt \iint_D G_w(\alpha - \beta, z - \xi, \tau - t)p(\beta, \xi, t)dS. \tag{3}$$

Here  $G_w(\alpha, z, \tau)$  is a non-stationary spatial function of influence for the shell which represents a solution of the following problem

$$\frac{\partial^2 \mathbf{G}}{\partial \tau^2} = L \cdot \mathbf{G} + \boldsymbol{\delta}, \mathbf{G} = (G_u, G_v, G_w, G_{\chi_1}, G_{\chi_2})^T, \boldsymbol{\delta} = [0, 0, \delta(\alpha)\delta(z)\delta(\tau), 0, 0]^T, \tag{4}$$

$$\mathbf{G}|_{\tau=0} = \dot{\mathbf{G}}|_{\tau=0} = \mathbf{0},$$

where  $\delta(\alpha), \delta(z), \delta(\tau)$  are the Dirac delta functions.

## 2 Non-stationary Spatial Function of Influence for Cylindrical Shell

To solve the problem (4) we will expand the required and prescribed functions in trigonometric series of Fourier by angular coordinate  $\alpha$ . By applying the Fourier integral transformation by coordinate  $z$  and Laplace integral transformation by time (here in after  $F$  means the function’s transform by Fourier,  $L$  is Laplace transform,  $q$  and  $s$  are parameters of Fourier and Laplace transformation) to the obtained equations we will reach a system of algebraic equations with regards to Fourier Laplace transforms.

The transforms of coefficients of expansions of the required function of influence will take the following structure:

$$G_{w,n}^{FL}(q, s) = \sum_{j=1}^4 P_j(q^2, s^2, n^2) / \sum_{l=1}^5 R_l(q^2, s^2, n^2), \tag{5}$$

where  $P_j(q, s, n)$  and  $R_l(q, s, n)$  are homogeneous polynomials of degree  $j$  and  $l$  correspondingly with coefficients depending on dimensionless parameters  $\eta, \gamma, k$  and the number of terms of series  $n$ . They are too cumbersome to be described here in a specific form.

Notwithstanding the obvious difficulties of joint inversion of Fourier and Laplace transforms (5), it is possible to propose an analytical way of constructing originals, base on the link of the inversion integral of Fourier transformation with Fourier series at a variable interval. The final formula for computing the joint inverse Fourier-Laplace transform is

$$G_{w,n}(z, \tau) = \frac{1}{2l(\tau)} G_{w,n}^{FL^{-1}}(0, s) H[l(\tau) - |z|] + \frac{1}{l(\tau)} \sum_{m=1}^{\infty} \left\{ G_{w,n}^{FL^{-1}}[\pi m/l(\tau), s] \cos[\pi m z/l(\tau)] \right\} H[l(\tau) - |z|], \tag{6}$$

where  $L^{-1}$  denotes the inverse Laplace transform,  $l(\tau) = \eta k \tau$ ,  $H(x)$  is the Heaviside function.

### 3 The Computation of the Normal Displacements of the Shell

#### 3.1 Numerical Algorithm

Let us assume that a rest shell at an initial moment of time is affected by non-stationary pressure of the following form:

$$P(\alpha, z, \tau) = \sin(\pi \alpha/\alpha_*) \cdot \sin(\pi z/z_*) \cdot [H(z) - H(z - z_*)] \cdot [H(\alpha) - H(\alpha - \alpha_*)] \cdot H(\tau), \tag{7}$$

which corresponds to a sudden application of pressure to the shell, distributed over area  $D = \{(\alpha, z) : 0 \leq \alpha \leq \alpha_*, 0 \leq z \leq z_*\}$  by law  $\sin(\pi \alpha/\alpha_*) \cdot \sin(\pi z/z_*)$ .

Normal displacements of the shell are found by formula (3) where surface integral adapted to the geometry of  $D$  area is substituted with an iterated integral:

$$w(\alpha, z, \tau) = \int_0^{\tau} dt \int_0^{\alpha_*} d\beta \int_0^{z_*} G_w(z - \xi, \alpha - \beta, \tau - t) p(\xi, \beta, t) d\xi, \quad p(\xi, \beta, t) = \xi \beta. \tag{8}$$

For finding integral in (8) we use a quadrature formula of the rectangle method:

$$w(\alpha, z, \tau) \approx \Delta t \Delta \xi \Delta \beta \sum_{i=1}^N \sum_{j=1}^M \sum_{k=1}^K G_{ijk}(\alpha, z, \tau) P_{ijk}, \tag{9}$$

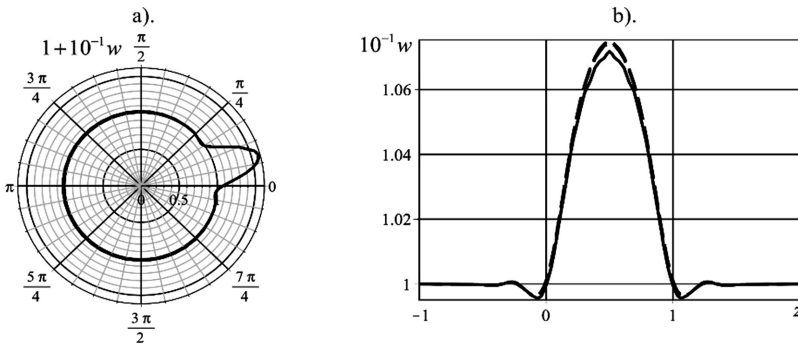
$$K = [\tau / \Delta t], \quad \Delta \xi = z_*/M, \quad \Delta \beta = \alpha_*/N,$$

$$G_{ijk}(\alpha, z, \tau) = G_w(\alpha - i\Delta\beta, z - j\Delta\xi, \tau - k\Delta t), \quad P_{ijk} = p(i\Delta\beta, j\Delta\xi, k\Delta t),$$

where  $[\tau / \Delta t]$  indicates an integer part of a number.

### 3.2 Calculation Example

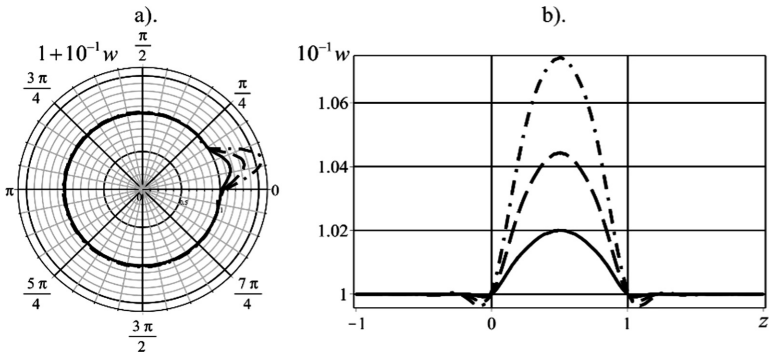
In calculations let us assume that  $\alpha_* = \pi/6$ ,  $z_* = 1$ ,  $\Delta t = 0.05$ . Figure 2a shows graphs of distribution of normal displacements with respect to angular coordinate  $\alpha$  at time  $\tau = 2$  with various values of  $N$  and  $M$ . Solid curve corresponds to the case of  $N = 10, M = 10$ ; dashed curve corresponds to  $N = 20, M = 20$ ; dash-and-dot curve corresponds to  $N = 30, M = 30$ . The graphs are drawn in a polar coordinate system linked with the shell cross section  $z = 0.5$ . Similar distributions of normal displacements on coordinate  $z$  with  $\alpha = 0$  c are shown in Fig. 2b. As seen from the analysis of the results, in the second and third cases the results are virtually identical, therefore, in further calculations under formula (9) it is assumed that  $N = 20, M = 20$ .



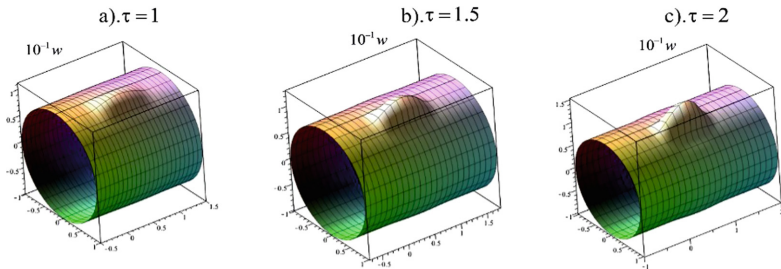
**Fig. 2.** Distributions of normal displacements with various number of discrete elements of body under pressure

Figure 3a represents distributions of normal displacements of the shell in the cross section  $z = 0.5$  at various times. Solid curve corresponds to time  $\tau = 1$ , dashed curve means  $\tau = 1.5$ , and dash-and-dot curve indicates  $\tau = 2$ . Distributions of normal displacements at coordinate  $z$  with  $\alpha = 0$  are shown in Fig. 3b.

Spatial distributions of normal displacements over the shell’s surface at various times are shown in Fig. 4a–c. Figure 4a corresponds to time  $\tau = 1$ , 4b.— $\tau = 1.5$ , 4c.— $\tau = 2$ .



**Fig. 3.** Distributions of normal displacements at various times



**Fig. 4.** Spatial distributions of normal displacements

**Acknowledgements.** The authors would like to acknowledge the financial support of the Russian Foundation for Basic Research (project № 19-08-01023 A).

**References**

1. Tarlakovskii, D.V., Fedotenkov, G.V.: Two-dimensional nonstationary contact of elastic cylindrical or spherical shells. *J. Mach. Manuf. Reliab.* **43**(2), 145–152 (2014)
2. Tarlakovskii, D.V., Fedotenkov, G.V.: Fedotenkov nonstationary 3D motion of an elastic spherical shell. *Mech. Solids* **50**(2), 208–217 (2015)
3. Mikhailova, E.Yu., Fedotenkov, G.V.: Nonstationary axisymmetric problem of the impact of a spherical shell on an elastic half-space (initial stage of interaction). *Mech. Solids* **46**(2), 239–247 (2011)
4. Mikhailova, E.Y., Tarlakovskii, D.V., Fedotenkov, G.V.: Transient contact problem for liquid filled concentric spherical shells and a rigid barrier. In: *Proceedings of the First International Conference on Theoretical, Applied and Experimental Mechanics* (2018), pp. 385–386
5. Fedotenkov, G.V., Mikhailova, E.Y., Kuznetsova, E.L., Rabinskiy, L.N.: Modeling the unsteady contact of spherical shell made with applying the additive technologies with the perfectly rigid stamp. *Int. J. Pure Appl. Math.* **111**(2), 331–342 (2016)



# Nonstationary Dynamic Problems for Elastic and Viscoelastic Piecewise Homogeneous Bodies

Pshenichnov Sergey<sup>(✉)</sup>

Institute of Mechanics, Lomonosov Moscow State University,  
Michurinsky Prospect 1, Moscow 119192, Russia  
serp56@yandex.ru

**Abstract.** The problems of transient wave processes in linearly viscoelastic piecewise homogeneous bodies with small deformations, boundedness of the disturbances propagation region, and creep boundedness of the material of homogeneous components of the bodies are considered. The issues related to the construction of solutions of such problems by the method of the integral Laplace transform with respect to time and subsequent reversal are touched upon. The statements about the properties of the Laplace transform simplifying the construction of the originals are formulated. The case when all homogeneous components of the body are linearly elastic is considered.

**Keywords:** Dynamics of viscoelastic bodies · Piecewise homogeneous bodies · Wave processes

## 1 Introduction

The study of transient wave processes in linear-viscoelastic piecewise-homogeneous bodies using analytical and numerical-analytical methods is very important, however, the results known today (some of which are reflected, for example, in [1–7]) are not exhaustive. Still, the study of the influence of the hereditary properties of the material on nonstationary processes in bodies with an arbitrary number of boundaries of the contact between the homogeneous components arouses interest. This paper presents theoretical results related to the construction of the solutions of dynamic linear viscoelasticity problems for piecewise homogeneous bodies with an arbitrary number of the components.

## 2 Mathematical Formulation of the Problem

Let us consider the nonstationary dynamic problem for a body occupying a domain  $\Omega$  with a boundary  $\Sigma$  and consisting of  $N$  homogeneous isotropic linear-viscoelastic components:  $\Omega = \Omega_1 \cup \Omega_2 \cup \dots \cup \Omega_N$  ( $\Omega_i$  and  $\Omega_j$  do not intersect at internal points if  $i \neq j$ ). On the contact surfaces between these components the conditions of continuity

of displacement and stresses vectors are satisfied. For each component of the body we write the equations of dynamics ( $n = 1, 2, \dots, N$ ):

$$(\hat{\lambda}_n + \hat{\mu}_n) \text{grad div } \mathbf{u}^{(n)}(\mathbf{x}, t) + \hat{\mu}_n \Delta \mathbf{u}^{(n)}(\mathbf{x}, t) + \mathbf{f}^{(n)}(\mathbf{x}, t) = \rho_n \ddot{\mathbf{u}}^{(n)}(\mathbf{x}, t) \quad (1)$$

and the material relations

$$\tilde{\boldsymbol{\sigma}}^{(n)}(\mathbf{x}, t) = \hat{\mu}_n \text{Def } \mathbf{u}^{(n)}(\mathbf{x}, t) + \hat{\lambda}_n \text{div } \mathbf{u}^{(n)}(\mathbf{x}, t) \tilde{\mathbf{I}}, \quad \mathbf{x}(x_1, x_2, x_3) \in \Omega_n. \quad (2)$$

For components with numbers  $1 \leq m \leq N$ , having the common points with a boundary  $\Sigma$ , we present the boundary conditions

$$\tilde{\boldsymbol{\alpha}}^{(m)}(\mathbf{x}) \tilde{\boldsymbol{\sigma}}^{(m)}(\mathbf{x}, t) \mathbf{n} + \tilde{\boldsymbol{\beta}}^{(m)}(\mathbf{x}) \mathbf{u}^{(m)}(\mathbf{x}, t) = \mathbf{p}^{(m)}(\mathbf{x}, t), \quad \mathbf{x} \in \Sigma, \quad t > 0 \quad (3)$$

On the contact surface of adjacent components with numbers  $p$  and  $q$  write down the relationships

$$\mathbf{u}^{(p)}(\mathbf{x}, t) = \mathbf{u}^{(q)}(\mathbf{x}, t), \quad \tilde{\boldsymbol{\sigma}}^{(p)}(\mathbf{x}, t) \mathbf{n} = \tilde{\boldsymbol{\sigma}}^{(q)}(\mathbf{x}, t) \mathbf{n}, \quad \mathbf{x} \in \Sigma_{pq} \quad (4)$$

For each component, we set the initial conditions

$$\mathbf{u}^{(n)}(\mathbf{x}, 0) = \mathbf{b}_1^{(n)}(\mathbf{x}), \quad \dot{\mathbf{u}}^{(n)}(\mathbf{x}, 0) = \mathbf{b}_2^{(n)}(\mathbf{x}), \quad \mathbf{x} \in \Omega_n \quad (5)$$

A dot above a letter means a time derivative;  $\tilde{\boldsymbol{\sigma}}^{(n)}$  is the stress tensor;  $\mathbf{u}^{(n)}$ ,  $\mathbf{p}^{(m)}$ ,  $\mathbf{f}^{(n)}$ ,  $\mathbf{b}_1^{(n)}$ ,  $\mathbf{b}_2^{(n)}$  are the vectors of displacements, the vectors of boundary actions, the volume forces, and the initial displacements and velocities related to the component of the body with the corresponding number;  $\rho_n$  is density;  $\tilde{\boldsymbol{\alpha}}^{(m)}$ ,  $\tilde{\boldsymbol{\beta}}^{(m)}$  are the tensors of rank 2 determining the type of boundary conditions;  $\mathbf{n}$  is the unit outward normal to the corresponding boundary;  $\Delta$  is the Laplace operator;  $\tilde{\mathbf{I}}$  is the unit tensor;  $\hat{\lambda}_n$ ,  $\hat{\mu}_n$  are the operators of the form

$$\begin{aligned} \hat{\lambda}_n &= \frac{1}{3} [3K_0^{(n)}(1 - \hat{T}_v^{(n)}) - 2G_0^{(n)}(1 - \hat{T}_s^{(n)})], & \hat{\mu}_n &= G_0^{(n)}(1 - \hat{T}_s^{(n)}), \\ \hat{T}_v^{(n)} \xi(t) &= \int_0^t T_v^{(n)}(t - \tau) \xi(\tau) d\tau, & \hat{T}_s^{(n)} \xi(t) &= \int_0^t T_s^{(n)}(t - \tau) \xi(\tau) d\tau \end{aligned} \quad (6)$$

where  $G_0^{(n)}$ ,  $K_0^{(n)}$  are the instantaneous values of the shear modulus and volume compression;  $T_v^{(n)}(t)$ ,  $T_s^{(n)}(t)$  are the volume and shear relaxation kernels of the body's component with the number  $n$ . It is assumed that the disturbances propagation domain is bounded.



### 3 The Problem in Transforms

Let us apply the integral Laplace transform with respect to time to (1)–(4), denoting the transforms of the variables

$$\mathbf{u}^{(n)}(\mathbf{x}, t), \tilde{\boldsymbol{\sigma}}^{(n)}(\mathbf{x}, t), \mathbf{f}^{(n)}(\mathbf{x}, t), \mathbf{p}^{(m)}(\mathbf{x}, t), T_v^{(n)}(t), T_s^{(n)}(t)$$

correspondingly through

$$\mathbf{U}^{(n)}(\mathbf{x}, s), \tilde{\mathbf{S}}^{(n)}(\mathbf{x}, s), \mathbf{F}^{(n)}(\mathbf{x}, s), \mathbf{P}^{(m)}(\mathbf{x}, s), \Theta_v^{(n)}(s), \Theta_s^{(n)}(s), \quad s \in C.$$

Taking into account (6) and the initial conditions (5), we obtain the problem for the transforms, which includes the dynamic equations ( $n = 1, 2, \dots, N$ )

$$\begin{aligned} (\Lambda_n(s) + M_n(s)) \text{grad div } \mathbf{U}^{(n)}(\mathbf{x}, s) + M_n(s) \Delta \mathbf{U}^{(n)}(\mathbf{x}, s) \\ - \rho_n s^2 \mathbf{U}^{(n)}(\mathbf{x}, s) + \rho_n [s \mathbf{b}_1^{(n)}(\mathbf{x}) + \mathbf{b}_2^{(n)}(\mathbf{x})] + \mathbf{F}^{(n)}(\mathbf{x}, s) = \mathbf{0}, \quad \mathbf{x} \in \Omega_n \end{aligned} \tag{7}$$

material relations

$$\begin{aligned} \tilde{\mathbf{S}}^{(n)}(\mathbf{x}, s) = M_n(s) \text{Def } \mathbf{U}^{(n)}(\mathbf{x}, s) + \Lambda_n(s) \text{div } \mathbf{U}^{(n)}(\mathbf{x}, s) \tilde{\mathbf{I}}, \\ \Lambda_n(s) = \frac{1}{3} [3K_0^{(n)}(1 - \Theta_v^{(n)}(s)) - 2G_0^{(n)}(1 - \Theta_s^{(n)}(s))], \quad M_n(s) = G_0^{(n)}(1 - \Theta_s^{(n)}(s)) \end{aligned} \tag{8}$$

the boundary conditions for the components which have points on the boundary  $\Sigma$

$$\tilde{\boldsymbol{\alpha}}^{(m)}(\mathbf{x}) \tilde{\mathbf{S}}^{(m)}(\mathbf{x}, s) \mathbf{n} + \tilde{\boldsymbol{\beta}}^{(m)}(\mathbf{x}) \mathbf{U}^{(m)}(\mathbf{x}, s) = \mathbf{P}^{(m)}(\mathbf{x}, s), \quad \mathbf{x} \in \Sigma, \quad 1 \leq m \leq N \tag{9}$$

and conditions on the contact surface of adjacent components with numbers  $p$  and  $q$

$$\mathbf{U}^{(p)}(\mathbf{x}, s) = \mathbf{U}^{(q)}(\mathbf{x}, s), \quad \tilde{\mathbf{S}}^{(p)}(\mathbf{x}, s) \mathbf{n} = \tilde{\mathbf{S}}^{(q)}(\mathbf{x}, s) \mathbf{n}, \quad \mathbf{x} \in \Sigma_{pq} \tag{10}$$

Assuming that the solution  $\mathbf{U}^{(n)}(\mathbf{x}, s)$  of the problem (7)–(10) is constructed, we establish a number of its properties which simplify the construction of the original. For this aim, in addition to problem (1)–(5), we consider the problem of damped free oscillations of the same piecewise-homogeneous body.

### 4 The Problem of Free Vibrations

Let the body oscillate in the absence of volume forces and boundary actions ( $\mathbf{f}^{(n)} \equiv \mathbf{0}$  and  $\mathbf{p}^{(m)} \equiv \mathbf{0}$ ) after such a period of time from the beginning, that the character of the oscillations practically does not depend on the way they are excited. So the lower

integration limit in operators (6) of the material relations (2) is  $-\infty$ . Representing the nontrivial solution of this problem in the form

$$\mathbf{u}^{(n)}(\mathbf{x}, t) = \mathbf{V}^{(n)}(\mathbf{x}, s) e^{st}, \quad s \in \mathcal{C},$$

we obtain the spectral problem

$$\begin{aligned} (\Lambda_n(s) + M_n(s)) \text{grad div } \mathbf{V}^{(n)}(\mathbf{x}, s) + M_n(s) \Delta \mathbf{V}^{(n)}(\mathbf{x}, s) - \rho_n s^2 \mathbf{V}^{(n)}(\mathbf{x}, s) &= \mathbf{0}, \\ \tilde{\mathbf{S}}^{(n)}(\mathbf{x}, s) &= M_n(s) \text{Def } \mathbf{V}^{(n)}(\mathbf{x}, s) + \Lambda_n(s) \text{div } \mathbf{V}^{(n)}(\mathbf{x}, s) \tilde{\mathbf{I}}, \quad \mathbf{x} \in \Omega_n, \\ \tilde{\boldsymbol{\alpha}}^{(m)}(\mathbf{x}) \tilde{\mathbf{S}}^{(m)}(\mathbf{x}, s) \mathbf{n} + \tilde{\boldsymbol{\beta}}^{(m)}(\mathbf{x}) \mathbf{V}^{(m)}(\mathbf{x}, s) &= \mathbf{0}, \quad \mathbf{x} \in \Sigma, \\ \mathbf{V}^{(p)}(\mathbf{x}, s) = \mathbf{V}^{(q)}(\mathbf{x}, s), \quad \tilde{\mathbf{S}}^{(p)}(\mathbf{x}, s) \mathbf{n} = \tilde{\mathbf{S}}^{(q)}(\mathbf{x}, s) \mathbf{n}, \quad \mathbf{x} \in \Sigma_{pq} \end{aligned} \tag{11}$$

eigenvalue  $s$  of which determines the frequency and damping coefficient of the free oscillations of the body.

### 5 Some Properties of the Solutions for the Transforms

Let us consider the connection of the branch points and poles of the components  $\{U_i^{(n)}(\mathbf{x}, s)\}$ ,  $i = 1, 2, 3, n = 1, 2, \dots, N$  of vectors  $\{\mathbf{U}^{(n)}\}$  characterizing the solution of the problem (7)–(10) with the spectrum of the problem (11). Let  $E_s$  be the set of eigenvalues of the problem (11), and  $E_{br}$  be the union of sets of branch points of the functions  $\Theta_v^{(n)}(s)$ ,  $\Theta_s^{(n)}(s)$  and the components  $P_i^{(m)}(\mathbf{x}, s)$ ,  $F_i^{(n)}(\mathbf{x}, s)$ ,  $i = 1, 2, 3$  of the vectors  $\mathbf{P}^{(m)}$  and  $\mathbf{F}^{(n)}$ ,  $n = 1, 2, \dots, N$ ,  $1 \leq m \leq N$ . In the particular case  $E_{br}$  may be empty.

**Statement 1** Suppose the set  $E_s$  is at most countable, and the set  $E_{br}$  is finite. Then, for all  $\mathbf{x} \in \Omega$  the branch points of any component  $U_i^{(n)}(\mathbf{x}, s)$  of the solution  $\mathbf{U}^{(n)}$  of the problem in transforms (7)–(10) can be only the elements of  $E_{br}$ .

**Remark 1** In the problem (1)–(5) it is assumed that the perturbation propagation domain is bounded, therefore the countability of the set  $E_s$  is quite natural. If the set  $E_{br}$  is empty, then all components  $U_i^{(n)}(x, s)$  of the solution of the problem (7)–(10) have no branch points. In many cases it is not immediately obvious, but is revealed after a series of calculations, often very laborious.

**Statement 2** Suppose  $s_\lambda \neq 0$  is a pole of the functions  $U_i^{(n)}(\mathbf{x}, s)$  and their derivatives with respect to coordinates  $U_{i,j}^{(n)}(\mathbf{x}, s)$ ,  $U_{i,jk}^{(n)}(\mathbf{x}, s)$  for all  $\mathbf{x} \in \Omega_n$  ( $i, j, k = 1, 2, 3, n = 1, 2, \dots, N$ ) and is not a singular point of  $\mathbf{P}^{(m)}(\mathbf{x}, s)$ ,  $\mathbf{F}^{(n)}(\mathbf{x}, s)$ ,  $\Theta_v^{(n)}(s)$ ,  $\Theta_s^{(n)}(s)$ . Then  $s_\lambda$  is an eigenvalue of the problem (11).

**Remark 2** If the conditions of the Statement 2 are fulfilled for  $s_\lambda \neq 0$  and at least one of the kernels  $T_v^{(n)}$ ,  $T_s^{(n)}$  for at least one  $n$  is not zero, then  $\text{Re}(s_\lambda) < 0$ . In this case, the

sets of poles of functions  $U_i^{(n)}(\mathbf{x}, s)$  may have finite limit points. These points in the case of bounded creep of the material are located to the left of the imaginary axis.

### 6 The Forms of the Solution in Originals

Let us establish the connection between the original problem (1)–(5) and the static problem of the theory of elasticity. In addition to the boundedness of perturbation propagation domain, we assume that the following conditions are met. At least one of the kernels  $T_v^{(n)}, T_s^{(n)}$  of at least one homogeneous component of the body is not zero; the creep of all components is limited; the displacements of the body as a rigid whole are excluded; boundary actions and the volume forces are such that there are limits

$$\lim_{t \rightarrow \infty} \mathbf{p}^{(m)}(\mathbf{x}, t) = \mathbf{p}_0^{(m)}(\mathbf{x}) \text{ and } \lim_{t \rightarrow \infty} \mathbf{f}^{(n)}(\mathbf{x}, t) = \mathbf{f}_0^{(n)}(\mathbf{x}), n = 1, 2, \dots, N, 1 \leq m \leq N.$$

Then there is a limit  $\lim_{t \rightarrow \infty} \mathbf{u}^{(n)}(\mathbf{x}, t) = \mathbf{u}_0^{(n)}(\mathbf{x})$ , where  $\mathbf{u}_0^{(n)}$  is a solution of the problem of the static theory of elasticity with long-term moduli  $\Lambda_n(0) = \lambda_\infty^{(n)}, M_n(0) = \mu_\infty^{(n)}$  which includes the equations:

$$(\lambda_\infty^{(n)} + \mu_\infty^{(n)}) \text{grad div} \mathbf{u}_0^{(n)}(\mathbf{x}) + \mu_\infty^{(n)} \Delta \mathbf{u}_0^{(n)}(\mathbf{x}) + \mathbf{f}_0^{(n)}(\mathbf{x}) = \mathbf{0}, \quad \mathbf{x} \in \Omega_n;$$

boundary conditions

$$\tilde{\boldsymbol{\alpha}}^{(m)}(\mathbf{x}) [\mu_\infty^{(m)} \text{Def} \mathbf{u}_0^{(m)}(\mathbf{x}) + \lambda_\infty^{(m)} \text{div} \mathbf{u}_0^{(m)}(\mathbf{x}) \tilde{\mathbf{I}}] \mathbf{n} + \tilde{\boldsymbol{\beta}}^{(m)}(\mathbf{x}) \mathbf{u}_0^{(m)}(\mathbf{x}) = \mathbf{p}_0^{(m)}(\mathbf{x}), \quad \mathbf{x} \in \Sigma$$

and the conditions of continuity of displacement and stress vectors on the contact surface of adjacent components, which are omitted here.

When all the above conditions are fulfilled, as well as the corresponding asymptotic relations in the vicinity of the accumulation points of the poles  $U_i^{(n)}(\mathbf{x}, s)$ , the theoretical concepts presented here make it possible to construct a solution of the problem (1)–(5) in the originals or in the form of series of residues at the poles of the transforms (if there are no branch points)

$$\mathbf{u}^{(n)}(\mathbf{x}, t) = \mathbf{u}_0^{(n)}(\mathbf{x}) + \sum_k \underset{s \neq 0}{\underset{s=s_k}{\text{Res}}} [\mathbf{U}^{(n)}(\mathbf{x}, s) e^{st}], \quad t > 0, \tag{12}$$

or (both in the absence and in the presence of branch points) in the form

$$\mathbf{u}^{(n)}(\mathbf{x}, t) = \frac{1}{2} \mathbf{u}_0^{(n)}(\mathbf{x}) + \frac{1}{\pi} \int_0^\infty \text{Re}[\mathbf{U}^{(n)}(\mathbf{x}, i\omega) e^{i\omega t}] d\omega, \quad t > 0 \tag{13}$$

where the integrand has no singularities as  $\omega \rightarrow 0$ .

Let the following conditions be satisfied

$$\mathbf{f}^{(n)}(\mathbf{x}, t) \equiv \mathbf{0} \text{ and } \mathbf{p}^{(m)}(\mathbf{x}, t) = \mathbf{p}_0^{(m)}(\mathbf{x}) \varphi(t). \quad (14)$$

If we construct a solution  $\mathbf{u}^{(n)}$  under the condition  $\varphi(t) = h(t)$  (which is Heaviside function), then using convolution, we can obtain a solution with another  $\varphi(t)$ , which does not necessarily have a limit as  $t \rightarrow \infty$ .

Let us pay attention to two special cases, when the solution is significantly simplified. The first one is when all homogeneous components of the body are linearly elastic ( $T_v^{(n)}(t) \equiv 0, T_s^{(n)}(t) \equiv 0$ ), the initial conditions are zero  $\mathbf{b}_1^{(n)}(\mathbf{x}) \equiv \mathbf{0}, \mathbf{b}_2^{(n)}(\mathbf{x}) \equiv \mathbf{0}$ , equalities (14) are fulfilled and  $\varphi(t) = h(t)$ . It can be shown that in this case all the poles of the transforms  $\mathbf{U}^{(n)}(\mathbf{x}, s)$  are located on the imaginary axis and they are simple. Representing the original in the form of an infinite sum of residues actually means the series expansion in eigenforms of free vibrations of the considered piecewise-homogeneous body. Note that formula (13) is not applicable for a linearly elastic body.

Another case is when all body components are viscoelastic, but their hereditary properties are characterized by only one kernel, the same for all components

$$T_v^{(n)}(t) \equiv T_s^{(n)}(t) \equiv ae^{-bt}, \quad n = 1, 2, \dots, N, \quad 0 < a < b/2. \quad (15)$$

Moreover, the initial conditions are zero and equalities (14) are fulfilled with  $\varphi(t) = h(t)$ . Then the poles of the transforms  $\mathbf{U}^{(n)}(\mathbf{x}, s)$  will also be simple. They are located to the left of the imaginary axis (except  $s = 0$ ) and they are easy to find.

**Comments.** Basing on the above theoretical propositions, the solutions were constructed for a number of nonstationary dynamic problems for multilayer bodies with plane-parallel, spherical and cylindrical boundaries of elastic and viscoelastic homogeneous layers. The cases, when the relaxation kernels of the material of the layers were not interconnected, were considered. Wave processes in multilayer cylinders with a large number of coaxial layers were investigated. This allowed to make the transition to the study of the dynamics of cylinders with continuous radial inhomogeneity of the material [8].

**Acknowledgments.** The reported study was funded by Russian Foundation for Basic Research, according to the research projects No. 19-08-00438 a, 18-08-00471 a.

## References

1. Sabodash, P.F.: Propagation of longitudinal viscoelastic waves in a three-layer medium. *Polym. Mech.* **7**(1), 124–128 (1971). [in Russian]
2. Kozlov, V.I., Kucher, N.K.: Dynamic behavior of multilayer cylindrical structures with transient loads. *Strength Mater.* **12**(5), 639–648 (1980). [in Russian]
3. Nuriev, B.R.: Impact on a viscoelastic layered composite. *Izv. Akad. Nauk AzSSR. Ser. Fiz-Tekh. Mat. Nauk* **4**, 35–41 (1985). (in Russian)
4. Songnan, L., Ping, G.: Dynamic response of layered viscoelastic half-space and its application to dynamic foundation problems. *Hubnan Daxue Xuebao J. Hunan Univ.* **20**(1), 57–64 (1993)

5. Lokshin, A.A.: The head wave at the boundary of two hereditary-elastic half-spaces. The case of a linear source. *J. Appl. Math. Mech.* **58**(1), 171–176 (1994)
6. Hyung Suk Lee: Viscowave—a new solution for viscoelastic wave propagation of layered structures subjected to an impact load. *Int. J. Pavement Eng.* **15**(6), 542–557 (2014)
7. Hashemi, S.H., Khaniki, H.B.: Dynamic behavior of multi-layered viscoelastic nanobeam system embedded in a viscoelastic medium with a moving nanoparticle. *J. Mech.* **33**(5), 559–575 (2017)
8. Korovaytseva, E.A., Pshenichnov, S.G.: The study of transient wave propagation in linearly visco-elastic bodies subject to the continuous heterogeneity of the material. *Prob. Strength Plast.* **78**(3), 262–270 (2016). [in Russian]



# The Wave Field of a Layer with a Cylindrical Cavity

Anna Fesenko<sup>(✉)</sup> and Nataly Vaysfel'd

Department of Mathematics, Physics and Information Technologies, Odessa I.I. Mechnikov National University, Dvoryanska Str.2, 65082 Odessa, Ukraine  
8lanna8l@gmail.com, vaysfeld@onu.edu.ua

**Abstract.** The wave field of an infinite elastic layer weakened by a cylindrical cavity is constructed in this paper. The ideal contact conditions are given on the upper and bottom faces of the layer. The normal dynamic tensile load is applied to a cylindrical cavity's surface at the initial moment of time. The Laplace and finite sin- and cos- Fourier integral transformations are applied successively directly to axisymmetric equations of motion and to the boundary conditions, on the contrary to the traditional approaches, when integral transformations are applied to solutions' representation through harmonic and biharmonic functions. This operation leads to a one-dimensional vector inhomogeneous boundary value problem with respect to unknown transformations of displacements. The problem is solved using matrix differential calculus. The field of initial displacements is derived after application of inverse integral transformations. The normal stress on the faces of the elastic layer are constructed and investigated depending on the mechanical and dynamic parameters.

**Keywords:** Elastic layer · Dynamic load · Cylindrical cavity · Integral transformation

## 1 Introduction

The presence of cracks in elastic bodies causes a stress concentration and significantly affects at the stress state of engineering constructions. A typical and sufficiently investigated problem of this class is the axisymmetric problem of the elasticity on the stress state of a layer, weakened by a cylindrical defect, when different boundary conditions are set on layer's faces and defect's surface. Existing research can be divided into three approaches: (1) a construction of an analytic solution of the problem in an explicit form [1, 2]; (2) a construction of an analytic-numerical solution, when the problem is reduced either to an integral equation or to an infinite system of algebraic equations, which are solved numerically [3, 4]; (3) a numerical solving of the problem [5, 6]. The problem of elasticity for an infinite layer with a cylindrical cavity in a static statement was considered by Popov [1], where an exact solution was obtained. In this paper authors extended this method on the analogical problem in the dynamic statement, where the boundary resonance phenomenon was investigated.

### 2 The Statement of the Problem

An elastic layer of thickness  $h$  ( $G$  is a shear modulus,  $\mu$  is a Poisson's ratio,  $\rho$  is density), describing in the cylindrical coordinate system by the correspondences:  $a < r < \infty$ ,  $-\pi < \varphi \leq \pi$ ,  $0 \leq z \leq h$  is weakened by a cylindrical cavity  $0 \leq r \leq a$ ,  $0 < \varphi \leq \pi$ ,  $0 \leq z \leq h$ . The layer's upper and bottom faces are in the conditions of ideal contact with a rigid base (the layer is supported by a smooth foundation without a friction)

$$u_r(r, 0, t) = 0, \quad \tau_{zr}(r, 0, t) = 0, \quad u_z(r, h, t) = 0, \quad \tau_{zr}(r, h, t) = 0 \quad (1)$$

The cylindrical cavity's surface  $r = a$  is under the influence of the normal dynamic tensile force  $P = P(z, t)$ , applied at the initial moment  $t = 0$ , the tangential loading is absent

$$\sigma_r(a, z, t) = P(z, t), \quad \tau_{rz}(a, z, t) = 0 \quad (2)$$

Thus, the problem was reduced to solving axisymmetric equations of motion with respect to the functions  $u_r(r, z, t) = u(r, z, t)$ ,  $u_z(r, z, t) = w(r, z, t)$  in a cylindrical coordinate system

$$\begin{aligned} r^{-1} \frac{\partial}{\partial r} \left[ r \frac{\partial}{\partial r} u(r, z, t) \right] - r^{-2} u(r, z, t) + \frac{\kappa - 1}{\kappa + 1} \frac{\partial^2}{\partial z^2} u(r, z, t) + \frac{2}{\kappa + 1} \frac{\partial^2}{\partial r \partial z} w(r, z, t) \\ = \frac{\kappa - 1}{\kappa + 1} \frac{\rho}{G} \frac{\partial^2 u(r, z, t)}{\partial t^2} \\ r^{-1} \frac{\partial}{\partial r} \left[ r \frac{\partial}{\partial r} w(r, z, t) \right] + \frac{\kappa + 1}{\kappa - 1} \frac{\partial^2}{\partial z^2} w(r, z, t) + \frac{2}{\kappa - 1} r^{-1} \frac{\partial}{\partial r} \left[ r \frac{\partial}{\partial z} u(r, z, t) \right] \\ = \frac{\rho}{G} \frac{\partial^2 w(r, z, t)}{\partial t^2} \end{aligned} \quad (3)$$

where  $\kappa = 3 - 4\mu$  and subjected to the mixed boundary conditions (1), (2). Here  $c_1^2 = \frac{\kappa + 1}{\kappa - 1} G / \rho$ —squared velocity of longitudinal wave propagation,  $c^2 = G / \rho$ —squared velocity of shear wave propagation. So,  $c_1^2 = \frac{\kappa + 1}{\kappa - 1} c^2$ .

### 3 Solving the Problem

The following change of the variables was done

$$\begin{aligned} \rho = a^{-1} r, \quad \xi = h^{-1} z, \quad \tau = ca^{-1} t, \quad u(a\rho, h\xi, ca^{-1}\tau) = U(\rho, \xi, \tau), \\ w(a\rho, h\xi, ca^{-1}\tau) = W(\rho, \xi, \tau) \end{aligned} \quad (4)$$

Consequently, the movement equations (3) can be written in the form

$$\begin{aligned} \rho^{-1} \frac{\partial}{\partial \rho} \left[ \rho \frac{\partial}{\partial \rho} U \right] - \rho^{-2} U + \frac{\kappa-1}{\kappa+1} \alpha^2 \frac{\partial^2}{\partial \xi^2} U + \frac{2}{\kappa+1} \alpha \frac{\partial^2}{\partial \rho \partial \xi} W &= \frac{\kappa-1}{\kappa+1} \frac{\partial^2 U(\rho, \xi, \tau)}{\partial \tau^2} \\ \rho^{-1} \frac{\partial}{\partial \rho} \left[ \rho \frac{\partial}{\partial \rho} W \right] + \frac{\kappa+1}{\kappa-1} \alpha^2 \frac{\partial^2}{\partial \xi^2} W + \rho^{-1} \frac{2}{\kappa-1} \alpha \frac{\partial}{\partial \rho} \left[ \rho \frac{\partial}{\partial \xi} U \right] &= \frac{\partial^2 W(\rho, \xi, \tau)}{\partial \tau^2} \end{aligned} \quad (5)$$

$1 < \rho < \infty, \quad 0 < \xi < 1, \quad \tau > 0, \quad \alpha = a/h$

Boundary conditions (1), taking into account the replacement (4), are transformed into form

$$\frac{\partial}{\partial \xi} U(\rho, 0, \tau) = 0, \quad \frac{\partial}{\partial \xi} U(\rho, 1, \tau) = 0, \quad W(\rho, 0, \tau) = 0, \quad W(\rho, 1, \tau) = 0 \quad (6)$$

as the boundary conditions (2) take the form

$$\frac{\partial}{\partial \rho} U(1, \xi, \tau) + \frac{3-\kappa}{1+\kappa} \left[ U(1, \xi, \tau) + \alpha \frac{\partial}{\partial \xi} W(1, \xi, \tau) \right] = aG^{-1} \frac{\kappa-1}{\kappa+1} P(\xi, \tau) \quad (7)$$

$$\alpha \frac{\partial}{\partial \xi} U(1, \xi, \tau) + \frac{\partial}{\partial \rho} W(1, \xi, \tau) = 0 \quad (8)$$

In order to reduce the problem to the one-dimensional one, the finite sin- and cos-Fourier integral transformations with regard of the variable  $\xi$  and Laplace integral transformation with regard of the variable  $\tau$  are applied successively to the differential equations (5) and boundary conditions (6)–(8).

As a result, Eq. (5) can be written

$$\begin{aligned} \rho^{-1} \frac{\partial}{\partial \rho} \left[ \rho \frac{\partial}{\partial \rho} U_{\lambda p}(\rho) \right] + \frac{2}{\kappa+1} \lambda_* \frac{\partial}{\partial \rho} W_{\lambda p}(\rho) - \rho^{-2} U_{\lambda p}(\rho) \\ - \frac{\kappa-1}{\kappa+1} \lambda_*^2 U_{\lambda p}(\rho) - \frac{\kappa-1}{\kappa+1} p^2 U_{\lambda p}(\rho) = 0 \end{aligned} \quad (9)$$

$$\begin{aligned} \rho^{-1} \frac{\partial}{\partial \rho} \left[ \rho \frac{\partial}{\partial \rho} W_{\lambda p}(\rho) \right] - \rho^{-1} \frac{2}{\kappa-1} \lambda_* \frac{\partial}{\partial \rho} \left[ \rho U_{\lambda p}(\rho) \right] - \frac{\kappa+1}{\kappa-1} \lambda_*^2 W_{\lambda p}(\rho) - p^2 W_{\lambda p}(\rho) = 0 \\ 1 < \rho < \infty, \quad \lambda_* = \lambda \alpha \end{aligned}$$

During this operation the boundary conditions (6) are automatically satisfied, and conditions (7), (8) have the form

$$\begin{aligned} U'_{\lambda p}(1) + \frac{3-\kappa}{1+\kappa} [U_{\lambda p}(1) + \lambda_* W_{\lambda p}(1)] &= aG^{-1} \frac{\kappa-1}{\kappa+1} P_{\lambda p} \\ W'_{\lambda p}(1) - \lambda_* U_{\lambda p}(1) = 0, \quad P_{\lambda p} &= \int_0^\infty \left( \int_0^1 P(\xi, \tau) \cos \lambda_n \xi d\xi \right) e^{-p\tau} d\tau \end{aligned} \quad (10)$$



For solving a one-dimensional boundary value problem (9), (10) a second-order matrix differential operator and the unknown vector of displacements' transformations are set

$$L_2 = \begin{pmatrix} \rho^{-1} \frac{\partial}{\partial \rho} \left[ \rho \frac{\partial}{\partial \rho} \right] - \rho^{-2} - \frac{\kappa-1}{\kappa+1} (\lambda_*^2 + p^2) & \frac{2}{\kappa+1} \lambda_* \frac{\partial}{\partial \rho} \\ -\frac{2}{\kappa-1} \lambda_* \rho^{-1} \frac{\partial}{\partial \rho} [\rho] & \rho^{-1} \frac{\partial}{\partial \rho} \left[ \rho \frac{\partial}{\partial \rho} \right] - \frac{\kappa+1}{\kappa-1} \lambda_*^2 - p^2 \end{pmatrix}$$

$$\mathbf{y}(\rho) = \begin{pmatrix} U_{\lambda p}(\rho) \\ W_{\lambda p}(\rho) \end{pmatrix}$$

Let's set up the boundary functional corresponding to the boundary conditions (10)

$$U[\mathbf{y}(1)] = \mathbf{A} \cdot \mathbf{y}(1) + \mathbf{I} \cdot \mathbf{y}'(1), \quad \mathbf{A} = \begin{pmatrix} \frac{3-\kappa}{1+\kappa} & \frac{3-\kappa}{1+\kappa} \lambda_* \\ -\lambda_* & 0 \end{pmatrix}, \quad \mathbf{I} = \begin{pmatrix} 1 & 0 \\ 0 & 1 \end{pmatrix}$$

In these notations the boundary value problem (9), (10) is written down in a next form

$$L_2 \mathbf{y}(\rho) = \mathbf{f}(\rho), \quad 1 < \rho < \infty, \quad U[\mathbf{y}(1)] = \gamma \tag{11}$$

In order to get a general decreasing solution when  $\rho \rightarrow \infty$  of the vector homogeneous equation in (11), the solution of the matrix differential equation

$$L_2 \mathbf{Y}(\rho) = 0, \quad 1 < \rho < \infty \tag{12}$$

should be constructed previously.

With the help of the auxiliary matrix

$$\mathbf{H}(\rho, \xi) = \begin{pmatrix} H_1^{(1)}(\rho \xi) & 0 \\ 0 & H_0^{(1)}(\rho \xi) \end{pmatrix}$$

where  $H_m^{(1)}(z)$  is the Hankel first order function,  $m = 0, 1$ , an important relationship has been proven [1]

$$L_2 \mathbf{H}(\rho, \xi) = -\mathbf{H}(\rho, \xi) \cdot \mathbf{M}(\xi)$$

$$\mathbf{M}(\xi) = \begin{pmatrix} \xi^2 + \frac{\kappa-1}{\kappa+1} (\lambda_*^2 + p^2) & \frac{2}{\kappa+1} \xi \lambda_* \\ \frac{2}{\kappa-1} \xi \lambda_* & \xi^2 + \frac{\kappa+1}{\kappa-1} \lambda_*^2 + p^2 \end{pmatrix} \tag{13}$$

$$\det \mathbf{M} = \left[ \xi - i \sqrt{\lambda_*^2 + p^2} \right] \left[ \xi + i \sqrt{\lambda_*^2 + p^2} \right] \left[ \xi - i \sqrt{\lambda_*^2 + \frac{\kappa-1}{\kappa+1} p^2} \right] \left[ \xi + i \sqrt{\lambda_*^2 + \frac{\kappa-1}{\kappa+1} p^2} \right]$$

Further, with the help of the equality (13), one can be convinced that the solution of the matrix equation (12) is

$$\mathbf{Y}(\rho) = \frac{1}{2\pi i} \int_C \mathbf{H}(\rho, \xi) \cdot \mathbf{M}^{-1}(\xi) d\xi$$

where  $C$  is the closed contour covering the origin and two poles of the first multiplicity  $\xi = i\sqrt{\lambda_*^2 + p^2}$ ,  $\xi = i\sqrt{\lambda_*^2 + \frac{\kappa-1}{\kappa+1}p^2}$  lying in the upper half-plane. Applying the methods of contour integration, the matrix is derived

$$\begin{aligned} \mathbf{Y}(\rho) = & \frac{1}{2p^2} \begin{pmatrix} i\frac{\kappa+1}{\kappa-1} \frac{\lambda_*^2}{\delta_1} H_1^{(1)}(i\rho\delta_1) & \lambda_* H_1^{(1)}(i\rho\delta_1) \\ i\frac{\kappa+1}{\kappa-1} \lambda_* H_0^{(1)}(i\rho\delta_1) & -i\delta_1 H_0^{(1)}(i\rho\delta_1) \end{pmatrix} \\ & + \frac{1}{2p^2} \begin{pmatrix} -i\frac{\kappa+1}{\kappa-1} \delta_2 H_1^{(1)}(i\rho\delta_2) & -\lambda_* H_1^{(1)}(i\rho\delta_2) \\ -i\frac{\kappa+1}{\kappa-1} \lambda_* H_0^{(1)}(i\rho\delta_2) & i\frac{\lambda_*^2}{\delta_2} H_0^{(1)}(i\rho\delta_2) \end{pmatrix} \end{aligned}$$

where  $\delta_1 = \sqrt{\lambda_*^2 + p^2}$ ,  $\delta_2 = \sqrt{\lambda_*^2 + \frac{\kappa-1}{\kappa+1}p^2}$ .

Taking into account the results in [1] and the range of the parameter  $1 < \rho < \infty$ , a decreasing solution of the matrix equation is constructed

$$\begin{aligned} \mathbf{Y}_{\lambda,p}(\rho) = & \frac{1}{p^2} \begin{pmatrix} -i\frac{\kappa+1}{\kappa-1} \frac{\lambda_*^2}{\delta_1} K_1(\rho\delta_1) & -\lambda_* K_1(\rho\delta_1) \\ -i\frac{\kappa+1}{\kappa-1} \lambda_* K_0(\rho\delta_1) & -\sqrt{\lambda_*^2 + p^2} K_0(\rho\delta_1) \end{pmatrix} \\ & + \frac{1}{p^2} \begin{pmatrix} i\frac{\kappa+1}{\kappa-1} \delta_2 K_1(\rho\delta_2) & \lambda_* K_1(\rho\delta_2) \\ i\frac{\kappa+1}{\kappa-1} \lambda_* K_0(\rho\delta_2) & \frac{\lambda_*^2}{\delta_2} K_0(\rho\delta_2) \end{pmatrix} \end{aligned}$$

where  $K_m(z)$  is the Macdonald function,  $m = 0, 1$ .

The solution of the one-dimensional problem (11) is written in the form [1]

$$\mathbf{y}(\rho) = \mathbf{Y}_{\lambda,p}(\rho) \cdot \begin{pmatrix} iC_0 \\ C_1 \end{pmatrix} \tag{15}$$

The reality of the solution's values (15) is guaranteed by the special choice of constants  $C_0, C_1$ , which can be found from the boundary conditions (10).

The solution of the one-dimensional value problem (11) in transformation domain was constructed.

In order to get the solution of initial problem (1–3), the inverse integral transformations should be applied.

The field of the initial displacements of the infinite elastic layer with the cylindrical cavity was derived.

The case of steady-state oscillations is considered below. With this aim the substitution  $p = i\omega$ ,  $p^2 = -\omega^2$  was made ( $p$ —Laplace transformation parameter,  $\omega$ —circular frequency of steady-state oscillations. The normal stress on the lower face of the layer  $\xi = 0$ ,  $1 < \rho < \infty$  was investigated, depending on different mechanical

characteristics: Poisson's ratio  $\mu = 1/3$  or  $\mu = 1/4$ , ratio of cavity radius to layer thickness  $\alpha = a/h$ , different variants of natural oscillation frequencies  $\omega = 0.1, 0.3, 0.5, 1, 2, 3$ . The possibility of the appearance of tensile stress on the lower face of the layer was considered. The dynamic load of constant intensity was set on the cylindrical surface of the cavity.

## 4 Conclusions

1. The dynamic problem's solution of the elasticity for a cylindrical cavity was derived, when on the faces of the infinite layer the ideal contact conditions are given.
2. The results were detailed for the case of steady-state oscillations.

## References

1. Popov, G.Y.: An exact solution of the elasticity theory problem for an infinite layer weakened by a cylindrical cavity. *Doklady Akad. Nauk SSSR*, **451**(5), 1–4 (2013)
2. Menshykov, O., Menshykova, M., Vaysfeld, N.: Exact analytical solution for a pie-shaped wedge thick plate under oscillating load. *Acta Mech.* **228**(12), 4435–4450 (2017). <https://doi.org/10.1007/s00707-017-1938-9>
3. Malitz, P.Y., Privarnikov, A.K.: The application of weber-type transformations to the solution of elasticity problems for layered media with a cylindrical hole. *J. Voprosu prochnosti i plastichnossty* 56–64 (1971)
4. Arutunyan, N.H., Abramyan, B.L.: Some axisymmetric problems for a half-space and an elastic layer with a vertical cylindrical notch. *J. Izv. AN Arm. SSR. Mekhanika* **22**(3), 3–13 (1969)
5. Jain, N.K., Mittal, N.D.: Finite element analysis for stress concentration and deflection in isotropic, orthotropic and laminated composite plates with central circular hole under transverse static load. *Mater. Sci. Eng.* **498**, 115–124 (2008)
6. Zheng, Y., Chang-Boo, K., Chongdu, C., Hyeon Gyu, B.: The concentration of stress and strain in finite thickness elastic plate containing a circular hole. *Int. J. of Solids Struct.* **45**(3–4), 713–731 (2008)



# Features of Subsonic Stage of Contact Interaction of Viscoelastic Half-Plane and Absolutely Rigid Striker

Ekaterina Korovaytseva<sup>(✉)</sup> and Dmitry Tarlakovskii

Institute of Mechanics, Lomonosov Moscow State University,  
Michurinsky Prospect, 1, Moscow 119192, Russia  
katrell@mail.ru

**Abstract.** Non-stationary dynamic contact problem for viscoelastic half-plane and absolutely rigid striker at subsonic stage of interaction is considered. Viscoelastic properties of half-plane material are described by exponential relaxation kernel. Free slipping is considered as contact boundary condition. Green function for normal displacement at the boundary of the half-plane is obtained using generalized convolution method. The resolving equation system consists of the striker motion equation, integral representation of half-plane boundary normal displacement, contact area boundary equation and the relation connecting half-plane boundary normal displacement and striker displacement. Equation system is solved numerically by meshing integration area and constructing equations difference scheme. The solution of the problem is obtained for the case of three types of surfaces constraining the striker: parabolic, circular and hyperbolic cylinders. Time dependencies of the striker velocity, resulting force for contact stresses and radius and contact area expansion velocity are obtained. The influence of relaxation kernel parameters on the mentioned contact interaction characteristics is analyzed.

**Keywords:** Viscoelasticity · Contact problem · Half-plane · Absolutely rigid striker · Green function

## 1 Problem Statement

In rectangular Cartesian coordinate system we consider viscoelastic half-plane  $x_3 \geq 0$ . At the initial time  $t = 0$  absolutely rigid striker of mass  $m$  starts indenting into the half-plane.

Dimensionless equations of half-plane motion have the form [1]

$$D(\tau) * \left( \beta^2 \frac{\partial \theta}{\partial x_1} + \gamma^2 \Delta u_1 \right) = \ddot{u}_1, \quad D(\tau) * \left( \beta^2 \frac{\partial \theta}{\partial x_3} + \gamma^2 \Delta u_3 \right) = \ddot{u}_3,$$

$$D(\tau) = \delta(\tau) - M(\tau), \quad \theta = \frac{\partial u_1}{\partial x_1} + \frac{\partial u_3}{\partial x_3}, \quad \Delta = \frac{\partial^2}{\partial x_1^2} + \frac{\partial^2}{\partial x_3^2}, \quad \gamma^2 = 1 - \beta^2, \quad \beta^2 = \frac{\lambda + \mu}{\lambda + 2\mu}.$$

(1)

Here  $\tau$  is time;  $u_k$  are components of displacement vector;  $M(\tau)$  is relaxation kernel;  $\lambda, \mu$  are elastic Lamé constants.

We suppose that at initial time medium is at rest:

$$u_1|_{\tau=0} = u_3|_{\tau=0} = \dot{u}_1|_{\tau=0} = \dot{u}_3|_{\tau=0} = 0. \tag{2}$$

The striker is constrained by smooth convex cylindrical surface, the equation of which in a coordinate system  $Cx_1x_3'$  referred to its mass center  $C$  we write down as follows:

$$\begin{aligned} x_3' &= x_3 + l = f(x_1), \\ f(-x_1) &= f(x_1), f'(x_1) < 0 (x_1 \neq 0), f'(0) = 0, f''(x_1) < 0. \end{aligned} \tag{3}$$

Here  $l$  is the distance between mass center and stagnation point.

Striker motion along the axis  $Ox_3$  without external forces action is described by the following initial problem

$$\begin{aligned} m\ddot{u}_{c3} &= R_3, \quad R_3(\tau) = \int_{-b(\tau)}^{b(\tau)} \sigma_{330}(x_1, \tau) dx_1, \quad \sigma_{330} = \sigma_{33}|_{x_3=0} \\ u_{c3}|_{\tau=0} &= u_{c30}, \quad \dot{u}_{c3}|_{\tau=0} = v_{c30}, \end{aligned} \tag{4}$$

where  $u_{c3}$  is striker mass center displacement;  $R_3$  is contact force;  $[-b(\tau), b(\tau)]$  is contact area.

We suppose that half-plane boundary outside contact area is free, and interaction of the striker and half-plane is modeled by the condition of free slipping.

Contact area radius is

$$b = f^{-1}(l - u_{c3}). \tag{5}$$

Besides, we must require the displacements to be constrained.

Integral equation connecting half-plane boundary normal displacement and contact stresses has the form

$$w(x_1, \tau) = G_{30}(x_1, \tau) * \sigma_{330}(x_1, \tau), \tag{6}$$

where the function  $G_{30}(x_1, \tau)$  corresponds to the problem (1), (2) and boundary conditions

$$\sigma_{13}|_{x_3=0} = 0, \quad \sigma_{33}|_{x_3=0} = \delta(x_1)\delta(\tau). \tag{7}$$

On the other hand, the following relation connects half-plane boundary normal displacement with the striker displacement:

$$w = u_{e3} + f(x_1) - l. \tag{8}$$

So the resolving equation system has the form (4)–(6), (8), and for its solution we have to determine Green function  $G_{30}(x_1, \tau)$ .

## 2 Green Function Construction

Equation system (1) solution at initial conditions (3) and boundary conditions (13) we shall seek in accordance with the statement proved in [2] in the form

$$\mathbf{u}(x_1, x_3, \tau) = \int_0^\infty \mathbf{u}_e(x_1, x_3, \alpha) W_\sigma(\alpha, \tau) d\alpha. \tag{9}$$

Here  $\mathbf{u}_e$  is constrained displacement vector with coordinates  $u_{e1}$  and  $u_{e3}$ , corresponding to two-dimensional elastic problem

$$\begin{aligned} \left( \beta^2 \frac{\partial \theta}{\partial x_1} + \gamma^2 \Delta u_{e1} \right) &= \ddot{u}_{e1}, & \left( \beta^2 \frac{\partial \theta}{\partial x_3} + \gamma^2 \Delta u_{e3} \right) &= \ddot{u}_{e3}, \\ \mathbf{u}_e|_{\alpha=0} = \frac{\partial \mathbf{u}_e}{\partial \alpha} \Big|_{\alpha=0} &= \mathbf{0}, & \sigma_{13}^e \Big|_{x_3=0} = 0, & \sigma_{33}^e \Big|_{x_3=0} = \delta(x_1) \delta(\alpha). \end{aligned}$$

The relation (9) on the surface  $x_3 = 0$  can be written down as follows:

$$G_{30}(x_1, \tau) = \int_0^\infty G_{3e}(x_1, \alpha) W_\sigma(\alpha, \tau) d\alpha \tag{10}$$

So the function  $G_{3e}(x_1, \alpha)$  in (10) represents Lamb’s problem solution obtained in [3]:

$$G_{3e}(x_1, \alpha) = [G_{3e,r}(x_1, \alpha) + G_{3e,s}(x_1, \alpha)] H(\alpha - |x_1|), \tag{11}$$

where

$$\begin{aligned} G_{3e,r}(x_1, \alpha) &= G_{3e,1}(x_1, \alpha) H(\eta|x_1| - \alpha) + G_{3e,3}(x_1, \alpha) H(\alpha - \eta|x_1|), \\ G_{3e,k}(x_1, \alpha) &= G_{3e,k}(x_1, \alpha) - G_{3e,s}(x_1, \alpha), \quad k = 1, 3 \\ G_{3e,1}(x_1, \alpha) &= \frac{\eta^4 x_1^2 (\eta^2 x_1^2 - 2\alpha^2)^2}{\pi P_4(x_1^2, \alpha^2)} \sqrt{\alpha^2 - x_1^2}, \\ P_4(x_1, \alpha) &= (\eta^2 x_1 - 2\alpha)^4 - 16\alpha^2 (\alpha - \eta^2 x_1) (\alpha - x_1), \end{aligned}$$

$$\begin{aligned}
 G_{3e,3}(x_1, \alpha) &= \frac{\eta^4 x_1^2 R_{22}(x_1^2, \alpha^2)}{\pi P_4(x_1^2, \alpha^2)} \sqrt{\alpha^2 - x_1^2}, \\
 G_{3e,s}(x_1, \alpha) &= \frac{a_s \alpha}{x_1^2 - c_R^2 \alpha^2}, \quad a_s = \frac{R_{22}(c_R^2, 1) \sqrt{1 - c_R^2}}{\pi \eta^4 P_2}, \\
 R_{22}(x_1, \alpha) &= (\eta^2 x_1 - 2\alpha)^2 + 4\alpha \sqrt{\alpha - x_1} \sqrt{\alpha - \eta^2 x_1}, \\
 P_2 &= c_R^4 - 2\phi^2 c_R^2 + i^2, \quad \phi^2 = 2(1 - \kappa) - c_R^2/2, \quad i^2 = 16(\eta^2 - 1)/(\eta^8 c_R^2),
 \end{aligned}$$

$c_R$  is Rayleigh wave propagation velocity.

Then for Green function for viscoelastic half-plane  $G_{30}(x_1, \tau)$  determination we have to construct the function  $W_\sigma(\alpha, \tau)$ .

In accordance with [2], the function  $W_\sigma$  in (9) is constrained solution of one-dimensional viscoelastic problem

$$\begin{aligned}
 \ddot{W}_\sigma &= D(\tau) * \frac{\partial^2 W_\sigma}{\partial \alpha^2}; \\
 W_\sigma|_{\tau=0} &= \dot{W}_\sigma|_{\tau=0} = 0, \quad \alpha \geq 0; \\
 [D(\tau) * W_\sigma(\alpha, \tau)]|_{\alpha=0} &= \delta(\tau), \quad \tau \geq 0.
 \end{aligned} \tag{12}$$

The solution of the problem (12) is found using Laplace transform and the results of the work [4]. Restricting ourselves by the case of exponential relaxation kernel  $M(\tau) = ae^{-\vartheta\tau}$ , we have

$$W_\sigma(\alpha, \tau) = e^{-\vartheta\tau} F(\alpha, \tau), \tag{13}$$

where

$$\begin{aligned}
 F(\alpha, \tau) &= e^{-(c_1 a - \vartheta)\alpha} \left[ \delta(\tau - \alpha) + \sum_{m=0}^{\infty} \frac{d_{m+1}(\alpha)}{m!} (\tau - \alpha)^m \right] H(\tau - \alpha), \\
 d_m(\alpha) &= \sum_{k=0}^m a^k g_{m-k}(\alpha), \quad g_l(\alpha) = \sum_{n=1}^l \frac{(-1)^n \alpha^n h_{l-n,n}}{n!}, \quad h_{p,q+1} = \sum_{n=0}^p h_{p-n,q} e_n \quad (q \geq 1), \\
 h_{p,1} &= e_p, \quad e_p = r_{p+1} a^{p+1}, \quad r_n = \left[ \frac{2n+1}{2(n+1)} a - \vartheta \right] c_n, \quad c_n = \frac{(2n-1)!!}{2^n n!}.
 \end{aligned}$$

Taking into account (10), (11) and (13), we can write down the expression for viscoelastic half-plane Green function  $G_{30}(x_1, \tau)$  in the form

$$\begin{aligned}
 G_{30}(x_1, \tau) &= I_0 + I_r + I_s, \\
 I_0 &= e^{-c_1 a \tau} [G_{3e,r}(x_1, \tau) + G_{3e,s}(x_1, \tau)], \\
 I_r &= e^{-\vartheta \tau} \int_{|x|}^{\tau} G_{3e,r}(x_1, \alpha) e^{-(c_1 a - \vartheta) \alpha} \sum_{m=0}^{\infty} \frac{d_{m+1}(\alpha)}{m!} (\tau - \alpha)^m d\alpha, \\
 I_s &= e^{-\vartheta \tau} \int_{|x|}^{\tau} G_{3e,s}(x_1, \alpha) e^{-(c_1 a - \vartheta) \alpha} \sum_{m=0}^{\infty} \frac{d_{m+1}(\alpha)}{m!} (\tau - \alpha)^m d\alpha.
 \end{aligned}$$

### 3 Contact Problem Solution Algorithm

So finally contact problem for the subsonic stage of interaction is determined by closed equation system

$$\begin{aligned}
 m\ddot{u}_{c3} &= \int_{-b(\tau)}^{b(\tau)} \sigma_{330}(x_1, \tau) dx_1, \quad u_{c3}|_{\tau=0} = u_{c30}, \quad \dot{u}_{c3}|_{\tau=0} = v_{c30}, \\
 b &= f^{-1}(l - u_{c3}), \\
 w(x_1, \tau) &= G_{30}(x_1, \tau) * \sigma_{330}(x_1, \tau), \\
 w &= u_{c3} + f(x_1) - l
 \end{aligned} \tag{14}$$

The solution of the problem is constructed using time and coordinate mesh representation of the resolving equations integration area and the following construction of difference scheme for these equations and quadrature formulae for the integrals. We shall mesh the plane  $R_{x_1}^2$  using mesh with uniform step  $\delta$ :  $\tau_i = i\delta$ ,  $\xi_j = j\delta$  ( $i = 0, 1, 2, \dots; j \in Z$ ).

We shall assign the functions of one and two variables in the relations (14) to mesh functions

$$\begin{aligned}
 u_{c3,i} &= u_{c3}(\tau_i), \quad b_i = b(\tau_i), \quad v_{c3,i} = v_{c3}(\tau_i), \quad f_j = f(x_{1,2j}), \\
 \sigma_{ij} &= \sigma_{330}(x_{1,2j}, \tau_i), \quad w_{ij} = w(x_{1,2j}, \tau_i).
 \end{aligned}$$

The choice of double step for space coordinate is determined by symmetry of the problem, as well as by characteristics of the quadrature formulae used.

Then the difference scheme for the system (14) at the point  $\tau = \tau_n, x_1 = x_{1,2m}$  has the form



$$\begin{aligned}
 \sigma_{nm} &= \sum_{i=1}^{n-1} \sum_{j=p_i}^{q_i} a_{n-i,2m-j} \sigma_{ik_j} - \frac{w_{nm}}{\delta}, \\
 w_{nm} &= u_{c3,n} + f_m + u_{c0}, \\
 u_{c3,n} &= u_{c3,n-1} + V_{n-1} \delta, \\
 V_n &= V_{n-1} + R_{n-1} \frac{\delta}{m}, \\
 R_n &= 2\delta \left( \sigma_{n0} + 2 \sum_{j=1}^{l_n} \sigma_{nj} \right), \\
 b_n &= f^{-1}(-u_{c3,n} - u_{c0}).
 \end{aligned}
 \tag{15}$$

Here

$$\begin{aligned}
 p_i &= \max(-2l_i, k_{i1}), \quad l_i = \left[ \frac{b_i}{2\delta} \right], \quad k_{i1} = i + 2m - n - 1, \\
 q_i &= \min(2l_i + 1, k_{i2}), \quad k_{i2} = -i + 2m + n, \quad k_j = \left[ \frac{j}{2} \right], \\
 a_{nm} &= \frac{1}{2} \int_{-1}^1 \int_{-1}^1 G_{30}(2m + 1 - v, 2n + 1 - u) dudv.
 \end{aligned}$$

Initial conditions for the system (15) have the form

$$u_{c3,0} = u_{c30}, \quad V_0 = V_{30}, \quad \sigma_{0m} = -V_{30}.$$

As an example of the constructed algorithm using contact problem for three types of surfaces constraining the striker is considered: parabolic, circular and hyperbolic cylinders. Time dependencies of the striker velocity, resulting force for contact stresses and radius and contact area expansion velocity are obtained. The influence of relaxation kernel parameters on the mentioned contact interaction characteristics is analyzed.

**Acknowledgements.** The reported study was funded by RFBR and Moscow city Government, according to the research project No. 19-38-70005 mol\_a\_mos.

## References

1. Gorshkov, A.G., Medvedskii, A.L., Rabinskii, L.N., Tarlakovskii, D.V.: Waves in Continuous Media. Physmatlit, Moscow (2004)
2. Ilyasov, MKh: Non-Stationary Viscoelastic Waves. Azerbaijan Hava Yollary, Baku (2011)
3. Gorshkov, A.G., Tarlakovskii, D.V.: Dynamic Contact Problems with Moving Borders. Physmatlit, Moscow (1995)
4. Korovaytseva, E.A., Pshenichnov, S.G., Tarlakovskii, D.V.: Propagation of one-dimensional non-stationary waves in viscoelastic half space. Lobachevskii J. Math. **38**, 827–832 (2017)



# The Unsteady Contact Interaction Problem of an Absolutely Rigid Body and a Membrane

Elena Yu Mikhailova<sup>1</sup> (✉), Grigory V. Fedotenkov<sup>1,2</sup>,  
and Dmitry V. Tarlakovskii<sup>1,2</sup>

<sup>1</sup> Moscow Aviation Institute (National Research University),  
Volokolamskoyeshosse 4, Moscow 125993, Russia  
mihel6@yandex.ru

<sup>2</sup> Institute of Mechanics Lomonosov Moscow State University,  
Michurinsky Prospekt 1, Moscow 119192, Russia

**Abstract.** This article investigates the vertical impact of an absolutely rigid body (indenter) on a membrane. The supersonic (initial) and subsonic stages of unsteady interaction are considered. The solution at the initial stage of contact interaction is reduced to solving a differential equation. A resolving system of equations was obtained for the problem at subsonic stage. The Green's function for the membrane is found and a numerical-analytical algorithm is constructed to solve the system. The unknown functions calculation results are presented in the graph form.

**Keywords:** Superposition method · Transient function · Laplace and fourier integral transforms · Membrane · Absolutely rigid body · Unsteady contact problem

## 1 Problem Formulation

We consider the contact interaction process of an absolutely rigid body bounded by a smooth convex cylindrical surface  $\Pi$  (indenter) with a flat membrane. The indenter moves with velocity  $V_0$  in direction of the normal vector to membrane plane. The contact between the absolutely rigid body and the membrane is adhesive-free (Fig. 1). Outside the contact area  $\Omega = [-b(\tau), b(\tau)]$  the membrane is free from external loads ( $\tau$  is a dimensionless time).

Mathematical model of the problem contains [1, 2]

– indenter motion equation

$$m\ddot{h}(\tau) = R(\tau), \quad R(t) = \int_{-b(t)}^{b(t)} P(t, x) dx \quad (1)$$

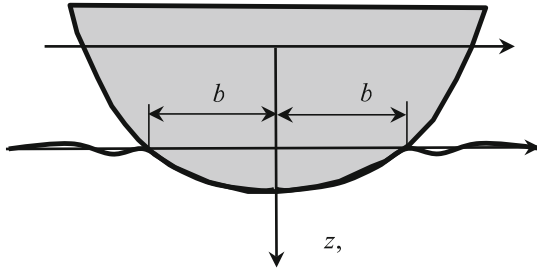


**Fig. 1.** Problem formulation

– membrane motion equation

$$\ddot{u}(\tau, x) = u''(\tau, x) + P(\tau, x) \tag{2}$$

boundary conditions of contact for the indenter and the membrane

$$u(\tau, x) = f(x) + h(\tau) - l, \quad |x| \leq b(\tau), \tag{3}$$

– relation to determine the radius of the contact area

$$b(t) = f^{-1}(l - h), \tag{4}$$

– initial conditions (at the initial time the membrane is in an unperturbed state)

$$u|_{\tau=0} = \dot{u}|_{\tau=0} = 0, \tag{5}$$

$$h|_{\tau=0} = 0, \quad \dot{h}|_{\tau=0} = V_0, \tag{6}$$

All variables and parameters are presented in a dimensionless form (the prime indicates the dimensionless values):

$$\tau = \frac{at}{L}, \quad u' = \frac{u}{L}, \quad h' = \frac{h}{L}, \quad x' = \frac{x}{L}, \quad l' = \frac{l}{L}, \tag{7}$$

$$V'_0 = \frac{V_0}{a}, \quad R' = \frac{R}{\rho a^2}, \quad P' = \frac{PL}{\rho a^2}, \quad m' = \frac{m}{\rho L}.$$

Here  $u(t, x)$  is a membrane deflection,  $a^2$  is the wave propagation velocity in the membrane,  $P(t, x)$  is a contact pressure,  $m$  is the linear weight,  $h(t)$  is an indentation depth,  $R(t)$  is a linear contact force,  $\rho$  is the membrane density,  $l$  is the distance from the mass center to the frontal point of the indenter,  $L$  is the characteristic linear parameter,  $t$  is a dimensional time.

In Formulas (1)–(6) and further primes are omitted. The dots denote derivatives by dimensionless time  $\tau$  and the primes denote derivatives by dimensionless spatial variable  $x$ .

According to [2], there are two speed stages of interaction between the indenter and the membrane: supersonic and subsonic.

## 2 Solution of the Problem at the Supersonic Interaction Stage

At the supersonic (initial) stage, the expansion speed of the contact area exceeds the speed of wave propagation in the membrane. It leads to the fact that there are no movements on the border

$$u(\tau, \pm b) = 0 \tag{8}$$

and inside the contact area of the indenter and the membrane

$$u(\tau, x) = u(\tau, x)H(b - |x|). \tag{9}$$

The found partial derivatives (11) by variables  $x$  and  $\tau$  taking into account (5), (8) we substitute into Formula (4) and obtain an expression for the contact pressure at the supersonic interaction stage  $\dot{b}(\tau) \geq 1$ :

$$P(\tau, x) = P_r + P_s, \tag{10}$$

where  $P_r(\tau, x) = \ddot{h}(\tau) - f''(x)$  is the regular component and  $P_s(\tau, x) = Q(\tau)[\delta(x + b) + \delta(x - b)]$  is the singular component of contact pressure,  $Q(\tau) = \dot{h}\dot{b} + f'(b)$  is the concentrated forces. Thus, for the supersonic interaction stage we obtain that the contact pressure is not a continuous function at the boundary of the contact area. In this case, concentrated forces appear on the border of contact area.

The equation for contact force  $R(\tau)$  on the interval  $(-b(\tau), b(\tau))$  is

$$-R(\tau) = -R_r(\tau) - R_s(\tau) = \int_{-b(\tau)}^{b(\tau)} P_r(\tau, x)dx + \int_{-b(\tau)}^{b(\tau)} P_s(\tau, x)dx = 2 \frac{\partial}{\partial \tau} (\dot{h}b). \tag{11}$$

We integrate the indenter motion equation (2) with considering the initial conditions (6) and Eq. (11). So, we get

$$\dot{h}(\tau) = \frac{mV_0}{m + 2b(\tau)}. \tag{12}$$

Then  $\dot{b}(\tau)$  can be defined as follows:

$$\dot{b}(\tau) = b'(h)\dot{h}(\tau) = b'(h) \frac{mV_0}{m + 2b(\tau)}. \tag{13}$$

Using the solution of ODE (12) with the initial conditions (6), (4) and (13) we obtain analytical dependencies  $h(\tau)$ ,  $\dot{h}(\tau)$ ,  $b(\tau)$ ,  $\dot{b}(\tau)$  for circular and elliptic (with semi-axes  $a = b = 1$ ), parabolic, hyperbolic (with semi-axes  $a = b = 1$ ) cylinders.

### 3 Solution of the Problem at the Subsonic Interaction Stage

Based on the principle of superposition the membrane deflection can be represented as a convolution [1, 3, 4]:

$$u(\tau, x) = G(\tau, x) * p(\tau, x) = \int_0^\tau \int_{-b(\tau)}^{b(\tau)} G(\tau - t, x - \xi) \cdot p(\tau, \xi) d\xi dt. \tag{14}$$

Here  $G(x, \tau)$  is the Green function, which is defined as the solution of the following boundary value problem:

$$\ddot{G}(\tau, x) = G''(\tau, x) + \delta(\tau)\delta(x), G|_{\tau=0} = \dot{G}|_{\tau=0} = 0, \tag{15}$$

where  $\delta(x)$  is Dirac delta function,  $p$  is the contact pressure.

After the Laplace and Fourier transforms, we obtain the solution of problem (15) as an expression for the Green’s function for the membrane:

$$G(\tau, x) = \frac{1}{2}H(\tau - |x|), \tag{16}$$

where  $H(x)$  is the Heaviside step function.

In the subsonic interaction stage, the basic equation of the resolving system of equations has the form (14). In addition to it, the mathematical model describing this stage of contact between the indenter and the membrane includes the following relations:

$$\begin{aligned} u(\tau, x) &= f(x) + h(\tau) - l, & h(\tau) &= \int_0^\tau V(t)dt, \\ b(\tau) &= f^{-1}(l - h(\tau)), \\ mV(\tau) &= \int_0^\tau R(t)dt, & R(\tau) &= \int_{-b(\tau)}^{b(\tau)} p(\tau, x)dx, \end{aligned} \tag{17}$$

where  $V(\tau)$  is speed of indentation.

The solution of the system of Eqs. (14), (17) is sought on the plane  $R_{t\xi}^2$  on which the grid is applied with a uniform step  $\delta$ :

$$\begin{aligned} t_i &= i\delta, & \xi_j &= j\delta, & R_{t\xi}^2 &= \bigcup_i \bigcup_j K_{ij} (i = 1, 2, 3, \dots; j \in \mathbb{Z}), \\ K_{ij} &= \{(t, \xi) | t_{i-1} \leq t \leq t_i, \xi_{j-1} \leq \xi \leq \xi_j\}. \end{aligned} \tag{18}$$

We assign to functions  $h(t), b(t_i), f(\xi), p(t, \xi), u(t, \xi)$  the grid functions  $h_i = h(t_i), b_i = b(t_i), f_i = f(\xi_i), p_{ij} = p(t_i, \xi_j), u(t_i, \xi_j)$ .

The difference scheme for system (14), (17) is explicit and has the following form

$$\begin{aligned}
 u_{nm} &= \frac{\delta^2}{4} \left( \sum_{i=n_s}^{n-1} \sum_{j=p_i}^{q_i} p_{ij} + \varepsilon_{nm} p_{nm} \right) + \sum_{i=0}^{n_s} (I_{1,i} - I_{2,i}) \\
 &\quad + \delta \sum_{i=i_r}^{n_s} \left( \dot{h}_i \dot{b}_i - \frac{\dot{h}_i}{\dot{b}_i} \sqrt{1 + \dot{b}_i^2} \right), \\
 I_{1,i} &= (x_2(t_i) - x_1(t_i)) (\ddot{h}(t_{i+1}) - \ddot{h}(t_i)), \\
 I_{2,i} &= \delta (f'(q_i) - f'(p_i)), \quad u_{nm} = h_n + f_m - l, \\
 h_n &= h_{n-1} + V_{n-1} \delta, \quad V_n = V_{n-1} + R_{n-1} \frac{\delta}{m}, \\
 R_n &= \delta \left( p_{n0} + 2 \sum_{j=1}^{l_n} p_{nj} \right), \quad b_n = f^{-1}(l - h_n), \quad \dot{b}_n = \dot{b}(t_n), \\
 \dot{b}_n &= -\frac{V_n}{f'(b_n)}.
 \end{aligned} \tag{19}$$

A program of numerical integration has been constructed based on the difference scheme (19). In the numerical calculation, the grid step was taken to be 0.005,  $m = 1, V_0 = 1, l = 1$ . The results were obtained for a parabolic indenter (the dependences on the depth of indentation, the indentation speed, the radius of contact area, the expansion speed of the contact area on time, the dependence of the pressure distribution over the contact area on the temporary layer with the number  $k$  and the pressure distribution on time at the frontal point.

**Acknowledgements.** The authors would like to acknowledge the financial support of the Russian Foundation for Basic Research (project № 19-08-01023 A).

## References

1. Gorshkov, A.G., Medvedsky, A.L., Rabinsky, L.N., Tarlakovsky, D.V.: Waves in Continuum Media. Fizmatlit, Moscow (2004). (in Russian)
2. Gorshkov, A.G., Tarlakovsky, D.V.: Dynamic Contact Problems with Moving Boundaries. Fizmatlit, Moscow (1995). (in Russian)
3. Mikhailova, E.Y., Tarlakovskii, D.V., Fedotenkov, G.V.: Transient Contact Problem for Liquid Filled Concentric Spherical Shells and a Rigid Barrier. In: Proceedings of the First International Conference on Theoretical, Applied and Experimental Mechanics, 385–386 (2018)
4. Fedotenkov, G.V., Mikhailova, E.Y., Kuznetsova, E.L., Rabinskiy, L.N.: Modeling the unsteady contact of spherical shell made with applying the additive technologies with the perfectly rigid stamp. Int. J. Pure Appl. Math. **111**(2), 331–342 (2016)



# Static and Dynamic Models of Bending for Elastic Sandwich Plates

M. Yu. Ryazantseva<sup>1(✉)</sup> and E. I. Starovoitov<sup>2</sup>

<sup>1</sup> Institute of Mechanics, Lomonosov Moscow State University,  
Michurinsky Prospect, 1, Moscow 119192, Russia  
m-rznt@yandex.ru

<sup>2</sup> Belarusian State University of Transport, Gomel, Belarus

**Abstract.** This work is an attempt to solve the problem how to describe static and dynamic bending deformations of elastic sandwich plates in the frame of two-dimensional theories. We focus here on the case of so-called hard-skin plates, i.e. the sandwich plates the faces of which are very hard. We consider only the hard-skin plates of symmetric structure on thickness. In this case the any static and dynamic problem can be represented as a superposition of two problems: one considers the deformations “in plane of the plate” (tension deformations) and the other considers deformations “out of plane of the plate” (bending deformations). It is proposed to solve the problem of static and dynamic bending for hard-skin plates on the basis of governing two-dimensional models derived from linear three-dimensional elasticity with the help of variational asymptotic method [1]. We show in which cases the bending problem must be solved on the basis the equations considering transverse shear effects both in statics and dynamics.

**Keywords:** Sandwich elastic plate · Asymptotic theory · Transverse shear effect

## 1 Introduction

Among various modern composite materials having wide industrial applications, the sandwich composites occupy the special place due to their superior mechanical properties and enhanced manufacturing technology. We consider here the problem how to describe static and dynamic bending of elastic sandwich plates of symmetric structure on thickness (hard-skin plates) on the basis of linear two-dimensional theories. As far as the mechanical characteristics of the layers are of different orders of magnitude, the normal fibers cannot remain normal to the mid-surface in the course of deformation. Therefore stress-strain state of such plates cannot be described by classical plate theory. The deviations from classical theory are characterized by transverse shear effect and its contribution in the picture of deformation can be the leading order. So to derive a two-dimensional theory of static and dynamic bending for sandwich plates from three-dimensional elasticity theory it is necessary to determine the leading

effects in the course of static and dynamic deformation. It can be realized with the help of asymptotic analysis of three-dimensional elastic energy functional on the basis of technique worked out by Berdichevsky [1].

## 2 Statement of the Problem

Consider a three-layered elastic plate of symmetric structure on thickness (denoted by  $h$ ). Each layer is made of homogeneous isotropic material, the contact between the layers is ideal. We denote the thicknesses of the center layer and the outer layers by  $h_c$  and  $h_s$  respectively. Indices c and s mark the value in the inner layer (core) and in the outer layers s (skin). For symmetric sandwich plates we have:  $h = h_c + 2h_s$ . Denote by  $x^\alpha (\alpha = 1, 2)$  the Cartesian coordinates in the mid-plane of the plate, and by  $x$  the normal coordinate to mid-plane. In given case the elastic properties  $\lambda, \mu$  and density  $\rho$  are the even functions of  $x$ . The displacements of any point of the plate with coordinates  $x, x^\alpha$  are denoted by  $w^\alpha (\alpha = 1, 2), w$ . For static and dynamic bending of symmetric sandwich plates functions  $w^\alpha$  are odd functions of  $x$  and  $w$  is even function of  $x$ .

The problem is to carry out the two-dimensional bending static and dynamic equations from three-dimensional elasticity as the theories of leading approximation for symmetric hard-skin plates.

## 3 An Asymptotic Theory the Static Bending of Sandwich Plates

The problem of deriving a two-dimensional asymptotic theory for statics of hard-skin plates from three-dimensional elasticity theory was solved by Berdichevsky [2]. An asymptotic theory was obtained as a governing theory of leading approximation using the variational asymptotic method. It was shown that besides the small parameter  $h/l$  ( $l$ —the characteristic length of the stress state along the plate) the additional small parameter  $\Lambda = \mu_c h_c / \mu_s h_s$  takes place for elastic sandwich plates.

The key role in developing an asymptotic bending theory is played by interplay of two small parameters which are connected with the relation:

$$\frac{\mu_c h_c}{\mu_s h_s} = \left(\frac{h}{l}\right)^\alpha.$$

Three different static bending situations were obtained and described in the leading approximation:

- $0 < \alpha < 2$ —the sandwich plate can be described by classical plate theory;
- $\alpha > 2$ —the sandwich plate behaves as a membrane and can be described by membrane equation;
- $\alpha = 2$ —the sandwich plate must be described by the theory considering the transverse shear effect.



For last case the governing two-dimensional bending equations for hard-skin plates are derived by an asymptotic analysis of linear three-dimensional elasticity as a theory of leading approximation [2].

#### 4 A Theory of Dynamic Bending of Sandwich Plates

In dynamics the two-dimensional equations can be obtained from static equations by adding the leading inertia terms to the static equations only in the case of low-frequency vibration, i.e. when the characteristic frequency  $\omega$  satisfies the condition:

$$\omega \sim \frac{1}{l} \sqrt{\mu_c / \rho_c}.$$

If this condition does not hold, then a two-dimensional theory must include high-frequency effects. Such theory cannot be constructed as an asymptotic theory, and therefore it is necessary to combine an asymptotic analysis with heuristic approach. The main idea assumed as a basis of deriving the two-dimensional dynamic theory of hard-skin elastic plates is to consider the interaction of low-frequency mode of vibrations (classical form) with first high-frequency form. The main hypotheses of the bending theory, considering the classical flexural mode and first high-frequency mode describing the transverse shear, can be represented in the following expressions for the displacements:

$$w = u + \frac{h^2}{4} \Delta u y(\zeta); \quad w_x = \chi_x \frac{h}{2} q(\zeta) - \frac{h}{2} u_{,x} \zeta; \quad \zeta = 2x/h$$

Function  $u(x^\alpha, t)$  describes the bending of mid-surface of the hard-skin plate. Functions  $\chi_\beta(x^\alpha, t)$  describe the effect of transverse shear. The displacement distributions on the thickness are described by the functions  $y(\zeta)$ ,  $q(\zeta)$ , respective analytic forms were obtained in [3] from the solution of appropriate eigenvalue problem in long-wave approximation.

The development starts with variation formulation of three-dimensional elasticity dynamic problem with expressions for displacements represented above. The governing two-dimensional equations are constructed applying the asymptotic analysis and averaging method to three-dimensional energy functional. The averaged equations obtained in such way contain all leading effects.

As a result for hard-skin plates we construct the two-dimensional dynamic equations as a theory of leading approximation, which is asymptotically correct on the long waves and qualitative correct on the sufficiently short waves. The obtained governing two-dimensional equations can be represented as generalization Timoshenko and Reissner-like theory on the case of elastic hard-skin plates.

## 5 Conclusion

As it is known from reviews (see, for example [4, 5]), the models based on the system of kinematical hypotheses are often too complicated and computationally inefficient to be used in practice. Therefore the statics of symmetric hard-skin elastic plates is proposed to study on the basis of asymptotic theory [2]. The dynamic behavior of symmetric hard-skin elastic plates is proposed to study on the basis of two-dimensional averaged theory considering the high-frequency vibration mode. The governing hyperbolic equations allow describing such effects as transverse shear and geometric dispersion of waves in long-wave approximation. It was shown in which cases the bending problem of hard-skin plates must be solved on the basis the equations considering transverse shear effects both in statics and dynamics.

**Acknowledgements.** The reported study was funded by Russian Foundation for Basic Research, according to the research projects No. 18-58-00008.

## References

1. Berdichevski, V.L.: Variational Principles of Continuum Mechanics. Springer, Berlin (2009)
2. Berdichevski, V.L.: An asymptotic theory of sandwich plates. *Int. J. Eng. Sci.* **48**, 383–404 (2010)
3. Ryazantseva, M.Y.: Harmonic running waves in sandwich plates. M.Yu. Ryazantseva, F.K. Antonov. *Int. J. Eng. Sci.* **59**, 184–193 (2012)
4. Heng, H., Belouettar, S., Potier-Ferry, M., Daya, E.M.: Review and assessment of various theories for modeling sandwich composites. *Composite Structure*, vol. 84, pp. 282–292. Elsevier (2008)
5. Noor, A.K., Burton, W.S.: Computational models for sandwich panels and shells. *Appl. Mech. Rev.* **49**(3) (1996)



# Analysis of Vibration Insulation Properties of a Plate in an Elastic Medium Under the Influence of Different Types of Waves

N. A. Lokteva<sup>1</sup>(✉) and D. V. Tarlakovskii<sup>2</sup>

<sup>1</sup> Moscow Aviation Institute (National Research University), Moscow 125993,  
80 GSP -3, Volokolamskoye Shosse 4, Russia  
nlok@rambler.ru

<sup>2</sup> Institute of Mechanics Lomonosov Moscow State University,  
Moscow 119192 Michurinski Prospekt 1, Russia  
tdvhome@mail.ru

**Abstract.** The vibration-absorbing properties of the plate under the action of the flat, cylindrical and spherical harmonic wave in the soil are studied. In the soil model, an elastic isotropic medium is used. The motion of the plate is described by the system of equations of Paimushin V.N. The mathematical formulation of the problem includes the assignment of the incident wave, the equations of motion of the soil and the plates, the boundary conditions for the slab and the soil, the conditions at infinity, and the conditions of contact of the earth with the obstacle, where we neglect the connection of the plate to the ground. The kinematic parameters of the plate and the parameters of the disturbed stress-strain state of the soil are represented in the form of double trigonometric series satisfying the boundary conditions. After that, the constants of integration, displacement and vibration acceleration are determined. The main goal is to determine the total vector field of acceleration for each type of waves.

**Keywords:** Soil · Plate · V.T. paymushin model · Flat wave · Cylindrical wave · Spherical harmonic wave · Frequency · Vibrations · Vibration absorption · Vibration acceleration

## 1 Introduction

Increasingly, there is a need to protect existing buildings and structures from the negative anthropogenic impact arising from the introduction of new infrastructure into the already existing urban environment. Buildings are often exposed to huge dynamic loads coming from industrial machinery, or transport (such as shallow-depth railroad systems, heavy trucks, railway trains) that causes [1]. Vibration-absorbing barriers placed between the vibration source and the protected object is an efficient way of foundation protection against ground vibrations [2, 3].

The mechanics of sound waves passing through obstacles has been studied quite widely. The sound insulation properties of single-layer and multilayer plates of unlimited and real sizes are investigated. The influence of geometrical dimensions, methods of fixing, physical and mechanical properties of plates on their vibration-

insulating characteristics is analyzed. At the same time the study of sandwich plate dynamics requires proper accounting for both transverse shear and transverse normal stress in the filling layer, otherwise the dynamic stress state can be computed with severe errors. On the other hand, the effect of the ingoing wave shape on the sound absorption properties of plane sandwich barriers must be studied in details to be a basis of further engineering estimates. We studied the sound-absorbing properties of plates subjected to the effects of subsurface various types of harmonic waves, against the background of new improved models with a lamellar plate, taking into account all the effects present. Depending on the position of the wave source, the plate is affected differently. In practice, in the case of a close position of a point source, a spherical wave arises; in the case of a linear source configuration, a cylindrical wave, if the source is far away, then a plane wave.

## 2 The Interaction of a Different Harmonic Wave with a Three-Layer Plate

Let us consider the rectangular plate that consists of three layers—two bearing layers and a honeycomb filling. The origin of the coordinate system is placed in the upper right-handed corner of the plate. Oz-axis is directed normally to the plate surface into the medium “2”, Ox and Oy lie in plate’s plane. Let  $w$  be the displacement of points of the medium “2” normal to the plate, and let  $u$  be the corresponding tangential displacement. Superscript denotes the media number while the subscript denotes the axis along which the displacement takes place, 1-x, 2-y. The Plate divides the medium into 2 parts: media “1” and “2” [4]. Harmonic wave rides on the plate from the medium “1”.

To appreciate vibration absorbing properties of obstacle, term “vibration acceleration” is used. The acceleration modulus is calculated using the formula (1).

$$a = \sqrt{a_x^2 + a_y^2 + a_z^2}. \quad (1)$$

The mathematical formulation of the problem includes the task of the incident wave, the equations of motion of the soil and the plate, boundary conditions for the plate and the ground, conditions at infinity, as well as the conditions of contact of the soil with an obstacle, where we neglect the adhesion of the plate with the ground. Besides, the motion of the medium is given when different waves are applied.

## 3 Dynamic Equations of Soil

The Model of isotropic elastic medium is used below [4, 5]. Its motion is described by the dynamic equations of the elasticity theory together with Cauchy relations and constitutive equations of the Hookean law [6].

Only harmonic waves with the frequency  $\omega$  are considered. Finally, for the scalar and vector potentials we obtain

$$\Delta\varphi + k_1^2\varphi = 0, \Delta\psi + k_2^2\psi = 0, k_j = \omega/c_j$$

$$u_1 = \frac{\partial\varphi}{\partial x} + \frac{\partial\psi_3}{\partial y} - \frac{\partial\psi_2}{\partial z}, u_2 = \frac{\partial\varphi}{\partial y} + \frac{\partial\psi_1}{\partial z} - \frac{\partial\psi_3}{\partial x}, w = \frac{\partial\varphi}{\partial z} + \frac{\partial\psi_2}{\partial x} - \frac{\partial\psi_1}{\partial y}$$

where:  $u_1, u_2$  and  $w$  are movements along the axes  $Ox, Oy$  and  $Oz$ .

Since the medium «2» is not bounded by the coordinate  $z$ , then the Somerfield radiation condition acts as a boundary condition [6].

### 4 Ingoing Harmonic Waves

The medium motion is described by the Helmholtz equation

$$\Delta\Phi_a + k_1^2\Phi_a = 0, k_1 = \omega/c_1 \tag{2}$$

While the first boundary condition is the Sommerfeld one, the second corresponds to the boundedness at the infinity:

$$\frac{\partial\Phi_a}{\partial r} + ik_1\Phi_a = 0 \left( \frac{1}{r} \right), r \rightarrow \infty \tag{3}$$

where  $r$ —radius-vector length.

Then, based on the value  $\sigma_{33}|_{t=0, z=0} = p_*$  the value of displacements and stresses is determined. For the plane harmonic wave on the plate surface, the solution of Eq. (2) with the dynamic equations and (3) taken into account is

$$u_1 = u_{1*} = u_2 = u_{2*} \equiv 0, w = w_* = \frac{ik_1 p_*}{\rho\omega^2} e^{-ik_1 z} = \frac{ip_*}{\rho c_1 \omega} e^{-ik_1 z},$$

$$\sigma_{11} = \sigma_{11*} = \kappa p_* e^{-ik_1 z}, \sigma_{33} = \sigma_{33*} = p_* e^{-ik_1 z},$$

$$\sigma_{22} = \sigma_{22*} = p_* e^{-ik_2 z}, \sigma_{13} = \sigma_{12} = \sigma_{13*} = \sigma_{12*} \equiv 0. \tag{4}$$

For the cylindrical harmonic wave

$$u_* = \frac{p_* x d}{\rho c_1^2 N r_{10}} H_1^{(2)}(k_1 r_{10}), w_* = \frac{d^2 p_*}{\rho c_1^2 N r_{10}} H_1^{(2)}(k_1 r_{10}),$$

$$\sigma_{11*} = \frac{p_* d}{N r_{10}^2} \left[ (1 + \kappa) r_{10} H_1^{(2)}(k_1 r_{10}) - k_1 r_{10}^2 H_2^{(2)}(k_1 r_{10}) \right],$$

$$\sigma_{13*} = -(1 - \kappa) \frac{p_* d^2 k_1 x}{N r_{10}^2} H_2^{(2)}(k_1 r_{10}), \sigma_{22} = \sigma_{12} = \sigma_{22*} = \sigma_{12*} \equiv 0,$$

$$\sigma_{33*} = \frac{p_* d}{N r_{10}^2} \left[ (1 + \kappa) r_{10} H_1^{(2)}(k_1 r_{10}) - k_1 r_{330}^2 H_2^{(2)}(k_1 r_{10}) \right]. \tag{5}$$

where:  $r_{10} = \sqrt{x^2 + d^2}, r_{110} = \sqrt{x^2 + \kappa d^2}, r_{330} = \sqrt{\kappa x^2 + d^2}, d$  is the distance from the source to the barrier.

$$\begin{aligned}
 u_{1*} &= \frac{(x+x_{1*})p_*r_*^2}{r^2N} \left( -ike^{-ikr} - \frac{ke^{-ikr}}{r} \right), u_{2*} = \frac{(y+x_{2*})p_*r_*^2}{r^2N} \left( -ike^{-ikr} - \frac{ke^{-ikr}}{r} \right) \\
 w_* &= \frac{(z+d)p_*r_*^2}{r^2N} \left( -ike^{-ikr} - \frac{ke^{-ikr}}{r} \right). \\
 \sigma_{11*} = \sigma_{22*} = \sigma_{33*} &= \frac{3\lambda p_*r_*^2}{r^2N} \left( -ike^{-ikr} - \frac{ke^{-ikr}}{r} \right) + \frac{3\lambda p_*r_*^2}{r^2N} \left( -ike^{-ikr} - \frac{ke^{-ikr}}{r} \right), \\
 \sigma_{13} = \sigma_{12} = \sigma_{13*} = \sigma_{12*} &\equiv 0.
 \end{aligned} \tag{6}$$

where  $x_*, y_*$  are the coordinates of the source, and  $d$  is the distance from the source to the barrier. The radius-vector— $r = \sqrt{(x-x_*)^2 + (y-y_*)^2 + (z+d)^2}$ .

## 5 The Plate Geometry

The plate consists of three layers, two bearing layers and the filling one. The Plate motion is described by Paimushin equation system [7, 8], which takes into account structural features of the plate formula (7).

Bearing layers are isotropic and have thickness  $2t$  and elasticity modulus  $E$  and Poisson's ratio  $\nu$ . The filling layer of thickness  $2h$  is orthotropic and honeycomb structure with the compression modules  $E_3$  and shear modulus  $G_1, G_2$  in axial directions  $Ox, Oy$ . The axis  $Oz$  is directed from layer number "1" to layer number "2". The plate is simply supported on the contour.

A special case of transversally soft filler layer is considered, when  $G_1 = G_2 = G$ . The normal pressures  $p_1$  and  $p_2$  act on bearing layers. Then the dynamic equations of the plate take the form [5, 6].

$$\begin{aligned}
 \rho_c \ddot{u}_1^c &= L_{11}(u_1^c) + L_{12}(u_2^c), \rho_c \ddot{u}_2^c = L_{21}(u_1^c) + L_{22}(u_2^c), \\
 \rho_a \ddot{u}_1^a &= L_{11}(u_1^a) + L_{12}(u_2^a) + 2q^1, \rho_a \ddot{u}_2^a = L_{21}(u_1^a) + L_{22}(u_2^a) + 2q^2, \\
 \rho_c \ddot{w}_c - \frac{m_c \Delta \ddot{w}_c}{\rho_{wq}} + \frac{\rho_{wq}(\ddot{q}_{,x}^1 + \ddot{q}_{,y}^1)}{\rho_{wq}} &= -D\Delta^2 w_c + 2k_1(q_{,x}^1 + q_{,y}^1) + p_1 - p_2, \\
 \rho_{aw} \ddot{w}_a - \frac{m_a \Delta \ddot{w}_a}{\rho_{wq}} &= -D\Delta^2 w_a - 2c_3 w_a + p_1 + p_2, \\
 \frac{\rho_{q1} \ddot{q}^1}{\rho_{wq1}} - \frac{\rho_{wq1} \ddot{w}_{c,x}}{\rho_{wq1}} &= u_1^a - k_1 w_{c,x} - k_2(q_{,x}^1 + q_{,y}^2)_{,x} + k_{31} q^1, \\
 \frac{\rho_{q2} \ddot{q}^2}{\rho_{wq2}} - \frac{\rho_{wq2} \ddot{w}_{c,y}}{\rho_{wq2}} &= u_2^a - k_1 w_{c,y} - k_2(q_{,x}^1 + q_{,y}^2)_{,y} + k_{32} q^2.
 \end{aligned} \tag{7}$$

where:

$$u_i^c = u_i^{(1)} + u_i^{(2)}, u_i^a = u_i^{(1)} - u_i^{(2)} (i = 1, 2); w_c = w_0^{(1)} + w_0^{(2)}, w_a = w_0^{(1)} - w_0^{(2)}.$$

In the equation system (5.1) the further notation is used:  $w_c, w_a$ —deflections;  $q^1, q^2$ —transverse shear stresses in the filling along the  $x$ -axis and  $y$ -axis;  $\rho_{(k)}$ —the mass density of bearing layers and the filling;  $u_1^{(k)}$  and  $u_2^{(k)}$ —tangential displacements

along the  $x$ -axis and  $y$ -axis respectively in the  $k^{th}$  bearing layer.  $B$  and  $D$ —tangent and bending stiffness of the tangent plate.  $w^{(k)}$ —the deflection of bearing layer. Conditions on the simply supported contour of the plate.

### 6 Conditions on the Contact Surface

The pressure amplitude of the wave coming from the medium «1» is equal to the sum of the normal stress in the medium and stress, arising as a result of the wave action.

$$p_1 = \left( \sigma_{33}^{(1)} + \sigma_{33*} \right) \Big|_{z=0}, p_2 = -\sigma_{33}^{(2)} \Big|_{z=0}. \tag{8}$$

In the second medium, the pressure amplitude is the same as the normal stress for the plane and spherical waves

$$\begin{aligned} (w^{(1)} + w_*) \Big|_{z=0} &= w_0^{(1)}, w^{(2)} \Big|_{z=0} = w_0^{(2)}, \\ \sigma_{13}^{(1)} \Big|_{z=0} = \sigma_{13}^{(2)} \Big|_{z=0} &= 0, \sigma_{12}^{(1)} \Big|_{z=0} = \sigma_{12}^{(2)} \Big|_{z=0} = 0, \sigma_{23}^{(1)} \Big|_{z=0} = \sigma_{23}^{(2)} \Big|_{z=0} = 0. \end{aligned} \tag{9}$$

For the cylindrical wave

$$\sigma_{13}^{(1)} \Big|_{z=0} = \sigma_{13}^{(2)} \Big|_{z=0} = 0, \sigma_{12}^{(1)} \Big|_{z=0} = \sigma_{12}^{(2)} \Big|_{z=0} = 0, \sigma_{22}^{(1)} \Big|_{z=0} = \sigma_{22}^{(2)} \Big|_{z=0} = 0. \tag{10}$$

Medium displacements, summed up with ingoing wave displacements, are equal to the displacement of the first plate bearing layer. The displacement of the second medium is the same as the displacement of the second plate bearing layer.

### 7 Computing of the Fourier Coefficients for the Potentials in Ambient Media

All unknown function, as well for the plate as for both media, are decomposed into trigonometric series and satisfy the boundary conditions of the simple support [9]. The wave equations in the potentials are also represented through the Fourier coefficients (6.1):

$$\begin{aligned} \frac{\partial^2 \varphi_{nm}^{(l)}}{\partial z^2} + \varphi_{nm}^{(l)} (k_1^2 - (\lambda_{1n}^2 + \lambda_{2m}^2)) &= 0, \\ \frac{\partial^2 \psi_{i\ nm}^{(l)}}{\partial z^2} + \psi_{i\ nm}^{(l)} (k_1^2 - (\lambda_{1n}^2 + \lambda_{2m}^2)) &= 0, i = 1, 2, 3 \end{aligned} \tag{11}$$

Solution of these equations must satisfy the Sommerfeld.

General solution of the wave Eq. (11) is given by the following way

$$\varphi_{nm}^{(j)}(z, \omega) = C_{1nm}^{(j)}(\omega) \left[ e^{ik_{1nm}(\omega^2)z} H(k_1 - (\lambda_{1n} + \lambda_{2m})) + e^{k_{1nm}(\omega^2)z} H((\lambda_{1n} + \lambda_{2m}) - k_1) \right],$$

$$\psi_{inn}^{(j)}(z, \omega) = C_{2inn}^{(j)}(\omega) \left[ e^{ik_{2nm}(\omega^2)z} H(k_2 - (\lambda_{1n} + \lambda_{2m})) + e^{k_{2nm}(\omega^2)z} H((\lambda_{1n} + \lambda_{2m}) - k_2) \right],$$

$$j = 1, 2.$$

To determine the constants we have to use the conditions of the contact between the plate and the medium (8), (9) for the plane and spherical waves and (8), (10) for the cylindrical wave. This requires that the stresses, deformations and displacements will be expressed in term of potentials so that allows one to determine the constants from the boundary conditions. The integration constants are determined from the boundary conditions. Further, the acceleration modulus is determined.

## References

1. Umek A.: Dynamic responses of building foundations to incident elastic waves. Ph.D. Thesis. Illinois, Ill. Inst. Technol (1973)
2. Kostrov, B.V.: Motion of a rigid massive wedge inserted into an elastic medium under the effect of plane wave. *Prikl. Mat. Mekh.* **28**(1), 99–110 (1964). (In Russian)
3. Rylko, M.A.: On the motion of a rigid rectangular insertion under the effect of plane wave. *Mekh. Tverd. Tela.* **1**, 158–164 (1977). (In Russian)
4. Rakhmatulin, K.A., Sunchalieva, L.M.: Elastic and elastoplastic properties of the ground upon dynamic loads on the foundation. Department in VINITI, pp. 4149–83 (1983) (In Russian)
5. Berezhnoi, D.V., Konoplev, Y.G., Paimushin V.N., Sekaeva, L.R.: Investigation of the interaction between concrete collector and dry and waterlogged grounds. *Trudy Vseros. nauch. konf. "Matematicheskoe modelirovanie i kraevye zadachi"* [Proc. All-Russ. Sci. Conf. "Mathematical Simulation and Boundary Value Problems"]. Part 1. Mathematical Models of Mechanics, Strength and Reliability of Structures. Samara, SamGTU, pp. 37–39 (2004) (In Russian)
6. Gorshkov, A.G., Medvedskii, A.L., Rabinskii, L.N., Tarlakovskii, D.V.: Waves in Continuum Media, p. 472. *Fizmatlit, Moscow* (2004). (In Russian)
7. Ivanov, V.A., Paimushin, V.N.: Refined formulation of dynamic problems of three-layered shells with a transversally soft filler is a numerical-analytical method for solving them. *Appl. Mech. Tech. Phys.* **36**(4), 147–151 (1995)
8. Ivanov, V.A., Paimushin, V.N.: Refinement of the equations of the dynamics of multilayer shells with a transversally soft filler. *Izv. RAS. MTT* **3**, 142–152 (1995)
9. Sheddon, I.: *Fourier Transforms*, p. 542. McGraw Hill, New York (1951)





# Studying of Influence of the Material Anisotropy on the Limit State of an Orthotropic Plate Weakened by a Periodic System of Collinear Cracks Under Biaxial Loading

Olga Bogdanova<sup>(✉)</sup>

S. P. Timoshenko Institute of Mechanics  
of National Academy of Sciences of Ukraine, Nesterov Str., 3,  
02053 Kiev, Ukraine  
o. bogdanova@i.ua

**Abstract.** On the basis of a modified Dugdale model, we investigate the influence of the anisotropy of the material, in particular, differences between the ultimate tensile strength and ultimate compressive strength, on the limit state of an orthotropic plate weakened by a periodic system of periodic collinear cracks under biaxial external loading. As a strength criterion, the Hoffman strength criterion is considered. Strength diagrams of an orthotropic plate with a crack for different strength and crack resistance parameters are obtained.

**Keywords:** Periodic system of collinear cracks · Critical loading · Biaxial loading · Orthotropic materials · Hoffman strength criterion

## 1 Introduction

In recent years, in fracture mechanics, the two-level approach has been developed. According to it, on the macrolevel, in a larger part of a body with a crack, methods of continuum mechanics are used, and, on the second level, in process zones near the crack front, in which partial fracture of the material has occurred, the fracture process is investigated with the help of specific modeling of physical features of concrete materials. At present, this approach is called fracture mesomechanics. Methods of fracture mesomechanics enable one to study fracture processes of various natural and artificial materials such as rocks, wood, concretes, ceramics, polymers, composites, etc. The study of fracture of anisotropic materials arouses particular interest of researchers.

As is shown by experiments, in many cases, process zones in thin plates are narrow wedge-shaped regions of a discontinuous semi-broken material on extensions of cracks. On the basis of these experimental data, in [1], the authors proposed a model that, like the Leonov–Panasyuk–Dugdale model, considers a process zone in the form of a notch to the faces of which self-balancing compressive stresses are applied. However, in contrast to the Leonov–Panasyuk–Dugdale model, the parameters of the model proposed in [1] are determined on the basis of the fact that the strength criterion

of the material in the process zone is satisfied, which makes it possible to take into account the influence of forces acting along the plane of the crack because this cannot be achieved using the indicated model.

In the present paper, on the basis of the general solution obtained in [1] and Hoffman strength criterion, the influence of the anisotropy of the material (the differences between moduli of elasticity along axes of orthotropy and between the ultimate tensile strength and ultimate compressive strength) on the limit state of a thin orthotropic plate weakened by a periodic system of collinear cracks under conditions of biaxial external loading is investigated.

## 2 Model of a Crack in an Orthotropic Material

Consider a thin orthotropic plate with periodic system of collinear cracks of length  $2l$  located along the axis of orthotropy which coincides with the  $Ox$ -axis. The centers of the cracks are located at the points  $x_n = 2nD$  ( $x_n = 0, \pm 1, \pm 2, \dots, y = 0$ ). The plate is stretched by a homogeneous load applied at infinity

$$\sigma_y = p > 0, \sigma_x = q, \tau_{xy} = 0 \text{ by } z \rightarrow \infty (z = x + iy).$$

We replace the process zones formed under the action of the load near the crack tips by additional cuts of length  $d$  on the continuations of the cracks whose lips are subjected to the action of stresses  $\sigma_x^0, \sigma_y^0$ . Assume that the limiting state of the material in the process zones is described by a strength criterion

$$F(\sigma_1, \sigma_2, C_i) = 0, \tag{1}$$

where  $\sigma_1, \sigma_2$  are the principal stresses and  $C_i$  are constants of the material.

In view of the symmetry of the problem, the directions  $x$  and  $y$  are principal. Therefore, the stresses  $\sigma_x^0, \sigma_y^0$  satisfy the condition of strength (1) in the process zone. These stresses are found from the solution of the system of two equations [1]:

$$\sigma_x^0 = \beta(\sigma_y^0 - p) + q, \quad F(\sigma_x^0, \sigma_y^0, C_i) = 0, \tag{2}$$

$\beta = \sqrt{E_1/E_2}$ ;  $E_1, E_2$ —are the elasticity moduli of the material in directions 1 and 2.

For the numerical analysis and conclusions the Hoffman criterion of strength is used. It is a generalization of the von Mises–Hill criterion, which takes into account the dependence of the difference between the tensile and compressive strength of unidirectional composite materials. For the plane stressed state, this criterion has the form

$$\frac{\sigma_1^2 - \sigma_1\sigma_2}{\sigma_1^c\sigma_1^t} + \frac{\sigma_2^2}{\sigma_2^c\sigma_2^t} + \frac{\sigma_1^c - \sigma_1^t}{\sigma_1^c\sigma_1^t}\sigma_1 + \frac{\sigma_2^c - \sigma_2^t}{\sigma_2^c\sigma_2^t}\sigma_2 + \frac{\tau_{12}^2}{\tau_0^2} = 1, \tag{3}$$

where  $\sigma_1^t, \sigma_2^t$  are ultimate strengths in tension along the axes  $Ox$  and  $Oy$ ,  $\sigma_1^c, \sigma_2^c$  are ultimate strengths in compression along the axes  $Ox$  and  $Oy$ , and  $\tau_0$  is the ultimate strength in shear along the principal directions.

The crack opening displacement  $\delta(x, l, L)$  at a point  $x$  from the segments  $|x - x_n| \leq L, y = 0$  is given by the formula [2]:

$$\delta(x) = \frac{2T_0\sigma_y^0 l \sin \alpha}{\pi \alpha} \int_{\omega}^{\sec \rho} \ln \left( \frac{1 + \xi \cos^2 \rho + \sin \rho \sqrt{1 - \xi^2 \cos^2 \rho} \xi - 1}{1 - \xi \cos^2 \rho + \sin \rho \sqrt{1 - \xi^2 \cos^2 \rho} \xi + 1} \right) \frac{d\xi}{\sqrt{1 - \xi^2 \sin^2 \alpha}}, \tag{4}$$

where

$$T_0 = \frac{1}{\sqrt{E_1 E_2}} \sqrt{2 \left( \sqrt{\frac{E_1}{E_2}} - \nu_{12} \right) + \frac{E_1}{G_{12}}}, \rho = \frac{\pi p}{2\sigma_y^0}, \alpha = \sin \frac{\pi l}{2D}, \omega = \frac{\sin \frac{\pi x}{2D}}{\sin \alpha}.$$

It is clear that the integral in relation (3) is computed in the finite form as  $D \rightarrow \infty$ , which corresponds to the case of a single crack [1].

The size of process zone is determined by the ratio [2]

$$\frac{\sin \frac{\pi l}{2D}}{\sin \frac{\pi x}{2D}} = \cos \frac{\pi p}{2\sigma_y^0} \tag{5}$$

### 3 The Limit State of the Plate

We choose the critical crack opening displacement criterion as a fracture criterion, then the start of the crack occurs at the moment the crack tip opening displacement attains a certain limit value  $\delta_c$ , i.e.  $\delta(l) = \delta_c$ . Then, basing on (4), the field of ultimate loads  $p_*$  can be defined by [2]

$$\begin{aligned} \sigma_y^0(p_*, q_*) \frac{\sin \alpha}{\alpha} \int_1^{\sec \rho_*} \ln \left( \frac{1 + \xi \cos^2 \rho_* + \sin \rho_* \sqrt{1 - \xi^2 \cos^2 \rho_*} \xi - 1}{1 - \xi \cos^2 \rho_* + \sin \rho_* \sqrt{1 - \xi^2 \cos^2 \rho_*} \xi + 1} \right) \frac{d\xi}{\sqrt{1 - \xi^2 \sin^2 \alpha}} \\ = 2\sigma_y^0(p_*^{(1)}, 0) \ln \sec \frac{\pi p_*^{(1)}}{2\sigma_y^0(p_*^{(1)}, 0)}, \end{aligned} \tag{6}$$

where  $\rho_* = \frac{\pi p_*}{2\sigma_y^0(p_*, q_*)}$ ,  $p_*^{(1)}$  is the limit load in uniaxial loading of the plate with a single crack. The change in  $p_*^{(1)}$  from zero to the ultimate strength of the material in the direction  $y$  corresponds to the change in the length of the crack from infinity to zero, i.e., includes the whole range of change in the length of the crack.

Since the stresses  $\sigma_y^0$ , which depend on the constants that characterize the mechanical properties of the material, enter into the determining relations (6), it is clear that the limit state of the plate depends also on these constants.

However, it should be noted that the limit state of the plane weakened by a system of cracks is not always determined by the fracture criteria of type (6). If the external load is such that the condition  $d = D - l$  is satisfied, then the emergence of prefracture zones of two neighboring cracks occurs, which can also be thought to be the condition of limit state. In view of (5), this condition takes the form

$$\frac{D}{l} = \frac{\pi}{2 \arcsin(\cos \rho^{(d)})}, \quad \rho^{(d)} = \frac{\pi p_*^{(d)}}{2\sigma_y^0(p_*^{(d)})} \tag{7}$$

The relation (6) determines the load  $p_*^{(d)}$  at which the areas of process zones of neighboring cracks occur.

### 4 Results and Discussion

Figure 1 shows limit fracture curves obtained on the basis of (6) (solid curves), curves of coalescence of process zones obtained on the basis of (7) (dashed curves) for  $\beta = 0.1, 0.5, 0.9$  and  $p_*^{(0)}/\sigma_2^p = 0.5$ , and a limit strength curve for a defect-free material (3) for  $\sigma_1^p/\sigma_2^p = 0.8, \sigma_1^c/\sigma_2^p = 0.4, \sigma_2^c/\sigma_2^p = 0.5$  (curve 4);  $D/l = 5$ .

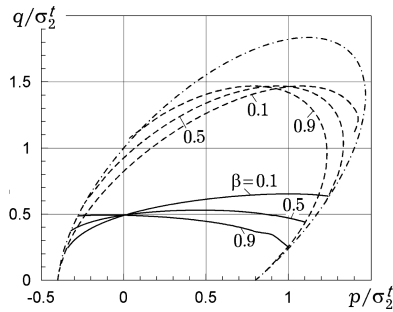
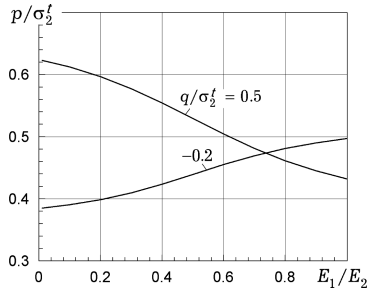


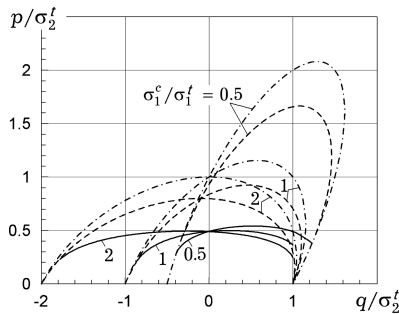
Fig. 1. The critical load and coalescence of process zones for different  $E_1/E_2$

Figure 2 shows dependences of the limit load  $p_*/\sigma_2^p$  on the ratio of the moduli of elasticity  $E_1/E_2$  for  $q/\sigma_2^p = -0.2, 0.5$  for material with the same ultimate strengths. As can be seen from the obtained results, an increase in the degree of anisotropy of the material leads to a decrease in the limit load  $p$  acting perpendicularly to the line of the cracks in the region of tensile loads  $q$  acting along the line of the cracks and to an increase in the limit load  $p$  in the region of compressive loads  $q$ .



**Fig. 2.** Dependence of critical load on the ratio of the moduli of elasticity  $E_1/E_2$

Figure 3 shows limit fracture curves obtained on the basis of (6) (solid curves), curves of coalescence of process zones obtained on the basis of (7) (dashed curves), and the corresponding limit strength curves (3) for  $\sigma_1^c/\sigma_1^t = 0.5, 1.0, 2.0$ , and  $\beta = 0.5$ ,  $p_*^{(0)}/\sigma_2^t = 0.5, \sigma_1^t/\sigma_2^t = 1.0$ .

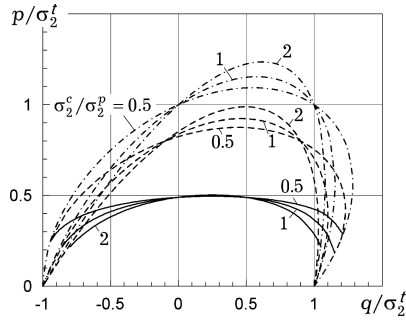


**Fig. 3.** Dependence of critical load on the ratio of tensile and compressive strengths for different  $\sigma_1^c/\sigma_1^t$

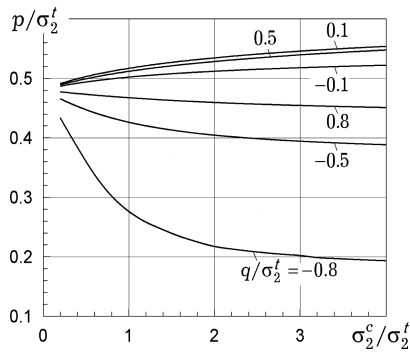
Figure 4 shows limit fracture curves obtained on the basis of (6) (solid curves), curves of coalescence of process zones obtained on the basis of (7) (dashed curves), and the corresponding limit strength curves (3) for  $\sigma_2^c/\sigma_2^t = 0.5, 1.0, 2.0$ , and  $\beta = 0.5$ ,  $p_*^{(0)}/\sigma_2^t = 0.5, \sigma_1^t/\sigma_2^t = 1.0$ .

Figure 5 shows dependences of the dimensionless limit load  $p_*/\sigma_2^t$  of the ultimate strength in compression along the axis of orthotropy  $Oy$  to the ultimate strength in tension along the same axis for different values of the load acting along the line of the crack  $q/\sigma_2^t = -0.8, -0.5, -0.1, 0.5, 0.8$  and  $\sigma_1^t/\sigma_2^t = 1.0$ .

Figure 6 shows the dependences of the dimensionless limit load  $p_*/\sigma_2^t$  on the ratio of the ultimate strength in compression along the axis of orthotropy  $Ox$  to the ultimate



**Fig. 4.** Dependence of critical load on the ratio of tensile and compressive strengths for different  $\sigma_2^c/\sigma_2^t$



**Fig. 5.** Dependence of critical load on the ratio of tensile and compressive strengths  $\sigma_2^c/\sigma_2^t$

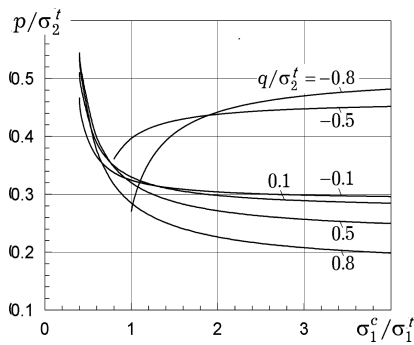


**Fig. 6.** Dependence of critical load on the ratio of tensile and compressive strengths  $\sigma_1^c/\sigma_1^t$

strength in tension along the axis of orthotropy  $Oy$   $\sigma_1^c/\sigma_2^t$  for different values of the load acting along the line of the crack  $q/\sigma_2^t = -0.8, -0.5, -0.1, 0.5, 0.8$  and  $\sigma_1^t/\sigma_2^t = 1.0$ .

## 5 Conclusions

The proposed modification of the Leonov-Panasyuk-Dagdale crack model to the case of orthotropic materials allows to effectively solve problems of the destruction of orthotropic bodies with cracks, the material of which satisfies the condition of the strength of the general form.

As it follows from the presented results, the difference between the ultimate tensile strength and ultimate compressive strength along each direction influences substantially the limit state of the orthotropic plate weakened by a periodic system of collinear cracks.

## References

1. Kaminsky, A.A., Bogdanova, O.S., Bastun, V.N.: On modeling cracks in orthotropic plates under biaxial loading: synthesis and summary. *Fatigue Fract. Eng. Mater. Struct.* **5**(34), 345–355 (2011)
2. Bogdanova, O.S.: Limiting state of an elastoplastic orthotropic plate with a periodic system of collinear cracks. *Int. Appl. Mech* **5**(43), 539–546 (2008)



# The Boundary-Element Approach to Modeling the Dynamics of Poroelastic Bodies

Leonid Igumnov<sup>(✉)</sup>, Svetlana Litvinchuk, Aleksandr Ipatov,  
and Tatiana Iuzhina

Research Institute for Mechanics, Lobachevsky State University  
of Nizhni Novgorod, 23 Prospekt Gagarina (Gagarin Avenue) BLDG 6,  
603950 Nizhny Novgorod, Russia  
igumnov@mech.unn.ru

**Abstract.** The present paper is dedicated to dynamic behavior of poroelastic solids. Biot's model of poroelastic media with four base functions is employed in order to describe wave propagation process, base functions are skeleton displacements and pore pressure of the fluid filler. In order to study the boundary-value problem boundary integral equations (BIE) method is applied, and to find their solutions boundary element method (BEM) for obtaining numerical solutions. The solution of the original problem is constructed in Laplace transforms, with the subsequent application of the algorithm for numerical inversion. The numerical scheme is based on the Green-Betty-Somigliana formula. To introduce BE-discretization, we consider the regularized boundary-integral equation. The collocation method is applied. As a result, systems of linear algebraic equations will be formed and can be solved with the parallel calculations usage. Modified Durbin's algorithm of numerical inversion of Laplace transform is applied to perform solution in time domain. A problem of the three-dimensional poroelastic prismatic solid clamped at one end, and subjected to uniaxial and uniform impact loading and a problem of poroelastic cube with cavity subjected to a normal internal pressure are considered.

**Keywords:** Poroelasticity · Boundary element method (BEM) · Boundary integral equation (BIE) · Laplace transform inversion · Durbin's algorithm

## 1 Introduction

Mechanics of poroelastic materials is relevant to such disciplines as geophysics, geo- and biomechanics, seismology, constricting, petroleum engineering. Wave propagation in porous media is an important issue of these disciplines. Porous medium is a solid with pore system, filled with a liquid or gas. Research of wave propagation processes in saturated porous continua began from the works of Y.I. Frenkel [1] and M. Biot [2]. Biot's model is based on the description of how two phases—porous elastic skeleton and gas or liquid filler—interact. Historically Biot's theory was the first model to predict all three possible types of waves in porous continuum: fast shear wave, fast and slow compression waves. Both fast waves are in their nature close to the ones of elastic



continuum, and slow compression wave presence is the principal difference between elastic and poroelastic continua. This wave is caused by transfer of pore filler particles with respect to the skeleton.

Traditional methods for solving problems of deformable solids mechanics are the finite element method (FEM) and boundary element method (BEM). A detailed review of studies devoted to the modelling of liquid-saturated porous media using BEM and FEM is presented in M. Schanz [3]. This paper is dedicated to the development of 3d poroelastodynamic problems numerical modeling technique based on Boundary Element Method (BEM) usage in Laplace domain and time-stepping schemes for Laplace transform numerical inversion. Specially designed software allows analyzing wave processes in homogeneous and piecewise homogeneous solids. Finite and semi-finite solids can be considered.

## 2 Solution Method

### 2.1 Poroelastic Formulation

We consider a homogeneous solid  $\Omega$  in three-dimensional space  $R^3$ , and  $\Gamma = \partial\Omega$  is the boundary of  $\Omega$ . Porous material of a volume  $V$  can be constructed as follows:

$$V = V^f + V^s \tag{1}$$

where  $V$  is the total volume,  $V^f$  is the summary pore volume and  $V^s$  is the volume of the skeleton. It is assumed that filler can openly seep through the pores and all closed pores are assumed as a part of the skeleton.

Considering a boundary-value problem for Biot’s model of fully saturated poroelastic continuum in Laplace domain in terms of four unknowns (displacements  $\bar{u}_i$  and pore pressure  $\bar{p}$ ) the set of differential equations take the following form [4]:

$$G\bar{u}_{i,jj} + \left(K + \frac{G}{3}\right)\bar{u}_{j,ij} - (\psi - \beta)\bar{p}_{,i} - s^2(\rho - \beta\rho_f)\bar{u}_i = -\bar{F}_i, \tag{2}$$

$$\frac{\beta}{s\rho_f}\bar{p}_{,ii} - \frac{\phi^2 s}{R}\bar{p} - (\psi - \beta)s\bar{u}_{i,i} = -\bar{a}, \quad x \in \Omega,$$

$$\bar{u}'(x, s) = \tilde{u}', \quad x \in \Gamma^u, \quad \bar{u}' = (\bar{u}_1, \bar{u}_2, \bar{u}_3, \bar{p}), \tag{3}$$

$$\bar{t}'_n(x, s) = \tilde{t}'_n, \quad x \in \Gamma^\sigma, \quad \bar{t}' = (\bar{t}_1, \bar{t}_2, \bar{t}_3, \bar{q}).$$

where  $\Gamma^u$  and  $\Gamma^\sigma$  denotes boundaries for boundary conditions of 1st and 2nd kind respectively,  $G, K$  are elastic moduli,  $\phi = V^f/V$  is porosity,  $\bar{F}_i, \bar{a}$  are bulk body forces,

$$\beta = \frac{\kappa\rho_f\phi^2 s}{\phi^2 + s\kappa(\rho_a + \phi\rho_f)}, \psi = 1 - \frac{K}{K_s} \text{ and}$$

$$R = \frac{\phi^2 K_f K_s^2}{K_f(K_s - K) + \phi K_s(K_s - K_f)}$$

are constants reflecting interaction between skeleton and filler,  $\kappa$  is permeability. Further,  $\rho = \rho_s(1 - \phi) + \phi\rho_f$  is a bulk density,  $\rho_s, \rho_a, \rho_f$  are solid, apparent mass density and filler density respectively,  $K_s, K_f$  are elastic bulk moduli of the skeleton and filler respectively. Apparent mass density  $\rho_a = C\phi\rho_f$  was introduced by Biot to describe dynamic interaction between fluid and skeleton.  $C$  is a factor depending on the pores geometry and excitation frequency.

## 2.2 Boundary-Element Approach

Fundamental and singular solutions are considered in term of singularity isolation. Numerical scheme is based on the Green-Betti-Somigliana formula. Boundary-value problem (2)–(3) can be reduced to the BIE system as follows [5, 6]:

$$\frac{1 - \alpha_\Omega}{2} v_i(\mathbf{x}, s) + \int_\Gamma (T_{ij}(\mathbf{x}, \mathbf{y}, s) v_j(\mathbf{y}, s) - T_{ik}^0(\mathbf{x}, \mathbf{y}, s) v_i(\mathbf{x}, s) - U_{ij}(\mathbf{x}, \mathbf{y}, s) t_j(\mathbf{y}, s)) d\Gamma = 0 \quad (3)$$

where  $U_{ij}, T_{ij}$ —fundamental and singular solutions,  $T_{ij}^0$  contains the isolated singularities,  $\mathbf{x} \in \Gamma$ —is an arbitrary point. Coefficient  $\alpha_\Omega$  equals 1 in case of finite domain and -1 in case of infinite domain.

Boundary surface of our homogeneous solid is discretized by quadrangular and triangular elements are assumed as singular quadrangular elements. We use reference elements: square  $\xi = (\xi_1, \xi_2) \in [-1, 1]^2$  and triangle  $0 \leq \xi_1 + \xi_2 \leq 1, \xi_1 \geq 0, \xi_2 \geq 0$ , and each boundary element is mapped to a reference one by the following formula:

$$y_i(\xi) = \sum_{l=1}^8 N^l(\xi) y_i^{\beta(k,l)}, \quad i = 1, 2, 3, \quad (4)$$

where  $l$ —local node number in element  $k, \beta(k, l)$ —global node number,  $N^l(\xi)$ —shape functions. To discretize the boundary surface eight-node biquadratic quadrilateral elements are used, generalized displacements and tractions—are approximated by linear and constant shape functions, respectively.

Subsequent applying of collocation method leads to the system of linear equations. As the collocation nodes we take the approximation nodes of boundary functions. Gaussian quadrature is used to calculate integrals on regular elements. But if an element contains a singularity, algorithm of singularity avoiding or order reducing is applied. When singularity is excluded we use an adaptive integration algorithm. An appropriate order of Gaussian quadrature is chosen from primarily known necessary precision, if it is impossible, the element is subdivided to smaller elements recursively. Solving the system of linear equations leads to the solution of the initial boundary-value problem in Laplace domain.

### 2.3 Laplace Transform Inversion

The inverse Laplace transform is defined as the following contour integral

$$L^{-1}\{\bar{f}(\mathbf{x}, s)\} = f(\mathbf{x}, t) = \frac{1}{2\pi i} \int_{\alpha-i\infty}^{\alpha+i\infty} \bar{f}(\mathbf{x}, s)e^{st} ds, \tag{5}$$

where  $\alpha > 0$  is the arbitrary real constant greater than the real parts of all singularities in  $\bar{f}(\mathbf{x}, s)$ . When values of  $\bar{f}(\mathbf{x}, s)$  are available only at the sample points, analytical evaluation of integral in Eq. (5) is impossible. Supposing  $s = \alpha + i\omega$  we have the following Durbin’s method [7] (for convenience the spatial variable  $\mathbf{x}$  is omitted hereinafter):

$$f(0) = \frac{1}{\pi} \int_0^\infty \text{Re}[\bar{f}(\alpha + i\omega)] d\omega, \tag{6}$$

$$f(t) = \frac{e^{\alpha t}}{\pi} \int_0^\infty \{ \text{Re}[\bar{f}(\alpha + i\omega)] \cos \omega t - \text{Im}[\bar{f}(\alpha + i\omega)] \sin \omega t \} d\omega, t > 0. \tag{7}$$

In order to overcome a drawback of constant integration step Zhao [8] introduced new approach. Let  $R$  be large real number and defining the nodes as  $0 = \omega_1 < \omega_2 < \dots < \omega_n < \omega_{n+1} = R$  we approximate Eqs. (6) and (7) as

$$f(0) = \frac{1}{\pi} \sum_{k=1}^n \int_{\omega_k}^{\omega_{k+1}} \text{Re}[\bar{f}(\alpha + i\omega)] d\omega, \tag{8}$$

$$f(t) = \frac{e^{\alpha t}}{\pi} \sum_{k=1}^n \int_{\omega_k}^{\omega_{k+1}} \{ \text{Re}[\bar{f}(\alpha + i\omega)] \cos(\omega t) - \text{Im}[\bar{f}(\alpha + i\omega)] \sin(\omega t) \} d\omega \tag{9}$$

In each segment  $[\omega_k, \omega_{k+1}]$ :  $F_k = \text{Re}[\bar{f}(\alpha + i\omega_k)]$ ,  $G_k = \text{Im}[\bar{f}(\alpha + i\omega_k)]$ ,  $k = \overline{1, n}$ , the real and imaginary parts of  $\bar{f}(s)$  are approximated as follows:

$$\text{Re}[\bar{f}(\alpha + i\omega)] \approx F_k + \frac{F_{k+1} - F_k}{\omega_{k+1} - \omega_k} (\omega - \omega_k), \tag{10}$$

$$\text{Im}[\bar{f}(\alpha + i\omega)] \approx G_k + \frac{G_{k+1} - G_k}{\omega_{k+1} - \omega_k} (\omega - \omega_k), \tag{11}$$

Substituting Eqs. (10) and (11) into Eqs. (8) and (9) and making direct integration we obtain

$$f(0) \approx \sum_{k=1}^n \left[ \frac{(F_{k+1} - F_k)\Delta_k}{2\pi} \right], \quad (12)$$

$$f(t) \approx \frac{e^{\alpha t}}{\pi t^2} \sum_{k=1}^n \left[ \frac{F_{k+1} - F_k}{\Delta_k} (\cos(\omega_{k+1}t) - \cos(\omega_k t)) + \frac{G_{k+1} - G_k}{\Delta_k} (\sin(\omega_{k+1}t) - \sin(\omega_k t)) \right], \quad (13)$$

where  $t > 0, \Delta_k = \omega_{k+1} - \omega_k$ .

### 3 Conclusions

Boundary integral equations method and boundary element method are applied in order to solve three dimensional boundary-value problems. Regularized BIE system is considered. We used mixed boundary elements to perform the spatial discretization. Gaussian quadrature and hierarchic integrating algorithm are used for integration over the boundary elements. Numerical inversion of Laplace transform is done by means of modified Durbin's algorithm.

We obtained numerical solutions of following dynamic problems: a problem of the three-dimensional poroelastic prismatic solid clamped at one end, and subjected to uniaxial uniform impact loading and a problem of poroelastic cube with cavity subjected to a normal internal pressure are considered.

**Acknowledgements.** This work was supported by a grant from the Government of the Russian Federation (contract No. 14.Y26.31.0031).

### References

1. Frenkel, J.: On the theory of seismic and seismoelectric phenomena in a moist soil. *J. Phys.* **8**, 230–241 (1944)
2. Biot, M.A.: Theory of propagation of elastic waves in a fluid-saturated porous solid. *J. Acoust. Soc. Am.* **28**(2), 168–191 (1956)
3. Schanz, M.: Poroelastodynamics: linear models, analytical solutions, and numerical methods. *Appl. Mech. Rev.* **62**(3), 030803-1–030803-15 (2009)
4. Schanz, M.: *Wave Propagation in elastic and Poroelastic Continua*. Springer, Berlin (2001)
5. Cruze, T.A., Rizzo, F.J.: A direct formulation and numerical solution of the general transient elastodynamic problem I. *J. Math. Anal. Appl.* **22**(1), 244–259 (1968)
6. Ugodchikov, A.G., Hutoryanskii, N.M.: *Boundary element method in deformable solid mechanics*. Kazan State University, Kazan (1986)
7. Durbin, F.: Numerical inversion of Laplace transforms: an efficient improvement to Dubner and Abate's method. *Comput. J.* **17**(4), 371–376 (1974)
8. Zhao, X.: An efficient approach for the numerical inversion of Laplace transform and its application in dynamic fracture analysis of a piezoelectric laminate. *Int. J. Solids Struct.* **41**, 3653–3674 (2004)



# Modeling Surface Waves on a Partially Saturated Poroelastic Half-Space

Leonid Igumnov, Svetlana Litvinchuk<sup>(✉)</sup>, Andrey Petrov,  
and Igor Vorobtsov

National Research Lobachevsky State University of Nizhny Novgorod, 23  
Prospekt Gagarina, 603950 Nizhny Novgorod, Russia  
igumnov@mech.unn.ru

**Abstract.** Defining relations for a partially saturated porous Biot medium, written in the variables of displacements of the skeleton and pore pressures of the fillers, are considered. The initial system of partial differential equations includes five functions (a displacement vector and two pore pressures). The model of the material corresponds to a three-component medium. A system of equations in partial derivatives and boundary-value conditions are written in Laplace transform for time variable and in direct time with initial conditions. The boundary-value problem is analyzed using the method of boundary integral equations, their solutions being sought with the boundary-element method. The numerical scheme is based on using the Green-Bettie-Somigliana formula. Quadratic interpolation polynomials are taken as form functions in describing the boundary of the body. Unknown boundary fields are sought through nodal values in interpolation nodes. The element-by-element numerical integration uses Gauss method and an adaptive integration algorithm. The boundary-element schemes are constructed, based on the consistent approximation of the boundary functions and the collocation method. The solution of the formulated system of linear algebraic equations is sought using the block-type Gauss method. The boundary integral equation method in combination with the technique of searching a boundary-element solution is oriented at a dynamic problem of an isotropic homogeneous partially saturated poroelastic half-space. The time-stepping method for numerical inverting the Laplace transform is used to obtain the solution in the time domain.

**Keywords:** Poroelasticity · Biot's theory · Boundary integral equation · Time-Step method

## 1 Models and Methods

A poroelastic medium is represented using the following mathematical model of a heterogeneous material: an elastic matrix phase and two filler phases—a liquid and a gas filling the pore system. All the three phases are assumed to be compressible. Temperature variations are neglected. Such a poroelastic material can be considered as partially saturated, and its model is called a “three-phase” model. Dynamic equations of a porous medium can be written in terms of representations of displacements of solid  $\hat{u}_i$

and descriptions of pore pressures of the fillers  $\hat{p}^w$  and  $\hat{p}^a$  [1], where symbol “^” denotes Laplace transform with complex variable  $s$ .

The boundary-element technique is based on the use of a regularized boundary integral equation direct approach:

$$\int_{\Gamma} (\mathbf{T}(\mathbf{x}, \mathbf{y}, s)\mathbf{u}(\mathbf{x}, s) - \mathbf{T}^0(\mathbf{x}, \mathbf{y})\mathbf{u}(\mathbf{y}, s))d\Gamma = \int_{\Gamma} \mathbf{U}(\mathbf{x}, \mathbf{y}, s)\mathbf{t}(\mathbf{x}, s)d\Gamma, \mathbf{x}, \mathbf{y} \in \Gamma, \Gamma = \partial\Omega, \tag{1}$$

where  $\mathbf{U}(\mathbf{x}, \mathbf{y}, s)$  and  $\mathbf{T}(\mathbf{x}, \mathbf{y}, s)$  are matrices of fundamental and singular solutions, respectively,  $\mathbf{T}^0(\mathbf{x}, \mathbf{y})$  contains isolated singularities,  $\mathbf{x}$  is integration point,  $\mathbf{y}$  is observation point,  $\mathbf{u}$  is generalized displacement vector,  $\mathbf{t}$  is generalized force vector.

To solve Eq. (1), the boundary surface  $\Gamma$  is divided into the generalized eight-node quadrangular elements. Generalized boundary functions of the first kind are approximated bilinearly, and generalized boundary functions of the second kind are assumed to be constant over the element. Integrals in discretized boundary integral equations are calculated using Gaussian quadrature in combination with singularity decreasing and eliminating algorithms [2].

The solution in the time domain is obtained using the time-step method of numerical inversion of the Laplace transform. This method is based on the operational calculus of integrating original  $f(s)$  of representation  $\hat{f}(s)$ . In general, the integral

$$y(t) = \int_0^t f(\tau)d\tau \tag{2}$$

is approximated as follows [3]:

$$y(0) = 0, \quad y(n\Delta t) = \sum_{k=1}^n \omega_k(\Delta t), \quad n = 1, \dots, N, \tag{3}$$

$$\omega_k(\Delta t) = \frac{R^{-k}}{L} \sum_{l=0}^{L-1} \hat{f}(s)se^{-k\phi i}, \quad \phi = \frac{2\pi l}{L}, \tag{4}$$

where  $N$  is number of time steps,  $L$  is number of nodes for numerically integrating on argument  $\phi$ .

## 2 Results and Discussion

The problem of the Heaviside-type load  $H(t)$  acting on the surface of a poroelastic half-space is considered [4]. A vertical load  $t_3 = -1000 \text{ N/m}^2 \cdot H(t)$  is specified on a surface area of  $1 \text{ m}^2$ , the rest of the surface is traction-free and impermeable. The parameters of the partially saturated porous material correspond to those of Massilon sandstone [1].

In Fig. 1, the color pictures of the vertical displacement and pore water pressure results  $u_3$  and  $p^w$  at  $t \approx 0.07$  s are given. The Rayleigh wave is clearly observed. Besides, the reflection surface wave can be observed due to the different boundary conditions on the loaded and free surfaces.

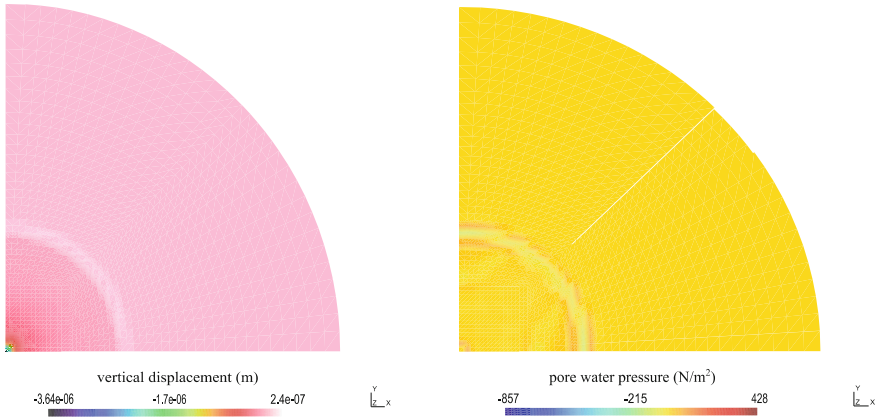


**Fig. 1.** Vertical displacement  $u_3$  and pore water pressure  $p^w$  distributions at  $t \approx 0.07$  s

### 3 Conclusion

Boundary-element solutions of the problem of a force in the form of Heaviside function acting on a punch on a partially saturated poroelastic half-space are presented. Boundary-element solutions for displacement and pore pressures are constructed.

**Acknowledgements.** This work was supported by a grant from the Government of the Russian Federation (contract No. 14.Y26.31.0031).

### References

1. Li, P., Schanz, M.: Time domain boundary element formulation for partially saturated poroelasticity. *Eng. Anal. Boundary Elem.* **37**(11), 1483–1498 (2013)
2. Goldshteyn, R.V.: *Boundary Integral Equations Method: Numerical Aspects & Application in Mechanics*. Mir, Moscow (1978)
3. Lubich, C.: Convolution quadrature and discretized operational calculus. I *Numerische Mathematik* **52**(2), 129–145 (1988)
4. Belov, A., Amenitskiy, A., Litvinchuk, S., Petrov, A.: Boundary-element analysis of the problem of a prismatic body acting on a half-space in a porous-elastic formulation. *Probl. Strength Plast.* **74**, 154–159 (2012)

**Part V**  
**Symposium on: “Elastostatic  
and Elastodynamic Problems  
for Thermosensitive  
and Nonhomogeneous Solids”  
by Roman Kushnir**





# Residual Strength and Reliability of Corroded Pipelines—Monte-Carlo Approach for Consideration of Spatially Nonuniform Material Properties

Alexey Milenin<sup>(✉)</sup>, Elena Velikoivanenko, Galina Rozyinka,  
and Nina Pivtorak

E.O. Paton Electric Welding Institute of NAS of Ukraine,  
03150, 11, K. Malevich Str., Kiev, Ukraine  
asmilenin@ukr.net

**Abstract.** Assessment of the residual strength and workability of pipelines with detected corrosion defects assumes implementation of the limiting state criteria, which relate the parameters of pipe material and actual geometry of structure with the system of operating loading. Since the finite-element modeling is widely used for the expert analysis of the results of technical diagnostics and gives the opportunity to decrease the conservativeness of reliability determination, development of corresponding numerical techniques with regard to specific pipeline element are actual. This work proposes the numerical approach of statistical analysis of corroded pipelines limiting state. It consists in consideration of natural nonuniformity of the material properties within the limits of the finite-element description of the combined development of stress-strain state and ductile subcritical damage up to the limiting state using Monte-Carlo procedure. It allows taking into account of spatial stochastic distribution of such material characteristics as yield stress, microcleavage stress, initial concentration of nucleated porosity of ductile fracture, critical value of plastic strain, etc. It is shown, that this approach has lower conservativeness, than conventional ones, those presuppose the consideration of uniform material properties, but remains responsive enough for solution of typical engineering problems.

**Keywords:** Corroded pipeline · Limiting state · Probability of fracture · Monte-Carlo method · Ductile fracture

## 1 Introduction

Statistical prediction of the strength and reliability of critical structures is actual alternative to the deterministic methods of design and expert analysis. It allows avoiding the conservative assumption that most design parameters and material properties are known constants. Concerning the assessment of the state of main and technological pipelines under internal pressure, one of the most typical problem is the determination of strength and reliability taking into account the presence of operating defects such as

corrosion (erosion) metal losses. The stress concentration in the region of wall thinning causes the increase of the material susceptibility to nucleation and propagation of fracture under comparatively low external loading.

There are a number of standard algorithms, those allow assessing the level of defected pipe strength degradation due to corrosion or erosion metal loss. They presuppose using the set of input parameters, such as physical mechanical properties of material, actual geometry of structure, characteristics of resistance to specific type of fracture. Also the assumption about material uniformity and isotropy is usually made. To decrease the conservativeness of corroded pipe limiting state assessment taking into account stochastic spatial distribution of material properties the methods of statistical theory of strength can be used. The most straightforward way of mathematical description of these phenomena is Monte-Carlo approach. But the implementation of this approach demands the precise description of subcritical and critical fracture of pipe under operational load as well as high-performance software for its fulfilling.

Within the limits of this work it is proposed the methodology for the numerical prediction of the strength and reliability of corroded pipelines with spatially nonuniform properties by means of Monte-Carlo approach for implementation of statistical strength theory along with finite-element description of the state of specific structure.

## 2 Numerical Procedure for Probabilistic Analysis of Residual Strength of Pressurized Pipeline with Corrosion Defect

### 2.1 Assumptions, Mathematical Model and Finite-Element Implementation

As the subcritical fracture of the material of pressurized pipeline with detected surface three-dimensional metal loss (Fig. 1) is determined by ductile mechanism (that consists in nucleation and propagation of microporosity of some volume concentration  $f$ ) the variable load bearing cross-section of the structure should be taken into account at the finite-element (FE) simulation of the state of stresses and strains. For predicting ultimate limiting state of pipeline with local corrosion metal loss of certain size under the internal pressure the pipeline material was considered as elastic-plastic medium, where the strain tensor increment  $d\varepsilon_{ij}$  was expressed as follows:

$$d\varepsilon_{ij} = d\varepsilon_{ij}^e + d\varepsilon_{ij}^p + \delta_{ij}(d\varepsilon_T + df/3) \quad (1)$$

where  $d\varepsilon_{ij}^e$ ,  $d\varepsilon_{ij}^p$ ,  $\delta_{ij} d\varepsilon_T$ ,  $\delta_{ij} df/3$  are the components of the strain tensor increment due to elastic, plastic, thermal and fracture deformation mechanisms, respectively,  $i, j = r, \beta, z$  (Fig. 1),  $\delta_{ij}$  is Kronecker symbol.

For numerical prediction of porosity nucleation in material of pressurized pipeline with surface corrosion metal loss the strain-based criterion was used:

$$\int \frac{d\varepsilon_i^p}{\varepsilon_c} > 1 \quad (2)$$

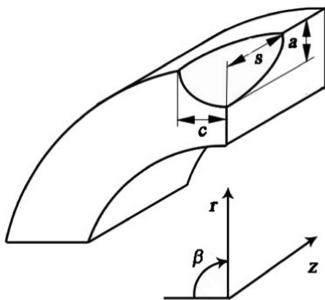


**Fig. 1.** Scheme of pipeline element with external corrosion defect of semiellipsoidal shape in cylindrical coordinate system

where  $d\epsilon_i^p = \frac{\sqrt{2}}{3} \sqrt{d\epsilon_{ij}^p d\epsilon_{ij}^p}$  is the increment of plastic strain intensity,  $\epsilon_c$  is the critical value of plastic strain.

Fulfillment of (2) means that porosity of certain concentration  $f_0$  nucleates. The further growth of voids depends on stress triaxiality  $T$ , i.e. the ratio of the hydrostatic  $\sigma_m$  to equivalent  $\sigma_{eq}$  stress and the intensity of the plastic strain  $\epsilon_i^p$  according to Rice-Tracey law [1]:

$$df = \begin{cases} 1.28 \exp(\frac{3}{2}T) d\epsilon_i^p, & \text{if } T = \frac{\sigma_m}{\sigma_{eq}} > 1 \\ 1.28(T)^{1/4} \exp(\frac{3}{2}T) d\epsilon_i^p, & \text{if } \frac{1}{3} \leq T \leq 1 \end{cases} \quad (3)$$

Numerical solution of the boundary-value problem for continuum with nonuniform bearing cross-section has been carried out by tracing the elastic-plastic deformations and the ductile fracture void concentration in structure at loading to the ultimate limit state within the framework of finite element description. The relationship between strains and stresses was determined by generalized Hooke’s law and the associated law of plastic flow, according to the next relationships [2]:

$$\Delta\epsilon_{ij} = \Psi(\sigma_{ij} - \delta_{ij}\sigma_m) + \delta_{ij}(K\sigma_m + \Delta\epsilon^r + \Delta f/3) - \frac{1}{2G}(\sigma_{ij} - \delta_{ij}\sigma_m)^* + (K\sigma_m)^* \quad (4)$$

where  $K = (1-2\nu)/E$ ,  $G = 0.5E/(1 + \nu)$ ,  $E$  is Young modulus,  $\nu$  is Poisson’s ratio, symbol “\*” refers to the variable of the previous tracing step,  $\Psi$  is the state function of the material, which is determined by the level of plastic deformation according to plastic flow surface  $\Phi$ , that was considered according to Gurson-Tvergaard-Needleman model [3]:

$$\Phi = \left(\frac{\sigma_{eq}}{\sigma_Y}\right)^2 - (q_3 f')^2 + 2q_1 f' \cosh\left(q_2 \frac{3\sigma_m}{2\sigma_Y}\right) \quad (5)$$

where  $q_1, q_2, q_3$  are the constants,  $f'$  is the equivalent concentration of voids,  $\sigma_Y$  is yield stress.

It was considered that specific FE lost its load bearing capacity in case of fulfilling the one of three conditions of numerical criterion of brittle-ductile fracture [4]:

$$\begin{aligned} \Psi - \frac{1}{2G} &\geq \frac{\varepsilon_f - (\varepsilon_i^p)^*}{1.5\sigma_s(\varepsilon_i^p)}; \\ f' &\geq f_F = \frac{1}{q_1} \exp\left(-\frac{3q_2\sigma_m}{2\sigma_Y}\right); \\ \frac{\sigma_1}{1 - 2f/3} &> S_K, \end{aligned} \quad (6)$$

where  $S_K$  is the microcleavage stress,  $\varepsilon_f$  is the critical strain (material deformability) according to Mackenzie rule.

As it can be seen, there is a number of material properties, those influence on the results of prediction of ultimate limiting state of corroded pipeline ( $E$ ,  $\sigma_Y$ ,  $f_0$ ,  $\varepsilon_c$ ,  $\varepsilon_f$ ,  $S_K$ ). The choice of their values determines the analysis conservativeness and they have certain spatial distribution because of material natural nonuniformity.

## 2.2 Monte-Carlo Algorithm for Probability Assessment

Monte-Carlo procedure for prediction of failure probability of corroded pipeline element taking into account spatial material nonuniformity consists in series of calculations of ultimate pressure in pipeline with arbitrary spatial variation of chosen properties according their density of distribution. Thus, within the limits of representative sampling (number of numerical tests  $N_r$ ) the failure probability for specific corroded pipe under pressure  $P$  is assessed as

$$p(P) = N_p/N_r \quad (7)$$

where  $N_p$  is the number of tests, for which (6) is fulfilled at pressures equal or less than  $P$ .

The choice of  $N_r$  has a key importance for the correct prediction of  $p(P)$  and the decrease the calculation time. Here the next algorithm was used:

1. Comparatively low initial value of  $N_0$  (about 100–200) is chosen and the dependence  $p_0(P)$  is obtained.
2. Next value  $N_1$  was equaled to double the initial one ( $N_1 = 2N_0$ ) and for  $N_1$  the dependence  $p_1(P)$  was obtained according to (7).
3. If quadratic deviation between dependences  $p_0$  and  $p_1$ , was higher of equal, than critical one  $\Delta_c$ , than next step of tracing was implemented, i.e.  $N_2 = 2N_1$  with subsequent calculation of  $p_2$  and quadratic deviation between dependences  $p_1$  and  $p_2$ .
4. If for some  $k$ -th step the deviation between dependences  $p_{k-1}$  and  $p_k$ , was lower than  $\Delta_c$ , it was concluded, that  $N_{k-1}$  tests was enough for representative sampling ( $N_{k-1} = N_r$ ) and  $p_{k-1}$  was accepted as the true value of failure probability, i.e.  $p_{k-1}(P) = p(P)$ .

This calculation algorithm is the laborious one, so for its implementation the novel methods of parallel and hybrid computation were used [5].

### 3 Results and Discussion

As a case of study it was considered the pressurized steel pipeline element (the outer diameter  $D = 1420$  mm and the wall thickness  $t = 20$  mm) with the individual corrosion metal loss of semiellipsoidal shape on outer surface of the pipe ( $2s \times 2c \times a = 20 \times 20 \times 10$  mm). The material of pipeline was steel 17G1S-U ( $E = 206$  GPa,  $\nu = 0.3$ ,  $\sigma_Y = 365\text{--}490$  MPa,  $S_K = 800\text{--}1000$  MPa,  $f_0 = 0.001\text{--}0.01$ ,  $\varepsilon_c = 0.001\text{--}0.05$ ). It was accepted that some parameters have Weibull spatial distribution, that's why the choice of stochastically distributed characteristic  $X$  for specific FE can be made at every numerical test by using following expression:

$$X_{ijk} = [-\ln(1 - RND)]^{\frac{1}{\eta_X}}(B_X - A_X) + A_X, \quad (i, j, k = r, \beta, z), \quad (8)$$

where  $RND$  is random value from the range (0;1),  $A_X$ ,  $B_X$ ,  $\eta_X$  are the constants of Weibull spatial distribution for characteristic  $X$ .

For the considered example of pipeline element with external defect it was accepted that some material properties have stochastic spatial distribution, namely, yield stress  $\sigma_Y$  ( $A_\sigma = 365$ ,  $B_\sigma = 450$ ,  $\eta_\sigma = 4$ ), concentration of nucleated porosity  $f_0$  ( $A_f = 0.001$ ,  $B_f = 0.0052$ ,  $\eta_f = 2$ ), critical value of plastic strain  $\varepsilon_c$  ( $A_\varepsilon = 0.001$ ,  $B_\varepsilon = 0.0024$ ,  $\eta_\varepsilon = 2$ ), microcleavage stress  $S_K$  ( $A_S = 800$ ,  $B_S = 937$ ,  $\eta_S = 4$ ). As it can be seen in Fig. 2, the consideration of spatial distribution of these variables leads to the fluctuation of the field of stresses over the cross-section of the defective pipe in comparison with conventional calculation with constant values of properties ( $\sigma_Y = 427$  MPa,  $f_0 = 0.0055$ ,  $\varepsilon_c = 0.026$ ,  $S_K = 900$  MPa). Nevertheless the stress fields are very similar from the point of view of maximum values of equivalent stress or the areas of high stress concentration.

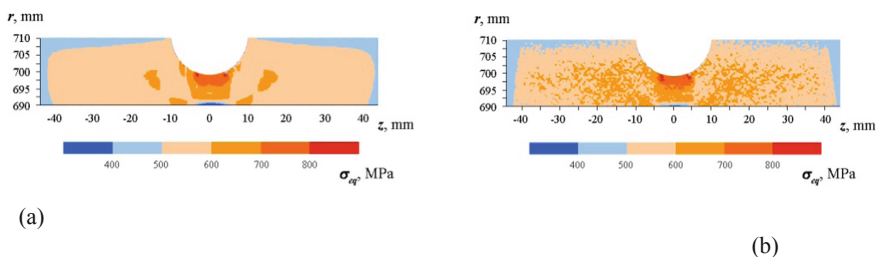


**Fig. 2.** Examples of equivalent stress distribution in pipeline ( $D \times t = 1420 \times 20$  mm, steel 17G1S-U) with external corrosion defect ( $2s \times 2c \times a = 20 \times 20 \times 10$  mm) under limiting internal pressure 14.0 MPa: **a**—conventional calculation with constant material properties; **b**—Monte-Carlo calculation

Frequency of fulfilling of (6) for considered pipeline with external defect under certain pressure within the limits of representative sampling allows assessing the probability of failure  $p$ . The chosen algorithm of need number of test  $N_r$  for representative sampling showed fast converging to the stationary state (see Fig. 3 a): it was

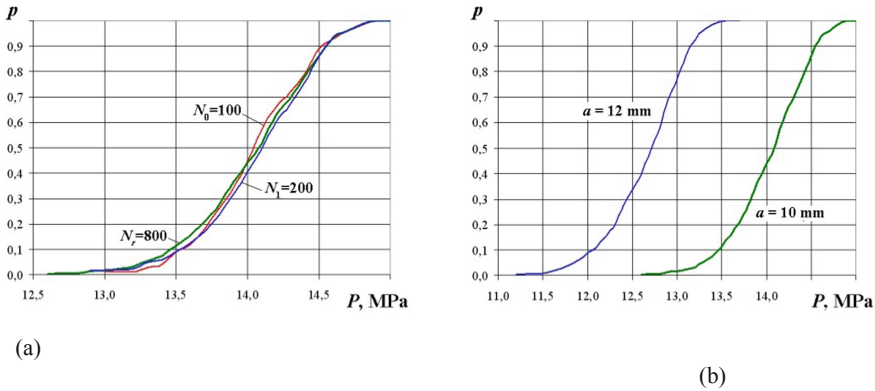


**Fig. 3.** Dependencies of failure probability  $p$  of pipeline ( $D \times t=1420 \times 20$  mm, steel 17G1S-U) with external corrosion defect ( $2s \times 2c \times a=20 \times 20 \times 10$  mm) on internal pressure  $P$ : **a**—at different number of tests Monte-Carlo sampling ( $N_0 = 100$  is the initial value;  $N_1$  is the second iteration;  $N_r=800$  is accepted representative sampling); **b**—for different depths  $a$  of the defect

needed five series of calculations to find true value of  $N_r$  equaled to 800 ( $\Delta_c=0.01$ ). As the calculation results showed, the considered pipeline can fail within the range of internal pressure from 12.6 to 14.8 (for defects of greater depth  $a$  see Fig. 3 b this range is naturally shifted to 11.2–13.5 MPa). In case of using of the most unfavorable set of possible values of input data the conventional calculation gave the limiting pressure  $P = 12.5$  MPa, whereas the most favorable input data combination leads to the value of limiting pressure about  $P = 15.6$  MPa. It can be concluded that implementation of Monte-Carlo approach allows reducing the conservativeness of reliability analysis of defective structure.

## References

- Chen, Z., Butcher, C.: Micromechanics Modelling of Ductile Fracture. Springer, Netherlands (2013). <https://doi.org/10.1007/978-94-007-6098-1>
- Makhnenko, V.: Problems of examination of modern critical welded structures. Paton Weld. J. **5**, 21–28 (2013)
- Xue, L.: Damage accumulation and fracture initiation in uncracked ductile solids subject to triaxial loading. Int. J. Solids Struct. **44**(16), 5163–5181 (2007). <https://doi.org/10.1016/j.ijsolstr.2006.12.026>
- Milenin, O.S.: Numerical prediction of the current and limiting states of pipelines with detected flaws of corrosion wall thinning. J. Hydrocarbon Power Eng. **4**(1), 26–37 (2017)
- Velikoivanenko, E.A., Milenin, A.S., Popov, A.V., Sidoruk, V.A., Khimich, A.N.: Methods and technologies of parallel computing for mathematical modeling of stress-strain state of constructions taking into account ductile fracture. J. Autom. Inf. Sci. **46**(11), 23–35 (2014). <https://doi.org/10.1615/JAutomatInfSci.v46.i11.30>



# Actual Problems of Structural Integrity Assessment of WWER-1000 Pressure Vessel Internals

O. V. Makhnenko and S. M. Kandala<sup>(✉)</sup>

E.O. Paton Electric Welding Institute of the NAS of Ukraine, Kyiv, Ukraine  
makhnenko@paton.kiev.ua, st\_kan@ukr.net

**Abstract.** The problem of numerical prediction of the process of radiation swelling in internal elements for assessment of structural integrity and prolonging the lifetime of the WWER-1000 reactors is quite actual. The critical element is core baffle, which is operating under high gradients of neutron irradiation and temperature. The influence of features of various fuel campaigns and their sequence on the distribution and the maximum value of radiation swelling, as well as, on stresses and distortions in the baffle after long-term service. The consequences of a possible decrease in the efficiency of cooling on the external surface of the baffle in the event of a gap closing between the barrel and the baffle due to radiation swelling or prediction tolerances are reviewed. According to result of modeling the recommendation for numerical assessment of residual life of internal baffle WWER-1000 reactor are formulated.

**Keywords:** Reactor WWER-1000 · Internals · Baffle · Barrel · Radiation swelling · Heat exchange

## 1 Consideration of the Sequence of Fuel Campaigns for Prediction of Radiation Swelling in Core Baffle

The main element of the internals, which determines and limits the residual life of the WWER-1000 reactors when extending the service life, is the reactor core baffle, which is operating under conditions of high gradients of neutron irradiation and temperature. The lifetime of the baffle is primarily determined by its progressive distortion, caused by radiation swelling. From the standpoint of ensuring the structural integrity of internal elements, the stress state plays an important role, which can also significantly depends on the process of radiation swelling.

The baffle is a cylindrical shell, consisting of rings, fastened with pins (Fig. 1). The rings of the baffle have an outer cylindrical surface and a faceted inner surface that follows the boundaries of the reactor core. The design is symmetrical, therefore, for modeling a section of 30-degree sector is considered. Material is austenitic stainless steel 08Cr18Ni10Ti.

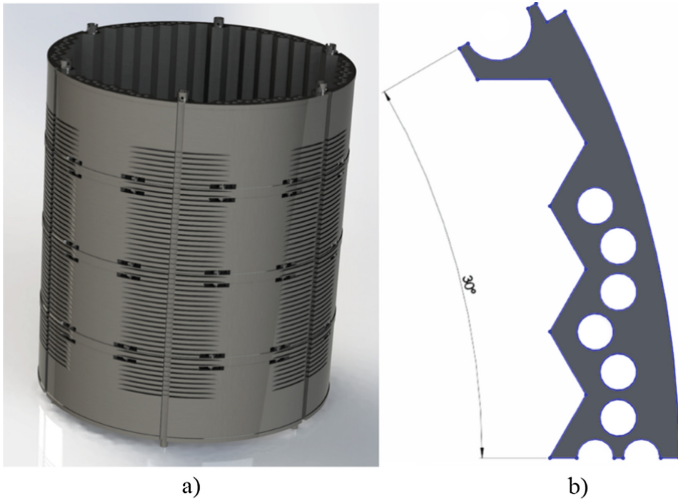


**Fig. 1.** Core baffle: **a** 3D model; **b** 30-degree sector

For the prediction of radiation swelling the following model was used [2]:

$$S = C_D \cdot D^n \cdot f_1(T) \cdot f_2(\sigma_m, \sigma_{eq}) \cdot f_3(\dot{\epsilon}), S > 0 \tag{1}$$

where

$$f_1(T) = \exp(-r \cdot (T - T_{max})^2); f_2(\sigma_m, \sigma_{eq}) = 1 + 8 \cdot 10^{-3} (0.85 \cdot \sigma_m + 0.15 \cdot \sigma_{eq})$$

$$f_3(\dot{\epsilon}) = \exp(-\eta \cdot \dot{\epsilon}); C_D = 1.035 \cdot 10^{-4}; n = 1.88; r = 1.825 \cdot 10^{-4};$$

$$T_{max} = 470^\circ\text{C}; P = 4 \cdot 10^{-3} \text{MPa}^{-1}; \eta = 8.75.$$

In the formulation of the problem, the relationship between the rate of strain of radiation creep and the rates of accumulated dose and complete swelling was taken into account [2]:

$$\frac{d\epsilon^{cr}}{dt} = \left( B_0 \frac{dD}{dt} + \omega \frac{dS}{dt} \right) \sigma_{eq} \tag{2}$$

### 1.1 The Results of the Calculation

The input data on the distribution in the volume of the baffle of accumulated dose (fluence) and heat release under the influence of gamma radiation can significantly affect the results of numerical prediction of radiation swelling of the material during long-term operation (30–60 years) [1].



To determine the influence of the fuel campaigns sequence and the averaging over fuel campaigns by input data on heat release and accumulated damaging dose, two most different fuel campaigns were chosen [3]. Based on these two campaigns, following five different operational scenarios for the long-term reactor operation were considered:

1. fuel campaign No. 1 for 60 years;
2. fuel campaign No. 2 for 60 years;
3. fuel campaign No. 1 for first 30 years and No. 2 for next 30 years;
4. fuel campaign No. 2 for first 30 years and No. 1 for next 30 years;
5. averaging of the fuel campaigns No. 1 and No. 2 for 60 years.

Analysis of the results of computation for all five scenarios shows that maximum values and distributions of temperature and swelling have a significant difference. The maximum value 5.05% of the radiation swelling of the baffle corresponds to scenario No. 2, since it is characterized by the highest temperature 412 °C and the level of the accumulated dose of radiation 95 d.p.a.. The minimum value 0.1% of the radiation swelling of the baffle material is typical for the scenario No. 1, where the maximum temperature is 365 °C, the maximum accumulated dose of radiation is 22 d.p.a. The calculation results are presented in Table 1 (Fig. 2).

**Table 1.** The results of the calculation for the considered scenarios

Max. values	Scenario No. 1	Scenario No. 2	Scenario No. 3	Scenario No. 4	Scenario No. 5
Dose, d.p.a.	22.25	95.31	47.28	47.28	51.25
Swelling, %	0.09	5.05	1.38	1.37	0.59
Temperature, °C	365	412	365–412	412–365	374
Stresses, MPa	189	253	231	222	192
Displacements, mm	9.45	11.20	10.47	10.42	9.90

Calculation for the two fuel campaigns, but in their different sequence (Scenarios No. 3 and No. 4) did not lead to significant differences in the results at the end of the operation for 60 years, but the kinetics of the development of radiation swelling may differ.

The averaging of the fuel campaigns (Scenario No. 5) by input data on heat release and accumulated damaging dose leads to a significant deviation of the results in comparison with Scenarios No. 3 and No. 4. Therefore, not taking into account the sequence of fuel campaigns and averaging by input data may significantly affect on the accuracy of prediction the stress-strain state and radiation swelling in core baffle.

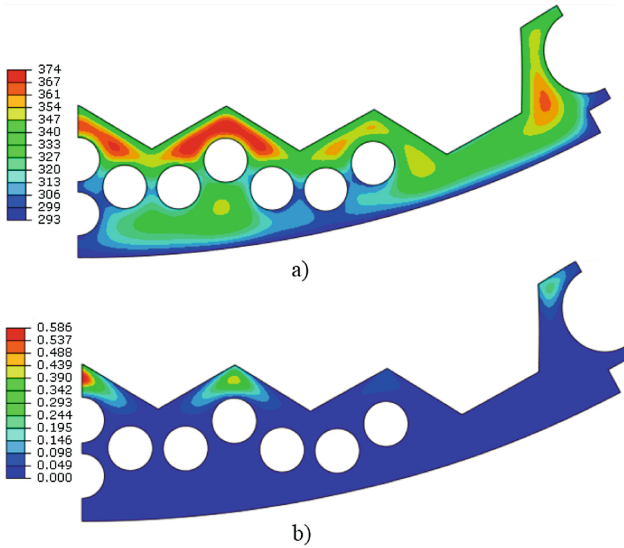


**Fig. 2.** The calculation results for the averaged data (scenario No. 5): **a** stationary temperature field, (°C), **b** swelling of the baffle material after the operation for 60 years, (%)

## 2 The Effect of Closing the Gap on the Stationary Temperature Field and the Shaping of the Baffle

The gap between the core baffle and the barrel can be closure during operation in result of radial distortions due to radiation swelling of baffle and possible quite large deviations of gap dimension from the project value (2.5 mm). That’s why the reduction of the cooling efficiency on the external surface of the baffle due to the closure of the gap between the barrel and the core baffle is quite probable for the WWER-1000 units.

In the computational research, three different cases of the temperature state of the baffle during operation were considered depending on the cooling efficiency on the outer surface, which is determined by the boundary conditions, namely the value of the heat transfer coefficient.

For the first case, the conditions of normal operation were specified according to Table 2. In the second case, the possible closure of the gap and, accordingly, the lack of cooling in the theoretically contact area was considered (Fig. 3). For the third case, low efficiency of cooling was modeled over the entire outer surface of the baffle.

**Table 2.** The main thermal and hydraulic parameters on the surfaces of the baffle [1]

	Coolant temperature, °C	Heat transfer coefficient, $W\ m^{-2}\ c^{-1}$
Inner surface of the baffle	320	15,000–40,000
Outer surface of the baffle	292	2000–6000
Cooling channels	292	1000–5000

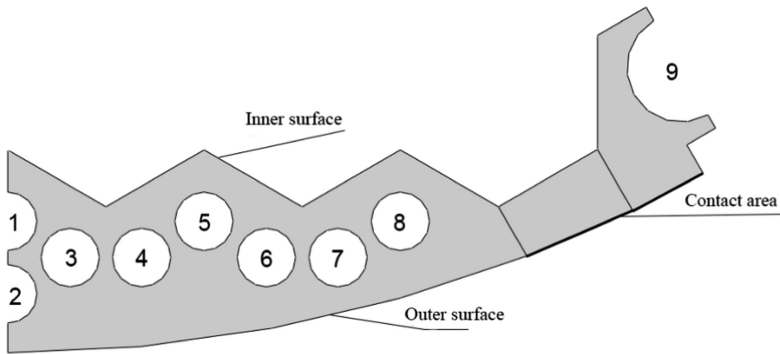


**Fig. 3.** Section of the core baffle, sector 30°

As can be seen from Fig. 4 all of the calculated cases are characterized by specific temperature fields with significant differences in the magnitude and the distribution.

The change in temperature field has a significant effect on the distortion of the baffle. So, calculation results for the second case in comparison with the normal cooling conditions (first case) show the increase in the maximum radial displacements from 9.5 to 10.0 mm with the same character of distribution (the maximum radial displacement on the outer surface of the baffle is near the channel No. 9). For the closing the gap over the entire outer surface of the baffle (third case), the maximum radial displacement 11.1 mm are in another zone of the external surface of the baffle near the channel No. 2.

It should be noted, that the considered rather conservative cases of reducing the cooling efficiency of the baffle do not affect the level of maximum radiation swelling, since in the calculated areas of temperature increase the accumulated fluence is quite low that does not lead to change of radiation swelling of the baffle material.

### 3 Conclusions

- From the point of view of reliability of prediction of radiation swelling of the baffle material during long-term operation it is necessary to take into account the features of fuel campaigns, as well as their sequence.
- The averaging of the fuel campaigns by input data on heat release and accumulated damaging dose leads to a significant deviation of the results. The averaging can be used only for future fuel campaigns at prolonging the lifetime of WWER-1000 reactors.
- Reducing the efficiency of cooling on the outer surface of the baffle due to closure of the gap between the baffle and the barrel can lead to a significant change in the distribution of the temperature state in the baffle during operation.

- Radial displacements also have significant changes due to reducing the efficiency of cooling, which can lead to an increase in stresses in the contact zone, both in the barrel and in the baffle.
- At the same time, there is no noticeable influence of cooling conditions on the outer surface of core baffle on the radiation swelling of the baffle material.

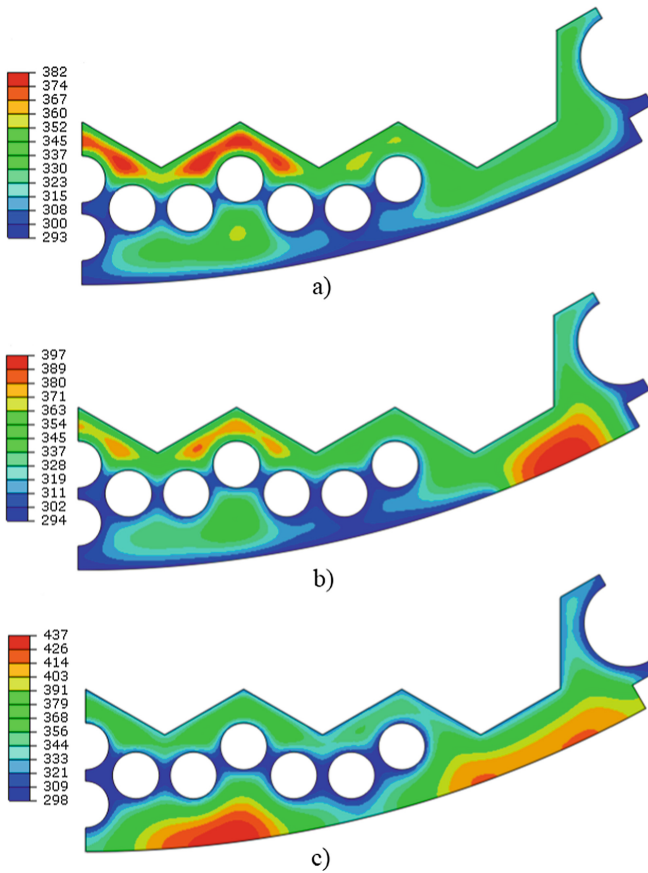


**Fig. 4.** Stationary temperature field of the baffle taking into account, °C: **a** the gap between the baffle and the barrel; **b** the closure of the gap in the zone of probable contact; **c** the closure of the gap over the entire outer surface of the baffle

## References

1. Harutyunyan, D., Mirzov, I., Schulc, M.: Void swelling in VVER-1000 pressure vessel internals. M&C 2017. In: International Conference on Mathematics & Computational Methods Applied to Nuclear Science & Engineering, Jeju, Korea, April 16–20, 2017, on USB (2017)
2. Margolin, B.Z., Murashova, A.I., Neustroev, V.S.: Analysis of influence of stressed state type on radiation swelling and radiation creep of austenitic steels. *Probl. Prochn.* **3**, 5–24 (2012)
3. Mirzov, I., Kandala, S.: Method of Parametric Assignment of Input Data for Irradiation Swelling Calculation of VVER1000 Internals. *Nucl. Radiat. Saf.* **3**, 23–27 (2016)



# Vibration of Titanium Blades of Turbomachines for Nuclear Power Plants with Erosive Damage

Yurii Vorobiov<sup>1</sup>, Oleg Makhnenko<sup>2</sup>(✉), Nataliia Ovcharova<sup>1</sup>,  
and Anton Olkhovskiy<sup>1</sup>

<sup>1</sup> A. Podgorny Institute of Mechanical Engineering Problem of NASU,  
Kharkiv 61046, Ukraine

vorobyov.yuriy@gmail.com

<sup>2</sup> E. O. Paton Electric Welding Institute of NASU, Kiev 03680, Ukraine  
makhnenko@paton.kiev.ua

**Abstract.** The influence of erosion damages on the vibration features of the working titanium blades of the last stage of the steam turbine with a capacity of 1 GW for a nuclear power plant is considered. Erosion damages of these blades were observed after 180 thousand hours of operation. Morphological and fractographic studies have shown the nature of erosion damages, but did not reveal degradation of the mechanical properties of the material. Such damages cause the stress concentration, that leading to a decrease of fatigue limit and residual life. A finite element model of the blade has been developed, which has a denser mesh in the area of damage. Numerical studies have revealed features of stress concentration in the damages zone. The degree of reduction of blade fatigue and residual life is determined. It is shown that mechanical treatment of the erosion damage zones allows to increase the fatigue limit and residual resource.

**Keywords:** Erosion damage · Vibration · Blade · Life · Titanium alloy

## 1 Introduction and Problem Statement

Turbine blades vibration, especially with erosion damages is of great interest and the results of their research are reflected in a number of publications [1–5].

The influence of erosion damages on the features of the vibrations of the last stage working blades of the low-pressure cylinder of the K-1000-60/3000 steam turbine for the nuclear power plant is considered. During the long time use in wet-steam environment which is typical for the last stages of steam turbines, especially for NPP turbines, there is a noticeable erosion of the blades. The greatest danger arises due to the formation of craters and slit-type damages at the upper third parts of the blade leading edge. Such damages cause concentration of stresses, which leads to a decrease in fatigue limit and residual life. The radius in the mouth of erosion damage is noticeable larger than that of a fatigue crack. The main danger for damaged blades is vibration. Further studies have shown that the mechanical treatment of the erosion damage zones can increase the fatigue limit and residual life.

The blade, whose vibrations are under investigation, is made of the TS5 titanium alloy (Ti-5Al-1.5 V) and has a length of 1200 mm. The morphological and fractographic analysis of the properties of titanium blade in the erosion zone after more than 180 thousand hours of operation was performed [4, 5].

The morphology of erosive damages to the blade contains deep cavities with arrow-like edges in the form of pyramidal elements with distances between them 400–700  $\mu\text{m}$  and the radius of each of them is 0.02–0.05 mm in the mouth of the damage. The main erosion damage has a saw-tooth character (Fig. 1).

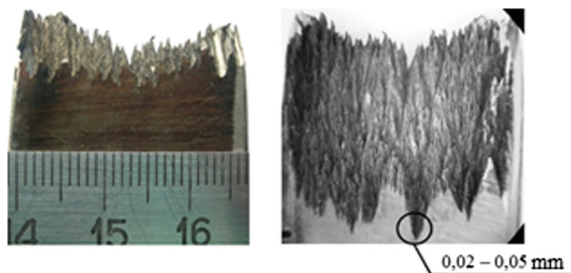


**Fig. 1.** General view of erosion damages on the back (left) and front (right) side of the blade

With such damages to the edge-to-edge contact, no damages can be observed. The morphological and fractographic analysis showed that the mechanical properties of the TS5 titanium alloy in the erosion zone in general meet the requirements of the Technical Specifications [5]. The degradation of the blade material mechanical properties after 180,000 h of operation, which should be taken into account in the blade models, were not observed. The damages in blade body are modeled by cutouts in the blade finite-element grid with a depth of 1–3 mm, width of 1–2 mm, radius of 0.02–0.05 mm in the mouth of the damage (Fig. 1). Therefore, there has been developed a blade finite element model, having a more condensed grid in the damage area, but a less condensed one in the rest of area (Fig. 2).

Using these models, the vibrations of the blades without damage and with different numbers of damage and in different places along the length of the blades in the stress localization zone due to the features of the vibration forms have been studied.

## 2 Numerical Studies of Blade Vibration

The frequencies variation and stresses for the cases of a different numbers of damages were studied. The natural frequencies of the blade in case of damage change slightly. Of much more interest is the distribution of vibration stresses in a damage area. Multivariate studies of the blades vibrations with a different number of damages, which are located in different places along the blade length, have been performed. It is shown that the greatest danger is represented by erosion damages, which are located in places of stresses localization under some modes of vibration. The greatest stress localization

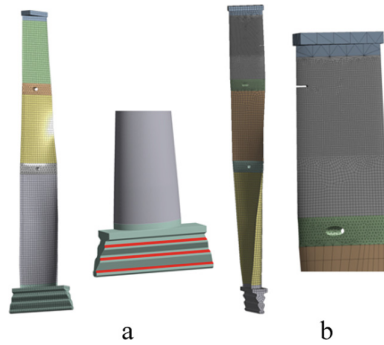


**Fig. 2.** Finite-element models of working blades without damage (a) and with a dense grid in the area of damage (b)

is observed for the third and sixth modes of vibrations. Therefore, Fig. 3 shows the vibration forms and the distribution of vibration stresses with one's damage for the third mode.

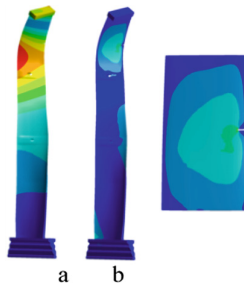


**Fig. 3.** The third mode of vibrations (a) and vibration stress distribution (b) in the area of localization of stress

This is evident from the coincidence of erosion damage and stress localization in the third mode. But real erosion damages are located in groups near each other. Therefore further studies of vibrations of the blades were carried out with a different number of damages located side by side in the stress localization zone. In Fig. 4 the distribution of vibration stresses for the third mode with a different number of damages is shown.

The study of vibrations with different number of damages shows that an increase in the number of damages leads to an increase in the size of the zone of increased stresses, but does not cause a greater concentration of stresses.

Multivariate calculations of vibrations of the blades with different number of damages made it possible to obtain a qualitative idea of the regularities of stress concentration in the blades with various forms of vibrations. But to consider the real



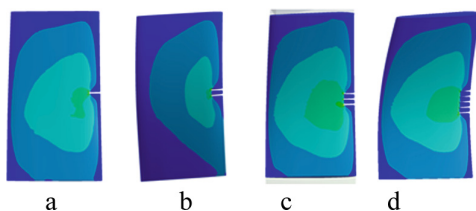


**Fig. 4.** Fragments of vibration stress distribution in the area of stresses localization for the third mode with one (a), two (b), three (c) and five (d) damages

stress concentration coefficients necessary calculations of the forced vibrations of the blades, at least under conditional loads.

Due to the lack of initial data, for the analysis of forced vibrations the conditional level of the load acting on the blade during vibrations in the flow can be used. The variable component of the gas-dynamical force of the flow acts on the working blades, causing the blade to vibrate.

The variable component can be decomposed into a harmonic series [3]. The amplitudes of these harmonic components forces are unknown. They can be estimated only roughly based on available source data. The frequencies of the harmonics that are dangerous can be determined. In the operating conditions always there is disturbing force which frequency is a multiple of the number of revolutions per minute  $n = 3000$ , which corresponds to  $\Omega = 50$  Hz. In addition, the harmonics caused by the guide blades has a frequency  $nz$ , where  $z$ —number of blades guide stage. The frequency of this harmonic is  $\omega_z = 50 \times 42 = 2100$  Hz. The amplitude of harmonic component with frequency  $\omega_z = 2100$  Hz will be taken as a distributed load equal to  $P_z = 2.47 \times 10^{-3}$  MPa.

Investigations of vibrations of the blades with one, two and three damages located side by side in the zone of stress localization under the action of harmonic component with a frequency of 2100 Hz were carried out. So in Fig. 5 the locations of vibration stresses in the blades with two damages are presented.

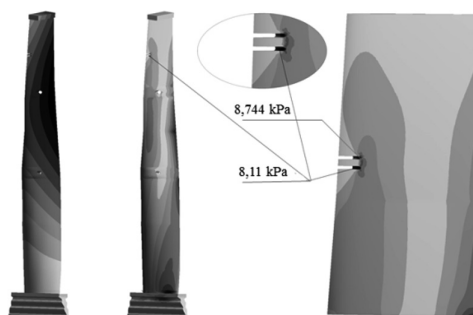


**Fig. 5.** Distribution of displacement and vibration stress when exposed harmonic component frequency of 2100 Hz

The comparison of the study's results of vibrations of the blades with a different number of damages in the zone of maximum stresses under the action of harmonic component with a frequency of 2100 Hz and results for the blade without damage shows that the stress concentration coefficients are within the range 1.2–3.1. This makes it possible to estimate the reduction in fatigue of the blade and the decrease the residual life.

Based on literature data and calculation results, the fatigue limit can be reduced to 330 MPa. But the residual life remains more than  $N = 10^7$  cycles [5, 6].

There is a lot of experience in analyzing the effect of damage on the compressor blades of aircraft gas turbine engines. Compressor blades are subject to dust erosion, water droplets, pieces of ice and other foreign objects. At the same time there are dents and other damages with a size of 350–800  $\mu\text{m}$ , with a radius at the mouth of damages 0.02–0.07 mm. These types of damage were investigated similarly [6]. They show the decrease in the fatigue limit of the blades and a residual resource of more than  $N = 10^7$  cycles. The operating experience of compressor blades shows that the significant increase the fatigue limit of the blades and a residual life can be achieved by mechanical surface treatment. This experience also can be used for titanium steam turbine blades with erosion damage.

### 3 The Effect of Machining on the Fatigue Limit and the Resource of Blades with Damage

Effective types of machining are the smoothing of the damage zone by turning and milling. Even more effective is further grinding and polishing. Such an increase of the fatigue limit is observed even for titanium alloys that have a relatively low degree of fatigue [6].

The TS5 titanium alloy (Ti-5Al-1.5 V) has good technological properties, rather high corrosion and erosion resistance. Therefore, it was chosen for the blades of the last turbine stages for nuclear power plants operating in a wet steam environment. The samples of material near the zone of damage to the blade after of 180 thousand hours operation were taken. On these samples, static and fatigue tests were performed using the MTS 810 machine at loading amplitudes of 350 MPa [5]. The results of these tests are presented in Table 1.

**Table 1.** Mechanical properties of the blade material (alloy TS5) near the damage zone

Number of samples	The yield stress $\sigma_{0.2}$ , MPa	Ultimate strength $\sigma_v$ , MPa	Fatigue limit $\sigma_{-1}$ , MPa	Residual life
1–3	832–838	911–920		
4–6			350–450	$N > 10^7$

Based on the results of the fatigue tests, it was found that for the given loading amplitudes, after reaching  $10^7$  cycles the destruction of samples № 4–6 was not observed, it means that the fatigue limit  $\sigma_{-1} > 350$  MPa.

Therefore, even after the operation for the 180,000 h, the blades have a residual fatigue life of  $N = 10^7$  cycles, that was also found as a result of numerical calculations. Thus, different approaches to estimating the reduction between the fatigue of the blade material after the damage and residual life give the same results.

The displacements and stresses distributions on the blade with machining are shown in Fig. 6. It is evident a decrease stresses concentration after the machining.

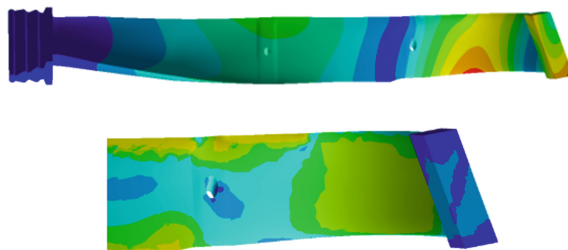


**Fig. 6.** Distribution of displacements (up) and fragment of vibration stresses (down) of a blade with machining

## 4 Conclusions

One can recommend such measures to prevent dangerous vibration stresses in the blades of the last stage of the turbine K-1000-60/3000 [5]:

- periodic testing of vibration frequencies of blades and impellers, if the frequencies deviate from the reference frequencies by 8–10%, stop and repair is necessary;
- checking the quality and possible damages of the damping wire ties in the wheel;
- if the turbines stop for a preventive inspection and repair then it is recommended for the damages that are more than 500  $\mu\text{m}$  in depth, smooth the damage zone by milling, grinding and subsequent polishing;
- if possible, apply a protective coating on the surface that has undergone a mechanical treatment;
- if possible, replacement of the impeller blade set with damage is recommended.

## References

1. Shubenko, A.L.: Effect of erosion on the main operational characteristics of the working blade of the last stage of a low-pressure cylinder of a powerful steam turbine. *J. Mech. Eng.* **13**(1), 3–10 (2010)
2. Zinkovskiy, A.P.: Effect of energy dissipation in a material on oscillations of blades with inhomogeneities. *Aerosp. Tech. Technol.* **9**(96), 132–137 (2012)
3. Borovkov, V.M., Getsov, L.B., Vorobyev, Yu.S.: *Materials and Strength of TPP Equipment*. Politekh, St. Petersburg, Russia (2008)

4. Vorobiov, Yu.S.: Problems of the use of new materials for turbine blade systems. In: Bulletin of the NTU 'KhPI'. Series: Power and Heat Engineering Processes and Equipment, vol. 9 (1181), pp. 44–49 (2016)
5. Vorobiov, Yu.S.: Vibration features of titanium alloy blades with erosive damages. J. Mech. Eng. **21**(4), 13–21 (2018)
6. Petukhov, A.N.: Fatigue Resistance to GTE Components. Mashinostroyeniye, Moscow, Russia (1993)



# Influence of Residual Stresses in the Cladding Zones of RPV WWER-1000 on Integrity Assessment

Oleh Makhnenko and Elena Kostenevich<sup>(✉)</sup>

The E. O. Paton Electric Welding Institute, 11 Kazimir Malevich Str.,  
Kiev 03680, Ukraine

makhnenko@paton.kiev.ua, alenakostenevich@gmail.com

**Abstract.** One of the current problems of the structural integrity assessment of the reactor pressure vessel WWER-1000 is the determination of resistance to brittle fracture taking into account the residual stresses after cladding of the protective anticorrosion layer and heat treatment. Existing data on the residual stresses do not take into account possible microstructural transformations in the base material steel 2.5Cr-Mo-V (15H2NMFA). Mathematical modeling of residual stresses taking into account microstructural phase transformations determines a compression stress area in the heat affected zone of the base material as result of martensite formation. These results were confirmed by dilatometric analysis and metallography of the steel 15H2NMFA templates. The evaluation of resistance to brittle fracture under the thermal shock load showed, that calculated compression residual stresses in the base material HAZ reduce value SIF for cracks of a depth up to 7 mm.

**Keywords:** RPV · Nozzle zone · Cladding · Thermal shock · Brittle fracture · SIF

The reactor pressure vessel (RPV) WWER-1000 is a welded shell structure from the perlitic 2.5Cr-Mo-V steel (15H2NMFA) with anticorrosion cladding on the inner surface. Residual stresses (RS) caused by welding and cladding can significantly influence on the assessment of the brittle fracture of the RPV structures.

Currently for the evaluation of the brittle fracture resistance of the RPV are used the distributions of the residual stresses, which are presented in various standard documents and guidelines, such as VERLIFE [1], MRK-SHR-2000 [2], and others [3]. These RS distributions are quite different relative to the size of the tensile stresses zone in the base material.

There are the experimental and calculation data on the distribution of RS in the structural elements after cladding for another reactor steel—SA533 [4] and SA508 [5] similar by chemical content. They have shown, that microstructural phase transformations during cladding, namely the formation of bainite and martensite at the cooling, cause the producing of compressive stresses in the heat affected zone (HAZ) with the subsequent transition to the tensile stresses zone.

## 1 Objectives of Research

Existing data of the distribution of RS in the cladding zones RPV WWER-1000 do not take into account possible microstructural transformations in the HAZ of the base material during the anticorrosion layer cladding. This question is required the additional study.

## 2 Determination of Microstructural Phase Composition

The results on evaluation of brittle fracture of the cladding zones RPV were obtained in the different parts of the model of the RPV nozzle zone: cylindrical part of the RPV and nozzle Dy850 part. The RPV nozzle zone (Fig. 1a) is not located near the active zone RPV and not exposed to intensive radiation embrittlement, but it is dangerous area in resistance to brittle fracture during emergency situation “pressurized thermal shock” (PTS) [6], because through nozzles into RPV fed cold boric water.

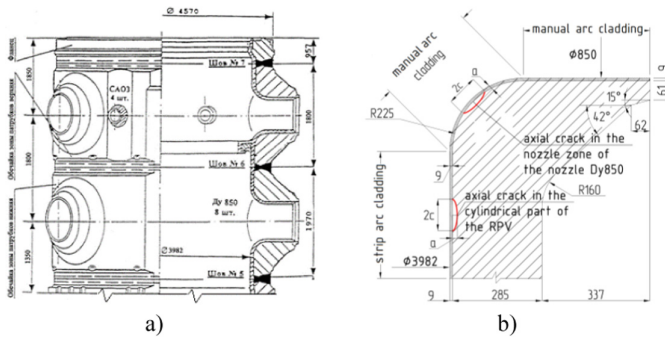


**Fig. 1.** The nozzle zone of the RPV WWER-1000 (a) and scheme of the nozzle Dy850 (b)

The inner surface is cladded by anticorrosion material of a total thickness 9 mm. The arc cladding of the cylindrical part of the RPV shell is carried out under a flux with strip electrode in two layers with preheating up to 250 °C in the following conditions:  $I = 600\text{--}650$  A,  $U = 32\text{--}36$  V, cladding speed  $v = 2$  mm/s [7]. The inner surface of the nozzles Dy850, including rounded corner, is cladded by manual arc cladding with coated electrodes under the conditions:  $I = 130\text{--}150$  A,  $U = 26\text{--}30$  V,  $\varnothing$  electrodes 4–5 mm,  $v = 0.83$  mm/s (Fig. 1b). The base material of the RPV is low-alloy steel of high strength 2.5Cr-Mo-V steel (15H2NMFA), cladding austenitic materials: the first layer—25Cr-13Ni (SV-07H25N13), the second layer—20Cr-10Ni (SV 04H20N10G2B).

Literature review has shown the existence of rather different data on the phase composition of the RPV base material: perlite, bainite, bainite-martensite. Also there is no complete diagram of the anisotropic austenite decomposition (CCT diagram) with data relative to the maximum content of the phase components for the cooling rates

during welding or cladding. According to existing metallurgical diagrams it is impossible to determine the microstructure phase composition during cladding.

For the calculation of the maximum content of the phase components and kinetic of microstructural phase transformations, a model based on the Avrami equation [8] (austenite decomposition into ferrite, perlite and bainite) was used:

$$V_j = 1 - \exp(-bt^n) \tag{1}$$

$V_j$ —current mass fraction,  $t$ —isothermal transformation time,  $b$ ,  $n$ —coefficients determined on the basis of parameters of the TTT-diagrams (diagrams of isothermal decomposition of austenite).

The simulation of microstructural transformations in conditions of continuous cooling and the calculation of the maximum mass fraction of bainite and ferrite-perlite is carried out on the basis of the additivity rule for isothermal transformations. The kinetic of martensitic transformation is described by the Koistinen-Marburger equation [9]:

$$V_j = 1 - \exp(-b(M_s - T)^n) \tag{2}$$

where  $M_s$ —temperature of the martensite start;  $b = 0.011$ ;  $n = 1$ .

As a result of the simulation of the microstructural phase state (Fig. 2) we obtain in the HAZ of the base material approximately the content of martensite 55% and bainite 45% for the strip cladding. Ferrite-perlite is not formed. For manual cladding of the inner surface of the nozzle Dy850 the predominant content of martensite is up to 80%.

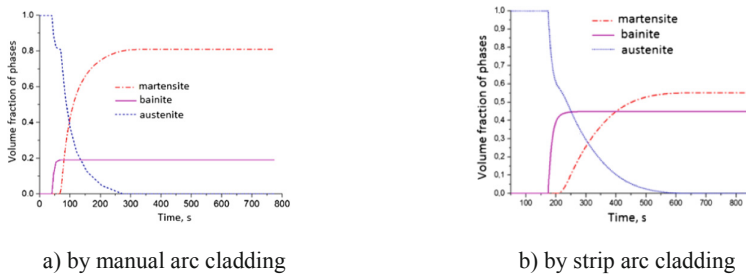


**Fig. 2.** Prediction of kinetic of the microstructural transformations during cooling in the HAZ

To validate the calculation data the dilatometric analysis of the austenite decomposition for real cladding thermocycle and metallography with templates from 2.5Cr-Mo-V steel (15H2NMFA) were done.

The common CCT diagrams are built for linear cooling rates. For real welding (cladding) process the cooling speed is not linear. Dilatothermy and metallography study for the real thermal cycle of welding by heating up to 1000 °C with characteristic curve of cooling at average speed of 5 °C/s in a temperature range of 500–800 °C and for thermal cycle with a cooling at a constant speed were conducted Fig. 3.

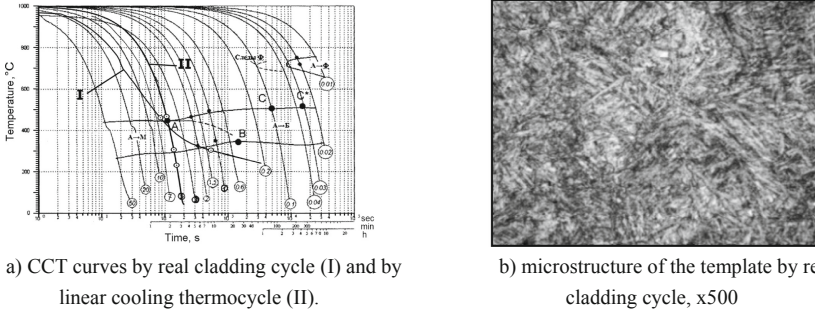


**Fig. 3.** The CCT diagram (a) and martensitic-bainite microstructure of the template (b)

According to the results of metallography, the structure of the template obtained for constant cooling rate of 5 °C/s is a martensite, of another template—for the real cladding cycle is heterogeneous and consists of 80–90% martensite and 10–20% of lower bainite.

### 3 Determination of RS Taking into Account Microstructural Phase Transformations

To simulate the stress-strain state of a material, a model of thermoviscoplasticity was used [10]. The general deformation tensor  $\epsilon_{ij}$  in welding processes can be represented as a sum of tensors: elastic  $\epsilon_{ij}^e$ , plastic  $\epsilon_{ij}^p$ , and creep deformations  $\epsilon_{ij}^c$ .

$$\epsilon_{ij} = \epsilon_{ij}^e + \epsilon_{ij}^p + \epsilon_{ij}^c \tag{3}$$

In accordance with Hooke’s law and with the von Mises yield criterion, the relationship between stresses and deformations has the form:

$$\epsilon_{ij} = \left[ \frac{\sigma_{ij} - \delta_{ij}\sigma}{2G} + \delta_{ij}(K\sigma + \varphi) \right] + \lambda(\sigma_{ij} - \delta_{ij}\sigma) + \Omega(\sigma_{ij} - \delta_{ij}\sigma) \tag{4}$$

where  $\sigma = \frac{1}{3}(\sigma_{rr} + \sigma_{\beta\beta} + \sigma_{zz})$ ;  $\sigma_{ij}$ —the stress tensor;  $\delta_{ij}$ —unit tensor;  $\lambda$ —scalar function, which depends on the stresses and properties of the material;  $\Omega$ —the creep function at temperature T; K—bulk modulus; G—shear modulus;  $\nu$ —Poisson’s ratio;  $\varphi$ —volume effects caused by the change of temperature and microstructural transformations.

By microstructural phase transformation at any point  $r, \beta, z$  at time  $t$ , the total effect of volume changes of the temperature  $T_0$  to  $T(t)$  is determined as by [10]:

$$3\varphi = \frac{\sum V_j(T, t)\gamma_j(T) - \sum V_j(T_0)\gamma_j(T_0)}{\sum V_j(T_0)\gamma_j(T_0)} \tag{5}$$



where  $V_j(T)$ —the mass fraction of the  $j$ -th phase at temperature  $T$ ;  $\gamma_j(T)$ —the volume of a unit mass of the  $j$ -th phase at temperature  $T$ . Values  $\gamma_j(T)$  for the construction steels are presented according to [10].

For both technologies of cladding the simulation of microstructural transformations leads to nonuniformity in the distribution of RS in thickness and along the surface of the cladding and the appearance of the compressive stresses zone in the HAZ. The compression reaches 400 MPa, the tensile RS are up to 750 MPa.

For mathematical modeling of the heat treatment process, the creep function of the material was used, which was determined in [11] on the base of existing experimental data for 2.5Cr-Mo-V steel (15H2NMFA) [12]. The relationship between stresses intensity  $\sigma_i$  and creep strain rate has the form:

$$d\epsilon^c = A \cdot \sigma_i^n \cdot dt \tag{6}$$

at temperature 650 °C,  $d\epsilon^c = 0.17 \times 10^{-20} \cdot \sigma_i^6 \text{ s}^{-1}$ —for base material,  $d\epsilon^c = 1.85 \times 10^{-18} \cdot \sigma_i^{4.82} \text{ s}^{-1}$ —for cladding material.

Figure 4 shows the distribution of the hoop component of the RS through the nozzle thickness after heat treatment (high tempering at 650 °C and duration 20 h). In the HAZ of the base material till the depth 7 mm the compression RS (up to -350 MPa) were defined. For both cladding technologies, the magnitude of the tension RS in the base material, taking into account microstructural transformations, is up to 150 MPa.

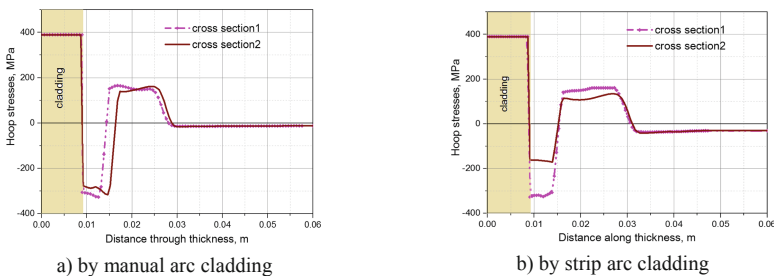


Fig. 4. Distribution of hoop RS  $\sigma_{\theta\theta}$  after heat treatment through thickness

#### 4 Assessment of Brittle Fracture on the Results of RS Modeling

The assessment of brittle strength in the cladding zones was carried out using the method of weight functions. For cylindrical part RPV it was carried out using analytical recommendations of VERLIFE for cracks of the axial and circumferential orientation, for the nozzle zone Dy850—only for axial cracks. The allowable values of SIF may be obtained from the following dependence:  $K_{Ic} = \min[26 + 36 \exp(0.02 \cdot (T - T_k)), 200]$ , where  $T_k$  is the critical temperature of brittleness. The value of the stress intensity

factors (SIF) for crack at the deepest point was determined for depth  $a = 7$  mm. The calculation model was loaded according to the PTS parameters [6]. Brittle strength was evaluated at various stress-deformed states—without taking into account the RS, with RS according to the VERLIFE [1], with the predicted RS taking into account microstructural phase transformation.

SIF determined with RS according to the VERLIFE for the sub-clad crack by  $a = 7$  mm, located in the nozzle zone Dy850 (Fig. 5a) and in the cylindrical part RPV (Fig. 5b), are highest. Values of the SIF obtained at the calculated stresses taking into account microstructural transformations are very low, because these cracks are located in the zone of calculated compression RS. The value of SIF without RS is smaller in two to three times than SIF with the RS taken into account.

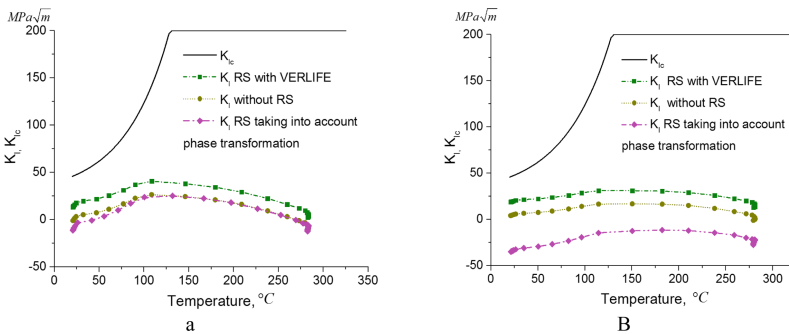


**Fig. 5.** SIF by PTS at the top of the axial sub-clad crack ( $a = 7$  mm;  $a/c = 0.3$ ), located **a** in the nozzle zone Dy850, **b** in the cylindrical part RPV

### 5 Conclusion

Consideration of residual stresses after arc cladding of a protective anticorrosion layer and heat treatment of the RPV WWER-1000 in the structural integrity assessment is mandatory.

For the base material of RPV WWER-1000 2.5Cr-Mo-V steel (15H2NMFA) the CCT-curve for characteristic thermocycle at cladding of the nozzle zone was obtained. These experimental data correlate with the calculated data, obtained on the base of the Avrami equation, because the martensitic content in the microstructure of the reactor steel after the cladding has been defined.

The calculated RS obtained taking into account the microstructural phase transformations showed, that due to the formation of the bainite-martensitic microstructure in the HAZ of the base material a stress compression zone (−100 to −300 MPa) appears with depth up to 7 mm. This factor makes it possible to reduce the conservatism of the brittle fracture estimates for sub-clad cracks up to 7 mm deep.

## References

1. VERLIFE: Guidelines for Integrity and Lifetime Assessment of Components and Piping in WWER NPPs During Operation "VERLIFE". IAEA, Vienna (2013)
2. Procedure for Lifetime Assessment of RPV in WWER During Operation MPK-CXP-2000. St. Petersburg, Moscow, 52 p (2000) (in Russian)
3. Kostylev, V.I., Margolin, B.Z.: Determination of residual stress and strain fields caused by cladding and tempering of reactor pressure vessels. *Int. J. Press. Ves. Piping* **77** (2000)
4. Katsuyama, J., Udagawa, M., Nishikawa, H., Nakamura, M., Onizawa, K.: Evaluation of weld residual stress near the cladding and J-weld in reactor pressure vessel head for the assessment of PWSCC behavior. In: *E-Journal of Advanced Maintenance*, vol. 2, pp. 50–64. Japan Society of Maintenology (2010)
5. Dupas, P., Moinereau, D.: Evaluation of cladding residual stresses in clad blocks by measurements and numerical simulations. *J. Phys. IV Colloque* **06(C1)**, C1-187–C1-196 (1996)
6. Guidance on the Reactor Pressure Vessel PTS Assessment for WWER Nuclear Power Plants. International Atomic Energy Agency, WWER-SC-157 (1996)
7. PNAE G-7-009-89 Equipment and Piping of Nuclear Power Installations. Welding and Overlaying Welding. Basic Provisions. Moscow (2003) (in Russian)
8. Avrami, M.: Kinetics of phase change. *J. Chem. Phys.* **7(12)**:1103–1112 (1939); **8(2)**:212–224 (1940); **9(2)**:177–184 (1941)
9. Koistinen, D.P., Marburger, R.E.: A general equation prescribing the extent of the austenite-martensite transformation in pure iron-carbon alloys and plain carbon steels. *Acta Metall.* **7**, 59–60 (1959)
10. Makhnenko, V.I., Velikoivanenko, E.A., Pochinok, V.E., Makhnenko, O.V., Rozyinka, G. Ph., Pivtorak, N.I.: Numerical methods for the prediction of welding stress and distortions. *Weld. Surf. Rev.* **13(Part 1)**, 146 p (1999)
11. Makhnenko, V.I.: Resource of Safety Service of Welded Joints and Assemblies of Current Structures, 618 p. Naukova Dumka, Kiev (2006) (in Russian)
12. Margolin, B.Z., Varovin, A.Ja., Kostylev, V.I.: Determination of residual stresses in reactors VVER after multipass welding, welding and high temperature tempering. *Autom. Weld. J.* (10) (2005) (in Russian)

**Part VI**  
**Symposium on: “Dynamic Problems  
in Mechanics of Coupled Fields,”**  
**by Roman Kushnir**



# Damping of Hydroelastic Vibrations of the Plate Using Shunted Piezoelectric Element. Part I: Numerical Model

Sergey Lekomtsev<sup>(✉)</sup> , Dmitrii Oshmarin ,  
and Natalya Sevodina 

Institute of Continuous Media Mechanics of the Ural Branch, Russian Academy of Science, Acad. Korolev Str. 1, Perm 614013, Russian Federation  
lekomtsev@icmm.ru

**Abstract.** In this work, we investigate the possibility of using a piezoelectric element connected to an external electric RL-circuit for passive vibrations damping of a cantilevered plate interacting with a quiescent fluid. The behavior of piezoelectric elements is described by the equations of electrostatics of deformable electroelastic media within the framework of quasi-static approximation. The motion of an ideal fluid in the case of small perturbations is considered in the framework of acoustic approximation. Small strains in a thin plate are determined using the Reissner–Mindlin theory. A mathematical formulation of the problem of electroelasticity elastic body with external electric circuits is based on the Lagrange variational principle, which includes the expression for hydrodynamic pressure. The acoustics equations together with the boundary conditions and the impermeability condition are converted to a weak form using the Bubnov–Galerkin method. The numerical implementation of the problem is carried out using an original approach, which is based on the ANSYS finite element package integrated with the program that implements the algorithm for solving the non-classical eigenvalue problem by the Muller method. This allows us to evaluate the values of the parameters of the external RL-circuit, which could provide the most effective damping of vibrations at a certain frequency.

**Keywords:** Fluid-structure interaction · Vibration damping · Finite element method

## 1 Introduction

Piezoelectric elements embedded or attached to the surface of various structures can be used as an effective tool for control of the dynamic behavior of the resulting systems. In the case of passive vibration damping, the surfaces of piezoelectric element covered with electrodes are shunted to the external electric circuit. Changing the values of the parameters of circuit components (resistance, inductance, capacitance), one can provide maximum damping of vibrations at a certain frequency.

A mathematical formulation of the problem presented below develops the idea and the method of solution, which are described in detail in [1], and is considered to be their generalization to structures interacting with a quiescent fluid. The parameters of the

resistance and inductance elements of the RL-circuit providing maximum vibration damping are selected based on the results of solving the problem of natural and harmonic hydroelastic vibrations of piecewise-homogeneous electroelastic bodies with external passive electric circuits.

## 2 Mathematical Model

### 2.1 Plate with Electroelastic Body

The variational equation of motion of the body of volume  $V = V^p + V^s$ , consisting of an elastic plate of volume  $V^s$  and an attached piezoelectric element of volume  $V^p$ , connected to an external electric circuit, is formulated on the basis of the relations of Reissner–Mindlin theory, linear theory of elasticity and quasi-static Maxwell equations [1–4]. Both, the supply and release of energy from the deformed piezoelectric element are realized through the electroded coatings applied to some parts of the body surface. Having negligible mass, they are assumed to be ideal conductors. Because of the electrode-covered surfaces, the system under consideration can be connected to the external electric circuits of arbitrary configuration, including resistive elements ( $R$ ), capacitive elements ( $C$ ) or inductive elements ( $L$ ). If these circuits are not connected to an external voltage source, they are classified as internal elements of the system (a structure with piezoelectric element and shunting circuit). The final resolving equation in the matrix form can be written as:

$$\begin{aligned} & \int_{V^p} (\delta \boldsymbol{\varepsilon}^p)^T \boldsymbol{\sigma}^p dV - \int_{V^p} (\delta \mathbf{E})^T \mathbf{d} dV + \int_{V^p} (\delta \mathbf{u}^p)^T \rho^p \mathbf{u}^p dV - \int_{V^p} \delta \mathbf{u}^p \mathbf{f}^p dV - \int_{S^p} q_e \delta \varphi dS \\ & + \int_{S^s} (\delta \boldsymbol{\varepsilon}^s)^T \mathbf{T}^s dS + \int_{V^s} (\delta \mathbf{u}^s)^T \rho^s \mathbf{u}^s dV - \int_{V^s} \delta \mathbf{u}^s \mathbf{f}^s dV - \int_{S_e^s} (\delta \mathbf{u}^s)^T \mathbf{t}^s dS \\ & + \sum_{k=1}^{n_L} \frac{1}{L_k} \iint (\varphi_1^{L_k} - \varphi_2^{L_k}) \delta \varphi dt dt + \sum_{q=1}^{n_R} \frac{1}{R_q} \int (\varphi_1^{R_q} - \varphi_2^{R_q}) \delta \varphi dt + \sum_{r=1}^{n_C} C_r (\varphi_1^{C_r} - \varphi_2^{C_r}) \delta \varphi = 0, \end{aligned} \tag{1}$$

where the generalized vector of forces and moments for the plate  $\mathbf{T}^s$  is defined by

$$\mathbf{T}^s = \{N_{xx}, N_{yy}, N_{xy}, M_{xx}, M_{yy}, M_{xy}, Q_x, Q_y\}^T = \mathbf{D}^s \boldsymbol{\varepsilon}^s,$$

and for the isothermal processes, the following physical relations are valid for piezoelectric element

$$\begin{aligned} \boldsymbol{\sigma}^p &= \left\{ \sigma_{xx}^p, \sigma_{yy}^p, \sigma_{zz}^p, \tau_{xy}^p, \tau_{yz}^p, \tau_{zx}^p \right\}^T = \mathbf{D}^p \boldsymbol{\varepsilon}^p - \boldsymbol{\beta} \mathbf{E}, \\ \mathbf{d} &= \{D_x, D_y, D_z\}^T = \boldsymbol{\beta}^T \boldsymbol{\varepsilon}^p + \mathbf{e} \mathbf{E}. \end{aligned}$$

Here, the superscripts “ $p$ ” and “ $s$ ” refer the corresponding variables to the piezoelectric element and the plate. The following notations are accepted:  $\delta$  is the variation

of the corresponding variable; column vectors  $\boldsymbol{\varepsilon}$  contain the components of strain tensors and are defined according to the well-known relations [2, 3];  $\mathbf{D}$  are the elastic constant matrices;  $\boldsymbol{\beta}$ ,  $\mathbf{e}$  are the matrices of piezoelectric and dielectric coefficients;  $\mathbf{f}$ ,  $\mathbf{t}$  are the vectors of the body and surface forces;  $\rho$  is the material density;  $\mathbf{u}^p$  is the piezoelectric element's displacements vector;  $\mathbf{u}^s$  is the generalized displacement vector for the plate which includes rotation angles;  $\mathbf{d}$ ,  $\mathbf{E}$  are the electric flux density and electric field intensity vectors; the potentiality condition is fulfilled for an electric field  $-\mathbf{E} = \{\varphi_{,x}, \varphi_{,y}, \varphi_{,z}\}$ , here  $\varphi$  is electric potential;  $\varphi_1^{el} - \varphi_2^{el}$  is the potential difference for the corresponding element of electric circuit ( $el = L_k, R_q, C_r$ );  $n_L, n_R, n_C$  are the numbers of inductive, resistive and capacitive elements;  $L_k, R_q, C_r$  are the values of inductance, resistance and capacitance for the corresponding element of electric circuit;  $q_e$  is the free charges surface density;  $S_\sigma^s$  is the part of the plate surface subjected to loads  $\mathbf{t}^s$ ;  $S^p = S_{el}^p + S_0^p$  is the surface of piezoelectric body, where  $S_{el}^p$  and  $S_0^p$  are the parts of the surface covered with electrodes and free of electrodes, respectively.

On the electrode-free parts of the surface of piezoelectric body  $S_0^p$  there are no free electric charges. Based on the form of the Maxwell equations used in this study, an electric boundary condition for  $S_0^p$  can be written as

$$\int_{S_0^p} \mathbf{n}^T \mathbf{d} dS = 0, \quad (2)$$

where  $\mathbf{n}$  is the outward normal vector to the surface.

Supposing that one of the electrode-covered surfaces of the piezoelectric element is grounded, i.e. has a zero-value electric potential, the electric boundary condition for this part of the surface can be written in the following form

$$\varphi = 0, \mathbf{x} \in S_{el}^p. \quad (3)$$

When an external voltage supply is absent, the other parts of the electrode surface are considered free. In this case, the open circuit mode is realized. On the other hand, it can be treated as having zero-value electric potential (3), in which case the short circuit mode is realized.

## 2.2 Fluid-Structure Interaction

The motion of an ideal compressible fluid in region  $V^f$  in the case of small perturbations is described by the well-known Euler equations, continuity equation and state equation [5]. The elimination of velocity  $\mathbf{v}$  from these equations gives the Helmholtz equation governing the hydrodynamic pressure  $p$

$$\nabla^2 p = \ddot{p}/c^2, \quad (4)$$

where  $c$  is the speed of sound in the medium.

On the boundary  $S_\sigma^s$  coupling between the motion of fluid and structure occurs, which can be described as

$$(\mathbf{n}^f)^T \dot{\mathbf{v}} = \ddot{w}, \quad \text{and} \quad \frac{\partial p}{\partial n} = -\rho^f (\mathbf{n}^f)^T \dot{\mathbf{v}}, \tag{5}$$

where  $\mathbf{n}^f$  is the vector of outward normal to the fluid region,  $w$  is the normal displacement of the plate.

In the simplest case the boundary condition on the free surface of the fluid  $S_{free}$  is written as  $p = 0$ . At the interface between the fluid and rigid wall  $S_w$ , the condition  $(\mathbf{n}^f)^T \dot{\mathbf{v}} = 0$  is prescribed.

A weak form of Eq. (4) after integration by parts and substitution of the boundary conditions described above leads to [5]

$$\int_{V^f} \delta p \left( \frac{1}{c^2} \ddot{p} + \nabla^2 p \right) dV + \int_{S_\sigma} \delta p \dot{w} dS = 0. \tag{6}$$

The traction integral in Eq. (1) can be expressed as

$$\int_{S_\sigma} (\delta \mathbf{u}^s)^T \mathbf{t}^s dS = \int_{S_\sigma} (\delta \mathbf{u}^s)^T \mathbf{n}^f p dS \tag{7}$$

because positive pressure is defined in compression and  $\mathbf{n}^s = -\mathbf{n}^f$ . Thus, we can finally write that  $\mathbf{t}^s = -p\mathbf{n}^s = p\mathbf{n}^f$ .

### 2.3 Harmonic and Natural Vibrations

Let us consider a perturbed motion of the fluid and the plate with the attached piezoelectric element defined as  $\mathbf{U}(\mathbf{x}, t) = \{\mathbf{u}^p(\mathbf{x}, t), \varphi(\mathbf{x}, t), \mathbf{u}^s(\mathbf{x}, t), \mathbf{p}(\mathbf{x}, t)\} = \tilde{\mathbf{U}}(\mathbf{x}) \exp(i\lambda t)$ , where  $\tilde{\mathbf{U}}(\mathbf{x})$  is the function of coordinates and  $\lambda = \omega + i\gamma$  is the characteristic parameter. Here,  $\omega$  corresponds to the circular natural frequency of vibrations and  $\gamma$  is the rate of its damping. Taking into account the above mentioned form of solution, the Eqs. (1) and (6) can be written as

$$\begin{aligned} & \int_{V^p} (\delta \varepsilon^p)^T \boldsymbol{\sigma}^p dV - \int_{V^p} (\delta \mathbf{E})^T \mathbf{d} dV - \lambda^2 \int_{V^p} (\delta \mathbf{u}^p)^T \rho^p \mathbf{u}^p dV - \int_{V^p} \delta \mathbf{u}^p \mathbf{f}^p dV - \int_{S^p} q_e \delta \varphi dS \\ & + \int_{S^s} (\delta \varepsilon^s)^T \mathbf{T}^s dS - \lambda^2 \int_{V^s} (\delta \mathbf{u}^s)^T \rho^s \mathbf{u}^s dV - \int_{V^s} \delta \mathbf{u}^s \mathbf{f}^s dV - \int_{S_\sigma} (\delta \mathbf{u}^s)^T \mathbf{n}^f p dS \\ & - \sum_{k=1}^{n_L} \frac{1}{\lambda^2 L_k} (\varphi_1^{L_k} - \varphi_2^{L_k}) \delta \varphi + \sum_{q=1}^{n_R} \frac{1}{i\lambda R_q} (\varphi_1^{R_q} - \varphi_2^{R_q}) \delta \varphi + \sum_{r=1}^{n_C} C_r (\varphi_1^{C_r} - \varphi_2^{C_r}) \delta \varphi = 0, \tag{8} \end{aligned}$$

$$\int_{V^f} \delta p \left( -\frac{\lambda^2}{c^2} p + \nabla^2 p \right) dV - \lambda^2 \int_{S_\sigma} \delta p w dS = 0$$



For the problem of natural vibrations under zero-value boundary conditions in the absence of body forces instead of (8) we have

$$\begin{aligned}
 & \int_{V^p} (\delta \boldsymbol{\varepsilon}^p)^T \boldsymbol{\sigma}^p dV - \int_{V^p} (\delta \mathbf{E})^T \mathbf{d} dV - \lambda^2 \int_{V^p} (\delta \mathbf{u}^p)^T \boldsymbol{\rho}^p \mathbf{u}^p dV \\
 & + \int_{S^s} (\delta \boldsymbol{\varepsilon}^s)^T \mathbf{T}^s dS - \lambda^2 \int_{V^s} (\delta \mathbf{u}^s)^T \boldsymbol{\rho}^s \mathbf{u}^s dV - \int_{S_o^s} (\delta \mathbf{u}^s)^T \mathbf{n}^f p dS \\
 & - \sum_{k=1}^{n_L} \frac{1}{\lambda^2 L_k} (\varphi_1^{L_k} - \varphi_2^{L_k}) \delta \varphi + \sum_{q=1}^{n_R} \frac{1}{i \lambda R_q} (\varphi_1^{R_q} - \varphi_2^{R_q}) \delta \varphi + \sum_{r=1}^{n_C} C_r (\varphi_1^{C_r} - \varphi_2^{C_r}) \delta \varphi = 0.
 \end{aligned} \tag{9}$$

### 3 Numerical Formulation

A solution to the problem is found with the use of the finite element method (FEM). Implementation of the FEM standard procedures [1, 5, 6] leads to the matrix equations

$$(-\lambda^2 \mathbf{M} + \mathbf{K} + \mathbf{C}(\lambda)) \tilde{\mathbf{U}} = \mathbf{F} \tag{10}$$

and

$$(-\lambda^2 \mathbf{M} + \mathbf{K} + \mathbf{C}(\lambda)) \tilde{\mathbf{U}} = 0, \tag{11}$$

where

$$\mathbf{M} = \begin{bmatrix} \mathbf{M}^p & \mathbf{0} & \mathbf{0} & \mathbf{0} \\ \mathbf{0} & \mathbf{0} & \mathbf{0} & \mathbf{0} \\ \mathbf{0} & \mathbf{0} & \mathbf{M}^s & \mathbf{0} \\ \mathbf{0} & \mathbf{0} & \boldsymbol{\rho}^f \mathbf{Q}^T & \mathbf{M}^f \end{bmatrix}, \quad \mathbf{K} = \begin{bmatrix} \mathbf{K}^p & \mathbf{K}^{p\varphi} & \mathbf{0} & \mathbf{0} \\ (\mathbf{K}^{p\varphi})^T & \mathbf{K}^\varphi & \mathbf{0} & \mathbf{0} \\ \mathbf{0} & \mathbf{0} & \mathbf{K}^s & -\mathbf{Q} \\ \mathbf{0} & \mathbf{0} & \mathbf{0} & \mathbf{K}^f \end{bmatrix}, \quad \mathbf{C}(\lambda) = \begin{bmatrix} \mathbf{0} & \mathbf{0} & \mathbf{0} & \mathbf{0} \\ \mathbf{0} & \mathbf{C}^\varphi(\lambda) & \mathbf{0} & \mathbf{0} \\ \mathbf{0} & \mathbf{0} & \mathbf{0} & \mathbf{0} \\ \mathbf{0} & \mathbf{0} & \mathbf{0} & \mathbf{0} \end{bmatrix},$$

$$\mathbf{F} = \{\mathbf{F}^p, \mathbf{F}^\varphi, \mathbf{F}^s, \mathbf{0}\}^T, \quad \mathbf{C}^\varphi(\lambda) = - \sum_{k=1}^{n_L} \frac{1}{\lambda^2 L_k} \mathbf{K}_{L_k}^\varphi + \sum_{q=1}^{n_R} \frac{1}{i \lambda R_q} \mathbf{K}_{R_q}^\varphi + \sum_{r=1}^{n_C} C_r \mathbf{K}_{C_r}^\varphi.$$

Here, the matrices  $\mathbf{K}_{L_k}^\varphi$ ,  $\mathbf{K}_{R_q}^\varphi$ ,  $\mathbf{K}_{C_r}^\varphi$  contain the coefficients 1 and -1 only in positions that refer to the nodal variables of the corresponding elements. The remaining typical matrices of individual finite elements are determined in the known manner [5, 6]. Discretization of the fluid, piezoelectric element and plate computational domains is based on the spatial 20-node brick elements and the 8-node flat rectangular finite elements with a quadratic approximation of the unknown variables.

The problem of natural vibrations (11) leads to the equation, which differs from the standard description of the generalized eigenvalue problem due to the matrix  $\mathbf{C}(\lambda)$ . The solution was performed using the capabilities of the ANSYS software package for generating and assembling of finite element matrices and the program written in FORTRAN language for computation of complex eigenvalues by the Mueller method using the sparse matrix technology for basic operations.

## 4 Conclusion

A mathematical formulation of the natural vibration problem for a piecewise-homogeneous electroelastic body connected to a shunt external electric circuit and interacting with a quiescent fluid has been proposed. The results of solving this problem are the complex eigenvalues characterizing both the natural vibration frequencies and the rate of its damping. The relations for the numerical implementation of the problem on the basis of finite element method have been derived. This problem can serve as a useful tool for studying the dynamic behavior of electromechanical structures interacting with fluids. Since the results of the problem solution do not depend on the initial conditions and loading modes, it can also serve as a basis for constructing efficient algorithms for evaluation of optimal dissipative properties of structures or the development of new dynamic behavior control strategies.




The study was supported by the grant of the Russian Scientific Foundation (project No. 18-71-10054).

## References

1. Matveenko, V.P., Iurlova, N.A., Oshmarin, D.A., Sevodina, N.V., Iurlov, M.A.: An approach to determination of shunt circuits parameters for damping vibrations. *Int. J. Smart Nano Mater.* **9**(2), 135–149 (2018)
2. Reddy, J.N.: *An Introduction to Nonlinear Finite Element Analysis*, 2nd edn. Oxford University Press, Oxford (2015)
3. Washizu, K.: *Variational Methods in Elasticity and Plasticity*. Pergamon Press, London (1982)
4. Parton, V.Z., Kudryavtsev, B.A.: *Electromagnetoelasticity of Piezoelectric and Electroconductive Bodies*. Nauka, Moscow (1988)
5. Zienkiewicz, O.C., Taylor, R.L.: *The Finite Element Method*, vols. 1–2, 5th edn. Butterworth-Heinemann, Oxford (2000)
6. Allik, H., Hughes, J.R.: Finite element for piezoelectric vibration. *Int. J. Numer. Methods Eng.* **2**(2), 151–157 (1970)



# Damping of Hydroelastic Vibrations of the Plate Using Shunted Piezoelectric Element. Part II: Experiment

Maksim Iurlov<sup>(✉)</sup> , Alexander Kamenskikh, Sergey Lekomtsev ,  
and Dmitrii Oshmarin 

Institute of Continuous Media Mechanics of the Ural Branch, Russian Academy of Science, Acad. Korolev Str. 1, Perm 614013, Russian Federation  
yurlov@m@yandex.ru

**Abstract.** In this work, we explore the possibilities of passive damping the resonance vibrations of a cantilevered duralumin plate located on the free surface of a quiescent fluid. The harmonic excitation with a specified frequency is provided by the electromagnetic field, which is generated under a combined action of a light neodymium magnet attached to the structure and a superposed coil. Passage of the alternating current produced by the generator through the coil generates an electromagnetic force, which oscillates the plate. The oscillations are damped by a piezoelectric element connected to an external passive electric RL-circuit. Measurements of the plate vibrations are taken using a Polytec PDV-100 digital laser vibrometer with a sampling frequency of 48 kHz. The amplitude-frequency characteristics of the plate were obtained from the experimental studies. The values of inductance and resistance parameters of the external RL-circuit were selected in such a way as to ensure the most effective damping of the harmonic vibrations of the plate. It was shown that the peak value of the vibration velocity can be reduced by 20 times in air environment and by 2.5 times in the case of interaction with fluid.

**Keywords:** Fluid-structure interaction · Vibrations damping · Plate

## 1 Introduction

Nowadays, many advanced technological solutions in different branches of industry make wide use of thin plates. Dangerous vibrations of these structures are frequently caused by their interaction with a liquid. High requirements to the safety of facilities, in which these solutions are applied, suggest not only a preliminary assessment of the system behavior under normal and abnormal operating conditions but also the feasibility of controlling the dynamic processes occurring in them. Nowadays, piezoelectric elements attached or embedded in the structure are widely used for these purposes. A detailed overview of their application in submerged systems is presented in [1]. This review paper analyzes and systematizes various technical applications, summarizes the most significant results in such areas as: modal analysis, active sound and vibration control, energy harvesting and atomic force microscopes in submerged systems. Most

of the experimental studies listed in [1], devoted to the control of hydroelastic vibrations of plates, are based on the active method. In this case the dynamic characteristics are governed using the systems with active feedback. Such an approach is used for example in works [2, 3]. In the paper [2], the authors investigate the effect of the active vibration control on the reduction of the sound generated by a circular plate interacting with a fluid is examined. Paper [3] is concerned with the active vibration control of a vertical cantilever rectangular plate partially submerged into a fluid using two piezoelectric sensors and two actuators located on the plate. MIMO (Multiple-Input Multiple-Output) positive position feedback controller was designed and applied to estimate the control efficiency. It should be noted, that for known and time-constant frequency of external excitation, oscillations can be very effectively damped by a passive manner. In this work, we explore the possibilities of damping the resonance vibrations of a cantilevered duralumin plate interacting with a quiescent fluid through the use of a piezoelectric element connected to an external electric RL-circuit.

## 2 Experimental Setup

The experimental setup is a thick-walled prismatic tank, in which a thin plate of length  $a$ , width  $b$  and thickness  $h$  is used instead of the top cover (see Fig. 1). One of its edges was rigidly fixed by a clamping plate, which was bolted to the structure walls by screws with a force of 70 cN m. The vibrations of the plate were excited by an electromagnetic field. For this purpose, a light neodymium magnet with a mass of 0.10 g was glued to the plate. Vibrations were induced by a coil mounted on the U-shaped frame. An electric current of a given frequency or a rectangular pulse of duration of 0.5 ms passed to the coil through the amplifier from the Tektronix AFG3021C signal generator. Under the action of the resulting electromagnetic force on the magnet the plate was set in motion. The tank was installed on a metal base, the horizontal position of which was regulated by means of lifting legs and laser inclinometer. The tank was filled with a fluid until the latter reached the lower surface of the plate.

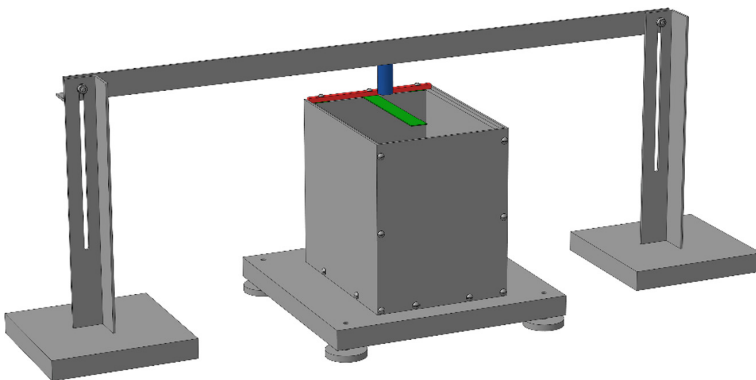


**Fig. 1.** Three-dimensional model of the experimental setup

The study of the natural frequencies and harmonic vibrations of the plate was performed using the method of laser vibrometry. The readings were taken with a Polytec PDV-100 digital vibrometer with a sampling frequency of 48 kHz and a resolution of 0.3  $\mu\text{m/s}$  in the velocity range of 500 mm/s. The device was positioned in such a manner that the angle between the laser ray and the surface of the plate was 45°. This made it possible to investigate not only bending vibrations, but also membrane vibrations. The natural vibration frequencies of the plate were determined from the Fourier transform of the signal received after the sample was subject to a short-term rectangular pulse of duration of 0.5 ms. For the excitation of harmonic vibrations, an alternating current of frequency equal to the eigenfrequency of the plate was passed to the coil from the generator through a power amplifier. During the experiment, the effective value of the alternating current was controlled by an ammeter and, if necessary, kept constant.

Plates in the form of a rectangle with  $a = 150$  mm,  $b = 10$  mm,  $h = 0.94$  mm were cut from the sheet of D16 AT duraluminium by electro-erosion to a tolerance of  $\pm 0.02$  mm. Thickness was defined as an average value obtained from ten measurements at various points. A piezoelectric element measuring  $30 \times 20 \times 0.36$  mm was made of PZT-19 piezo-ceramics and glued to the upper surface of the plate. The physical coil in the shunt circuit was replaced by a compact inductance equivalent circuit—a gyrator. Its main function is to make the input voltage and current of the circuit behave like the voltage and current in an inductor using for this purpose a capacitor and operational amplifiers.

Damping of the plate vibrations was carried out in several steps. First, the natural frequencies of the sample were determined in the open-circuit (OC) and short-circuit (SC) modes. Then, based on the results of numerical simulation by the finite element method or calculation by formulas [4], the parameters of inductance and resistance of the external RL-circuit were selected in such a way as to provide the most effective suppression of harmonic vibrations at a given frequency. At the final stage, amplified alternating current was passed to the coil to force harmonic vibrations of the plate, with the piezoelectric element being connected to an external open or closed electric RL-circuit. Measurements of the plate velocity were taken simultaneously at the control point. Processing of the recorded vibrogram data allowed us to build its envelope and the variation of the vibration frequency with time. In order to reduce the effect of noise in the experimental data, which can strongly distort the overall picture, the raw recorded signal was pre-filtered in the vicinity of the examined frequency using a Fourier filter.

### 3 Results

#### 3.1 Vibrations of the Plate in Air Environment

The effectiveness of suppressing structure vibrations in a passive manner strongly depends on the location of the piezoelectric element. In this study, it was determined from the condition of maximum of the electromechanical coupling coefficient, obtained for a particular vibration mode by solving a modal problem by the finite element

method. Location of the piezoelectric element near the fixed edge of the plate ensures its effective operation at the first two bending modes. In the experiments, in order to reduce the risk of damage, it was glued to the plate surface at a distance of 2 mm from the clamped edge.

The average values of the obtained natural frequencies of the plate in air environment and located on the layer of a fluid are shown in Table 1. The cells contain the values of the mean square deviation calculated from 10 measurements. Before each new measurement, the fluid was pumped out and the plate was demounted. The “Mode” column includes the classification of vibration modes (B—bending, T—torsional, M—membrane) and the number of node lines in the transverse and longitudinal directions. The data obtained from the formulas given in [4] were used to select the values of inductance and resistance parameters of an external RL-circuit connected to the piezoelectric element. These parameters can provide the most effective damping of harmonic oscillations at frequencies  $\omega_1$  ( $L = 597.90$  H,  $R = 28,776$   $\Omega$ ),  $\omega_2$  ( $L = 19.56$  H,  $R = 4658$   $\Omega$ ) and  $\omega_4$  ( $L = 2.89$  H,  $R = 1355$   $\Omega$ ). The torsional mode ( $\omega_3$ ) was not considered in this study, because the electromechanical coupling coefficient for this mode was very small (damping would not be effective).

**Table 1.** Natural frequencies of cantilever plate with piezoelectric element

No.	In air environment			On the fluid		
	Mode	SC	OC	Mode	SC	OC
$\omega_1$	B (0–0)	40.54 $\pm$ 0.14	40.72 $\pm$ 0.14	B (0–0)	21.07 $\pm$ 0.32	21.07 $\pm$ 0.32
$\omega_2$	B (1–0)	224.36 $\pm$ 1.11	225.16 $\pm$ 0.80	B (1–0)	119.64 $\pm$ 0.88	119.79 $\pm$ 1.03
$\omega_3$	T (0–1)	544.14 $\pm$ 0.67	543.75 $\pm$ 0.44	B (2–0)	325.94 $\pm$ 2.00	326.12 $\pm$ 2.07
$\omega_4$	B (2–0)	584.53 $\pm$ 2.57	585.72 $\pm$ 2.06	T (0–1)	368.85 $\pm$ 1.30	369.01 $\pm$ 1.19
$\omega_5$	M (0–0)	730.60 $\pm$ 1.83	731.15 $\pm$ 1.73	M (0–0)	658.57 $\pm$ 3.55	658.65 $\pm$ 3.64

Traditional approaches to vibration damping with the help of piezoelectric patches shunted by resonant RL-circuits [4] involve the adjustment of external circuits to provide a minimum amplitude for a given shape of natural vibrations (the corresponding curves are indicated as “Hagood” at Fig. 2). This can be very useful in practical applications where the frequency of external actions changes with time. This naturally leads to a slight shift of the resonant peak relative to the original non-damped system, which is caused by the appearance of an additional frequency in the spectrum due to the interaction between the inductive element of the external circuit and the intrinsic capacitance of the piezoelectric element [4, 5]. Another way to facilitate the vibration damping is to shift the resonant frequency of the structure to some safe range other than the frequency range of the external excitation. This variant is suitable for the situations, in which the frequency of external excitation takes a fixed value and does not change with time. The implementation of this approach, leads to a slight decrease in the amplitude of vibrations compared to the undamped structure due to the energy dissipation on the circuit elements. As an example, Fig. 2a shows the amplitude-frequency characteristic plotted for manually sampled parameters of the RL-circuit, which provide a minimum velocity value in the frequency range of 39–41 Hz (see curve “manual”).

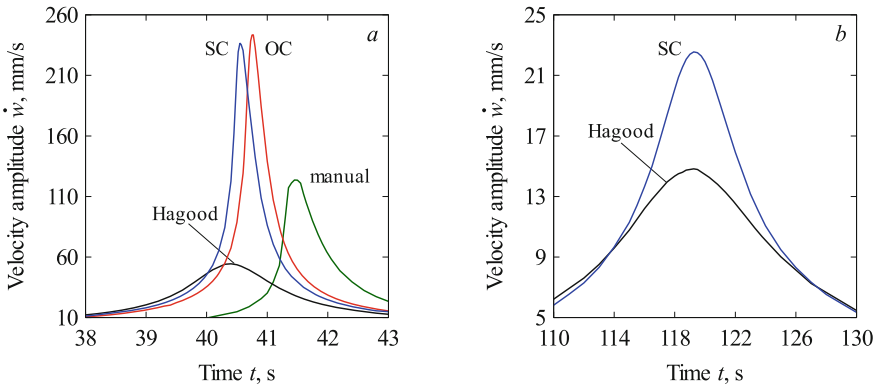


**Fig. 2.** Amplitude-frequency characteristics of the plate in air environment (a) and located on the free surface of the fluid (b).

Figure 3 presents the envelopes of harmonic vibrations of the plate at the first three bending modes (on the SC frequencies, manual tuning) and demonstrates their passive suppression. The results depicted in the figure show a decrease in the velocity amplitude  $\omega_1$  and  $\omega_2$  by 20 times after closing the external RL-circuit connected to the piezoelectric element. Note that its location for  $\omega_4$  is not optimal, so that the amplitude decreases only by 3.2 times. We should also note that it turned out to be impossible to hold the initial velocity of 200 mm/s, because the excitation coil was not designed for high voltage. The analysis of the above dependences allows us to conclude that the damping rate and the time of the transient process are different for each of the examined vibration modes.

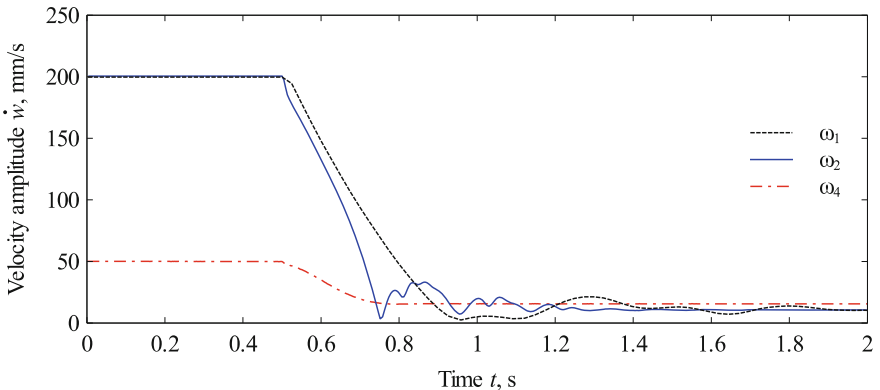


**Fig. 3.** Damping of vibrations of the plate in air environment at different SC frequencies.

### 3.2 Vibrations of the Plate Located on the Free Surface of the Fluid

Similar studies were carried out for a plate interacting with a fluid. Figure 4 illustrates the process of damping the harmonic vibrations at different SC frequencies. It should be noted, that frequencies SC and OC for mode  $\omega_1$  was close to each other (see Table 1). It means that the electromechanical coupling coefficient was very small, so damping was not effective. For second bending mode  $\omega_2$  the velocity amplitude decreases up to 2.5 times in the case of manual tuning of RL-circuit. The resonant frequency of the system shifts from range 117–121 Hz similar to behavior of “manual” curve at Fig. 2a. This results demonstrates that damping of the resonance vibrations of the plate interacting with a quiescent fluid through the use of a shunted piezoelectric element is less effective.

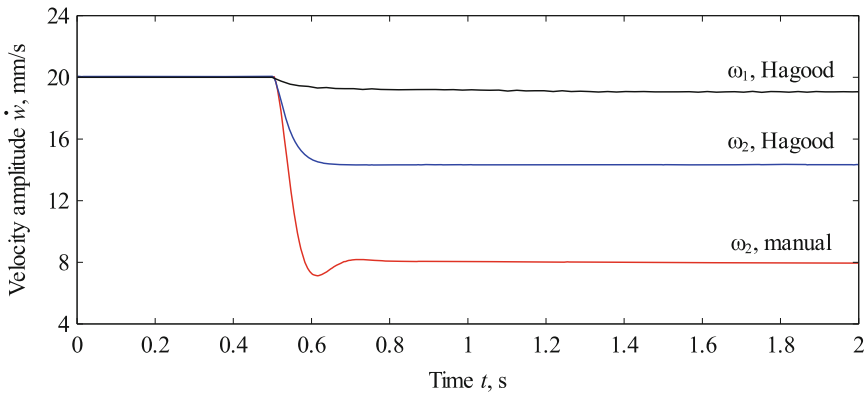


**Fig. 4.** Damping of hydroelastic vibrations of the plate located on the free surface of the fluid at different SC frequencies.

**Acknowledgments.** The study was supported by the grant of the Russian Scientific Foundation (project No. 18-71-10054).

### References




1. Presas, A., Luo, Y., Wang, Z., Valentin, D., Egusquiza, M.: A review of PZT patches applications in submerged systems. *Sensors* **18**(7), 2251 (2018)
2. Leniowska, L.: Effect of active vibration control of a circular plate on sound radiation. *Arch. Acoust.* **31**(1), 77–87 (2006)
3. Kwak, M.K., Yang, D.-H.: Dynamic modelling and active vibration control of a submerged rectangular plate equipped with piezoelectric sensors and actuators. *J. Fluids Struct.* **54**, 848–867 (2015)



4. Hagood, N.W., von Flotow, A.: Damping of structural vibrations with piezoelectric materials and passive electrical networks. *J. Sound Vib.* **146**(2), 243–268 (1991)
5. Matveenko, V.P., Iurlova, N.A., Oshmarin, D.A., Sevodina, N.V., Iurlov, M.A.: An approach to determination of shunt circuits parameters for damping vibrations. *Int. J. Smart Nano Mater.* **9**(2), 135–149 (2018)



# Stationary Dynamic Acoustoelasticity Problems of a Thin Plate in a Perfect Compressible Fluid, Taking into Account the Dissipation of Energy in the Plate and Liquid

V. N. Paimushin<sup>1,2</sup> , R. K. Gazizullin<sup>1</sup> ,  
and D. V. Tarlakovskii<sup>3</sup> 

<sup>1</sup> Kazan National Research Technical University Named After  
A. N. Tupolev - KAI, Kazan, Russia  
vpajmushin@mail.ru

<sup>2</sup> Kazan Federal University, Kazan, Russia

<sup>3</sup> Lomonosov Moscow State University, Moscow, Russia

**Abstract.** We propose the refined equations of motion of the plate and the fluid with additional accounting of the energy dissipation in the material of the plate and fluid based on the Thompson–Kelvin–Voight hysteresis model. These equations are used for the formulation of stationary dynamic problems in the field of acoustoelasticity of thin plates surrounded on both sides by acoustic media, which is represented as a perfect compressible fluid. Refinement of fluid behavior is based on the assumption that the pressure increment in fluid is proportional not only to volumetric deformation, but also to its velocity. This assumption allows us to obtain the generalized Helmholtz wave equation by introducing into consideration the complex velocity of sound according to the representation of Skudrzyk to account for energy dissipation. The equations of the plate motion are based on the classical Kirchhoff-Love model.

**Keywords:** Problems of acoustoelasticity · Perfect compressible fluid · Energy dissipation · Thompson–Kelvin–Voight model · Complex sound velocity · Generalized helmholtz equation

## 1 Introduction

It should be emphasized that the most dangerous regime of the dynamic deformation of structures is the resonant mode, which is realized in a structure when the frequency of its natural vibrations coincides with the frequency of external cyclic action. Under such conditions of loading, as is known, the amplitude values of parameters of the dynamic stress and strain state of structures increase many times, which, in turn, leads also to a sharp change in the parameters of sound waves being formed. It should be pointed out that most correct, profound and meaningful theoretical study on the dynamic processes of deformation of thin-walled structural elements being deformed in an acoustic

medium is possible only with regard for the damping properties of the material, structures as a whole, as well as energy dissipation in acoustic media surrounding the structure.

## 2 Generalized Wave Equation

We assume that the material of the plate has well-pronounced viscoelastic properties for the description of which in the case of a uniaxial stress-strain state the simplest relationship between stress  $\sigma$ , strain  $\varepsilon$ , and strain-rate  $\dot{\varepsilon} = \partial\varepsilon/\partial\tau$ , according to the well-known Thompson–Kelvin–Voight model [1, 2], can be represented in the form of the dependences

$$\sigma = E\varepsilon + \beta\dot{\varepsilon}. \tag{1}$$

Here,  $E$  is the dynamic modulus of elasticity,  $\beta$  is the viscosity coefficient of the material. In the case of harmonic vibrations at a frequency  $\omega$ , when  $\varepsilon = \varepsilon_0 \sin \omega t$  ( $\varepsilon_0$  is the strain amplitude), this coefficient is connected with the logarithmic decrement of vibrations  $\delta$  used in the literature by the dependence  $\delta = \beta\pi\omega/E$ .

As is known [2], the introduced into consideration quantity  $\delta$  characterizing the internal friction of the material, is determined as a half of the relative energy dissipation per unit volume of the material for a single cycle of vibrations with a period  $T$

$$\delta = \frac{\Delta W}{2W} = \frac{\beta\pi\omega}{E}, \quad W = \frac{E\varepsilon_0^2}{2}, \quad \Delta W = \int_0^T \sigma d\varepsilon = \int_0^T (E\varepsilon + \beta\dot{\varepsilon})d\varepsilon = \beta\varepsilon_0^2\pi\omega.$$

At harmonic vibrations of the bar, stresses and strains varying with time according to the law  $\varepsilon = \varepsilon_0 e^{i\omega\tau}$ ,  $\sigma = \sigma_0 e^{i\omega\tau}$ , where  $i = \sqrt{-1}$ —is the imaginary unit. Substituting these results in relation (1), we obtain  $\sigma_0 = E(1 + i\delta/\pi)\varepsilon_0$ . As follows from here, the introduced coefficient of viscosity  $\beta$  should also be considered as the imaginary part of the complex modulus of elasticity, which is widely used in the mechanics of viscoelastic bodies.

Consider a thin plate of thickness  $t$ , whose space is related to a Cartesian coordinate system  $Oxyz$  so that  $-t/2 \leq z \leq t/2$ . We assume that the plate on two sides is surrounded by acoustic media with densities  $\rho_1, \rho_2$ , and sound velocities  $c_1, c_2$ , occupying the half-spaces  $V_1(0 \geq z \geq -\infty), V_2(0 \leq z \leq +\infty)$ , and the plate itself is in the bending dynamic strained state, changing in time  $\tau$  with a circular frequency  $\omega$ . At such deformation, obviously, harmonic acoustic (sound) waves must arise in the media  $V_1$  and  $V_2$ . These waves are described by the following wave equations for the velocity potentials  $\Phi_k(x, y, z)$  [3–5]:

$$\frac{\partial^2 \Phi_k}{\partial x^2} + \frac{\partial^2 \Phi_k}{\partial y^2} + \frac{\partial^2 \Phi_k}{\partial z^2} - \frac{1}{c_k^2} \frac{\partial^2 \Phi_k}{\partial \tau^2} = 0; \quad k = 1, 2, \tag{2}$$

if there is no overflow of the medium from one half-space to the other. The increments of pressures  $p_k$  and velocities  $v_x^k, v_y^k, v_z^k$  in media “1” and “2” are determined via the functions  $\Phi_k$  as follows:

$$p_k = -\rho_k \frac{\partial \Phi_k}{\partial \tau}, \quad v_x^k = \frac{\partial \Phi_k}{\partial x}, \quad v_y^k = \frac{\partial \Phi_k}{\partial y}, \quad v_z^k = \frac{\partial \Phi_k}{\partial z}. \quad (3)$$

At the interaction of the plate with acoustic media without separation, solutions of the equations of motion of the plate and acoustic media (2) at points of the planes  $z = -t/2$  and  $z = t/2$  for a small thickness  $t$  must satisfy the conditions

$$\dot{w} = v_z^1, \quad \dot{w} = v_z^2. \quad (4)$$

We should note that, in the described model of the dynamic behavior of acoustic media there are no components accounting the dissipation of energy in the media (unlike model (1) used for a deformable solid).

In accordance with the results of [5, 6], there is another variant of the formulation of the problem under consideration, which is absolutely equivalent to the one described above. Following these works, instead of the velocities of points of acoustic media, the components of their displacement vectors are introduced into consideration. Through them, the volumetric strains of media in spaces  $V_k$  are determined by the relations

$$\varepsilon^k = u_{x,x}^k + u_{y,y}^k + u_{z,z}^k, \quad (5)$$

which are related to pressure increments by physical relations of the form [6]

$$p_k = -K_k \varepsilon^k = -\rho_k c_k^2 \varepsilon^k. \quad (6)$$

Here,  $K_k = \rho_k c_k^2$  denotes the modules of volumetric adiabatic compression of acoustic media. For them, the equations of motion are of the form [6]

$$\frac{\partial p_k}{\partial x} + \rho_k \ddot{u}_x^k = 0, \quad \frac{\partial p_k}{\partial y} + \rho_k \ddot{u}_y^k = 0, \quad \frac{\partial p_k}{\partial z} + \rho_k \ddot{u}_z^k = 0. \quad (7)$$

In the case of introducing into consideration as unknown functions  $\varphi_k(x, y, z, \tau)$ , that are the potentials of displacements,

$$u_x^k = \frac{\partial \varphi_k}{\partial x}, \quad u_y^k = \frac{\partial \varphi_k}{\partial y}, \quad u_z^k = \frac{\partial \varphi_k}{\partial z}, \quad (8)$$

Equation (7) with an accuracy of an arbitrary nonessential function of time are reduced to dependencies

$$p_k = -\rho_k \ddot{\varphi}_k, \tag{9}$$

which differ from dependencies contained in (3). Substitution of (8) into (5) leads to the relation [6]  $\varepsilon^k = \Delta\varphi_k$ , where  $\Delta$ —the Laplace operator. Using this relation as well as relations (9), the dependences (6) can be reduced to the equations of the continuity of strains [6]

$$c_k^2 \Delta\varphi_k - \ddot{\varphi}_k = 0, \tag{10}$$

having the same form as Eq. (2). However, we should note that,  $\Phi_k(x, y, z, \tau) \neq \varphi_k(x, y, z, \tau)$ .

In case of the considered statement of the problem, instead of conditions (4), the kinematic conjugation conditions by displacements are formulated [6]

$$w = u_z^k = \frac{\partial\varphi_k}{\partial z}. \tag{11}$$

Instead of model (6) of purely elastic deformation of acoustic media, by analogy with relations (1), we adopt the model of viscoelastic volumetric deformation

$$p_k = -\rho_k c_k^2 \left( 1 + \frac{\eta_k^*}{\omega} \frac{\partial}{\partial \tau} \right) \varepsilon_k = -\rho_k c_k^2 \left( 1 + \frac{\eta_k^*}{\omega} \frac{\partial}{\partial \tau} \right) \Delta\varphi_k, \tag{12}$$

introducing into consideration the coefficients of viscosity of media  $\eta_k^*$  to be determined experimentally. In the case of using (12) instead of (10) we obtain the equations

$$c_k^2 \left( 1 + \frac{\eta_k^*}{\omega} \frac{\partial}{\partial \tau} \right) \Delta\varphi_k - \ddot{\varphi}_k = 0, \tag{13}$$

representing the generalized Helmholtz wave equations, compiled with additional accounting of dissipative energy losses in acoustic media under its volume adiabatic compression. If the deformation process is harmonic, then functions  $\varphi_k$  must be represented as  $\varphi_k = \tilde{\varphi}_k e^{i\omega\tau}$  and, Eq. (13) reduced to the form

$$c_k^2 (1 + i\eta_k^*) \Delta\tilde{\varphi}_k + \omega^2 \tilde{\varphi}_k = 0. \tag{14}$$

Without losing the meaningfulness of Eq. (14), it is permissible to replace it with equation  $c_k^2 (1 + i\eta_k)^2 \Delta\tilde{\varphi}_k + \omega^2 \tilde{\varphi}_k = 0$ , if we enter into consideration complex velocity of sound  $c_k = c_k (1 + i\eta_k)$ , according to Skudrzyk [7]. It is easy to make sure that the parameters  $\eta_k^*$  and  $\eta_k$  entered into consideration are related to each other by dependency  $\eta_k^* \approx 2\eta_k$ . Determining the viscosity parameter of acoustic media  $\eta$ , introduced into consideration, requires appropriate experimental studies and is an independent problem.

### 3 The Equation of a Thin Plate Motion, Taking into Account the Energy Dissipation in the Plate Material and Acoustic Media

In the case of using relations of the form (1) for the description of bending dynamic strained state, the differential equation of the plate motion, based on the Kirchhoff–Love hypotheses, can be reduced to the form ( $w$  is the deflection, and  $\rho_p$  is the density of the plate material)

$$D\nabla^2\nabla^2w + \tilde{D}\nabla^2\nabla^2\dot{w} + \rho_p t\ddot{w} - p = 0, \tag{15}$$

where  $p = q_* + q, D = \frac{Et^3}{12(1-\nu^2)}, \tilde{D} = \frac{\beta t^3}{12(1-\nu^2)} = \frac{\delta}{\pi\omega}D$ .

In Eq. (15)  $q_*$  represents a certain specified external transverse load, and, for determining the aerodynamic load  $q$ , formed due to the interaction of the plate with the surrounding acoustic media, using the flat reflection hypothesis and introducing complex sound speeds according to the equality  $q = p_1|_{z=0} - p_2|_{z=0}$  we arrive at the expression

$$q = -C\dot{w}, \quad C = \rho_1 c_1^* + \rho_2 c_2^* = \rho_1 c_1 + \rho_2 c_2 + \underline{i(\rho_1 c_1 \eta_1 + \rho_2 c_2 \eta_2)}. \tag{16}$$

Here, the underlined components are responsible for taking into account the energy dissipation in acoustic media surrounding the plate.

If a flat harmonic wave with pressure  $p_*$  and frequency  $\omega$  falls on the plate, then, as a results of its interaction with the plate in the surrounding half-spaces  $V_1$  and  $V_2$ , acoustic waves are induced, which are reflected and radiated in the first medium and radiated in the second medium. These waves with respect to the velocities potentials  $\Phi_*, \Phi_1, \Phi_2$  in case of the refined formulation of acoustoelasticity problems can be described by generalized wave equations

$$c_1^{*2}\Phi_{*,zz} - \ddot{\Phi}_* = 0, \quad c_k^{*2}(\Phi_{k,xx} + \Phi_{k,yy} + \Phi_{k,zz}) - \ddot{\Phi}_k = 0$$

written with additional accounting the energy dissipation by introducing into consideration the complex velocity of sound according to Skudrzyk [7]. At the same time, the aerohydrodynamic load acting on the plate  $p$  will be equal to

$$p = q_* + q = (p_* + p_1 - p_2)|_{z=0},$$

and the components of the velocities  $v_z^*, v_z^k$ , at the interaction of the plate with acoustic media without separation, must satisfy the conditions

$$\dot{w} = (v_z^1 + v_z^2)|_{z=0}, \quad \dot{w} = v_z^2|_{z=0}.$$

On the basis of the constructed equations, exact analytical solutions are found for the problems of free vibrations of a rectangular plate hinged around the contour with the definition of complex eigenfrequencies, as well as for the problems of the forced

vibrations of the plate under the action of a flat mono-harmonic incident sound wave with determination of sound transmission loss, of plate's stress-strain state parameters and of the laws of sound pressures change in fluid on the distance from the plate.

The analysis of the constructed solutions has showed that correct and more meaningful solutions of the considered class problems in the field of plate acoustoelasticity are possible only in case of description of the fluid behavior on the basis of non-simplified three-dimensional wave equations with additional accounting of energy dissipation. Moreover, it becomes possible to drastically clarify the laws of decreasing of reflected and emitted sound waves pressures amplitude values as they move away from the plate.

**Acknowledgments.** This research was supported by a grant from the Russian Science Foundation (project № 19-19-00058).

## References

1. Panovko, Y.G.: Vnutrennee trenie pri kolebaniyah uprugih sistem [Internal Friction at Vibrating of Elastic Systems]. Fizmatgiz, Moscow (1960). (in Russian)
2. Pisarenko, G.S., Yakovlev, A.P., Matveev, V.V.: Vibropogloshchayushchie svojstva konstrukcionnyh materialov: Spravochnik [Vibration Absorption Properties of Structural Materials: A Handbook]. Naukova Dumka, Kiev (1971). (in Russian)
3. Grigolyuk, E.I., Gorshkov, A.G.: Nestacionarnaya gidrouprugost' obolochek [Nonstationary Hydroelasticity of Shells]. Sudostroenie, Leningrad (1974). (in Russian)
4. Guz, A.N., Kubenko, V.D.: Metody rascheta obolochek. Tom 5. Teoriya nestacionarnoj aehroidrouprugosti obolochek [Methods for Calculating Shells. Volume 5 Theory of Nonstationary Aeroelasticity of Shells]. Naukova Dumka, Kiev (1982). (in Russian)
5. Gorshkov, A.G., Morozov, V.I., Ponomarev, A.T., Shklyarchuk, F.N.: Aehroidrouprugost' konstrukcij [Aeroelasticity of Constructions]. Fizmatgiz, Moscow (2000). (in Russian)
6. Shklyarchuk, F.N., Grishanina, T.V.: Primenenie metoda otsekov k raschetu kolebanij zhidkostnyh raket-nositelej [Application of the Compartment Method to the Calculation of Liquid Launch Vehicles Oscillations]. MAI Publishing House, Moscow (2017). (in Russian)
7. Skudrzyk, E.: The Foundations of Acoustics. Basic Mathematics and Basic Acoustics. Springer, New York (1971)



# Dynamics and Elastic Stability of an Electrostatically Actuated Microbeam Under Ultrafast Laser Pulse

A. V. Lukin<sup>1</sup>✉, D. A. Indeitsev<sup>1,2</sup>, I. A. Popov<sup>1</sup>, O. V. Privalova<sup>1</sup>,  
and L. V. Shtukin<sup>1,2</sup>

<sup>1</sup> Department of Mechanics and Control Processes, Peter the Great St.  
Petersburg Polytechnic University, St. Petersburg, Russia  
lukin\_av@spbstu.ru

<sup>2</sup> Institute for Problems in Mechanical Engineering, Russian Academy of  
Sciences (IPME RAS), St. Petersburg, Russia

**Abstract.** Laser-induced vibrations and elastic stability of a clamped-clamped beam electrostatic transducer are considered under ultrafast laser pulse. It is assumed that laser pulse acts as volume heat generation with Gaussian time-profile localized in near-surface layer of the beam. Temperature load non-stationarity and non-homogeneity through length and thickness lead to appearance of thermal-induced mechanical moment and axial forced acting on the beam, which can result in buckling phenomena. Semi-analytical methods for solution of nonlinear boundary-value problems are used for static equilibrium determination of the beam in the electric field of one stationary electrode. Analytical solution of non-stationary temperature problem in the beam volume is obtained. Finally, areas in parameter space of system geometrical and mechanical properties along with laser pulse characteristics are determined which correspond to elastic stability of initial equilibrium form of the beam subjected to laser pulse.

**Keywords:** MEMS · Bernoulli-Euler beam · Laser pulse · Elastic stability

## 1 Introduction

The problem of dynamic stability of constructional elements is a practically important area of research, far from being completely studied. For example, as shown in [1–3], critical values of dynamic forces leading to a loss of stability can significantly differ from known static (Eulerian) values. The aforesaid phenomenon occurs in applications of laser technologies for nondestructive testing of constructions and studying the physical properties of materials at the micro- and nanoscale level [4–6], as well as in technological processes of laser forming [7], additive manufacturing [8] and in nano- and microsystem engineering production [9, 10]. The necessity of solving problems of this class arises also in studying the working capacity of nano- and microelectromechanical systems in resonant operating modes under conditions of impact-impulse thermal actions [11]. In [12–15] it was pointed out that the dynamics of the Bernoulli–Euler beam under laser pulse action is significantly affected by thermal moments



caused by a nonuniform temperature distribution over the volume of an elastic element. In this work, we investigate the action of axial (membrane) thermal forces on dynamics and stability of the considered elastic element of MEMS.

## 2 Problem Statement

We consider the problem about the pulse laser action on an elastic element of the electrostatic transducer (Fig. 1) with allowance for the initial deflection caused by the action of the electrostatic field. For the model describing the dynamics of this element, we chose the Bernoulli–Euler beam model. A feature of its behavior in this problem is the necessity to take into account the preliminary stress–strain state. This is caused by two factors. First, the assembly technology is such that the initial length of an unstrained beam can exceed the distance between the bearings, which creates an additional compressive stress. Second, a stationary potential difference  $V$  with a fixed electrode is transmitted to the beam as a movable electrode, which creates a preliminary beam deflection under the action of attractive forces in the electrostatic field.

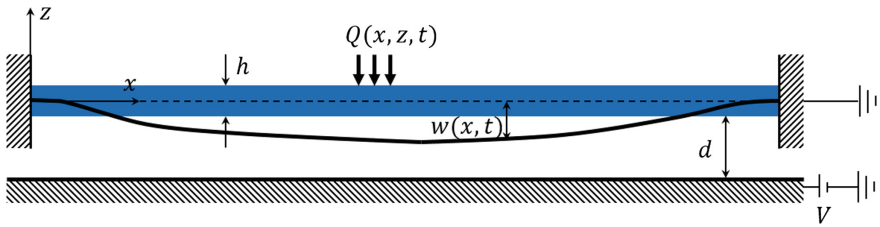


Fig. 1. Schematic of a MEMS capacitive transducer under laser heating

We assume that the action of a laser pulse on the beam surface is reduced mainly to the appearance of a thermal front propagating over the bulk of the beam. The nonuniformity and nonstationarity of the temperature field both in thickness and in length of the beam in the general case lead to the appearance of a bending moment and axial force, which are responsible for the eventual loss of stability. To simplify the problem to some extent, we assume that the laser action is uniform over the beam length. We take that the volumetric heat release during the action of the laser has the form [16]

$$Q(z, t) = H(t) \cdot \frac{R_a L_0}{\delta t_p^2} t \cdot \exp\left(\frac{z - \frac{h}{2} - t}{\delta} - \frac{t}{t_p}\right), \tag{1}$$

where  $H(t)$  is the Heaviside function,  $L_0$  is the parameter characterizing the action power,  $R_a$  is the absorption index of the irradiated surface,  $\delta$  is the characteristic depth of the pulse penetration into the material, and  $t_p$  is the pulse duration.

For a broad class of nano- and microelectromechanical electrostatic transducers, the distance between electrodes  $d$  is considerably less than the thickness of the elastic

element  $h$ , which allows one to use geometrically linear equations of transverse deflections. Under the aforesaid assumptions, the fundamental equations describing the dynamic bending of a beam in the physically nonlinear coupled thermoelectroelasticity problem under consideration have the form

$$EI \frac{\partial^4 w}{\partial x^4} + \rho b h \frac{\partial^2 w}{\partial t^2} + M_T + P \frac{\partial^2 w}{\partial x^2} = \frac{\epsilon_r \epsilon_0 b V^2}{2(d-w)^2},$$

$$P = P_0 + P_T - \frac{E b h}{2L} \int_0^L \left( \frac{\partial w}{\partial x} \right)^2 dx, \quad P_T = E b \alpha_T \int_{-\frac{h}{2}}^{\frac{h}{2}} \theta dz, \quad M_T = E b \alpha_T \int_{-\frac{h}{2}}^{\frac{h}{2}} z \frac{\partial^2 \theta}{\partial x^2} dz,$$
(2)

$$k \left( \frac{\partial^2 \theta}{\partial x^2} + \frac{\partial^2 \theta}{\partial z^2} \right) + Q(x, z, t) = \rho c_v \frac{\partial \theta}{\partial t} + \beta T_0 \frac{\partial e}{\partial t}.$$

Here,  $x$  and  $z$  are the longitudinal and vertical coordinates, respectively;  $t$  is time;  $w(x, t)$  is the transverse displacement of the geometric center of the beam cross section;  $\theta(x, z, t) = T(x, z, t) - T_0$  is the change in the temperature relative to the reference temperature  $T_0$ ;  $b, h, L$ , and  $d$  are the geometric parameters of the system: the width, height, and length of the beam and the initial gap between the electrodes, respectively;  $I = \frac{bh^3}{12}$  is the moment of inertia of the cross section;  $E$  is the Young modulus;  $\nu$  is the Poisson ratio;  $\rho$  is the material density;  $\alpha_T$  is the thermal linear expansion coefficient;  $\epsilon_r \epsilon_0$  is the dielectric permittivity of the medium in the gap between the electrodes;  $k$  is the heat conductivity coefficient of the beam material;  $c_v$  is the specific heat capacity;  $\beta = \frac{E \alpha_T}{1-2\nu}$  is the coefficient associating the temperature increment with the rate of change in the deformed body volume;  $e = -z \frac{\partial^2 w}{\partial x^2}$ ; and  $P = E b h \frac{\Delta L}{L}$  is the axial force caused by technology factors (is the initial deviation of the beam length from the length corresponding to the stress-free state).

### 3 Determination of the Beam Equilibrium Shape in Static Electric Field

The boundary value problem for finding the initial equilibrium state (the static deflection) is obtained from the general system of equations (2) by truncation of the inertial terms when the thermal action is absent. To obtain an approximate solution, the authors used the Galerkin method where the coordinate functions are chosen in the form of eigenfunctions of a compressed fixed-ended beam in the absence of an electric field (Fig. 2). Note that a well-known catastrophic bifurcation with disappearance of equilibrium shapes is observed in the system when the physical parameter  $\lambda = \frac{6\epsilon_r \epsilon_0 L^4 V^2}{E h^3 d^3}$  reaches a certain critical value (a regular extreme point or pull-in instability [17]).

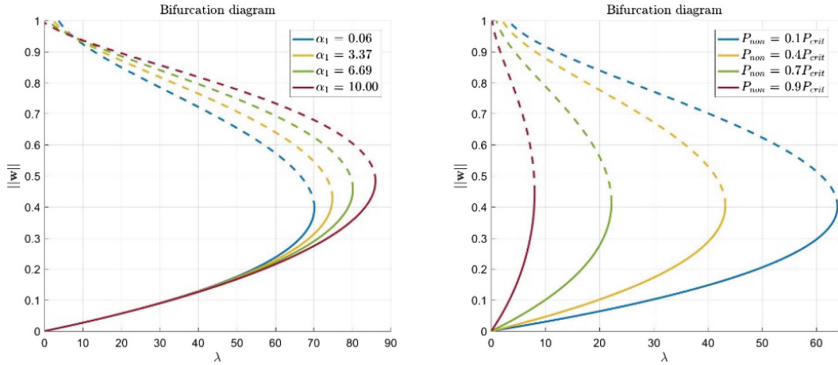


Fig. 2. Microbeam equilibria for various  $\alpha_1 = 6\left(\frac{d}{h}\right)^2$  and  $P_{non} = 12\frac{L}{h}\frac{\Delta L}{h}$

### 4 Investigation of Beam Stability Under Laser Action

The force and moment actions on the elastic element under consideration during a laser pulse are determined from the solution of the non-stationary heat conduction problem in the beam material (Fig. 3).

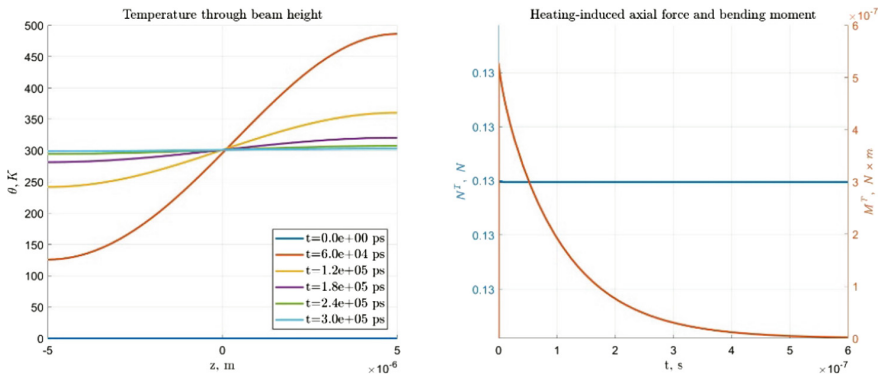


Fig. 3. Thermal response of a microbeam

The exhaustive investigation of the dynamics of the system requires solving the nonlinear initial-boundary value problem, which can be carried out using approximate analytical methods. The upper estimate of the critical parameters of the action can be obtained by analyzing the linearized motion equation obtained from (2) by Taylor series expansion of nonlinear summands and truncation of the leading powers of the unknown function:

$$EI \frac{\partial^4 w_d}{\partial x^4} + \rho b h \frac{\partial^2 w_d}{\partial t^2} + \left[ P_0 + Eb\alpha_T \int_{-\frac{h}{2}}^{\frac{h}{2}} \theta(z, t) dz - \frac{Ebh}{2L} \int_0^L \left( \frac{\partial w_s}{\partial x} \right)^2 dx \right] \frac{\partial^2 w_d}{\partial x^2} - \frac{Ebh}{L} \int_0^L \frac{\partial w_s}{\partial x} \frac{\partial w_d}{\partial x} dx \cdot \frac{\partial^2 w_s}{\partial x^2} - \frac{\epsilon_r \epsilon_0 b V^2}{(d - w_s)^3} w_d = -Eb\alpha_T \int_{-\frac{h}{2}}^{\frac{h}{2}} \theta(z, t) dz \cdot \frac{\partial^2 w_s}{\partial x^2} \tag{3}$$

Note that the motion Eq. (3) in the presence of an electric field (and nonzero static deflection  $w_s$  related to it) is nonautonomous: the nonstationary temperature distribution leads to the appearance of a transverse force acting on the beam.

The solution to dynamic problem (3) is found in the form of a Galerkin series in eigenmodes of both ends of a fixed beam with allowance for axial compression by the force  $P_0$ . Writing the projection conditions, we come to the following system of linear equations with variable coefficients for the coordinate functions  $\eta_j(t)$ :

$$M\ddot{\boldsymbol{\eta}} + [N + L(t)]\boldsymbol{\eta} = \mathbf{H}(t), \tag{4}$$

where  $M$  and  $N$  are definite constant matrices;  $L(t)$  is a matrix with time-dependent coefficients; and  $\mathbf{H}(t)$  is the column vector of right-hand sides.

Applying the theorem about the sufficient condition of the Lyapunov stability of the solution [15] to system (4) allows one to reduce the analysis of stability to the determination of signs for the real parts of eigenvalues of the system.

Leaving in expansion (4) only the oscillation mode corresponding to the lower frequency, we obtain simple expression for the lower estimate of the critical laser pulse power in terms of the geometric parameters of the system, the mechanical properties of the material, the axial force value and external factors related to the action of the laser pulse and electrostatic field:

$$Q_{crit} = \frac{\rho c_v}{Eb\alpha_T t_p \delta (1 - e^{-h/\delta}) e} \cdot \left\{ \frac{EIA_{11} - \frac{Ebh}{L} C_{11} - \epsilon_r \epsilon_0 b V^2 D_{11}}{-B_{11}} - P_0 + \frac{Ebh}{2L} \int_0^L \left( \frac{\partial w_s}{\partial x} \right)^2 dx \right\}, \tag{5}$$

where  $A_{11}, B_{11}, C_{11}$  and  $D_{11}$  are certain projection coefficients.

Figure 4 shows the calculated conservative estimate for the boundary of the stability region in the space of laser pulse parameters  $(t_p, \delta, Q_{max})$ .

Comparison of the results of [8, 9] with the critical laser pulse power obtained above points to the fact that the loss of stability of the initial equilibrium shape of the Bernoulli–Euler beam due to the presence of a compressing axial force of thermal origin can occur at considerably lesser laser pulse powers than is necessary for reaching dangerous deflections due to the bending moment. The last must be taken into account in practical calculations of the elastic elements of nano- and microsystem engineering, as well as other constructions under the action of pulse thermal loads.

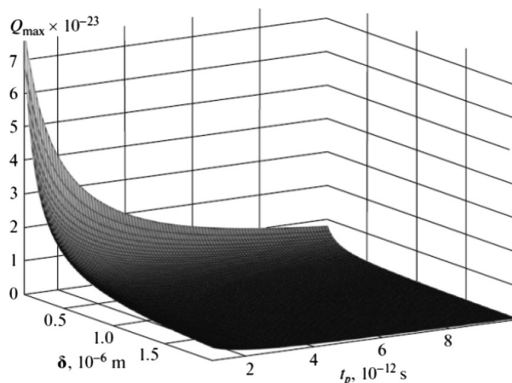


**Fig. 4.** Region of elastic stability

**Acknowledgements.** This work was supported by the Russian Foundation for Basic Research, project no. 17-01-0414.

## References

1. Lavrent'ev, M.A., Ishlinskii, A.Y.: Dokl. Akad. Nauk SSSR **64**(6), 779 (1949)
2. Morozov, N.F., Tovstik, P.E.: Dokl. Phys. **58**, 510 (2013)
3. Belyaev, A.K., Morozov, N.F., Tovstik, P.E., Tovstik, T.P.: Vestn. St. Petersburg Univ.: Math. **49**(1), 53 (2016)
4. Champion, A., Bellouard, Y.: Direct volume variation measurements in fused silica specimens exposed to femtosecond laser. Optical Mater. Express **2**(6) (2012)
5. Li, C., et al.: Laser induced surface acoustic wave combined with phase sensitive optical coherence tomography for superficial tissue characterization. Biomed. Opt. Expr. **5**(5) (2014)
6. Otsuka, P., et al.: Time-domain imaging of gigahertz surface waves on an acoustic metamaterial. New J. Phys. **20** (2018)
7. Shen, H., Zhou, W., Wang, H.: Laser forming of doubly curved plates using minimum energy principle and comprehensive strain control. Int. J. Mech. Sc. **145** (2018)
8. Russel M.A., Souto-Iglesias A. Numerical simulation of Laser Fusion Additive Manufacturing processes using the SPH method, Comp. Meth. Appl. Mech. Eng. 341 (2018)
9. Zheng, Z., et al.: Femtosecond laser inscribed small-period long-period fiber gratings with dual-parameter sensing. IEEE Sens. J. **18**(3) (2018)
10. Xiong, Q, et al.: Thermal damage and ablation behavior of graphene induced by ultrafast laser irradiation. J. Therm. Stresses (2018)
11. Yang, T., Bellouard, Y.: Laser-induced transition between nonlinear and linear resonant behaviors of a micromechanical oscillator. Phys. Rev. Appl. **7** (2017)
12. Sun, Y., et al.: Laser-induced vibrations of micro-beams under different boundary conditions. Int. J. Solids Struct. **45** (2008)
13. Sun, Y., et al.: Thermoelastic response of a simply supported beam irradiated by a movable laser pulse. Canad. J. Phys. (2017)
14. Yang, X., et al.: An exact analytical solution for thermoelastic response of clamped beams subjected to a movable laser pulse. Symmetry **10**, 139 (2018)

15. Sun, Y., et al.: Thermodynamic response of beams on winkler foundation irradiated by moving laser pulses. *Symmetry* **10**, 328 (2018)
16. Tang, D.W., Araki, N.: Wavy, wavelike, diffusive thermal responses of finite rigid slabs to high-speed heating of laser-pulses. *Int. J. Heat Mass Transf.* **42** (1999)
17. Zhang, W., Yan, H., Peng, Z., Meng, G.: *Sens. Actuators A* **214**, 187 (2014)

# Author Index

## A

Abuzaid, Wael, 45  
Adegbenjo, Adewale, 9, 27  
Adeyemi, Oluseyi A., 9, 27  
Afanasieva, O. A., 193  
Alayande, S. O., 27  
An, Xiaopin, 15  
Arkhyenko, Kostyantyn, 199

## B

Bello, Kazeem A., 9  
Bigoni, Davide, 175  
Bogdanova, Olga, 304  
Bogdanov, Vyacheslav, 110, 114  
Brynk, Tomasz, 65

## C

Capuani, Domenico, 175  
Chen, Daolun, 126  
Chen, Po-Yu, 84  
Chernyakov, Yuri, 205  
Chirol, Clément, 168  
Combes, Bertrand, 168

## D

Daidié, Alain, 168  
Danoglidis, Panagiotis A., 36, 54  
Dare, E. O., 27  
Demydov, Oleksandr, 215  
Dovzhyk, Mykhailo, 114

Dvorak, Jiri, 39

## E

Edokpayi, J. N., 27

## F

Falara, Maria G., 36, 75  
Fedotkov, Grigory V., 264, 289  
Fesenko, Anna, 277  
Figueroa, Carlos Gabriel, 161

## G

Gafurov, U. S., 193  
Gao, Hao, 135  
Gazizullin, R. K., 364  
Gdoutos, Emmanuel E., 54, 75  
Giarola, Diana, 175  
Goji, Tsukasa, 182

## H

He, Cheng, 87  
Hrbek, Vladimir, 3  
Hua, Guo, 48  
Huang, Suxia, 15  
Hwang, Chi-Hung, 94

## I

Igumnov, Leonid, 311, 316  
Indeitsev, D. A., 148, 370  
Ipatov, Aleksandr, 311

Iurlov, Maksim, 357  
Iuzhina, Tatiana, 311

**J**

Jacobo, Víctor Hugo, 161

**K**

Kamenskikh, Alexander, 357  
Kandala, S. M., 327  
Karma, Alain, 101  
Kayumov, R. A., 29  
Kholmogorov, S. A., 29  
Kipnis, A. L., 106, 110  
Kishore, M. N., 142  
Konsta-Gdoutos, Maria S., 36, 54, 75  
Korovaytseva, Ekaterina, 283  
Kostenevich, Elena, 341  
Kral, Petr, 39  
Krasnikov, Vasilii S., 59  
Kryvyi, Oleksandr, 187, 199  
Kulkarni, Rishikesh, 71  
Kunets, Yaroslav, 209  
Kuo, Tzu-Yu, 94  
Kuo, Yu-Wei, 80  
Kushnir, Roman, 209  
Kvapilova, Marie, 39  
Kyrylova, Olga, 236

**L**

Lapusta, Nadia, 156  
Leblond, Jean-Baptiste, 101  
Lekomtsev, Sergey, 351, 357  
Liang, Taosha, 48  
Li, Hezong, 15  
Li, Qiusheng, 15  
Litvinchuk, Svetlana, 311, 316  
Liu, Yang, 48, 87  
Loboda, Volodymyr, 205  
Lokteva, N. A., 298  
Lukin, A. V., 370

**M**

Maglogianni, Myrsini, 36  
Ma, Hongyi, 21  
Makhnenko, Oleg, 334  
Makhnenko, Oleh, 341  
Makhnenko, O. V., 327  
Matus, Valeriy, 209  
Mayer, Alexander E., 59, 119  
Mayer, Polina N., 119  
Mikhailova, Elena Yu, 289  
Milenin, Alexey, 321  
Misharin, A. S., 229  
Mitin, Andrey Yu, 264

Morozov, Yurii, 187  
Msagati, T. A. M., 27  
Mysov, K., 242

**N**

Nazarenko, Vladimir, 114  
Nazarenko, V. M., 106

**O**

Oke, Wasiu A., 9  
Olaffson, Simon, 154  
Olkhovskiy, Anton, 334  
Oshmarin, Dmitrii, 351, 357  
Ovcharova, Nataliia, 334

**P**

Paimushin, V. N., 29, 364  
Patriarca, Luca, 45  
Petrov, Aleksandr, 205  
Petrov, Andrey, 316  
Pivtorak, Nina, 321  
Ponson, Laurent, 101  
Popov, I. A., 370  
Popov, V. G., 229  
Popov, Vsevolod, 215, 222, 236  
Prado, Armando Ortiz, 161  
Prikazchikov, D., 248  
Privalova, O. V., 370  
Protserov, Yu., 248

**R**

Rafik, Vincent, 168  
Ramírez, Miguel Ángel, 161  
Rastogi, Pramod, 71  
Ren, Facai, 15  
Rozyinka, Galina, 321  
Ruphakety, Rajesh, 154  
Ryazantseva, M. Yu., 294

**S**

Sanket, Hedduri, 142  
Scherbakov, Vasily, 259  
Schouwenaars, Rafael, 161  
Semenov, B. N., 148  
Sergey, Pshenichnov, 270  
Ševčík, Radek, 3  
Sevodina, Natalya, 351  
Shtukin, L. V., 370  
Sklenicka, Vaclav, 39  
Skubov, D. Yu., 148  
Song, Xiu, 48, 87  
Starovoitov, E. I., 294  
Steblyanko, Pavel, 205  
Sung, Po-Chi, 80



Suresh, Nagesh, [142](#)

**T**

Tarlakovskii, Dmitry V., [29](#), [254](#),  
[264](#), [283](#), [289](#), [298](#), [364](#)

Trofymchuk, Oleksandr, [209](#)

**U**

Uenishi, Koji, [182](#)

**V**

Vasudevan, Aditya, [101](#)

Vavilov, D. S., [148](#)

Vaysfeld, Nataly, [242](#), [248](#), [277](#)

Velikoivanenko, Elena, [321](#)

Vestyak, V. A., [254](#)

Vestyak, Vladimir, [259](#)

Vorobiov, Yurii, [334](#)

Vorobtsov, Igor, [316](#)

**W**

Wang, Changlu, [135](#)

Wang, Lei, [48](#), [87](#)

Wang, Simon S., [15](#)

Wang, Wei-Chung, [80](#), [84](#), [94](#)

Wang, Yanzhong, [135](#)

Wu, Long, [135](#)

**X**

Xie, Liyang, [21](#)

Xu, Guoliang, [21](#)

Xu, Zichun, [135](#)

**Z**

Zemskov, A. V., [193](#)

Zhang, Yaping, [135](#)

Zhelyazov, Todor, [154](#), [159](#)